UNIVERSITÀ DEGLI STUDI DI MODENA E
REGGIO EMILIA

Dipartimento di Scienze Fisiche, Informatiche e Matematiche

School of Graduate Studies in Physics and Nanosciences

Disciplinary Scientific Sector FIS/07

Mechanobiology of biosystems: from lipid bilayers to *in-vitro* cells

Supervisor:
Prof. Andrea Alessandrini

PhD Candidate:
Gregorio Ragazzini

Director of the PhD school:
Prof. Stefano Frabboni

Academic Year 2020/2021

Abstract (Italian)

Le proprietà meccaniche dei sistemi biologici hanno una grande importanza nel determinare il loro comportamento. Molti potenziali farmaci possono modificare le proprietà meccaniche della membrana biologica e indirettamente modulare la funzione di proteine di membrana. Analogamente, molti stati patologici a livello cellulare presentano un fenotipo con proprietà meccaniche alterate e la modifica di tali proprietà è tipicamente il risultato di una riorganizzazione del citoscheletro. Allo stesso tempo, le cellule sondano le proprietà reologiche della matrice extracellulare (ECM) attivando, a seconda della risposta ottenuta, diversi percorsi biochimici. Tali fenomeni sono spesso caratterizzati da una riorganizzazione citoscheletrica a seguito di stimoli periodici, come avviene ad esempio nel sistema cardiovascolare o nei polmoni. La scienza che tratta questi fenomeni è la meccanobiologia. Il lavoro di questa tesi di dottorato è dedicato all'analisi delle proprietà meccaniche di costituenti biologici, da semplici modelli di membrana, come doppi-strati-lipidici supportati (SLB) e vescicole giganti unilamellari (GUV), a sistemi quali colture cellulari *in-vitro*. Le tecniche di indagine usate hanno coinvolto: microscopia ottica in contrasto di fase, DIC e fluorescente; microscopia a forza atomica (AFM). Sono stati sviluppati, all'interno della tesi, metodi di analisi e dispositivi dedicati per specifiche applicazioni e misure di campioni. È stato progettato, testato e impiegato un incubatore per esperimenti di live-cell imaging da integrare direttamente sul tavolino (on-stage) di un microscopio ottico. Sono stati ottenuti simultaneamente parametri di migrazione di cellule esposte a diversi trattamenti, o poste su substrati aventi diversa rigidità meccanica. Lo stesso incubatore è stato ridisegnato per poter alloggiare uno stretcher uniassiale in grado di fornire al substrato specifiche funzioni periodiche di deformazione e valutare la conseguente risposta delle cellule in termini di migrazione e polarizzazione. Tra i metodi di indagine, è stata sviluppata l'analisi quantitativa di migrazione di singola cellula, ed è stato impiegato il modello "Persistence-Random-Walk". Lo scopo era quello di analizzare l'effetto citostatico di un potenziale farmaco nelle cellule U87MG, usate come modello del glioblastoma multiforme. L'analisi effettuata ha infatti mostrato l'efficacia sia citostatica che antimitotica della molecola. Sono stati indagati inoltre i possibili meccanismi biochimici alla base di tali effetti. Nel contesto dei SLB e GUV è stata implementata rispettivamente l'analisi sulla tensione di linea di domini che simulano lipid-rafts e la costante di bending, basandosi sulla teoria delle fluttuazioni di membrana. Nel primo caso sono stati confrontati i risultati sulla misura della tensione di linea di miscele ternarie costituite da diverse componenti rilevanti nella formazione di lipid-rafts. Nel secondo caso, è stato valutato il ruolo di molecole esogene (peptidi antimicrobici e lipopeptidi) nella determinazione della costante di bending. Nella caratterizzazione visco-elastica del citoscheletro con AFM, è stato implementato un software basato sul modello di Ting, in grado di estrapolare i parametri viscoelastici dalle singole curve andata-ritorno. Si è studiato l'effetto del potenziale farmaco prima citato, sulle proprietà reologiche di cellule U87MG al fine di correlare migrazione e proprietà meccaniche cellulari. Sono stati sviluppati software dedicati alla ricerca di eventi Jump-Through-Force nell'analisi di SLB per valutare alterazioni nelle fasi Solido-ordinata (S_o) Liquido-Disordinata (L_d) in mappe di Force-Volume. In particolare, sono state investigati gli effetti sulle proprietà meccaniche di SLB sotto l'effetto di molecole esogene come la daptomicina.

Abstract (English)

Thesis project and aims

Mechanical properties of biological systems play a crucial role for their behavior. For example, many drugs could modify mechanical properties of the biological membrane and indirectly modulate transmembrane protein functions. Similarly, many pathological conditions at the cellular level are characterized by a phenotype with altered mechanical properties, where these alterations are due to cytoskeleton reorganization. At the same time, cells continuously probe rheological properties of extracellular matrix (ECM) enabling, depending on response obtained by the substrate, different downstream signaling cascades. In many cases, cytoskeleton reorganization occurs also when cells are experiencing periodic mechanical stimuli, as it happens for example in the cardiovascular system or in lungs. All these aspects are treated by a recent interdisciplinary branch of physic and biology sciences called “Mechano-biology”.

This PhD thesis work has been devoted to study some specific aspects of mechanical properties of biological systems: from simple models of the biological-membrane, like supported-lipid-bilayer (SLB) or giant-unilamellar-vesicle (GUV), to *in-vitro* cells. Investigation techniques exploited in this work include: phase-contrast optical microscopy, DIC and fluorescence microscopy and atomic force microscopy (AFM). In the thesis we developed methods for the quantitative analysis and devices dedicated to specific applications and measurements of biological properties. An on-stage cell incubator for live cell imaging has been designed, tested and employed successfully. From time-lapse microscopy experiments we obtained different quantitative migration parameters both for cell exposed to different drugs and for cells seeded on substrates with different mechanical rigidity. In the context of these cell migration assays, we focused on two different topics: Firstly, the glioblastoma multiforme (GBM) which is one of the most common malignant primary brain tumors and, despite a strong effort dedicated to finding an effective therapy, it is still characterized by a very poor prognosis. We investigated the antimitotic and cytostatic effect of a potential antitumoral drug *in-vitro* assay in collaboration with the Department of Life Sciences, University of Modena and Reggio Emilia. Secondly, we exploited the on-stage live cell incubator to investigate the interaction of mineral fibres with macrophages. This investigation is related to the chronic lung inflammation and the subsequent development of lung malignancies due to mineral fibres inhalation and it has been developed in collaboration with the Department of Chemical and Geological Sciences and the Department of Life Sciences, University of Modena and Reggio Emilia.

The same cell incubator has been modified to include an uniaxial stretcher to provide specific periodic deformation stimuli to the substrate on which cells are growing, and we studied the effect of the periodic stimulation on cell migration and orientation

Among the different analysis methods, a single cell migration analysis protocol has been developed, exploiting the “Persistence-Random-Walk” model. The ultimate goal was that of analyzing the cytostatic effect of a potential drug for the U87MG cell line, employed as model of the glioblastoma multiforme disease. The analysis has in fact shown the efficiency of this molecule for blocking both migration and replication of this cell line. Furthermore, possible biochemical mechanisms of action involved in these effects have been investigated.

In the context of SLBs and GUVs, a line tension analysis of domains recapitulating lipid-raft and a bending constant measurement have been implemented, in both cases exploiting the Flickering spectroscopy theory. In the former case, domain line tension results for ternary mixtures containing different components relevant for lipid-rafts formation have been compared for different lipid compositions. In the latter case, the role of exogenous molecules (antimicrobial peptides and lipopeptides) on the bending constant has been investigated. In viscoelastic characterization of the cell cytoskeleton through AFM, a Ting model-based software has been implemented, allowing to extrapolate viscoelastic parameters from single indentation-retraction curves. Using this method, the effect of the previously mentioned potential drug has been

investigated, trying to correlate rheological properties to migration capabilities of U87MG. Finally, software dedicated to Jump-Through-Force curves by AFM to identify specific events on SLB in Force-Volume maps have been developed. In particular, SLB S_o-L_d phases coexistence alterations under exogenous drug like Daptomycin have been investigated.

Thesis outline:

1. Chapter “Introduction”: A brief and exhaustive state of the art regarding the current knowledge concerning mechanobiology and the specific motor clutch model, relevant in the context of cell migration and cyclic stretching is provided.
2. Chapter “Measurement methods”: A complete overview of the underlying mathematical basis regarding Flickering-based theories is illustrated. A contour evaluation algorithm with sub-pixel resolution for both GUVs and lipid domains is also implemented. The data-analysis protocol for single cell migration, reorientation and polarization are illustrated and implemented. The theoretical framework of the “Persistence-Random-Walk” model is also introduced. A brief review regarding the pre-processing steps for AFM force curves (in particular the contact point determination), then the Hertzian-based models are presented. After illustrating the main limitations of the Hertz model for the mechanics of cells the Ting model theory is introduce and, subsequently, its implementation for cell viscoelasticity characterization is illustrated.
3. Chapter “Devices development”: A custom-built (Arduino-based) On-Stage cell incubator for time-lapse cell imaging assays and its development is presented. Additional features including automated autofocus and motorized stage are also included. Then, a stretcher device compatible with the presented cell incubator set-up is developed and validated.
4. Chapter “Results”: In this chapter the different findings obtained during PhD work are summarized. In particular, line tension and bending findings are illustrated basing on related published articles. Jump-Through-Force analysis of SLB exposed to exogenous drug is showed as well. Then, the main results regarding U87MG cell migration assays and related viscoelastic characterization exploiting Ting model are presented. In particular, correlations between cell motility variation and rheological behavior when U87MG are exposed to exogenous drugs are investigated.
5. Conclusion and final remarks: Here the different contributions for combined techniques, devices and aim achieved during the PhD training have summarized.

Chapter 1

Introduction

Brief introduction to Mechanobiology

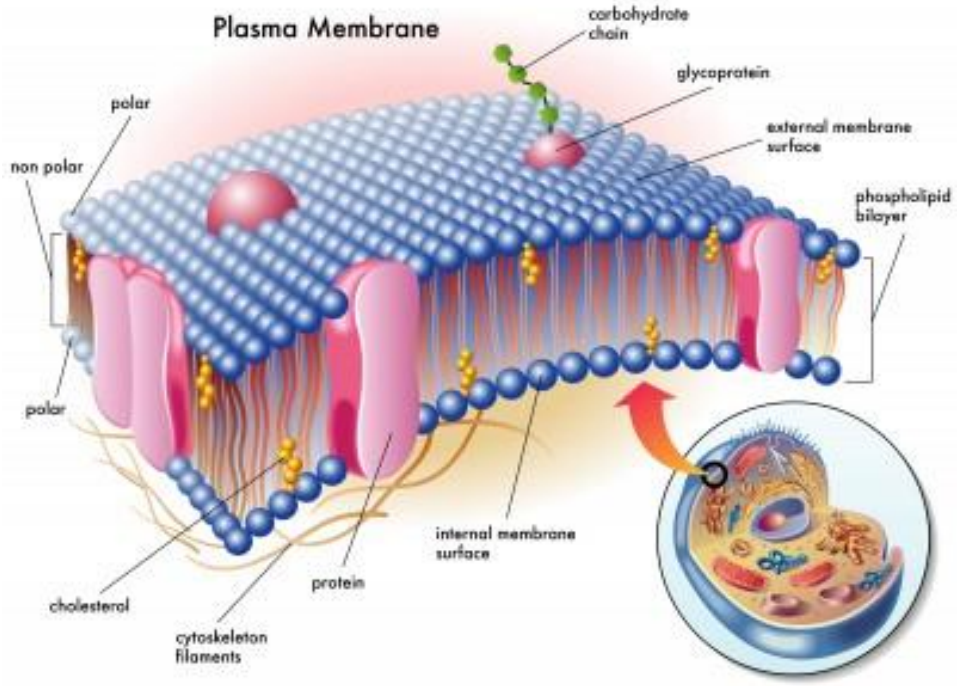

Figure 1: Representative picture of the plasma-membrane, highlighting its main components.

Image taken from: https://biology.tutorvista.com/animal-and-plant-cells/plasma-membrane.html

Cell biology related disciplines in the last few decades have shown that main cell processes are governed not only by biochemical stimuli, but also by physical cues, like geometry, external cellular matrix stiffness or traction forces [1]–[3]. These external mechanical stimuli are involved in many processes such as cell development and migration [4] and at the same time, cells are able to respond to external physical stimuli by deeply reorganizing the cytoskeleton, which provides the main mechanical structure to the cell. This situation highlights the need of an interdisciplinary approach in biomedical sciences. Mechanobiology, i.e. the transduction of mechanical signals into biochemical ones by cells [5], constitutes a relatively recent science field. It is based on the biochemistry of biological systems but requires also knowledge of mathematical and physical aspects to better understand cell processes like division, differentiation, migration and development and to build devices that are able to explore these properties. This new discipline builds its

foundations also on the explanation of biological functions involved in both healthy and disease conditions exploiting mechanical aspects. It also has to be approached at different hierarchical levels, from molecular to tissues scale. In fact, all characteristic metric scales spanning from nanometric to millimeter size are relevant in mechanobiology study. Considering for example proteins: conformational changes are involved at molecular level in gene transcriptions, protein complexes are associated in cell motility, adhesion and material transport at the cellular level [6]. Finally, forces provided at molecular and cellular level can reshape tissues, chemical and physical stimuli generated between cells and among cell by extracellular matrix environment form the basis for tissues scaffold and architecture engineering in regenerative medicine. Also the cell microenvironment and its nano-topography provides deep implication in subsequent cell mechanotransduction [7]. Since cell processes span over six orders of magnitude, from nanometric scale to millimeter, and many subcellular structures up to tissues are involved, a multidisciplinary framework is fundamental. In particular, research teams need to involve, apart from the biological component, also physicists, chemists and mathematicians, which provide the intuitions of mechanical aspects together to appropriate computational models [8]. This is needed to collect, re-elaborates the vast data obtained from experimental study, and provide appropriate models for a specific frame-work, even if a unified mechanobiology theory, which spans from molecular players to tissues is completely out of range, at the moment. A major effort is still needed to shed light on the complex hierarchy roles of cell mechanics, from proteins to tissues and organs. The quantitative and numerical approach to mechanobiology can be divided into three different instances [9]. First, physics and mathematical modeling provide numerical quantification of the processes under study, a starting point for novel and still hidden potential mechanism involved in mechano-transduction framework. Second, since in mechanobiology experiments the results appear sometime counterintuitive or even conflictual, new interpretation approaches could be tested through mathematical modeling combined to large data set available from observations. Finally, computational models developed to explain to novel mechanism of action can be tested, selecting new and specific experiments to be performed. Mechanobiology applications are essential in biomedicine screening research and in regenerative medicine.

One of the most important players of all mechanobiology works at the molecular level is represented by the “integrin-based adhesion complex” known also as “Focal-Adhesions”. This molecular player is closely bound to actin cytoskeleton and, from the other side, to extracellular matrix. These complexes, together with cytoskeleton elements, are able to recognize not only biochemical factors but also many different substrate mechanical properties, like stiffness, viscosity, geometry or ligand spacing [1]–[3]. This series of capabilities is directly translated at the cellular level, developing traction forces that are relevant for many biological processes, like cell migration healing, angiogenesis, or metastasis. Considering this basic and essential example, mechanobiology could provide guidelines in prediction of physiological and even pathological event progression by measuring magnitude and direction of involved traction forces [10]. Remaining on the molecular scale, among other single-molecule mechanobiology examples, two main subjects have been explored: “Motor-tracks” and “Ion-channels” [6]. The former constitutes a large family of transporters for molecular components inside cells. Usually, molecular motors are represented by actin and microtubule-based complexes, which move along specific tracks. Kinesin protein motor for example moves along microtubule network inside a cell with the purpose of transporting cargos where they should be transferred; myosin motor instead, is responsible for example of our muscle contraction and is associated to actin filaments. The latter subject is constituted by protein families able to allow ion transport across the membrane by the formation of pores. These proteins regulate the ion flow between inside and outside of the cell. Activation mechanisms of ion channel obviously are affected by the hydrophobic chains of the lipids constituting the membrane, their exposure to the aqueous medium, and charges displacement inside the lipid bilayer. Nevertheless, also other physical factors play a role in channel activation, like the lipid lateral tension, which could introduce conformational changes in transmembrane protein and subsequently activate/de-activate the ion channel by lateral pressure tuning. A second example of ion channel activation introduced by a variation in a physical parameter is the voltage-gated channels family [11], which are sensitive to voltage difference across the plasma-membrane that can have also mechanical effects due to capacitive aspects. Moving inside the eukaryotic cell and passing from molecular scale to organelle size, we can focus on the nucleus. The nucleus represents the headquarters of the cell itself, and contains all the

information needed for any cell activity, from single proteins synthesis to cell division, hosting the entire genetic material constituted by long DNA sequences closely packed by histones, forming chromosomes. Although nucleus shape and size could deeply influence genome functions and expressions, the nucleus mechanical properties are still poorly explored. Nevertheless, initial studies [12] have shown some interesting connection between pre-stressed eukaryotic internal structures of the nucleus and surrounding cytoplasm environment, mainly through two different pieces of evidence. First, it has been shown that heterochromatin nodes ablation results in anisotropic shrinkage of the nucleus structure. Second, depolymerization of actin and microtubule experiments at cytoplasmatic level exerts forces on the nucleus. These starting results should spur further experimental investigation in nucleus reshaping and re-sizing and mechanically induced genome expressions and protein translocation. As asserted above, sensing and exerting forces capabilities are relevant both in physiological and in pathological scenarios. In particular, changes in mechanical properties are often associated to pathophysiological initialization and progression. To this ensemble we include diseases associated to initial inflammatory response of lung cells after combustion-generated ambient, or engineered manufactured, nanoparticle exposure. It has been shown [13] that heathy lung cells after particles exposure changed their mechanical properties, depending on particle composition, size and dose. This cell mechanical sensitivity to external particle exposure constitutes an initial step toward respiratory diseases or even aggravation of pre-existing pathology. At the tissue level, forces involved in this scenario are needed for cell-cell adhesion, responsible for reshaping and resizing of the multicellular system itself [14]. The challenging issue is to address the mechano-transduced forces involved in the corresponding multicellular processes and function response. Many works proposed a series of different modes and models for mechano-sensing of different relevant physical parameters, fundamental in a wide range of biological functions. These models span from balancing between cell-matrix and cell-cell forces adhesion via the cytoskeleton to line tension and stresses redistribution upon cell proliferation or collective cell migration. For example, a theoretical work [16A] proposed a mathematical model, based on differential adhesion of epithelium cells. It has been shown that differential adhesion is needed to maintain the right cell positioning during cell evolution. Furthermore, without differential adhesion, cell migration alone will result in a completely random process. An interesting example regarding mechanobiology influence at cell and tissue levels are represented by the role of extracellular matrix elasticity for cell evolution. In fact, it has been shown that differentiation of stem cells and metastasis of cancer cells are governed not only by biochemical factor, but also extracellular matrix stiffness plays a crucial role [15]. Naive mesenchymal stem cells evolve in different phenotypes depending on substrate elasticity. In particular, extracellular matrix rigidity, which mimics specific tissue phenotype rigidity will differentiate stem cell in the same tissue phenotype [16]. For example, soft substrates recapitulating the brain extracellular matrix micro-environment have a neurogenic behavior, substrates with intermediate stiffness resembling muscle extracellular matrix have myogenic capability, and finally more rigid substrates, which mimic bone have an osteogenic role. Note that extracellular matrix Young modulus spans over six orders of magnitude, from few kPa for neuronal tissue, to several GPa for bone tissue. Extracellular matrix rigidity plays other crucial roles also, in cell spreading and migration [17]. Early in-vitro experiments showed that cells on softer substrate were characterized by higher motility and were less spread than on stiffer substrate. Furthermore, on softer substrate focal adhesions were less developed than on stiffer substrate, confirming that this latter structure and its dynamics is closely involved in the mechano-transduction process between cytoskeleton and substrate. More quantitatively, previous experiments showed the existence of a substrate Young modulus optimum value for traction force, adhesion and migration. This value is around ≈5 kPa and many results confirmed that this is a typical critical value. This nominal value of the Young modulus can be better understood following several physical arguments. First, focal adhesion organization is the main tool, which provides mechanical sensing and transmission capabilities with the surrounding cell environment, typical focal adhesion size is around the micrometer scale, and the forces sensed and exerted from focal adhesion are around ≈5 nN of magnitude [18]. Second, the perception of the external environment rigidity is unlikely obtained with an absolute and independent measurement by the cell. More probable, the cell senses the external rigidity and compares its magnitude with an internal reference value, and the more reliable candidate is the cell stiffness itself or the mechanical properties of the polymers constituting the cytoskeleton. We will expect that this reference value will not differ significantly from the threshold value mentioned above. Further AFM forces measurements,

adopting polymer physics principles for the cytoskeleton, showed that the typical cell stiffness is in the kPa range, around ≈5 kPa, supporting the previous findings of the Young modulus threshold value. Other pieces of evidence about substrate rigidity sensing of cell is reported by a special mechano-sensitive molecule, "talin" [19]–[21]. This protein is highly sensitive upon loading rate exerted between the cell and the extracellular matrix substrate, and its partial unfolding driven by force rates governs subsequent vinculin-talin binding. Talin-vinculin binding constitutes a starting point for further focal adhesion growth, its role is fundamental for cell adhesion and migration. We will discuss about talin unfolding in the Motor-clutch section.

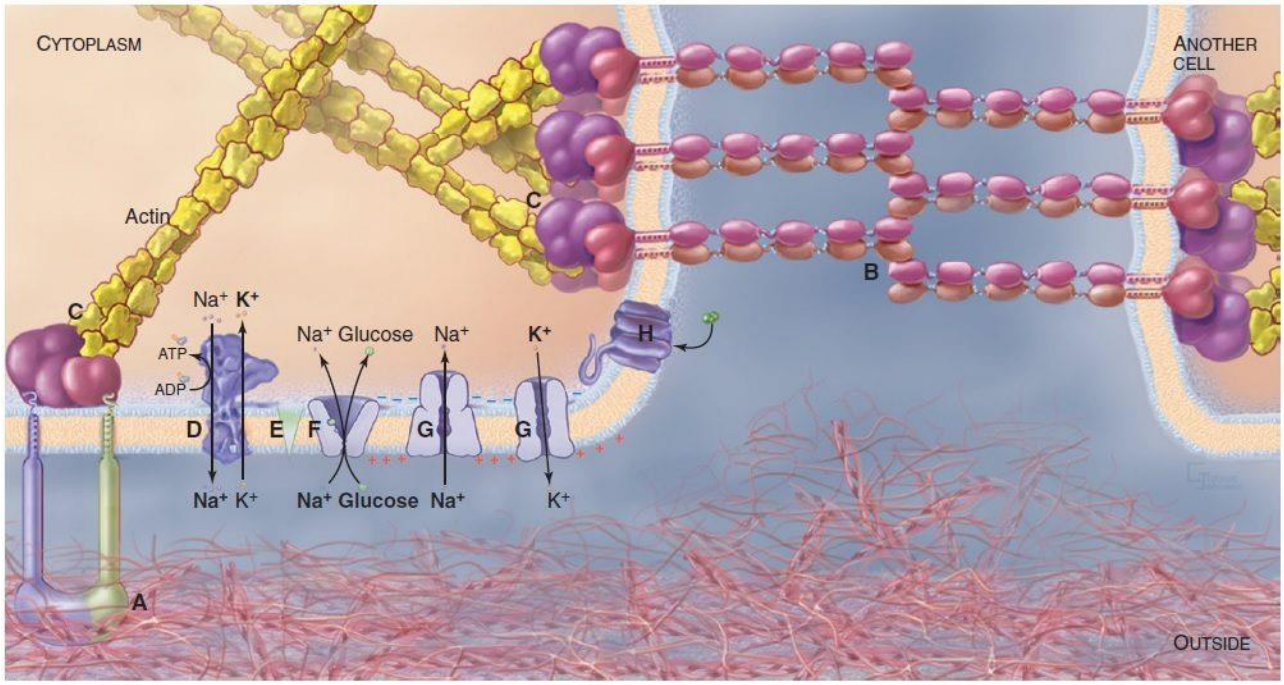

Figure 2: Main plasma-membrane interaction to inner part of the cell and surrounding environment: A) transmembrane adhesion protein anchored the membrane to the extracellular matrix. B) Receptor-proteins, like cadherins bound two different cells. C) Receptors dedicated to force transmission from actin to cytoskeleton. D-G) Various examples of plasma-membrane selective permeability abilities:

Image taken from: https://alevelbiology.co.uk/notes/plasma-membrane-structure-and-functions/

The cell substrate stiffness microenvironment is not the only physical parameter which can affect cell capabilities. Processes that can be modulated by mechanical cues include differentiation, migration and adhesion and living cells in their physiological environments are continuously exposed to stretching or compressing deformations. These situations include both the case of uniaxial stretching, such as for cells of the skeletal-muscle tissues or cells in the walls of vessels exposed to a periodic stretching given by the blood pressure oscillations, and of isotropic stretching, as in the case of hollow structures such as the heart or lungs. Stretching a cell could affect in different ways its behaviour. For example, stretch-activated ion channels such as piezo-channels [22] could be induced to activate, leading to a change of the flux across the membrane of Ca^{2+} ions, generating in this way a cascade of biochemical processes. At the same time, every deformation of the substrate on which cells are growing acts on the focal adhesion complexes, transmitting the mechanical signal to the cytoskeleton inside the cell [22]–[25]. Given the mainly dynamic nature of the cell cytoskeleton, a stretching acting on the sticking points of the cells to the substrate, could interfere with the polymerization and depolymerisation processes of its elementary units. To shed light on the role of mechanical stimulation on the cell activity, devices that are able to apply well defined deformations to the substrate have been developed [26], [27]. If cells sufficiently adhere to the underlying substrate, without sliding, a strain of the substrate can be transmitted to their internal structures. These devices, even if they cannot recapitulate the

very complex scenario occurring *in vivo*, can provide very useful information on the biological effects of mechanical deformations of the cells, better approaching specific physiological situations. Indeed, the physiological environment of several cells includes periodic mechanical stimuli, but cells that physiologically reside in regions without mechanical signals also share the same type of reactions when exposed to periodic stretching. This behaviour appears so as a common aspect of the molecular machinery constituting the parts of the cells in mechanical contact with the external environment. It has been demonstrated that cyclic stretching can lead to alterations of the gene expression profile of cells. This phenomenon typically concerns the proteins of the cytoskeleton or associated with it and the proteins of the extracellular matrix [28]–[30]. One of the effects of periodic stretching on cells that has been deeply investigated is their reorientation relative to the stretching direction in order to maintain a tensional homeostasis [31]–[37]. There is large evidence that cells with a bipolar shape such as fibroblasts tend to reorganize their orientation almost perpendicularly to the direction of periodic stretching as a consequence of the development of an oriented structure of stress fibers. Studying the details of this effect can largely help in understanding the mechanobiology of the cell/substrate interaction. In the literature there are works that have been carried out exploiting different types of cell stretching devices [38]**.** The large majority of the devices are custom-made, although some systems are also commercially available. The stretcher can be uniaxial, bi-axial or radial (isotropic).

In the context of mechanosensing, any deformation in the geometry of the substrate on which the cells are growing can be transmitted inside the cell causing a sequence of biochemical reactions to begin if there is a mechanical connection between the cell and the substrate [39]. Focal adhesions (FAs) are complexes working as mechanonsensors used by the cells to probe their mechanical environment and integrins are transmembrane proteins inside FAs used by cells to establish this connection [3]. They provide a bridge between the internal cytoskeleton and the extracellular matrix. The stretching action is able to affect the activation of relevant molecules inside the FA complexes such as the FA kinase (FAK) [40]. Forces applied from outside to the cytoskeleton are able to affect the dynamical structure of this molecular construct. As far as mechanochemistry is concerned, it is important to consider that the mechanical transmission chain in composed by proteins interacting with each other with mainly two different types of bonds [41]. The first type is the “slip bond” and its lifetime decreases if a force trying to break it is applied to the partners [42]. The second type is called “catch bond” [43] and is characterized by the fact that there is an initial increase of the bond lifetime when a force is applied to it but , upon a further increase of the force, the lifetime starts decreasing. We will provide a complete overview of the “slip bond” and “catch bond” in the motor clutch model section.

Introduction to motor-clutch dynamics model

An example of a mechanobiological mechanism for which analytical models have been developed is represented by the traction force exerted by cells on the extracellular matrix. This model will be exploited in this thesis in the context of migration of cells as a function of substrate rigidity.

The capabilities of cell to carry out its main functions [16], [44], [45], including proliferation [46] depend on cell ability to exert forces in the surrounding cells and its microenvironment [47]–[49]. In this section we will introduce how cells are able to generate forces, and how these forces are transmitted to the extracellular matrix at molecular level using the molecular clutch hypothesis. Finally, we will provide different cues about how the clutch model could explain the mechano-transduction downstream events needed for cell functions.

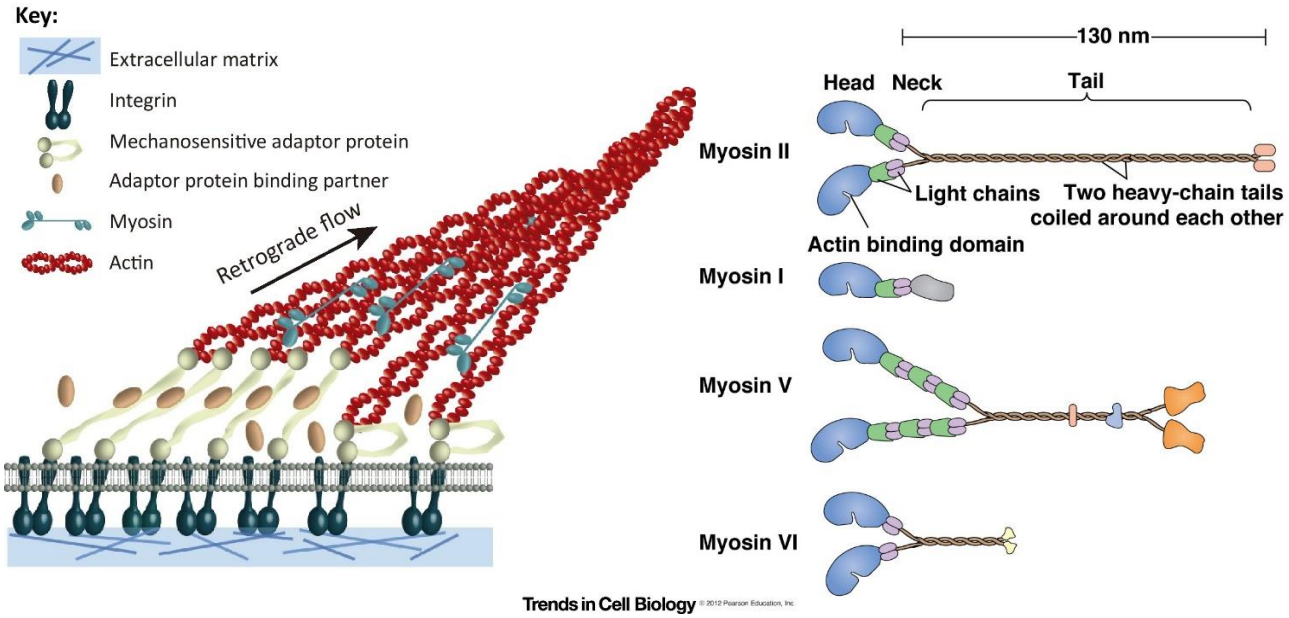

Figure 3 (left): Representative picture of the actin retrograde flow induced by myosin motors, and subsequent force transmission to the extracellular matrix by adaptor-protein complex.

Figure 3 (right): Myosin molecular motor different configuration

Image taken from: Control of Mechanotransduction by Molecular Clutch Dynamics [C]; BIOL2060

The principal actors involved in exerting forces by the cell are represented by actin and myosin. Actin allows cell to apply force through two major processes: actin polymerization and actin contraction, where myosin II molecular motor plays a crucial role. Once the force is generated by actin and myosin processes the stimuli must be transmitted toward the extracellular matrix. A wide range of adaptor proteins bound to actin are involved in force transmission. Nevertheless, adaptor proteins represent just a single step in force transmission process, in fact adaptor proteins are linked to actin on one edge, and are bound to transmembrane protein to the other edge, which behave like a bridge between the adaptor protein and the extracellular microenvironment. Usually, the molecular structures constituted by actin, adaptor proteins, and transmembrane proteins are defined as cell-matrix and cell-cell adhesion complexes, depending on the type of transmembrane protein involved. If force is transmitted to extracellular matrix, integrins constitute the principal transmembrane protein [50], if force is transmitted to other cell, cadherins represent the typical transmembrane protein [51]. These adhesion complexes, which are deeply dynamic, are fundamental for appropriate force transmission, exhibiting a precise spatial organization needed for specific adhesion between cell and cell and cell to its microenvironment. Otherwise, in this regime nonspecific interaction would bring to repulsive processes. Reassuming, in the inner part of the cell actin-based processes are pushing against the membrane through actin polymerization and actin contractility powered by myosin, produces a constant actin flow, called retrograde flow since is more accentuated at the cell edge and it moves toward cell center [52], [53]. Lamellipodia and stress fiber are examples of adhesion complex integrins-based (cell-microenvironment) involved in retrograde flow [54], [55], but similar examples can be found experimentally shifting to cadherins-based adhesion complex (cell-cell). As mentioned above, adhesion complexes constitute a highly dynamic system where a continuous binding and unbinding process between different molecular elements regulates force transmission and influence the retrograde flow. When adaptor and transmembrane protein are bounded together the adhesion complex is able to transmit force toward extracellular matrix and, if the system is “engaged” with the extracellular matrix, the actin contraction provided by myosin motor is rigidly opposed resulting in a slowing down of the retrograde flow [19]. we will see later that retrograde flow is inversely connected to cell migration speed [52], [56], [57]. As opposite condition, when the adaptor protein and its transmembrane protein counterpart are loosely interacting with

the extracellular matrix, the system is disengaged, force transmission is stopped and retrograde flow speeds up. To resembling the dynamical relation between cytoskeleton-external microenvironment and cell migration in [20] the "molecular clutch" model was introduced and named like this according to relationship between axles and the mechanical engine in a motor machine. As the different shafts can transmit motion from to engine to the wheels only when they are correctly positioned, cell can coordinate its protrusions when the different molecular element in adhesion complexes are correctly engaged.

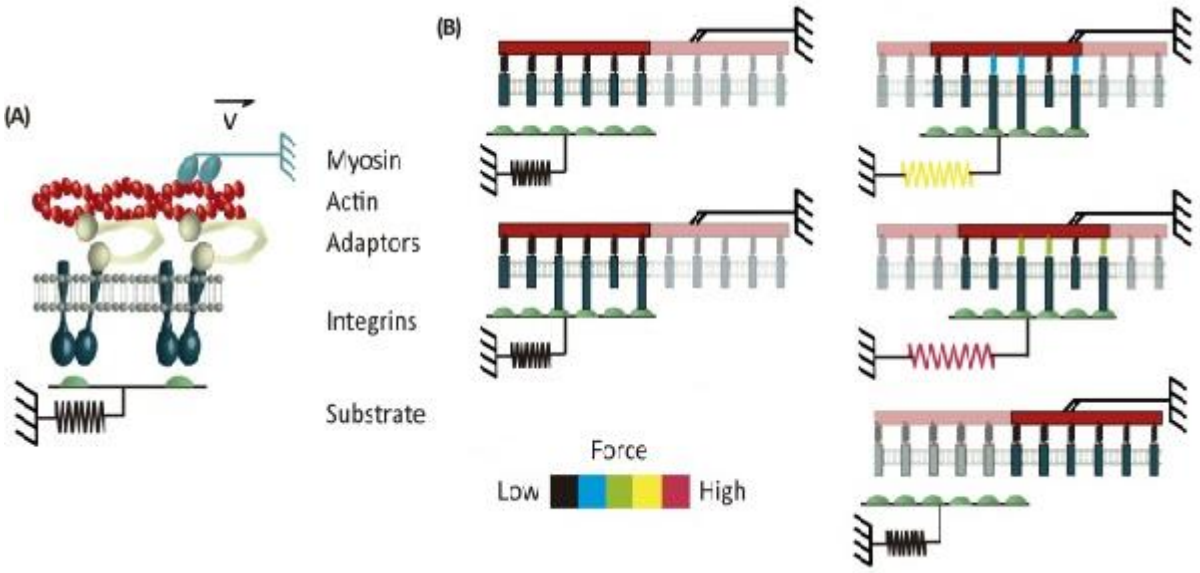

Figure 4 (A): Motor-clutch model scheme (B): Different motor-clutch model configuration, varying the number of motors and the clutches engaged to the substrate.

Image taken from: Control of Mechanotransduction by Molecular Clutch Dynamics [C];

Since motor-clutch model regulates both cell movement and force transmission, it has deeply implication in the onset of mechano-transduction events. Many different aspects about biochemical and mechanical properties of mechano-sensitive players have been widely studied in the literature, and the motor-clutch model could provide more quantitative modelling and prediction about other underling mechano-transduction pathways still unexplored. We will see how clutch model results can be spent not only in the well-studied case of integrin-based complexes in cell-extracellular matrix context, but it can be also exploited for other specific adhesion complexes. Furthermore, molecular-clutch outputs are ascribed directly not to forces per se, but more specifically to the force loading rate.

There are different molecular pathways where force transmission is involved through clutch model and we will summarize them. Notwithstanding the molecular complexity arising from cell-extracellular matrix adhesion, we can define which are the principal molecular player involved in clutch model: starting from external microenvironment and moving toward the plasma-membrane we first find transmembrane protein constituted by integrins/cadherins and other molecular ligands. Proceeding from the cell membrane to the inner of the cell itself we have adaptor proteins, followed by myosin II motor and actin filament pulled by molecular motors. Depending on the adaptor and transmembrane proteins involved, force transmission can be affected in a straightforward manner: by direct interaction between integrins and extracellular matrix [58], [59], or by adaptor proteins, which directly mediate interaction between integrin and the actin filament, like alfa-actinin [60], filamin [61], tensin [62], kindilin [63] and talin [64]–[66]. Force transmission occurs also in a secondary way, by indirect interaction between integrin and actin. Adaptor proteins involved in this scenario are: vinculin [64], [67]–[69], FAK (Focal Adhesion Kinase) paxillin, and kank [70]. Similarly, in cell-cell adhesion at intercellular level force transmission occurs both in a straightforward and in an indirect way, where integrins are substituted by cadherins-based complexes [71]. Nevertheless, just few adaptor proteins

have been experimentally observed in the force transmission chain, both in cadherin and integrin-based complexes, like vinculin [72]; It is possible that more adaptor proteins affect force transmission in both cell-extracellular matrix and cell-cell adhesion contexts.
Now that we have shed light on the major molecular players involved in the motor-clutch model, we will show how the model can regulate and trigger specific force transmission. The principal property of the clutch model resides in its intrinsic highly dynamic engagement and disengagement rates of the involved molecular components. If more and more adaptor and transmembrane proteins are engaged connecting actin filament to the extracellular environment, the force will be transmitted more efficiently. Nevertheless, the high number of elements (influencing each other) and the complexity of the model require specific mathematical modelling to describe the nontrivial and counterintuitive consequences of the model. Motor-clutch formulation can be proposed using different models, depending on the type of molecular elements and the chosen number, the extracellular mechanical properties and so on. In literature many computational simulation studies [73]–[76], and analytical solution to proposed models [76]–[80] have been developed.

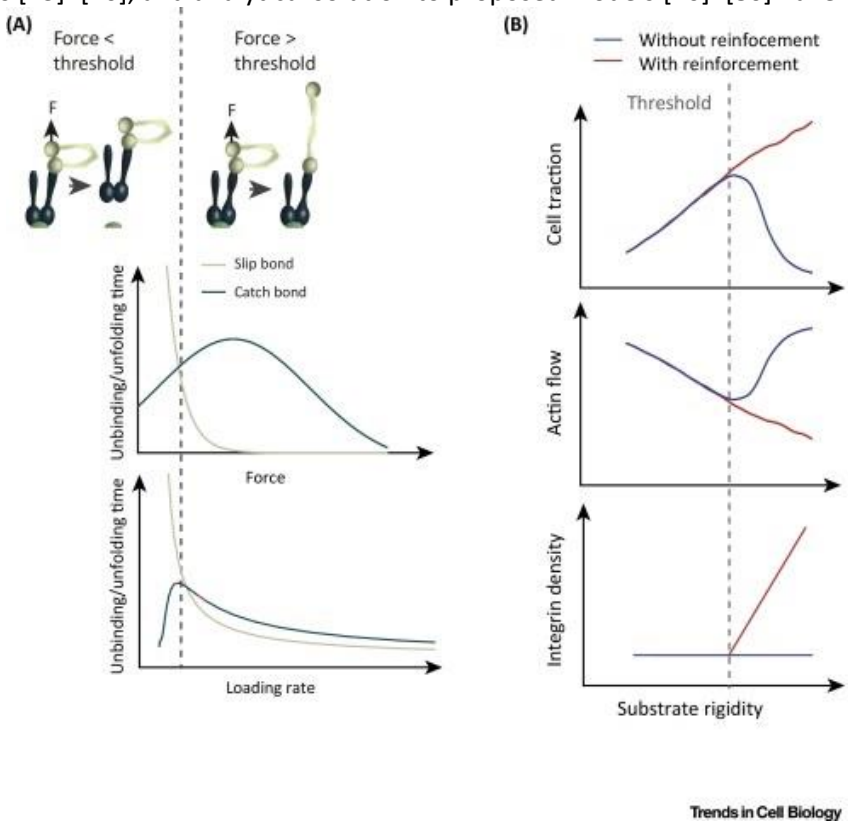

Figure 5 (A): Lifetime of slip and catch (catch-slip) bonds comparison as function of Force and loading rate. (B): Description of force transmission, retrograde flow and integrin density proposed by clutch model increasing substrate rigidity, considering the presence/absence of focal adhesion reinforcement.

Image taken from: Control of Mechanotransduction by Molecular Clutch Dynamics [C];

In [73] Odde et al provided a clutch model, which is highly sensitive to two characteristic properties: the number of clutch motor elements available and bonds (slip and catch) lifetime. As already mentioned, the retrograde actin flow generated by myosin motors depends inversely on the number of clutch elements engaging the substrate [59], [64], [73], [81]. On its turn, actin flow speed decreases as the force transmission is enhanced by the clutches, and the total exerted force reaches it maximum in stalling condition, whose upper limit is fixed by the maximal force that a myosin motor can provide (~2 pN) [82]. The work quantified the actin flow in the extreme regimes: when the system is completely disengaged and no clutches are present between actin and extracellular matrix, resulting in the maximal retrograde flow, around 120 nm/s; when all the clutches are simultaneously engaged to the substrate, corresponding to minimal flow rates around 10

nm/s, since lower speed has not been observed [81]. The second property is the lifetime of bonds involving adaptors, transmembrane proteins, and the microenvironment. In fact, characteristic lifetimes of these bonds are directly affected by the force amount that is transmitted by the molecular partners to the bond itself. Usually, proposed models consider just one type of bond and this selection is performed by looking for the weakest link in the chain from the actin filament to extracellular matrix (integrins-based adhesion) [59], [83], [84], or alternatively from cell to cell (cadherins-based adhesion) [73], [85]. Nevertheless, previous experimental findings showed a variety of different retrograde flow rates response, depending on the clutch elements involved [54]. Maybe, considering only one contribution provided by the weakest link is just a first approximation, likely the model should take into account a superposition of the different clutch elements lifetime reflecting an integrated and more realistic response in force transmission and retrograde flow. Different clutch model formulations are strictly bounded to particular clutch elements selection, which is justified by the particular adhesion complexes under investigation. notwithstanding the wide variety of clutch models, simulations share a common dynamic evolution: at the initial condition the system, constituted by a set of clutches, results completely disengaged, so actin contractility evolves freely and the retrograde flow is maximum. As many clutches start to bind with a characteristic binding rate, the system becomes gradually engaged, actin contraction pull on the substrate exerting progressively higher force. Since bonds involved in the clutches are sensitive to the amount of force transmission, after reaching maximum force traction corresponding to a completely engaged system, molecular chain elements gradually broke up since unbinding events overcome binding events. The catastrophic disengagement cascade ends, since initial conditions are restored, and the cycle can begin again. This periodic and dynamic engagement/disengagement circle is called “load and fall”. Force transmission is optimized in the “load and fall” regime, but for particular molecular player properties and microenvironment conditions. Among the different external microenvironmental parameters, substrate rigidity plays a crucial role in the optimal “load and fall” cycling for maximum force transmission. In fact, as mentioned before, the principal parameter that carried out the exerting force transmission tuning is the loading rate, rather than the force itself. Loading rate is directly bounded to the retrograde actin flow by the substrate rigidity itself [86]. For rigidities higher than the optimum value, clutches transmit load faster than the maximum loading rate supported by the bounded molecular elements, so individual clutch binding elements are progressively released since unbinding rate dominates, before additional force could be transferred to the substrate. The system rapidly collapses and the number of engaged clutches reaches zero, both for instantaneous and stationary regimes, the “load and fall” condition is substituted by the “frictional slippage”, where actin contraction acts in a freely and completely disengaged environment, and force transmission contributions are negligible. Instead, for lower rigidities than the optimum value, actin contraction provided by myosin induced too slow loading rate, and single clutches disengage before the force has been completely transmitted. Alternatively, the mean lifetime of clutches bond elements is too short to allow force transmission correctly in this low rigidity regime. This behavior has been observed experimentally in [73] and [87]. Comprehensively, motor clutch model suggests a biphasic behavior between substrate rigidity and force transmission, which gradually increases increasing stiffness and then drastically slow down for rigidities above the optimum value [73]. Nevertheless, many experimental studies provided a monotonic enhancement in transmission force when rigidity is progressively increased [58], [78], [88], [89]. This discrepancy could be explained considering talin unfolding, a mechano-transduction phenomenon already mentioned in the previous section, and its connection to focal adhesion grows over the threshold rigidity [64].

Alternatively, it is possible to study how optimum rigidity value is affected by the loading rate, for example modifying the number of active motors in actin contractility [64]. In that paper it has been shown how inhibition of myosin II molecular motor introduced a shift in the optimum rigidity value toward higher value, where, in control condition, “frictional slippage” is expected. Furthermore, it is possible to modify two clutches parameter simultaneously, like the number of motors together with the number of clutches, experimentally realized in [90], [91] to test clutch model simulation predictions. Considering not a purely elastic substrate, but a viscoelastic behavior can deeply affect cell response. In [92] paper it has been show how clutch model applied to a viscoelastic extracellular matrix could predict corresponding cell reorganization.

Clutch model is fundamental not only in force transmission processes, but also for force transduction regulation, and we will provide an intriguing example. Mechano-transduction property is defined as an ensemble of cell capabilities to convert forces into a biochemical cascade signaling, which is able to affect cell function itself. Usually, in mechano-transduction events specific mechano-sensing molecules are strictly involved, and these molecular players are believed to change their biochemical properties upon external mechanical stimuli, like applied stress or shear flow. The best known example of mechano-sensing mechanism is represented by the partial talin unfolding together with vinculin, needed for actin-integrin binding. Nevertheless, focusing on single molecular mechano-sensor is not enough to describe and recapitulate force transduction regulation in the highly dynamic force transmission scenario, where the motor clutch model finds its place. To provide a substrate rigidity sensitivity to the system, motor clutch model needs at least two mechanosensory players with different mechanosensitive capability. Consider again the actin-integrin clutch, which interacts with extracellular matrix exploiting talin. This simple element of the clutch model constitutes already a substrate rigidity threshold sensor. Nevertheless, it cannot be explained analyzing talin unfolding process alone, but it must be compared to integrin-extracellular matrix fibronectin protein binding. More precisely, the time involved in the unbinding/unfolding of the two bonds, which is force dependent, must be compared. In the former case (talin unfolding), the process is described by the Bell model [93], meaning that the time required for single unfolding event decreases exponentially increasing the exerted force, suggesting that talin folding events rate increases at high substrate regimes. The latter case (integrin and extracellular matrix binding), is described by a catch bond (catch-slip bond). So, time needed to break up the integrin bond follows a biphasic behavior, first increases increasing the applied force, and then decreases upon further increase of the force, like a normal slip bond. Combining the two bonds time-vs-force behaviors we can observe a crossover between the slip and catch bond processes. The exerted force value provided by the substrate, where the two bonds curve cross each other, marks the rigidity threshold value above that talin unfolding and subsequent talin-vinculin bindings dominates. Then, talin-vinculin binding promotes further focal adhesion growth [68], [94]. This example clarifies that talin unfolding act as nonspecific rigidity sensor, since it could be activated without a precise rigidity threshold, unless integrin binding is taken into account. Following the previous description, it seems that exerted force magnitude controls the slip and catch bonds, rather than loading rate. Nevertheless, similar behaviors could be extended referring to applied loading rate. Furthermore, for long time it has been questioned if cell mechanical sensing is affected more by force magnitude or loading rate, experimental evidences have shown the presence of force fluctuation at cellular level [95]–[97], suggesting that they play a crucial role in cell functions and development. So, motor clutch model, confirming this first experimental cues, could better shed light on this debate [98]. As mentioned above, focal adhesion growth reinforcement caused by talin unfolding at high substrate rigidity regime could explain the discrepancy between biphasic and monotonic behavior of force transmission (upon increasing rigidity). In fact, cells that experiencing adhesion reinforcement are able to enhance their clutch binding rate, because there are more and more integrins available to bind, resulting in higher retrograde actin flow and preventing the force transmission decay expected in biphasic regime. Obviously, as well as substrate rigidity, there are other internal and external mechanical parameters affecting force mechano-transduction in clutch model. For example, in [99] it has been demonstrated that spatial arrangement of ligands combined to two different mechano-sensors provide cell sensing capability of extracellular matrix ligands distribution, and regulate subsequent focal adhesion formations. Force transduction capabilities prediction arising from clutch model are based on life-time curve interception belonging to two different bonds. Nevertheless, clutch model findings do not place any limitation about the type of couple of bonds involved, previously we considered a slip and a catch-slip bonds, but similar force transduction abilities could be predicted by the model using any type of bonds couples, as long as life-time interception curves exists.

So far, we demonstrated the clutch model validity regarding force transmission and transduction. Traction force could, at first sight, directly explain subsequent cell migration. Nevertheless, single measurement of force transmission generated by the cell are several orders of magnitude higher than the force amount needed for cell migration, while summing up the overall traction forces acting on cell will result in a zero force value [100]. These experimental evidences suggest that traction force does not act as propulsion source for cell migration. Although traction forces are not directly linked to cell migration, pieces of evidence [52],

[56], [101] show a connection between cell migration speed and retrograde actin flow, one of the main features of clutch model. It has been shown previously that for a specific actin polymerization, corresponding to minimum retrograde flow, cell exhibits maximum traction force, this condition constitutes the favorite one for fastest migration. This finding is strictly applicable for leading edge migration condition [73], belonging to the initial clutch models proposed. In a more realistic description more protrusions pulling on cell must be taken into account, as provided by Bangasser et al [90]. They predicted an optimal substrate rigidity not only for maximum traction force, but also for fastest cell migration changing the number of clutches and motors in the model, highlighting that maximum force transmission does not corresponds necessarily to fastest migration.
Furthermore, motor clutch model prediction on cell migration regulation could be exploited not only for single cell migration, but also for collective durotaxis [46]. In this scenario epithelial cell are sensitive to substrate gradient rigidity, moving toward stiffer substrate area. It has been shown that collective migration is cancelled by motors inhibition using blebbistatin, when cell-cell junctions are suppressed. Thus, durotaxis constitutes a long-range interaction of cell-cell adhesions, where the clutches placed at the two opposite edges, at the softer and the stiffer substrate area play a crucial role.

Role of the plasma-membrane as mechano-sensor and mechano-transducer

The plasma-membrane constitutes a physical barrier between the inner and the outer part of the cell. This is just one of the different roles associated to the plasma-membrane. Since the plasma-membrane is in direct contact with the external environment, represented by the other cells, and the cytoskeleton, it is affected by different mechanical and chemical stimuli. This wide range of external stimuli constitutes a set of stresses that the cell must overcome and respond to. For this reason, the cell membrane represents a mechano-sensor, between mechanical stimulus and consequent cell mechanical response. Furthermore, mechanical response acts as a trigger for the subsequent downstream biochemical responses located inside the cell and the nucleus, the plasma-membrane behaves also as a mechano-transducer. The simultaneous roles of sensor and transducer provided by the cell membrane, is fundamental for all cell process such as proliferation, division, differentiation and migration [102]–[110]. Cell mechanical responses induced by external stresses are usually provided in order to maintain the integrity of the cell itself, and the subsequent biochemical signaling cascade is relevant both in healthy and in diseases scenarios. Among the different molecular actors and parameters, which act as sensor and transducer in the plasma-membrane we can mention: membrane-protein folding/unfolding, membrane tension, membrane curvature and domain re-arrangement in the membrane. Since we mentioned above the wide range of stresses to which the cell is exposed, it is useful to separate the different type of external mechanical stimuli, which can be classified in three different stresses classes: Tensile, Compressive, and Shear stress. In the next sections we will focus on each single class, recalling the principal molecular actors and parameters involved, and introducing different examples of sensor and transducer cases associated to each class. We should specify, that usually a combination of simultaneous external stresses act on the plasma-membrane, in this scenario we should treat the membrane as an entire three-dimensional system. This more exhaustive description is for the moment set aside, and we will focus on only a single type of mechanical stress at a time, considering the plasma-membrane as two-dimensional system.

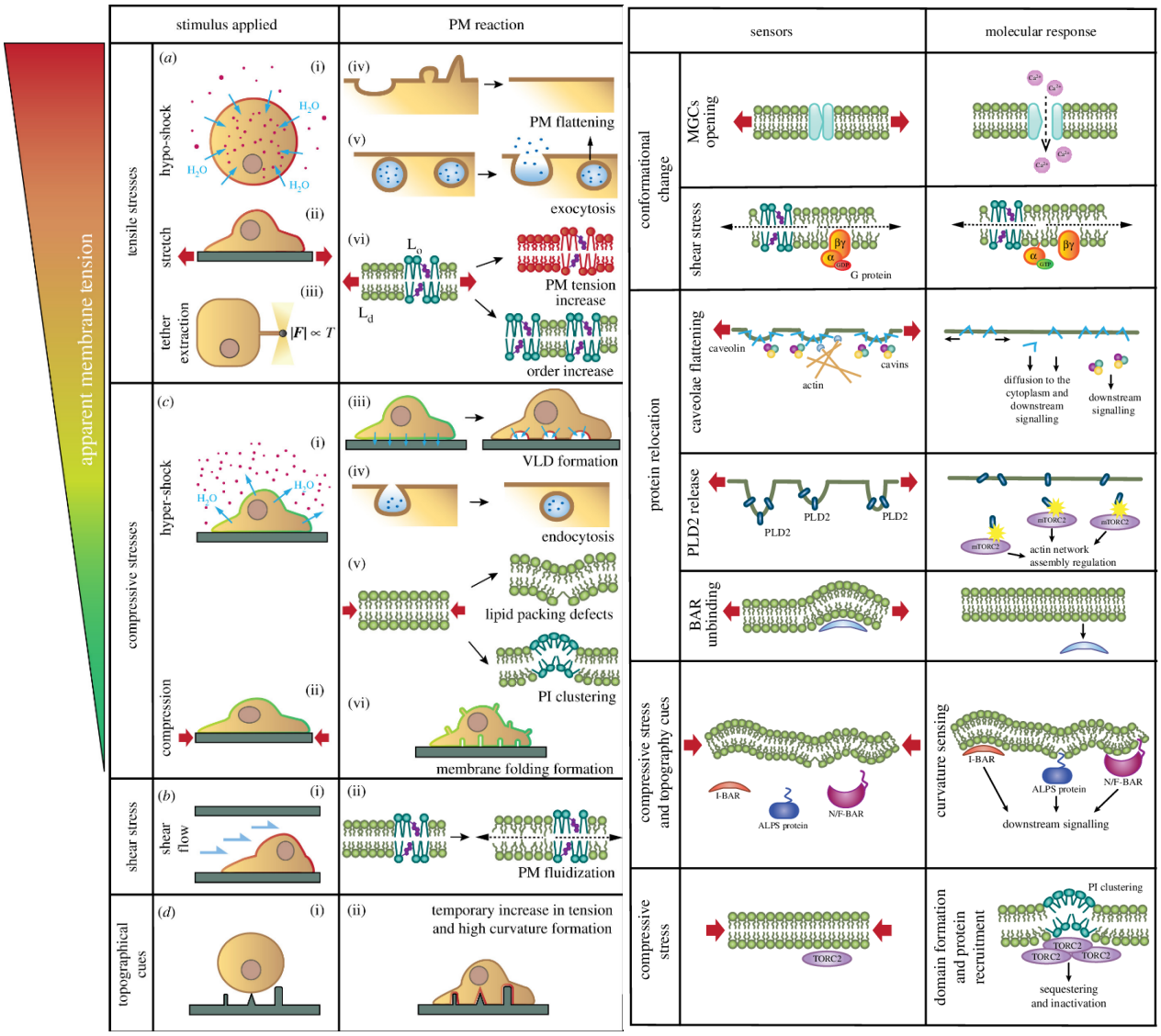

Figure 6 (A): Scheme of mechanical stimuli experienced from the plasma membrane, highlighting the subsequent main membrane reactions (B): Ensemble of the different molecular sensors and related mechanical stresses acting on the membrane.

Image taken from: The plasma membrane as mechanochemical transducer [D];

- **Tensile stresses (discussion and examples of sensor/transducer cases)**

Tensile stress can be achieved by osmotic procedures [111]–[113], usually using hypotonic treatment, both in suspended and adherent cells. The typical cell response consists in membrane buckling, a plasma-membrane area expansion, and a volume expansion of the cell itself. Alternatively, focusing on adhering cells an uniaxial or isotropic stretching can be applied on cell membrane mechanically stretching the substrate [112], [114]. In both the mentioned experimental approaches, the final result is an increase of the plasma-membrane apparent tension. In fact, hypotonic treatment acts not only on the plasma-membrane, but also on the surrounding cytoskeleton architecture, so part of the increasing tension is transferred on the cytoskeleton [115], [116] which is strongly bound to the plasma-membrane. The role of the cytoskeleton scaffold in this case, is to prevent cell lysing or rupture, since the plasma-membrane alone can endure only ~3-5% area expansion corresponding to a tension rupture amount of few mN/m (dyn/cm) magnitude (at 25°C is 10-12 mN/m and at 50°C is between 3 and 4 mN/m) [Elastic Area Compressibility Modulus Of Red Cell

Membrane E. A. Evanes, R. Waugh, and L. Melnik Biophysical Journal Volume 16 1976] [107], [117]. Depending on the cell type, cell-membranes have different responses to minimize tension increment provided by osmotic destabilization. In particular, cell membranes can supply additional lipids during area expansion, and buffer the tension increases. First, we consider plasma-membrane having high density folds. Folds can be released by plasma-membrane flattening, when is needed upon cell volume expansion [111], [112], [118]. Second, we consider cells that release internal liposomes, through exocytosis processes, in response to plasma-membrane tension increment [114], [119]–[122]. In both cases the cell carries out a mechano-protective process to compensate plasma-membrane tension increase. This cell response upon osmotic changes shows that not only the amount of stretching sensed by the cell is relevant, but also the overall membrane lipid reservoir must be taken into account [123]. The total amount of lipid fold or endo-membranes contained in the cell depends on the cell type, and usually cell lines exposed to frequent osmotic instabilities or external stretch are coupled with overall higher lipid reserves. For example, caveolae are highly abundant specifically in smooth muscle cells, which are highly exposed to stretch, and in endothelial cells, which are highly exposed to shear flows). Now we focus on a consequence related to plasma-membrane tension increment, the subsequent lipid bilayer thickness decrease [117]. This results in a complex rearrangement in the elements contained in the cell membrane. In order to prevent water exposure of the hydrophobic chains, conformational change in trans-membrane protein can occur, or a decrement in the lipid packing that will favor diffusion in the bilayer.

We will proceed introducing different examples of molecular actors involved as sensors of tensile stresses, relevant at short-time scale. The first example are the integral membrane proteins, which undergo conformational changes upon tension increase and subsequence membrane expansion. In this family of proteins, we can mention the “mechanically gated channels” [124]–[127]. This type of protein is exposed to conformational changes also when shear flow is applied [124], [128], [129]. Nevertheless, if channel activation is induced by share stress or by tensile stress caused by hydrostatic pressure remains unclear. Another cue about protein conformational changes is the hydrophobic mismatch, which occurs when lipid-bilayer thickness is modified. As we mentioned above, upon tensile stress also changes in the lipid-bilayer are involved. In the studies of bacterial-channels it has been shown that also changes in plasma-membrane thickness [130], together with area expansion and tension increment [131], can affect activation of these channels. Introduction of membrane thickness and subsequent hydrophobic mismatch [117] to which internal membrane proteins are exposed could reveal that several other transmembrane proteins work as tensile stress sensor [132].

The second molecular actor that acts as sensor upon tensile stress is represented by all proteins involved in relocation processes when caveolae and other invaginations are unfolded. We will focus first on caveolae flattening when plasma-membrane undergoes tensile stress, the first role of this response process is to prevent further tension increase. This results in tension buffering of the membrane, and it could be thought as a sort of “mechanically gated channels” activation prevention. As final result, caveolae flattening represents also and indirect mechano-transduction protection upon unwanted activation of transmembrane channel gates [133]. During caveolae flattening many different proteins are easily diffused through the cytoplasm, (for example caveolin-1, caveolin-3 and caveolae-associated protein 1) and to the nucleus (EH-domain containing protein 2). Moreover, caveolae disassembling results in a decrement in sphingolipid packing [134], favoring glycosphingolipid replacement in the membrane, since in flattened and unpacked caveolae diffusion is increased. Finally, upon stretch release, caveolae are re-assembled [135], but the basic mechanism that stays behind this process remains unclear. It has been proposed that “Bin-amphiphysin-Rvs” domain-protein could be involved as actor in caveolae biogenesis [136], so proteins like “protein kinase C and casein kinase substrate in protein neuron 2” could act as precursor-sensors of tension decrease in the membrane. Regarding other invaginations unfolding, there are many examples that show how enhanced phase separation induced by tension increment leads to relocation of anchored and embedded proteins [137]–[141].

- **Compressive stresses (discussion and examples of sensor/transducer cases)**

Compressive stresses could be thought as the opposite of tensile stress stimuli, and they occur typically in two different ways. Mechanically, when the stretch is released compressive solicitation can also be achieved by hyperosmotic treatment, followed by tension decrease [113], [142], [143]. The plasma-membrane tends to bend more its surface in order to accommodate apparent tension decrements [117]. Upon hypertonic treatment, cells passively form dome-like, caveolae and other invaginations structures at the micrometer-scale as a consequence of water expulsion from the inner of the cell, but usually lipid reservoirs don't form [112], [113], [115]. Otherwise, when mechanical de-stretch occurs, cell membrane spontaneously folds in form of sub-micrometer dot-like shaped or longer tubes reservoirs. In this case the plasma-membrane deform locally its structure in order to accommodate the lipid excess originated from compression. Even if unlikely in de-stretching stimuli, in the case of osmotic changes a volume decrease is also involved leading to a minor area exceeding, so other additional membrane structures different from invaginations are not required to compensate the minimal area increment. As a conclusion, in hypertonic treatment, changes both in the cell shape and its volume are involved, but minor effects in plasma-membrane topography have been observed [111].

Like in tensile stress, also in compressive stress lipid re-organization is involved. Tension decrease and subsequent formation of highly curved structures in the bilayer are strongly correlated to lipid domains defects, clustering and sorting. Experiments involving GUVs have shown lipid packing defects formation when highly curved structures are present, both in liquid ordered and liquid disordered phases [144]–[146]. From the theoretical point of view, some correlations between lipid clustering and lipid bilayer curvature have been proposed, and then confirmed by simulations [147].

We will proceed focusing and retrieving the principal actors involved as sensors of compressive stress stimuli. As seen before, the plasma-membrane undergoes deformations upon compression. Sensors that we are introducing are able to detect this highly curved membrane structure, representing indirect measurements of compressive applied stresses. One of the most important compressive stress protein sensors (CPS) is represented by the "Bin-amphiphysin-Rvs" domain-proteins [148]. This wide protein family contains many different types of molecules having their own specific intrinsic curvature: For example, N-BAR protein contain a high intrinsic curvature, and it could be described as a banana-shaped molecule, which interacts strongly in the presence of highly curved membrane-structures, providing a scaffold for this regions. F-BAR domain, similarly to N-BAR domains, acts as support for plasma-membrane curved region having reduce curvature compared to N-BAR protein [149]. Finally, I-BAR protein, could be thought as a bearing with negative curvature [150], opposite to N-BAR and F-BAR domains, which binds to membrane regions having negative curvature. In all three described cases, positive BAR domain binds to negatively charged polar head of lipids, and this process is favored by the fact that both BAR domain and membrane regions have similar intrinsic curvature.

The second type of curvature-sensor actor is represented by amphipathic helix motifs domain. As mentioned before, compressive stress is also able to increase lipid packing/domain defects. These helices present in the cell's inner region in form of soluble proteins, can strongly interact via protein folding in membrane regions enriched of lipid domain defects, acting as defect sensor and screening. One of the first examples discovered is the ARFGAP1 (ADP-ribosylation factor GTPase-activating protein 1) protein [151], which represents a specific protein of a wide range of helix motifs packing-sensor family "ALPS". Nevertheless, there are many examples of protein containing ALPS motifs that behave also as curvature-sensing [152]–[159], like N-BAR domain proteins. It's likely that in proteins containing both ALPS and curvature-sensor domains, the different domains act as curvature detection in a cooperative process [160].

Since now, we have introduced many examples of curvature sensing proteins (CPS), nevertheless these proteins can also induce specific curvature on plasma-membrane [138], [155], [161]. From a theoretical point of view, sensing and inducing curvature are both simultaneous results of the same framework [162]. This framework connects and couple the bilayer free energy, chemical potential of the proteins involved and the curvature topography. For this reason, it is generally impossible to uncouple curvature sensing and

formation, except for extreme cases of highly diluted or crowded protein, or fixing membrane shape. In cell experiments, it has been shown how CPS organization remodel the plasma-membrane and most of related results are focused on CPS inducing-curvature of cellular membrane in order to promote specific cellular functions [163], [164]. Instead, the major experimental works of vitro assays developed since now, have been focused more on the sensing role of CPS protein. For this purpose, sensing of liposomes with different curvature has been studied [158], [159], also tether lipid assay and tether extraction from supported lipid bilayer has been investigated [161], [165]. CPS are capable of recognizing convex and concave curvature, choosing the appropriate intrinsic protein, nevertheless it is more intriguing to investigate the former, which can be analyzed by lipid tether experiments [166]. Only experiments setup that involved models of the plasma-membrane are dedicated to curvature sensing, decoupling curvature induction. In fact, CPS present in cell contain additional domains, many of these have a secondary role in the biochemical signaling cascade process. In most cases it remains unclear if protein recruitment in the curved plasma-membrane regions is produced by sensing process or for other reasons. Nevertheless, it is believed that BAR proteins recruitment in specific curved region to stimulate subsequent mechano-transduction cascade is induced by pre-existing curvature on the membrane, rather in planar region that has been bended by external forces [167].
Finally, there are also example of CPS proteins that act in membrane sensing as response to membrane re-shaping after the application of external mechanical stimuli. This happens in bacteria [168], and studies focused on artificial reconstructed substrate topography [71], [169]. In the latter case specific CPS recruitment occurs, like N-BAR or I-BAR, depending on the shape and size of the substrate pattern. Moreover, topography modification in the membrane can stimulate CPS recruitment and subsequent mechano-transduction cascade, which is concluded by enhanced endocytosis [170].

- **Shear stresses (discussion and examples of sensor/transducer cases)**

Since cells are surrounded by aqueous medium, there are many scenarios where a water flux acts on plasma-membrane surface, like in blood vessels. The flowing medium generates a shear flow on the plasma-membrane. From a theoretical point of view, a shear flow acts on the surface generating a shear stress and a tensile stress at the same time, and it is not possible to disjoint the two types of stresses. Nevertheless, it has been shown experimentally in many different papers that shear flow introduces a fast disordering in the plasma membrane. Furthermore, a specific study has revealed that rapid disordering occurring in the membrane is directly related to shear stress only, rather than to tensile stress [171]. Disordering in the plasma-membrane is associated to increased diffusion both in cells and in GUVs, and the fluidification acts independently on the particular lipid phase considered (Liquid-ordered or Liquid-disordered) [172].
G-proteins family represents an important example of shear stress sensors in the plasma-membrane. In particular, shear stimuli are essential in G-protein activation, since it induces the protein conformational change needed [70]. As mentioned before, upon shear flow, membrane undergoes fluidity increment, which favors G-protein rotational mobility and subsequent conformational change [171].
Shear flow is also responsible in vascular endothelial growth factor receptors and its phosphorylation, nevertheless the exact process involved between shear flow and these receptors is still unclear [171].

Role of lateral tension and fluidity in the plasma-membrane

In previous section we emphasized the different mechanical stimuli arising from external environment directed toward the plasma-membrane. The membrane is continuously exposed to tensile and stretch stresses, or other poking by extracellular matrix, cytoskeleton, or others biochemical imbalance. Now that we tried to address the different mechanical stresses to the mechano-sensing molecules present in the

plasma membrane, in this section we will argue how these mechanical local perturbations and their results perturbate and propagate in surrounding environment of plasma-membrane. More precisely, we will discuss how tension and mechano-sensor transmembrane proteins could diffuse from the point of application of the external stimuli. Think for example about relevant experimental frameworks constituted by micro-pipette aspiration or tether pulling. In this experimental setup we introduced a local perturbation to the membrane, and we could investigate how fast and how far perturbation could propagate. In literature this debate has been deeply treated, resulting sometimes in apparently contradictory results [173]. In fact, analysis of time propagation of tension shows a widely spread timescale, diverging by ~10^6 orders of magnitude comparing papers in the literature. Maybe this drastically high discrepancy among different works could be affected not only by the particular conditions chosen by the authors, but also by active cell response governing its growth and functions. For example, plasma-membrane could regulate transmembrane protein distribution during cell activities, consequently affecting tension propagation.
The first question we can address is: "plasma-membrane is really well reproduced by lipid bilayer model systems regarding mechanical properties ensemble?". In the real cell membrane, the main components are the different phospholipid species, constituting the lipid-bilayer, although, all the other organic molecule, like cholesterol and transmembrane proteins are equally biochemically relevant. In most cases purified lipid bilayers reproduce quite well mechanical features of plasma-membranes, like bending and stretching constant. Nevertheless, some other physical or chemical cell membrane properties could be not well reproduced by purified bilayer models, for example tension propagation. Historically, the first model of the plasma membrane, proposed in 1972, was the "fluid mosaic model" [174]. It considers a liquid lipid bilayer, where transmembrane proteins dispersed inside are able to move freely, and it is mechanically characterized by only two parameters, the bending and the stretching constant, meaning that the system opposes resistance upon in plane and out of plane deformation, but it can flow freely within its own plane. Later on, experimental pieces of evidence have shown that several transmembrane proteins are not able to move freely in the bilayer [175], [176], in particular diffusion coefficient deviation of this proteins emerged between cell membrane and pure bilayer enriched of that proteins [101], [177], [178]. Gradually, successive models [179], [180] added in the bilayer other biological components, taking into account related constrains, like transmembrane protein fixed position or additional specific interaction between two proteins. Every time cell membrane experimental evidence showed additional constrains, these were transferred in revised models. Nevertheless, possible mechanical properties alteration provided by these additional constrain must be also investigated, in order to test actual validity of cell membrane model [173].

• Tension propagation and stretch in membranes

If a membrane is exposed to external pulling or poking and the subsequent balancing flow is impeded, for example by immobilized transmembrane proteins, the membrane will experience a stretching, identified by the stretch modulus E. Experimentally, stretching of membrane is observed every time a change in tension occurs, followed by subsequent area rearrangement. Stretch parameter E is measured comparing tension variation $\Delta\sigma$, and fractional area changes $\Delta A/A$, as defined in [eq: 0]

$$E = \frac{\Delta\sigma}{\frac{\Delta A}{A}} = \frac{\Delta\sigma}{\Delta A} A \ [0]$$

Where A in the dominator constitutes the initial area value. Nevertheless, in this definition we must mention that A includes only membrane region where tension changes are distributed. As a first attempt, we can expose the entire membrane to external tension application, such that A constitutes the initial whole projected area membrane, as performed in [181] using full cell aspiration. Otherwise, when the tension is imposed locally, A must be redefined including regions surrounding the point of application, and A boundaries depending on tension propagation spreading [182]. The crucial question is, in fact, the spreading tension propagation that limits prediction, introducing great uncertainties on A estimation. As we will see afterwards, E experimental estimation arising from purified lipid bilayer (E≈10^5 pN*µm^{-1} [183], [184]) differs

significantly from real cell membrane (E≈40 pN*μm^{-1} [181]) for two fundamental aspects; Firstly, in plasma-membrane are present lipid reservoirs, which dynamically and deeply interfered in A parameter evolution and estimation. Secondary, in E definition [eq: 0] time does not appear explicitly, so we expected E measurement as a constant and intrinsic mechanical property belonging to the membrane, considering the membrane in a physical equilibrium state within measuring time interval. We will see that this assumption is easily applicable on purified lipid bilayer, like GUV, whereas is no more believable in cell membrane context. In a purified and free double layer thermal fluctuation introduce undulations in the membrane topography, which are suddenly suppressed when the membrane is stretched. While fluctuations represent a positive entropy contribution derived from thermal noise, stretching counterbalances decreasing configurational entropy. Experimental findings in pure lipid bilayer, previously cited, show that membrane is almost inextensible under stretching application, and mathematical models for free membrane scenario are in good agreement with experiments [185], more precisely, these models set an upper limit for E estimation. If transmembrane proteins are dislocated into the membrane, they affect deeply stretching modulus estimation for various reasons: proteins able to bend during conformational changes introduces a coupling between their bending properties and membrane stretching. At low tension regime, proteins that introduce bend contribution concordantly to other molecules bending properties, will arise attractive interaction between them, favoring protein clustering [186]. Also changes in conformational entropy of the membrane could favor attractive interaction between bending-sensitive proteins [187]. At high tension regime, large area membrane regions owing elevate curvature are entropically discouraged. Another example is provided by proteins which membrane-bound and free-solution states are governed by membrane tension changes, like BAR-protein previously cited [Compressive stresses sub-section] [110], [141], and alternatively protein could control membrane tension upon bleb formation [182]. Finally, cytoskeleton could deeply interfere in membrane stretching properties, since cytoskeleton elements locally poke and interact to standing above membrane; introducing an “apparent” stretch modulus membrane, which is highly sensitive to cytoskeletal mechanics details [188], [189]. Furthermore, membrane tension could be partially transferred to cytoskeleton-elements, catastrophically changing the tension perceived by mechano-sensing molecule, like ion channels [190]. Finally, as mention above, time does not appear explicitly in E definition [eq: 0]. We can compare the time interval propagation, relaxation and dynamic involved in pure lipid bilayer and in cell membrane. Considering a GUV having a radius r≈10μm, since main thermodynamic process occurring is thermal fluctuation the time expected for the largest wavelength relaxation is Δt≈0.1s [191]. Passing towards real cell membrane, multiple factors must be considered, transmembrane proteins and cytoskeleton in particular. These two main features reduce significantly membrane dynamics, so rearrangements of tension and area need additional time, even up to hour time scales.

Now that we have highlighted the main factors affecting stretching constant in pure bilayer and cell-membrane, we can move towards stretching estimation for real cell membranes. Stretching parameter measurements obtained from tether pulling reveal an irregular behavior gradually increasing extracted tubes length. In fact, this technique shows a complex tension membrane dynamics during tube extraction [175], [191]. For tubes extraction event of length up to ≈10 μm the apparent stretching value is almost zero [191], since the membrane can provide additional lipids amount from internal reservoirs, tension perturbation and subsequent propagation are negligible, while projected area increases [105], [182], [192], [193]. During tube extraction, the force needed to accomplish the process remains almost constant, this is the main reason why there is no net tension propagation in the membrane. Experimental works like [181], showed that continuing tether extraction with further stretch of the tube a not null E value has been observed in the order of E≈40 pN*μm^{-1}. Although this stretching constant is approximatively five orders of magnitude lower than E observed in pure bilayer, it is probable that further tube stretching should exhibit an E value close to that of pure lipid bilayer one. As mentioned above, a stretching constant value E≈10^5 pN*μm^{-1} for pure lipid bilayer implies an almost inextensible membrane, while in cell membrane having a lower stretching constant suggests a major capability to endure external mechanical perturbations. In fact, a lower stretching modulus means a minor resistance upon tension perturbation, more importantly, stretching parameter in cell membrane vary significantly during tether extraction. This first insight shed light on the mechano-protection role of cytoskeleton for the plasma- membrane [190], [194]–[196]. Several pieces of experimental evidence [191] showed that cell membrane stretch have both a plastic and an elastic component behavior. From all

these data, it is highly likely that stretching parameter in cell membrane is not a distinct variable (how it happens in purified bilayer), whereas it results from a superposition of different active responses depending on actual physiological conditions.

• Membrane fluidity: Stokes' theory in 2D and 3D like system

As mentioned in the introduction section, comparing works that analyzed tension propagation in the plasma-membrane suggests completely different rebalancing timescales, passing from almost instantaneous force propagation to the whole membrane, within millisecond [197], to almost no long-range propagation, since it occurs in the order several minutes [175]. First, we will provide some qualitative cues about membrane flow, comparing theoretical predictions for two and three dimensions environments. Membrane will flow, whit a speed v, upon tension gradient $\nabla\sigma$ following equation [eq:1]:

$$v = \frac{k}{\eta}\nabla\sigma \ [1]$$

Where k and η are respectively, the Darcy permeability of the array obstacles present in the membrane (for example transmembrane protein bounded to the cytoskeleton), and the membrane viscosity. In two dimensions the obstacles have planar shape (circular shape for simplicity), and the Darcy permeability k behaves following [eq: 2][17] and is dimensionally expressed as an area.

$$k \approx -\frac{a^2[1+\ln(\Phi)]}{8\Phi} \ [2]$$

where "a" represent the single area obstacle and ϕ constitutes the area fraction of the obstacles ensemble dispersed in the available membrane area, so ϕ parameter is strictly minor than unity. Observing [eq: 2], Darcy permeability is well summarized starting from pure geometrical indexes. For highly diluted obstacles the Darcy permeability in a two dimensions system diverges proportionally to $\phi^{-1}\cdot\ln(\phi^{-1})$ product. If we consider sphere-shaped obstacles, passing to three dimensions system, the Darcy permeability diverge slowly, proportionally to ϕ^{-1} [198], as we will see further, this different behavior between 2D and 3D approaches will lead to deeply significant implications in flow membrane understanding. Before discussing about biological consequences arising from these mathematical discrepancy, we will briefly summarize how mathematical efforts evolved starting from initial findings. Treating viscous liquid framework, in 1851 Stokes developed the drag flow profile of a sphere falling down in a viscous medium [199]. These early studies focused on slow speed regime, when viscous force exceeds inertial contribution (Reynolds number Re<<1), show that the flow speed profile v_f decay asymptotically linearly increasing the distance r from sphere center $v_f \propto r^{-1}$. Passing from three dimensions to two dimensions system, and substituting the flowing sphere with a circular disc the flow speed profile surrounding the object decay asymptotically slower than in the 3D case, proportionally to the logarithm of the distance from disc center: $v_f \propto [\ln(r)]^{-1}$. According to these 2D viscous liquid flow profile results, it is not possible to have a null flow speed far from the disc, unless disc is in static condition, independently of how large are the boundaries containing the fluid. It emerges that boundaries in 2D system affect deeply the flow liquid, introducing the so called "Stokes' paradox". Historically, before the appearance of implications in cell membrane studies, Stokes' paradox directly hindered Einstein diffusion theory in 2D environment for almost 70 years. In 1975 Saffman and Delbrück [200] first considering biological implication of the Stokes' paradox (in a pure 2D membrane all transmembrane protein are unable to diffuse), assuming that the plasma-membrane does not behave as a pure 2D material. Water layers having their own viscosity and surrounding both sides of the membrane contribute to remove logarithmic divergence, ensuring a partial transmembrane diffusion in the membrane. Logarithmic divergence damping occurs above a characteristic length-scale, the so called Saffman-Delbrück length:

$$l = \frac{\mu'}{\mu}h$$

Where μ' constitutes the 3D membrane viscosity, μ is the aqueous medium viscosity, and h is the typical membrane thickness, approximatively 5 nm. Usually the viscosity ration is $\mu'/\mu \approx 100 \div 1000$, consequently the Saffman-Delbrück length $l \approx 1\mu m$, and Saffman-Delbrück theoretical expectation has been confirmed in pure lipid bilayer experiments containing diluted trackers.

In the previous examples we have considered circular and spherical objects in the 2D and 3D scenario respectively, which moving through the viscous fluid, produce a liquid flow around the object edges. We can alternatively describe a liquid flow that encounter a pattern of random static obstacles and ask how the array obstacles affect flow propagation. Boundary conditions require that flow must vanish at the obstacle edges. So, as long as the obstacles are enough dispersed, and the mean distance between two nearest obstacles is higher than Saffman-Delbrück length, the logarithmic divergence quenching is applicable. Thus, for plasma-membrane containing dilute obstacles 3D corrections can be invoked and the boundary condition of null fluid flux at the obstacle edges is verified, while no zero fluid speed is maintained far from obstacles. Instead, for highly packed obstacles array Saffman-Delbrück correction is not applicable, since mean distance between nearest obstacle is negligible if compared to the characteristic length l. In this condition logarithmic divergence dominates, thus is difficult to imagine a not null membrane flux across the obstacles pattern. In other words, Stokes' paradox show us that membrane flow is highly sensitive to immobilized obstacles, even at very low obstacle area fraction ϕ. Similarly, in 3D context where an ensemble of identical objects is moving through the viscous medium; If we considered again a spherical-shaped element, the spheres will diffuse easily in the medium, even at relatively high concentration. If we considered a rod-shaped element, the rods will not diffuse inside the medium, but they will prefer to form aggregates, even at very low concentration regime. In [173] the authors compared how obstacles array affects membrane flow, highlighted by Darcy permeability, and tracker diffusion comparing the different theoretical behavior as a function of the ϕ parameter. They observe a catastrophic decrease of Darcy permeability upon ϕ increment $[10^{-4} \div 0.1]$, of at least 1000-times, while tracker diffusion decreases of about 10-times in the same ϕ interval. This theoretical prediction suggest how diffusion of tracers is less affected by obstacle area fraction, while even for low values of the ϕ parameter, membrane flow could be easily suppressed. In fact, tracer diffusion studies are fairly consistent to theoretical expectations.

Finally, we will provide some cue about membrane flow regulation by the cell itself through transmembrane protein clustering, since Darcy permeability [eq: 1] is highly sensitive to a and ϕ geometrical parameters. In fact [201], [202], receptor clustering is often related to many different downstream signaling. If a given number of N_p of transmembrane protein equally dispersed in the membrane is substituted by several clusters (N), where each single cluster contain N_c transmembrane protein ($N_p = N * N_c$) we expect that Darcy permeability increases by a N_c factor. So, when transmembrane protein ensemble forms cluster, the membrane flow will propagate easily through the obstacles. There are also examples where the fraction of immobilized transmembrane proteins is changed, manipulating ϕ parameter leaving *a* constant [203].

Bibliography

[1] B. Geiger and A. Bershadsky, “Exploring the neighborhood: Adhesion-coupled cell mechanosensors,” *Cell*, vol. 110, no. 2, pp. 139–142, 2002, doi: 10.1016/S0092-8674(02)00831-0.

[2] A. Bershadsky, M. Kozlov, and B. Geiger, “Adhesion-mediated mechanosensitivity: a time to experiment, and a time to theorize,” *Curr. Opin. Cell Biol.*, vol. 18, no. 5, pp. 472–481, 2006, doi: 10.1016/j.ceb.2006.08.012.

[3] B. Geiger, J. P. Spatz, and A. D. Bershadsky, “Environmental sensing through focal adhesions,” *Nat. Rev. Mol. Cell Biol.*, vol. 10, no. 1, pp. 21–33, 2009, doi: 10.1038/nrm2593.

[4] T. Iskratsch, H. Wolfenson, and M. P. Sheetz, “Appreciating force and shape-the rise of mechanotransduction in cell biology,” *Nat. Rev. Mol. Cell Biol.*, vol. 15, no. 12, pp. 825–833, 2014, doi: 10.1038/nrm3903.

[5] V. Vogel and M. Sheetz, “Local force and geometry sensing regulate cell functions,” *Nat. Rev. Mol. Cell Biol.*, vol. 7, no. 4, pp. 265–275, 2006, doi: 10.1038/nrm1890.

[6] S. V. Mikhailenko, Y. Oguchi, and S. Ishiwata, “Insights into the mechanisms of myosin and kinesin molecular motors from the single-molecule unbinding force measurements,” *J. R. Soc. Interface*, vol. 7, no. SUPPL. 3, pp. 295–306, 2010, doi: 10.1098/rsif.2010.0107.focus.

[7] M. Chighizola *et al.*, “Mechanotransduction in neuronal cell development and functioning,” *Nanoscale*, vol. 12, no. 27, pp. 701–720, 2020, doi: 10.1007/s12551-019-00587-2.

[8] C. T. Lim, A. Bershadsky, and P. Sheetz, “Mechanobiology,” no. April, pp. 291–293, 2010.

[9] U. S. Schwarz, “Mechanobiology by the numbers: A close relationship between biology and physics,” *Nat. Rev. Mol. Cell Biol.*, vol. 18, no. 12, pp. 711–712, Dec. 2017, doi: 10.1038/nrm.2017.109.

[10] S. Suresh, “Biomechanics and biophysics of cancer cells,” *Acta Biomater.*, vol. 3, no. 4, pp. 413–438, 2007, doi: 10.1016/j.actbio.2007.04.002.

[11] K. Yoshimura and M. Sokabe, “Mechanosensitivity of ion channels based on protein-lipid interactions,” *J. R. Soc. Interface*, vol. 7, no. SUPPL. 3, 2010, doi: 10.1098/rsif.2010.0095.focus.

[12] A. Mazumder and G. V. Shivashankar, “Emergence of a prestressed eukaryotic nucleus during cellular differentiation and development,” *J. R. Soc. Interface*, vol. 7, no. SUPPL. 3, 2010, doi: 10.1098/rsif.2010.0039.focus.

[13] L. Müller, M. Riediker, P. Wick, M. Mohr, P. Gehr, and B. Rothen-Rutishauser, “Oxidative stress and inflammation response after nanoparticle exposure: Differences between human lung cell monocultures and an advanced three-dimensional model of the human epithelial airways,” *J. R. Soc. Interface*, vol. 7, no. SUPPL. 1, 2010, doi: 10.1098/rsif.2009.0161.focus.

[14] J. H. Kim, L. J. Dooling, and A. R. Asthagiri, “Intercellular mechanotransduction during multicellular morphodynamics,” *J. R. Soc. Interface*, vol. 7, no. SUPPL. 3, 2010, doi: 10.1098/rsif.2010.0066.focus.

[15] M. Makale, “Cellular mechanobiology and cancer metastasis,” *Birth Defects Res. Part C - Embryo Today Rev.*, vol. 81, no. 4, pp. 329–343, 2007, doi: 10.1002/bdrc.20110.

[16] A. J. Engler, S. Sen, H. L. Sweeney, and D. E. Discher, “Matrix Elasticity Directs Stem Cell Lineage Specification,” *Cell*, vol. 126, no. 4, pp. 677–689, 2006, doi: 10.1016/j.cell.2006.06.044.

[17] R. J. Pelham, Y. L. Wang, F. G. M. Russel, J. M. Bindels, and C. H. Van, “Cell locomotion and focal adhesions are regulated by substrate flexibility,” *Proc. Natl. Acad. Sci.*, vol. 94, no. 25, pp. 13661–13665, Dec. 1997, doi: 10.1073/pnas.94.25.13661.

[18] N. Q. et al Balaban, “Force and focal adhesion assembly: a close relationship studied using elastic

micropatterned substrates," *Nat. Cell Biol.*, vol. 3, pp. 466–473, 2001, doi: 10.1053/j.gastro.2004.10.010.
[19] S. E. Lee, R. D. Kamm, and M. R. K. Mofrad, "Force-induced activation of Talin and its possible role in focal adhesion mechanotransduction," *J. Biomech.*, vol. 40, no. 9, pp. 2096–2106, 2007, doi: 10.1016/j.jbiomech.2007.04.006.
[20] C. Ciobanasu, B. Faivre, and C. Le Clainche, "Actomyosin-dependent formation of the mechanosensitive talin-vinculin complex reinforces actin anchoring," *Nat. Commun.*, vol. 5, p. 3095, 2014, doi: 10.1038/ncomms4095.
[21] M. Yao, B. T. Goult, H. Chen, P. Cong, M. P. Sheetz, and J. Yan, "Mechanical activation of vinculin binding to talin locks talin in an unfolded conformation," *Sci. Rep.*, vol. 4, 2014, doi: 10.1038/srep04610.
[22] B. Coste *et al.*, "Piezo1 and Piezo2 Are Essential Components of Distinct Mechanically Activated Cation Channels," *Science*, vol. 330, no. October, pp. 7–12, 2010.
[23] M. A. Schwartz, "Integrins and Extracellular Matrix in Mechanotransduction," *Cold Spring Harb Perspect Biol*, pp. 1–13, 2010, doi: 10.2147/CHC.S21829.
[24] U. S. Schwarz and M. L. Gardel, "United we stand - Integrating the actin cytoskeleton and cell-matrix adhesions in cellular mechanotransduction," *J. Cell Sci.*, vol. 125, no. 13, pp. 3051–3060, 2012, doi: 10.1242/jcs.093716.
[25] J. Z. Kechagia, J. Ivaska, and P. Roca-Cusachs, "Integrins as biomechanical sensors of the microenvironment," *Nat. Rev. Mol. Cell Biol.*, vol. 20, no. 8, pp. 457–473, 2019, doi: 10.1038/s41580-019-0134-2.
[26] A. W. Holle *et al.*, "Cell-Extracellular Matrix Mechanobiology: Forceful Tools and Emerging Needs for Basic and Translational Research," *Nano Lett.*, vol. 18, no. 1, pp. 1–8, 2018, doi: 10.1021/acs.nanolett.7b04982.
[27] D. Y. M. Leung, S. Glagov, and M. B. Mathews, "A new in vitro system for studying cell response to mechanical stimulation," *Exp. Cell Res.*, vol. 109, no. 2, pp. 285–298, 1977, doi: 10.1016/0014-4827(77)90008-8.
[28] M. Reichenbach, K. Reimann, and H. Reuter, "Gene expression in response to cyclic mechanical stretch in primary human dermal fibroblasts," *Genomics Data*, vol. 2, pp. 335–339, 2014, doi: 10.1016/j.gdata.2014.09.010.
[29] T. Korff, K. Aufgebauer, and M. Hecker, "Cyclic stretch controls the expression of CD40 in endothelial cells by changing their transforming growth factor-β1 response," *Circulation*, vol. 116, no. 20, pp. 2288–2297, 2007, doi: 10.1161/CIRCULATIONAHA.107.730309.
[30] S. Lehoux and A. Tedgui, "Cellular mechanics and gene expression in blood vessels," *J. Biomech.*, vol. 36, no. 5, pp. 631–643, 2003, doi: 10.1016/S0021-9290(02)00441-4.
[31] K. Hayakawa, N. Sato, and T. Obinata, "Dynamic reorientation of cultured cells and stress fibers under mechanical stress from periodic stretching," *Exp. Cell Res.*, vol. 268, no. 1, pp. 104–114, 2001, doi: 10.1006/excr.2001.5270.
[32] K. Kurpinski, J. Chu, C. Hashi, and S. Li, "Anisotropic mechanosensing by mesenchymal stem cells," *Proc. Natl. Acad. Sci. U. S. A.*, vol. 103, no. 44, pp. 16095–16100, 2006, doi: 10.1073/pnas.0604182103.
[33] V. P. Shirinsky *et al.*, "Mechano-chemical control of human endothelium orientation and size," *J. Cell Biol.*, vol. 109, no. 1, pp. 331–339, 1989, doi: 10.1083/jcb.109.1.331.
[34] B. Liu *et al.*, "Role of cyclic strain frequency in regulating the alignment of vascular smooth muscle cells in vitro," *Biophys. J.*, vol. 94, no. 4, pp. 1497–1507, 2008, doi: 10.1529/biophysj.106.098574.
[35] U. S. Kaunas R, Nguyen P, R. Kaunas, P. Nguyen, S. Usami, and S. Chien, "Cooperative effects of Rho and mechanical stretch on stress fiber organization," *Proc Natl Acad Sci U S A. 2005 Nov 1;102(44)15895-900.*, vol. 102, no. 44, p. 900, 2005, doi: 10.1073/pnas.0506041102.
[36] R. A. Brown, R. Prajapati, D. A. McGrouther, I. V. Yannas, and M. Eastwood, "Tensional homeostasis in dermal fibroblasts: Mechanical responses to mechanical loading in three-dimensional substrates," *J. Cell. Physiol.*, vol. 175, no. 3, pp. 323–332, 1998, doi: 10.1002/(SICI)1097-4652(199806)175:3<323::AID-JCP10>3.0.CO;2-6.

[37] K. D. Webster, W. P. Ng, and D. A. Fletcher, “Tensional homeostasis in single fibroblasts,” *Biophys. J.*, vol. 107, no. 1, pp. 146–155, 2014, doi: 10.1016/j.bpj.2014.04.051.
[38] H. Kamble, M. J. Barton, M. Jun, S. Park, and N. T. Nguyen, “Cell stretching devices as research tools: Engineering and biological considerations,” *Lab Chip*, vol. 16, no. 17, pp. 3193–3203, 2016, doi: 10.1039/c6lc00607h.
[39] B. D. Hoffman, C. Grashoff, and M. A. Schwartz, “Dynamic molecular processes mediate cellular mechanotransduction,” *Nature*, vol. 475, no. 7356, pp. 316–323, 2011, doi: 10.1038/nature10316.
[40] J. I. Andersen, C. P. Pennisi, T. Fink, and V. Zachar, “Focal Adhesion Kinase Activation Is Necessary for Stretch-Induced Alignment and Enhanced Differentiation of Myogenic Precursor Cells,” *Tissue Eng. - Part A*, vol. 24, no. 7–8, pp. 631–640, 2018, doi: 10.1089/ten.tea.2017.0137.
[41] Y. Wang, J. Yan, and B. T. Goult, “Force-Dependent Binding Constants,” *Biochemistry*, vol. 58, no. 47, pp. 4696–4709, 2019, doi: 10.1021/acs.biochem.9b00453.
[42] E. Evans, “Probing the Relation Between Force Lifetime and Chemistry,” *Annu. Rev. Biophys. Biomol. Struct.*, vol. 30, pp. 105–128, 2001.
[43] B. T. Marshall, M. Long, J. W. Piper, T. Yago, R. P. McEver, and C. Zhu, “Direct observation of catch bonds involving cell-adhesion molecules,” *Nature*, vol. 423, no. 6936, pp. 190–193, 2003, doi: 10.1038/nature01605.
[44] F. et al. Bosveld, “Mechanical Control of Morphogenesis by Fat/Dachsous/Four-Jointed Planar Cell Polarity Pathway,” *Science (80-.).*, vol. 336, no. May, pp. 724–728, 2012, doi: 10.1101/2020.01.06.896266.
[45] Y. A. Miroshnikova *et al.*, “Tissue mechanics promote IDH1-dependent HIF1α-tenascin C feedback to regulate glioblastoma aggression,” *Nat. Cell Biol.*, vol. 18, no. 12, pp. 1336–1345, 2016, doi: 10.1038/ncb3429.
[46] R. Sunyer *et al.*, “Collective cell durotaxis emerges from long-range intercellular force transmission,” *Science (80-.).*, vol. 353, no. 6304, pp. 1157–1161, 2016, doi: 10.1126/science.aaf7119.
[47] D. Ng *et al.*, *The Vibrio cholerae Minor Pilin TcpB Initiates Assembly and Retraction of the Toxin-Coregulated Pilus*, vol. 12, no. 12. 2016.
[48] T. Betz, D. Koch, Y. B. Lu, K. Franze, and J. A. Käs, “Growth cones as soft and weak force generators,” *Proc. Natl. Acad. Sci. U. S. A.*, vol. 108, no. 33, pp. 13420–13425, 2011, doi: 10.1073/pnas.1106145108.
[49] P. Roca-Cusachs, V. Conte, and X. Trepat, “Quantifying forces in cell biology,” *Nat. Cell Biol.*, vol. 19, no. 7, pp. 742–751, 2017, doi: 10.1038/ncb3564.
[50] P. Roca-Cusachs, T. Iskratsch, and M. P. Sheetz, “Finding the weakest link-exploring integrin-mediated mechanical molecular pathways,” *J. Cell Sci.*, vol. 125, no. 13, pp. 3025–3038, 2012, doi: 10.1242/jcs.095794.
[51] B. Ladoux, W. J. Nelson, J. Yan, and R. M. Mège, “The mechanotransduction machinery at work at adherens junctions,” *Integr. Biol. (United Kingdom)*, vol. 7, no. 10, pp. 1109–1119, 2015, doi: 10.1039/c5ib00070j.
[52] Y. L. Wang, “Exchange of actin subunits at the leading edge of living fibroblasts: Possible role of treadmilling,” *J. Cell Biol.*, vol. 101, no. 2, pp. 597–602, 1985, doi: 10.1083/jcb.101.2.597.
[53] J. A. and mitchison T. J. Theriot, “Actin microfilamnt dynamics in locomoting cells,” *Nature*, vol. 352. pp. 126–131, 1991.
[54] Y. J. Liu *et al.*, “Differential Transmission of Actin Motion Within Focal Adhesions,” no. January, pp. 111–116, 2007.
[55] L. M. Owen *et al.*, “A cytoskeletal clutch mediates cellular force transmission in a soft, three-dimensional extracellular matrix,” *Mol. Biol. Cell*, vol. 28, no. 14, pp. 1959–1974, 2017, doi: 10.1091/mbc.E17-02-0102.
[56] C. H. Lin and P. Forscher, “Growth cone advance is inversely proportional to retrograde F-actin flow,” *Neuron*, vol. 14, no. 4, pp. 763–771, 1995, doi: 10.1016/0896-6273(95)90220-1.
[57] B. Liu, T. J. Kim, and Y. Wang, “Live cell imaging of mechanotransduction,” *J. R. Soc. Interface*, vol. 7, no. SUPPL. 3, 2010, doi: 10.1098/rsif.2010.0042.focus.
[58] H. B. Schiller *et al.*, “β 1 - And α v -class integrins cooperate to regulate myosin II during rigidity

sensing of fibronectin-based microenvironments," *Nat. Cell Biol.*, vol. 15, no. 6, pp. 625–636, 2013, doi: 10.1038/ncb2747.
[59] A. Elosegui-Artola *et al.*, "Rigidity sensing and adaptation through regulation of integrin types," *Nat. Mater.*, vol. 13, no. 6, pp. 631–637, 2014, doi: 10.1038/nmat3960.
[60] P. Roca-Cusachs, A. Del Rio, E. Puklin-Faucher, N. C. Gauthier, N. Biais, and M. P. Sheetz, "Integrin-dependent force transmission to the extracellular matrix by α-actinin triggers adhesion maturation," *Proc. Natl. Acad. Sci. U. S. A.*, vol. 110, no. 15, 2013, doi: 10.1073/pnas.1220723110.
[61] A. J. Ehrlicher, F. Nakamura, J. H. Hartwig, D. A. Weitz, and T. P. Stossel, "Mechanical strain in actin networks regulates FilGAP and integrin binding to filamin A," *Nature*, vol. 478, no. 7368, pp. 260–263, 2011, doi: 10.1038/nature10430.
[62] K. Clark *et al.*, "Tensin 2 modulates cell contractility in 3D collagen gels through the RhoGAP DLC1," *J. Cell. Biochem.*, vol. 109, no. 4, pp. 808–817, 2010, doi: 10.1002/jcb.22460.
[63] M. Theodosiou *et al.*, "Kindlin-2 cooperates with talin to activate integrins and induces cell spreading by directly binding paxillin," *Elife*, vol. 5, no. JANUARY2016, pp. 1–24, 2016, doi: 10.7554/eLife.10130.
[64] A. Elosegui-Artola *et al.*, "Mechanical regulation of a molecular clutch defines force transmission and transduction in response to matrix rigidity," *Nat. Cell Biol.*, vol. 18, no. 5, pp. 540–548, 2016, doi: 10.1038/ncb3336.
[65] K. Austen *et al.*, "Extracellular rigidity sensing by talin isoform-specific mechanical linkages," *Nat. Cell Biol.*, vol. 17, no. 12, pp. 1597–1606, 2015, doi: 10.1038/ncb3268.
[66] P. Ringer *et al.*, "Multiplexing molecular tension sensors reveals piconewton force gradient across talin-1," *Nat. Methods*, vol. 14, no. 11, pp. 1090–1096, 2017, doi: 10.1038/nmeth.4431.
[67] C. Grashoff *et al.*, "Measuring mechanical tension across vinculin reveals regulation of focal adhesion dynamics," *Nature*, vol. 466, no. 7303, pp. 263–266, 2010, doi: 10.1038/nature09198.
[68] A. Carisey *et al.*, "Vinculin regulates the recruitment and release of core focal adhesion proteins in a force-dependent manner," *Curr. Biol.*, vol. 23, no. 4, pp. 271–281, 2013, doi: 10.1016/j.cub.2013.01.009.
[69] D. W. Dumbauld *et al.*, "How vinculin regulates force transmission," *Proc. Natl. Acad. Sci. U. S. A.*, vol. 110, no. 24, pp. 9788–9793, 2013, doi: 10.1073/pnas.1216209110.
[70] Z. Sun *et al.*, "Kank2 activates talin, reduces force transduction across integrins and induces central adhesion formation," *Nat. Cell Biol.*, vol. 18, no. 9, pp. 941–953, 2016, doi: 10.1038/ncb3402.
[71] W. Zhao *et al.*, "Nanoscale manipulation of membrane curvature for probing endocytosis in live cells," *Nat. Nanotechnol.*, vol. 12, no. 8, pp. 750–756, 2017, doi: 10.1038/nnano.2017.98.
[72] C. Bertocchi *et al.*, "Nanoscale architecture of cadherin-based cell adhesions," *Nat. Cell Biol.*, vol. 19, no. 1, pp. 28–37, 2017, doi: 10.1038/ncb3456.
[73] C. E. Chan and D. J. Odde, "Traction dynamics of filopodia on compliant substrates," *Science (80-.).*, vol. 322, no. 5908, pp. 1687–1691, 2008, doi: 10.1126/science.1163595.
[74] B. L. Bangasser, S. S. Rosenfeld, and D. J. Odde, "Determinants of maximal force transmission in a motor-clutch model of cell traction in a compliant microenvironment," *Biophys. J.*, vol. 105, no. 3, pp. 581–592, 2013, doi: 10.1016/j.bpj.2013.06.027.
[75] J. Escribano, M. T. Sánchez, and J. M. García-Aznar, "A discrete approach for modeling cell–matrix adhesions," *Comput. Part. Mech.*, vol. 1, no. 2, pp. 117–130, 2014, doi: 10.1007/s40571-014-0006-7.
[76] B. Sabass and U. S. Schwarz, "Modeling cytoskeletal flow over adhesion sites: Competition between stochastic bond dynamics and intracellular relaxation," *J. Phys. Condens. Matter*, vol. 22, no. 19, 2010, doi: 10.1088/0953-8984/22/19/194112.
[77] B. L. Bangasser and D. J. Odde, "Master equation-based analysis of a motor-clutch model for cell traction force," *Cell. Mol. Bioeng.*, vol. 6, no. 4, pp. 449–459, 2013, doi: 10.1007/s12195-013-0296-5.
[78] M. Ghibaudo *et al.*, "Traction forces and rigidity sensing regulate cell functions," *Soft Matter*, vol. 4, no. 9, pp. 1836–1843, 2008, doi: 10.1039/b804103b.
[79] P. Sens, "Rigidity sensing by stochastic sliding friction," *Epl*, vol. 104, no. 3, 2013, doi: 10.1209/0295-5075/104/38003.
[80] M. Srinivasan and S. Walcott, "Binding site models of friction due to the formation and rupture of

bonds: State-function formalism, force-velocity relations, response to slip velocity transients, and slip stability," *Phys. Rev. E - Stat. Nonlinear, Soft Matter Phys.*, vol. 80, no. 4, pp. 1–15, 2009, doi: 10.1103/PhysRevE.80.046124.

[81] M. L. Gardel, B. Sabass, L. Ji, G. Danuser, U. S. Schwarz, and C. M. Waterman, "Traction stress in focal adhesions correlates biphasically with actin retrograde fl ow speed," *J. Cell Biol.*, vol. 183, no. 6, pp. 999–1005, 2008, doi: 10.1083/jcb.200810060.

[82] J. E. Molloy, J. E. Burns, B. Kendrick-Jones, R. T. Tregear, and D. C. S. White, "Movement and force produced by a single myosin head," *Nature*, vol. 378, no. 6553. pp. 209–212, 1995, doi: 10.1038/378209a0.

[83] Y. Aratyn-Schaus and M. L. Gardel, "Transient frictional slip between integrin and the ECM in focal adhesions under myosin II tension," *Curr. Biol.*, vol. 20, no. 13, pp. 1145–1153, 2010, doi: 10.1016/j.cub.2010.05.049.

[84] M. Ishibashi *et al.*, "Integrin LFA-1 regulates cell adhesion via transient clutch formation," *Biochem. Biophys. Res. Commun.*, vol. 464, no. 2, pp. 459–466, 2015, doi: 10.1016/j.bbrc.2015.06.155.

[85] G. Jiang, G. Giannone, D. R. Critchley, E. Fukumoto, and M. P. Sheet, "Two-piconewton slip bond between fibronectin and the cytoskeleton depends on talin," *Nature*, vol. 424, no. 6946, pp. 334–337, 2003, doi: 10.1038/nature01805.

[86] A. Elosegui-Artola, X. Trepat, and P. Roca-Cusachs, "Control of Mechanotransduction by Molecular Clutch Dynamics," *Trends Cell Biol.*, vol. 28, no. 5, pp. 356–367, 2018, doi: 10.1016/j.tcb.2018.01.008.

[87] M. F. Fournier, R. Sauser, D. Ambrosi, J. J. Meister, and A. B. Verkhovsky, "Force transmission in migrating cells," *J. Cell Biol.*, vol. 188, no. 2, pp. 287–297, 2010, doi: 10.1083/jcb.200906139.

[88] J. P. Califano and C. A. Reinhart-King, "Substrate stiffness and cell area predict cellular traction stresses in single cells and cells in contact," *Cell. Mol. Bioeng.*, vol. 3, no. 1, pp. 68–75, 2010, doi: 10.1007/s12195-010-0102-6.

[89] S. Ghassemi *et al.*, "Cells test substrate rigidity by local contractions on submicrometer pillars," *Proc. Natl. Acad. Sci. U. S. A.*, vol. 109, no. 14, pp. 5328–5333, 2012, doi: 10.1073/pnas.1119886109.

[90] B. L. Bangasser *et al.*, "Shifting the optimal stiffness for cell migration," *Nat. Commun.*, vol. 8, no. May, pp. 1–10, 2017, doi: 10.1038/ncomms15313.

[91] A. H. Mekhdjian *et al.*, "Integrin-mediated traction force enhances paxillin molecular associations and adhesion dynamics that increase the invasiveness of tumor cells into a three-dimensional extracellular matrix," *Mol. Biol. Cell*, vol. 28, no. 11, pp. 1467–1488, 2017, doi: 10.1091/mbc.E16-09-0654.

[92] M. Bennett, M. Cantini, J. Reboud, J. M. Cooper, P. Roca-Cusachs, and M. Salmeron-Sanchez, "Molecular clutch drives cell response to surface viscosity," *Proc. Natl. Acad. Sci. U. S. A.*, vol. 115, no. 6, pp. 1192–1197, 2018, doi: 10.1073/pnas.1710653115.

[93] G. I. Bell, "Models for the Specific Adhesion of Cells to Cells," *Adv. Appl. Probab.*, vol. 12, no. 3, pp. 566–567, 1978, doi: 10.1017/s0001867800035254.

[94] P. Atherton, B. Stutchbury, D. Jethwa, and C. Ballestrem, "Mechanosensitive components of integrin adhesions: Role of vinculin," *Exp. Cell Res.*, vol. 343, no. 1, pp. 21–27, 2016, doi: 10.1016/j.yexcr.2015.11.017.

[95] S. V. Plotnikov, A. M. Pasapera, B. Sabass, and C. M. Waterman, "Force fluctuations within focal adhesions mediate ECM-rigidity sensing to guide directed cell migration," *Cell*, vol. 151, no. 7, pp. 1513–1527, 2012, doi: 10.1016/j.cell.2012.11.034.

[96] X. Serra-Picamal *et al.*, "Mechanical waves during tissue expansion," *Nat. Phys.*, vol. 8, no. 8, pp. 628–634, 2012, doi: 10.1038/nphys2355.

[97] G. Meacci *et al.*, "α-Actinin links extracellular matrix rigidity-sensing contractile units with periodic cell-edge retractions," *Mol. Biol. Cell*, vol. 27, no. 22, pp. 3471–3479, 2016, doi: 10.1091/mbc.E16-02-0107.

[98] Z. Wu, S. V. Plotnikov, A. Y. Moalim, C. M. Waterman, and J. Liu, "Two Distinct Actin Networks Mediate Traction Oscillations to Confer Focal Adhesion Mechanosensing," *Biophys. J.*, vol. 112, no. 4, pp. 780–794, 2017, doi: 10.1016/j.bpj.2016.12.035.

[99] R. Oria *et al.*, “Force loading explains spatial sensing of ligands by cells,” *Nature*, vol. 552, no. 7684, pp. 219–224, 2017, doi: 10.1038/nature24662.
[100] T. Oliver, M. Dembo, and K. Jacobson, “Separation of propulsive and adhesive traction stresses in locomoting keratocytes,” *J. Cell Biol.*, vol. 145, no. 3, pp. 589–604, 1999, doi: 10.1083/jcb.145.3.589.
[101] J. Lee, A. Ishihara, J. A. Theriot, and K. Jacobson, “Principles of locomotion for simple-shaped cells,” *Nature*, vol. 362, no. 6416, pp. 167–171, 1993, doi: 10.1038/362167a0.
[102] B. Pontes *et al.*, “Membrane tension controls adhesion positioning at the leading edge of cells,” *J. Cell Biol.*, vol. 216, no. 9, pp. 2959–2977, 2017, doi: 10.1083/jcb.201611117.
[103] P. Chugh *et al.*, “Actin cortex architecture regulates cell surface tension,” *Nat. Cell Biol.*, vol. 19, no. 6, pp. 689–697, 2017, doi: 10.1038/ncb3525.
[104] C. Simon, V. Caorsi, C. Campillo, and C. Sykes, “Interplay between membrane tension and the actin cytoskeleton determines shape changes,” *Phys. Biol.*, vol. 15, no. 6, 2018, doi: 10.1088/1478-3975/aad1ab.
[105] N. C. Gauthier, M. A. Fardin, P. Roca-Cusachs, and M. P. Sheetz, “Temporary increase in plasma membrane tension coordinates the activation of exocytosis and contraction during cell spreading,” *Proc. Natl. Acad. Sci. U. S. A.*, vol. 108, no. 35, pp. 14467–14472, 2011, doi: 10.1073/pnas.1105845108.
[106] A. D. Lieber, Y. Schweitzer, M. M. Kozlov, and K. Keren, “Front-to-rear membrane tension gradient in rapidly moving cells,” *Biophys. J.*, vol. 108, no. 7, pp. 1599–1603, 2015, doi: 10.1016/j.bpj.2015.02.007.
[107] A. D. Lieber, S. Yehudai-Resheff, E. L. Barnhart, J. A. Theriot, and K. Keren, “Membrane tension in rapidly moving cells is determined by cytoskeletal forces,” *Curr. Biol.*, vol. 23, no. 15, pp. 1409–1417, 2013, doi: 10.1016/j.cub.2013.05.063.
[108] J. H. R. Hetmanski *et al.*, “Membrane Tension Orchestrates Rear Retraction in Matrix-Directed Cell Migration,” *Dev. Cell*, vol. 51, no. 4, pp. 460-475.e10, 2019, doi: 10.1016/j.devcel.2019.09.006.
[109] A. R. Houk *et al.*, “Membrane tension maintains cell polarity by confining signals to the leading edge during neutrophil migration,” *Cell*, vol. 148, no. 1–2, pp. 175–188, 2012, doi: 10.1016/j.cell.2011.10.050.
[110] K. Tsujita, T. Takenawa, and T. Itoh, “Feedback regulation between plasma membrane tension and membrane-bending proteins organizes cell polarity during leading edge formation,” *Nat. Cell Biol.*, vol. 17, no. 6, pp. 749–758, 2015, doi: 10.1038/ncb3162.
[111] A. Pietuch, B. R. Brückner, and A. Janshoff, “Membrane tension homeostasis of epithelial cells through surface area regulation in response to osmotic stress,” *Biochim. Biophys. Acta - Mol. Cell Res.*, vol. 1833, no. 3, pp. 712–722, 2013, doi: 10.1016/j.bbamcr.2012.11.006.
[112] A. J. Kosmalska *et al.*, “Physical principles of membrane remodelling during cell mechanoadaptation,” *Nat. Commun.*, vol. 6, 2015, doi: 10.1038/ncomms8292.
[113] J. Dai, M. P. Sheetz, X. Wan, and C. E. Morris, “Membrane tension in swelling and shrinking molluscan neurons,” *J. Neurosci.*, vol. 18, no. 17, pp. 6681–6692, 1998, doi: 10.1523/jneurosci.18-17-06681.1998.
[114] N. E. Vlahakis, M. A. Schroeder, R. E. Pagano, and R. D. Hubmayr, “Role of deformation-induced lipid trafficking in the prevention of plasma membrane stress failure,” *Am. J. Respir. Crit. Care Med.*, vol. 166, no. 9, pp. 1282–1289, 2002, doi: 10.1164/rccm.200203-207OC.
[115] C. E. Morris and U. Homann, “Cell surface area regulation and membrane tension,” *J. Membr. Biol.*, vol. 179, no. 2, pp. 79–102, 2001, doi: 10.1007/s002320010040.
[116] R. Alert, J. Casademunt, J. Brugués, and P. Sens, “Model for probing membrane-cortex adhesion by micropipette aspiration and fluctuation spectroscopy,” *Biophys. J.*, vol. 108, no. 8, pp. 1878–1886, 2015, doi: 10.1016/j.bpj.2015.02.027.
[117] O. P. Hamill and B. Martinac, “Molecular basis of mechanotransduction in living cells,” *Physiol. Rev.*, vol. 81, no. 2, pp. 685–740, 2001, doi: 10.1152/physrev.2001.81.2.685.
[118] A. G. Clark, O. Wartlick, G. Salbreux, and E. K. Paluch, “Stresses at the cell surface during animal cell morphogenesis,” *Curr. Biol.*, vol. 24, no. 10, pp. R484–R494, 2014, doi: 10.1016/j.cub.2014.03.059.
[119] J. L. Fisher, I. Levitan, and S. S. Margulies, “Plasma membrane surface increases with tonic stretch of

alveolar epithelial cells," *Am. J. Respir. Cell Mol. Biol.*, vol. 31, no. 2 I, pp. 200–208, 2004, doi: 10.1165/rcmb.2003-0224OC.
[120] N. Groulx, F. Boudreault, S. N. Orlov, and R. Grygorczyk, "Membrane reserves and hypotonic cell swelling," *J. Membr. Biol.*, vol. 214, no. 1–2, pp. 43–56, 2006, doi: 10.1007/s00232-006-0080-8.
[121] T. Van der Wijk, S. F. B. Tomassen, A. B. Houtsmuller, H. R. De Jonge, and B. C. Tilly, "Increased vesicle recycling in response to osmotic cell swelling. Cause and consequence of hypotonicity-provoked ATP release," *J. Biol. Chem.*, vol. 278, no. 41, pp. 40020–40025, 2003, doi: 10.1074/jbc.M307603200.
[122] N. E. Vlahakis, M. A. Schroeder, R. E. Pagano, and R. D. Hubmayr, "Deformation-induced lipid trafficking in alveolar epithelial cells," *Am. J. Physiol. - Lung Cell. Mol. Physiol.*, vol. 280, no. 5 25-5, pp. 938–946, 2001, doi: 10.1152/ajplung.2001.280.5.l938.
[123] M. A. A. Jumaa, S. Dewitt, and M. B. Hallett, "Topographical interrogation of the living cell surface reveals its role in rapid cell shape changes during phagocytosis and spreading," *Sci. Rep.*, vol. 7, no. 1, pp. 1–11, 2017, doi: 10.1038/s41598-017-09761-6.
[124] S. S. Ranade, R. Syeda, and A. Patapoutian, "Mechanically Activated Ion Channels," *Neuron*, vol. 87, no. 6, pp. 1162–1179, 2015, doi: 10.1016/j.neuron.2015.08.032.
[125] A. R. Battle, P. Ridone, N. Bavi, Y. Nakayama, Y. A. Nikolaev, and B. Martinac, "Lipid-protein interactions: Lessons learned from stress," *Biochim. Biophys. Acta - Biomembr.*, vol. 1848, no. 9, pp. 1744–1756, 2015, doi: 10.1016/j.bbamem.2015.04.012.
[126] F. Sachs, "Mechanical Transduction and the Dark Energy of Biology," *Biophys. J.*, vol. 114, no. 1, pp. 3–9, 2018, doi: 10.1016/j.bpj.2017.10.035.
[127] B. Martinac *et al.*, "Tuning ion channel mechanosensitivity by asymmetry of the transbilayer pressure profile," *Biophys. Rev.*, vol. 10, no. 5, pp. 1377–1384, 2018, doi: 10.1007/s12551-018-0450-3.
[128] A. H. Lewis and J. Grandl, "Mechanical sensitivity of Piezo1 ion channels can be tuned by cellular membrane tension," *Elife*, vol. 4, no. December2015, pp. 1–17, 2015, doi: 10.7554/eLife.12088.
[129] K. A. Gerhold and M. A. Schwartz, "Ion channels in endothelial responses to fluid shear stress," *Physiology*, vol. 31, no. 5, pp. 359–369, 2016, doi: 10.1152/physiol.00007.2016.
[130] Y. R. Guo and R. MacKinnon, "Structure-based membrane dome mechanism for piezo mechanosensitivity," *Elife*, vol. 6, pp. 1–19, 2017, doi: 10.7554/eLife.33660.
[131] E. S. Haswell, R. Phillips, and D. C. Rees, "Mechanosensitive channels: What can they do and how do they do it?," *Structure*, vol. 19, no. 10, pp. 1356–1369, 2011, doi: 10.1016/j.str.2011.09.005.
[132] A. L. Le Roux, X. Quiroga, N. Walani, M. Arroyo, and P. Roca-Cusachs, "The plasma membrane as a mechanochemical transducer," *Philos. Trans. R. Soc. B Biol. Sci.*, vol. 374, no. 1779, 2019, doi: 10.1098/rstb.2018.0221.
[133] L. Kozera, E. White, and S. Calaghan, "Caveolae act as membrane reserves which limit mechanosensitive ICl,swell channel activation during swelling in the rat ventricular myocyte," *PLoS One*, vol. 4, no. 12, 2009, doi: 10.1371/journal.pone.0008312.
[134] O. L. Gervásio, W. D. Phillips, L. Cole, and D. G. Allen, "Caveolae respond to cell stretch and contribute to stretch-induced signaling," *J. Cell Sci.*, vol. 124, no. 21, pp. 3581–3590, 2011, doi: 10.1242/jcs.084376.
[135] B. Sinha *et al.*, "Cells respond to mechanical stress by rapid disassembly of caveolae," *Cell*, vol. 144, no. 3, pp. 402–413, 2011, doi: 10.1016/j.cell.2010.12.031.
[136] R. G. Parton and M. A. Del Pozo, "Caveolae as plasma membrane sensors, protectors and organizers," *Nat. Rev. Mol. Cell Biol.*, vol. 14, no. 2, pp. 98–112, 2013, doi: 10.1038/nrm3512.
[137] A. Diz-Muñoz *et al.*, "Membrane Tension Acts Through PLD2 and mTORC2 to Limit Actin Network Assembly During Neutrophil Migration," *PLoS Biol.*, vol. 14, no. 6, pp. 1–30, 2016, doi: 10.1371/journal.pbio.1002474.
[138] M. P. Sheetz, J. E. Sable, and H. G. Döbereiner, "Continuous membrane-cytoskeleton adhesion requires continuous accommodation to lipid and cytoskeleton dynamics," *Annu. Rev. Biophys. Biomol. Struct.*, vol. 35, pp. 417–434, 2006, doi: 10.1146/annurev.biophys.35.040405.102017.
[139] M. Vidal-Quadras *et al.*, "Endocytic turnover of Rab8 controls cell polarization," *J. Cell Sci.*, vol. 130,

no. 6, pp. 1147–1157, 2017, doi: 10.1242/jcs.195420.
[140] P. Y. Tan and R. Zaidel-Bar, “Transient membrane localization of SPV-1 drives cyclical actomyosin contractions in the C elegans spermatheca,” *Curr. Biol.*, vol. 25, no. 2, pp. 141–151, 2015, doi: 10.1016/j.cub.2014.11.033.
[141] M. Simunovic and G. A. Voth, “Membrane tension controls the assembly of curvature-generating proteins,” *Nat. Commun.*, vol. 6, no. May, 2015, doi: 10.1038/ncomms8219.
[142] K. Xie, Y. Yang, and H. Jiang, “Controlling Cellular Volume via Mechanical and Physical Properties of Substrate,” *Biophys. J.*, vol. 114, no. 3, pp. 675–687, 2018, doi: 10.1016/j.bpj.2017.11.3785.
[143] M. Riggi *et al.*, “Decrease in plasma membrane tension triggers PtdIns(4,5)P 2 phase separation to inactivate TORC2,” *Nat. Cell Biol.*, vol. 20, no. 9, pp. 1043–1051, 2018, doi: 10.1038/s41556-018-0150-z.
[144] N. S. Hatzakis *et al.*, “How curved membranes recruit amphipathic helices and protein anchoring motifs,” *Nat. Chem. Biol.*, vol. 5, no. 11, pp. 835–841, 2009, doi: 10.1038/nchembio.213.
[145] J.-B. M. M. Pinot, S. Vanni, E. Ambroggio, D. Guet, B. Goud, “Feedback between membrane tension, lipid shape and curvature in the formation of packing defects M. Pinot, S. Vanni, E. Ambroggio, D. Guet, B. Goud, J.-B. Manneville 1,” *BioRxiv*, 2018.
[146] J. B. Larsen *et al.*, “Membrane curvature enables N-Ras lipid anchor sorting to liquid-ordered membrane phases,” *Nat. Chem. Biol.*, vol. 11, no. 3, pp. 192–194, 2015, doi: 10.1038/nchembio.1733.
[147] H. Koldsø, D. Shorthouse, J. Hélie, and M. S. P. Sansom, “Lipid Clustering Correlates with Membrane Curvature as Revealed by Molecular Simulations of Complex Lipid Bilayers,” *PLoS Comput. Biol.*, vol. 10, no. 10, 2014, doi: 10.1371/journal.pcbi.1003911.
[148] B. J. Peter *et al.*, “BAR Domains as Sensors of Membrane Curvature: The Amphiphysin BAR Structure,” *Science (80-.).*, vol. 303, no. 5657, pp. 495–499, 2004, doi: 10.1126/science.1092586.
[149] A. Frost, P. De Camilli, and V. M. Unger, “F-BAR Proteins Join the BAR Family Fold,” *Structure*, vol. 15, no. 7, pp. 751–753, 2007, doi: 10.1016/j.str.2007.06.006.
[150] T. H. Millard *et al.*, “Structural basis of filopodia formation induced by the IRSp53/MIM homology domain of human IRSp53,” *EMBO J.*, vol. 24, no. 2, pp. 240–250, 2005, doi: 10.1038/sj.emboj.7600535.
[151] J. Bigay, J. F. Casella, G. Drin, B. Mesmin, and B. Antonny, “ArfGAP1 responds to membrane curvature through the folding of a lipid packing sensor motif,” *EMBO J.*, vol. 24, no. 13, pp. 2244–2253, 2005, doi: 10.1038/sj.emboj.7600714.
[152] B. Antonny, “Mechanisms of membrane curvature sensing,” *Annu. Rev. Biochem.*, vol. 80, pp. 101–123, 2011, doi: 10.1146/annurev-biochem-052809-155121.
[153] G. Drin and B. Antonny, “Amphipathic helices and membrane curvature,” *FEBS Lett.*, vol. 584, no. 9, pp. 1840–1847, 2010, doi: 10.1016/j.febslet.2009.10.022.
[154] K. L. Madsen, V. K. Bhatia, U. Gether, and D. Stamou, “BAR domains, amphipathic helices and membrane-anchored proteins use the same mechanism to sense membrane curvature,” *FEBS Lett.*, vol. 584, no. 9, pp. 1848–1855, 2010, doi: 10.1016/j.febslet.2010.01.053.
[155] J. M. Isas, M. R. Ambroso, P. B. Hegde, J. Langen, and R. Langen, “Tubulation by amphiphysin requires concentration-dependent switching from wedging to scaffolding,” *Structure*, vol. 23, no. 5, pp. 873–881, 2015, doi: 10.1016/j.str.2015.02.014.
[156] N. A. McDonald, C. W. Vander Kooi, M. D. Ohi, and K. L. Gould, “Oligomerization but Not Membrane Bending Underlies the Function of Certain F-BAR Proteins in Cell Motility and Cytokinesis,” *Dev. Cell*, vol. 35, no. 6, pp. 725–736, 2015, doi: 10.1016/j.devcel.2015.11.023.
[157] H. Yamamoto, A. Kondo, and T. Itoh, “A curvature-dependent membrane binding by tyrosine kinase Fer involves an intrinsically disordered region,” *Biochem. Biophys. Res. Commun.*, vol. 495, no. 1, pp. 1522–1527, 2018, doi: 10.1016/j.bbrc.2017.12.009.
[158] V. K. Bhatia *et al.*, “Amphipathic motifs in BAR domains are essential for membrane curvature sensing,” *EMBO J.*, vol. 28, no. 21, pp. 3303–3314, 2009, doi: 10.1038/emboj.2009.261.
[159] V. K. Bhatia, N. S. Hatzakis, and D. Stamou, “A unifying mechanism accounts for sensing of membrane curvature by BAR domains, amphipathic helices and membrane-anchored proteins,”

Semin. Cell Dev. Biol., vol. 21, no. 4, pp. 381–390, 2010, doi: 10.1016/j.semcdb.2009.12.004.
[160] Z. Chen, C. Zhu, C. J. Kuo, J. Robustelli, and T. Baumgart, "The N-Terminal Amphipathic Helix of Endophilin Does Not Contribute to Its Molecular Curvature Generation Capacity," *J. Am. Chem. Soc.*, vol. 138, no. 44, pp. 14616–14622, 2016, doi: 10.1021/jacs.6b06820.
[161] B. Sorre *et al.*, "Nature of curvature coupling of amphiphysin with membranes depends on its bound density," *Proc. Natl. Acad. Sci. U. S. A.*, vol. 109, no. 1, pp. 173–178, 2012, doi: 10.1073/pnas.1103594108.
[162] T. Baumgart, B. R. Capraro, C. Zhu, and S. L. Das, "Thermodynamics and mechanics of membrane curvature generation and sensing by proteins and lipids," *Annu. Rev. Phys. Chem.*, vol. 62, pp. 483–506, 2011, doi: 10.1146/annurev.physchem.012809.103450.
[163] S. Suetsugu, S. Kurisu, and T. Takenawa, "Dynamic shaping of cellular membranes by phospholipids and membrane-deforming proteins," *Physiol. Rev.*, vol. 94, no. 4, pp. 1219–1248, 2014, doi: 10.1152/physrev.00040.2013.
[164] H. T. McMahon and E. Boucrot, "Membrane curvature at a glance," *J. Cell Sci.*, vol. 128, no. 6, pp. 1065–1070, 2015, doi: 10.1242/jcs.114454.
[165] C. Zhu, S. L. Das, and T. Baumgart, "Nonlinear sorting, curvature generation, and crowding of endophilin N-BAR on tubular membranes," *Biophys. J.*, vol. 102, no. 8, pp. 1837–1845, 2012, doi: 10.1016/j.bpj.2012.03.039.
[166] P. Bassereau *et al.*, "The 2018 biomembrane curvature and remodeling roadmap," *J. Phys. D. Appl. Phys.*, vol. 51, no. 34, 2018, doi: 10.1088/1361-6463/aacb98.
[167] M. Kaksonen and A. Roux, "Mechanisms of clathrin-mediated endocytosis," *Nat. Rev. Mol. Cell Biol.*, vol. 19, no. 5, pp. 313–326, 2018, doi: 10.1038/nrm.2017.132.
[168] K. S. Ramamurthi, S. Lecuyer, H. A. Stone, and R. Losick, "Geometric cue for protein localization in a bacterium," *Science (80-.).*, vol. 323, no. 5919, pp. 1354–1357, 2009, doi: 10.1126/science.1169218.
[169] H. Y. Lou, W. Zhao, Y. Zeng, and B. Cui, "The Role of Membrane Curvature in Nanoscale Topography-Induced Intracellular Signaling," *Acc. Chem. Res.*, vol. 51, no. 5, pp. 1046–1053, 2018, doi: 10.1021/acs.accounts.7b00594.
[170] M. Goudarzi *et al.*, "Bleb Expansion in Migrating Cells Depends on Supply of Membrane from Cell Surface Invaginations," *Dev. Cell*, vol. 43, no. 5, pp. 577-587.e5, 2017, doi: 10.1016/j.devcel.2017.10.030.
[171] K. Yamamoto and J. Ando, "Vascular endothelial cell membranes differentiate between stretch and shear stress through transitions in their lipid phases," *Am. J. Physiol. - Hear. Circ. Physiol.*, vol. 309, no. 7, pp. H1178–H1185, 2015, doi: 10.1152/ajpheart.00241.2015.
[172] K. Yamamoto and J. Ando, "Endothelial cell and model membranes respond to shear stress by rapidly decreasing the order of their lipid phases," *J. Cell Sci.*, vol. 126, no. 5, pp. 1227–1234, 2013, doi: 10.1242/jcs.119628.
[173] A. E. Cohen and Z. Shi, "Do Cell Membranes Flow Like Honey or Jiggle Like Jello?," *BioEssays*, vol. 42, no. 1, pp. 1–13, 2020, doi: 10.1002/bies.201900142.
[174] S. . Singer and G. L. Nicolson, "Singer1972.Pdf," *Science*, vol. 175. pp. 720–731, 1972.
[175] Z. Shi, Z. T. Graber, T. Baumgart, H. A. Stone, and A. E. Cohen, "Cell Membranes Resist Flow," *Cell*, vol. 175, no. 7, pp. 1769-1779.e13, 2018, doi: 10.1016/j.cell.2018.09.054.
[176] A. Kusumi *et al.*, "Dynamic organizing principles of the plasma membrane that regulate signal transduction: Commemorating the fortieth anniversary of singer and nicolson's fluid-mosaic model," *Annu. Rev. Cell Dev. Biol.*, vol. 28, pp. 215–250, 2012, doi: 10.1146/annurev-cellbio-100809-151736.
[177] J. M. Sanderson, "Resolving the kinetics of lipid, protein and peptide diffusion in membranes," *Mol. Membr. Biol.*, vol. 29, no. 5, pp. 118–143, 2012, doi: 10.3109/09687688.2012.678018.
[178] D. E. Koppel, M. P. Sheetz, and M. Schindler, "Matrix control of protein diffusion in biological membranes," *Proc. Natl. Acad. Sci. U. S. A.*, vol. 78, no. 6 I, pp. 3576–3580, 1981, doi: 10.1073/pnas.78.6.3576.
[179] G. L. Nicolson, "The Fluid - Mosaic Model of Membrane Structure: Still relevant to understanding the structure, function and dynamics of biological membranes after more than 40 years," *Biochim. Biophys. Acta - Biomembr.*, vol. 1838, no. 6, pp. 1451–1466, 2014, doi:

10.1016/j.bbamem.2013.10.019.
[180] A. D. Dupuy and D. M. Engelman, “Protein area occupancy at the center of the red blood cell membrane,” *Proc. Natl. Acad. Sci. U. S. A.*, vol. 105, no. 8, pp. 2848–2852, 2008, doi: 10.1073/pnas.0712379105.
[181] D. Needham and R. M. Hochmuth, “A sensitive measure of surface stress in the resting neutrophil,” *Biophys. J.*, vol. 61, no. 6, pp. 1664–1670, 1992, doi: 10.1016/S0006-3495(92)81970-7.
[182] I. Lavi, M. Goudarzi, E. Raz, N. S. Gov, R. Voituriez, and P. Sens, “Cellular Blebs and Membrane Invaginations Are Coupled through Membrane Tension Buffering,” *Biophys. J.*, vol. 117, no. 8, pp. 1485–1495, 2019, doi: 10.1016/j.bpj.2019.08.002.
[183] W. Rawicz, K. C. Olbrich, T. McIntosh, D. Needham, and E. A. Evans, “Effect of chain length and unsaturation on elasticity of lipid bilayers,” *Biophys. J.*, vol. 79, no. 1, pp. 328–339, 2000, doi: 10.1016/S0006-3495(00)76295-3.
[184] W. Rawicz and E. Evans, “Entropy-Driven Tension and Bending Elasticity in Condensed-Fluid Membranes,” *Phys. Rev. Lett.*, vol. 64, no. 17, p. 2094, 1990.
[185] W. Helfrich and R. M. Servuss, “Undulations, steric interaction and cohesion of fluid membranes,” *Nuovo Cim. D*, vol. 3, no. 1, pp. 137–151, 1984, doi: 10.1007/BF02452208.
[186] M. Goulian, R. Bruinsma, and P. Pincus, “Long-range forces in heterogeneous fluid membranes,” *Epl*, vol. 23, no. 2, pp. 125–128, 1993, doi: 10.1209/0295-5075/23/2/014.
[187] H. K. Lin, R. Zandi, U. Mohideen, and L. P. Pryadko, “Fluctuation-induced forces between inclusions in a fluid membrane under tension,” *Phys. Rev. Lett.*, vol. 107, no. 22, pp. 2–6, 2011, doi: 10.1103/PhysRevLett.107.228104.
[188] R. Nambiar, R. E. McConnell, and M. J. Tyska, “Control of cell membrane tension by myosin-I,” *Proc. Natl. Acad. Sci. U. S. A.*, vol. 106, no. 29, pp. 11972–11977, 2009, doi: 10.1073/pnas.0901641106.
[189] S. KRISHNASWAMY, “A COSSERAT-TYPE MODEL FOR THE RED BLOOD CELL WALL,” vol. 34, no. 8, pp. 873–899, 1996.
[190] C. D. Cox *et al.*, “Removal of the mechanoprotective influence of the cytoskeleton reveals PIEZO1 is gated by bilayer tension,” *Nat. Commun.*, vol. 7, pp. 1–13, 2016, doi: 10.1038/ncomms10366.
[191] D. Raucher and M. P. Sheetz, “Characteristics of a membrane reservoir buffering membrane tension,” *Biophys. J.*, vol. 77, no. 4, pp. 1992–2002, 1999, doi: 10.1016/S0006-3495(99)77040-2.
[192] T. A. Masters, B. Pontes, V. Viasnoff, Y. Li, and N. C. Gauthier, “Plasma membrane tension orchestrates membrane trafficking, cytoskeletal remodeling, and biochemical signaling during phagocytosis,” *Proc. Natl. Acad. Sci. U. S. A.*, vol. 110, no. 29, pp. 11875–11880, 2013, doi: 10.1073/pnas.1301766110.
[193] A. M. ari. Sokac, “A membrane reservoir at the cell surface: unfolding the plasma membrane to fuel cell shape change,” *Bioarchitecture*, vol. 4, no. 2, pp. 39–46, 2014, doi: 10.4161/bioa.29069.
[194] C. E. Morris, “Mechanoprotection of the Plasma Membrane in,” vol. 6, no. September, pp. 703–720, 2001.
[195] M. Glogauer, P. Arora, D. Chou, P. A. Janmey, G. P. Downey, and C. A. G. McCulloch, “The role of actin-binding protein 280 in integrin-dependent mechanoprotection,” *J. Biol. Chem.*, vol. 273, no. 3, pp. 1689–1698, 1998, doi: 10.1074/jbc.273.3.1689.
[196] H. P. Lo *et al.*, “The caveolin-Cavin system plays a conserved and critical role in mechanoprotection of skeletal muscle,” *J. Cell Biol.*, vol. 210, no. 5, pp. 833–849, 2015, doi: 10.1083/jcb.201501046.
[197] K. Keren *et al.*, “Mechanism of shape determination in motile cells,” *Nature*, vol. 453, no. 7194, pp. 475–480, 2008, doi: 10.1038/nature06952.
[198] J. Happel, “Viscous flow in multiparticle systems: Slow motion of fluids relative to beds of spherical particles,” *AIChE J.*, vol. 4, no. 2, pp. 197–201, 1958, doi: 10.1002/aic.690040214.
[199] G. G. Stokes, “On the Effect of the Internal Friction of Fluids on the Motion of Pendulums,” *Math. Phys. Pap.*, pp. 1–10, 2010, doi: 10.1017/cbo9780511702266.002.
[200] P. G. S. A. M. DELBROCK, “Brownian motion in biological membranes,” vol. 72, no. 8, pp. 3111–3113, 1975.
[201] N. C. Hartman and J. T. Groves, “Signaling clusters in the cell membrane,” *Curr. Opin. Cell Biol.*, vol. 23, no. 4, pp. 370–376, 2011, doi: 10.1016/j.ceb.2011.05.003.

[202] M. L. Dustin and J. T. Groves, “Receptor signaling clusters in the immune synapse,” *Annu. Rev. Biophys.*, vol. 41, no. 1, pp. 543–556, 2012, doi: 10.1146/annurev-biophys-042910-155238.
[203] A. J. Borgdorff and D. Choquet, “Regulation of AMPA receptor lateral movements,” *Nature*, vol. 417, no. 6889, pp. 649–653, 2002, doi: 10.1038/nature00780.

Chapter 2

Measurement methods

Fluctuations Spectroscopy Techniques

Cell membrane constitutes the physical barrier for cells, and it could be considered, to a first approximation, simply as a pure lipid bilayer. Furthermore, many inner cell organelles have their own barrier constituted by a lipid bilayer. The whole biological membrane, and in particular the lipid bilayer skeleton, is essential for cell stability, permeability, and functioning. Investigating mechanical and physical properties of pure lipid bilayers is crucial, since, for some relevant aspects, they recapitulate the main mechanical features and interactions of biological membranes.

In the following sections we will introduce the basic concepts of differential geometry, capable to properly describe the fluctuating 2D membrane of GUVs; using the quasi-spherical approximation, we will describe how surface undulations can be split into a stationary and a time-dependent part. exploiting the previous statements, we will define the appropriate Hamiltonian for surface mechanical energy, highlighting the bending contribution. We will demonstrate that the eigenfunctions able to solve the Hamiltonian of the membrane fluctuations in any point are the spherical harmonics. Alternatively, fluctuations could be expanded using spherical harmonics, and the coefficients are obtained by theoretical solutions proposed from surface Hamiltonian. Membrane thickness is approximatively 5 nm, while GUV's radius is around 10÷40 µm, and usually optical microscopy is employed to follow membrane undulations. Due to the vast discrepancy between membrane thickness and radius and the depth of field of optical microscopy, only a limited part of the vesicles in a given frame is in focus. We typically concentrate on the equatorial plane, which provide the greatest observable radius fluctuation. Albeit the solution obtained for the energy surface described by the Hamiltonian is applicable in any point of the fluctuating membrane, due to the previously mentioned experimental limitation, the fluctuations expected by theoretical framework of Hamiltonian must be exploited focusing on the equatorial plane condition. Starting from equatorial plane contour fluctuations, we will define the autocorrelation function and since contour fluctuations can be expressed using spherical harmonic basis, the autocorrelation function can be expanded using this mathematical basis as well. Then we will invoke the equipartition theorem and we will correlate the expansion coefficients of the autocorrelation function to the searched intrinsic membrane feature, its bending constant. Alternatively, the autocorrelation function can be expanded using the Fourier series basis. In both cases the bending constant and the reduced membrane tension can be obtained using a non-linear fitting procedure, based on the Levenberg-Marquardt algorithm. We will discuss deeply the advantages and drawbacks of each approach making appropriate comparisons. Finally, we will provide a set of basic rules needed to identify the quality of the fit obtained, suitable for both proposed approaches, based on general arguments depending on the investigated vesicles shape, size and the range of the obtained parameters observed after the flickering analysis.

- **Flickering Spectroscopy on GUVs:**
  - **Differential geometry and calculating curvatures**

Giant unilamellar vesicles that are fluctuating are constituted by a lipid bilayer in the fluid state. The thickness of the bilayer is approximatively equal to the double of a single acyl chain length, and it measures about 40-50 Å, a negligible value if compared to the radius vesicles, which is several micrometers. The vesicle is surrounded by aqueous medium both from the inner and the outer of the membrane itself, and during bilayer fluctuations the membrane is considered impermeable to water transfer from inside to the outside and vice versa. Combining these arguments, we can approximate the membrane bilayer as a pure two-dimensional system, exposed to three dimensional aqueous medium, which undergoes thermal fluctuations. These thermal fluctuations, resulting from thermal noise contribution, perturb the membrane from its theoretical

sphere-shape. So, the lipid bilayer can be considered quasi-spherical-shaped, and the spherical coordinate properly describe each point of its surface. [Eq 1] resumes the representation of a generic point belonging to the membrane surface, relating cartesian coordinates to the more suitable polar s one.

$$\begin{cases} x = R[1 + u(\theta, \varphi, t)] \sin(\theta) \cos(\varphi) \\ y = R[1 + u(\theta, \varphi, t)] \sin(\theta) \sin(\varphi) \\ z = R[1 + u(\theta, \varphi, t)] \cos(\theta) \end{cases} [1]$$

where (x;y;z) represent the cartesian coordinates of the vector placed in the center of mass of the liposome (characterized by a triad of mobile coordinates ($x_0(t);y_0(t);z_0(t);$)) and pointing toward the point "P" of the membrane (see figure 1). Alternatively, the point "P" can be identified using the polar spherical coordinates (ρ=r;θ;φ) where θ and φ are the polar and the azimuthal angles. For simplicity, we place the origin of the frame of reference in the center of mass of the liposome itself, and we rewrite the radius r as ρ=r=R(1+u(θ,φ,t)) where R is the equivalent radius of a sphere having the same volume of the liposome and u represents the relative radius fluctuations. Since we are considering a quasi-spherical condition, we expect that amplitude radius fluctuations expressed by the function u to be small, i.e. u(θ,φ,t)<<1. Furthermore, in the absence of thermal noise we expect a pure spherical shape of the liposome, meaning that amplitude fluctuations mediated in time should be equal to zero $\langle u(\theta,\varphi,t) \rangle_t = 0$; we will come back on this aspect later.

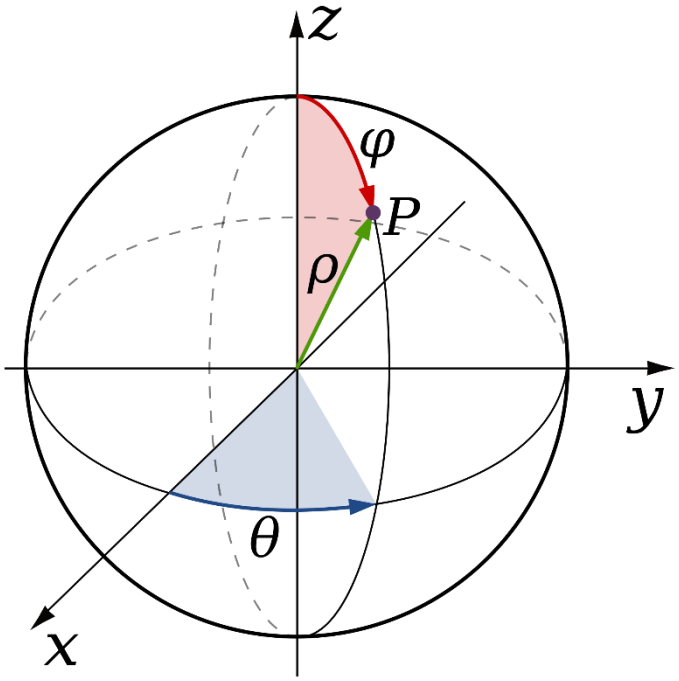

Figure 1: Representation of a generic point P belonging to the membrane surface, exploiting spherical coordinates: ρ=r=R(1+u(ϑ,φ,t))

Now we will resume some brief general aspects regarding differential geometry, very important in two-dimensional membrane surface context. Starting from the radial vector $\vec{r}(\theta, \varphi)$, which identifies the surface point "P" of the quasi-spherical liposome in the polar coordinates frame of reference, we can define the metric tensor, $g^{\alpha\beta}(\theta, \varphi)$ [Eq 2]:

$$g^{\alpha\beta}(\theta, \varphi) = \begin{pmatrix} \vec{r_\theta} \cdot \vec{r_\theta} & \vec{r_\theta} \cdot \vec{r_\varphi} \\ \vec{r_\varphi} \cdot \vec{r_\theta} & \vec{r_\varphi} \cdot \vec{r_\varphi} \end{pmatrix} [2] \; where \cdot is \; the \; scalar \; product$$

Where $\overrightarrow{r_\theta} = {}^{\partial \vec{r}}/_{\partial \theta}$ and $\overrightarrow{r_\varphi} = {}^{\partial \vec{r}}/_{\partial \varphi}$ represent the partial derivatives of the radial-vector with respect the θ and φ angles. $\overrightarrow{r_\theta}$ and $\overrightarrow{r_\varphi}$ are a couple of vectors tangent to the surface membrane where $\vec{r}$ is pointing to ("P"). The metric tensor also admits its inverse matrix defined as follows [Eq 3]:

$$g_{\alpha\beta}(\theta,\varphi) = \frac{1}{\det\left[g^{\alpha\beta}\right]}\begin{pmatrix} \overrightarrow{r_\varphi}\cdot\overrightarrow{r_\varphi} & -\overrightarrow{r_\varphi}\cdot\overrightarrow{r_\theta} \\ -\overrightarrow{r_\theta}\cdot\overrightarrow{r_\varphi} & \overrightarrow{r_\theta}\cdot\overrightarrow{r_\theta} \end{pmatrix} [3]$$

The metric tensor $g^{\alpha\beta}(\theta,\varphi)$ can be used to reconstruct locally around "P" the membrane surface, since it constitutes a new two-dimensional frame of reference for the area membrane around the radial-vector. Furthermore, the couple of vectors $\overrightarrow{r_\theta}$ and $\overrightarrow{r_\varphi}$ can be used to identify the surface membrane normal vector $\vec{n}$, as follows [Eq 4]:

$$\vec{n}(\theta,\varphi) = \frac{\overrightarrow{r_\theta}\times\overrightarrow{r_\varphi}}{\left|\overrightarrow{r_\theta}\times\overrightarrow{r_\varphi}\right|} [4]$$

Considering $\vec{n}$, we can define $\overrightarrow{n_\theta} = {}^{\partial \vec{n}}/_{\partial \theta}$ and $\overrightarrow{n_\varphi} = {}^{\partial \vec{n}}/_{\partial \varphi}$. Since $\vec{n}$ is obtained by the product vector between $\overrightarrow{r_\theta}$ and $\overrightarrow{r_\varphi}$, it is perpendicular to the plane containing this couple of vectors $\overrightarrow{r_\theta}$ and $\overrightarrow{n_\varphi}$ and we will have that $\vec{n}\cdot\overrightarrow{n_\theta} = 0$ and $\vec{n}\cdot\overrightarrow{n_\varphi} = 0$. In other words, the partial derivates $\overrightarrow{n_\theta}$ and $\overrightarrow{n_\varphi}$ are contained in the same plane constructed starting from the vectors $\overrightarrow{r_\theta}$ and $\overrightarrow{n_\varphi}$, so they are both tangents to the membrane surface and can be expressed as a linear combination of $\overrightarrow{r_\theta}$ and $\overrightarrow{n_\varphi}$ vectors. The partial derivates of the normal vector $\vec{n}$ can be used to define the useful curvature tensor, $C^{\alpha\beta}(\theta,\varphi)$ as follows [Eq 5]:

$$C^{\alpha\beta}(\theta,\varphi) = \begin{pmatrix} \overrightarrow{n_\theta}\cdot\overrightarrow{n_\theta} & \overrightarrow{n_\theta}\cdot\overrightarrow{n_\varphi} \\ \overrightarrow{n_\varphi}\cdot\overrightarrow{n_\theta} & \overrightarrow{n_\varphi}\cdot\overrightarrow{n_\varphi} \end{pmatrix} [5]$$

In fact, for each point "P" the membrane surface in the neighborhood of that point can be described starting from its principal curvatures c_1 and c_2 that are perpendicular to each other and locally reconstruct the surface in "P". In figure 2 two typical examples are reported, where c_1 and c_2 are defined as the inverse of the maximum R_1 and minimum R_2 radius perpendicular respectively to each other and describing the surface curvatures:

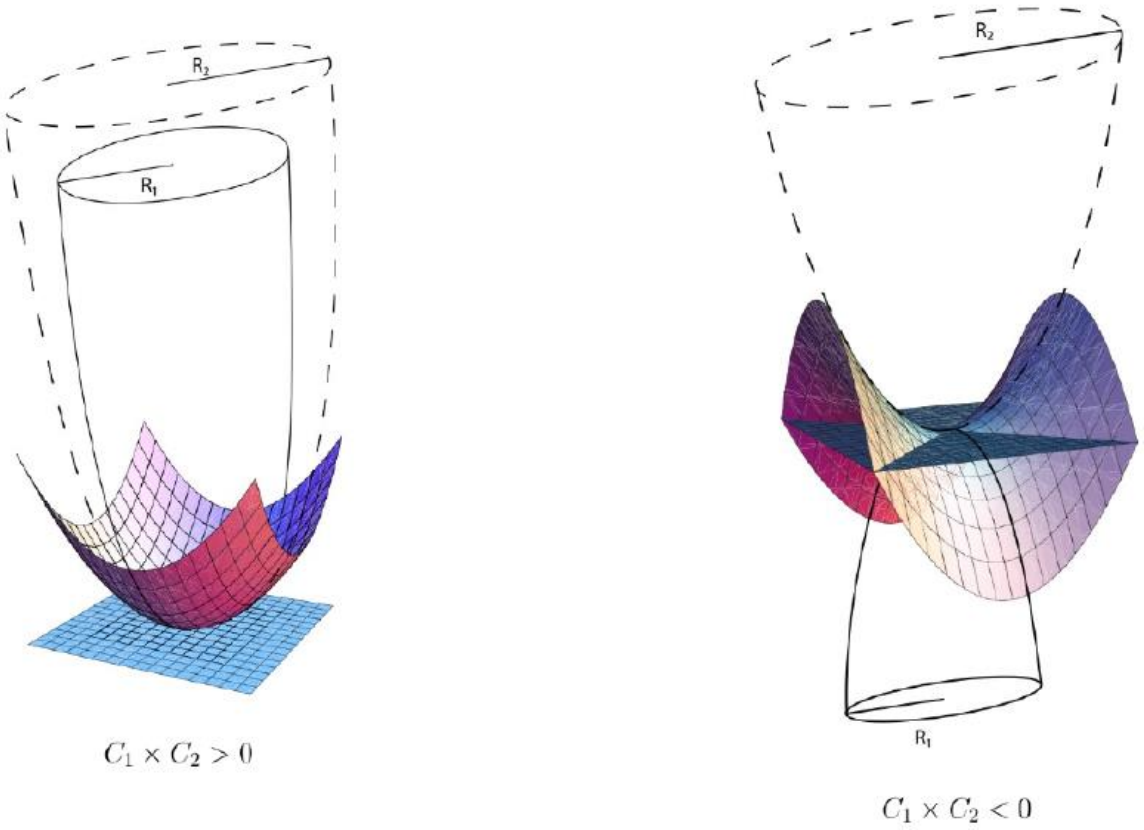

Figure 2: Principal curvatures examples for two different conditions: Ellipsoidal surface (left) and saddle surface (right)

Starting from the curvature $C^{\alpha\beta}(\theta,\varphi)$ and the inverse metric $g_{\alpha\beta}(\theta,\varphi)$ tensors we can define a practical tool, $C^{\alpha}_{\beta}(\theta,\varphi)$ [Eq 6] which is still a tensor able to connect together the two principal curvatures c_1 and c_2. Alternatively, we can consider c_1 and c_2 as the inverse of the maximum R_1 and minimum R_2 radius perpendicular respectively to each other and describing the surface curvatures.

$$C^{\alpha}_{\beta}(\theta,\varphi) = C^{\alpha\gamma}(\theta,\varphi)g_{\gamma\beta}(\theta,\varphi)[6]$$

In fact, this tensor has two important properties:

The trace corresponds to the mean curvature: $Tr\left[C^{\gamma}_{.\gamma}\right] = c_1 + c_2$; while the determinant corresponds to the Gaussian curvature $det\left[C^{\alpha}_{.\beta}\right] = c_1 c_2$. The quantities: $c_1 + c_2$ and: $c_1 c_2$ are invariants quantities, which are unaffected by the particular representation adopted.

Now that we have provided the appropriate mathematical framework, based on differential geometry for the two-dimensional description of the membrane surface, we can proceed introducing the Hamiltonian for the total mechanical free energy of the lipid bilayer itself.

• Introducing the Helfric's free energy Hamiltonian

Early theoretical investigations regarding the mechanical free energy of the lipid bilayer started in 1970' thanks to different researchers [1]–[3]. Their predictions regarding the free energy Hamiltonian were supported by geometrical and symmetry arguments, depending strictly on the quasi-spherical condition. In particular, they asserted that only the shape of the vesicles influences the total free energy of the membrane,

and the structure of the Hamiltonian is independent of the particular parametrization chosen for the fluctuating surface description. Since the mean curvature and the Gaussian curvature are surface invariants the Hamiltonian should depend strictly on these two parameters. [Eq 7] represents the complete form of the surface free energy obtained by previous authors:

$$H = \sigma \int dA + \frac{\kappa}{2}\int (c_1 + c_2 - c_0)^2 dA + \kappa_{Gauss}\int (c_1 \cdot c_2) dA \,[7]$$

This Hamiltonian is composed by three different terms, and each one of these highlights a different additional cost for the total free energy of the membrane.

The first term $\sigma \int dA$: represents the energy cost required to increase the area membrane after its formation. A further area increase is weighted by surface tension σ, which is expressed as an energy per unit of area. The surface tension parameter does not behave as a pure constant. In fact, during self-formation of the vesicles the surface tension can be neglected, considering it equal to zero. But once the vesicles in formed encapsulating the inner aqueous medium from the external environment, any additional volume accommodation from the outside will require an additional area membrane contribution, and in this case a net surface tension should be considered. In the introduction chapter we will connect surface tension changes due to external mechanical stimuli, the subsequent area increment and the stretching parameter; in this chapter we will focus on vesicle exposed just to thermal noise and no other stimuli will be considered. In [Eq 7] we considered the surface tension σ as a constant parameter set outside the total area integral, implying that we are measuring the free energy contribution provided by the membrane tension during self-formation of the vesicles. Resuming the previously mentioned arguments about this term of the Hamiltonian, we can neglect surface tension contribution since we are referring just to the vesicle after formation process and affected lonely by thermal noise perturbations.

The second term, $\frac{\kappa}{2}\int (c_1 + c_2 - c_0)^2 dA$, represents the energy cost of bending deformations of the membrane surface. It measures the energy cost required for curvature deviations starting from the mean value: c_1+c_2, taking into account also the presence of a possible spontaneous curvature c_0. The coefficient c_0 arises from intrinsic membrane and bulk properties, such as an asymmetry in the lipid composition of the two leaflets, which could provide a spontaneous bending of the membrane area. The coefficient κ is in fact the bending energy constant, and the bending contribution depends on the quadratic difference between mean and spontaneous curvatures.

The last term $\kappa_{Gauss}\int (c_1 \cdot c_2) dA$ represents the energy cost required if a gaussian curvature is imposed on the surface membrane, so it constitutes a pure topologically dependent contribution where κ_{Gauss} is the Gaussian elastic modulus. Using the Gauss-Bonnet theorem [4], [5] developed in the differential geometry field, we can solve analytically the third contribute. This theorem in fact connect the surface geometry directly to its topological features. It asserts that whenever the gaussian curvature is integrated on a compact surface (closed and limited area of integration), like in this case, the result is a topological invariant, as showed in [Eq 8]

$$\int (c_1 \cdot c_2) dA = 4\pi(1 - G)[8]$$

The key parameter for the integral evaluation is "G": the number of handles present in the integrating surface. Since we are considering a quasi-spherical shape, the total area of the vesicles, which does not contains any handles, the final result of the third term is a constant contribution equal to $4\pi\kappa_{Gauss}$. In fact, upon thermal fluctuation the membrane vesciscle remains compact limited and closed, dividing the inner and the outer aqueous medium. Summarizing the previous considerations, the free energy Hamiltonian

under equilibrium condition F_c can be rewritten, neglecting constant contributions, using only the second term [Eq 9]:

$$F_c = \frac{\kappa}{2}\int (c_1 + c_2 - c_0)^2 dA \text{ [9]}$$

The last equation represents the appropriate free energy Hamiltonian of a vesicles exposed to thermal noise, and it constitutes the starting point for further surface fluctuation analysis.

• Minimum of the free energy Hamiltonian

The next goal is to solve the free energy Hamiltonian, searching his local minimum, using the surface fluctuation amplitudes, described by u(θ,φ,t) function. Upon just thermal fluctuation, net volume flux of aqueous medium between the inside and the outside of the membrane is negligible, implying volume conservation of the quasi-spherical vesicles. This constrain condition must be impoed using [Eq 10]:

$$V\{u\} = \oint v(u)d\theta d\varphi = \iint_{0\,0}^{\pi\,2\pi} v(u)d\theta d\varphi = \iint_{0\,0}^{\pi\,2\pi} R^3\left(\frac{1}{3} + u + u^2\right)\sin\theta\, d\theta d\varphi \text{ [10]}$$

Where $v(u)$ represents the vesicles volume density, which can be described using the surface fluctuation function u(θ,φ,t). Integrating the volume density function over the entire vesicle we obtain the total volume $V\{u\}$, which is maintained constant during thermal noise exposition. The surface fluctuation function u is parametrized separating the spatial component, resembled by R, and the angular dependency ascribed to θ and φ. As mentioned above, R represents the radius of the sphere able to contain the same volume $V\{u\}$, of the studied vesicle, so: $R = \sqrt[3]{\frac{3}{4\pi}V\{u\}}$

As said in the introduction chapter, local surface tension changes introduce stretch response and subsequent area variation. Nevertheless, for pure lipid bilayer, the energy cost required for area expansion when the vesicle is under thermodynamic equilibrium is drastically elevated. Experimental evidences confirm that pure lipid bilayer surface is almost inextensible, in fact stretching constant for this model membrane is approximatively ~10^5 pN*μm^{-1}, this contribution can be rewritten emphasizing the fact that represents an energetic cost upon area expansion: ~10^{-1}pN*((μm)$^{-2}$). These arguments clearly confirm that in absence of external mechanical stimuli, thermal fluctuations alone are unable to produce surface membrane expansion. We can conclude that also total surface membrane remains constant upon thermal noise exposition, this second constrain can be written using [Eq 11]

$$S\{u\} = \oint s(u)d\theta d\varphi = \iint_{0\,0}^{\pi\,2\pi} s(u)d\theta d\varphi = \iint_{0\,0}^{\pi\,2\pi} R^2\left(1 + u + 2u^2 + \frac{1}{2}(\nabla u)^2\right)\sin\theta\, d\theta d\varphi \text{ [11]}$$

Where s(u) is the surface density, which is integrated considering the compact closed and limited vesicle surface. [Eq 11] can be solved, and its result can be written highlighting the relative area excess "s_+" with respect the non-perturbated surface $4\pi R^2$, when the vesicles behave as a pure and stable sphere of radius R. Accordingly, we have $S\{u\} = 4\pi R^2(1 + s_+)$. In the equation the gradient operator applied to the fluctuation function u appears. This operator (squared) can be rewritten in the polar coordinates basis, which is more suitable for further analysis: $(\nabla u)^2 = \left(u_\theta^2 + \frac{u_\varphi^2}{\sin(\theta)^2}\right)$ The terms u_θ^2 and u_φ^2 indicate the square value of the partial derivatives of u with respect to the two angular parameters θ and φ.

At this point, it is strictly convenient to rewrite the surface fluctuations u(θ,φ,t) separating the static contribution u_0(θ,φ) from temporal dependent variations δu(θ,φ,t) [Eq 12 a], where the static part u_0(θ,φ) emphasizes the non-instantaneous surface deviations from the spherical condition [Eq 12b].

$$u(\theta,\varphi,t) = u_0(\theta,\varphi) + \delta u(\theta,\varphi,t)\ [12a];\ < u(\theta,\varphi,t) >_t = u_0(\theta,\varphi) \xrightarrow{yields} < \delta u(\theta,\varphi,t) >_t = 0\ [12b]$$

The free energy Hamiltonian of the vesicles under thermodynamic equilibrium conditions [Eq 9] has a minimum level, which is raised up by thermal fluctuations. These thermal induced surface perturbations correspond to thermal noise provided by the water surrounding vesicle environment. Related to this minimum free energy level, we expect to find an equilibrium-shape for the vesicle (an analytical solution for the fluctuations function u(θ,φ,t)), and its configuration can be found imposing the minimum of the free energy. Looking again at the total free energy of the vesicle surface [Eq 9], we defined c_0 as the spontaneous surface vesicles curvature, this term is null if the membrane is symmetric. More precisely, whenever the two leaflets composing the bilayer have the same composition, then $c_0 = 0$. From now on we will always consider pure lipid bilayers having symmetric composition. In [Eq 13], where f_c indicates the free energy density, we rewrite the free energy of the vesicles defined in [Eq 9], explicating its dependence on fluctuation function and their partial derivatives:

$$F_c\{u\} = \oint f_c\left(u, u_\theta, u_\varphi, u_{\theta\theta}, u_{\varphi\varphi}\right) d\theta d\varphi = \frac{\kappa}{2} \iint_0^{\pi\, 2\pi} (4 - 4\nabla^2 u + 4u\nabla^2 u + (\nabla^2 u)^2 + 2(\nabla u)^2) \sin\theta\, d\theta d\varphi\ [13]$$

where $(\nabla u)^2 = \left(u_\theta^2 + \frac{u_\varphi^2}{\sin(\theta)^2}\right)$ is the gradient operator applied to u, and squared, already mentioned in [Eq 11]. $\nabla^2 u$ is the Laplacian operator applied to u function, whose expression form using the more useful spherical coordinates is the following: $\nabla^2 u = \left(u_{\theta\theta} + \cot\theta\, u_\theta + \frac{u_{\varphi\varphi}}{(\sin\theta)^2}\right)$.

The minimum free energy search, from a physical perspective, must be achieved with additional conditions; imposing into the Hamiltonian the previously mentioned boundaries associated to fixed volume vesicle (no aqueous medium exchange between inside and outside of the membrane) and fixed surface vesicle (negligible stretch contribution). From a mathematical perspective, we can tackle this problem introducing a new functional "F" without constrains that contains the free energy, the surface, the volume of the vesicle and two additional parameters σ and Δp acting as Lagrange multipliers, which must have a specific physical meaning [Eq 14]:

$$F\{u\} = F_c\{u\} + \sigma S\{u\} - \Delta p V\{u\} [14]$$

The Lagrange multipliers are represented respectively by σ the surface tension, a small contribution, but must take into account whenever the surface vesicles is close after its formation, and Δp which identifies the hydrostatic pressure difference between the inner and the outer part of the vesicles. Using this new framework, the two boundary conditions are substituted by the presence of the Lagrange multipliers. Note that the functional is applied on the fluctuations function u(θ,φ,t), which can be rewritten specifying the stationary and the time-dependent contributions. Next goal is to solve this variational problem, looking for specific fluctuations function u(θ,φ,t) which minimize the functional F. In the variational context the search of the maxima or minima of the related functional (extrema research) is always involved and in this case we are setting the ordinary conditions for minimum functional value.

The first condition is reported in [Eq 15], the first variation of the functional $F\{u_0, \delta u\}$ must be null:

$$\delta F\{u_0, \delta u\} = \delta F_c\{u_0, \delta u\} + \sigma \delta S\{u_0, \delta u\} - \Delta p \delta V\{u_0, \delta u\} = 0 \quad [15]$$

This equation has an important physical meaning, if the fluctuation function stationary part $u_0(\theta,\varphi)$ minimizes the functional F, this implies that its first variation of the functional δF with respect to all small perturbations of u, represented by δu must be zero. Equivalently, the overall work executed by the external forces acting on the surface membrane is zero, and the corresponding stationary part of the fluctuations function u_0 reproduces the equilibrium shape. Note that just [Eq 15] is unable to specify if the solution $u_0(\theta,\varphi)$ obtained for this shape equilibrium condition reflects a stable, a not-stable or even saddle conditions. Eq 15 is composed by three different terms, and each one of these can be rewritten explicating the stationary $u_0(\theta,\varphi)$ and perturbating $\delta u(\theta,\varphi,t)$ fluctuation functions [Eq 16 a-c]:

$$\begin{cases} \delta F_c = \dfrac{\partial F_c}{\partial u}\delta u = \kappa \displaystyle\iint_{0\,0}^{\pi\,2\pi} [(\nabla^2[\nabla^2 u_0] + 2\nabla^2 u_0)\sin\theta]\delta u d\theta d\varphi \; [16a] \\ \delta S = \dfrac{\partial S}{\partial u}\delta u = R^2 \displaystyle\iint_{0\,0}^{\pi\,2\pi} [(2 + 2u_0 - \nabla^2 u_0)\sin\theta] d\theta d\varphi \; [16b] \\ \delta V = \dfrac{\partial V}{\partial u}\delta u = R^3 \displaystyle\iint_{0\,0}^{\pi\,2\pi} [(1 + 2u_0)\sin\theta] d\theta d\varphi \; [16c] \end{cases}$$

Now that we have written the different variation contributions δF_c, δS, and δV, differentiating upon fluctuations variation δu, we can observe that all the integrals have a common factor: $\sin\theta\, \delta u d\theta d\varphi$, this allows us to directly sum the functions under the integrals, we finally rewrite the [Eq 15] in a more suitable form, [Eq 17]:

$$\nabla^2(\nabla^2 u_0) + (2 - \bar{\sigma})\nabla^2 u_0 + 2(\bar{\sigma} - \bar{p})u_0 = \bar{p} - 2\bar{\sigma} [17]$$

This equation-form is called Euler-Lagrange Equation and is satisfied by all the u_0 functions able to reproduce equilibrium shape for the surface vesicles. $\bar{\sigma}$ represent the reduced surface tension, and it depends upon the ratio between the tension and the bending constant multiplied by the square of R. Similarly, $\bar{p}$ represent the reduced pressure difference. In the first member of [Eq 17] we note different terms, and each one is applied to u_0 function. Accordingly, we can rewrite the first member highlighting that it can be thought as a linear differential operator "L": $L = \nabla^2(\nabla^2 \cdot) + (2 - \bar{\sigma})\nabla^2 \cdot + 2(\bar{\sigma} - \bar{p})$, which depends on the Laplacian operator: $\nabla^2 = \left(\partial_{\theta\theta} + \cot\theta\, \partial_\theta + \frac{\partial_{\varphi\varphi}}{(\sin\theta)^2}\right)$. In the second member of [Eq 17] we have a constant term depending only on the reduced tension and pressure, which are constant parameters. As we will see later, for small fluctuation intensities compared to the equilibrium shape, we can approximate $\bar{p} \approx 2\bar{\sigma}$ and subsequently the second membrane of [Eq 17] will become zero. Taking a look to the new obtained equation, it now corresponds to a canonical eigenfunction-eigenvalue problem depending on a linear combination of the Laplacian: $\nabla^2(\nabla^2 u_0) + (2 - \bar{\sigma})\nabla^2 u_0 + 2(\bar{\sigma} - \bar{p})u_0 = 0 \xrightarrow{yields} \nabla^2(\nabla^2 u_0) + (2 - \bar{\sigma})\nabla^2 u_0 = 2(\bar{p} - \bar{\sigma})u_0$
Since the L operator is a linear combination of constant terms and the Laplacian, and the eigenfunctions of

the Laplacian are the spherical harmonics [Eq 18 a-c], we can expand the stationary part of fluctuations u_0 using the spherical harmonics basis with the appropriate coefficients [Eq 18 d]:

$$\begin{cases} Y_n^m(\theta,\varphi) = \Theta_n^m(\theta)\cdot\Phi_n^m(\varphi) = (-1)^m\sqrt{\dfrac{(2n+1)(n-m)!}{4\pi(n+m)!}}P_n^m(\cos\theta)e^{im\varphi}\,[18\ a] \\ \Theta_n^m(\theta) = (-1)^m\sqrt{\dfrac{(2n+1)(n-m)!}{2(n+m)!}}P_n^m(\cos\theta)\,[18\ b] \\ \Phi_n^m(\varphi) = \dfrac{1}{\sqrt{2\pi}}e^{im\varphi}\,[18\ c] \\ u_0(\theta,\varphi) = \sum_{n=0}^{N_{Max}}\sum_{m=-n}^{m=n}A_n^m\cdot Y_n^m(\theta,\varphi)\,[18\ d] \end{cases}$$

where $P_n^m(\cos\theta)$ are the associated Legendre polynomials, the index *m* and *n* constitute the order and the degree of the decomposition, respectively. Although from the mathematical point of view the spherical harmonics expansion of an arbitrary function can be done considering an infinite sum, the series expansion of $u_0(\theta,\varphi)$ has a cut-off limit N_{Max} . This is due to the fact that the surface membrane structure is discretized, and not continue. In particular, the total number of the lipids and molecules N_{Lipids} constituting the surface sets this limit, as follow: N_{Max}=$\sqrt{N_{Lipids}}$. The underling idea is that the total number of independent amplitudes, will be equal to the number of molecular elements available in the membrane. (For a fixed oscillator of degree n, there are 2n+1 amplitude contributions, since m spans from -n to +n. So, summing up the total number of enabled amplitudes m, it scales approximatively as N_{Max}^2)

Until now, we have solved the equilibrium condition for the total free energy of the vesicle, demonstrating that the most suitable representation for the stationary solution function u_0 are the spherical harmonics. Now we must introduce a second condition, similar to [Eq 15], which ensures that our equilibrium condition is related to a minimum value for our functional F (or alternatively a minimum for the free energy F_c), thus to a stable scenario. This condition is reported in [Eq 19], which involves the second variation δ^2F of the functional F:

$$\delta^2F\{u_0,\delta u\} = \delta^2F_c\{u_0,\delta u\} + \sigma\delta^2S\{u_0,\delta u\} - \Delta p\delta^2V\{u_0,\delta u\} \geq 0 \quad [19]$$

Starting from [Eq 19] and proceeding differentiating up to second order with respect to fluctuations δu the different components of the equation, we can demonstrate that [Eq 19] has a quadratic form with respect to time-dependent fluctuations δu and its partial derivates $(\delta u_\theta, \delta u_\varphi, \delta u_{\theta\theta}, \delta u_{\varphi\varphi})$. Furthermore, adopting integration by parts we can rewrite [Eq 19] in a more suitable way [Eq 20], emphasizing the presence of a linear differential operator $L'(u_0)$, (which depends on the u_0 function), acting on δu.

$$\delta^2F\{u_0,\delta u\} = \kappa\oint\delta u[L'(u_0)\cdot\delta u]d\theta d\varphi \quad [20]$$

This linear differential operator $L'(u_0)$, results really similar to the already introduced L during equilibrium discussion, since both are linear combinations of the Laplacian operator. In the previous case [Eq 17], L operator acted on the stationary part u_0, and we expanded the u_0 solution using the spherical harmonics basis [Eq 18 d]. Similarly, now $L'(u_0)$ is applied to time-dependent fluctuations δu, so it is convenient to adopt the spherical harmonics expansion for the δu function also [Eq 23 a]. Again, we can go back [Eq 20] to an equivalent eigenfunction(δu)-eigenvalue(λ) problem with respect to the $L'(u_0)$ operator [Eq 21]:

$$L'(u_0)\delta u = \lambda \delta u \; [21]$$

Furthermore, considering quadratic approximation, the operator $L'(u_0)$ loses its dependence from function u_0 and becomes identical to L. ($L'(u_0) \xrightarrow{yields} L$), so the eigenvalue equation assumes a simpler form [Eq 22]:

$$L\delta u = [\nabla^2(\nabla^2 \cdot) + (2-\bar{\sigma})\nabla^2 \cdot + 2(\bar{\sigma} - \bar{p}) \cdot]\delta u = \lambda \delta u \quad [22]$$

Using spherical harmonics expansion for fluctuation function [Eq 23 a] (note that the coefficients of the expansion $U_n^m(t)$ are time dependent, and the sum is truncated to N_{Max} for the same arguments cited before during u_0 spherical harmonic decomposition [Eq 18 d]), and adopting spherical harmonics properties, in particular the relationship joining the spherical harmonics and the Laplacian operator [Eq 23 b], we can analytically solve [Eq 22].

$$\begin{cases} \delta u(\theta, \varphi, t) = \sum_{n=0}^{N_{Max}} \sum_{m=-n}^{m=n} U_n^m(t) \cdot Y_n^m(\theta, \varphi) \quad [23\ a] \\ \nabla^2 \cdot Y_n^m(\theta, \varphi) = -n(n+1) Y_n^m(\theta, \varphi) \quad [23\ b] \end{cases}$$

In particular, we can identify the eigenvalue λ of this equation as a series of terms $\lambda_n(\bar{\sigma}, \bar{p})$ which depend on *n*, the reduced surface tension and pression, as follow [Eq 24 a-b]:

$$\begin{cases} \lambda_n(\bar{\sigma}, \bar{p}) = n^2(n+1)^2 - (2-\bar{\sigma})n(n+1) + 2(\bar{\sigma} - \bar{p}) \quad [24\ a] \\ alternatively: \\ \lambda_n(\bar{\sigma}, \bar{p}) = (n-1)(n+2)[\bar{\sigma} + n(n+1)] + 2(2\bar{\sigma} - \bar{p}) \quad [24\ b] \end{cases}$$

As we will see later, the second rearrangement [Eq 24 b] is more suitable for further experimental analysis. So, [Eq 22] can be completely rewritten using [Eq 25]:

$$L\delta u = \lambda \delta u = \sum_{n=0}^{N_{Max}} \lambda_n(\bar{\sigma}, \bar{p}) \sum_{m=-n}^{m=n} U_n^m(t) \cdot Y_n^m(\theta, \varphi) \; [25]$$

Now we almost have all the components required to locally describe the total free energy of the vesicle, around its equilibrium configuration, which is [Eq 26]:

$$F\{u_0,\delta u\} = F\{u_0\} + (\delta F\{u_0\} = 0) + \frac{1}{2}\delta^2 F\{\delta u\} \xrightarrow{yields} F\{u_0,\delta u\} - F\{u_0\} = \frac{1}{2}\delta^2 F\{\delta u\} [26]$$

Considering again [Eq 20], we can evaluate the analytical result of this integral exploiting spherical harmonics properties, in particular the $Y_n^m(\theta,\varphi)$ orthonormality, since the fluctuation function δu is described through this basis decomposition. Moreover, we previously required that surface perturbations do not have stationary part ($< \delta u(\theta,\varphi,t) >_t = 0$) and the equilibrium shape should be spherical. Since in the spherical harmonic basis the degree value *n=1* describes fluctuations different from usual spherical-shaped, we will have $< U_1^m(t) >_t = 0$. The second variation of the functional F will be [Eq 27 d]:

$$\frac{1}{2}\delta^2 F\{\delta u\} = \frac{\kappa}{2}\oint \delta u[L\delta u]d\theta d\varphi \quad [27\ a]$$

$$\frac{1}{2}\delta^2 F\{\delta u\} = \frac{\kappa}{2}\oint \sum_{n\prime=0}^{N_{Max}} \sum_{m\prime=-n\prime}^{m\prime=n\prime} U_{n\prime}^{m\prime}(t)\cdot Y_{n\prime}^{m\prime}(\theta,\varphi)\left[\sum_{n=0}^{N_{Max}} \lambda_n(\bar{\sigma},\bar{p}) \sum_{m=-n}^{m=n} U_n^m(t)\cdot Y_n^m(\theta,\varphi)\right] d\theta d\varphi [27\ b]$$

$$\frac{1}{2}\delta^2 F\{\delta u\} = \frac{\kappa}{2}\sum_{n\prime=0}^{N_{Max}} \sum_{m\prime=-n\prime}^{m\prime=n\prime} U_{n\prime}^{m\prime}(t)\left[\sum_{n=0}^{N_{Max}} \lambda_n(\bar{\sigma},\bar{p}) \sum_{m=-n}^{m=n} U_n^m(t)\right]\delta_{nn\prime}\delta_{mm\prime} [27\ c]$$

$$\frac{1}{2}\delta^2 F\{\delta u\} = \frac{\kappa}{2}\lambda_0(\bar{\sigma},\bar{p})\left|U_0^0(t)\right|^2 + \frac{\kappa}{2}\sum_{n=2}^{N_{Max}} \lambda_n(\bar{\sigma},\bar{p}) \sum_{m=-n}^{m=n} |U_n^m(t)|^2 [27\ d]$$

The first term, $\frac{\kappa}{2}\lambda_0(\bar{\sigma},\bar{p})\left|U_0^0(t)\right|^2$, constitutes the deviation of the surface membrane related to static translations of the center of mass. The relevant contribution is the second one, which shows how the free energy raises from its minimum value, proportionally to the square value of the amplitudes $|U_n^m(t)|^2$. This energy enhancement is ensured as long as $\lambda_n(\bar{\sigma},\bar{p})$ coefficients are strictly positive. Thus, the surface membrane is fluctuating as a pure collective Brownian motion given by approximatively $2N_{Max}$ independent harmonic oscillators, with a related amplitude $|U_n^m(t)|^2$.

• Squared fluctuations amplitude expression

We will proceed by investigating the distribution probability of the square amplitudes $|U_n^m(t)|^2$. Following statistical mechanics, we expect a Boltzmann distribution [Eq 28]:

$$f(U_n^m) = \frac{e^{-\frac{\kappa}{2}\sum_{n=2}^{N_{Max}} \lambda_n(\bar{\sigma},\bar{p}) \sum_{m=-n}^{m=n} |U_n^m(t)|^2 \frac{1}{k_B T}}}{\int e^{-\frac{\kappa}{2}\sum_{n=2}^{N_{Max}} \lambda_n(\bar{\sigma},\bar{p}) \sum_{m=-n}^{m=n} |U_n^m(t)|^2 \frac{1}{k_B T}} d\, U_n^m} [28]$$

Where $f(U_n^m)$ is the frequency (probability) of obtaining a given amplitude fluctuation $U_n^m(t)$.

Recalling the most probable expected amplitude, which is given by [Eq 29], and exploiting the ergodic hypothesis we can connect thermal moments of $U_n^m(t)$ to its time average.

$$\langle U_n^m U_{n'}^{m'} \rangle = \int U_n^m U_{n'}^{m'} f(U_n^m) d\, U_n^m = \delta_{nn'}\delta_{mm'}\langle |U_n^m(t)|^2 \rangle \quad [29]$$

Finally, invoking the equipartition theorem, which asserts that each independent mode in [Eq 27 d] contributes with a constant weight $\frac{k_B T}{2}$ (where k_B is the Boltzmann constant and T the absolute temperature), we will obtain [Eq 30]:

$$\frac{\kappa}{2}\lambda_n(\bar{\sigma},\bar{p})\langle |U_n^m(t)|^2 \rangle_t = \frac{k_B T}{2} \xrightarrow{yields} \langle |U_n^m(t)|^2 \rangle_t = \frac{k_B T}{\kappa}\frac{1}{\lambda_n(\bar{\sigma},\bar{p})} n \geq 2; |m| \leq n [30]$$

Recalling [Eq 24 b] we can obtain the final equation for the time-mediated squared fluctuation amplitudes $\langle |U_n^m(t)|^2 \rangle_t$ for spherical vesicles [Eq 31]:

$$\langle |U_n^m(t)|^2 \rangle_t = \frac{k_B T}{\kappa}\frac{1}{(n-1)(n+2)[\bar{\sigma}+n(n+1)]+2(2\bar{\sigma}-\bar{p})} [31]$$

Furthermore, exploiting the small perturbation approximation we are allowed to apply the well-known Laplace equation, which connects reduced membrane tension and pressure difference: $\bar{p} \approx 2\bar{\sigma}$. So, the second term in the denominator can be removed and we write [Eq 32], presented for the first time in [6], and we will use it for further experimental relationships.

$$\langle |U_n^m(t)|^2 \rangle_t = \frac{k_B T}{\kappa}\frac{1}{(n-1)(n+2)[\bar{\sigma}+n(n+1)]} \quad [32]$$

[Eq 31] and its approximation form for small fluctuations [Eq 32] show how all independent oscillators provide a constant contribution dependent only on the degree index *n*, independently of order *m*. This property is due to the fact that we are in a pure spherical symmetry condition. The couple of parameters: $(\kappa, \bar{\sigma})$ constituting the unknown physical properties of the vesicles, in particular the searched bending energy, which must remain constants upon degree *n≥2* increment. There are several fitting procedures exploitable and able to measure these parameters $(\kappa, \bar{\sigma})$, and we will see them later.

• Angular Correlation function

From a hypothetical point of view, if the experimental value of the whole 3-dimensional fluctuations function δu(θ,φ,t) was available, we could directly fit [Eq 32], simply decomposing δu(θ,φ,t) in the spherical harmonic basis. Nevertheless, optical microscopy is unable to acquire simultaneously the entire 3-dimensional structure of the quasi-spherical vesicles surface. Flickering spectroscopy technique reveals only the two-dimensional equatorial plane of the liposome, resembling its cross-section corresponding to θ=π/2. This condition is obtained when the focal plane of the microscope is placed at the section corresponding to the maximum vesicle diameter fluctuations, and equatorial-plane contour is observed with maximum contrast. Following the work of Fernandez-Puente et al [7], it is possible to correlate the previous theoretical finding for a membrane elasticity model in a 3-dimensional framework with the experimental quantities provided by the 2-dimensional equatorial-plane contours series. In particular, exploiting the angular correlation function, evaluated at equatorial plane (θ=π/2), defined in [Eq 33 c]. [Eq 33 a] represents the cross-sectional radius $r(\varphi, t)$, which describes the overall equatorial contour as a function of φ angle at a given frame t. [Eq 33 b] provides the average equatorial radius, integrating over φ angle , measured at a given frame t:

$$\begin{cases} r(\varphi,t) = R\left[1 + u\left(\theta = \frac{\pi}{2}, \varphi, t\right)\right] [33\ a] \\ r(t) = \frac{1}{2\pi}\int_0^{2\pi} r(\varphi,t)d\,\varphi [33\ b] \\ \xi(\gamma,t) = \frac{1}{2\pi R^2}\int_0^{2\pi}\big(r(\varphi+\gamma,t) - r(t)\big)\big(r(\varphi,t) - r(t)\big)d\,\varphi = \frac{1}{2\pi R^2}\left[\int_0^{2\pi} r(\varphi+\gamma,t)r(\varphi,t)d\varphi - r(t)^2\right] [33\ c] \end{cases}$$

Substituting $r(\varphi,t)$ from [Eq 33 a] in the angular correlation function $\xi(\gamma,t)$ [Eq 33 c] we will obtain a more suitable equation [Eq 34 a], where we can exploit spherical harmonics decomposition of fluctuation function $u(\theta,\varphi,t)$ (see Eq 18 d; Eq 23 a), for $\theta = \frac{\pi}{2}$ and obtain [Eq 34 b]. The symbol ~ means the complex conjugate component:

$$\xi(\gamma,t) = \frac{1}{2\pi R^2}\int_0^{2\pi}\left(u\left(\frac{\pi}{2},\varphi,t\right)\right)\left(\tilde{u}\left(\frac{\pi}{2},\varphi+\gamma,t\right)\right)d\,\varphi \quad [34\ a]$$

$$\xi(\gamma,t) = \frac{1}{2\pi}\int_0^{2\pi}\left(\sum_{n=0}^{N_{Max}}\sum_{m=-n}^{m=n} U_n^m(t)Y_n^m\left(\frac{\pi}{2},\varphi\right)\right)\left(\sum_{n\prime=0}^{N_{Max}}\sum_{m\prime=-n\prime}^{m\prime=n\prime} \widetilde{U_{n\prime}^{m\prime}(t)}\widetilde{Y_{n\prime}^{m\prime}}\left(\frac{\pi}{2},\varphi+\gamma\right)\right)d\,\varphi \quad [34\ b]$$

We can extract the coefficients of the expansions $U_n^m(t)$ and $\widetilde{U_{n\prime}^{m\prime}(t)}$ from the integral since they just depend on time:

$$\xi(\gamma,t) = \sum_{n=0}^{N_{Max}}\sum_{m=-n}^{m=n}\sum_{n\prime=0}^{N_{Max}}\sum_{m\prime=-n\prime}^{m\prime=n\prime} U_n^m(t)\,\widetilde{U_{n\prime}^{m\prime}(t)}\,\frac{1}{2\pi}\int_0^{2\pi} Y_n^m\left(\frac{\pi}{2},\varphi\right)\widetilde{Y_{n\prime}^{m\prime}}\left(\frac{\pi}{2},\varphi+\gamma\right)d\varphi \quad [35]$$

Adopting the already cited spherical harmonics orthogonal properties, regarding φ angle, we can solve the integral and write [Eq 36]:

$$\xi(\gamma,t) = \sum_{n=0}^{N_{Max}}\sum_{n\prime=0}^{N_{Max}}\sum_{m=-n}^{m=n} U_n^m(t)\widetilde{U_{n\prime}^{m}(t)}\,Y_n^m\left(\frac{\pi}{2},0\right)\widetilde{Y_{n\prime}^{m}}\left(\frac{\pi}{2},\gamma\right) [36]$$

Now we introduce the function: $\xi(\gamma) = \langle\xi(\gamma,t)\rangle_t$, which represents the angular correlation average with respect to time [Eq 37]:

$$\xi(\gamma) = \langle\xi(\gamma,t)\rangle_t = \sum_{n=0}^{N_{Max}}\sum_{n\prime=0}^{N_{Max}}\sum_{m=-n}^{m=n}\langle U_n^m(t)\widetilde{U_{n\prime}^{m}(t)}\rangle_t\,Y_n^m\left(\frac{\pi}{2},0\right)\widetilde{Y_{n\prime}^{m}}\left(\frac{\pi}{2},\gamma\right) [37]$$

Since the only time-dependent part in the formula is the product: $\langle U_n^m(t)\widetilde{U_{n\prime}^{m}(t)}\rangle_t$, we can invoke again the previous finding regarding statistical mechanics [Eq 29], recalling independency between different modes. The time-mediated angular correlation function can be rewritten as follow [Eq 38]:

$$\xi(\gamma) = \langle\xi(\gamma,t)\rangle_t = \sum_{n=2}^{N_{Max}}\sum_{m=-n;m\neq 0}^{m=m}\langle|U_n^m(t)|^2\rangle_t\,Y_n^m\left(\frac{\pi}{2},0\right)\widetilde{Y_n^m}\left(\frac{\pi}{2},\gamma\right)$$

Finally, recalling [Eq 32] we can replace, for *n≥2*, the squared time-mediated fluctuation amplitudes with the unknown physical parameters: $(\kappa,\bar{\sigma})$, obtaining [Eq 39]:

$$\xi(\gamma) = \sum_{n=2}^{N_{Max}} \sum_{m=-n;m\neq 0}^{m=m} \frac{k_B T}{\kappa} \frac{1}{(n-1)(n+2)[\bar{\sigma}+n(n+1)]} Y_n^m\left(\frac{\pi}{2},0\right) \widetilde{Y_n^m}\left(\frac{\pi}{2},\gamma\right) [39]$$

This final result shows how the time-averaged angular correlation function, (which could be experimentally evaluated from vesicles contour resumed analyzing images of the vesicles acquired at equatorial plane), is related to the searched physical parameters: $(\kappa, \bar{\sigma})$. From this point, we can proceed using two different pathways depending on the mathematical basis chosen for the angular correlation function decomposition. In the next section we will introduce the so call "Old" or "Classical" approach, since it was the first one to be exploited. In this case we will decompose the angular correlation time-averaged using Legendre polynomials basis.

▪ Classical Approach

Looking again at [Eq 39], we can highlight how the experimental quantity $\xi(\gamma)$, which represents the time-mediated angular correlation, is described by a sum of $N_{Max}(N_{Max}+1)-2$ terms, each one of these is constituted by two separated components. The former is represented by an unknown factor: $\frac{k_B T}{\kappa} \frac{1}{(n-1)(n+2)[\bar{\sigma}+n(n+1)]}$, depending on $(\kappa, \bar{\sigma})$, the searched parameters. The latter component is represented by a factorized couple of Laplace's spherical harmonics $Y_n^m\left(\frac{\pi}{2},0\right) \widetilde{Y_n^m}\left(\frac{\pi}{2},\gamma\right)$ which could be thought still as a mathematical basis for angular correlation decomposition. Nevertheless, in [Eq 39] the second sum specifies $m \neq 0$ and the couple of harmonic functions are evaluated for two different angular conditions. Thus, exploiting directly [Eq 39] decomposing angular correlation in the spherical harmonic basis to extrapolate $(\kappa, \bar{\sigma})$ is not suitable. Nevertheless, we can take back this incomplete harmonic basis decomposition into a new one structure, involving a different mathematical representation, the Legendre's polynomials. Using the spherical harmonics theorem [Eq 40 a], which connects the sum over m of the couple of factorized harmonic functions $Y_n^m\left(\frac{\pi}{2},0\right) \widetilde{Y_n^m}\left(\frac{\pi}{2},\gamma\right)$ to the associated Legendre's polynomials $P_n(\cos\gamma)$:

$$\begin{cases} P_n(\cos\lambda) = \dfrac{4\pi}{2n+1} \displaystyle\sum_{m=n}^{m=-n} \widetilde{Y_n^m}(\theta_1,\varphi_1) Y_n^m(\theta_2,\varphi_2) [40\ a] \\ \cos\lambda = \cos\theta_1\cos\theta_2 + \sin\theta_1\sin\theta_2\cos(\varphi_1-\varphi_2) \xrightarrow{yields} \cos\gamma\ [40\ b] \end{cases}$$

Since in [Eq 39] terms having $m=0$ are absent, we cannot use the theorem unless these $m=0$ terms have been subtracted from summation [Eq 41]. Note that the sum over m has been removed, since it is contained into $P_n(\cos\gamma)$:

$$\xi(\gamma) = \frac{k_B T}{4\pi\kappa} \sum_{n=2}^{N_{Max}} \left[\frac{2n+1}{(n+2)(n-1)(\bar{\sigma}+n(n+1))}\right] P_n(\cos\gamma) - \frac{k_B T}{4\pi\kappa} \sum_{n=2}^{N_{Max}} \left[\frac{Y_n^0\left(\frac{\pi}{2},0\right) \widetilde{Y_n^0}\left(\frac{\pi}{2},\gamma\right)}{(n+2)(n-1)(\bar{\sigma}+n(n+1))}\right] P_0(\cos\gamma) [41]$$

Considering again [Eq 32], which correlates the squared average-time amplitudes $\langle |U_n^m(t)|^2 \rangle_t$ to the searched parameters $(\kappa, \bar{\sigma})$, we can rewrite the experimental time-averaged angular correlation as follows [Eq 42]:

$$\xi(\gamma) = + \sum_{n=2}^{N_{Max}} \langle B_n(t) \rangle_t P_n(\cos\gamma) + \langle B_0 \rangle_t P_0(\cos\gamma) [42]$$

Where two different contribution can be highlighted: the first contribution resumes the angular correlation decomposition using Legendre's polynomials for *n≥2*, the second contribution recapitulates the overall $m=$

0 terms, which are absent in [Eq 39] definition, and are ascribed to the zero Legendre's polynomial component $P_0(\cos\gamma)$. More precisely [Eq 43]:

$$\langle B_n(t)\rangle_t = \begin{cases} \dfrac{2n+1}{4\pi}\,\langle |U_n^m(t)|^2\rangle_t ; for\ n \geq 2 \\ -\sum_{l=2}^{N_{Max}} Y_l^0\left(\frac{\pi}{2},0\right)\widetilde{Y_l^0}\left(\frac{\pi}{2},\gamma\right)\langle \left|U_l^0(t)\right|^2\rangle_t ; for\ n=0 \end{cases} \quad [43]$$

Only the first contribution is suitable for further fitting analysis in order to extrapolate $(\kappa, \bar{\sigma})$ parameters. The zero-order contribution $\langle B_0\rangle_t$ refers to vesicles radius changes over time, which are negligible [8]. Thus, $\langle B_0\rangle_t$ contribution to the fitting analysis is not relevant for bending constant evaluation. Introducing the theoretical expected $B_n(\kappa, \bar{\sigma})$ values, defined in [Eq 44], we can compare them to the corresponding experimental quantities $\langle B_n(t)\rangle_t$ for $(\kappa, \bar{\sigma})$ extrapolation:

$$B_n(\kappa,\bar{\sigma}) = \frac{2n+1}{4\pi}\frac{k_B T}{\kappa(n-1)(n+2)[\bar{\sigma}+n(n+1)]} \quad [44]$$

Now, the angular correlation function can be evaluated from the reconstructed contour coordinates of each vesicle image (See "Contour Evaluation Algorithm" section). Usually, for each analyzed vesicle a series of approximatively N_{images}~2000÷4000 images is acquired, with a frame rate of about 20 ms, depending on optical magnification conditions. Reasonably, investigated vesicles are imaged for a few minutes. The experimental angular correlation function is then decomposed into the Legendre's polynomial basis and a set of B_n coefficients for each image is evaluated. Before proceeding to the time-averaged coefficient calculation $< B_n >_t$ mediating the different N_{images} contribution arising from the image series, we must highlight an experimental construction limitation: the image acquisition time of the CCD camera. In particular, the images of the GUVs are taken every t_s=40 µs, and, consequently, modes having a relaxation time smaller than t_s cannot be observed. For this reason, all contributions coming from these not-observable modes must be however included in the analysis. Now we want to relate the theoretically corrected values (actually unknown) $B_n(t)$, which will be exploited in [Eq 44-46] for bending analysis, to the experimental quantities $B_n'(t)$ just obtained from autocorrelation function. More precisely, to relate the theoretical expected values $B_n(t)$ to the experimental quantities $B_n'(t)$, $B_n(t)$ terms must be multiplied by a correction coefficient. This time-integration correction factor has been previously introduced in [9]. In order to obtain $B_n(t)$, the corrected value of the experimental $B_n'(t)$, a couple of non-linear equations [Eq 45 a-b] must be numerically solved:

$$\begin{cases} \tau_n^m = \dfrac{4\pi\eta R^3}{k_B T}\left(2-\dfrac{1}{n(n+1)}\right) B_n [45\ a] \\ B_n' = 2\left(\dfrac{\tau_n^m}{t_s}\right)^2\left[\dfrac{t_s}{\tau_n^m} + e^{-\frac{t_s}{\tau_n^m}} - 1\right] B_n [45\ b] \end{cases}$$

A correlation time τ_n^m is introduced for each B_n mode. The parameter η represents the viscosity of the medium surrounding the liposome. R is the GUV radius, k_B is the Boltzmann constant and T is the temperature (in Kelvin). The new set of coefficients $B_n(t)$ is used to evaluate the time-mean coefficient $< B_n >_t$, then the least-squared "*LS*" fitting procedure [Eq 46] is performed through a non-linear Levenberg-Marquardt algorithm:

$$LS(\kappa,\bar{\sigma}) = \sum_{n=2}^{n=N_{lim}}\left[\frac{B_n(\kappa,\bar{\sigma}) - \langle B_n(t)\rangle_t}{STD_n}\right]^2 \quad [46]$$

where STD_n represents the corresponding standard-deviation of the associated $\langle B_n(t)\rangle_t$ mean coefficient. The set of coefficients $(\kappa, \bar{\sigma})$ that minimizes $LS(\kappa, \bar{\sigma})$ will be extrapolated as the bending constant and reduced surface tension, respectively, which describes the investigated vesicle. As show in [Eq 46] the least-squared problem involves several modes, starting from the second up to certain N_{lim} index. The fitting procedure and subsequent $(\kappa, \bar{\sigma})$ parameter extractions are highly sensitive to the number of modes chosen in the procedure, for several reasons.

First, looking again at [Eq 43] for *n≥2* we can observe how the decomposition coefficients $B_n(t)$ arise from strictly positive quantities $|U_n^m(t)|^2$, for this reason $B_n(t)$ negative coefficients contributions must be removed from calculation: $\langle B_n(t)\rangle_t$, since they have not physical meaning. Second, nevertheless squared deviations in [Eq 46] are weighted by STD_nwe must also consider that $B_n(\kappa, \bar{\sigma})$ scales proportionally to ~n^{-2} with respect to the order index, meaning that higher order contributions are less detectable in the fitting approach. Furthermore, these higher order modes are related to spatial scale fluctuations comparable to the pixel resolution of camera itself, or alternatively their correlation-time are comparable to the integration time t_s. For these arguments, summation in [Eq 46] is truncated to $N_{lim} = 14$. Third, the lower modes correspond to the longest space scale fluctuations, whose relaxation occurs even in several seconds, depending on the vesicle diameter size. Thus, although low order modes are easily detectable, they are characterized by poor statistical analysis. In fact, imaged vesicles acquisition should be prolonged up to approximatively ~10÷15 min to record enough relaxation events for these lower modes (n=2÷3), which is experimentally inapplicable due to vesicle translation out of ROI (Region-Of-Interest) boundaries. For these arguments, usually the lowest order considered in the fitting procedure is n=4 [10]. In Fig 3 an example of the Legendre's Polynomial coefficients decomposition and subsequent fitting for a DOPC vesicle to extrapolate $(\kappa, \bar{\sigma})$ parameters set is reported.

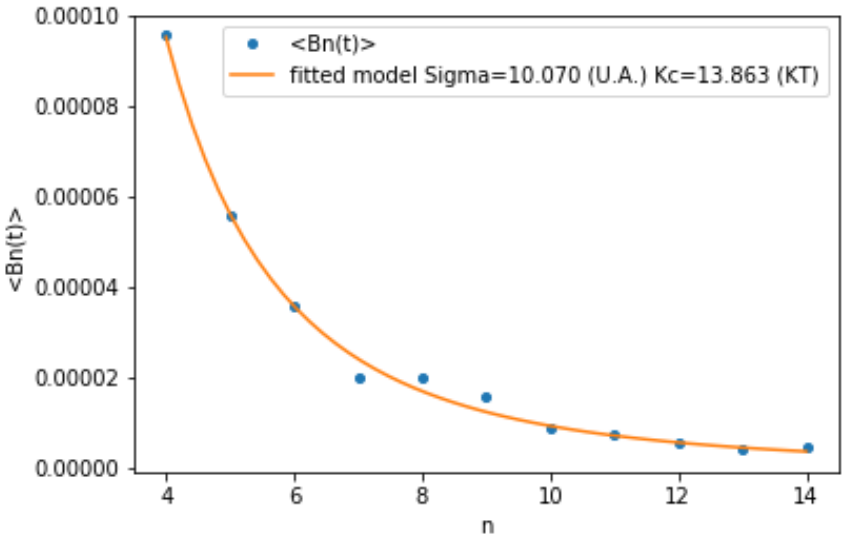

Figure 3: Time averaged Legendre's Polynomial coefficients <$B_n(t)$> (blue dots) obtained from angular autocorrelation decomposition of a DOPC vesicle and subsequent fitting (yellow curve) to extrapolate the Bending constant: K_c=13.86 K_bT and the reduced surface tension: $\bar{\sigma}$=10.07

Recalling some of the hypothesis/assumptions introduced during previous theoretical derivation, we should consider quasi-spherical vesicles whose fluctuations are clearly observable, not simply imputable to camera integration-time noise. For these reasons the vesicles should not be too small, not too tensed, otherwise surface tension will suppress thermal noise, and no surface defects should be present. Using these criteria, following [11] work, we developed the following protocol in order to choose correctly the investigated vesicles:

- vesicles with radius smaller than 10 µm has been discarded;
- vesicles with a resulting reduced surface tension $\bar{\sigma}$ out of this range [-4÷50] are discarded (negative $\bar{\sigma}$ value suggest a particular fluctuating vesicles and are still acceptable unless quasi-spherical shape is maintained. Too high $\bar{\sigma}$ values imply poor bending constant detection);
- vesicles with surface defects or not conserving quasi-spherical shape or its radius are discarded,
- vesicles containing smaller vesicles are discarded.

Statistical Approach

As mentioned above, using Legendre's polynomial decomposition of the angular correlation factor, only approximatively 10÷12 modes, spanning from [2°÷14°] are suitable for the fitting procedure. In Fig 4 the frequency distribution of the Legendre's polynomial decomposition coefficients B_n of angular correlation function obtained from a series of 1500 images of a fluctuating DOPC vesicle is reported.

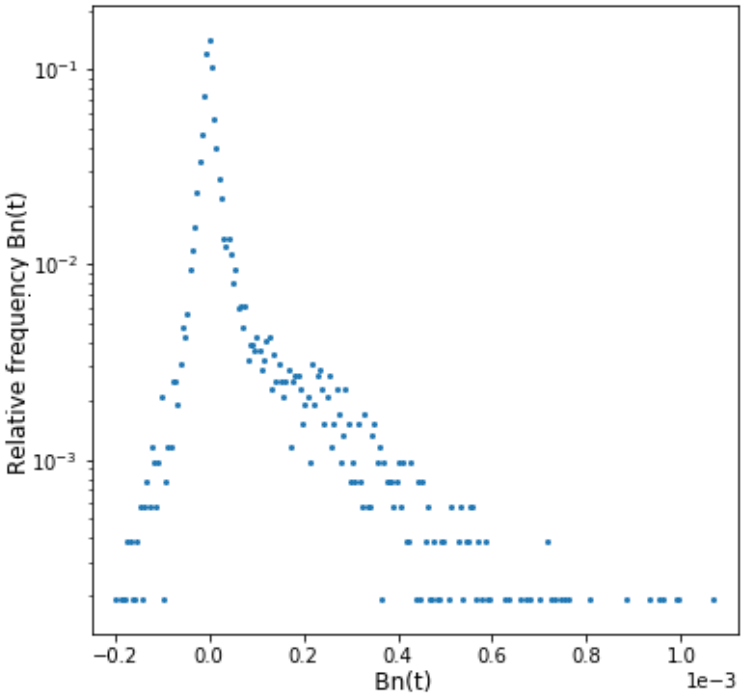

Figure 4: Frequency distribution of the Legendre's Polynomial coefficients $B_n(t)$ obtained from the angular autocorrelation function of a DOPC fluctuating vesicle (≈1500 frames).

The vertical axis, representing the event-frequency, is a logarithmic scale to highlight how largely frequency coefficients B_n could vary, depending on the considered index mode. In particular, two key aspects appear in the frequency distribution factor.

Firstly, although a small fraction of experimental coefficients B_n has negative contributions, a clearly asymmetric distribution shifted toward positive values can be observed from Fig 4. Confirming that B_n coefficients are strictly positive, since they are connected to the squared fluctuation amplitudes from [Eq 43]. Negative contributions are present for two different reasons: they could be referred to the zero-order index *n=0*, which should in fact be strictly negative [Eq 43] and is not included in the fitting procedure. Alternatively, these negative contributions could be related to higher index orders (above 14°) where time-relaxation is comparable to the camera integration-time itself and various experimental noises could occur.

The second aspect that arises from Fig 4, looking at positive contributions, is that the higher B_n coefficients present in the decomposition, ascribed to the first modes involved in the analysis, constitute a minority. While, most of the B_n are however positive but are not included in the fitting procedure for several reasons described in the "Old" approach section. Essentially, these positive contributions obtained from Legendre decomposition arise from higher modes and are systematically ignored. Thus, the old approach poses a further question, "Does it exist a different method able to include also the higher modes? Since they constitute a not negligible frequency population?"

The "Statistical" approach has been introduced in order to respond to these crucial issues arising from the "Old" approach [12]. In particular, it exploits part of the higher modes not originally involved in the "Old" approach. As highlighted by its definition, "Statistical" approach proposes a method that introduces a new mathematical basis to decompose angular correlation, and exploit how their coefficients decomposition is statistically distributed, instead of simply evaluate their arithmetic means for further fitting procedure. The goal is to redefine angular correlation decomposition using the Fourier basis. In this approach free energy and angular correlation are rewritten as a superposition of a new set of independent modes, and each mode owns its characteristic angular-periodicity, and we are focused on how each mode is statistically distributed. We will start from the radius fluctuations, passing toward free energy, to finally obtain angular correlation Fourier decomposition. We will demonstrate that angular correlation can be written as a pure cosine decomposition, and each coefficient obtained from its decomposition follows a mono-exponential decay, suitable to extrapolate the bending constant through a non-linear fitting procedure.
Starting from vesicles radius description, which has been previously decomposed using spherical harmonic [Eq 18 d; Eq 23 a]:

$$r(\theta,\varphi,t) = R[1+u(\theta,\varphi,t)] = R\left[1+\frac{A_0^0+U_0^0(t)}{\sqrt{4\pi}}+\sum_{n\geq 2;|m|\leq n} U_n^m(t)Y_n^m(\theta,\varphi)\right] [47]$$

we can rearrange the last term, containing fluctuations analysis, as follows [Eq 48]:

$$r(\theta,\varphi,t) = R\left[1+\frac{A_0^0+U_0^0(t)}{\sqrt{4\pi}}+\sum_{n\geq 2}\left(a_n^0\overline{P_n^0(\cos\theta)}+\sum_{0<m\leq n}(a_n^m\cos(m\varphi)+b_n^m\sin(m\varphi))\,\overline{P_n^m(\cos\theta)}\right)\right] [48]$$

where the new terms: $\overline{P_n^m(\cos\theta)}$ and a_n^m, b_n^m have been introduced following [Eq 49 a-b]:

$$\begin{cases} \overline{P_n^m(x)} = (-1)^m\sqrt{\dfrac{(2n+1)(n-m)!}{4\pi(n+m)!}}P_n^m(x) \xrightarrow{yields} Y_n^m(\theta,\varphi) = \overline{P_n^m(\cos\theta)}e^{im\varphi} [49\ a] \\ U_n^m(t) = \dfrac{a_n^m(t)-ib_n^m(t)}{2} [49\ b] \end{cases}$$

[Eq 48] has been obtained manipulating [Eq 47] and adopting [Eq 49 a-b] definition. [Eq 48] represents the vesicles radius description using a different mathematical basis: The Fourier decomposition, and will be useful in further angular correlation redefinition.

Now we recall [Eq 27 d], which describes the overall elastic energy of the vesicles around its equilibrium state, as a sum of squared amplitude fluctuations $|U_n^m(t)|^2$, multiplied by the eigenvalues $\lambda_n(\bar{\sigma},\bar{p})$. Using previous Laplace equation $\bar{p} \approx 2\bar{\sigma}$ we rewrite: $\lambda_n(\bar{\sigma},\bar{p}) \approx \lambda_n(\bar{\sigma}) = (n-1)(n+2)[\bar{\sigma} + n(n+1)]$

$$\frac{1}{2}\delta^2 F\{\delta u\} = \frac{\kappa}{2}\lambda_0(\bar{\sigma},\bar{p})\left|U_0^0(t)\right|^2 + \frac{\kappa}{2}\sum_{n=2}^{N_{Max}}\lambda_n(\bar{\sigma})\sum_{m=-n}^{m=n}|U_n^m(t)|^2\ [27\ d']$$

We can rearrange the summation separating positive order *m* contribution from negative ones [Eq 27 d'']:

$$\frac{1}{2}\delta^2 F\{\delta u\} = \frac{\kappa}{2}\lambda_0(\bar{\sigma},\bar{p})\left|U_0^0(t)\right|^2 + \frac{\kappa}{2}\sum_{n=2}^{N_{Max}}\lambda_n(\bar{\sigma})\left[|U_n^0(t)|^2 + \sum_{1\le m\le n}(|U_n^m(t)|^2 + |U_n^{-m}(t)|^2)\right][27\ d'']$$

Then we exploit the following relation that bounds squared amplitudes fluctuation between spherical harmonic (having opposite order index *m*) and Fourier decompositions [Eq 50]:

$$|U_n^m(t)|^2 + |U_n^{-m}(t)|^2 = \frac{1}{2}(|a_n^m(t)|^2 + |b_n^m(t)|^2)[50]$$

As final result, we can redefine the total free energy around its equilibrium state using Fourier basis [Eq 51].

$$\frac{1}{2}\delta^2 F\{\delta u\} = \frac{\kappa}{2}\lambda_0(\bar{\sigma},\bar{p})\left|U_0^0(t)\right|^2 + \frac{\kappa}{2}\sum_{n=2}^{N_{Max}}\lambda_n(\bar{\sigma})\left[|a_n^0(t)|^2 + \frac{1}{2}\sum_{1\le m\le n}(|a_n^m(t)|^2 + |b_n^m(t)|^2)\right][51]$$

What we have obtained is an alternative description of the total surface elastic energy, but still governed by a different set of independent harmonic oscillators. So, for each squared contribution: $|a_n^0(t)|^2$, $|a_n^m(t)|^2$, $|b_n^m(t)|^2$ we can invoke again the equipartition theorem and each squared amplitude in Fourier decomposition follows a Gaussian distribution. Thus, statistical distributions for a_n^0, $a_n^m$and b_n^m can be written using [Eq 52 a-b], where: $\alpha_n^0(x)$, $\alpha_n^m(x)$and $\beta_n^m(x)$ are the Boltzmann statistics of the corresponding amplitude: a_n^0, a_n^m and b_n^m respectively:

$$\begin{cases} \alpha_n^0(x) = \sqrt{\dfrac{\kappa\lambda_n(\bar{\sigma})}{2\pi k_b T}}\, e^{-\frac{\kappa\lambda_n(\bar{\sigma})x^2}{2k_b T}}\ [52\ a] \\ \alpha_n^m(x) = \beta_n^m(x) = \sqrt{\dfrac{\kappa\lambda_n(\bar{\sigma})}{4\pi k_b T}}\, e^{-\frac{\kappa\lambda_n(\bar{\sigma})x^2}{4k_b T}}\ [52\ b] \end{cases}$$

Now we rewrite the fluctuations radius at the equatorial plane $\theta = \frac{\pi}{2}$, obtaining [Eq 53] (From now on we will consider an implicit time dependence of a_n^0, a_n^m and b_n^m coefficients):

$$r(\varphi,t) = R\left[1 + \frac{A_0^0 + U_0^0(t)}{\sqrt{4\pi}} + \sum_{n\ge 2}\left(a_n^0\overline{P_n^0(0)} + \sum_{0<m\le n}(a_n^m\cos(m\varphi) + b_n^m\sin(m\varphi))\,\overline{P_n^m(0)}\right)\right][53]$$

Similarly, we rewrite the mean radius at the equatorial plane [Eq 54]:

$$r(t) = \frac{1}{2\pi}\int_0^{2\pi} r(\varphi,t)d\,\varphi = R\left[1 + \frac{A_0^0 + U_0^0(t)}{\sqrt{4\pi}} + \sum_{n\ge 2}a_n^0\overline{P_n^0(0)}\right][54]$$

Subtracting from each other Eq 53 and Eq 54 we essentially remove the first two terms in $r(\varphi,t)$, obtaining [Eq 55]:

$$r(\varphi,t)-r(t)=R\left[\sum_{n\geq 2}\sum_{0<m\leq n}\left(a_n^m\cos(m\varphi)+b_n^m\sin(m\varphi)\right)\overline{P_n^m(0)}\right][55]$$

We can invert the order summation between degree *n* and order *m* index and rearrange the terms as follows, remembering that n has un upper limit N_{Max}, obtaining [Eq 56 d]:

$$\begin{cases} r(\varphi,t)-r(t)=R\sum_{0<m}^{N_{Max}}\left[\cos(m\varphi)\sum_{n\geq m}^{N_{Max}}a_n^m\overline{P_n^m(0)}+\sin(m\varphi)\sum_{n\geq m}^{N_{Max}}a_n^m\overline{P_n^m(0)}\right][56\ a] \\ \alpha^m=\sum_{n\geq m}^{N_{Max}}a_n^m\overline{P_n^m(0)}\ [56\ b] \\ \beta^m=\sum_{n\geq m}^{N_{Max}}b_n^m\overline{P_n^m(0)}\ [56\ b] \\ r(\varphi,t)-r(t)=R\sum_{0<m}^{N_{Max}}\left[\alpha^m\cos(m\varphi)+\beta^m\sin(m\varphi)\right][56\ d] \end{cases}$$

The new terms introduced α^m and β^m, are a linear combination of the a_n^m and b_n^m sets respectively, where the weights in the summation are represented by the $\overline{P_n^m(0)}$ constant. Since the original sets a_n^m and b_n^m follow a Gaussian distribution, the new variables α^m and β^m follow a Gaussian distribution as well. Nevertheless, since the different contributions in the sums [56 b-c] bring a different weight, depending on $\overline{P_n^m(0)}$ constant, the Boltzmann statistics of α^m and β^m must be re-normalized as follows [Eq 57]:

$$A^m(y)=B^m(y)=\sqrt{\frac{\kappa\lambda_n(\bar{\sigma})}{4\pi k_bT\sum_{n\geq m}\left[\overline{P_n^m(0)}\right]^2}}e^{-\frac{\kappa\lambda_n(\bar{\sigma})}{4k_bT}\frac{y^2}{\sum_{n\geq m}\left[\overline{P_n^m(0)}\right]^2}}[57]$$

α^m and β^m coefficients are in fact experimentally follow a gaussian distribution. As example, in Fig 5 the frequency distributions of α^8 and β^8 coefficient modes are reported:

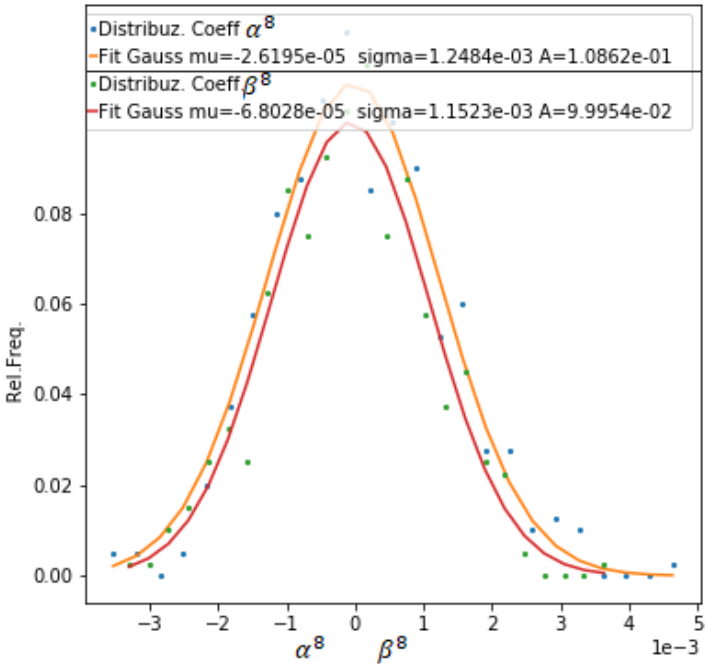

Figure 5: Experimental distribution of α^8 (blue dots) and β^8 (green dots) coefficient modes and subsequent gaussian fits, yellow and red curve, respectively

Finally, we can recall the angular correlation defined in [Eq 33 c], and, using the previously introduced quantities [56 b-c], after some rearrangement we can rewrite the angular correlation as follows [Eq 58]:

$$\xi(\gamma,t) = \frac{1}{2}\sum_{0<m}^{N_{Max}}\left[\left(\alpha^m(t)\right)^2 + \left(\beta^m(t)\right)^2\right]\cos(m\gamma) = \sum_{0<m}^{N_{Max}}\xi^m(t)\cos(m\gamma) \text{ [58]}$$

[Eq 58] shows how the angular correlation function can be decomposed in a pure cosine basis, where we have substituted $\xi^m(t) = \frac{1}{2}\left[\left(\alpha^m(t)\right)^2 + \left(\beta^m(t)\right)^2\right]$. Since both $\alpha^m(t)$ and $\beta^m(t)$ follow a Gaussian distribution, their squared values $\left(\alpha^m(t)\right)^2$ and $\left(\beta^m(t)\right)^2$ will follow a mono-exponential distribution. These couple variables $\left(\alpha^m(t)\right)^2$ and $\left(\beta^m(t)\right)^2$ are so distributed as a mono-exponential decay with the same features (See [Eq 57]), and are statistically independent. Thus, we expect that also $\xi^m(t)$ follows a mono-exponential distribution, since it is written as the product of $\left(\alpha^m(t)\right)^2$ and $\left(\beta^m(t)\right)^2$ distributions. We will obtain that the $\xi^m(t)$ distribution: $\Xi^m \propto exp\left[-\frac{\kappa\lambda_n(\bar{\sigma})}{4k_bT}\cdot\frac{x^2+y^2}{\sum_{n\geq m}\left[P_n^m(0)\right]^2}\right]$ where x and x are representing $\alpha^m(t)$ and $\beta^m(t)$ space variables respectively. Adopting polar coordinates transformation defining *z* as: $z = \frac{1}{2}(x^2+y^2)$ where z represents ξ^m space variable, we can normalize the $\xi^m(t)$ distribution as follow [Eq 59]:

$$\Xi^m(\xi^m) = \frac{\kappa\lambda_n(\bar{\sigma})}{2\pi k_bT\sum_{n\geq m}\left[P_n^m(0)\right]^2}e^{-\frac{\kappa\lambda_n(\bar{\sigma})}{2k_bT}\frac{\xi^m}{\sum_{n\geq m}\left[P_n^m(0)\right]^2}} = \Delta^m e^{-\Delta^m\cdot\xi^m} \text{ [59]}$$

where in the last member we have substituted Δ^m using [Eq 60]

$$\Delta^m = \frac{\kappa\lambda_n(\bar{\sigma})}{2\pi k_b T \sum_{n\geq m}\left[\overline{P_n^m(0)}\right]^2} [60]$$

The Δ^m definition [Eq 60] highlights how the statistical distribution of the coefficient ξ^m obtained from cosine decomposition of angular correlation can be summarized including only three parameters $\left[\kappa; \lambda_n(\bar{\sigma}); \sum_{n\geq m}\left[\overline{P_n^m(0)}\right]^2\right]$. The first two are the searched physical parameters, while the latter is a pure mathematical factor. In particular, this sum converges quickly with the *n* index, avoiding possible fitting procedure issues arising in the denominator.

Thus, using angular correlation function experimentally evaluated for each vesicles frame $\xi(\gamma, t)$, we can decompose it using Fourier basis and confirm that it is a pure pair function, since recalling [Eq 58] it can be described as a pure cosine decomposition. From each vesicle frame we can then extrapolate a different set of $\xi^m(t)$ decomposition coefficients. For each mode *m* we can analyze its statistical distribution and confirm that corresponds to a mono-exponential decay, expecting strictly positive $\xi^m(t)$ coefficients for all modes. From the statistical distribution of $\xi^m(t)$ we can linearize its exponential decay and extrapolate the corresponding slope Δ^m, for each mode. Finally, the obtained set of slopes Δ^m arising from different modes can be exploited to extrapolate $(\kappa, \bar{\sigma})$ parameters using a non-linear Levenberg-Marquardt procedure. Some prescription should be highlighted during statistical distribution linearization, when the slopes Δ^m are evaluated. In Fig 6 the statistical distribution of the m=8 mode is reported.

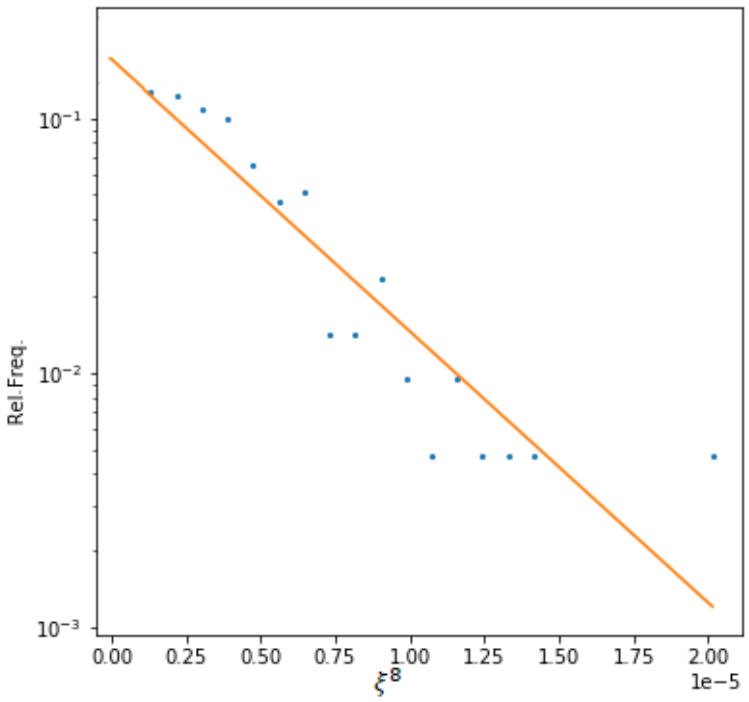

Figure 6: Statistical distribution for the 8-th mode experimentally obtained and plotted in linear-log scale (blue dot), and subsequent fitting procedure (yellow line) to extrapolate Δ^8slope

Some deviations from mono-exponential decay (see Fig 6) could occur at very low frequency regime (far right of the curve). These contributions constitute rare events whose statistical description is poorly explored, and these points should be removed from the fitting analysis. At very high frequency regime (far left of the curve) other deviations could appear due to the white noise arising from starting contour evaluation. Thus, very high frequencies should be fitted with a cut-off limit. Finally, rare but still possible $\xi^m(t)$ coefficients with negative values arising from cosine decomposition must be removed. In Fig 7 the experimental Δ^m coefficients obtained from the same DOPC vesicle analyzed in Fig 3 is reported, where we adopted the angular autocorrelation ("old-approach"), and subsequent non-linear fitting to extrapolates the $(\kappa, \bar{\sigma})$ parameters.

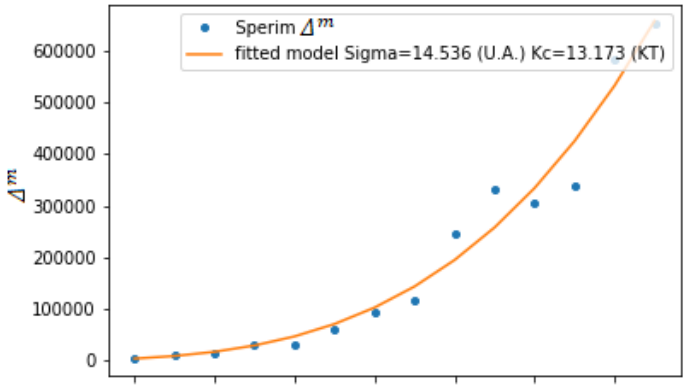

Figure 7: experimental coefficients obtained from a DOPC vesicle (blue dots) and subsequent fitting procedure (yellow curve) to extrapolate the Bending constant: K_c=13.86K_bT and the reduced surface tension: $\bar{\sigma}$=10.07

- **Contour Evaluation Algorithm**

In this subsection we will illustrate how our contour evaluation protocol has been developed following previous procedures, in particular [13]. Our contour analysis algorithm has been written using Python scripts. The vesicle frame acquired is a 12÷16-bit depth gray-scale image.

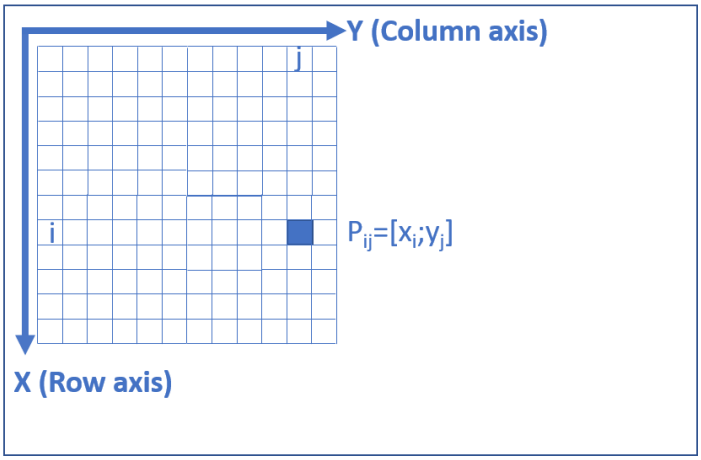

Figure 8: Pixel coordinates frame of reference of the liposome image

In the first step the image is read and numerically interpreted as a two-dimensional matrix object of size $[N_{rows};N_{columns}]$, where N_{rows} and $N_{columns}$ represent the number of rows and columns of the image, respectively. Each pixel intensity of the image spans over a range of: $[0\div2^{bit\text{-}depth}-1]$. In Fig 8 the frame of reference of the pixel coordinates is reported.

Next step consists of the identification of the vesicle's boundaries exploiting the rows pixel intensity profiles analysis. As mentioned above, the inner liposome volume is filled with sucrose dispersed in aqueous medium, while the surrounding medium is composed by water with glucose. Since the sucrose and glucose have two different refractive indexes, then the mean pixel intensities measured inside and outside the liposome are also different (we use phase imaging). Thus, we expect to measure a constant and flattened pixel intensity profile in rows that do not intercept the liposome boundaries. Instead, when the row profile intercepts the liposome boundaries we expect to see a double discontinuity; when the row passes through the glucose-lipid bilayer-sucrose and through the sucrose-lipid bilayer-glucose interfaces, respectively. In Fig 9b is reported a flattened row intensity profile that does not cross the vesicle boundaries (blue dotted line of Fig 9c), in Fig 9a another row intensity profile that crosses the vesicle boundaries and two discontinuity regions is shown

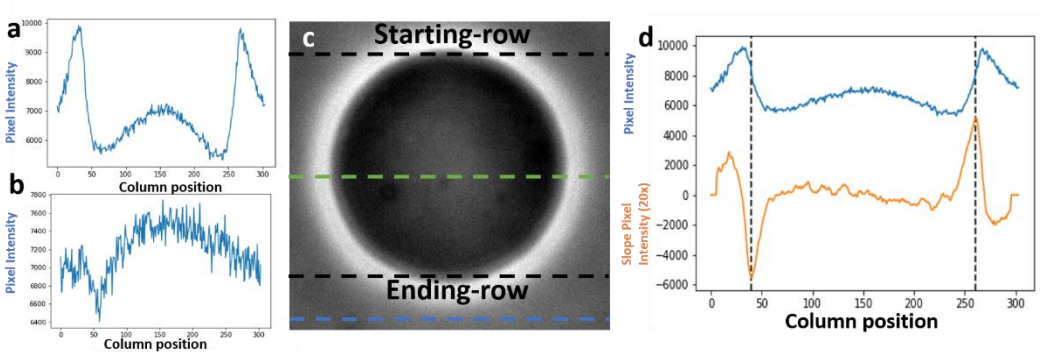

(green dotted line of Fig 9c). The vesicle boundaries search can be performed scanning the pixel intensity row

Figure 9: (a-b) pixel intensity row profile intercepting liposome boundary (green dotted line), and not intercepting the liposome (blue dotted line). (c) liposome frame at a given time frame. (d) Pixel intensity (blue line) and its slope along column (y) axis (orange line 20x magnified).

profiles (at fixed row index and scanning the column index coordinate) and establish an objective criterion to identify these profile discontinuities.

As first attempt we proposed a test-parameter based on the ratio between the mean intensity profile measured inside and outside the liposome. As shown in Fig 9a, when the columns coordinate in the row pixel intensity profile (along y-direction) is reaching or overcoming the liposome boundary, a local peak maximum is observable. Accordingly, the liposome contour in Fig 9c is surrounded by a circular brighter halo. Thus, identifying these two local maxima allows us to distinguish the internal and the external region of the liposome for a given row line. Further confirmation that the region between the two peaks is including the inner part of the liposome is based on the average intensity comparison measured inside and outside the peaks. In fact, the average intensity inside the liposome is lower than the mean intensity value outside, since the sucrose and glucose have different refractive indexes. Thus, the test-parameter regarding this intensity ratio [Eq 61] has been proposed:

$$I_{ratio} = \frac{\langle I_{Inside-liposome} \rangle}{\langle I_{Outside-liposome} \rangle} < I_{ratio-edge} [61]$$

where $\langle I_{Inside-liposome} \rangle$ and $\langle I_{Outside-liposome} \rangle$ are the average intensity measured inside and outside the two peaks, respectively, while $I_{ratio-edge}$ is the threshold edge parameter. The row profiles (along y-direction) are analyzed first from the top of the image corner row-index=0, running from left to right. When the [Eq 61] has been satisfied the same analysis is proposed starting from the bottom of the image corner, row-index= N_{rows}-1, when also the second research is concluded we have the starting-row-index and the ending-row-index, respectively. Nevertheless, this first approach based on the intensity-ratio- reveals some lacks, essentially related to the non-uniform illumination of the imaged area. Thus, a second method to evaluate the starting and the ending row indexes has been developed.

The second approach analyze again the row intensity profiles (along y-direction, at fixed row and varying column index), but in this case the slope signal of the pixel intensity is numerically evaluated. A moving window of 11 pixels size is used to extrapolate the mean slope around each pixel column coordinate, obviously the first and the last 5 pixels are ignored in the analysis. The slope intensity is averaged over 11 pixels in order to minimize image noise between neighboring pixels. When the row profile encounters the lipid-bilayer interface it undergoes a fast variation. More precisely, the row profile passing through the glucose-lipid bilayer-sucrose experiences a fast decrement, while passing through the sucrose-lipid bilayer-glucose it undergoes a fast increment. These fast variations are ascribable to the lipid bilayer barrier thickness, which is approximatively ≈4÷5 nm. Thus, these pixel intensity modifications are clearly observable when the slope pixel intensity is introduced (see Fig 9d) and the associated peaks are really sharped and easily detectable. In particular, a negative peak is associated to the glucose-lipid bilayer-sucrose interface, while a positive peak is ascribable to the sucrose-lipid bilayer-glucose interface. A second test-parameter is introduced, based on the pixel-separation between the position of the minimum and the maximum values in the row pixel slope profile. $Dist_{Min-Max}$ is the test parameter and it measures the separation, expressed in pixel unit, between the minimum (first interface, on the left) and the maximum (second interface, on the right) in the row slope intensity profile. [Eq 62] represents the condition that must be satisfied to identify the starting-row or the ending-row index.

$$Dist_{Min-Max} = Pos_{Min} - Pos_{Max} > Dist_{Edge} [62]$$

where Pos_{Min} and Pos_{Max} represent the column position where it is placed, respectively, the minimum and the maximum value in the slope intensity profile, while $Dist_{Edge}$ is the edge parameter (≈30 pixels). Condition of [Eq 62] must be tested only when the peaks corresponding to Pos_{Min} and Pos_{Max} are quite sharp, otherwise, they could arise from background noise and the row profile is not crossing the liposome boundaries. This second approach was really robust and reliable, thus we adopted this option.

Since the criterion implemented to evaluate the starting-row and the ending-row index is equal, we expect that these row indexes are placed almost symmetrically from the liposome center row axis. The mean-row index: $\langle row \rangle$ evaluated averaging the starting and the ending row should almost intercept the liposome

center: $\langle row \rangle = (Starting_{row} + Ending_{row})/2$. Now, analyzing the slope pixel intensity profile of $\langle row \rangle$ we can provide a first estimation of liposome diameter D and center $[row_C; column_C]$ [Eq 63 a-c]:

$$\begin{cases} D = Pos_{Min}(\langle row \rangle_{slope}) - Pos_{Max}(\langle row \rangle_{slope}) \; [63a] \\ row_C = \langle row \rangle \; [63b] \\ column_C = Pos_{Min}(\langle row \rangle_{slope}) + \dfrac{D}{2} \; [63c] \end{cases}$$

The equatorial plane of the liposome is described by a fluctuating circular-shaped contour, thus, we can split up approximatively the contour perimeter in 8 regions equally spaced and define this quantity as: $Interval = \pi D/8$. This is just an approximation since the measured perimeter contour: $2p_{Real}$ is larger than the circular perimeter: $2p_{circ} = \pi D$, due to thermal fluctuations. The algorithm proposed reconstructs the contour perimeter step-by-step (pixel-by-pixel) through an iterative approach. Thus, we suppose to conclude the contour reconstruction when the iterate-index in close to: $2p_{circ}$, since all the geometrical parameters are expressed in pixel units. Using the $Interval$ parameter we can estimate which one of the 8 contour sectors we are building.

In the next step, we set the provisional contour starting-point using the previous information [Eq 64 a-b]. According to the frame of reference in Fig 10a, we specify that the starting-point is aligned to $row_C = \langle row \rangle$ along the vertical axis x, in the far right of the horizontal axis y, and the reconstruction contour is performed in the counterclockwise direction. Finally, the row-column pixel coordinates of contour points: $[row_i; column_i]$ (where the subscript i index refers to the i-th contour point) are converted in polar coordinates $[r_i; \theta_i]$ (where r_i and θ_i are the radial distance and the polar angle measured from the liposome center). The coordinates conversion from cartesian-to-polar is done accordingly to Fig 10b frame of reference.

$$\begin{cases} row_{Start} = \langle row \rangle \; [64a] \\ column_{Start} = Pos_{Max}(\langle row \rangle_{slope}) [64b] \end{cases}$$

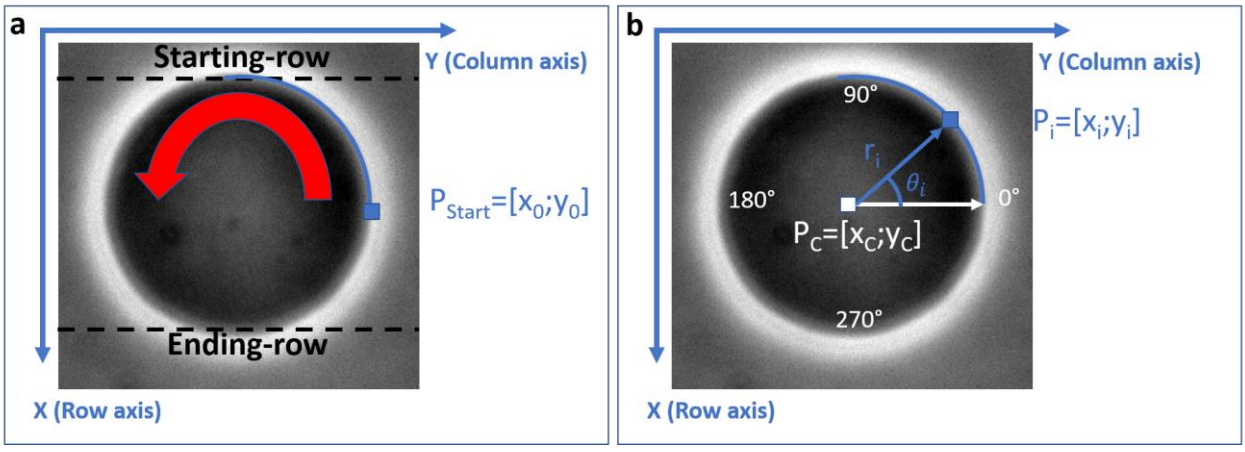

Figure 10: (a) Frame of reference for contour starting point and subsequent counterclockwise direction. (b) Planar to polar contour point conversion.

As mentioned early, the slope of the pixel intensity profile is a useful tool in the liposome boundaries evaluation. Since now, the slope of the pixel intensity profile has been exploited for the profiles of the rows, along y-direction, (constant row index and scanning the column index). Intuitively, this derivative-based approach is highly sensitive when the liposome lipid bilayer barrier is placed almost perpendicularly to the profile direction, since the scanning direction intercept the minimal cross-section barrier, whereas it is almost

ineffective when profile direction and liposome bilayer are mutually parallel. Accordingly, the slope pixel intensity along the row profile is maximized close to $row_{index} = \langle row \rangle$ and is instead insensitive around $row_{index} = \langle row \rangle \pm D/2$. Thus, a set of four directions namely: [x,y,v,w] has been proposed [13] to analyze and reconstruct locally the slope pixel intensity from these different directions, for a given contour point. In Fig 11 shown are the four direction profiles: along x-direction (column profile) is placed m_y gradient, which evaluates the slope pixel intensity at fixed column line (fixed y), and varying column index x; along y-direction (row profile) is placed m_x which evaluates the slope pixel intensity at fixed row line (fixed x) and varying the column index y (already adopted to extrapolate starting-row and the ending-row indexes). Thus, m_y gradient, which studies pixel intensity variation along x-direction (fixed column index y) is really efficient when we are moving using row profiles placed close the liposome center ($column_{index} \approx column_C$). We considered also two additional directions, v and w (and subsequent gradient m_v and m_w), which are placed mutually perpendicular and run diagonally with respect to x-direction (fixed-column y) and y-direction (fixed-row x). In v and w directions the pixel intensity is evaluated along the pixel diagonal displacement, since the row and column indexes are moved simultaneously. In fact, in w direction the row (x) and column (y) index increase together, in v direction the row index (x) increases while the column index (y) decreases. Since the pixel intensity profile is evaluated for a large displacement in v and w directions, along diagonal axis, actually $\sqrt{2}$ times the x and y directions, we expect a larger pixel intensity variation. Thus, the subsequent slopes measured in v and w direction are weighted and normalized by a factor $1/\sqrt{2}$. We expect that v and w directions provide a larger slope pixel intensity contribution for contour points placed between x-direction

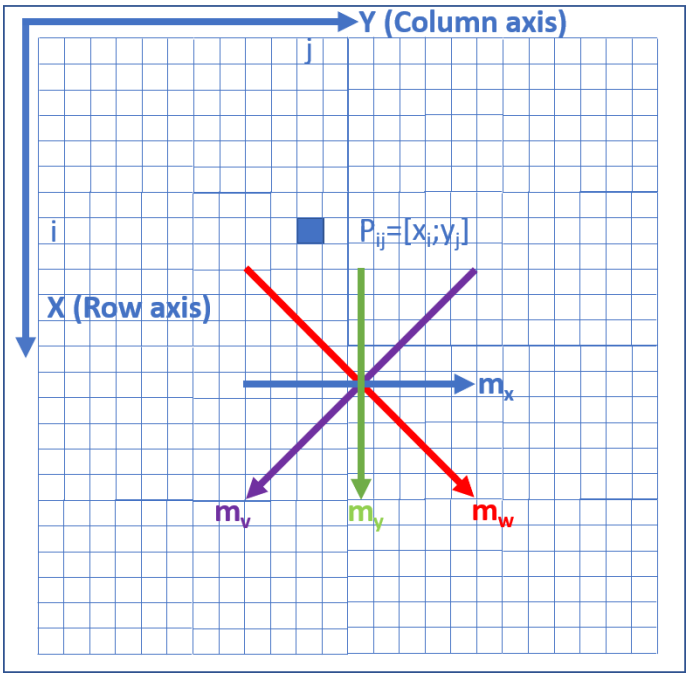

Figure 11: Frame of reference for the [x,y,v,w] set directions used for liposome boundaries evaluation.

(fixed column y) and y-direction (fixed row x). In particular, when contour points have polar angle $\theta \approx 45°$ and $\theta \approx 225°$ for v direction, and $\theta \approx 135°$ and $\theta \approx 315°$ for w direction. Adopting the gradient set: $[m_y,m_x,m_v,m_w]$ we are able to follow and reconstruct the liposome contour in the different portions of the image imposing a counterclockwise orientation.

Now we illustrate the gradient-based iterative method that provides a first estimation of the liposome contour with "pixel-resolution". Each iteration of the loop introduces an additional pixel point following a standard protocol described below. Exit from the loop is done once the initial contour starting point is recovered. A set of four matrices (3x3 shaped) is initialized: $[M_y,M_x,M_v,M_w]$. The matrix describe the gradient

pixel intensity in the adjacent 8 points of the current contour position: $P_{current}$, along the different directions mentioned above (along x-direction M_y; along y-direction M_x; along v-direction M_v; along w-direction M_w;). Not only the magnitude of each element in the four matrix is relevant, but also its sign. In fact, the magnitude (the absolute value) of the matrix element reveals how close the point is to the contour boundary. The sign of the matrix element reveals that portion of the liposome contour we are studying. For example, adopting: M_x gradient matrix centered in the starting-point [Eq 64 a-b] we expect that the matrix elements magnitude are higher if compared to the other gradient directions: M_y, M_v and M_w. Furthermore, since we are intercepting the sucrose-lipid bilayer-glucose interface the M_x matrix elements are all strictly positives. Thus, magnitude and sign of matrix elements can provide additional conditions to superimpose a counterclockwise orientation. Since the magnitude of the gradient matrix elements suggest us how close we are to the contour boundary with respect to a given direction, we defined a fifth matrix, M_{Mean}, defined as [Eq 65]:

$$M_{Mean} = \|M_y\| + \|M_x\| + \|M_v\| + \|M_w\| \text{ [65]}$$

M_{Mean} matrix represents the average gradient pixel intensity arising from the four directions in the adjacent positions of the current point, neglecting their specific sign (absolute value of the sum). Thus, M_{Mean} matrix could provide a first estimation of the next trial contour point. First, the central element is set to zero, since it is the current point of the contour. Then, a protocol of simple rules (shown below) is adopted to superimpose a counterclockwise orientation of the contour evaluation. The four gradient pixel intensity matrix: M_y, M_x, M_v and M_w are compared, choosing the matrix owing the highest absolute value element: M_{Max}. This selection shows us which is the dominant pixel intensity variation direction. If $M_{Max} = M_y$ the dominant direction is x, corresponding to $\vartheta \approx 90°$ or $\vartheta \approx 270°$. If $M_{Max} = M_x$ the dominant direction is y, corresponding to $\vartheta \approx 0°$ or $\vartheta \approx 180°$. If $M_{Max} = M_v$ the dominant direction is v, corresponding to $\vartheta \approx 45°$ or $\vartheta \approx 225°$. Finally, if $M_{Max} = M_w$ the dominant direction is w, corresponding to $\vartheta \approx 135°$ or $\vartheta \approx 315°$.

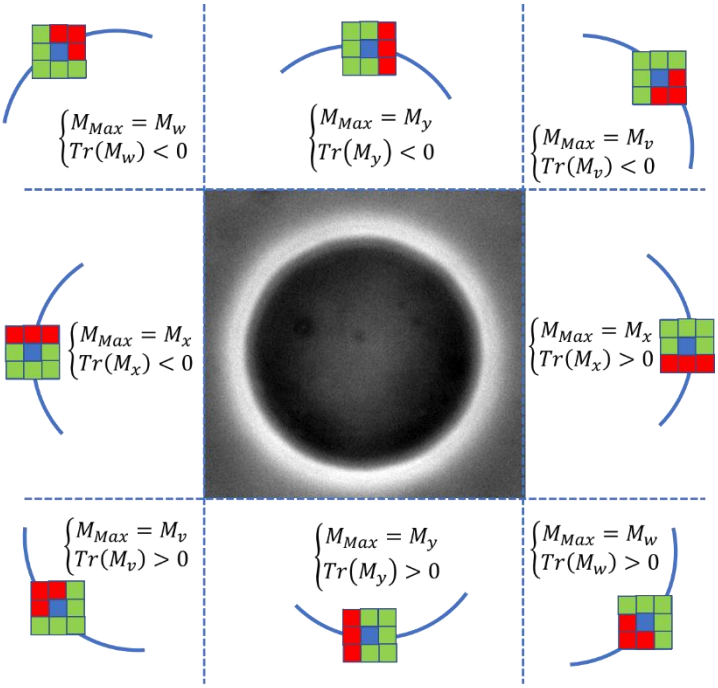

Figure 12: Graphical representation of the rules-set adopted to superimpose a counterclockwise contour evaluation. The 3x3 matrix represents the pixels under study: the current contour position (blue square), the possible next contour point (green squares) and the deleted points (red squares).

Then, the trace of M_{Max} is computed and its sign is investigated. Depending on the dominant gradient direction matrix M_{Max} and its trace sign, 8 possible different scenario are possible. The counterclockwise direction of the contour evaluation is imposed removing (setting to zero) 3 of the 8 elements of M_{Mean} matrix (the 8 adjacent points of the current position). The deleting choice of these 3 adjacent points is driven by the 8 scenarios proposed. In Fig 12 are summarized these 8 different scenario configuration and subsequent deleting choice.

Thus, after application of this protocol rules, in M_{Mean} matrix 5 non null elements remain as possible next trial point of the contour. The highest of these 5 candidates is chosen as next trial contour point, then we check that this trial point does not belong already to the previous contour point list. If the check is concluded successfully the current contour point is added to the previous contour point list, and the trial point becomes the current contour position, ready for the next iteration. If the check of the next trial contour point fails (this trial point already belongs to the contour points list), the corresponding M_{Mean} element is set to zero and the successive highest element in the matrix is set as next trial contour point and checked. This recursive trial contour point analysis is performed since a new correct contour point is obtained.

After the new contour point evaluation, we check two additional conditions related to the iterate-index $Iterate_{index}$.

Since the starting contour point defined in [Eq 64 a-b] is just a first approximation obtained using only m_x gradient, we decided to discard the first "delay" points, with $Delay = 30$. Thus, when $Iterate_{index} = Delay$ we discard these first points.

The second condition concerns the exit circumstance from the iterative loop, when the iteration-index: $Iterate_{index}$ is close to the supposed concluding iteration: $Iterate_{index} \approx 2p_{circ} = \pi D = 8 \cdot Interval$. This condition holds unless all the geometrical parameters are expressed in pixel units. Thus, when the current contour point is placed in the last of the 8 sub-sectors, $Iterate_{index} > 7 \cdot Interval$, we can measure the distance between the current and the starting contour points [Eq 66]:

$$Dist_{Current-Starting} = \sqrt{\left(x_{Current} - x_{Starting}\right)^2 + \left(y_{Current} - y_{Starting}\right)^2} \leq Dist_{Threshold} [66]$$

where x and y refer to the row and column index of the contour points, respectively. The $Dist_{Threshold}$ parameter is the distance threshold that allow the exit from the iterative loop. We set an intermediate distance parameter: $Dist_{Threshold} = 2\sqrt{2}$, equivalent to $\left|x_{Current} - x_{Starting}\right| \leq 2$ and $\left|y_{Current} - y_{Starting}\right| \leq 2$. Once the [Eq 66] is satisfied, the algorithm escapes from the first iterative contour evaluation loop.

Now we have a liposome contour evaluation with pixel resolution. The contour points expressed in cartesian coordinates $[row_i; column_i]$ ($[x_i; y_i]$) are exploited for the circular fitting, thus, the fitting radius r_{fit} and center $[row_C = x_C; column_C = y_C]$ are extrapolated. Then, the cartesian coordinates are converted in polar coordinates: $[r_i; \theta_i]$ adopting [Eq 67 a-b] (see Fig 10b planar-angular conversion):

$$\begin{cases} r_i = \sqrt{(x_i - x_C)^2 + (y_i - y_C)^2} \ [67a] \\ \theta_i = \tan^{-1}\left(\dfrac{x_i}{y_i}\right) \ [67b] \end{cases}$$

Note that the fitting radius r_{fit} is a theoretical parameter obtained approximating the liposome contour as pure circular-shaped figure. Thus, $\langle r \rangle_\vartheta \neq r_{fit}$, where $\langle r \rangle_\vartheta$ is the experimental radius averaged upon the polar angle θ. Furthermore, the contour perimeter: $2p_{Contour}$ is higher than the theoretical perimeter: $2p_{circ} = 2\pi r_{fit}$. The contour perimeter: $2p_{Contour}$ can be evaluated summing up the distances between neighboring

contour points ds_i [Eq 68]. Since the contour is evaluated with pixel resolution without overlapped points, the distance between neighboring points can have only two possible values: $ds_i = 1$ for vertically/horizontally aligned points, $ds_i = \sqrt{2}$ for diagonally aligned points:

$$2p_{Contour} = \sum_{i=1}^{N_{tot}-1} \sqrt{(x_{i+1} - x_i)^2 + (y_{i+1} - y_i)^2} + 2\sqrt{2} = \sum_{i=1}^{N_{tot}-1} ds_i + 2\sqrt{2} \text{ [68]}$$

where N_{tot} is total number of elements constituting the contour points list, and the term $2\sqrt{2}$ is the distance between the starting point ($[x_1, y_1]$) and the ending point ($[x_{N_{tot}}, y_{N_{tot}}]$). The circular fitting perimeter: $2p_{circ}$ and the contour perimeter: $2p_{Contour}$ can be compared, and we expect: $2p_{Contour} > 2p_{circ}$, due to thermal fluctuations. Thus, the perimeters ratio $2p_{Ratio}$ can be introduced [Eq 69]:

$$2p_{Ratio} = \frac{2p_{Contour}}{2p_{circ}} \text{ [69]}$$

The contour points list and the associated perimeter ratio [Eq 69] are stored.

Now we can evaluate again the liposome contour through an iterative approach, similarly to the first provided loop, but including in the end some modification. The criterions used to superimpose the counterclockwise direction and the first $Delay$ points remotion are unchanged.

In the second iterative loop we set as starting position the contour point belonging to the previous contour list, located in the $N_{tot} - Delay$ position. The check for the exit condition has been modified in this second loop. While in the first run we required a static escaping condition [Eq 66], here we used a dynamic solution. When we are approximatively in the last sub-sector of the contour perimeter, $Iterate_{index} > 7 \cdot Interval$, we cyclically measure the distance between the current point and the starting point: $Dist_{Current-Starting}$ [Eq 66]. Once we are close enough to the starting point, imposing $Dist_{Current-Starting} \leq 5\sqrt{2}$, or equivalently: $|x_{Current} - x_{Starting}| \leq 5$ and $|y_{Current} - y_{Starting}| \leq 5$, we initialize a distance function $Dist$ which measures the $Dist_{Current-Starting}$ as a function of the iteration-index for the next 20 iterations. Since we start to acquire and store the current distance $Dist_{Current-Starting}$ in the $Dist$ function when we are 5 pixels far from the initial point, we expect to complete the contour perimeter figure in less than 20 iterations. When the 20-th iteration from $Dist$ initialization has been computed, we interrupt the iterative-loop process, and we analyze $Dist$ as a function of the iteration-index. The minimum value: $Dist_{Min}$ of $Dist$ function and its corresponding iteration-index position $Iterate_{Min}$ are evaluated. The minimum value of $Dist$, $Dist_{Min}$ and its iteration position $Iterate_{Min}$ represent the contour perimeter closure. The iterations before $Iterate_{Min}$ complete the contour figure, the iterates successive to $Iterate_{Min}$ are retracing the contour perimeter, thus are removed. Finally, the circular fitting procedure is applied on the new contour data set.

Since now, we have essentially re-evaluated the contour perimeter with pixel resolution similarly to the first iterative loop proposed above. Here we introduce two additional post processing steps, which improve the liposome contour detection to sub-pixel resolution.

First, we adopted a new algorithm for contour point redefinition, which is based on the “radial-research”. For each point of the contour perimeter just obtained we reconstruct the straight line joining the contour point: $[x_i; y_i]$ to the liposome center: $[x_C; y_C]$. The points of this straight line placed around the contour point: $[x_i; y_i]$ (the distance between $[x_i; y_i]$ and the new points must be less than 10% of r_{fit}) are analyzed. The m_{Mean} parameter (similarly to M_{Mean} [Eq 65] for a single element) is evaluated for this new points, if a different point $[x_p; y_p]$ with respect to the contour point $[x_i; y_i]$ has a higher m_{Mean} value, then the previous contour point: $[x_i; y_i]$ is replaced by: $[x_p; y_p]$. We expect that the radial research will affect slightly the initial contour points list, and most of the points will remain unchanged.

The second and more relevant correction is the sub-pixel resolution adjustment, already implemented by [13]. Starting from a given i-th contour point, its coordinates $[x_i; y_i]$ are expressed with pixel resolution from previous steps, thus x_i and y_i are integer values. Adopting the sub-pixel resolution algorithm the contour point coordinates: $[x_i; y_i]$ are redefined with sub-pixel resolution introducing $\widetilde{x_i}$ and $\widetilde{y_i}$ which are fractional values. The proposed algorithm is defined in [Eq 70 a-b]:

$$\begin{cases} \widetilde{x_i} = \dfrac{x_i|m_{x_i}| + \overline{x_i}|m_{y_i}| + \overline{w_{x_i}}\left|m_{w_{x_i}}\right| + \overline{v_{x_i}}\left|m_{v_{x_i}}\right|}{|m_{x_i}| + |m_{y_i}| + \left|m_{w_{x_i}}\right| + \left|m_{v_{x_i}}\right|} & [70a] \\ \widetilde{y_i} = \dfrac{y_i|m_{y_i}| + \overline{y_i}|m_{x_i}| + \overline{w_{y_i}}\left|m_{w_{y_i}}\right| + \overline{v_{y_i}}\left|m_{v_{y_i}}\right|}{|m_{x_i}| + |m_{y_i}| + \left|m_{w_{y_i}}\right| + \left|m_{v_{y_i}}\right|} & [70b] \end{cases}$$

[Eq 70 a-b] constitute a couple of weighted average equations where the weights are $\left[|m_{x_i}|, |m_{y_i}|, \left|m_{w_{x_i}}\right|, \left|m_{v_{x_i}}\right|\right]$ and $\left[|m_{x_i}|, |m_{y_i}|, \left|m_{w_{y_i}}\right|, \left|m_{v_{y_i}}\right|\right]$ for [Eq 70a] and [Eq 70b], respectively. The barred values: $\left[\overline{x_i}, \overline{w_{x_i}}, \overline{v_{x_i}}\right]$ and $\left[\overline{y_i}, \overline{w_{y_i}}, \overline{v_{y_i}}\right]$ are defined through a geometrical construction rule. For a given direction (for simplicity we will focus on y-direction, the column axis, providing an example Fig 13) the pixel intensity profile is plotted (yellow line) and the related slope pixel intensity: m_{x_i} is used to linearize the pixel profile (green straight line) around the point coordinate: y_i(black vertical dotted line) .Then, the mean pixel intensity around the contour point coordinate y_i is evaluated (red dotted line) using a window of 31 points. Finally, the barred value: $\overline{y_i}$ (blue vertical dotted line) is found evaluating the interception coordinate between the pixel profile linearization and the mean pixel intensity.

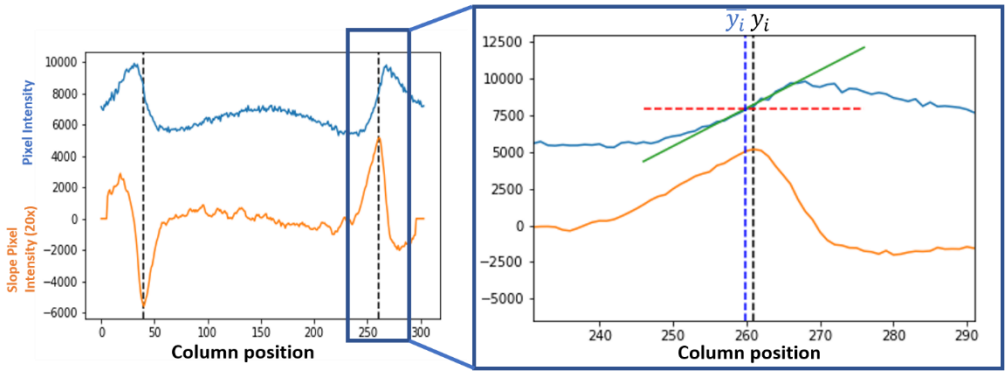

Figure 13: Graphical construction of the barred value ($\overline{y_i}$ vertical blue dotted line) starting from the original contour coordinate ($y_i$vertical black dotted line). In this example we showed only the contour column coordinate.

This geometrical construction is straightforward for $\overline{x_i}$ evaluation. For $\left[\overline{w_{x_i}}, \overline{v_{x_i}}\right]$ and $\left[\overline{w_{y_i}}, \overline{v_{y_i}}\right]$ first the $\overline{w}$ and $\overline{v}$ values are evaluated along w and v direction, respectively, using the same protocol adopted for $\overline{y_i}$ and $\overline{x_i}$. Then, $\left[\overline{w_{x_i}}, \overline{v_{x_i}}\right]$ and $\left[\overline{w_{y_i}}, \overline{v_{y_i}}\right]$ and subsequent weights $\left[\left|m_{w_{x_i}}\right|, \left|m_{v_{x_i}}\right|\right]$ and $\left[\left|m_{w_{y_i}}\right|, \left|m_{v_{y_i}}\right|\right]$ are obtained projecting barred values and weight along x and y direction, respectively.

The reason underlying the [Eq 70 a-b] weighted averages can be better understood providing an example. Suppose to adjust a contour point oriented close to $\theta_i \approx 0°$. For that direction we previously mentioned that the contour boundary is easily detectable from m_{x_i} slope, where m_{x_i} is the slope pixel intensity along y-direction evaluated at fixed x=x_i. Instead, $m_{y_i}$is less accurate for this contour point position. Alternatively, we can assert that y_i coordinate is evaluated with higher accuracy than x_i. For the moment we did not include the w and v slope weight corrections in the averages. After the geometrical construction mentioned in Fig 13 we have the $[\overline{y_i}, \overline{x_i}]$ data set, which essentially are an improvement of the initial coordinates. Since

the m_{x_i} slope have a higher accuracy than m_{y_i} we expect the $\overline{y_i}$ fractional value to be more accurate than $\overline{x_i}$.Thus, reasonably in [Eq 70b] the $\overline{y_i}$ value is weighted by $|m_{x_i}|$ to obtain a $\widetilde{y_i}$ value closer to the new fractional value. Instead, in [Eq 70a] $\overline{x_i}$ is weighted by $|m_{y_i}|$ to reproduce a closer value to the previous x_i integer value.

The sub-pixel resolution adjustment is applied for all points constituting the contour perimeter, then the new contour points list is converted in polar coordinates [Eq 67 a-b] and sorted with respect to the angular parameter θ_i. Finally, the distance between adjacent points is evaluated. If couples of adjacent points result higher than a given threshold ($\sim 2\ pixels$) additional points are inserted in these vacancy portions using the following protocol. First, the straight line joining the couple of points placed too far from each other is evaluated. Then, the points belonging to the straight line are added in the contour list. Finally, the additional points list is treated adopting the "radial-research" procedure and subsequent sub-pixel resolution adjustment described above. The additional contour points and the initial sub-pixel resolution list are merged and the resulting array is sorted with respect to the angular parameter ϑ_i. The contour and the fitting perimeter are evaluated, finally the parameters ratio is measured [Eq 69]. Then the perimeters ratio obtained from the previous iteration and the current are compared. If their difference is less than the imposed threshold: $2p_{Ratio_{Threshold}}$ (we set: $2p_{Ratio_{Threshold}} = 0.01$=1%) the entire contour evaluation procedure is concluded [Eq 71]:

$$\left|2p_{Ratio_{Current}} - 2p_{Ratio_{Previous}}\right| \leq 2p_{Ratio_{Threshold}} \quad [71]$$

Alternatively, an additional iteration loop contour evaluation is performed. In Fig 14 a flowchart reassumes the overall algorithm process.

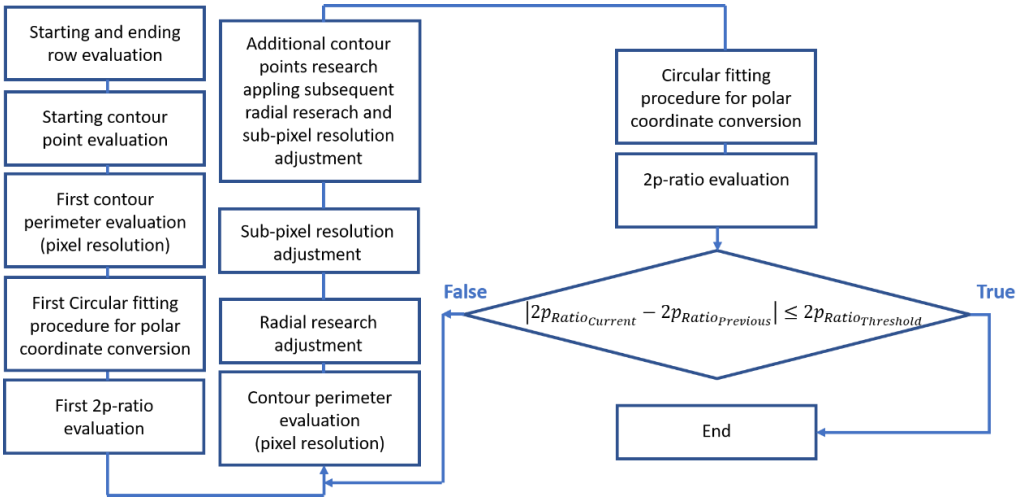

Figure 14: Summary contour evaluation algorithm flowchart

In Fig 15 the contour evaluation obtained from a DOPC vesicle applying the algorithm is shown. The direction slopes set [x,y,v,w] are highlighted in the final iteration of the recursive loop.

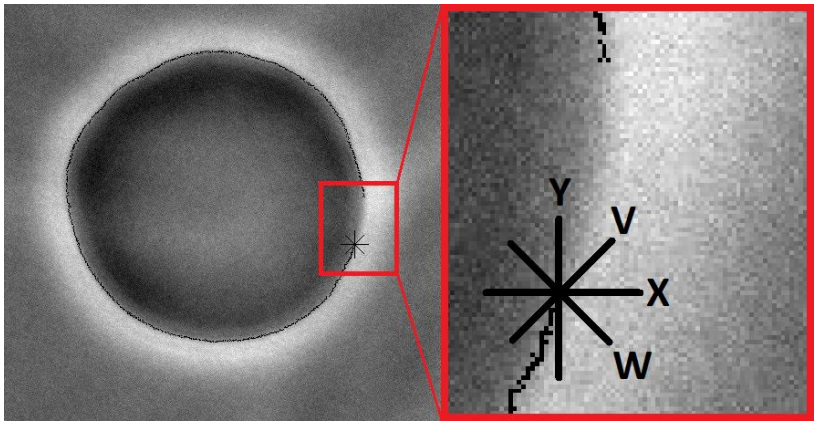

Figure 15: Contour evaluation reconstruction applying the algorithm on a DOPC vesicle. In the right-side the [x,y,z,w] direction slopes set is highlighted in the final steps of the recursive loop.

- **Flickering spectroscopy applied to boundary undulations of lipid fluid domains for Line Tension measurement**

In the previous section we deeply discussed and developed flickering spectroscopy as tool for bending constant measurement in GUVs. In this framework, usually the vesicles are constituted of a mono-component phospholipid specie in a homogeneous fluid phase, at most combined with cholesterol. In general, GUVs composed of ternary mixture are avoided, since they introduce spontaneous curvature between boundary domain demixing between fluid phases. Nevertheless, flickering spectroscopy technique can be exploited in line tension determination in ternary mixture, containing cholesterol, at the boundary domain coexistence between Liquid-Ordered (L_o) and Liquid-Disordered (L_d) phases, when GUVs are for example close to the mixing/demixing transition [14].

Line tension measurement at boundary fluid domains mismatch is a subject of many investigations, both from theoretical and experimental point of view. In some cases, inhomogeneity of proteins and lipids in the lateral distribution in lipid bilayers drives the subsequent line tension studies [15]. In fact, line tension regulates the fluid domain growth kinetics, fission and size, depending on its magnitude. Therefore, line tension modulation influences the protein-lipid heterogeneity composition in the plasma membrane. From this starting evidence, line tension constituted a crucial parameter in the functional regulations aspects in the biological membrane, like protein conformational changes or recruitment as mentioned in the introductive chapter.

In the next section we emphasize how flickering spectroscopy basis can be exploited not only in the 3-dimensional fluctuations of vesicles to measure the bending constant, but also in 2-dimensional in plane undulations at the boundary of different fluid domain in lipid bilayer, in order to estimate line tension. First, we will introduce the line tension concept in lipid bilayers following the historical development of this physical parameter, then we will focus on 2-phases interfaces (boundary tension). We will compare the different experimental framework able to measure line tension of lipid monolayer and lipid bilayer, and the different accessible ranges for each technique. We will recall the capillarity wave theory basis, which is behind the line tension measurement using the flickering spectroscopy approach. We will see also that line tension can be estimated using different methods, starting from contour evaluation of boundary fluid domain. In principle all the different approaches (radial fluctuations, angular correlation and relaxation time) are

interchangeable. Finally, we will focus on the best experimental conditions to obtain the most reliable results of line tension measurements using the flickering spectroscopy technique.

• Introduction

Liquid-Ordered (L_o) and Liquid-Disordered (L_d) phases have been initially hypothesized by Ipsen et al. [16] in 1987, and about two decades later experimental results [17], [18] confirmed the coexistence of these fluid phases on lipid bilayer arising from ternary mixture containing cholesterol and for some aspects resembling biological membranes. After these initial observations, the physical and chemical knowledge that is behind fluid phases mixing-demixing has been progressively expanded, as reported in different reviews as [19]. Molar ratio components and temperature regulate lipid phase transition between the homogeneous fluid phase and fluid phases coexistence. In fact, lipid phase transition has been deeply investigated exploring ternary mixture composition, (reproducing also molar components ratio far from physiological condition) and temperature[20]–[24]. Regarding fluid phases coexistence many physicochemical aspects has been treated, like domain diffusion [25] and mechanical properties of domains [21], [26], [27], which reflect 3-dimensional vesicle shape. Although, all these additional investigations are strictly connected to soft condensed matter physics issues, most of nowadays research interest is devoted to lipid-protein membrane heterogeneities at domain boundary level in living cells [28]. In fact, fluid domain microenvironment and its dynamics regulates biological functionality of transmembrane proteins. Thus, investigation of bulk domain properties has been integrated by studies of the boundary between fluid domains, which have increased progressively both from theoretical [29]–[32] and experimental [26], [33]–[35] point of view. A key parameter for the boundary fluid domain coexistence properties is the interfacial tension or simply line or boundary tension.

Before going into the details, we will recapitulate the “line tension” concept, from how it has been historically introduced for the first time to nowadays use in lipid monolayer/bilayer. The concept of line tension was firstly introduced by Gibbs in his theory of capillarity [36], which considers the more general case where three different phases coexist simultaneously. In fact, most of the experimental and theoretical line tension studies published since now consider 3-phases coexisting environments [37] spanning a wide range of different materials. Nevertheless, line tension is defined also in surface environments where at least two different phases coexist. Far from 3-phases coexistence, few works dedicated to surface phase mixing/demixing has been published, since few materials have been identified for the latter case. In fact, the substances that belong to surface phase coexistence and analyzed trough Langmuir technique can be grouped in three different families: Polymers [38], [39]; Surfactants [40]; and Lipids.

Here, we will report some literature examples regarding lipid-based phase coexistence. Firstly, we will focus on monolayer studies. Initially, C. Desai et al. [41] studied gas and liquid-expanded phase coexistence by the fluorescence microscopy technique, in particular its buckling instability heating the sample with constrained area, which allowed first line tension estimation for a 2-dimensional lipid system. Then, Fisher et al. [42] studied a similar system, where surfactant gas and liquid-expanded phases coexistence has been investigated to measure line tension parameter. In this case deformation forces has been exerted using laser tweezer. Finally, a liquid-liquid phase coexistence has been studied by McConnel et al. [43]. In this work lipid (Dimyristoylphosphatidylcholine DMPC) and cholesterol mixture monolayer has been investigated exploiting the Langmuir technique. Thus, shear flows and subsequent shape-distorting of the domains have been exploited to investigate liquid phase transition. Line tension has been measured using the recovery rate from distorted domain shape toward equilibrium condition, and values between ≈0.1÷10 pN has been observed, depending on the applied film pressure. This paper suggests, as expected, that line tension decreases dramatically close to the critical point. Similarly, in [44] liquid-liquid phase coexistence studied by thermally induced domain boundaries fluctuations confirmed that line tension magnitude is around ≈0.1 pN when the

system is close to a critical point. Considering theoretical support from continuum [43], [44] and microscopic models [29], [30], [45], these findings suggest that line tension values for lipid monolayer spans from 1 pN to 10 pN and collapse to 0.1 pN near a critical point.

Now we will consider studies regarding line tension evaluation in lipid bilayers. Line tension in lipid bilayer membrane arises in two different circumstances: firstly, whenever a pore formation event is involved, the energy cost to maintain membrane edge depends on line tension; secondly, at the boundary interface between phase-separated domains, as in monolayer environment. In the first case, line tension at the membrane edge has been investigated both experimentally [46]–[48] and theoretically [49], suggesting a line tension magnitude approximatively ≈10 pN. In the second scenario, where boundary domain interface is involved, several experimental setups allow different line tension measurement approaches. In fluid-fluid phase separation of GUVs, a first attempt based on shape analysis provided a coarse estimation of line tension around ≈1 pN [26], [33]. Further works [34] involving the micropipette aspiration technique in dumbbell-shaped vesicles containing liquid-liquid phase separation, provided a line tension value around ≈5 pN. This is a valuable technique to measure higher boundary domains line tension in GUVs but it become extremely imprecise below ≈0.5 pN regime. As mentioned above, low line tension regimes (≈0.5 pN or lower) appear and are strictly connected to mixing/demixing phase transition temperatures. Several experimental pieces of evidence such as for example in the work by Baumgart et al [26], show that in-plane domains boundary between fluid phases domains become nearly circular close to the temperature transition. In this scenario, low line tension associated to circular boundary domains fluctuations can be measured. Indeed, boundary domain thermal fluctuation can be spectrally analyzed by FFT (Fast Fourier Transform) decomposition and give access to line tension estimation. Invoking capillarity wave theory [26], [44], [50], the mean squared modes obtained from boundary undulation Fourier decomposition can be related to line tension magnitude. Several other studies have already tested this theoretical analysis, [14]. In particular Keller et al. [51] proposed a two dimensional Ising class model to describe ternary lipid mixture containing respectively high-melting-temperature, low-melting-temperature phospholipids and cholesterol near a critical point. In this work they correlate line tensions and correlation lengths concepts to temperature by introducing critical exponents. Since we cited several line tension evaluation approaches for lipid bilayer in the form of GUVs, we should also consider supported lipid bilayers (SLBs). In the latter case, AFM is a valuable technique, which is not available in the case of GUVs. SLB studies involving AFM technique suggest a different line tension evaluation method. In fact, line tension of boundary domains between fluid and solid phases has been established measuring domain nucleation rates [35].

• Capillarity wave theory

In this section we will recapitulate how surface domain fluctuations can be described through capillarity wave theory, focusing on fluid-fluid boundary interface between micrometer scale domains with constrained area. In liquid boundary domains having constrained area, if their fluctuations can be spectrally decomposed using Fourier basis and their power modes behave as independent harmonic oscillators, then spectral amplitudes are proportional to $(n^2 - 1)^{-1}$ where n represents the power mode number describing the n-th harmonic oscillator index.

Thermal undulations-based studies of fluid bodies with delimited boundaries have been deeply examined, both with theoretical and experimental approaches, including normal fluctuations (out of plane undulations), like double layer membrane in GUVs and red blood cells [52]–[55], where bending stiffness constant evaluation constitutes the core of the flicker spectroscopy analysis. This method, already described in the previous sections, is well characterized nowadays, since optical microscopy image acquisition has been gradually optimized increasing the method accuracy [9], [13], [56]. At the same time, in-plane fluctuations where we consider domain boundary at liquid-liquid interface when two fluid phases coexist, such as in

Langmuir monolayer of lipids [50] and polymers [57], have been previously studied. Next step is to expand the theoretical and experimental supports of thermal undulation boundary domains monolayer toward circular fluctuating boundary domains in GUVs membrane in the demixing region of their phase diagram. As we will see, bending elasticity in GUVs membrane and line tension in fluctuating liquid domains, share mathematical Fourier decomposition of experimental fluctuations, and they belong to the Flickering spectroscopies analysis. Nevertheless, in bending elasticity analysis of GUVs lower modes indexes are usually discarded [9], [13], due to poor statistic as already mentioned. Instead, in line tension analysis, higher power mode amplitudes are set aside since they significantly deviate from the theoretical behavior and many experimental limitations affect the obtained power modes.

Let us define the squared average (time mediated: from now on $\langle x \rangle$ constituted by the time average of x quantity) power amplitudes obtained from Fourier decomposition of domain undulation as: $\langle |u_n|^2 \rangle$. In [44] capillarity wave theory has been employed to relate line tension to these coefficients, in that case the study of a Langmuir lipid monolayer of a lipid mixture was involved. Now we will resume their theoretical framework and we will adopt it to the lipid bilayer environment. The starting point of capillarity wave theory assumes the existence of a model Hamiltonian (or effective Hamiltonian) and the fluctuations boundaries at the interface between different domains can be described solving the Hamiltonian itself [58], [59]. In our case, the Hamiltonian can be written as follows [Eq 1]:

$$H = L\sigma = \sigma \int_0^{2\pi} \sqrt{\left[r^2 + \left(\frac{dr}{d\theta} \right)^2 \right]} d\theta \; [1]$$

where L and r are geometrical parameters: L is the boundary contour length and r is the distance between the contour point and the center of mass of the domain. Finally, σ identify the line tension. The contour of the domain is parametrized through the polar angle θ. In fact, a crucial point in the Hamiltonian equation is the contour evaluation, and usually the analytical solution based on the polar angle parametrization results useful for practical purposes. For this reason, [Eq 1] is rewritten substituting exact L parametrization by its truncated expression [Eq 2] (where the Taylor expansion: $\lim_{x \to 0} \sqrt{1+x} \approx 1 + \frac{x}{2}$ has been exploited setting $x = \left(\frac{dr}{d\theta} / r \right)^2$). This assumption holds as far as the radial fluctuation with respect the polar angle $\frac{dr}{d\theta}$ are negligible if comparted to the radial distance r.

$$H = L\sigma = \sigma \int_0^{2\pi} \left[r + \frac{1}{2r} \left(\frac{dr}{d\theta} \right)^2 \right] d\theta \; [2]$$

The contour length L expansion can be truncated only for small radial fluctuations Δr compared to the equivalent radius R_0, defined as: $R_0 = \sqrt{\frac{A}{\pi}}$. R_0 represents the equivalent radius if the domain was replaced by a circle containing the same initial area A. Now, the radial coordinate $r = r(\theta)$ (expressed using polar angle) can be spectrally decomposed using Fourier basis [Eq 3 a-b]:

$$\begin{cases} r(\theta) = R_0 \left(1 + u_0 + \sum_{n=1}^{N/2} a_n \cos(n\theta) + b_n \sin(n\theta) \right) [3a] \\ r(\theta) = R_0 \left(1 + u_0 + \frac{1}{2} \sum_{n=-N/2; n \neq 0}^{n=N/2} u_n e^{in\theta} \right) with: |u_n| = \sqrt{{a_n}^2 + {b_n}^2} [3b] \end{cases}$$

Where the summations are truncated up to $\frac{N}{2}$, since the contour undulations are provided from optical microscopy images, thus N parameter depends by molecular details $N = \frac{L}{b}$ (where b is a cutoff length associated to molecular dimensions [59]). Using [Eq 3 a-b] the contour length L, and the area domain A can be Fourier decomposed as well [Eq 4-5]:

$$L = 2\pi R_0 \left[1 + u_0 + \frac{1}{4}\sum_n n^2 |u_n|^2\right] [4]$$

$$A = \pi R_0 \left[(1 + u_0)^2 + \frac{1}{2}\sum_n |u_n|^2\right] [5]$$

From the experimental perspective, we would like to establish line tension measurements for boundary domain with constrained area $A = \pi {R_0}^2$, as described in the introduction. This additional condition applied to [Eq 5] poses a further relation between Fourier coefficient [Eq 6]:

$$(1 + u_0)^2 = 1 - \frac{1}{2}\sum_n |u_n|^2 [6]$$

Now, we can apply the square root to [Eq 6] and assuming the sum over $|u_n|^2$ as a small contribution compared to the unity. We can then rewrite the right-hand side using the square root expansion and truncating it [Eq 7]:

$$(1 + u_0) = \sqrt{1 - \frac{1}{2}\sum_n |u_n|^2} \approx 1 - \frac{1}{4}\sum_n |u_n|^2 [7]$$

Using the latter approximation [eq 7] we can rewrite the contour length L [Eq 4], and in particular removing u_0 dependence from this equation, obtaining [eq 8]

$$L = 2\pi R_0 \left[1 + \frac{1}{4}\sum_n (n^2 - 1)|u_n|^2\right] [8]$$

Focusing on [Eq 8] just obtained, we can distinguish two different contributions. The first term represents the energy amount for the minimum equilibrium state $E_0 = 2\pi R_0 \sigma$, when the boundary behaves as a pure circular-shaped domain and thermal noise in not affecting its contour. The second term raises the energy of the domain from its minimum, by a contribution $\Delta E = \frac{\pi R_0 \sigma}{2}\sum_n (n^2 - 1)|u_n|^2$, due to the presence of thermal induced fluctuations of the contour boundaries. The energy amount ΔE just obtained is perfectly comparable to the expression derived by [44] for the lipid monolayer context. Under the approximations applied since now, we are allowed to invoke the equipartition theorem on the thermal energy terms: $\Delta E_n = \frac{k_b T}{2}$ .This assumption treats each energy thermal contribution ΔE_n in the sum as an independent harmonic oscillator with quadratic degree of freedom [Eq 9].

$$\langle |u_n|^2 \rangle = \frac{k_b T}{\pi R_0 \sigma (n^2 - 1)} [9]$$

Using [Eq 9] we can resume the line tension magnitude starting from the mean squared power modes amplitudes $\langle |u_n|^2 \rangle$ using a non-linear fitting procedure.

Equivalently to the equipartition theorem, we can tackle the line tension evaluation from a statistical perspective in the time-domain. We assume that each thermal energy contribution: $\Delta E_n = \frac{\pi R_0 \sigma}{2}(n^2 - 1)|u_n|^2$ in the sum $\Delta E = \frac{\pi R_0 \sigma}{2}\sum_n (n^2 - 1)|u_n|^2$ is an independent harmonic oscillator. Then, each harmonic oscillator characterized by its own vibrating amplitude $|u_n|$ can be associated at a given frame according to its probability distribution $P(|u_n|)$, which follows a gaussian distribution: $P(|u_n|) \propto e^{-\frac{\pi R_0 \sigma (n^2-1)|u_n|^2}{2k_b T}}$

This result is applicable to the entire set of experimental obtained squared power modes $|u_n|^2$. If the harmonic oscillator amplitude $|u_n|$ follows a gaussian distribution, then the variance of the squared power modes $Var[|u_n|^2]$ will be equal to: $Var[|u_n|^2] = \frac{k_b T}{\pi R_0 \sigma (n^2-1)}$. Now we recall the variance definition, which is: $Var[|u_n|^2] = \langle \Delta |u_n|^2 \rangle = \langle (u_n - \langle u_n \rangle)^2 \rangle = \langle |u_n|^2 - 2u_n \langle u_n \rangle + \langle u_n \rangle^2 \rangle = \langle |u_n|^2 \rangle - \langle u_n \rangle^2$. Since we expect no net deformation of the contour boundary from its mean circular shape during time, we can assume: $\langle u_n \rangle = 0$ and $\langle \Delta |u_n|^2 \rangle = \langle |u_n|^2 \rangle$. This latter statement, allow us to measure the line tension according to [Eq 9]

Furthermore, this latter approach gives us the opportunity to test if the squared power modes verify the previous assumptions regarding equipartition theorem, simply verifying if squared power modes follow a gaussian distribution. [Eq 9] can be rewritten in the real space fluctuations $\Delta r(\theta)$ by summing up the mean squared power modes, obtaining [Eq 10]

$$\langle \Delta r(\theta)^2 \rangle = \frac{3 k_b T R_0}{4\pi\sigma} [10]$$

Where $\langle \Delta r(\theta)^2 \rangle$ is mediated firstly over the polar angle at a given snapshot when a single frame is taken under study; secondly time mediated over the entire set of acquired frames.

Protocol regarding floating fluid domains appropriated selection is explained below.

• Contour Evaluation

Starting from the image set acquired for a single domain under study, next goal is to establish the contour coordinates [x,y] where the couple [x,y] refers to the pixel position running on the contour profile. As first attempt, we tried to adopt the same protocol used for phase contrast microscopy image in the bending analysis cited in previous section. Summarizing, in that method we reconstruct the contour profile by an iterative approach until a closed boundary is obtained. Finally, we improve the contour coordinates position resolution at sub-pixel scale using an algorithm based on mean gray scale. Nevertheless, this reliable method has been developed for gray scale frame obtained for phase contrast microscopy for imaging GUVs, now we are using the fluorescence microscopy technique on fluid L_o-L_d domains boundary. Testing this previous method on fluid domains imaged by fluorescence technique some issues emerged. During contour evaluation at the iterative section loop many unwanted events perturb the boundary reconstruction. These additional events include the presence of neighboring floating fluid domains, which not necessarily will join the domain under study. When suddenly additional neighboring domains appear in the field of view the contour iterative algorithm could accidentally consider also these domains in the contour evaluation. Finally, the contour profile obtained in this case will be partially the boundary of the original domain under study, joined to a portion of the second floating domain boundary, at least. Alternatively, if the second floating domain is only partially imaged in the view field, the iterative loop algorithm will crash whenever a field of view edge is reached. Due to this deleterious issue, the algorithm used after closing the first contour domain determination, which redefines the contour coordinates at sub-pixel resolution has been poorly tested. Although the iterative contour loop algorithm work quite well on isolated fluid domain, the presence of additional floating domains during exposure time yield almost unsuitable this contour evaluation protocol.

Following contour evaluation methods used by [60] and partially by [14], in our protocol discrete approximations of the domain contours are obtained by superposing a square mesh mask to the images, which are converted to binary afterwards (the ImageJ software was used), then, no additional refinements have been applied.

• Angular autocorrelation

After contour evaluation procedure, we can start the data analysis first evaluating the $R_0 = \sqrt{\frac{A}{\pi}}$ parameter. Acknowledgment of the contour coordinates [y,x] (pixel-scale) allow us to first establish if A and R_0 remain constant, neglecting pixelation and tracing noises, for the entire set frames acquired. Whenever this statement is infringed, then the imaged domain is discarded. Next step consists of evaluating the center of mass of the imaged domain [y_{CM},x_{CM}] , for each frame. Then we convert the [y,x] coordinates data set into polar coordinates $[r(\theta), \theta]$, where r is the radial distance measured from the center of mass. The statistical analysis approaches discussed below started manipulating the contour coordinates, expressed in the polar basis: $[r(\theta), \theta]$, and they concluded obtaining the line tension. In this section, we will show how line tension can be obtained from the squared power modes provided by the FFT spectral decomposition, exploiting two different methods: the former is based on direct radial distance FFT decomposition; the latter involve angular autocorrelation function.

In the former method, we can directly analyze the contour radial distance for each acquired image, and this imaged contour is associated at a given time frame t_i (where i-index runs from 1 up to N_{Frames} the total number of images acquired for the fluctuating domain boundary). Thus, we obtain the $u_n(t_i)$ modes amplitude from $r(\theta, t_i)$, the radial distance Fourier spectrum decomposed [Eq 3b] (actually: $r(\theta, t_i) - R_0$ if we want remove the unity contribution), and then we evaluate the squared modes $|u_n(t_i)|^2$. Finally, from the data-set resulting from each mode (each experimental data-set associated at a given mode contains N_{Frames} elements), we evaluate the time-mediated squared mode: $\langle |u_n|^2 \rangle_t = \frac{1}{N_{Frames}} \sum_{t=t_1}^{t_{N_{Frames}}} |u_n(t)|^2$ needed for line tension analysis [14]. In a similar manner, we can measure the amplitude of the different modes starting from the radial fluctuations, which are defined as $\Delta r(\theta) = r(\theta) - \langle r(\theta) \rangle_\theta$, where $\langle r(\theta) \rangle_\theta$ represents the radial distance mediated on the angular parameter, $\langle r(\theta) \rangle_\theta$. We first evaluate the mean radial distance: $\langle r(\theta) \rangle_\theta$ using [Eq 3b], demonstrating that is strictly connect to the sum of the squared mean modes: $\sum_n |u_n|^2$.We solve the integral $\langle r(\theta) \rangle_\theta$ [Eq 11] recalling that u_n are describing the thermal motion, which is completely random, thus their overall contribution mediated over the polar angle is null:

$$\langle r(\theta) \rangle_\theta = \frac{1}{2\pi} \int_0^{2\pi} r(\theta) d\theta = R_0(1 + u_0) + \frac{R_0}{4\pi} \int_0^{2\pi} \sum_{n;n\neq 0} u_n e^{in\theta} \, d\theta = R_0(1 + u_0) \; [11]$$

Substituting [Eq 11] in $\Delta r(\theta)$ definition shows us how the contribution $R_0(1 + u_0)$ is systematically canceled out in the radial fluctuations, in fact, $\Delta r(\theta) = \frac{R_0}{2} \sum_{n;n\neq 0} u_n e^{in\theta}$. Thus, when we decompose $\Delta r(\theta)$ using FFT we directly measure the power mode amplitudes $u_n(t_i)$ associated to the frame under study and line tension is evaluated following the same steps described above [14]. Furthermore, [Eq 11] can be rewritten in a more suitable way, recalling [Eq 7]: $\langle r(\theta) \rangle_\theta \approx R_0 \left(1 - \frac{1}{4} \sum_n |u_n|^2\right)$. This interesting finding shows how the angular-averaged radial distance is clearly different from the R_0 parameter and is even systematically less than R_0. Furthermore, angular averaged radial distance $\langle r(\theta) \rangle_\theta$ can be finally time mediated, simply averaging the different $\langle r(\theta, t_i) \rangle_\theta$ contribution frames $\langle \langle r(\theta) \rangle_\theta \rangle_t = \frac{1}{N_{Frames}} \sum_{t=t_1}^{t_{N_{Frames}}} \langle r(\theta, t) \rangle_\theta = R_0 \left(1 - \frac{1}{4} \sum_n \langle |u_n|^2 \rangle_t\right)$. Although the time and angular averaged radial distance contain the average squared power modes sum $\sum_n \langle |u_n|^2 \rangle_t$, a suitable process to decompose single $\langle |u_n|^2 \rangle_t$ term from the summation is not available. Nevertheless, the experimentally obtained $\langle \langle r(\theta) \rangle_\theta \rangle_t$ can be compared to the reconstructed experimental

quantity: $R_0\left(1-\frac{1}{4}\sum_n\langle|u_n|^2\rangle_t\right)$ exploiting $\langle|u_n|^2\rangle_t$ evaluated from $\Delta r(\theta)$ or $r(\theta)$ spectrally decomposed. This mathematical inference allows us to test again if the previous hypothesis conditions (like fixed area domain constriction) are really satisfied.

In the latter approach, we reconsider again the radial fluctuation function: $\Delta r(\theta)$, which is required to define the angular autocorrelation $c(\delta)$ [Eq 12]:

$$c(\delta)=\langle\Delta r(\theta+\delta)\cdot\Delta r(\theta)\rangle_\theta=\frac{1}{2\pi}\int_0^{2\pi}[r(\theta+\delta)-\langle r(\theta)\rangle_\theta]\cdot[r(\theta)-\langle r(\theta)\rangle_\theta]d\theta \quad [12]$$

where δ represents the phase shift. Solving the [Eq 12] integral, exploiting the orthogonal properties of the exponential terms $e^{in\theta}$, we can rewrite the angular autocorrelation function in a more suitable way [Eq 13] [14]:

$$c(\delta)=\frac{{R_0}^2}{2}\sum_n|u_n|^2\cos(n\delta) \quad [13]$$

In fact, $c(\delta)$ is described as the trace Fourier mode amplitudes. Thus, the squared power mode amplitudes $|u_n|^2$ can be obtained from the spectral cosine decomposition of the angular autocorrelation. Each contour frame provides its squared power mode dataset $|u_n(t_i)|^2$, and time averaging the contributions we obtain the average squared power mode amplitudes: $\langle|u_n|^2\rangle_t=\frac{1}{N_{Frames}}\sum_{t=t_1}^{t_{N_{Frames}}}|u_n(t)|^2$. Finally, we extrapolate the line tension magnitude.

• Relaxation time

In the previous section we discussed how to obtain the time-averaged squared power mode amplitudes: $\langle|u_n|^2\rangle_t$ starting from the radial fluctuation $\Delta r(\theta)$ or, alternatively, from the angular autocorrelation function $c(\delta)$, in order to extrapolate the line tension parameter σ. In this section we will introduce a different method, moving toward the time domain. As a starting point, the squared power modes amplitudes $|u_n|^2$ and their time-averaged $\langle|u_n|^2\rangle_t$ are still required. This approach has been firstly introduced in [14] in the context of membrane lipid bilayer and previously by [44], [61], [62] for lipid monolayers. In their works temporal fluctuations of the squared power mode amplitude with respect to time averaged value have been adopted [Eq 14]:

$$\Delta|u_n(t)|^2=|u_n(t)|^2-\langle|u_n(t)|^2\rangle_t \quad [14]$$

Then, exploiting these time fluctuations function $\Delta|u_n(t)|^2$, the time autocorrelation function has been defined has follow [Eq 15]:

$$g_n(\tau=n\Delta t)=\langle\Delta|u_n(t+\tau)|^2\cdot\Delta|u_n(t)|^2\rangle_t=\sum_{i=1}^{N_{Frames}-n}\frac{\Delta|u_n(t_{i+n}+\tau)|^2\cdot\Delta|u_n(t_i)|^2}{N_{Frames}-n} \quad [15]$$

Obviously, [Eq 15] must be time discretized , [Eq 15 right-hand member], since the time fluctuations $\Delta|u_n(t)|^2$ are evaluated between two different time frames, and the time shift τ can be only a discrete multiple of the time interval of the frame acquisition time Δt. Thus $\tau=n\Delta t$

The time autocorrelation function $g_n(t)$ behaves as a mono-exponential time decay function, with its related time constant τ_n.Thus, $g_n(t)\propto e^{-\frac{t}{\tau_n}}$, and the time autocorrelation function can be linearized as follows:

$\ln g_n(t) = \mathrm{a} + \mathrm{b}t = \mathrm{a} - \frac{t}{\tau_n}$ and finally the time constant τ_n can be evaluated starting from the slope b. The time constant is related to the line tension and to the power mode index n through the following relation [Eq 16]:

$$\tau_n = \frac{2\pi R_0 \eta}{\sigma} \frac{\left(n^2 - {}^1/_4\right)}{n^2(n^2-1)} [16]$$

In [14] the authors developed [Eq 16] starting from previous time autocorrelation theory [63], which has been exploited for lipid monolayer fluid-fluid domains in Langmuir experiments. In [61], [63] the authors constructed this time-dependent approach adjusting capillarity wave theory in the time-domain. In [Eq 16] the η parameter represent the surrounding aqueous medium viscosity, while the intrinsic lipid bilayer viscosity is neglected [64]. Note that moving from lipid monolayers, (where only the underling lipid interface interact with water), to bilayer environment, where the interacting aqueous surfaces are duplicated, the initial τ_n equation proposed by [61], [63] must be redefined. In fact, the original equation τ_n has been multiplied by a factor 2 in order to obtain [Eq 16].

The authors in [14] experimentally validated this time-dependent method, expecting and verifying an exponential decay of the time autocorrelation function respect time for the first fourth modes. Furthermore, they confirm a fast decrement of time constant: $\tau_n \propto n^{-2}$ as suggested from the theory. This approach allows also to extrapolate the viscosity coefficient, if the line tension has been obtained using the approaches discussed above [65].

• Experimental protocol and limitations

In this section we will illustrate the experimental protocol adopted for the fluctuating boundary domain video acquisition, accordingly to [14], [60]. Then, we will recapitulate the common experimental issues and limitations that affect experimental data acquisition and analysis.

After GUVs electro-formation, the vesicles have been slowly cooled at room temperature and stored at + 4°C. In the experimental setup for epifluorescence imaging the vesicles suspended in a 105-mM glucose solution were injected in a glass chamber embedded in another Teflon chamber custom built for controlling the temperature of the system and. A small hole was made in the spacer to insert the thermocouple probe inside the water solution. The bottom slide was pretreated with 10 mg/mL BSA to remove surface charges and to avoid strong adhesion between the bilayers and the glass, which could affect the phase behavior of the vesicles. About 200 mL of a 105-mM glucose solution was inserted into the chamber, and 50 mL of vesicle suspension was added. The chamber was sealed by vacuum grease and put in direct contact with a Peltier cell. From the opposite side, the Peltier cell was in contact with a circulating water chamber whose temperature was controlled by a circulating temperature control unit (Lauda Brinkmann, Delran, NJ). The Peltier cell was connected to a custom-developed control unit exploiting the proportional integral derivative system (PID) of an Arduino microprocessor. The system allowed for temperature jumps as fast as 15°C/min as well as controlled cooling or heating ramps. In Fig 1a is reported the temperature control unit together with the PID controller, in Fig 1b is showed a typical temperature heating ramp during experimental session.

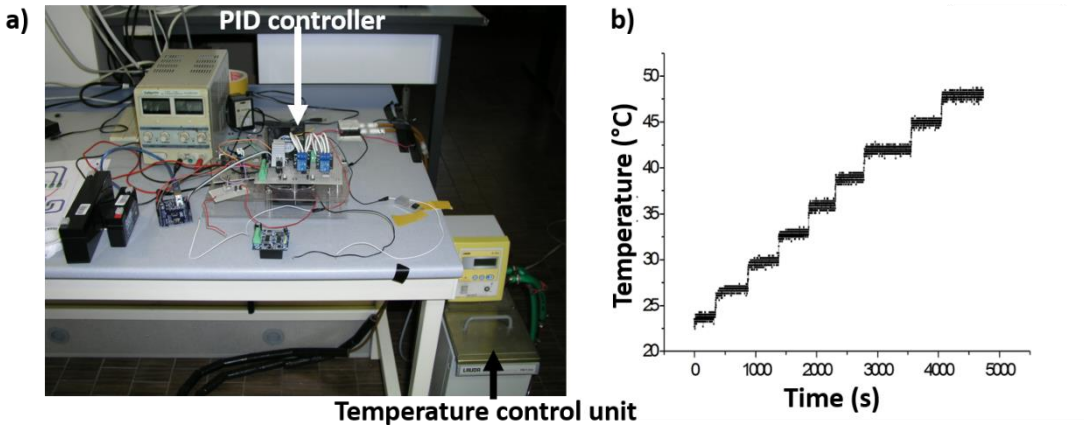

Figure 1: (a) PID controller and temperature control unit. (b) Temperature heating ramp example during GUVs coexisting phases analysis.

Since the GUVs have been prepared in 100m-M sucrose solution, they will fall down toward the bottom surface. When the vesicles reached the lower glass side the temperature has been rapidly increased from room temperature until only homogeneous fluid disordered phase L_d is obtained. Then, the temperature has been gradually moved toward L_o-L_d phase transition value for the given lipid mixture composition. When a stationary L_o phase appear from nucleation processes in the higher side of the vesicle, far from the glass interface, the boundary fluctuating domains can start. The challenging and crucial part consists of finding the appropriate vesicle, which must be in the appropriate range size, and stable. This guarantees to observe domains in the upper vesicle pole neglecting domain curvature projection out of the focusing plane. Furthermore, the same domain fluctuations can be acquired during time, preventing domain escaping from the ROI (Region-Of-Interest) due to vesicle rotation. When the appropriate vesicle has been selected, the domain under study must conserve its initial area, thus selected domain where neighboring domain coalesce in the former one must be discarded. Briefly, similarly to [14], [60] the protocol selection for the domains must possess several properties:

1-Their area must not exceed approximatively ≈20% of the total area of the GUV, otherwise domain area projection effects deeply influence the contour evaluation.

2-Their shape must be almost circular, accordingly to L_o-L_d boundaries. This caution should exclude induced photo-oxidation effects from illumination source, which usually remodel the circular boundaries.

3-Their radius must be not less than 3 µm, since smaller radius dimensions imaged in our optical setup are not capable to highlight net undulations boundaries with sufficient accuracy.

4- They must be planar and located at about the center of the GUV imaged surface, close to the vesicle pole. This additional condition ensures domain focus by the optical objective in its entire area and prevent area projection effects.

5-Their area must remain constant during the whole acquisition time. This condition is an indispensable hypothesis requirement. Furthermore, it excludes neighboring domain fusion events and domain alteration due to photo-induced effects.

In fact, selection of GUVs with appropriate domains is performed using as low as possible light intensity to prevent photo-oxidation. The images are collected by fluorescence microscopy; then, discrete approximations of the domain contours are obtained by superposing a square mesh mask to the images, which are converted to binary images (the ImageJ software was used). In Fig 2a a L_o domain frame captured from a DiphyPC-DPPC-Chol vesicle (1-1-1 molar ratio +0.5% Tx-Red), and subsequent square mesh mask process toward binary image 2b is reported.

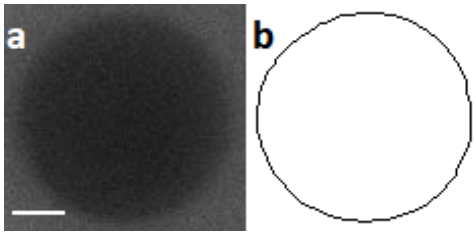

Figure 2: Boundary domain frame captured from a DiphyPC-DPPC-Chol vesicle (a) and contour reconstruction using a square mesh mask (b). Bar-size=2μm

The frames have been acquired using a CCD high-resolution video camera (QIcam FAST Cooled Mono 12-bits) or a CMOS camera (Hamamatsu ORCA-flash 4.0LT – C11440) connected to an inverted optical microscope (Olympus IX 70 microscope, Olympus, Tokyo, Japan). Texas Red-DHPE was included in the lipid mixtures at a molar concentration of 0.5–1% or lower. We used a 40x objective lens with inverted configuration for epifluorescence microscopy. In this configuration the pixel size it corresponds approximatively to 114 nm (Qicam FAST Cooled Mono 12-bits). When the appropriate fluctuating domain has been selected and the ROI has been resized, the exposition time ranged from 20 to 30 ms and the acquisition time from 30 to 50 ms (if we increase the acquisition time up to 250 ms the obtained results are very similar). Being the number of images for each sequence in the order of 600, the overall acquisition time takes 18-30 s. In fact, following the data analysis approach in [14], considering simulation studies, about ≥500 frames are required to measure line tension with enough accuracy.

We also search the maximum mode number N_{max}, which can be employed in the spectral squared power mode analysis. Setting the length $\Delta x_{lim} = 114\ nm$ corresponding to the pixel size, it poses a limit on the maximum mode number N_{max} which makes sense to be analyzed: the wavelengths of the Fourier components (e.g. in the autocorrelation function) are 2^n submultiples of the fundamental wavelength: $\lambda_1 = 2\pi R_0$, so that it is readily found that $N_{max} = \log_2(\lambda_1/\Delta x_{lim})$. Contours of domains with approximatively 3 μm radius can be analyzed up to the 6th mode.

In Fig 3a the experimental mean squared power modes $|u_n|^2$ obtained using the angular autocorrelation spectral decomposition of a L_o domain fluctuations captured from a DiphyPC-DPPC-Chol vesicle as function of the index mode (2°÷6° modes, red dots, are highlighted) are reported. Since the $|u_n|^2$ coefficients are proportional to $(n^2-1)^{-1}$ ([Eq 9]) we expect a straight line for the mean squared power modes as function of $(n^2-1)^{-1}$ and the slope reveals the line tension parameter, Fig 3b confirms theoretical behavior (2°÷6° modes, red dots, are highlighted).

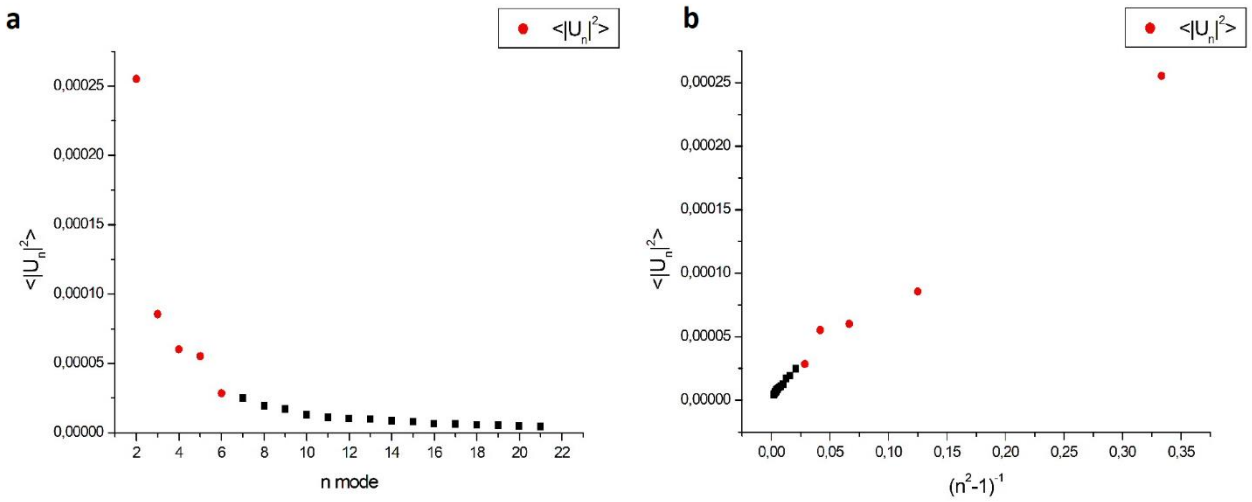

Figure 3: Experimental $|u_n|^2$ coefficients obtained from angular autocorrelation spectral decomposition of L_o fluctuating domain as function of mode index "n" (a), and $(n^2-1)^{-1}$ factor (b). First 2°÷6° modes are highlighted (red dots)

The problem of photo-oxidation has been considered already in ref. [60] and it is addressed here because we used a fluorophore concentration significantly higher (≈5 times) than in that work. To check the relevance of induced photo-oxidation on the domains, we partitioned the image sequence in four sub-sets made of the same number of frames. For each sub-set the line tension was estimated in order to reveal whether any systematic drift of line tension σ in time was detectable; our results did not show any such tendency. Eventually, we analyzed the dependence of the line tension as a function of domain radius and, within errors, no influence on the domain size was observed.

In Fig 4 we reported an example of line tension measurements in progressive sub-sets, each of these constituted by ≈ 150 frames, for L_o domain fluctuations captured from a DiphyPC-DPPC-Chol vesicle. In Fig 5 we analyzed line tension measurements as a function of domain radius for the same domain specie (L_o domain fluctuations captured from a DiphyPC-DPPC-Chol). In particular, we divided domain radius results in two sub-groups: R_0<3 µm and R_0>3 µm. As we stressed out above, fluctuations of domains having smaller radius (R_0<3 µm) are less detectable (less contour points and pixelation effect) resulting in poor statistical analysis for the $|u_n|^2$ coefficients. Comparing line tension result for these two sub-groups it appears the presence of a clear shift toward higher values moving from R_0<3 µm to R_0>3 µm, also the experimental accuracy is higher for R_0>3 µm sub-group. Probably, pixelation contributions and less contour points for R_0<3 µm sub-group yield apparent higher domain fluctuations and subsequently a distorted value for the line tension. This experimental comparison confirms how point 3 in the protocol is strictly required for accurate line tension measurements.

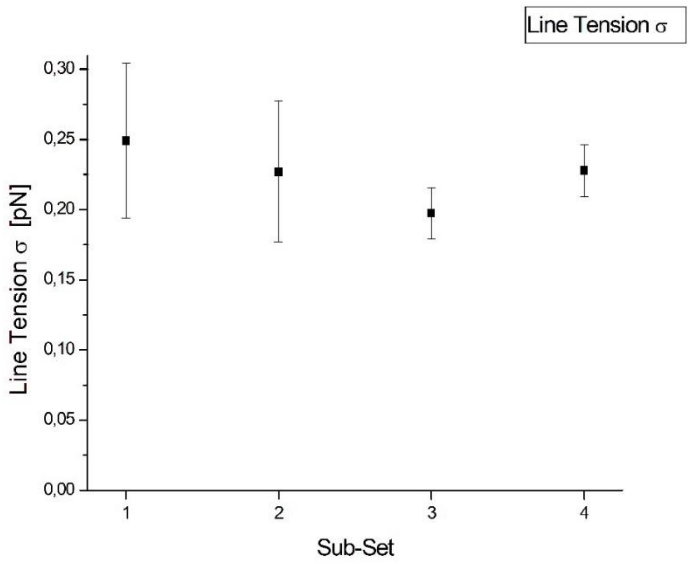

Figure 4: Line tension measurements for a L_o fluctuating domain (DiphyPC-DPPC-Chol 1:1:1) for progressive sub-set frames. No net deviation of line tension during time appears comparing the different sub-sets, confirming that photo-induced oxidation effects are negligible.

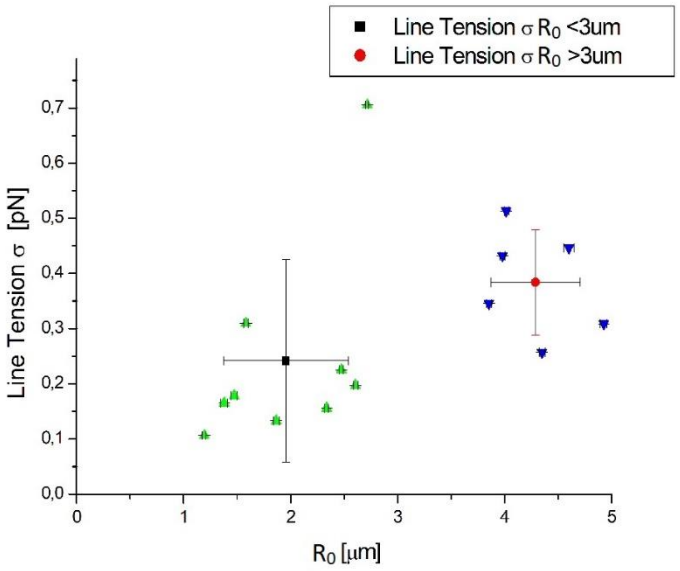

Figure 5: Line Tension measurements as function radius domain R_0 partitioned in wo sub-groups: R_0<3 µm (cluster of 9 domains, green triangles) and R_0>3 µm (cluster of 6 domains: blue triangles).

Finally, we want to point out how the mean power mode amplitude equation [Eq 9], needed for line tension evaluation, has been developed for finite system size. Instead, the equivalent [Eq 9] for continuum size domain will lead to $\langle|u_n|^2\rangle = \frac{k_bT}{\pi R_0 \sigma n^2}$. Note that [Eq 9] rewritten for continuum systems is really similar to: $\langle|u_n|^2\rangle \propto \frac{k_bT}{\sigma q^2}$ [59] where q represents the wave vector. Although several fluctuating modes are microscopically accessible for micrometer-scale phase-separated domain, finite size system approach should be taken into account, as indeed has been performed.

In a similar approach already treated in the bending constant analysis [Eq 45 a-b], an equivalent couple of equation corrections regarding the power mode amplitudes must be introduced to take into account camera exposure time. In fact, other than scan size limitation given by the optical system combined to the CCD camera resolution, also the exposition time must be considered. Finite frame exposition time, which theoretically should be null, poses an issue for faster fluctuating modes. In fact, these fast undulations cannot be followed by the CCD camera frames, and their contribution must be time averaged. This problem has been already treated for 3-Dimensional fluctuations of vesicles by [9], [13], [66]. Starting from angular autocorrelation function mediated over time, for a time interval up to the exposition time, a correction factor similar to [Eq 45 b] in the bending constant section can be introduced. This correction factor correlates the experimental squared power modes $|u_n{}'|^2$, which must be corrected and redefined, to the theoretically expected unknown values $|u_n|^2$, where the effect of an exposition time different from zero has been removed [Eq 17]:

$$|u_n{}'|^2 = 2\left(\frac{\tau_n}{\tau_s}\right)^2 \left[\frac{\tau_s}{\tau_n} + e^{-\frac{\tau_s}{\tau_n}} - 1\right] |u_n|^2 \quad [17]$$

In [Eq 17] the adjusting factor is governed by the ratio τ_s/τ_n where τ_n is the relaxation time, depending on the considered n-th fluctuating mode (which can be evaluated similarly to [Eq 45 a]), and τ_s is the camera exposition time. Note that for zero exposition time, or infinitely short if compared to exposition time the ratio τ_s/τ_n in the exponential term can be Taylor expanded and the experimental $|u_n|'^2$ and theoretical $|u_n|^2$ converge.

Following the simulation results proposed by [60] the flickering spectroscopy technique for line tension determination is a valuable approach for low range measurements [0.10÷0.50 pN]. In particular, for fluctuating domains with circular shape close to the fluid-fluid phase separation condition or to the critical point, where line tension collapses. Thus, flickering spectroscopy is a reliable and complementary approach to Micropipette aspiration technique for GUVs, when externally applied forces cannot be applied.

Cell Migration and orientation quantification parameters

In this section we will illustrate the quantitative-qualitative cell migration parameters, highlighting the advantages and drawbacks of each of them. Before the description and numerical implementation of the migration parameters:

- Wind-Rose Plot
- Mean Square Displacement (MSD)
- (Experimental) Mean-Speed-Modulus
- Directionality-Ratio
- Angular-Autocorrelation
- Final-Direction and $<|\sin(\theta_{Final})|>$
- Shape-Factor
- Reorientation-angle parameter and director index

we will illustrate the protocol adopted for cell migration imaging acquisition and subsequent manual tracking.

The parameter proposed refer to single cell migration, measured on isolated moving cell. Eventually, these parameters can be mediated on the overall cell sample data set. Firstly, we will propose the spatial parameters: the Mean-Square-Displacement (MSD) and the Mean-Speed-Modulus, which provide a first estimation of the area explored by the cell and its dynamics. Nevertheless, these metric parameters, even adopting mathematical models about the MSD, are unable to represent a complete overview of single cell migration. Thus, directional-based parameters of single cell migration are also proposed: the directionality-ratio, the angular-autocorrelation, the final direction assumed by the cell with respect to its starting position. Also, a director parameter needed to quantify the cell migration population starting from single cell analysis has been introduced: $<|\sin(\theta_{Final})|>$. Finally, the Persistence-Random-Walk, a mathematical model for MSD description and extrapolation of physical-dynamic cell features, has been described, implemented and exploited.

Furthermore, we studied also the cell morphology reorientation under periodic stretch of the underlying substrate. Thus, subsequent cell reorientation director parameter has been introduced.

All the scripts developed for cell migration and reorientation parameters quantification are written in Python language.

Here I will illustrate several motility parameters examples that can be reobtained and implemented from previous works mentioned below, and from papers written during the PhD course included in the thesis.

• Manual Tracking

After selection of the regions of interest of the cell sample, the image acquisition can finally start. The custom-built motorized stage can follow from 4 up to 8 different areas simultaneously and maintain the focus in each portion independently using the autofocus algorithm developed in the lab [67].

A sequence of images is acquired for each single area of interest with a specific time interval between two consecutive frames (typically every 3÷6 min). To proceed with the migration analysis, it is necessary to keep track of the individual cells during the entire film acquisition period. Since we are interested in studying the

migration of single cells, not all cells present at the beginning of the sequence in the area can be exploited for analysis. Cells that are in contact with other cells, cells that escape the imaged boundary field or cells that undergo cell division must be discarded. Selected cells are individually tracked manually using a free ImageJ (Manual Tracking) software plugin. This plugin is capable of recording progressive cell positions and instantaneous speed to a text file. We decided to follow a fully manual tracking since semi-automatic algorithm are not capable to track faithfully the center of mass of the cell during the entire sequence.

• Wind-Rose plot

After the manual-tracking process we have the track points coordinates list of the selected cell-set. The first and straightforward qualitative parameter that we can exploit is the Wind-Rose plot. All the two dimensional track cells can be rigidly translated to the origin point P_{Origin}=[0;0] of the frame of reference in the planar plane X-Y. Thus, the absolute tracking-point coordinates for a given cell $P_i = [X_i; Y_i]$,where the subscript -i refers to the image frame index, are converted in the relative coordinates by subtracting the cell starting point $P_0 = [X_0; Y_0]$ [Eq 1]:

$$p_i = P_i - P_0 = [X_i - X_0; Y_i - Y_0] = [x_i; y_i] \; [1]$$

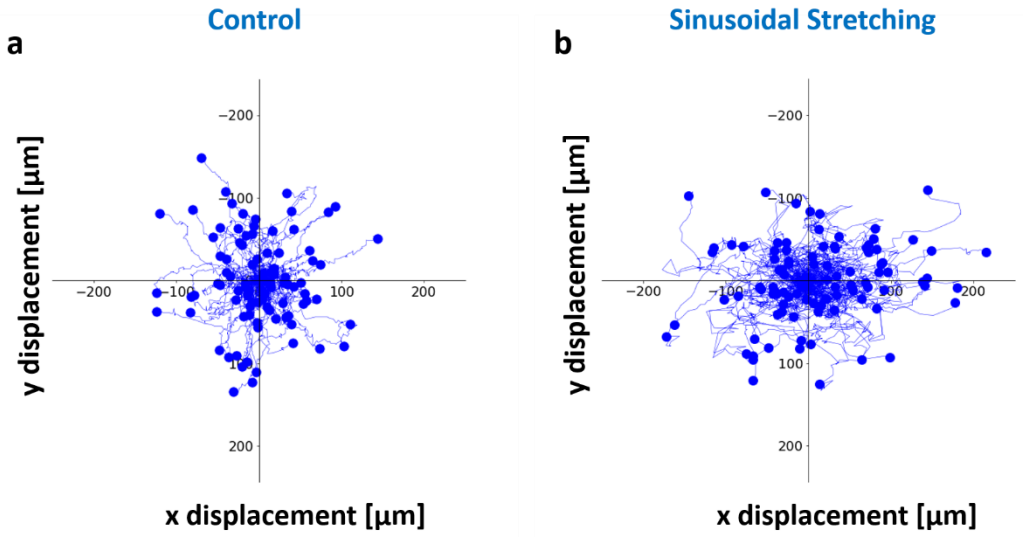

Figure 1: Wind-Rose plot comparison of BALB-3T3 under control condition (a) and under sinusoidal periodic stretching.

The relative-coordinates p_i obtained from the overall cell data-set are plotted in the X-Y plane, and each time frame constitutes a point in the X-Y frame of reference. The Wind-Rose plot provides a first estimation of the magnitude and behavior of the area explored by the cells set. In particular, the plot can dispense a starting guess regarding the anisotropic nature in the cell migration direction. In Fig 1 the Wind-Rose plot obtained from BALB-3T3 cell-line after 6 hours of live imaging in control condition (a) and under sinusoidal uniaxial stretching (b) is reported. The superposition of the cell tracking ensemble in control condition appears clearly isotropic (a), while in periodic stretching the cells explore the surrounding environment anisotropically [68]. In fact, the cell migration in Fig 1b is more oriented along the X direction.

• Migration Parameters Evaluation

Since the Wind Rose plot provides just a first cue regarding the magnitude and the nature of the area explored by the cell population, here we will summarize the principal quantitative parameters that describe the migration process from spatial and directional point of views.

• Mean-Square-Displacement

Starting from the cell coordinates $p_i = [x_i; y_i]$ associated with the i-frame at a given moment, many relevant migration parameters can be analyzed. The first kinematic parameter we will introduce is Mean-Square-Displacement (MSD). This parameter is provided by averaging the square displacement traveled by a single cell after a specific number of frames "*n*". Since the time interval between consecutive frames is fixed, henceforth Δt, the MSD evaluated after *n* frames will correspond to the averaged square displacement traveled by the cell after a time of $t = n\Delta t$. Therefore, the MSD will be described as a function of time. Taking into account that if the cell trace contains a total number of frames *N* (corresponding to *N* points labeled from 0 to *N-1*), the total amount of contributions needed to evaluate MSD after $t = n\Delta t$ is *N-n*, and the MSD function is defined as follows [Eq 2]:

$$MSD(t = n\Delta t) = \sum_{i=0}^{N-n-1} \frac{(x_{i+n} - x_i)^2 + (y_{i+n} - y_i)^2}{N - n} \quad [2]$$

From the experimental point of view, this index provides a first quantitative estimation of the area explored by the single cell during the observation time. The MSD pathway from individual cells can also be exploited for describing the overall behavior of the cells collected in the tracking procedure. If N_{Cells} is the number of cells selected in a given zone, we can introduce the overall mean square displacement, defining it as MSD_{All}, as follows [Eq 3]:

$$MSD_{All}(n\Delta t) = \sum_{i=1}^{N_{Cells}} \frac{MSD_{i-cell}(n\Delta t)}{N_{Cells}} \quad [3]$$

This parameter represents the average area explored by the set of cells chosen in the area of interest as a function of the elapsed time since the start of the image acquisition. The experimentally obtained MSD from single cell analysis is often used to test mathematical models that could describe a particular cell migration behavior. In a section below we will propose a mathematical model for MSD description, the PRW, which can be applied upon the environmental conditions adopted in our experimental setup.

• (Experimental) Mean-Speed-Modulus

Another quantitative cinematic parameter easily measurable from the cell tracking is the Experimental Speed Modulus, in particular the mean experimental speed modulus between adjacent frames. Typically, the cell motility behavior, when a time interval acquisition of several minutes is adopted (like in our experimental protocol), is a saltatory-like motion. Thus, the cell performs its translation in several steps before the process is concluded. First, the cell protrusions are elongated toward the motion direction, then the central cell body is moved, and finally the remaining back cell translates and the cell is ready for the next translation cycle. As mentioned above, the manual tracking is performed following the cell center of mass by the operator. Consequently, evaluating the displacement between adjacent frames: $d_{i+1;i} = \sqrt{(x_{i+i} - x_i)^2 + (y_{i+i} - y_i)^2}$ and normalizing it with respect to the time interval, the resulting plot as

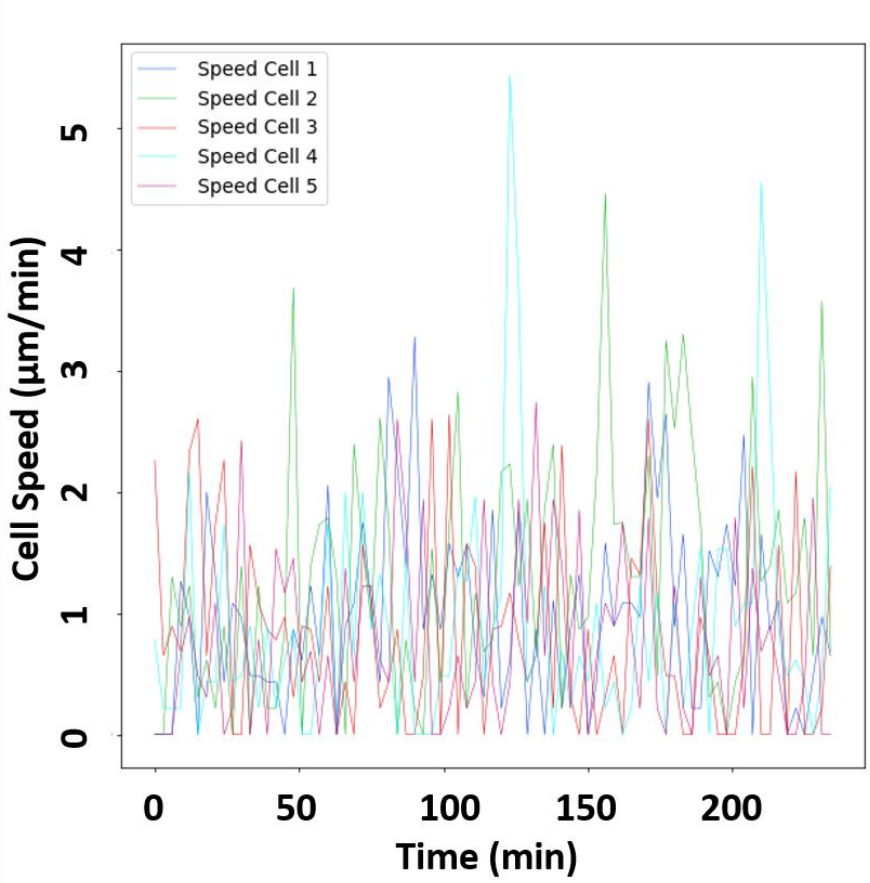

Figure 2: Instantaneous speed modulus measured from 5 tracked U87MG cell seeded on petri-dish under control condition.

function of the observation time $t=n\Delta t$ is a discontinuous segmented line. In Fig 2 are reported the instantaneous speed modulus profiles: $v_{i+1;i}$ obtained from 5 U87MG cells cultured on plastic petri-dish in control condition, the saltatory-based motion is clearly observable. Most of the "instantaneous-speed" $v_{i+1;i} = d_{i+1;i}/\Delta t$ between adjacent frames are almost null and just few plot points are significantly different from zero. These well localized sharp peaks highlight the saltatory cell migration behavior.

Thus, the "instantaneous" speed modulus can be used for investigating qualitative parameters to demonstrate the saltatory nature of the motion and the saltatory events rate. A more suitable and quantitative parameter is the mean experimental speed modulus $\langle v \rangle$. After measurement of displacements between couple of adjacent frames we evaluate their average normalized with respect to the time interval Δt. Since the tracking list points is constituted by N elements, we have N-1 contributions, which must be averaged [Eq 4].

$$\langle v \rangle = \sum_{i=0}^{N-2} \frac{\sqrt{(x_{i+1} - x_i)^2 + \left(y_{i+1} - y_i\right)^2}}{N-1} \frac{1}{\Delta t} \quad [4]$$

The mean experimental speed modulus constitutes the intrinsic speed parameter of the cell sample and can be compared to the speed fitting parameter extrapolated from specific MSD mathematical model, as we will see below.

- **Directionality-Ratio**

The previously introduced motility parameters constitute spatial-based index and provide information regarding the area explored by the cell (Wind-Rose plot and MSD) and the underlying dynamic cues that govern the processes (instantaneous and mean speed).

However, these parameters evaluated for a single cell or averaged for the entire cell population, are kinematic parameters that do not take into account any clues as to the directionality of migration. The simplest index that considers the role of cell directionality is the Directionality-Ratio, DR. It is defined as the ratio of the net distance between the starting point and the ending point for a given time interval $t = n\Delta t$: $d_{n;0}$ and the length traveled by the cell during the related image sequence [0;n]: $d_{tot} = \sum d_{i+1;i}$ [Eq 5].

$$DR(n\Delta t) = \frac{d_{n;0}}{d_{tot}} = \frac{\sqrt{(x_n - x_0)^2 + \left(y_n - y_0\right)^2}}{\sum_{i=0}^{N-2} \sqrt{(x_{i+1} - x_i)^2 + \left(y_{i+1} - y_i\right)^2}} \text{ [5]}$$

If a cell maintains its initial direction throughout its migration, DR will equal one. If a cell loses its initial direction, DR will be progressively less than one and the rate of this decay depends on how quickly the cell loses its original direction. However, this parameter is not the best index for cell direction analysis, as the DR also depends on the instantaneous speed and the distance traveled between consecutive frames. Essentially, the DR parameter provide only a partial information regarding the cell directionality migration, but it does not constitute a pure (angular)-geometrical index.

• Angular-Autocorrelation

Since the DR parameter does not provide an entire directional analysis overview, we move toward an angular-based director index. The next migration parameter we will introduce is the Direction-Autocorrelation, DA. Similarly, to DR, DA describes the ability of the cell to retain its initial direction over time, with the advantage that this is a pure geometric index, completely independent of the instantaneous cell speed [69]. Consider the trace of a single cell, defined by N couples $[x_i; y_i]$ representing the positions occupied by the cell in the stack of images. From this set of N coordinates, we can define N-1 segments, and fixing a common frame of reference X0Y, we can evaluate for each segment its length and its angle from a fixed axis (X or Y independently). Consider for example the couple of adjacent point $[x_0; y_0]$ and $[x_1; y_1]$ and fix the frame of reference X0Y: X horizontal axis with the positive semi-axis oriented to the right, and Y vertical axis with the positive semi-axis oriented downward (See Fig 3a). We can define the segment joining $[x_0; y_0]$ and $[x_1; y_1]$ as S_1 having a length given by [Eq 6a] and an angle given by [Eq 6b] measured from the positive X axis (See Fig 3a).

$$\begin{cases} |S_1| = \sqrt{(x_1 - x_0)^2 + \left(y_1 - y_0\right)^2} \text{ [6a]} \\ \theta_1 = \tan^{-1}\left(-\dfrac{y_1 - y_0}{x_1 - x_0}\right) \text{ [6b]} \end{cases}$$

Repeating this procedure for all the couples of adjacent points $[x_i; y_i]$ and $[x_{i+1}; y_{i+1}]$ we will obtain a complete set of N-1 segments, from S_1 to S_{N-1} and the corresponding set of angles from θ_1 to θ_{N-1}.

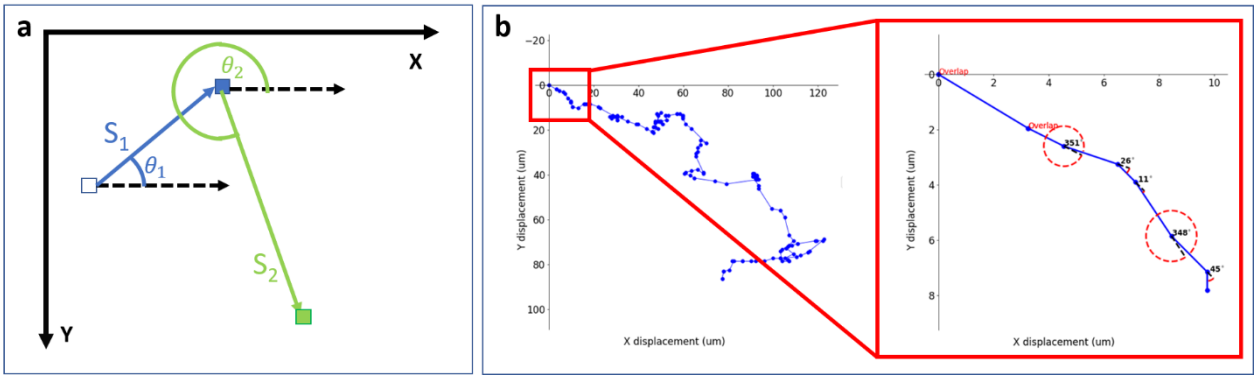

Figure 3: Representative XY frame of reference for S_n and ϑ_n geometrical construction (a). Example of cell tracking and subsequent $\Delta\vartheta_{n=1}$ evaluation for the first 10 segments (b).

As already mentioned, DA depends only on geometric factors. In fact, it is defined using only the set of angles $\theta_1 \div \theta_{N-1}$. DA can be expressed as a function of time DA = DA(nΔt), and measures the average $\cos(\Delta\theta_n)$ value, where $\Delta\theta_n = \theta_{i+n} - \theta_i$ represents the difference between angles associated to segments separated by *n* frames. In Fig 3b is reported the $\Delta\theta_{n=1}$ construction, for the first 10 steps of a given cell track. "OVERLAP" label in Fig 3b refers to couple of overlapped tracking points, thus $S_n=0$ and subsequent $\Delta\theta_n$ cannot be evaluated. Since we start from a set of N-1 segments and their corresponding angles, we will have N-n-1 cosine contributions for the evaluation of DA(nΔt) [Eq 7]:

$$DA(n\Delta t) = \sum_{i=1}^{N-n-1} \frac{\cos(\theta_{i+n} - \theta_i)}{N-n-1} \quad [7]$$

Since DA is defined as the average $\cos(\Delta\theta_n)$ value, we expect $-1 \leq DA \leq 1$. From the experimental point of view, DA = 1 represents a perfect straight path in which no change in direction occurs during cell migration, similarly to DR = 1. In fact, DA = 1 means $\Delta\theta_n = 0°$ constantly, describing a series of segments, not necessarily equally sized, all parallel and aligned along the same direction. Consider now the case DA = 0, corresponding to $\Delta\theta_n = \pm 90°$. If we focus only on adjacent segments (DA(t=Δt)), cell path is described by a random walk where every step segment is followed by a new one oriented perpendicularly to the previous one. Finally, considering the lower value DA = -1, in the limiting case of consecutive segments (DA(t=Δt)), the cell trace is characterized by a series of segments, where each couple of consecutive steps are oriented antiparallel to each other. During the manual-tracking procedure, cells could maintain their position for several frames before continuing their travel, meaning that several consecutive points are overlapped, and the corresponding steps are zero. Obviously, the angle direction cannot be evaluated for these steps, and this introduce a problem in the DA equation. There are many different ways to overcome this numerical evaluation issue: we can assume that the null step maintains the previous direction, or simply remove $\cos(\Delta\theta_n)$ contribution whenever null segments are involved. We have chosen the latter option. Similarly, to MSD [Eq 2], DA=DA(nΔt) is evaluated mediating N-n-1 contributions for a fixed n index. Thus, the DA parameter is truncated approximatively at $n \approx N \cdot 75\%$ since for higher n values NA becomes noisy due to low number of contributions in the sum.

The DA=DA(nΔt) function evaluated from isolated cells can finally be mediated for the overall cell data set.

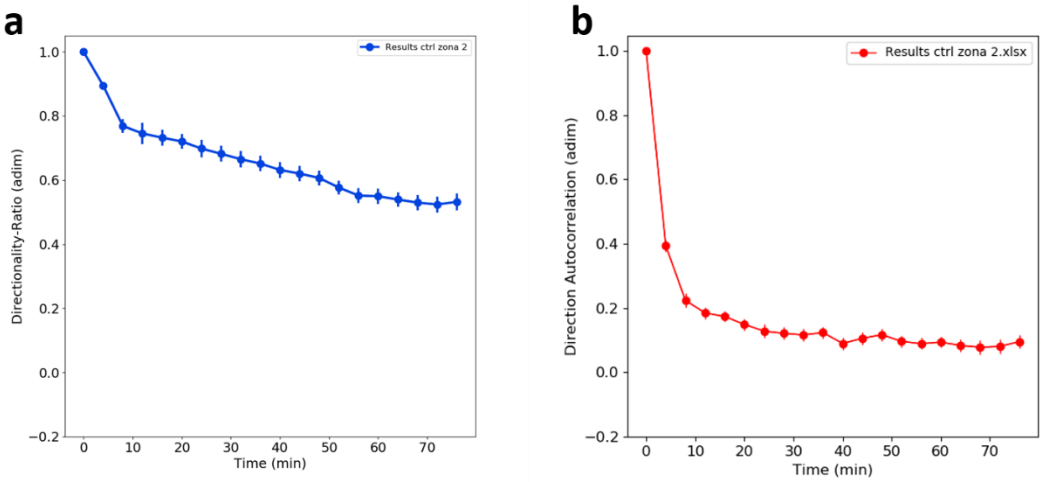

Figure 4: DR and DA comparison parameters obtained from U87MG cells seeded in petri-dish under control condition.

In Fig 4 is illustrated the DR (a) and DA (b) graphs comparison of U87MG cells in control condition. This comparison confirms how the DR is more fluctuating and noisy than DA, in fact DR is biased from the instantaneous mean speed while DA does not.

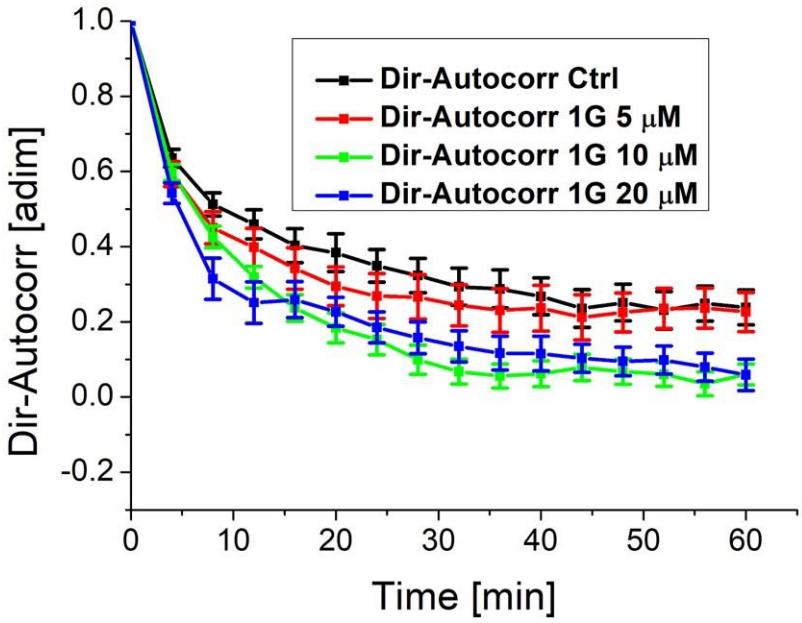

Figure 5: DA comparison of U87MG cells exposed to different concentration of 1G compound: Control (black dotted line),1G 5μM (red dotted line),1G 10μM (green dotted line) and 1G 20μM (blue dotted line), respectively.

In Fig 5 is reported the DA function comparison of U87MG cells seeded on plastic petri-dish in control condition (black dotted line) and exposed to several different exogenous 1G molecule concentration: 5μM (red dotted line), 10μM (green dotted line) and 20μM (blue dotted line), respectively. 1G is a molecule that we studied for its potential as a cytostatic drug (See Chapter results). The DA index decays faster under 1G exposition, especially for higher concentration levels. Thus, the inability of U87MG cell to maintain its initial direction even after few frames when exposed to 1G drug is highlighted from DA comparison and confirm 1G cytostatic effect.

- **Final-Direction and <|sin(θ$_{Final}$)|>**

The DA parameter introduced above describes the cell migration directionality during time. Thus, DA represents a kinetics director index of the directionality. The last directional parameter we will introduce is the final direction of migration assumed by the cell, θ_{Final}. It is defined as the angle of the segment joining the starting and the final points of the cell trace [Eq 8]:

$$\theta_{Final} = \tan^{-1}\left(-\frac{y_{n-1} - y_0}{x_{n-1} - x_0}\right) \quad [8]$$

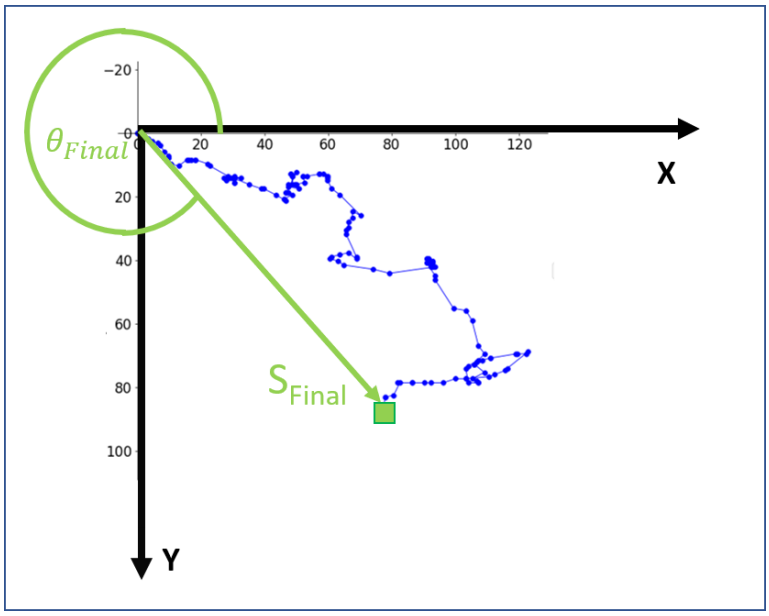

Figure 6: ϑ_{Final} geometrical construction for a given tracked cell.

Using the previous reference system X0Y, θ_{Final} is measured from the positive X axis and is a pure geometric index like DA. Unlike DA, θ_{Final} estimates the ending direction, neglecting the intermediate configuration assumed by the cell. Thus, θ_{Final} does not represent a kinetic index but can quantify the presence of anisotropic motility in the cell sample, regardless from the displacement traveled by the cell. Cells having the same final direction of migration but different final MSD are indistinguishable in this analysis. In Fig 6 is reported the θ_{Final} geometrical construction for a given tracked cell using the same frame of reference adopted in Fig 3b.

From the tracked cells list composed by N_{Cells} elements we will obtain the associated θ_{Final} data set. This directionality index allows us to establish if the overall cell migration behaves isotropically or a particular anisotropy exists and, in the latter case, its direction. Histogram of θ_{Final} parameter can provide a first estimation of the hypothetical preferred direction of migration, a flatted histogram suggests that the cell migration process is totally isotropic, the presence of a couple of peaks equally spaced with respect to the zero value suggests an anisotropic behavior. In order to better quantify the anisotropy direction we can define $|\sin(\theta_{Final})|$, where the symbol | | represents the absolute value, and finally compute the average value $<|\sin(\theta_{Final})|>$. If cell migration follows a purely isotropic dispersion we should expect $<|\sin(\theta_{Final})|>=2/\pi$, in fact passing from the discrete sum of the N_{Cells} terms to the continuous limiting case and solving the associated integral we find [Eq 9]:

$$< |\sin\theta_{Final}| >= \sum_{i=1}^{N_{Cells}} \frac{|\sin\theta_{i-Final}|}{N_{Cells}} \rightarrow \lim_{N_{Cells}\rightarrow+\infty} < |\sin\theta_{Final}| >= \frac{1}{2\pi}\int_{-\pi}^{\pi} |\sin\theta|\, d\theta = {}^{2}/_{\pi} \quad [9]$$

Any significant deviation from 2/π suggests the presence of an anisotropic behavior. In particular significant lower value ($<|\sin(\theta_{Final})|> << 2/\pi$) shows cell migration preference to follow X direction. Instead, significant higher level ($1 \geq <|\sin(\theta_{Final})|> >> 2/\pi$) suggests cell migration preference to maintain almost the Y direction. In Fig 7a1-a2 are reported the θ_{Final} histogram comparison between BALB-3T3 cultured on PDMS rigid substrate in control condition (Fig 7a1 no periodic stretching application) and under sinusoidal periodic stretching (Fig 7a2), respectively (See chapter Devices Development). The histogram of θ_{Final} obtained from cells traced in control condition appears fairly flattened and uniform with respect to the angular orientation range [-180÷180(°)], while the θ_{Final} parameter obtained under periodic stretching does not. In fact, the central regions around ≈±90° is less populated than the other orientations. This first qualitative guess is numerically confirmed by $<|\sin(\theta_{Final})|>$ parameter evaluated from control (red column bar) and under periodic stretching (black column bar) conditions (Fig 7b). In the control case the experimental $<|\sin(\theta_{Final})|>$ value follows the expected isotropic direction (pink column bar) [Eq 9], while in the periodic case the

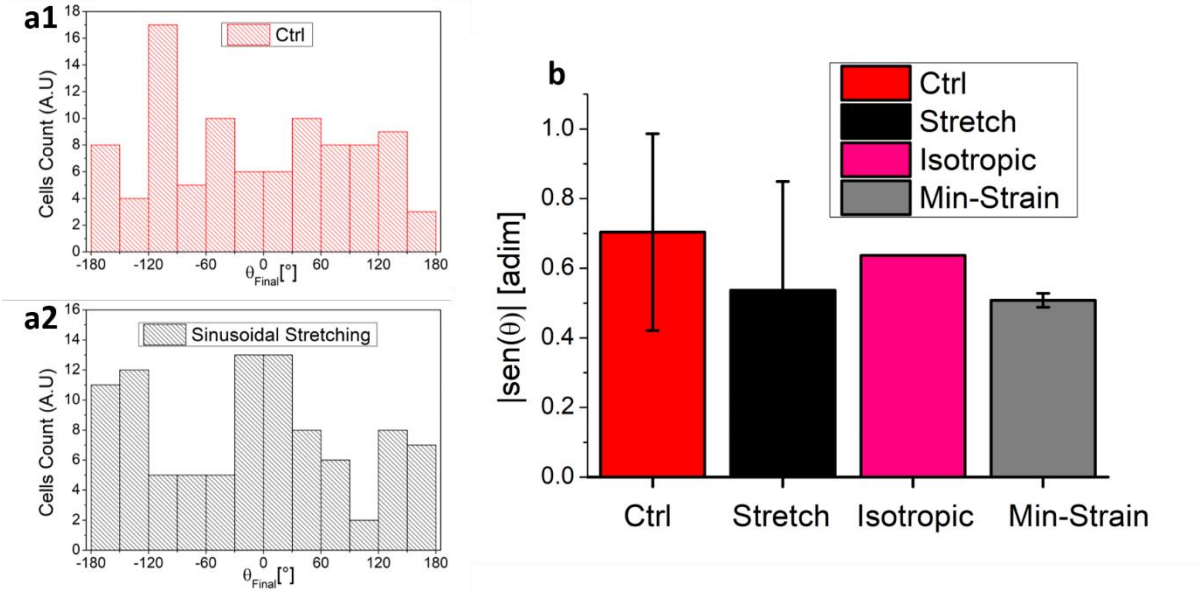

Figure 7: ϑ_{Final} histograms obtained from BALB-3T3 in control condition (1a red column bar) and under periodic stretching (2a black column bar). $<|\sin(\vartheta_{Final})|>$ bars plot comparison between experimental findings (control red column bar, periodic stretching black column bar) and theoretical isotropic (pink column bar) and min-strain (gray column bar) directions.

experimental $<|\sin(\theta_{Final})|>$ data is superimposable to the minimum-strain direction (gray column bar) derived from stretching calibration setup.

All the reported parameters have been numerically computed starting from excel raw data obtained from ImageJ plugin using home-made scripts developed in Python.

• Persistence Random Walk Model

Depending on the experimental conditions to which the cells are exposed during migration, it is possible to propose specific migration models. These mathematical models could depend on specific migration conditions, such as the presence of gradients of exogenous molecules acting as chemical attractors, or whether cells collectively move cooperatively or not. Furthermore, the physical conditions of the in vitro assay can influence the empirical parameters obtained from the model, which may be different from the intrinsic properties of cell motility. In the literature it has been often proposed that, in an isotropic environment, cells follow a Persistence-Random-Walk model PRW [70]. Thus, in our experimental studies, when no periodic stretching is applied and no exogenous molecule is present, this hypothesis is assumed. This mathematical model proposes two different cell motility behaviors, depending on the observation time

scale considered: for a short period of time the cells move in a fairly straight direction, while, for a long period of time, the cells behave in more casual way similar to a random walk. The time parameter that marks the transition from short to long time scale is the so called Persistence-Time P; accordingly, for time t << P we expect a linear trajectory, whereas, for t >> P, we have a completely randomized motion. The PRW model can be applied to a wide range of physical phenomena. For example, in the semi-rigid polymers context like DNA the "end-to-end distant correlation" has been exploited [71], which is pretty similar to PRW where the persistent-time is replaced by the persistent-length. In the cell motility context, the PRW model has been introduced independently by different authors, initially by Dunn et al. and then by Othmer et al. and Alt et al. [72]–[74] with different approaches. They derived the following equation [Eq 10]:

$$MSD_{PRW}(t) = 2S^2P\left[t - P\left(1 - e^{-t/p}\right)\right] \quad [10]$$

which states that the MSD in a two-dimensional system is governed by only two empirical parameters: S, i.e. the (fitting) speed modulus and the persistence time P, mentioned above. The fitting speed parameter S constitutes a model parameter and must not be confused with the mean experimental speed modulus $\langle v \rangle$, which is an intrinsic kinematic index introduced above. The fitting parameter S is the theoretical-speed that the cell should maintain during its path reproducing the PRW model with persistence time P extrapolated from the analysis. Thus, $\langle v \rangle$ and S must not be necessarily comparable since they concern to different kinematic speed concepts.

The three approaches proposed by the different authors differ from each other for the physical role assigned to the P parameter. Dunn et al. considered the MSD as a sequence of discrete adjacent segments approximating the real curvilinear cell trajectory, defining P as a pure directional persistence index unaffected by cell fitting speed modulus or direction. Othmer et al. proposed a different interpretation for the P parameter: they suggested that cell speed and orientation are not regulated by the same mechanism. According to their view, speed and directionality belong to separate underling processes. Cell speed changes are controlled by a Poisson process distribution with parameter λ, resembling the speed frequency changes. This assumption directly affects P, which finally results as a superposition of speed modification, defined by λ, and a directional factor Ψ_d which describe the average directional cosine [Eq 11]:

$$P = \frac{1}{\lambda(1 - \Psi_d)} \quad [11]$$

Similarly, Alt obtained the PRW equation on the basis of a speed autocorrelation function. The fit to each cell track to obtain the (S,P) parameters is performed using a non-linear Levemberg-Marquardt convergence-method. The fitting process is applied on the experimental MSD up to 75% of the total observation time. In fact, evaluation for longer times would results in a poor estimation of MSD, since the total number of contributions decreases following a *N-n* factor, where *N* is the total number frames constituting the movie, and *n* is the number of steps after that MSD is evaluated. After the fitting procedure, cells that provide P values near or below the acquisition time interval Δt, or significantly higher than the total observation time NΔt, are automatically discarded. Persistence times drastically outside the useful time range [Δt ; NΔt] are typically obtained when the expected biphasic cell migration behavior, which should be almost quadratic for t << P, and fairly linear for t >>P , has not been clearly observed, and obviously the PRW model cannot be applied to the considered cell [75]. In the former case, P < Δt, the cell follows a pure random walk migration, in the latter case, P >> NΔt, the cell is moving in an almost straight line for the entire time observation (MSD is in this case described by a purely quadratic curve), neglecting any random behavior. Our findings show that the majority of the analyzed cells followed the PRW model. Before identifying the most probable value for <S> and <P>, we must consider what is the statistical distribution for these two parameters. Following the previous works, the speed modulus distribution is described by a Gaussian curve, P instead, derived from a Poisson process, follows a Poisson distribution. In Fig 8 is reported the S and P statistical distribution obtained applying PRW on MSD evaluated from U87MG tracked cells set under control condition (Fig 8a1-b1) and

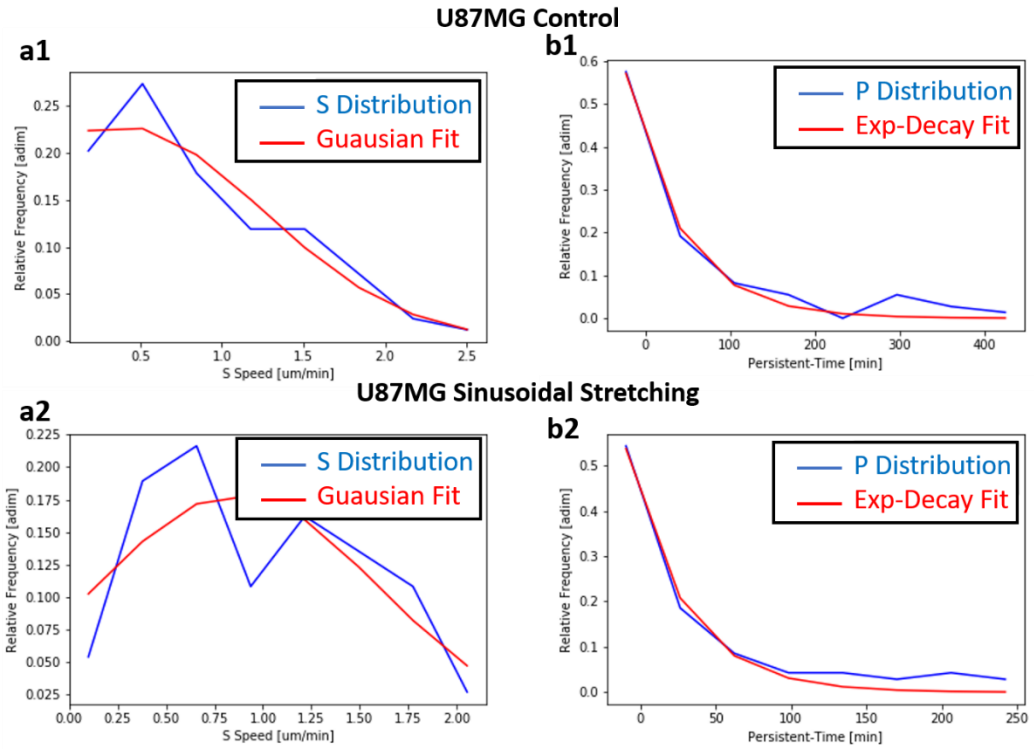

Figure 8: Statistical distribution panel of S and P fitting parameters obtained from PRW model applied on experimental MSD evaluated from single cells. In (a1-b1) figures are reported the S and P parameter, respectively, from U87MG under control condition. In (a2-b2) figures are reported the S and P parameter, respectively, from U87MG under sinusoidal stretching stimuli.

under periodic stretching (Fig 8a2-b2). The fitting speed S distributions (Fig 8a1-a2) follow fairly well a gaussian behavior, while the persistence time P distributions are ascribable to a Poisson-like distribution process (Fig 8b1-b2):

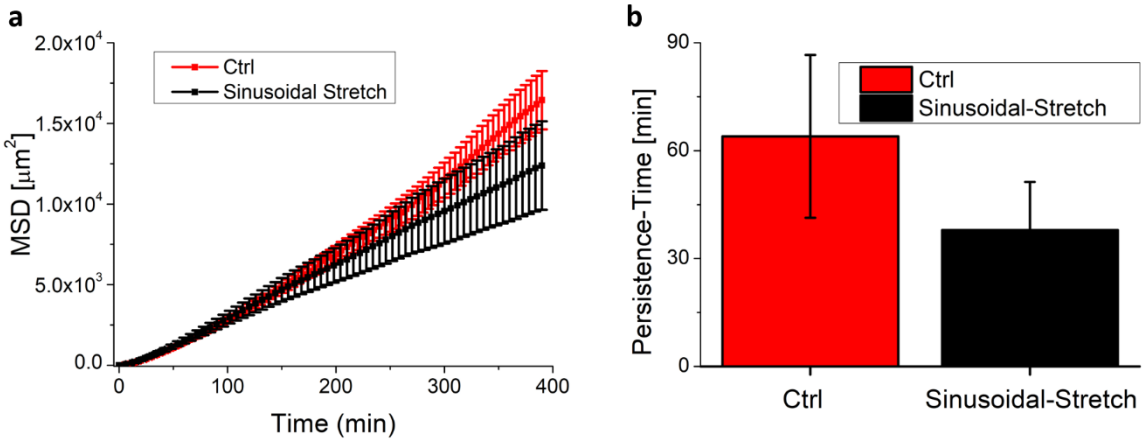

Figure 9: (a) Averaged MSD of U87MG cells in control condition (red squared dots) and under periodic stretching (black squared dots). (b) P fitting parameter comparison between U87MG in control condition (red column bar) and under periodic stretching (black column bar)

In Fig 9a are compared the experimental overall MSD averaging the MSD from single cells obtained under control condition (red squared dots) and applying the periodic stretching (black squared dots). The averaged MSD behavior under periodic stretching application is almost linear during the entire time observation, while a composed parabolic-linear profile is clearly observable in control condition. Accordingly, the persistence time P extrapolated in the control experiment is significantly higher than P obtained during periodic stretching (approximatively two-times-fold) (See Fig 8b1-b2 and Fig 9b).

The knowledge of <S> and <P>, global parameters representing the cell motility in a specific area, allows us to introduce another general physical parameter. Pointing out that the migration of a cell population in a given zone resembles a diffusive process, we can define the diffusivity μ starting from <S> and <P> parameters as follows [Eq 12]:

$$\mu = \frac{< S >^2 < P >}{2} \quad [12]$$

The factor two in the denominator summarizes that we are dealing with a diffusive process in a two-dimensional system.

• Shape-factor and orientation Parameters Evaluation

When cells from in-vitro experiments are manually tracked, in addition to migration analysis, the shape-factor is equally relevant. In our studies we focused on two major topics. Firstly, how cells react from exogenous molecule or drug exposure, evaluating their polarity. Secondly, how cells reorient their body under periodic stretching stimuli. In both cases a quantitative parameter summarizing cell polarity must be introduced. In the next section we will provide a shape-factor fitting parameter that allows us to measure shape-ratio of single cells. Shape-ratio index is required to tackle polarity study in the former task (exogenous drug exposure). The shape-factor fit is also exploited to evaluate the reorientation-angle, needed for the latter framework (stretching stimuli). Similarly to the final direction parameter: θ_{Final} introduced above, also in the reorientation angle a director index must be adopted to quantify the cells reorientation magnitude.

• Shape-Factor parameter

Usually, the cell shape can reasonably be approximated as an ellipsoidal body. This condition holds for the cell-lines exploited in our experimental setups, which are U87MG glioblastoma and BALB-3T3, respectively. In particular, for the case of U87MG line since it is a “multiform” tumor most of the cell ensemble contours are superimposable to an ellipsoidal shape. The relevant geometrical index summarizing the cell morphology are the major a and the minor b axis obtained from the ellipsoidal fitting applied on the cell contour. The cell contour is manually tracked and then the ellipsoidal fitting is applied using standard Image-J routines. Then, the shape-factor can be evaluated computing the aspect-ratio AR between the minor and the major axis [Eq 13].

$$AR = \frac{b}{a} \quad [13]$$

In Fig 10 the elliptical fitting applied on contour cell highlighting the major and minor axis is reported.

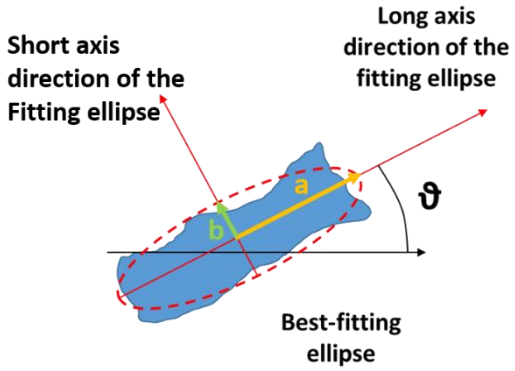

Figure 10: Graphical reconstruction of the elliptical fitting procedure (red dashed line) applied on contour cell (blue body).

The shape-factor runs in the [0÷1] range and represents a polarity index for the cell morphology. In fact, aspect-ratio closer to unity identify cellular shape where no dominant elongation direction is detectable, subsequently the cell is “depolarized”. Instead, aspect-ratio significantly lower than unity refers to cell contour having a sharped and easily observable elongation direction, thus the cell is highly “polarized”. In this description we are neglecting the cell orientation direction since we are simply testing the polarization level of the cell contour sample. The presence of cell polarization can provide cues regarding the cell motility capabilities. Usually, highly polarized cells have higher migration features, while low polarized cells do not. The aspect-ratio is a suitable index to test the efficacy of cytostatic drugs on cell lines, here we provide an example. We tested the cytostatic role of a novel potential-drug compound called “1G” that is a benzodiazepine-based molecule and has been initially synthesized searching an anti-epileptic role. Nevertheless, 1G compound showed a potential efficiency as antimitotic and cytostatic drug. Thus, we investigated 1G effect on immortalized glioblastoma tumor cell line, U87MG. In Fig 11 a-b two final snapshots after 12 hours of live imaging of cultured invitro U87MG in control condition (Fig 11a) and exposed to 1G 20µM (11b) are reported. Approximatively ≈25 cells have been selected and elliptically fitted to evaluate their aspect-ratio [Eq 13]. The image acquisition started immediately after cell seeding. In Fig 11c the mean aspect-ratio ± s.d. obtained from control (red column bar) and 1G 20µM exposition (green column bar) after 12 hours from initial seeding is reported. Most of the cells in control conditions are fairly polarized, in fact their mean AR is significantly lower than unity, while the majority of cells exposed to 1G result rounded and their mean AR is approximatively one. This AR suggest that the reduced motility of U87MG cell-line under 1G exposure is probably due to the depolarization process induced by the exogenous drug.

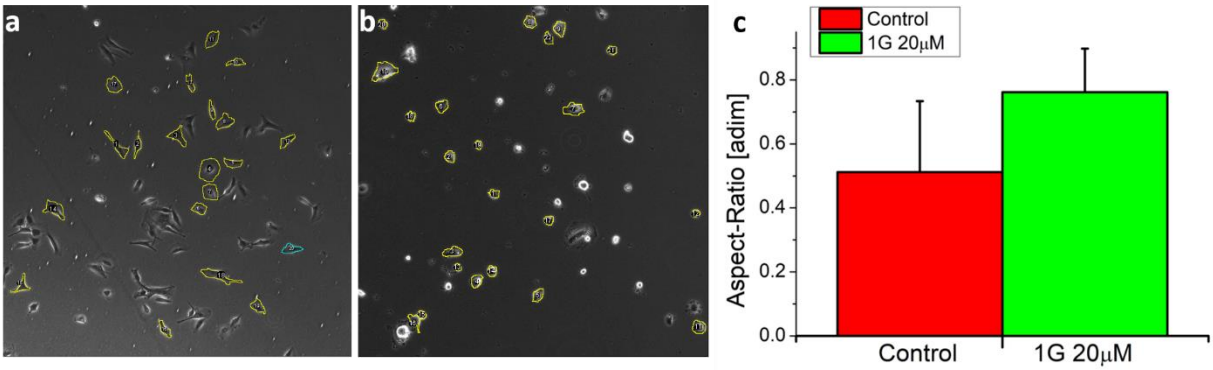

Figure 11: Final snapshots of the cells imaged areas after 12 hours from seeding in control condition (a) and under 1G 20µM exposition. AR comparison between control (red column bar) and 1G 20 M exposition (green column bar).

• Reorientation-angle parameter and director index

In the previous section we have introduced the AR parameter starting from the contour cell fitting, which is ascribable to an elliptical shape. In the topic treated above we were focused only on the polarization-depolarization evaluation, since this parameter is strictly connected to the cell motility features. However, the environmental condition both in control condition and during drug exposition are supposed to be isotropic, considering the drug diffusion equally spread in the cell microenvironment. This argument suggests us to neglect the particular major axis orientation with respect the axis of reference. Whenever the cells environment treated so far cannot be consider isotropic anymore, then also the reorientation angle must be included. This is the case of the second topic treated, when an uniaxial periodic stretching is applied we are introducing a mechanical anisotropy in the cell substrate.

In the literature there are many pieces of evidence reporting that cells exposed to a uniaxial cyclic stretching stimulus in a 2D environment reorient themselves in a direction almost perpendicular to the stretching one

[76]–[78]. If we assume that cells align along the direction of zero strain, we expect to see, after a certain period of continuous cyclic stretching, cells with the major axis of their fitted shape aligned along two mirror directions corresponding to the angle obtained for this specific orientation (the angle we are considering is evaluated with respect to the main stretching direction). Equivalently, the major axis direction obtained from the fit reproduce the cell orientation body. If the orientation angle is measured from the main-stretching direction, we expect to observe two possible mirror cell-reorientation directions. Thus, evaluating the major axis direction angle from a cell data-set the subsequent histogram should follow a double peak distribution. Here we assume that the direction of the cell major axis corresponds to the average direction of the stress fibers in the cell (we then experimentally validated this hypothesis). In our analysis we exposed BALB-3T3 cell line under uniaxial periodic stretching with sinusoidal waveform and frequency f=1Hz with maximum strain ≈10% for 6 hours. Accordingly, the ImageJ software was used to determine the average direction of the major axis of about 100 cells every 2h of stretching. In Fig 12c the major axis direction angle distributions obtained from the elliptical fitting each 2 hours of live imaging observation is reported. The major axis direction angle is measured from the horizontal X axis reference, which is placed perpendicular to the main strain direction (Y vertical axis). Direction angle histograms confirms the expected double peaks distribution placed symmetrically with respect the uniaxial main-strain anisotropy, even after just 2 hours of cycling stretching application.

We firstly tried to evaluate the most probable reorientation angles applying a gaussian fitting distribution on the histogram peaks. Nevertheless, the distribution of the cell orientation is typically not Gaussian. In some theoretical investigations, the energy associated to specific cell orientations has been considered and then the expected distribution has been derived on the basis of statistical mechanics. In the specific case, the Boltzmann factor has been exploited to derive the distribution.

Following these statistical mechanics basis we removed the Gaussian fit and we introduced a director for the average cell direction $\vartheta_{director} = \langle\vartheta\rangle$ and orientational order parameter S to represent the angular distribution. Where $\langle\vartheta\rangle$ is the arithmetic average of the major axis direction angle. Then the angular fluctuation $\Delta\vartheta = \langle\vartheta\rangle - \vartheta$ (where θ is the major axis direction extrapolated from a given cell) is introduced. A possible choice for the orientational order parameter S in 3D systems is [Eq 14]:

$$S = P_2(cos\Delta\vartheta) = \langle\frac{3cos^2\Delta\vartheta - 1}{2}\rangle \, [14]$$

as is quite common in the field of liquid crystals (note that S corresponds to the second order Legendre polynomial). In our case, we can use a 2D orientation order parameter defined as [Eq 15]:

$$S = \langle 2cos^2\Delta\vartheta - 1\rangle = \langle \cos 2\Delta\vartheta\rangle \, [15]$$

The average value of $\cos 2\Delta\vartheta$ is also defined as apolar order parameter. In fact, for cells represented as an ellipse, a vector **v** oriented along the direction of the major axis is equivalent to the –**v** vector. S = 0 case means an isotropic distribution of directions and the cells are equally oriented around average direction $\langle\vartheta\rangle$ with a mean dispersion $\langle|\Delta\vartheta|\rangle = \pi/4$. S = 1 means perfect order since the cell ensemble have the same identical orientation $\vartheta_i = \langle\vartheta\rangle$ and $\Delta\vartheta_i = 0$ for each i-th cell. S = -1 means perfect order in the direction perpendicular to the director $\langle\vartheta\rangle$. Another possibility would be that of using as a director the main-strain direction, and of calculating the orientational order parameter with respect to that direction. Subsequently, $\vartheta_{director} = \vartheta_{main-strain}$ and $\Delta\vartheta = \vartheta_{main-strain} - \vartheta$ (where ϑ still refers to the major axis direction extrapolated from a given cell). In this case S = 0 means isotropic orientation of cells, S = 1 corresponds to the situation where all the cells are oriented parallel to the stretching direction and S = -1 indicates that all the cells are oriented perpendicular to the stretching direction. We decided to calculate the average direction $\vartheta_{director}$ and the orientational order parameter S using the average cells direction as the director. We split the major axis orientations in two sub-groups [0÷90(°)] (right) and [90÷180(°)] (left), where the angle is measured from the horizontal axis of Fig XX and α=90° represents the main-stretch direction. Then we

evaluated the $\langle\vartheta\rangle$ and S parameter separately for each sub-group, obtaining $\langle\vartheta_{right}\rangle$, $\langle\vartheta_{left}\rangle$ and S_{right}, S_{left}, respectively . Thus, we expect a similar orientational order parameter: $S_{right} \approx S_{left}$ from the sub-groups for a given time observation. S value near to 1 indicate a narrow orientational distribution, while S near to 0 implicates an almost isotropic angular dispersion. In Fig 12a-b are reported the initial (a) and the final (b) snapshot of BALB-3T3 cells imaged field during sinusoidal stretching application, also the main-strain direction is emphasized. In Fig 12c is showed the experimental angular distribution histogram for 0,1,2,4 and 6 hours of live imaging observation. Figure 12d shows the average cell direction as a function of stretching time. The angles corresponding to the zero(min)-strain direction (blue and green dashed lines) and main-strain (black dashed line) are also reported in Figure 12d. It is to be stressed that the most probable reorientation process that we observed is represented by cells losing their orientation, becoming almost circular and then extending their body (and stress fibers) along the specific direction of almost zero-strain and not a slow rotation of flattened cells.

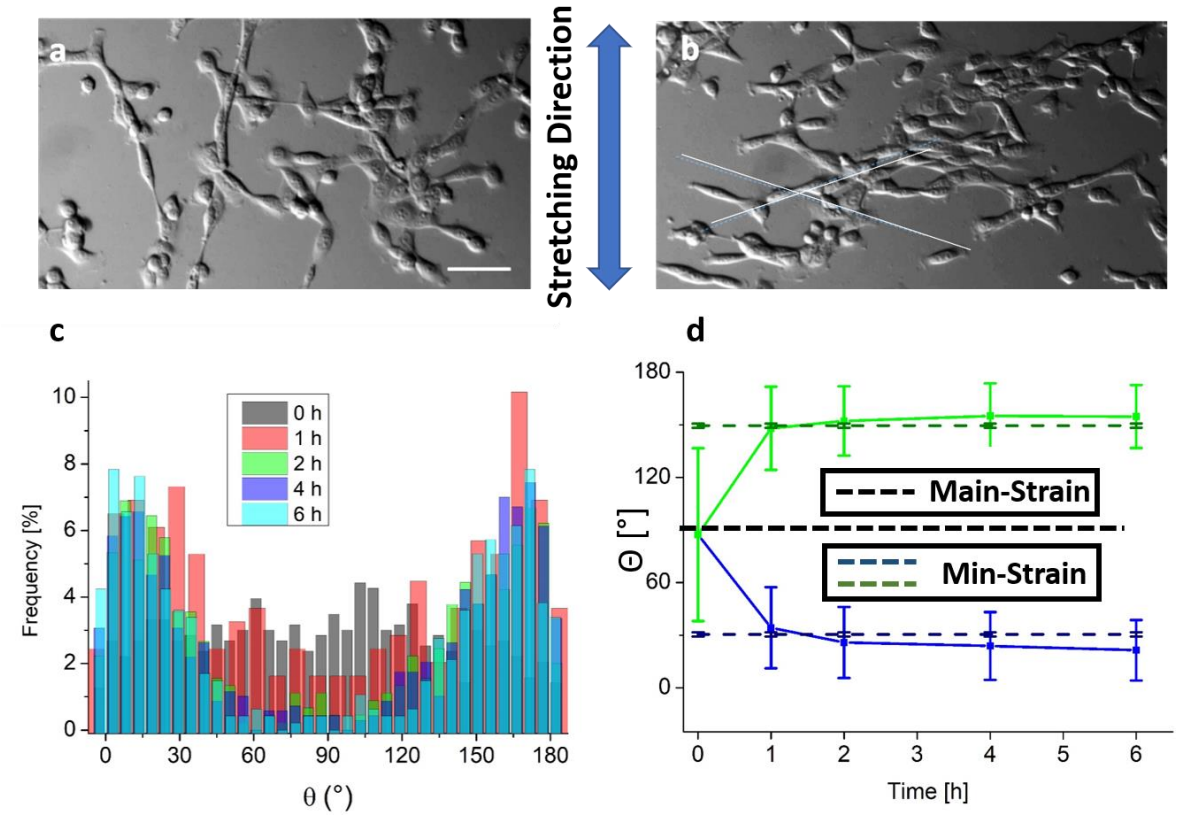

Figure 12: BALB-3T3 polarization process under sinusoidal stretching is showed: initial (a) and final (b) snapshot of cells in the imaged field. Also the main (blue vertical arrows) and the min strain (white crossed lines) directions are showed. (c) Statistical distribution of the cells direction distribution for several time-frames ([0,1,2,4,6] hours) during sinusoidal stretching. (d) Averaged cells polarization direction evaluated for the different time-frames previously analized in (c). Also the min-strain direction (blue and green dashed lines) and the main-strain direction (black dashed line) are reported in (d).

In order to have quantitative data about the angular distribution we determined the orientational order parameter S [Eq 15]. Accordingly, S = 0 means an isotropic distribution of directions, S = 1 means perfect order along the director and S = -1 means perfect order in the direction perpendicular to the director. The data are reported in Table 1:

	Average direction (director) with respect to the	**S parameter (calculated with respect to the director)**

Stretching time	perpendicular to the main stretching direction	
0 h		0.08
1 h	(34±23)°	0.71±0.30
	(148±23)°	0.70±0.30
2 h	(26±20)°	0.79±0.30
	(152±19)°	0.79±0.20
4 h	(24±19)°	0.80±0.30
	(154±18)°	0.81±0.20
6 h	(21±17)°	0.85±0.30
	(155±17)°	0.83±0.20

Table 1: values of the average direction of cells (± s.d.) and the corresponding S parameter at different time points of continuous cyclic stretching.

Cell Nano-Mechanics

In this section we will describe how AFM technique can be exploited as a powerful investigation device to obtain data about cell mechanical properties. In the previous section, we characterized cell migration properties introducing different parameter-indexes. Nevertheless, cell speed, MSD, and directional parameters alone provide only a partial cell features description. In fact, these migration indexes are strictly connected to cell mechanical and viscoelastic properties and their changes [79], [80]. In this section we will focus on the complete cell nano-mechanical investigation (viscoelasticity) through single Force-Displacement (F-D) AFM curves.

AFM is endowed with an almost unique capability: it can apply and measure vertical forces and height profiles sample with nano-scale resolution, and it can be exploited in vast variety of materials exposed to different external conditions: in vacuum, in air, and in aqueous environment. This allows us to study for example cells in their almost physiological conditions. Through AFM we can acquire vertical height profile of cells at the nano-scale level moving along the x-y plane up to 100/200 micrometers. In fact, cell samples topography has been already imaged by AFM technique in literature [81]. Moreover, since actually AFM cantilever provides a deflection signal for a given plane coordinates sample point (x_i,y_i), we can extrapolate force interactions between the AFM tip and the underlying cell. In fact, after initial pre-calibration of sensitivity parameters and cantilever elastic constant K_e , we can obtain the actual tip- sample interacting force curve. Thus, for a given sample-surface point (x_i,y_i), we can first obtain the deflection-scan displacement curve (Def-D) expressed in voltage units, then calibrating the piezo sensitivity parameter we can convert the Def-D curves in metric unit. Finally, the Deflection-Scan Displacement curves can be rewritten as Deflection-Indentation curves (Def-I), which correlate the actual cell indentation to the tip deflection (or alternatively to the force perceived by the tip). In this step several data treatments can be taken into account, such as the hydrodynamic drag evaluation and subsequent subtraction and the contact point (C-P) evaluation. Hydrodynamic drag affects the deflection signal along the entire scanning displacement, especially at high scan-displacement speed regime and is clearly observable in the non-contact regions. C-P represents the initial point of the vertical scan-displacement axis where the tip starts its interaction with the underlying cell surface. After these two sub-steps correction we can obtain the Deflection-Scan Displacement curves corrected from aqueous medium drag and measured from the C-P. Nevertheless, the horizontal axis (Scan-Displacement measured from the C-P) does not represent the real tip indentation applied to the cell surface. Since the sensitivity calibration has been obtained from the plastic/glass rigid substrate, cell indentation is referred to the underlying rigid substrate. Thus, cell indentation should be measured starting from the linear substrate deflection response used for sensitivity calibration. A linear fit representing the tip/rigid sample deflection is plotted and then subtracted from the Def-Scan Displacement curves, for both the approach and retraction regions. Thus, starting from the initial Deflection-Scan Displacement (Def-D) raw curves we have extrapolated the Indentation-Scan displacement cell curves (I-D) (where the cell substrate and hydrodynamic medium contribution have been removed). Finally, the Force-Indentation curves (F-I) can be evaluated by multiplying the Indentation axis to the tip elastic constant K_e previously measured.

Starting from Force-Indentation F-I curves we can provide some mechanical initial guess and cues. Initial cell studies involving AFM measurements proposed a pure elastic and isotropic description of the cell[82]. in these works, only the approach part of the F-I curve has been involved in the analysis. Considering the Hertz theory regarding contact mechanics and deformations of bodies with different geometries [83], [84], Young modulus E extrapolation of the cell from approach F-I curve can be obtained. These initial cell elasticity evaluations, based only on E parameter using non-linear fitting procedure of approach F-I curves rapidly showed their drawback. Even taking into account bottom-effect-correction model (BECC), cell nano-mechanics is not well described through pure elastic models. Firstly, cell mechanicsis clearly highly non-isotropic both along in-plane and vertical directions [85]. In fact, depending on the particular indented inner cell region, apparent Young modulus changes rapidly, since both plasma-membrane and cytoskeletal

environments provide their contribution to the overall measured indentations. Secondly, applying the Hertz indentations models to the retraction part of F-I curves, the extrapolated E parameter is always higher if compared to E value obtained from the approach region. Furthermore, comparing approach and retraction F-D or F-I curves, a clear hysteresis area is observed [86], [87], and usually the retraction part is located below the approach curve. These first insights clearly suggest that a pure elastic description for cell nano-mechanic is totally inappropriate, but it could provide a first approximation of E parameter for further analysis. Instead cell contain, at least, also a viscoelastic contribution, which must be quantified introducing a second mechanical parameter, which must be added to E quantification.

Further works dedicated to cell nano-mechanics measured by AFM moved from a pure elastic cell description toward viscoelastic modeling [88], [89]. Usually, in these works a dynamic force AFM setup was exploited, where two mechanical parameter G and G' are extrapolated as function of the driven cantilever oscillation frequency. These AFM setups required some additional modifications from original AFM configurations, which are also quite expensive, like lock-in device. Furthermore, this approach is employed in the frequency domain, whereas we coukld be interested in extrapolating the viscoelasticity of cell samples directly from initial single Def-D curves.

In fact, looking at the Def-D or F-D profiles, the hysteresis between the approach and retraction parts is clearly observable. Thus, viscoelastic behavior of cell is already contained into the F-D curve but it cannot be directly evaluated. Our next achievement is to adapt an analytical method that allows us to extrapolate viscoelasticity from F-D (F-I) curves. Following the protocols introduced by [90] and [91], which are based on Ting model [92], we developed our own step-by-step method to extrapolate the viscoelastic parameters and we applied this method to different cell lines exposed to different treatments. Then, we adapted and applied the same analysis protocol to force-volume maps (FV) to map viscosity and elasticity of whole cell regions exposed to different exogenous molecules.

Our AFM setup is constituted by a BioScope I microscope equipped with a Nanoscope IIIA controller (Veeco Metrology, Plainview, NY, U.S.A.). A custom temperature-controlled stage based on a circulating water bath combined to Peltier cell driven by PID controller has been exploited to control sample temperature. AFM was used in both imaging (tapping-mode) and force spectroscopy configurations, using triangular silicon nitride cantilevers (Bruker DNP-S) with nominal spring constants of 0.06 N/m. Force-Indentation curves has been acquired setting $\approx 100\, nm$ maximum indentation since we are adopting sharp-tip geometry (pyramidal-indenter).

- **Preliminary Calibrations on Deflection-Scan Displacement curves**

In this section we will recapitulate the steps needed to convert raw data curves (deflection-scan displacement data, Def-D, of the piezo expressed as volage) to deflection-scan displacement curves (Def-D) expressed in metric units. Then, we will focus on the hydrodynamic drag contribution, which affects Def-D curves during both approach and retraction regions, especially at high scan-displacement tip speeds. We will show how to remove this deleterious effect due to the aqueous medium. Finally, we will introduce the Contact-Point (C-P) concept, which specifies where actually the tip encounter the cell sample surface and its force interaction starts. Definition of C-P is extremely crucial for further analysis, in fact, we developed several iterative algorithm approaches to identify C-P along the scan displacement axis. We will show how the combinations of these different method allow us to better identify the C-P on the Def-D curves.

- **Sensitivity Evaluation**

After AFM tip mounting and photo-diode centering, the cantilever is inserted in the the aqueous medium. Using the imaging support given by the optical microscope a plastic/glass substrate region not covered with cells is selected. Finally, the approaching procedure toward the sample surface is performed. First manual stepping driven by the operator through the stepper motor is used to travel coarse the major distance between the tip and the surface. Then, when the tip-surface distance is less than approximatively ≈500um the automatic search of the underlying surface can start. During the procedure the piezo moves cyclically toward the surface as follows. First it travels down approximatively for 15 micrometers, then if in this initial approaching the sample surface is not reached the tip is retracted for half of the distance traveled by the stepper motor and the sequence is iterated until the surface is achieved.

When the tip reaches the sample surface, usually the setup is set to rest for several minutes. Since the cell sample is placed in a controlled temperature device, which is needed to maintain the sample at the physiological condition of +37°C, the piezo and the cantilever should reach a new thermodynamical equilibrium condition. In fact, the piezo sensitivity, the calibration parameter that we are going to measure, is highly sensitive to environment condition changes especially on temperature. After several minutes, when the aqueous medium and the piezo are thermically stable, the piezo sensitivity can be acquired. First, the AFM operating mode is set on single deflection-scan displacement curve. Then, several Def-D curves on the plastic/glass substrate are acquired minimizing the scan-displacement speed in order to reduce as much as possible the hydrodynamic drag. The substrate is chosen as surface of reference for sensitivity calibration, since it could be thought as an extremely rigid and non-deformable material. In fact, glass bulk is constituted by an almost infinity stiffness if compared to cantilever elastic constant and considering substrate and tip material. The scan-displacement range and the deflection setpoint are tuned in order to emphasize the region of interaction between the cantilever tip and the underlying glass surface. In fact, we are searching the linearity region of piezo response and detector sensitivity, needed for sensitivity calibration. The Deflection-scan Displacement curves (Def-D) graphs obtained from the rigid surface can be summarized as a flat curve, representing the non-contact region, followed by a linear region with almost constant slope, i.e. the contact region. A typical D-Def graph curve acquired on a rigid substrate (where the axis have been already inverted from Def-D curve for sensitivity calibration) is reported in Fig 1-left. The D-Def data raw curves are expressed initially in voltage unit, then only the scan-displacement axis can be converted in metric unit, which in fact describes the known vertical scanning of the cantilever. Focusing on the contact region (Fig 1-right zoom) we can compare the cantilever deflection amount and the subsequent vertical scan displacement variation. Since the surface behaves, at first approximation, as a non-deformable material, during deflection process the cantilever tip hypothetically does not indent the surface and the corresponding vertical scan-displacement variation is due only by pure elastic cantilever deflection in response to the underlying substrate. Thus, the sensitivity parameter can be inferred fitting the linear region and measuring the subsequent slope coefficient, which is expressed as a metric unit divided voltage unit (usually nm/V). The

optimal region used for linear regression is the central region of the detector, where the photodiode response linearity is maximized.

• Hydrodynamic drag correction

After initial piezo sensitivity calibration on the rigid substrate, the Def-D curves on cell sample acquisition can finally start. Usually, cell surface research is performed moving the AFM stage and looking the area of interest provided by the objective of the optical microscope. Once a specific cell is chosen, the AFM stage is moved in order to place the cantilever tip above the central region of the cell and several Def-D curves are acquired.

One of the key point-parameters during the Def-D curves acquisition is the scan displacement speed. As the cantilever tip moves faster on the underlying sample, more Def-D curves can be acquired during time. Nevertheless, as the scan displacement speed is increased also the hydrodynamic drag is enhanced. The hydrodynamic drag is introduced by the presence of the aqueous medium surrounding the cantilever; the surrounding medium is dragged by the cantilever movement and opposes the tip vertical translation. Thus,

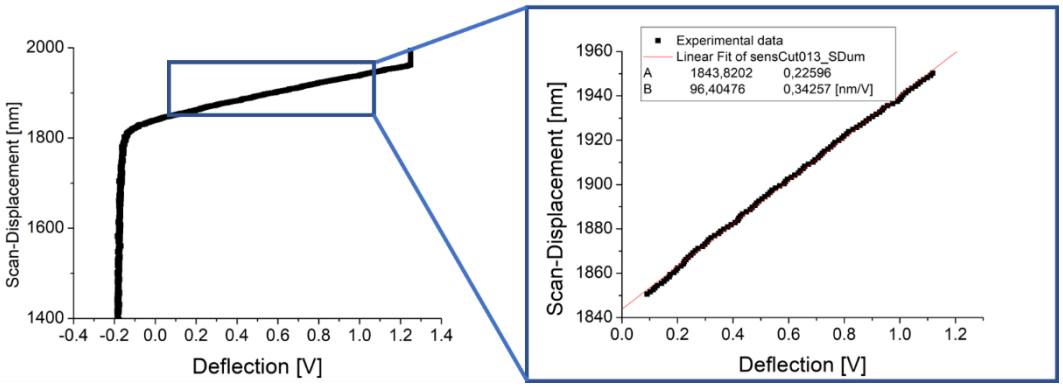

Figure 1: Sensitivity calibration from Scan Displacement-Deflection curve from glass substrate. (left) Deflection-vs-Scan Displacement. (right) zoom on the linearity region of the photodiode response and subsequent linear fitting for sensitivity measurement.

the tip undergoes additional deflection contribution arising from hydrodynamic drag, which depends on several terms like cantilever and tip geometry and scan displacement speed. When the AFM works in vacuum or air environment hydrodynamic drag is negligible. Conversely, hydrodynamic drag in water represents a non-neglectable contribution, both during approach and retraction regions. Thus, hydrodynamic drag provides an additional deflection during the entire scanning of the tip on the below cell surface, also in the contact part, and its contribution is perfectly equivalent in the approaching and retraction region. The hydrodynamic drag is the major deflection contribution during the non-contact region, when the tip does not interact with the underlying surface. Its contribution is clearly observable highlighting the deviations of the non-contact region in the approach and retract curves. The farther the initial part of the Def-D approaching region from the retraction section, the more the hydrodynamic drag deeply influences the deflection signal.

The hydrodynamic drag removal is performed as follow: first the Def-D curve in the approach part is taken into account, then the initial part of the curve (usually $\approx 1/3 \div 1/2$ of the entire scan-displacement, but still far from the contact region) is fitted by a parabolic fitting procedure, in order to remove the non-linear contributions that affects the Def-D curve at high scan displacement speed regime. Finally, the reconstructed parabolic behavior is removed along the entire scan displacement axis, in both the approach and retraction regions. This procedure allows removing also possible tilts in the force-curve plots due to the laser alignment. As final result, we have obtained the Def-D hydrodynamic drag corrected curves, where the non-contact region in the approach and retraction regions is represented by a perfectly fattened curve, meaning that no interaction is affecting the non-contact regime. A more rigorous procedure would require to take into

account the hydrodynamic drag also when the tip is in contact with the sample, but this approach is more critical in the case of dynamic modes of analysis of the sample rheological properties.

• Contact-Point search algorithms

After the pre-treating steps of detector sensitivity calibration and tilt and hydrodynamic drag correction, we finally obtain the corrected Deflection-Scan Displacement (Def-D) curves. These treated Def-D curves are composed by two different regimes, the non-contact (flat part) and the contact (non-linear part) regions. Between these two regimes is contained the contact-point (C-P), the scan-displacement coordinate where the cantilever tip first encounters the underlying cell surface. The C-P is a fundamental parameter, since it allows us to measure the height profile (the gap) between the cell surface measured from the cantilever tip in the non-contact region. More importantly, it provides us with a first estimation of the indentation amount in the cell sample in the contact-region, since the rigid substrate deflection contribution has not yet been removed. The C-P is easily detectable for Def-D curves measured on stiff material, like plastic/glass substrate, simply because there is a sudden, and monotonic deflection signal change behavior upon scan-displacement axis movement, as reported above. When the AFM tip deflection is measured on soft material, like on living cells, the change of the approach deflection signal along vertical scan displacement is less noticeable due to several reasons. Firstly, the non-contact region is characterized by low signal-to-noise ratio of the deflection signal, even after hydrodynamic drag subtraction. Secondly, the deflection profile in the contact region does not follow a pure linear behavior like in non-deformable material. Instead, the deflection response as a function of scan displacement, given the soft surface, provides a non-linear curve that must be treated carefully to correctly determine the C-P coordinate.

To avoid subjective manual C-P detection provided directly by the operator, first automatic C-P evaluation has been initially proposed by [93]. Furthermore, the typical amount of Def-D curves acquired at the end of any experiment is about several thousands, thus an automatic and well tested protocol is needed. Previous proposed C-P evaluation studies [93]–[97] considered several approaches. Nevertheless, most of these methods were focused on the Goodness-Of-Fit method (GOF). The GOF approach recursively fits a specific sub-section of the approaching Def-D curve with a given Deflection-Scan Displacement (or alternatively Force-Scan Displacement) theoretical relationship based on Hertzian models ((for example [Eq 1a-b])) through least-squares based algorithm. The unknown coefficient that is extrapolated by the GOF fitting procedure is typically the Young modulus E. For every experimental Def-D sub-section fitting, subsequent residuals sum is stored, and the C-P selection is based on searching the sub-section containing the minimum residuals amount. Thus, C-P evaluation based on GOF is strictly dependent on the particular experimental conditions used during Def-D set curves acquisition. In particular, several theoretical relations that bound Force and Deflection are proposed depending upon these experimental circumstances, like: tip and cantilever geometrical shapes, tip half-opening angle, and indentation/sample-height ratio. Usually, in the C-P evaluation based on GOF the underlying cell is treated as a pure elastic and isotropic material, and Sneddon's implementation of the Hertz theory for pyramidal or cone-shaped tip is used [98]. Alternatively, for cone tip where the indentation/sample-height ratio cannot be neglected in which the bottom effect arising from the rigid substrate affects the indentation process, also the Bottom-Effect-Cone-Correction (BECC) [99], [100] and more recently [101] is included. In [Eq 1a] is reported the Sneddon's equation for a cone-shaped tip, in [Eq 1b] BECC modified equation is reported, where θ represents the half-opening angle of the tip, E is the Young Modulus which is extrapolated from the fitting procedure, and h is the sample thickness at a given location:

$$\begin{cases} F = \dfrac{2E \tan\theta\, \delta^2}{\pi\,(1-\nu^2)} assuming\ \upsilon = 0.5 \xrightarrow{yields} F = \dfrac{8E \tan\theta\, \delta^2}{3\pi} [1a] \\ F = \dfrac{8E \tan\theta\, \delta^2}{3\pi}\left[1 + 1.7795^2 \dfrac{\tan\theta}{\pi^2}\dfrac{\delta}{h} + 16 \cdot 1.7795^2 (\tan\theta)^2 \left(\dfrac{\delta}{h}\right)^2\right] [1b] \end{cases}$$

The initial C-P evaluation works [93]–[97] confirmed how the different iterative searching methods provide similar C-P results. Here, we will summarize four different methods and we will show how a combination of them can achieve better accuracy results in C-P evaluation. In fact, erroneous C-P identifications that differ approximatively $\sim 50\ nm$ from real C-P position could produce faulty Young modulus values up to an order of magnitude [102]. This larger error propagation is easily explained just considering that the typical Force-Indentation ($F - \delta$) relationship for cone and pyramidal tip shapes follow a quadratic behavior: $F \propto \delta^2$.

The four C-P search algorithms proposed below are supposed to work in a similar way. Each proposed method is labeled by a test-parameter, which is sequentially evaluated for all the possible C-P candidate positions along the scan-displacement axis. As mentioned before, not the entire Def-D approach curve is really suitable for the C-P search algorithm, thus the C-P points under test are usually individually related to a sub-portion of the curve. In particular, the approaching Def-D curve is analyzed fragmentating it in sub-parts of equal size, and each sub-part is labeled by its specific trial C-P belonging to this sub-region. The window-size is defined depending on the chosen C-P searching algorithm. After the trial C-P set analysis we have the corresponding test-parameter data set, which we expect to vary smoothly far from C-P region, while it assumes a narrow peak in the region surrounding the C-P. This common test-parameter behavior for the proposed algorithms yield a fast and easily detectable C-P search, guaranteeing high accuracy for all proposed methods. Furthermore, since the four approaches provide similar test-parameter behavior as a function of the trial C-P coordinate, these methods can be combined together to yield the best C-P research.

The first algorithm proposed is the so called: Ratio-Of-Variances (ROV):

In the non-contact region we have a completely flat curve, since the tip does not mechanically interact with the underlying surface and only the thermal and instrumental noises could affect deflection signal. Thus, measuring the variance in a small window portion of the non-contact region we expect to measure only these noises. Instead, moving toward the contact region the tip senses a progressively higher interaction force with the cell surface confirmed by an increase of the deflection signal. Thus, the variance measured using the same window size in the contact region will be significantly higher if compared to the variance obtained in the non-contact region. If we move the window starting from the initial scan displacement points (the farthest from the cell surface) toward the contact region and we sequentially measure the window variance we expect to observe a step-like behavior in the portion surrounding the C-P. Obviously, the window-size must be sufficiently large to minimize accidental noise contribution, and the i-th trial C-P point is placed at the center of the window. Nevertheless, window variance profile does not fit the appropriate criteria described above. In particular, its relationship with respect to the i-th trial candidate does not follow a peak profile around the C-P region. Thus, several possible data modifications are required. The first, and more obvious, option consists on the numerical evaluation of the derivative of the variance with respect the i-th trial index. This suggestion will introduce one peak in the real C-P position, where the step-shaped profile of the variance is maximized. Summarizing, the variance signal is locally fitted point by point by a straight line having a fixed number of elements around the point of interest. The fitting region should be large enough to minimize noise fluctuations. Then, the slopes obtained from the sequential variance fitting are plotted and the trial point represented by the highest slope is chosen as best C-P. The derivative of the variance signal is a valuable test-parameter, but not the unique possible for the variance-based method. A second solution proposes to evaluate the variance of two equally spaced windows (of size N_{window}) located respectively at the left-side and at right-side of the i-th trial C-P. Then the ratio between the right-side and left-side window

is evaluated [Eq 2], where X_i denotes the scan-displacement coordinate. This test-parameter is called Ratio-Of-Variance (ROV):

$$ROV(i) = \frac{Var\left[X_i \div X_{i+N_{window}}\right]}{Var\left[X_{i-N_{window}} \div X_i\right]} [2]$$

As mentioned above, the variance in the non-contact region is due to instrumental and thermal noise contributions, which are almost constant along the scan-displacement axis. Thus, the ROV is close to unity in the non-contact region. Equivalently, in the pure contact region the Def-D curve follows a paraboloidal or similar behavior depending on the cantilever and tip geometrical features. Thus, ROV in the contact region is slightly above unity. Around the C-P the ROV increases since the variance in the non-contact region is significantly lower compared to the value obtained in the contact region as explained above. Thus, at the C-P location the ROV reaches its maximum value and around the C-P is well represented by a peak behavior. Note how the ROV method is robust with respect to the particular experimental condition, since it is unaffected by geometrical cantilever and tip construction features, and indentation-sample-height ratio as well. Furthermore, this method is numerically less expensive since just standard variances evaluation of the different windows is required. Thus, ROV approach could be used as first C-P evaluation, and only then several different more computationally expensive searching algorithms could be applied around this initial guess [103].

The second method illustrated is the previously mentioned GOF,

This is the most common strategy exploited so far. The Def-D curve is progressively fitted, each time changing the initial point, using the appropriate contact-mechanics model depending on the experimental conditions. Thus, the trial C-P candidates, representing the initial point for the fitting procedure, are sequentially tested starting from fart non-contact region toward the contact region. Since the horizontal axis in the least-squares fit algorithm constitutes the sample indentation, the i-th trial C-P candidate is tested setting the initial point $X_i = 0$ and $F_i = 0$ (for the scan-displacement and force coordinates) in the fitting procedure. Possible test-parameters associated to GOF approach could be: the mean-squared error [104], the residuals-sum, or the r^2 coefficient [97], [105]. These test-parameters profile plotted as a function of the trial C-P index share similar peak-shaped behavior. Obviously, for mean-squared error and residuals-sum the absolute minimum value constitutes the best C-P choice. Instead, for r^2 coefficient the maximum value, the closest to unity is set as C-P selection. This sequential C-P research method is quite computationally expensive if compared to ROV approach since non-linear fit algorithms are iteratively applied. Thus, it could be applied only in a limited Dev-D curve portion around the C-P previously evaluated from the ROV strategy. In Fig 2a is reported the C-P evaluation using the ROV method. In Fig 2b is reported the C-P evaluated using the GOF method, the initial guess I provided from the ROV C-P (vertical black dashed line).

The third method illustrated is based on Young modulus E variations (obtained by the fit procedure) observed applying sequentially the contact-mechanics model (ΔE method):

This method is a sort of additional study based on the GOF approach, described above. Whenever we apply the appropriate contact-mechanics model fit, (usually based on Hertzian models) we extrapolate the E coefficient that describes the elastic mechanical material property. This mechanical coefficient depends strictly on the C-P choice, or alternatively the initial point of the fitting procedure. When part of the non-contact is included in the model fitting the E coefficient is systematically underestimated. Alternatively, when the fitting initial point is well within the contact region, over the real C-P, the E coefficient is overestimated. Thus, E extrapolated from least-squares fitting, increases monotonically as the i-th trial C-P index runs along the scan-displacement, as reported by [93]. The E derivative with respect to the i-index (dE/di) can be introduced and numerically evaluated. We expect that its sign is strictly positive ($dE/di > 0$). Nevertheless, the derivate dE/di behavior could change depending on the contact-mechanics modelling. For Sneddon's

[Eq 1a] its value is almost constant while for BECC [Eq 1b] follows an exponential trend. In [103], where the Seddon's model for cone-shaped tip was exploited, they observed a small inflection in the E profile with respect to the i-index at the C-P coordinate, which is easily detectable in a logarithmic scale. Thus, this local minimum represents the ideal condition for C-P detection. The test-parameter proposed was ΔE, defined in [Eq 3], where minus sign was applied to convert the local minimum in a local maxima point. This test-parameter behaves like a peak-shaped curve around the C-P region, as required in the statements above. Like in GOF approach, the fitting procedure for E extrapolation is applied systematically along the scan-displacement. This least-squares procedure is quite numerically expensive, thus initial C-P guessing provided by ROV method should be considered.

$$\Delta E = -\frac{d[\ln(E)]}{di} [3]$$

The fourth and last method exploited is the Power-Law-Exponent (PLE) model

When GOF and ΔE methods are applied, [Eq 1a-1b] or adapted contact-mechanics modela are sequentially applied on portions of the Def-D curve and the unknown E coefficient is evaluated. In the case of Sneddon's model the applied force follows a quadratic profile with respect to the indentation amount, thus: $F \propto \delta^2$. This relationship could in principle be tested for the trial C-P set under study. In PLE approach we have two free parameters: the Young modulus, and the power law exponent x (E, X) instead of only E. We expect to reobtain X=2 only when the initial point for the fitting procedure is placed at the right C-P coordinate. Instead, when part of the non-contact region is included in the least-squares fit the x exponent will significantly decrease from its theoretical value. Similarly, when the initial fitting point is well-within the contact region x exponent will reproduce numerical deviation from the expected X=2 condition. This method must be adapted if a different contact-mechanics model describes the Force-Indentation theoretical behavior. An additional prescription must be highlighted, since power law exponent deviation could appear for high indentation regimes, when the theoretical model predictions are less reasonable. In this case, only a small portion of the Def-D (Force-D) curve should be fitted. For low deflection condition this additional caution can be neglected, since also bottom effects are negligible. If the Sneddon's model [Eq 1a] is replaced by BECC [1b], which actually is a Sneddon's correction, the pure quadratic profile is no more reliable especially for higher indentation/sample-thickness- ratio regimes. In the most general case, the following equation [Eq 4] has been developed by [103], the test-parameter PLE that reproduces the required peak-like profile around the C-P. $X_{expected}$ represents the power law exponent required by the appropriate contact-mechanics model, while X_i constitutes the power law coefficient associated to the i-th trial C-P extrapolated from the fitting procedure. When $X_{expected} \approx X_i$ the PLE function diverges, since the denominator is close to zero, and the C-P coordinate is easily detectable. Also, in the PLE approach an initial C-P guess provided by the ROV method can reduces the computational cost. In Fig 2c is illustrated the C-P evaluation using the PLE method using the ROV C-P as initial guess (vertical black dashed line).

$$PLE = \ln\left(\frac{1}{|X_{expected} - X_i|}\right) [4]$$

After the application of the proposed methods we have a set of four possible C-P candidates for each Dev-D curve. In [103] the authors proposed a specific new test-metric based on the product of the four singles test-parameters. We initially decided to evaluate the best C-P coordinate simply averaging the four parameters. Nevertheless, we systematically observe a large deviation in the C-P evaluated by ΔE if compared to the C-P obtained from the other approaches. Furthermore, the peak-shaped profile in the ΔE model is less

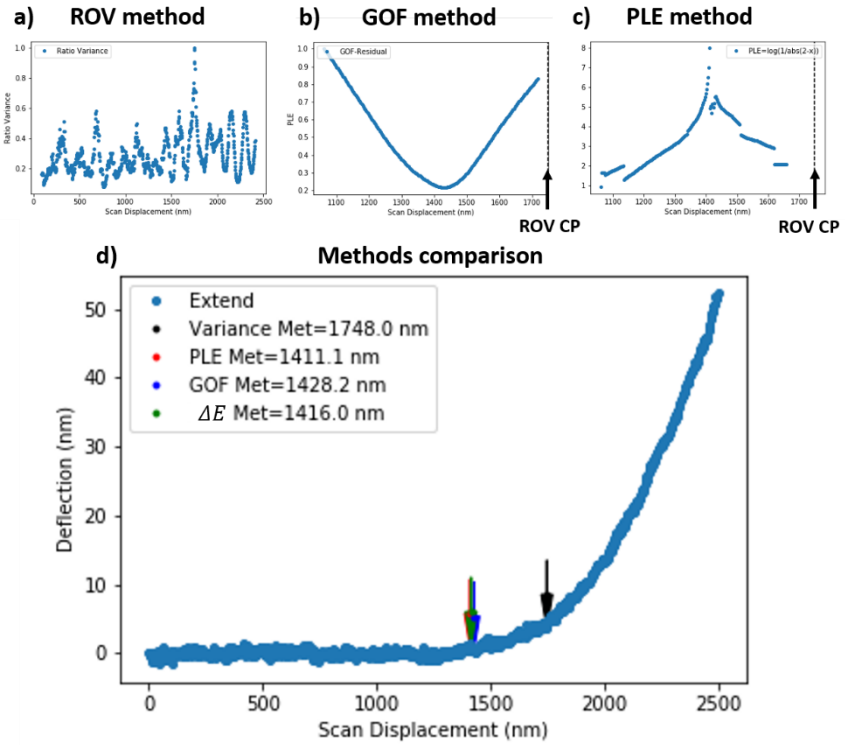

detectable. In fact, other similar spikes are frequently observed in the profile background and subsequent C-P evaluation sometimes is quite confusing. Thus, we decided to mediate only the GOF, VOR and PLE methods. In Fig 2d is reported an example of the C-P evaluation for a Def-D curve obtained from U87MG cell sample. Vertical arrows represent the different C-P methods results obtained.

Figure 2: Different Contact-Point evaluations adopting the proposed strategies on a U87MG Deflection-Scan Displacement curve. (a) Ratio-Of-Variance ROV, (b) Goodness-Of-Fit GOF, (c) Power-Law-Exponent, (d) comparison of the C-P methods. In b-c panel vertical black dashed line illustrates the C-P evaluated from ROV method.

It is interesting to note how the C-P searching algorithms are usually referred to Deflection-Indentation (Force-Indentation) curves, while we instead considered C-P evaluation in Deflection-Scan Displacement curve. Nevertheless, the Scan-Displacement to Indentation conversion is easily obtained by subtracting the Deflection-Scan-Displacement straight-line obtained from previous sensitivity calibration on the rigid substrate. Thus, the C-P search process and the Scan-Displacement-Indentation conversion can be exchanged in the data analysis sequence.

- # Hertz Model

The usually exploited model for contact mechanics in AFM investigation is the Hertz model. Originally, Hertz treated in 1881 [106] the contact mechanics and subsequent deformation between two solid spheres. In this description the first sphere (the indenter) is indenting the other one (the sample) and is considered infinitely rigid if compared to the sample stiffness. Thus, for spherical indenter the equation bounding the applied force F and the subsequent indentation δ in the sample is [Eq 5]:

$$F(\delta) = \frac{4\sqrt{R}}{3(1-\nu^2)} E_{Hertz} \delta^{\frac{3}{2}} [5]$$

Where ν constituted the Poisson ratio of the sample. Usually, for cell environment ν≈0.5 since it is constituted essentially of water and accordingly is assumed to be incompressible. E_{Hertz} is the sample elastic Young modulus, which summarize together with ν the mechanical features of the sample, assuming a pure linear elastic and isotropic environment. δ represents the vertical indentation of the sample. Usually, in the Hertz model and its modifications, the force F is proportional to a given power n of the indentation, $F \propto \delta^n$. Finally, R is the effective radius of curvature describing the indenter-sample coupling [Eq 6]:

$$\frac{1}{R} = \frac{1}{R_{Indenter}} + \frac{1}{R_{Sample}} [6]$$

In the limit of sample constituted by a flat surface (which corresponds to the indentation problem of an half-space with a rigid axisymmetric indenter and compatible with the Ting's solution) the radius curvature is described by the indenter radius: $R \approx R_{Indenter}$

Starting from Hertz contact-mechanics model developed for spherical-shaped indenter, since in AFM framework a multitude of other tip geometries are available, several modifications of [Eq 5] have been introduced to adopt other tip geometries [107], [108]. Below we will briefly report the most exploited tip geometries in AFM setup:

For conical indenters, the relationship between the applied force provided by the tip and subsequent vertical sample indentation is described in [Eq 7]:

$$F = \frac{2\tan(\theta)}{\pi(1-\nu^2)} E_{Hertz} \delta^2 [7]$$

Where θ is the previously mentioned half-opening angle of the cone. Note how setting ν≈0.5, which is usually adopted for cell sample, [Eq 7] become [Eq 1a].

Similarly, for pyramidal indenter the relation bounding the applied force F and the indentation is [Eq 8]:

$$F = \frac{1.4906\tan(\theta)}{2(1-\nu^2)} E_{Hertz} \delta^2 [8]$$

Where θ is the semi-included angle (axis-to-face) of the pyramidal. These cone-shaped and pyramidal-shaped tip geometries are really similar, and they share the same Force versus indentation relationship: $F \propto \delta^2$. The indentation profiles obtained from these tip geometries provided more local surface nano-mechanical information from the underlying surface sample depending on the opening angle value.

For flat cylindrical indenters [Eq 9] describes the relation between applied force and indentation of a half-space:

$$F = \frac{2R_{cilinder}}{1-\nu^2} E_{Hertz} \delta [9]$$

Where $R_{cilinder}$ represents the cylinder radius. This tip geometry could provide more surface-mediated nano-mechanical sample information.

In contact-mechanics Hertz-based models, [Eq 5,7,8,9] reported above, essentially two mechanical fit parameters resembling the pure elastic behavior of the sample are unknown (ν, E_{Hertz}). Nevertheless, for cell sample it is common choice setting ν≈0.5, considering it as an incompressible material and a time independent mechanical parameter. Thus, in further analysis the Poisson pre-factor $(1-\nu^2)$ is implicitly substituted by the numerical factor: $3/4$ and only the Young modulus remains unknown during fitting

procedure. As we will see next, the Poisson ratio could be in principle reintroduced as free parameter when more complex models (including poro-elasticity behavior) are taken into account.

In previous experimental works on cell nano-mechanics characterization based on AFM setups, Hertzian models have been deeply exploited in the Force-Indentation curve in the approaching region, after contact-point evaluation [108]–[113]. Previous work confirm how Hertzian models fit objectively well the experimental data, both for cells and hydrogels, at least for shallow indentation profiles and low scan piezo speed regime. Nevertheless, as already mentioned above, a clear hysteresis between the approach and retraction curve during the indentation cycle confirms the presence of a viscous component in the cell nano-mechanics. Since the Hertzian models involve only the approaching region and treat the cell surface as a pure elastic material they are unable to completely characterize the viscoelastic cell behavior. Before complete rejection of the Hertz model for the entire cell nano-mechanics characterization, we could at least consider if the extrapolated E_{Hertz} is a valuable "comparison-parameter" between different cell phenotypes, or for cell response upon exogenous drug exposure, providing a guess about cell health, tumor progression, differentiation or other cell features changes. In [90] the authors clearly confirm that elastic modulus E_{Hertz} obtained from approaching curve fitting not only is unable to recapitulate the entire cell viscoelasticity, but furthermore it cannot be exploited as "comparison-parameter" for cell viability, differentiation, tumor progression or other cell parameters. In fact, the measured E_{Hertz} parameter (which is actually a dummy or apparent mechanical parameter) could be arising from different combinations of the viscoelastic coefficients couple, which they will be introduced formally in the next section. Thus, for example in cell samples exposed to exogenous drugs a possible invariance of E_{Hertz} calculated considering only elastic contribution during experiment could instead hide deep cell viscoelasticity changes and subsequent cell condition modifications. In Fig 3 the approaching phase of a Force-Indentation curve is reported, using pyramidal indenter, obtained from a u87MG cell and subsequent Hertz model fitting. The fitting curve follows fairly well the experimental data.

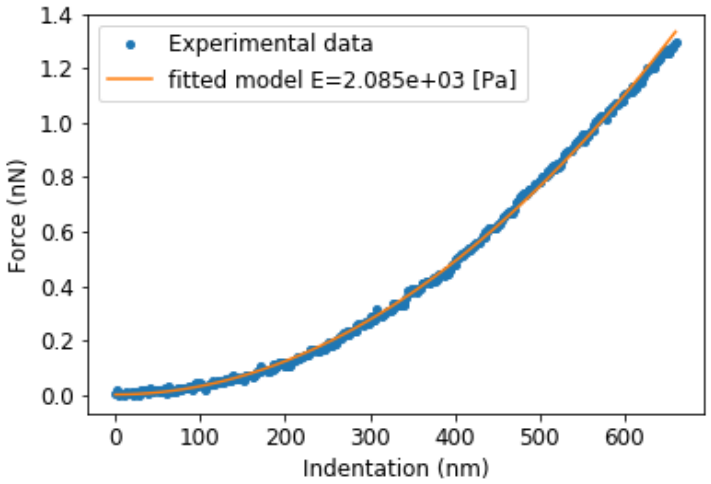

Figure 3: Example of Force-Indentation curve during the approaching phase obtained from U87MG cell sample (blue curve), and subsequent Hertzian model fitting (orange curve).

- **Ting Model**

In the previous section we have illustrated the most used contact-mechanics models derived from Hertz theory, and we have demonstrated how E_{Hertz} coefficient obtained from the fit is just a "dummy" or "apparent" cell mechanical parameter and is not able to clarify actual cell conditions or other main cell features modifications. Thus, in this section we will illustrate the theoretical framework provided by the Ting model exploited on the Force-Indentation (F-I) curves obtained on cells. The exploitation of the Ting model allows obtaining cell viscoelasticity data directly from single force curves. We will briefly summarize the experimental-theoretical steps that gradually moved the F-I analysis from the initial Hertz models toward a complete viscoelastic framework. Then, we will compare advantages and drawback between the Ting model and the other well-known viscoelastic approaches based on the AFM technique in the time and frequency domain.

Starting from previous results obtained by Hertz-based methods, which includes only the approaching part, a first attempt for viscoelasticity characterization could be introduced following Lee and Radok work [114]. The authors proposed an analytical solution for the indentation of a viscoelastic material based on the "elastic-viscoelastic" correspondence principle and the focal parameter becomes the contact-area a(t), which must necessarily increase during time. Thus, this theoretical framework is perfectly suitable in the approaching and holding phases of AFM curves but is no more exploitable in the retraction part. The Lee and Radok analytical method requires the knowledge of the solution for the equivalent elastic scenario problem. In fact, the time-stationary Young modulus behavior E_{Hertz}, is replaced by a relaxation function: E(t). Thus, the initial Young modulus: E_{Hertz} obtained from Hertzian models provides a starting guess for this relaxation function, which replace H_{Hertz}. The solution is based on the hereditary integral operator and in [Eq 10] the analytical resolution for a pyramidal-shaped tip, recalling [Eq 8] is proposed:

$$F\big(t,\delta(t)\big) = \frac{1.4906\tan(\theta)}{2(1-\nu^2)}\int_0^t E(t-\xi)\frac{\partial\delta^2}{\partial\xi}d\xi \; [10]$$

The applied force F is a time-dependent function and is evaluated solving the integral. The time extrema span from t=0 (representing the starting point of the indentation process and a(t=0)=0) to $t=t_m$ (where t_m represents the concluding frame of the approaching process). The variable ξ represents the fictitious time variable, required to solve the integral. The factor inside the integral is constituted by two different terms: $E(t-\xi)$ and $\frac{\partial\delta^2}{\partial\xi}$. The former factor represents the constitutive equation (relaxation function) for the time-dependent Young modulus, which is evaluated at the time-frame: $(t-\xi)$. Thus, the applied force F evaluated at the time-frame "t" is provided summing up the overall Young modulus contributions arising from the relaxation function $E(t-\xi)$ taking into account a shift (delay) time given by $(t-\xi)$ and due to the material response propagation, as expected for linear response theory. The latter factor: $\frac{\partial\delta^2}{\partial\xi}$ is the time derivative of the indentation function power 2, evaluated at the corresponding instantaneous fictitious time: ξ. Note that this time-derivative is applied to the power-law-indentation term expected for the Hertz model with a spherical-shaped indenter. The Lee and Radok solution can be easily adapted for the different indenter geometries. Accordingly, the pre-factor in front of the integral and the indentation-factor ratio inside it must be corrected. The constitutive relaxation function is an arbitrary time-dependent relation that contains several mechanical parameters resembling the viscoelastic behavior of the sample. Thus, the constitutive equation is chosen on the base of a realistic viscoelasticity model that well-describes the treated sample. We will see later several constitutive relaxation models motivating their viscoelastic fitting parameters. The Lee and Radok solution can be applied also in experimental processes where the shear modulus is exploited, using the well-known relation [Eq 11]:

$$G = \frac{E}{2(1+\nu)}\,[11]$$

Consequently, the pre-factor term in [Eq 10] must be rewritten if the shear relaxation modulus is used.

Although the Lee and Radok viscoelastic method introduces the relaxation modulus functions, it exploited only the approach region of the AFM force-indentation curves. Thus, viscoelasticity information arising from retraction region remains unknown, furthermore, it has been demonstrated [90] how Lee and Radok analytical solution is incomplete and could provide erroneous viscoelastic results.

The limitations of the Lee and Radok analytical solution arise essentially from the contact-area a(t) time progression, which must increase during indentation cycle, and makes the method incomplete. To exploit also the retraction region a more general viscoelastic theoretical framework, which is independent from a specific load history, must be developed. Nevertheless, many qualitative and phenomenological attempts have been proposed to measure the viscoelasticity from standard indentation cycle. Several works studied the hysteresis area between approaching and retraction phases [86], [112], [115]–[117], other investigated the relationship between the indentation-rate and the "apparent" Young modulus (still obtained from Hertzian models) [113], [115], [118]. Nonetheless, these empirical approaches results provide a non-complete viscoelastic description since they are not based on a rigorous theoretical framework.

In 1966 T.C.T.Ting [92] developed a new theoretical framework, which solved the indentation problem for a linear viscoelastic half-space material under a rigid axisymmetric indenter force application for an arbitrary load history. Thus, for this theoretical scenario the entire indentation cycle, involving approaching and retraction part can be exploited. Previous works already implemented and adapted the Ting model in the AFM force-indentation curves acquired from cell samples and soft hydrogels. In [90] the authors validated the method comparing the fitting results extrapolated from experimental data with theoretical prediction obtained from Finite-Element simulations (FE). In [91] the viscoelasticity parameters using Ting model extrapolated from experimental data were compared with usual AFM viscoelastic characterization in the frequency-domain. In the former work a spherical-shaped indenter geometry was used for the protocol implementation. In the latter paper a conical-shaped tip was adopted. More recently also [119] adopted the Ting model. Here, we will develop a similar protocol for pyramidal-shaped geometry indenter.

The analytical solution of the Ting theoretical framework for a pyramidal indenter during the entire indentation cycle is represented in [Eq 12a-c]:

$$\begin{cases} F\big(t,\delta(t)\big) = \dfrac{1.4906\tan(\theta)}{2(1-\nu^2)}\displaystyle\int_0^t E(t-\xi)\frac{\partial\delta^2}{\partial\xi}d\xi \ for\colon 0 \le t \le t_m [12a] \\ F\big(t,\delta(t)\big) = \dfrac{1.4906\tan(\theta)}{2(1-\nu^2)}\displaystyle\int_0^{t_1(t)} E(t-\xi)\frac{\partial\delta^2}{\partial\xi}d\xi \ for\colon t_m < t \le t_{ind} [12b] \\ with\colon \displaystyle\int_{t_1(t)}^{t} E(t-\xi)\frac{\partial\delta}{\partial\xi}d\xi = 0 \ for\colon t_m < t \le t_{ind} [12c] \end{cases}$$

where the time variable t runs along the overall indentation process, t=0 corresponds to the initial indentation state, $t=t_m$ constitutes the approaching conclusion (similarly to Lee and Radok method [Eq 10]), and $t=t_{ind}$ represents the complete indentation cycle end. δ is the indentation depth, E(t) is the constitutive relaxation function chosen for the Young modulus, and ξ is the fictitious time variable required for integral solution. The Ting model adaptation for AFM force-indentation curves is a clear extension of the previous solution provided by Lee and Radok. In fact, [Eq 12a] exploitable for the approaching phase is perfectly equivalent to [Eq 10]. $t_1=t_1(t)$ is an auxiliary time function required to fix the upper limit in the integral of [Eq 12b] for the force evaluation during the retraction phase. During indenter retraction ($t_m<t<t_{ind}$), the auxiliary time function t_1 ($0<t_1<t_m$) is evaluated using [Eq 12c], this nulling requirement of the integral represents the mathematical condition to superimpose $a(t)=a(t_1)$, meaning that the contact area in the actual frame t in the

retraction phase must be recovered during the approaching phase, in particular the time t_1 when this condition is satisfied. The auxiliary time function $t_1=t_1(t)$ has a deep physical implication, as the contact area $a(t_1(t))$ can be evaluated, and also the effective indentation $\delta_1(t_1(t))$ during the retraction process can be evaluated. The effective indentation can be though as the indentation measured relative to the relaxation of the surface after deformation produced by the indenter. As asserted above, the hysteresis between approaching and retraction in Force-Indentation curve (See Figure 4) appears since the deflection (or force) signal in the retraction is systematically lower than the approach signal. Thus, at a certain point in the retraction curve the force becomes null before the "absolute" indentation (measured from initial undeformed surface) has reached its initial starting point. If the force is null then the contact area is null, and subsequently also the effective indentation is null meaning that the relaxation process rate is slower than the cantilever-base retraction speed. Equivalently, when the indenter is still retracting from the sample, the

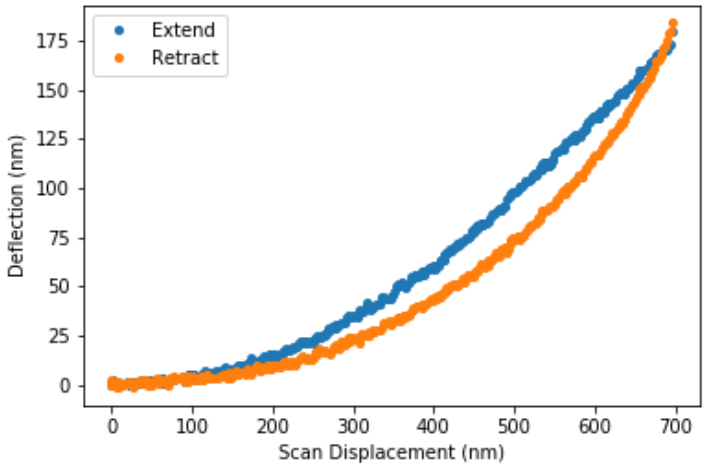

Figure 4: Example of Deflection-Scan Displacement curve obtained from U87MG cell sample (the substrate removal contribution has not been applied yet). A clear hysteresis appears between the approaching (blue curve) and retraction (orange curve) phase.

previous indentations states have not yet completely recovered because the relaxation surface process is too slow and the tip is physically detached from the underlying substrate and no net deflection is measured.

Cell sample mechanical-viscoelastic characterization has been developed exploiting several techniques other than AFM-based like for example micropipette-aspiration [120], [121], compression and stretching stimuli using a couple of microplates [122]–[124], optical-tweezers [115], [125] and magnetic twisting cytometry [126], [127]. For AFM-based nano-mechanics viscoelastic investigation the methods can be divided in two main groups: techniques exploiting the time domain [88], [128], [129], and techniques exploiting the frequency domain [105], [130]–[134].

In the time-domain experiments, usually creep and stress relaxation are the most exploited methods [88], [135], [136]. Typically, the experimental protocol for these setups forecasts a fast loading step- (which should be theoretically instantaneous) followed by a long hold phase. Nevertheless, in the loading phase even the maximum loading speed available from the device, which mimics the step, is not exploitable. In fact, the hydrodynamic and inertial effects deeply affect the deflection profile during the loading phase. Thus, the actual curve is a ramp-hold profile and the ramp-correction, or a global ramp-holding fitting should be implemented [137]–[139]. Furthermore, for long-time relaxation several issues in the interpretation could arise from thermal drift of the piezo and from active cell response [140], [141].

AFM experiments can be performed also in the frequency-domain. In this framework the cantilever base oscillates sinusoidally with a fixed amplitude and a pack of waves containing several harmonics is transferred

to the piezo at a specific point of the indentation curve [130], [131], [134], [142]–[144]. From the cantilever oscillation signal the amplitude and phase shift are acquired to evaluate the frequency-dependent complex Young modulus or shear modulus. Nevertheless, these experimental setups require additional modification from standard biologically oriented AFM-device, and also a higher expertise skills from the operators.

Since now, we have summarized the main advantages and drawbacks of usual AFM viscoelasticity characterization in the time and frequency domain. The Ting-based analytical solution allow us to directly obtain viscoelastic features of the sample starting just from standard approaching-retraction curves, and no additional modifications of the protocol or the device are required. The curves analysis obtained from Ting model adaptation owned a complete viscoelasticity overview, since it has a firm theoretical foundation over the entire indentation cycle. The Ting-based method can be applied on arbitrary indentation loading history curve, once its associated analytical solution has been theoretically evaluated. Thus, also ramp-holding profiles can for example be analyzed. Since all the data points of the curve are numerically treated in the Ting solution, (and no lag-times are required), also fast loading rate profiles can in principle be exploited, once the sampling rate has been previously adjusted. Thus, also a ramp-loading force profile can be analyzed using the Ting-based method. Once the loading history is experimentally accessible the Ting model can be exploited, also in experimental setups other than AFM. Bottom-Effect correction can be introduced in the analytical solution [Eq 12a-c] inside the integrals. In fact, basing on Finite-Element simulation, it has been demonstrated that this effect is unaffected by the loading history [145]. Thus, the Bottom-Effect correction can be defined just starting from: the geometrical indenter features, the sample thickness, and the indentation depth, while it is independent from the chosen relaxation modulus. Finally, several constitutive relaxation functions can be tested in the Ting analytical solution integrals to find out which one of these better recapitulates the viscoelasticity features of the sample.

On the other hand, several drawbacks regarding the Ting model adaptation should be highlighted. Obviously, since the method is employed on standard AFM indentation curves, it shares the usual uncertainties regarding AFM experiments, like cantilever spring constant and sensitivity calibration. Requirements arising from the Ting protocol guidelines are; the absence of strong adhesion forces during the retraction phase (which are not accounted in the analysis), and possible drift and active cell response especially for low piezo speeds. Finally, a high computational cost is required. In fact, each theoretical force coordinate is evaluated solving numerically the integral [Eq 12a] and a couple of integrals are numerically solved [Eq 12b-c] for each point of the retraction phase.

Recalling again the set of [Eq 12a-c] the Poisson ratio v is considered as constant and time-independent coefficient. In fact, it is kept aside from the solving integrals. As said above, we set v=0.5 since the cell sample are composed mainly by water. In a more realistic analysis, also the Poisson ratio can be treated as free and time-dependent parameter, introducing a poro-elastic component.

• Relaxation modulus (Constitutive equation)

In Lee-Radok [Eq 10] and Ting [Eq 12a-c] analytical solution definition for a linear viscoelastic material deformed by an axisymmetric indenter (with pyramidal-shaped tip), the viscoelastic constitutive relaxation function of Young modulus $E(t)$ has been introduced. A time-dependent relaxation modulus essentially describes how the Young modulus of the viscoelastic material dynamically evolves after external indentation stimuli. The relaxation modulus resembles the overall viscoelastic features of the sample and matches the arbitrary constitutive equations of the linear viscoelastic material. Thus, the relaxation modulus function and the constitutive equation essentially coincide and can be exchanged reciprocally. Usually, the relaxation modulus is a decaying function governed by several viscoelastic parameters resembling the material properties with a physical meaning. The relaxation modulus, or alternatively the constitutive equation, is

derived starting from a rheological modeling. There are many rheological models, and each one contains its set of viscoelastic fitting parameters. Essentially, the rheological modelling of a given viscoelastic material is built starting from two elementary components: a spring (elastic element) and a dashpot (damper element). A rheological model can contain an arbitrary number of springs and dashpots connected each other in series or in parallel, and subsequently the related constitutive equation can be defined with its viscoelasticity fitting parameters. However, among the multitude of different rheological models, just a few of them have been deeply exploited in viscoelasticity characterization: the Standard-Linear-Solid (SLS) and the Power-Law-Rheology (PRL). The SLS model usually describes well soft hydrogels, as demonstrated in [90]. In this model, the viscoelastic material is considered as a spring connected in parallel to a spring-dashpot series (see Fig 5a). In [Eq 13a] the associated relaxation modulus function is reported. The constitutive equation of SLS model is composed by three different viscoelastic fitting parameters: E_0, E_∞, and τ, which represent respectively, the instantaneous, the asymptotic Young modulus, and the relaxation time (time constant). Thus, the SLS proposes an instantaneous elastic response governed by E_0, which evolves following a unique viscoelastic process described by an exponential decay, reaching a long-time relaxation value E_∞. The PLR model usually describes fairly well cell sample, independently of the specific cell line [90]. It is composed by an infinite coupling of spring-dashpot series, and each spring-dashpot series element is connected in parallel with the others (see Fig 5b). In [Eq 13b] the most general relaxation modulus for the PLR model is reported. The constitutive equation of the PLR contains three different viscoelastic parameters, like the SLS: E_0, E_∞, and α. E_0 and E_∞ represent the same definition introduced in the SLS. Since the PLR mode is described by an infinite sum of different relaxation processes τ_i, the superposition of this relaxations provides a power law decay highlighted by the α parameter, which is the power law coefficient. t' represents just a small time offset value needed to normalize the ratio t/t' and actually does not constitute a fitting parameter. Commonly, the t' time offset is set equal to the sampling acquisition time.

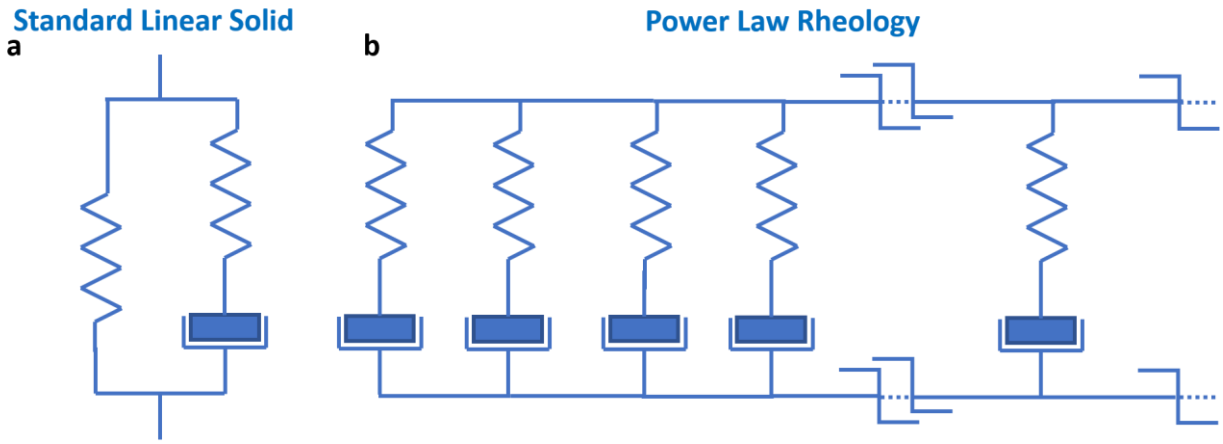

Figure 5: Spring&Dashpot modeling of the Standard-Linear-Solid (a) and the Power-Law-Rheology (b) viscoelasticity model.

$$E(t) = \begin{cases} E_\infty + (E_0 - E_\infty)e^{-\frac{t}{\tau}} \;\; SLS\;[13a] \\ E_\infty + \dfrac{E_0 - E_\infty}{\left(1 + \dfrac{t}{t'}\right)^\alpha} \;\; PLR\;[13b] \end{cases}$$

The SLS model describes a viscoelastic material that is ascribable to a specific single relaxation process, and the relaxation rate can be evaluated from the τ/t_{ind} ratio, where t_{ind} is observation time phenomena that coincides with the entire duration of the approach-retraction cycle. (Deborah's number). An higher τ/t_{ind} ratio means a slower relaxation process. The PLR represents a superposition of an infinite number of different relaxation processes, and the overall sum is described by α, the power law parameter. The α parameter spans between [0÷1], where α=0 describes a pure elastic-solid material, meaning that the dashpot elements are

negligible, and α=1 represents a pure fluid-like material. Thus, α quantify the relaxation amount, higher α values mean larger relaxation behavior, up to the limit α=1 where $E(t) \propto E_0 \frac{1}{1+t/t'}$.

The PLR model foundations are strictly related to the Soft-Glassy-Rheology theory (SGR) [146]. The SGR theory is based on the assumption that the material is composed by several internal structures, and the disorder and metastability arising from their superposition produces its observable behavior at the different observation ranges. The internal constitutive elements are bound together by weak attractive interactions, thus their resulting energy profile is assimilable to a well. The scale-free, or power-law, rheology is defined superimposing a large distribution (theoretically infinite) of well energy profiles and related element lifetimes. The ensemble of these energy well-traps, where the elements are temporary confined, defines the "effective-temperature" of the material, which reflects the thermal agitations of the constitutive elements and defines the jump-probability of the elements to jumps between different wells. The power law exponent α parameter represents this "effective-temperature", where higher α values means more fluid-like behavior. In fact, the jumps of the elements between energy wells is the theoretical basis for the fluid-like processes. Thus, α=0 represent a soft glassy material, which behaves as a pure elastic solid, while α=1 represents a pure viscous liquid, and 0<α<1 α values are related to partial elastic/viscous samples with a behavior from an elastic-solid to -a viscous fluid. The cytoskeleton micro-environment can be described by a PLR model [147], where the internal elements undergoes to disordering-reordering changes, and subsequently the reorganization of these elements is represented by the α parameter. Furthermore, changes in the effective-temperature parameter could be due to cell-processes like migration, differentiation, invasion and metastasis, thus providing a theoretical framework for these fundamental cell events. Previous rheological characterization oof living cell adopting PLR identified their rheology behavior as a soft glassy material close to glass transition $\alpha \sim [0.0 \div 0.2]$ [90], [147].

Before going on, we should mention that many PLR constitutive equations variations have been developed, depending on the particular time frame we want to highlight. The simplest form for the PLR is reported in [Eq 14], where E_1 refers to the modulus relaxation for t=1s and the time variable t is normalized with respect to 1s value [148].

$$E(t) = E_1 t^{-\alpha} [14]$$

Instead, [Eq 13b] [149], [150] have a more general structure where E_0 and E_∞ have the same meaning of the SLS model. Moreover, the unity addition removes the singularity for t = 0s. However, for cell experiments, especially in rheology framework, E_∞ is set to zero. Thus [Eq 13b] can be simplified using only two fitting viscoelastic parameters, obtaining [Eq 13b new]:

$$E(t) = E_0 \left(1 + \frac{t}{t'}\right)^{-\alpha} [13b\ new]$$

In [90], the authors tried to maintain the long-term relaxation modulus E_∞ as a free parameter and obtained values close to zero, if compared to E_0. Thus, simplifying [Eq 13b] removing the long-term, and taking into account that t' is set equal to the sampling time and subsequently $t' << t_{ind}$, [Eq 13b new] and [Eq 14] look really similar. In particular, [Eq 13b new] becomes $E(t)=E_1 t^{-\alpha}$ with $E_1 \approx E_0 t'^{\alpha}$.

Till now, we have proposed two possible relaxations modulus for an arbitrary linear viscoelastic constitutive equation, which will describe the viscoelasticity of the material. The former case, the SLS, is an extreme case where a specific single relaxation process describes the overall viscoelastic material behavior. The latter case, the PLR, on the opposite side considers an infinite superposition of different relaxation processes. However, plotting the relaxation modulus normalized to the instantaneous value E_0 (thus $E(t)/E_0$ ratio is plotted) as a function of time for the SLS and the PLR models and comparing them, they will show a really similar time-decay behavior (Fig 6a). This first comparison obtained from a linear time scale, which explore just a decade range, clearly shows how difficult is to test the proposed relaxation moduli on short time scale. Thus, to

evaluate that relaxation function better represents our viscoelastic sample, several experimental data-set of t_{ind} spanning over many time scale decades should be acquired and analyzed. To better justify this

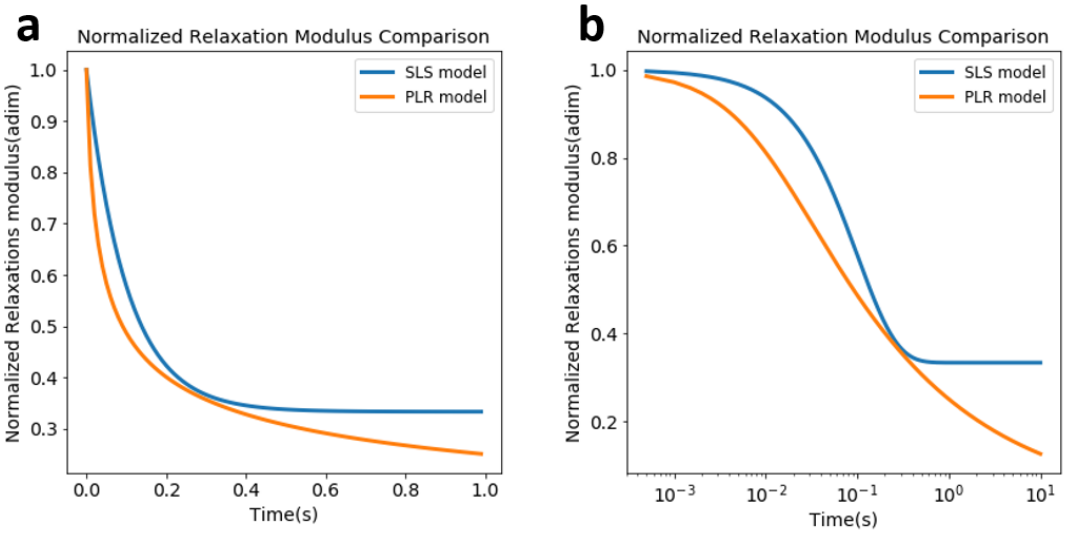

Figure 6: Normalized relaxation modulus comparison between SLS (blue curve) and PLR (orange curve) viscoelastic model; on linear-linear scale (a) and on logarithmic-linear scale (b). Two clear plateau are observable in the SLS model in Fig 6b, which PRL model does not own.

experimental choice, in Fig 6b the same normalized relaxation modulus of SLS and PLR models on a log-linear scales is reported, where several order of magnitudes in the time domain are explored. It clearly appears from Fig 6b, that the SLS presents two plateaus at the short and long-time scale regimes, respectively. Instead, the PLR is characterized by a more monotonic decay, since it is constituted by a continuous relaxation spectrum.

• Indentation and its derivatives Evaluation

In the first section we described the overall preliminary steps regarding the raw Deflection-Scan Displacement to Force-Indentation curves conversion (Calibration Sensitivity, Deflection relative to the substrate evaluation (Scan displacement to Indentation conversion) and Contact-Point (C-P) evaluation). Then we showed the limitations arising from pure Hertzian models adaptations, and then we introduced the Ting model for pyramidal-shaped indenter [Eq 12 a-c] and the relaxation modulus concepts [Eq 13a-b,13 b new].

In this subsection we will summarize the pre-processing and the sequential steps required for numerical implementation of the Ting model [Eq 12 a-c]. In the next subsection we will provide an exhaustive and step-by-step description of the numerical implementation. First, recalling the analytical solution proposed by Ting we can observe that the constitutive elements inside the integrals are essentially two. The relaxation modulus equation: $E(t-\xi)$ that is chosen arbitrary before numerical solution, to test its robustness, and $\frac{\partial \delta}{\partial \xi}$ or $\frac{\partial \delta^2}{\partial \xi}$ that are the rates of the indentation and of the squared indentation, respectively. Note also that all these terms are time-dependent function, the former $E(t-\xi)$ is a constitutive theoretical equation depending on the trial viscoelastic parameter ($[E_0,E_\infty,\tau]$ for the SLS, and $[E_0,\alpha]$ for the PLR) and can be easily evaluated by an appropriate sub-function in the algorithm; the latter $\left(\frac{\partial \delta}{\partial \xi} \text{ or } \frac{\partial \delta^2}{\partial \xi}\right)$ are experimental quantities that must be numerically evaluated starting from the indentation data $\delta(t)$. The rates $\left(\frac{\partial \delta}{\partial \xi} \text{ or } \frac{\partial \delta^2}{\partial \xi}\right)$ are

essentially data arrays and each element of the array is associated at a given time frame t_i where t_i moves between [0÷t_{ind}]. Thus, these experimental data arrays remain unchanged during integral numerical solution [Eq 12 a-c] and must be evaluated only once and this step constitutes the "zero-step" of the Ting model implementation.

Here we will focus on the numerical differentiation of δ and δ^2. First, we want to emphasize how not only the time-dependent force signal experimental data $F(t)$ is non-linear, but also the deflection signal $\delta(t)$ varying non-linearly during time. In fact, only the Scan Displacement, the vertical piezo movement or the cantilever base displacement, is performed at constant speed. Instead, the indentation speed is slower than

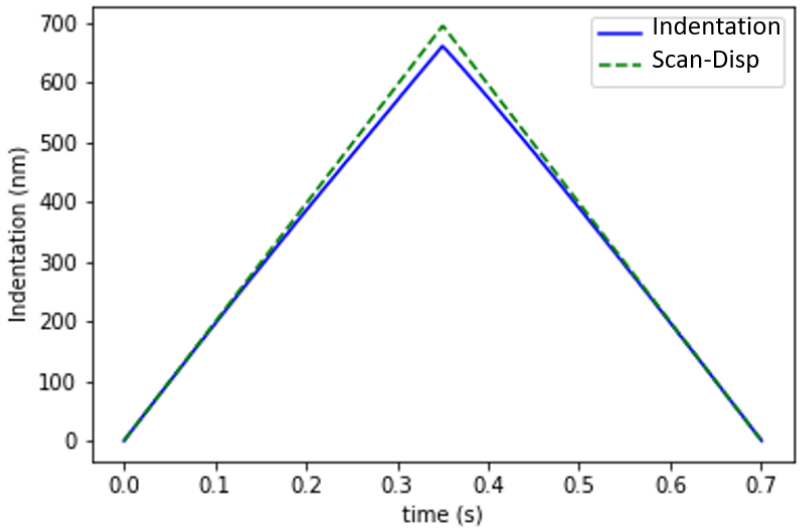

Figure 7: Indentation (blue curve) and Scan-Displacement (green dotted line) profile comparison as function of time. Experimental data obtained from U87MG cell sample

the Scan-Displacement speed. This is particularly true during the contact region, where the deflection signal is increasing significantly. The indentation-vs-Scan-Displacement speed discrepancy is clearly observable when the piezo direction is inverted, at the highest deflection signal regime and $t \approx t_m$ (see Fig 7).

Thus, the experimental indentation data $\delta(t)$ is almost superimposable to the theoretical Scan-Displacement signal at the beginning or close to the ending of the indentation cycle ($t \approx 0$ or $t \approx t_{ind}$), while is significatively lower close to piezo direction inversion $t \approx t_m$. Instead, the Scan-Displacement signal is described by a pure time-dependent linear behavior for the overall indentation time t_{ind}, as highlighted in Fig 7.

The numerical evaluations of the rates $\left(\frac{\partial\delta}{\partial\xi} \text{ and } \frac{\partial\delta^2}{\partial\xi}\right)$ are performed as follows. First numerical calculation of $\delta^2(t)$ vector elements is obtained from $\delta(t)$ data, then mean slopes with respect to time of the $\delta(t)$ and $\delta^2(t)$ data points are computed adopting a moving average filter of 5 points size, in order to reduce experimental noise contribution and minimize random spikes in the time-derivatives. In Fig 8 the experimental rates example plots are reported, $\frac{\partial\delta}{\partial\xi}$ in Fig 8a and $\frac{\partial\delta^2}{\partial\xi}$ in Fig 8b:

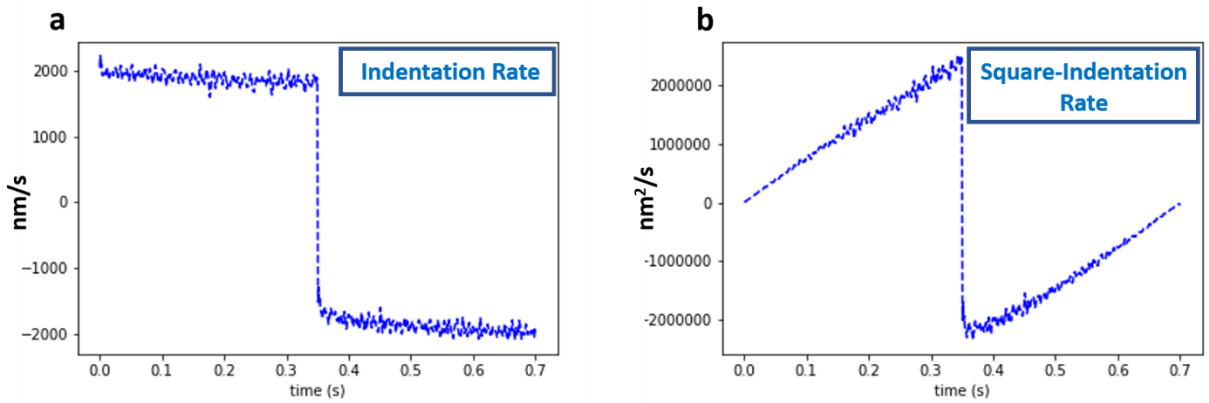

Figure 8: Indentation (a) and square indentation (b) rates obtained from experimental data of U87MG cell sample force curve. Some deviation from the theoretical Scan-Displacement speed magnitude (2000 nm/s) are observable close to t_m.

As expected, the experimental rates $\left(\frac{\partial\delta}{\partial\xi} \text{ and } \frac{\partial\delta^2}{\partial\xi}\right)$ are, in modulus, lower than the Scan-Displacement speed and the Scan-Displacement squared speed, respectively.

Now that the required experimental vectors: $\frac{\partial\delta}{\partial\xi}$ and $\frac{\partial\delta^2}{\partial\xi}$ have been evaluated in the "step-zero", we can start the numerical evaluation of the solution of integrals [Eq 12a-c]. The viscoelastic parameters ([E_0,E_∞,τ] for the SLS, and [E_0,α] for the PLR) referred to the associated relaxation modulus are extrapolated from the algorithm minimizing the following quantity *e* [Eq 15]:

$$e = \sum_{t_i=t_1}^{t_{ind}} \left(F_{t_i}^{Experim} - F_{t_i}^{Ting}([E_\infty, E_0, \tau]_{SLS}; [E_0, \alpha]_{PLR})\right)^2 \quad [15]$$

Where *e* is the sum of the squared errors (norm of residuals) between the experimental data and the Ting model. The $F_{t_i}^{Experim}$ represents the experimental force for a given time frame t_i, while $F_{t_i}^{Ting}$ is the theoretical force value reconstructed from the model for the same time frame. The main advantage of the Ting-based model is that the overall data-set: $\left(F_{t_i}^{Experim}; \delta_{t_i}^{Experim}\right)$ of the indentation cycle is exploited in the analytical solution for pyramidal-indenter. Thus, if few experimental data points $\left(F_{t_i}^{Experim}; \delta_{t_i}^{Experim}\right)$ are affected by noises, their contribution is minimum in the [Eq 15] sum, where all indentation cycle points square errors are evaluated. The algorithm starts setting an initial guess value for the viscoelastic parameters of the relaxation modulus chosen. Then, the theoretical Ting function is reconstructed and the norm of residuals *e* is evaluated. The algorithm repeats recursively the previous steps adjusting the viscoelastic parameters since the norm of residuals is minimized. The algorithm has been developed in Python language adopting a least-square fitting procedure based on Levenberg-Marquardt algorithm the viscoelastic parameters of the constitutive equation are extrapolated.

- **Constitutive equation models and step-by-step algorithm implementation**

In the previous subsection we discussed about the integrating function components of the solving formula of the Ting model [Eq 12a-c]. In particular, we focused on the indentation and square indentation rates $\left(\frac{\partial\delta}{\partial\xi} \text{ and } \frac{\partial\delta^2}{\partial\xi}\right)$ and their numerical evaluations. Then, we introduced our algorithm for Ting adaptation model protocol, suitable on our Force-Indentation experimental curves. The quality parameter of the algorithm e [Eq 15], which establishes when the iterative viscoelastic parameters research can be considered satisfied, has been defined.

Now we will focus on the second fundamental component of the integrating function [Eq 12a-c], the constitutive equation of the viscoelastic model $E(t)$ (the relaxation modulus). The $E(t)$ relaxation modulus represents the theoretical viscoelastic time evolution of our sample, and it is governed by its parameters. The numerical implementation of the relaxation modulus is straightforward since is easily evaluated once the time frame t_i and the viscoelastic parameters are known [Eq 13a,13 b new]. Thus, a dedicated sub-function in the algorithm is written for each proposed relaxation modulus, in our case we provide two different sub-function for the SLS and the PLR models, respectively. While the indentation and squared indentation rate arrays are evaluated only once as pre-processing step, the relaxation modulus must be computed recursively for each time frame t_i inside the solving integrals every time a new viscoelastic set parameter is proposed.

Now we describe the step-by-step procedure algorithm of our numerical implementation of the Ting model adaptation. Initially, the approaching Force-Indentation curve is fitted using the Hertzian model for pyramidal-shaped indenter [Eq 8]. The apparent Young modulus E_{Hertz} is stored and will be used as initial guess value for the viscoelastic constitutive equation parameter E_0, in particular, for both SLS and PLR models we set $E_0=2E_{Hertz}$. As mentioned above, the apparent Young modulus E_{Hertz} does not resemble the overall viscoelastic behavior of the sample, in fact application of the Hertzian model in the retraction phase will provide a higher E_{Hertz} value if compared with the previous one obtained fitting the approaching curve. Thus, we will expect a viscoelastic parameter $E_0>E_{Hertz}$ and declaring $E_0=2E_{Hertz}$ is a reasonable initial guess assignment. In the SLS model option we additionally set, $E_\infty=E_0$ as long-term modulus, and $\tau=1s$ as time decay, as initial guess declaration. In the PLR model we additionally define $\alpha=0.1$ as power law exponent initial guess. In fact, previous rheological studies on cell samples modelled successfully cellular environment as a soft glassy material with α close to glass transition $\sim[0.0 \div 0.2]$.

Now, after initial viscoelastic parameters assignment for the constitutive equation, the iterative procedure can finally start. The iterative viscoelastic set parameters research will be concluded once the e [Eq 15] minimization is satisfied.

First, the Ting solution for the approaching phase [Eq 12a] is numerically solved for every data point $\left(F_{t_i}^{Experim}; \delta_{t_i}^{Experim}\right)$, and the theoretical reconstructed points $F_{t_i}^{Ting}$ of the approach region are evaluated. Then, before computing the analytical solution for the retraction phase [Eq 12b], the auxiliary time function $t_1=t_1(t)$ must be numerically evaluated for each time frame t_i belonging to the retraction phase. Thus, for each data point of the retraction curve $t_m<t_i<t_{ind}$ the nullification condition of [Eq 12c] must be satisfied. The integral [Eq 12c] is thus discretized and treated as sum of elements composed by two factors: the relaxation modulus $E(t-\xi)$ (where the dependency from viscoelastic parameters has been omitted) and the indentation rate $\frac{\partial\delta}{\partial\xi}$ (and obviously the sampling time interval: $d\xi$). The analytical condition of [Eq 12c] can be rewritten and computed by the algorithm as follows [Eq 16]:

$$\sum_{t_n=t_1(t_i)}^{t_i} E(t_i - t_n) \cdot \frac{\partial \delta}{\partial \xi}(t_n) \cdot (t_n - t_{n-1}) \approx 0 \; [16]$$

[Eq 16] provides the numerical adaptation of [Eq 12c] condition, and extrapolates the auxiliary time function value $t_1(t_i)$ for a given time frame t_i belonging to the retraction phase: $t_m<t_i<t_{ind}$, while $t_1(t_i)$ that satisfied [Eq 16] belongs to the approaching phase: $0<t_1(t_i)<t_m$. More precisely, $t_1(t_i)$ is constituted by an array of $N_{ind}/2$ elements, where N_{ind} is the overall number of experimental data points of the indentation cycle, and it is not to be confused with $t_1 = 0$, which is the initial time frame of the experimental data-set. $E(t_i - t_n)$ and $\frac{\partial \delta}{\partial \xi}(t_n)$ are, respectively, the relaxation modulus and the indentation rate evaluated at the current time frame t_n, $(t_n - t_{n-1})$ is the time interval between the current time frame t_n, and the previous one t_{n-1}. Since the experimental sampling rate is constant, we expect $(t_n - t_{n-1})$ to be constant. An additional discussion should be made regarding the constitutive factor signs of [Eq 16] sum, which help the nullification condition search. The relaxation modulus is a decaying positive function: $E(t_i - t_n) > 0, \forall t_n$ as the time interval is also positive: $(t_n - t_{n-1}) > 0$, instead the indentation rate has two different sign assignment:

$$\frac{\partial \delta}{\partial \xi}(t_n) = \begin{cases} positive, & 0 < t_n < t_m \\ negative, & t_m < t_n < t_i < t_{ind} \end{cases}$$

In fact, during approaching phase: $0 < t_n < t_m$ the indentation increases during time, while during the retraction phase: $t_m < t_n < t_i < t_{ind}$, the indentation is decreasing over time. Thus, all contributions in [Eq 16] sum arising from retraction phase are strictly negative, while the contributions obtained from approaching phase are strictly positive. We decided to start the summation process from the upper limit $t_n = t_i$ and moving the lower limit, scanning the t_n toward the initial time frame. Thus, we gradually added previous time frames since nullification condition is satisfied. Once the auxiliary time function $t_1 = t_1(t_i)$ array has been numerically evaluated for each time frame t_i belonging to the retraction phase, we can proceed with the next step. In Fig 9a an example of the auxiliary t_1 time function research for a given t_i, where the trial frame time $t_{1\text{-trial}}$ is moved toward the starting frame is reported. In Fig 9b the numerical values (theoretically nulls) of the [Eq 16] integral as function of t_i ($t_m<t_i<t_{ind}$) is reported, in Fig 9c the subsequent $t_1(t_i)$ values that minimize the integral is shown. As shown in the plots, for the higher retraction time frames the nullification condition [Eq 16] is not satisfied, thus the auxiliary time function is set to $t_1(t_i)=0$, the starting time frame. For the higher times in the retraction phase $t_1(t_i)=0$ condition is the best numerical solution for

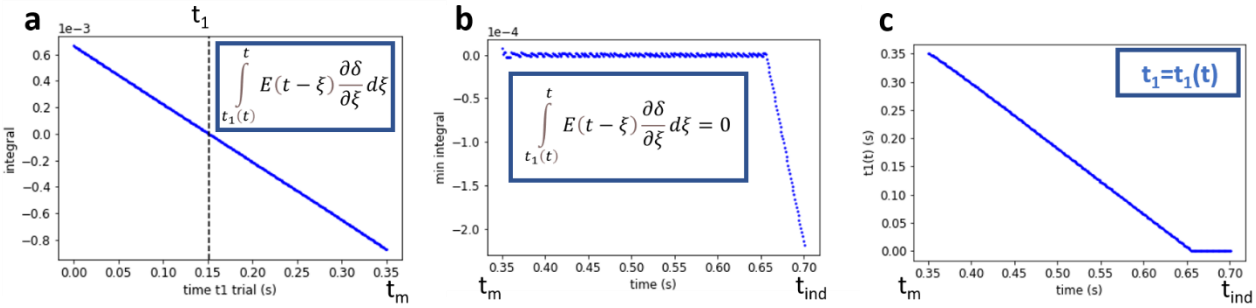

Figure 9: Auxiliary time function t_1 panel: (a) Graphical representation of the [Eq 12c 16] integral for a fixed t_i ($t_m< t_i< t_{ind}$) as function the $t_{1\text{-trial}}$ point, t1 choice is highlighted (vertical black dotted line). (b) Plot of [Eq 12c 16] integral nullification condition check. (c) Auxiliary time function $t_1=t_1(t)$ obtained from [Eq 12c 16] condition.

[Eq 16] minimization, in fact, $t_1(t_i)=0$ brings [Eq 16] closer to zero, as much as possible. This statement is in total agreement with the Ting theory, and it can be proved simply recalling the t_1 role, which is defined as $a(t_1(t_i))=a(t_i)$ where a is the contact-area. In the final frames of the retraction phase the contact area is zero, this condition during the approaching phase holds only for $t_1(t_i)=0$, as confirmed by Fig 9b-c.

Now, we are able to numerically compute [Eq 12b], which analytically resolves the indentation problem in the retraction phase adopting the Ting model. The [Eq 12a] for the approaching region and the [Eq 12b] for the retraction region are formally the same, except for the upper limit of the integral. Thus, this couple of equations can be treated recalling the same sub-function inside the algorithm. This sub-function discretizes the integrals [Eq 12 a-b] similarly to [Eq 12c] discretization, obviously the indentation rate is replaced by the squared indentation rate [Eq 17]:

$$F_{t_i}^{Ting}\left(t_i, \delta(t_i)\right) = \sum_{t_n=t_1}^{t_{lim}} E(t_i - t_n) \cdot \frac{\partial \delta^2}{\partial \xi}(t_n) \cdot (t_n - t_{n-1}) \begin{cases} t_{lim} = t_i, & 0 < t_i < t_m \\ t_{lim} = t_1(t_i), & t_m < t_i < t_{ind} \end{cases} [17]$$

Once the theoretical Ting function: $F_{t_i}^{Ting}$ has been reconstructed from the experimental data: $\left(t_i, \delta(t_i)\right)$ for a given viscoelastic parameters trial set (again the dependency of the viscoelastic parameters has been omitted in the relaxation modulus: $E(t_i - t_n)$), we can compute the norm of residual: e [Eq 15].

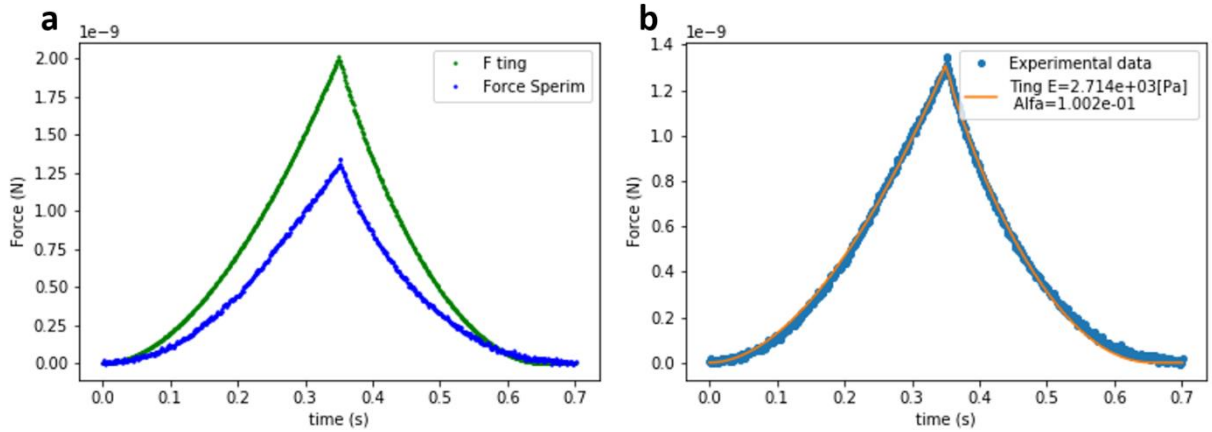

Figure 10: Example of viscoelastic parameters [E_0,α] extrapolation solving the Ting model through the iterative algorithm. The PLR model has been adopted as relaxation modulus. The experimental force-indentation curve has been obtained from a U87MG cell.

This step-by-step proposed algorithm protocol is repeated iteratively, and each time the viscoelastic parameters are adjusted, until the sum of residual is lower than the prefixed tolerance-convergence value. The resulting viscoelastic parameters set are chosen as the best combination, which better describes the experimental data for the given viscoelastic constitutive equation model. In Fig 10 an example of the iterative algorithm application on experimental indentation cycle adopting the PLR model, where the starting guess assignment (Fig 10a) and the final iterate results (Fig 10b) are highlighted is reported.

In Fig 11 the block diagram of the step-by-step procedure adopted by the algorithm is reported.

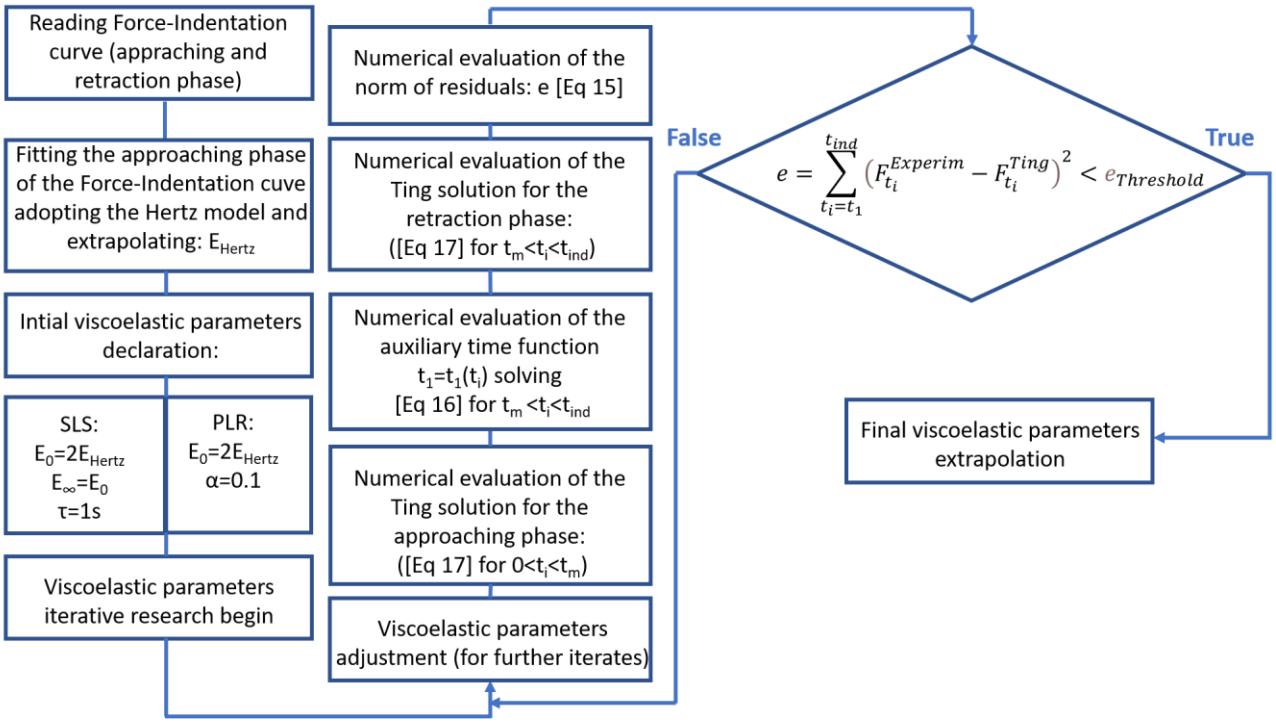

Figure 11: Summary flowchart description of the Ting model resolution algorithm adaptation for force-indentation cycle.

• Constitutive viscoelastic model equation choice

In the previous subsection we described how to adapt the Ting analytical solution [Eq 12a-c] for a numerical implementation [Eq 16-17]. The proposed algorithm treats the relaxation modulus as an priori assigned function, and the viscoelastic parameters set are tested during the fitting procedure.

Nevertheless, another option can be considered. Rewriting the resolutive equations [Eq 12a-c] by replacement of the integral with the Riemann sum, the relaxation modulus $E(t)$ can be extrapolated for each time frame t_i. In this case we obtain the empirical relaxation modulus: $E(t)$, which is a function dependding just on time t and no additional viscoelastic parameters are included. Thus, the extrapolated relaxation modulus $E(t)$ represents a constitutive viscoelastic model. The empirical $E(t)$ data can be compared to several known constitutive relaxation moduli, testing different viscoelastic parameter sets combination for each constitutive equation. Although this second approach does not impose any a priori constitutive equation inside the analytical solution [Eq 12a-c], the identification of the constitutive equation from the empirical $E(t)$ data is not simple or straightforward. Furthermore, the time derivative of the indentation and square indentation are pretty noisy, even applying a moving average filter of 5 points size, especially close the Contact-Point (C-P). Thus, extrapolation of the empirical relaxation modulus $E(t)$ and its level of accuracy are hindered due to noise coming from the time derivative [90].

Thus, we decided to adopt the same strategy mentioned early and also used in [90]. An arbitrary constitutive viscoelastic model is assigned, before applying the numerical evaluation [Eq 16-17] of the analytical Ting solution [Eq 12a-c]. To test the robustness of the trial constitutive model the associated viscoelastic parameters set are extrapolated for different experimental conditions. In particular, several indentation cycles are acquired at different indentation time t_{ind} on the same cell sample. The experimental protocol adopted is the following. We fixed the total Scan-Displacement of the piezo and we gradually increased the

Scan-Displacement speed, exploring approximatively one order and a half of magnitude of this parameter (Scan-Displacement Speed 0.40÷6.70 μm/s]). We examined approximatively ≈20 cells and for each cell we focused on the central region and we have taken several Deflection-Scan-Displacement (Def-D) curves for each Scan-Displacement speed. We expect that the viscoelastic parameters resembling the constitutive equation to be independent of the particular experimental condition used (in our case the Scan-Displacement Speed or the total cycle indentation time t_{ind}). Thus, if the viscoelastic parameters extrapolated from the different Scan-Displacement speeds are almost unchanged, then the chosen constitutive equation reassume well the viscoelastic behavior of the sample. Instead, if the viscoelastic parameters are not preserved for the different Scan-Displacement speeds tested, then the related constitutive equation does not describe well the sample and must be rejected.

The cell line used for the test of the relaxation modulus choice was U87MG. This cell line represents a deeply studied biological model for the glioblastoma-multiforme tumor. The cell sample was placed and cultured into a petri-dish and then transferred for AFM characterization using a device to control the temperature, which is maintained at +37°C. We acquired approximatively ≈3 indentation cycles for each Scan-Displacement speed [0.40; 1.00; 2.00; 2.66; 4.00; 6.70] μs/s analyzing the central area of the cell for a total number of ≈20 cells. Then, we processed the raw Deflection-Scan-Displacement (Def-D) curves obtaining the related Force-Indentation (Def-Ind) curves. Finally, the pre-processed curves were analyzed computing the numerical solution [Eq 16-17] of the Ting resolving equations [Eq 12a-c], first setting the PLR and then the SLS as constitutive viscoelastic model, for each Scan-Displacement speed condition.

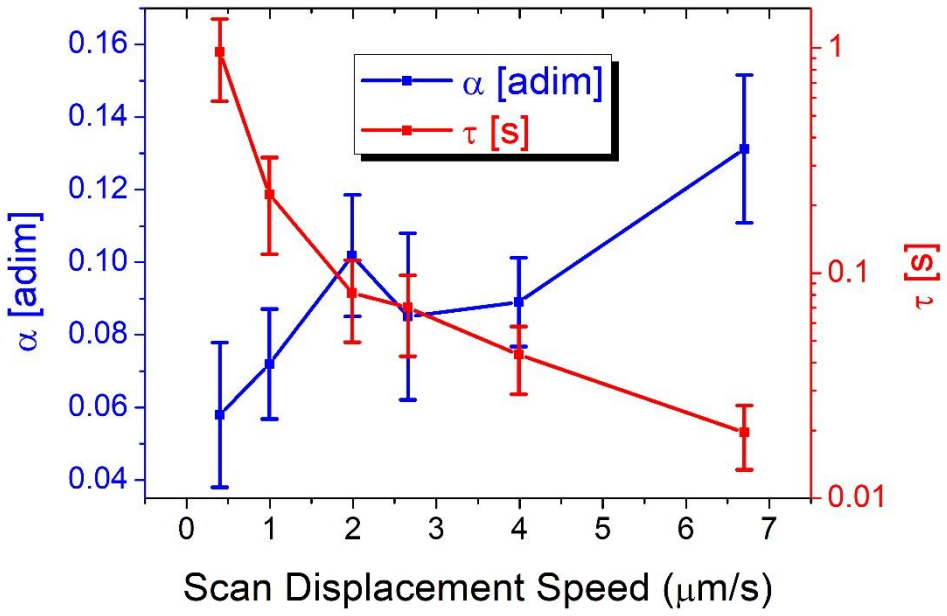

Figure 12: Viscoelastic model robustness comparison between PLR (α) and SLS (τ) for U87MG cell sample. α parameter (blue squares) is plotted in a linear scale, the τ parameter (red squares) is plotted on a logarithmic scale.

The obtained viscoelastic parameters set of the relative constitutive equations: $[E_0,\alpha]$ for the PLR and $[E_0,E_\infty,\tau]$ for the SLS were split up for the different Scan-Displacement speeds and finally compared. In particular, we compared the relaxation rate parameter of the proposed models: the power law exponent α from the PLR and the decaying time τ from the SLS. In Fig 12 power law exponent α and the decaying time τ as a function of the Scan-Displacement speed are reported. The Scan-Displacement speed is represented on a linear scale, like the power law exponent α, while the time decaying parameter τ is plotted on a logarithmic scale. Observing Fig 12, the decaying time parameter τ decreased dramatically over two orders of magnitude from τ≈1s to τ≈0.01s moving along the Scan-Displacement speed. Instead, the power law exponent α

gradually increased from α≈0.06 at the lowest speed to α≈0.14 at the highest speed. Nevertheless, the power law exponent is approximatively constant α≈0.10 in the other four intermediated Scan-Displacement speed conditions. The power law exponent α deviations observed at the Scan-Displacement speeds extrema could be reasonably related to the limitation of the PLR model, where its single α parameter is not able to captures the overall viscoelastic behavior for all the Scan-Displacement speeds. In fact, it has been demonstrated in several rheological experimental studies on cells [136], [151]–[153], where the PLR model has been exploited, that a single α parameter is not able to recapitulates the overall viscoelastic cell behavior along the entire time or frequency domain range. Instead, two or three distinct regimes has been observed, thus a specific power law exponent is required to describes each regime. Probably, the Scan-Displacement speed range adopted in our analysis crosses a power law exponent transition between two different regimes. However, from Fig 12 we can clearly assert that the PLR better reassumes the viscoelastic behavior of U87MG cells than the SLS. This conclusion also confirms how several relaxation processes (PLR) affect the viscoelasticity of the cell sample, rather the only a specific one (SLS). In the other viscoelastic characterization of cell samples adopting the Ting model analytical solution, the PLR constitutive equation will be exploited.

Bibliography

[1] P. B. Canham, “The minimum energy of bending as a possible explanation of the biconcave shape of the human red blood cell,” *J. Theor. Biol.*, vol. 26, no. 1, pp. 61–81, 1970, doi: 10.1016/S0022-5193(70)80032-7.

[2] W. Helfrich and I. Introduction, “Elastic properties of lipid bilayers: Theory and Possible Experiments / Helfrich_1973.pdf,” *Degruyter.Com*, pp. 693–703, 2013, [Online]. Available: https://www.degruyter.com/view/j/znc.1973.28.issue-11-12/znc-1973-11-1209/znc-1973-11-1209.xml.

[3] E. A. Evans, “Bending Resistance and Chemically Induced Moments in Membrane Bilayers,” *Biophys. J.*, vol. 14, no. 12, pp. 923–931, 1974, doi: 10.1016/S0006-3495(74)85959-X.

[4] H. J. Deuling and W. Helfrich, “Red blood cell shapes as explained on the basis of curvature elasticity,” *Biophys. J.*, vol. 16, no. 8, pp. 861–868, 1976, doi: 10.1016/S0006-3495(76)85736-0.

[5] H. J. Deuling and W. Helfrich, “The curvature elasticity of fluid membranes : A catalogue of vesicle shapes,” *J. Phys.*, vol. 37, no. 11, pp. 1335–1345, 1976, doi: 10.1051/jphys:0197600370110133500.

[6] S. T. Milner and S. A. Safran, “Dynamical fluctuations of droplet microemulsions and vesicles,” *Phys. Rev. A*, vol. 36, no. 9, pp. 4371–4379, 1987, doi: 10.1103/PhysRevA.36.4371.

[7] L. Fernandez-Puente, I. Bivas, M. D. Mitov, and P. Méléard, “Temperature and chain length effects on bending elasticity of phosphatidylcholine bilayers,” *Epl*, vol. 28, no. 3, pp. 181–186, 1994, doi: 10.1209/0295-5075/28/3/005.

[8] I. Bivas, P. Hanusse, P. Bothorel, J. Lalanne, and O. Aguerre-Chariol, “Application of the Optical Microscopy To the Determination of the Curvature Elasticity Modulus of Biological and Model

Membranes.," *Prog. Colloid Polym. Sci.*, vol. 73, p. 195, 1987, doi: 10.1007/3-798-50724-4_100.

[9] J. F. Faucon, M. D. Mitov, P. Méléard, I. Bivas, and P. Bothorel, "Bending elasticity and thermal fluctuations of lipid membranes. Theoretical and experimental requirements," *J. Phys.*, vol. 50, no. 17, pp. 2389–2414, 1989, doi: 10.1051/jphys:0198900500170238900.

[10] A. Mescola, N. Marín-Medina, G. Ragazzini, M. Accolla, and A. Alessandrini, "Magainin-H2 effects on the permeabilization and mechanical properties of giant unilamellar vesicles," *J. Colloid Interface Sci.*, vol. 553, pp. 247–258, 2019, doi: 10.1016/j.jcis.2019.06.028.

[11] J. Genova, *Marin Mitov Lectures. Measuring the Bending Elasticity of Lipid Bilayers.*, 1st ed., vol. 17. Copyright © 2013 Elsevier Inc. All rights reserved., 2013.

[12] P. Méléard, T. Pott, H. Bouvrais, and J. H. Ipsen, "Advantages of statistical analysis of giant vesicle flickering for bending elasticity measurements," *Eur. Phys. J. E*, vol. 34, no. 10, p. 116, 2011, doi: 10.1140/epje/i2011-11116-6.

[13] J. Pécréaux, H. G. Döbereiner, J. Prost, J. F. Joanny, and P. Bassereau, "Refined contour analysis of giant unilamellar vesicles," *Eur. Phys. J. E*, vol. 13, no. 3, pp. 277–290, 2004, doi: 10.1140/epje/i2004-10001-9.

[14] C. Esposito, A. Tian, S. Melamed, C. Johnson, S. Y. Tee, and T. Baumgart, "Flicker spectroscopy of thermal lipid bilayer domain boundary fluctuations," *Biophys. J.*, vol. 93, no. 9, pp. 3169–3181, 2007, doi: 10.1529/biophysj.107.111922.

[15] A. Bandara, A. Panahi, G. A. Pantelopulos, T. Nagai, and J. E. Straub, "Exploring the impact of proteins on the line tension of a phase-separating ternary lipid mixture," *J. Chem. Phys.*, vol. 150, no. 20, 2019, doi: 10.1063/1.5091450.

[16] J. Hjort Ipsen, G. Karlström, O. G. Mourtisen, H. Wennerström, and M. J. Zuckermann, "Phase equilibria in the phosphatidylcholine-cholesterol system," *BBA - Biomembr.*, vol. 905, no. 1, pp. 162–172, 1987, doi: 10.1016/0005-2736(87)90020-4.

[17] C. Dietrich *et al.*, "Lipid rafts reconstituted in model membranes," *Biophys. J.*, vol. 80, no. 3, pp. 1417–1428, 2001, doi: 10.1016/S0006-3495(01)76114-0.

[18] A. V. Samsonov, I. Mihalyov, and F. S. Cohen, "Characterization of cholesterol-sphingomyelin domains and their dynamics in bilayer membranes," *Biophys. J.*, vol. 81, no. 3, pp. 1486–1500, 2001, doi: 10.1016/S0006-3495(01)75803-1.

[19] S. L. Veatch and S. L. Keller, "Seeing spots: Complex phase behavior in simple membranes," *Biochim. Biophys. Acta - Mol. Cell Res.*, vol. 1746, no. 3, pp. 172–185, 2005, doi: 10.1016/j.bbamcr.2005.06.010.

[20] S. L. Veatch and S. L. Keller, "Organization in Lipid Membranes Containing Cholesterol," *Phys. Rev. Lett.*, vol. 89, no. 26, pp. 1–4, 2002, doi: 10.1103/PhysRevLett.89.268101.

[21] S. L. Veatch and S. L. Keller, "Separation of Liquid Phases in Giant Vesicles of Ternary Mixtures of Phospholipids and Cholesterol," *Biophys. J.*, vol. 85, no. 5, pp. 3074–3083, 2003, doi: 10.1016/S0006-3495(03)74726-2.

[22] S. L. Veatch, I. V. Polozov, K. Gawrisch, and S. L. Keller, "Liquid Domains in Vesicles Investigated by NMR and Fluorescence Microscopy," *Biophys. J.*, vol. 86, no. 5, pp. 2910–2922, 2004, doi: 10.1016/S0006-3495(04)74342-8.

[23] S. L. Veatch and S. L. Keller, "Miscibility phase diagrams of giant vesicles containing sphingomyelin," *Phys. Rev. Lett.*, vol. 94, no. 14, pp. 3–6, 2005, doi: 10.1103/PhysRevLett.94.148101.

[24] S. L. Veatch, K. Gawrisch, and S. L. Keller, "Closed-loop miscibility gap and quantitative tie-lines in

ternary membranes containing diphytanoyl PC," *Biophys. J.*, vol. 90, no. 12, pp. 4428–4436, 2006, doi: 10.1529/biophysj.105.080283.

[25] P. Cicuta, S. L. Keller, and S. L. Veatch, "Diffusion of liquid domains in lipid bilayer membranes," *J. Phys. Chem. B*, vol. 111, no. 13, pp. 3328–3331, 2007, doi: 10.1021/jp0702088.

[26] T. Baumgart, S. Hess, and W. Webb, "Imaging coexisting fluid domains in biomembrane models coupling curvature and line tension," *Nature*, vol. 425, no. October, pp. 821–824, 2003.

[27] K. Bacia, P. Schwille, and T. Kurzchalia, "Sterol structure determines the separation of phases and the curvature of the liquid-ordered phase in model membranes," *Proc. Natl. Acad. Sci. U. S. A.*, vol. 102, no. 9, pp. 3272–3277, 2005, doi: 10.1073/pnas.0408215102.

[28] M. Edidin, "The state of lipid rafts: From model membranes to cells," *Annu. Rev. Biophys. Biomol. Struct.*, vol. 32, pp. 257–283, 2003, doi: 10.1146/annurev.biophys.32.110601.142439.

[29] S. A. Akimov, P. I. Kuzmin, J. Zimmerberg, F. S. Cohen, and Y. A. Chizmadzhev, "An elastic theory for line tension at a boundary separating two lipid monolayer regions of different thickness," *J. Electroanal. Chem.*, vol. 564, no. 1–2, pp. 13–18, 2004, doi: 10.1016/j.jelechem.2003.10.030.

[30] P. I. Kuzmin, S. A. Akimov, Y. A. Chizmadzhev, J. Zimmerberg, and F. S. Cohen, "Line tension and interaction energies of membrane rafts calculated from lipid splay and tilt," *Biophys. J.*, vol. 88, no. 2, pp. 1120–1133, 2005, doi: 10.1529/biophysj.104.048223.

[31] S. A. Akimov, P. I. Kuzmin, J. Zimmerberg, and F. S. Cohen, "Lateral tension increases the line tension between two domains in a lipid bilayer membrane," *Phys. Rev. E - Stat. Nonlinear, Soft Matter Phys.*, vol. 75, no. 1, pp. 1–8, 2007, doi: 10.1103/PhysRevE.75.011919.

[32] V. A. J. Frolov, Y. A. Chizmadzhev, F. S. Cohen, and J. Zimmerberg, "'Entropic traps' in the kinetics of phase separation in multicomponent membranes stabilize nanodomains," *Biophys. J.*, vol. 91, no. 1, pp. 189–205, 2006, doi: 10.1529/biophysj.105.068502.

[33] T. Baumgart, S. Das, W. W. Webb, and J. T. Jenkins, "Membrane elasticity in giant vesicles with fluid phase coexistence," *Biophys. J.*, vol. 89, no. 2, pp. 1067–1080, 2005, doi: 10.1529/biophysj.104.049692.

[34] A. Tian, C. Johnson, W. Wang, and T. Baumgart, "Line tension at fluid membrane domain boundaries measured by micropipette aspiration," *Phys. Rev. Lett.*, vol. 98, no. 20, pp. 18–21, 2007, doi: 10.1103/PhysRevLett.98.208102.

[35] C. D. Blanchette, W. C. Lin, C. A. Orme, T. V. Ratto, and M. L. Longo, "Using nucleation rates to determine the interfacial line tension of symmetric and asymmetric lipid bilayer domains," *Langmuir*, vol. 23, no. 11, pp. 5875–5877, 2007, doi: 10.1021/la7004584.

[36] J. Gibbs, Willard and J. W. Gabriele, "On the Equilibrium of Heterogeneous Substances," pp. 360–375, 1879.

[37] B. V. Toshev, D. Platikanov, and A. Scheludko, "Line tension in three-phase equilibrium systems," *Langmuir*, vol. 4, no. 3, pp. 489–499, 1988, doi: 10.1021/la00081a001.

[38] E. K. Mann, S. Hénon, D. Langevin, and J. Meunier, "Molecular layers of a polymer at the free water surface : microscopy at the Brewster angle," *J. Phys. II*, vol. 2, no. 9, pp. 1683–1704, 1992, doi: 10.1051/jp2:1992228.

[39] M. J. Roberts, E. J. Teer, and R. S. Duran, "Measurement of line tension from cell coalescence events in a Langmuir film," *J. Phys. Chem. B*, vol. 101, no. 5, pp. 699–701, 1997, doi: 10.1021/jp953163w.

[40] P. Muller and F. Gallet, "First measurement of the liquid-solid line energy in a Langmuir monolayer," *Phys. Rev. Lett.*, vol. 67, no. 9, pp. 1106–1109, 1991, doi: 10.1103/PhysRevLett.67.1106.

[41] K. J. Stine, C. M. Knobler, and R. C. Desai, “Buckling instability in monolayer network structures,” *Phys. Rev. Lett.*, vol. 65, no. 8, pp. 1004–1007, 1990, doi: 10.1103/PhysRevLett.65.1004.

[42] S. Wurlitzer, P. Steffen, and T. M. Fischer, “Line tension of Langmuir monolayer phase boundaries determined with optical tweezers,” *J. Chem. Phys.*, vol. 112, no. 13, pp. 5915–5918, 2000, doi: 10.1063/1.481164.

[43] Benvegnu D. J.; McConnel J.M., “Line Tension between Liquid Domains in Lipid Monolayers,” *J. Phys. Chem.*, vol. 96, no. 16, pp. 6820–6824, 1992.

[44] R. E. Goldstein and D. P. Jackson, “Domain shape relaxation and the spectrum of thermal fluctuations in Langmuir monolayers,” *J. Phys. Chem.*, vol. 98, no. 38, pp. 9626–9636, 1994, doi: 10.1021/j100089a043.

[45] Y. Hu, K. Meleson, and J. Israelachvili, “Thermodynamic equilibrium of domains in a two-component langmuir monolayer,” *Biophys. J.*, vol. 91, no. 2, pp. 444–453, 2006, doi: 10.1529/biophysj.106.081000.

[46] D. V. Zhelev and D. Needham, “Tension-stabilized pores in giant vesicles: determination of pore size and pore line tension,” *BBA - Biomembr.*, vol. 1147, no. 1, pp. 89–104, 1993, doi: 10.1016/0005-2736(93)90319-U.

[47] P. H. Puech, N. Borghi, E. Karatekin, and F. Brochard-Wyart, “Line Thermodynamics: Adsorption at a Membrane Edge,” *Phys. Rev. Lett.*, vol. 90, no. 12, p. 4, 2003, doi: 10.1103/PhysRevLett.90.128304.

[48] E. Karatekin, O. Sandre, H. Guitouni, N. Borghi, P. H. Puech, and F. Brochard-Wyart, “Cascades of transient pores in giant vesicles: Line tension and transport,” *Biophys. J.*, vol. 84, no. 3, pp. 1734–1749, 2003, doi: 10.1016/S0006-3495(03)74981-9.

[49] J. De Joannis, F. Y. Jiang, and J. T. Kindt, “Coarse-grained model simulation of mixed-lipid systems: Composition and line tension of a stabilized bilayer edge,” *Langmuir*, vol. 22, no. 3, pp. 998–1005, 2006, doi: 10.1021/la051278d.

[50] M. . S. M. L. Seul, “Competing Interactions and Domain-Shape Instabilities in a Monomolecular Film at an Air-Water Interface,” *Phys. Rev. Lett.*, vol. 64, no. 16, pp. 1903–1908, 1990, doi: 10.1051/jphystap:018980070016101.

[51] A. R. Honerkamp-Smith *et al.*, “Line tensions, correlation lengths, and critical exponents in lipid membranes near critical points,” *Biophys. J.*, vol. 95, no. 1, pp. 236–246, 2008, doi: 10.1529/biophysj.107.128421.

[52] W. W. W. M. B. Schneider, J. T. Jenkins, “Thermal fluctuations of large quasi-spherical bimolecular phospholipid vesicles,” vol. 45, no. 1984, pp. 1457–1472, 1984.

[53] E. Sackmann, H. P. Duwe, and H. Engelhardt, “Membrane bending elasticity and its role for shape fluctuations and shape transformations of cells and vesicles,” *Faraday Discuss. Chem. Soc.*, vol. 81, no. 3, pp. 281–290, 1986, doi: 10.1039/DC9868100281.

[54] H. P. Duwe and E. Sackmann, “Bending elasticity and thermal excitations of lipid bilayer vesicles: Modulation by solutes,” *Phys. A Stat. Mech. its Appl.*, vol. 163, no. 1, pp. 410–428, 1990, doi: 10.1016/0378-4371(90)90349-W.

[55] H. Engelhardt, H. P. Duwe, and E. Sackmann, “Bilayer bending elasticity measured by Fourier analysis of thermally excited surface undulations of flaccid vesicles,” *J. Phys. Lettres*, vol. 46, no. 8, pp. 395–400, 1985, doi: 10.1051/jphyslet:01985004608039500.

[56] J. Henriksen, A. C. Rowat, and J. H. Ipsen, “Vesicle fluctuation analysis of the effects of sterols on membrane bending rigidity,” *Eur. Biophys. J.*, vol. 33, no. 8, pp. 732–741, 2004, doi: 10.1007/s00249-

004-0420-5.

[57] E. K. Mann, S. H. Langevin, and J. Meunier, “Hydrodynamics of domain relaxation in a polymer monolayer.” pp. 5708–5720, 1995.

[58] M. P. Gelfand and M. E. Fisher, “Finite-size effects in fluid interfaces,” *Phys. A Stat. Mech. its Appl.*, vol. 166, no. 1, pp. 1–74, 1990, doi: 10.1016/0378-4371(90)90099-E.

[59] S. A. Safran, “Statistical Thermodynamics of Surfaces, Interfaces, and Membranes,” *Westview Press. Boulder, CO*, 2003.

[60] R. D. Usery *et al.*, “Line Tension Controls Liquid-Disordered + Liquid-Ordered Domain Size Transition in Lipid Bilayers,” *Biophys. J.*, vol. 112, no. 7, pp. 1431–1443, 2017, doi: 10.1016/j.bpj.2017.02.033.

[61] H. A. Stone and H. M. Mcconnell, “Hydrodynamics of quantized shape transitions of lipid domains,” *Proc. R. Soc. London. Ser. A Math. Phys. Sci.*, vol. 448, no. 1932, pp. 97–111, 1995, doi: 10.1098/rspa.1995.0007.

[62] M. Seul, “Dynamics of domain shape relaxation in Langmuir films,” *J. Phys. Chem.*, vol. 97, no. 12, pp. 2941–2945, 1993, doi: 10.1021/j100114a019.

[63] J. C. Alexander, A. J. Bernoff, E. K. Mann, J. A. Mann, J. R. Wintersmith, and L. Zou, *Domain relaxation in Langmuir films*, vol. 571. 2007.

[64] P. G. S. A. M. DELBROCK, “Brownian motion in biological membranes,” vol. 72, no. 8, pp. 3111–3113, 1975.

[65] B. A. Camley, C. Esposito, T. Baumgart, and F. L. H. Brown, “Lipid bilayer domain fluctuations as a probe of membrane viscosity,” *Biophys. J.*, vol. 99, no. 6, pp. L44–L46, 2010, doi: 10.1016/j.bpj.2010.07.007.

[66] P. Méléard, J. F. Faucon, M. D. Mitov, and P. Bothorel, “Pulsed-light microscopy applied to the measurement of the bending elasticity of giant liposomes,” *Epl*, vol. 19, no. 4, pp. 267–271, 1992, doi: 10.1209/0295-5075/19/4/004.

[67] G. Ragazzini, A. Mescola, L. Corsi, and A. Alessandrini, “Fabrication of a low-cost on-stage cell incubator with full automation,” *J. Biol. Educ.*, vol. 53, no. 2, pp. 165–173, 2019, doi: 10.1080/00219266.2018.1451772.

[68] G. Ragazzini, J. Guerzoni, A. Mescola, D. Di Rosa, L. Corsi, and A. Alessandrini, “A Fully Integrated Arduino-Based System for the Application of Stretching Stimuli to Living Cells and Their Time-Lapse Observation: A Do-It-Yourself Biology Approach,” *Ann. Biomed. Eng.*, 2021, doi: 10.1007/s10439-021-02758-3.

[69] R. Gorelik and A. Gautreau, “Quantitative and unbiased analysis of directional persistence in cell migration,” *Nat. Protoc.*, vol. 9, no. 8, pp. 1931–1943, 2014, doi: 10.1038/nprot.2014.131.

[70] Lackey JM, “Cell Movement and Cell Behavior,” *Allen and Unwin*, 1986.

[71] C. Rivetti, M. Guthold, and C. Bustamante, “Scanning force microscopy of DNA deposited onto mica: Equilibration versus kinetic trapping studied by statistical polymer chain analysis,” *J. Mol. Biol.*, vol. 264, no. 5, pp. 919–932, 1996, doi: 10.1006/jmbi.1996.0687.

[72] G A Dunn, “Characterising a kinesis response: time averaged measures of cell speed and directional persistence,” *Agents Actions Suppl*, 1983.

[73] A. W. Othmer H. G. , Dunbar S. R., “Models of dispersal in biological systems.” p. j. Math. Biol. 263-298, 1988.

[74] Alt W., “CORRELATION ANALYSIS OF TWO-DIMENSIONAL LOCOMOTION PATHS,” *Biol. Motion*, p.

254, 1990.

[75] P. A. DiMilla, J. A. Quinn, S. M. Albelda, and D. A. Lauffenburger, “Measurement of individual cell migration parameters for human tissue cells,” *AIChE J.*, vol. 38, no. 7, pp. 1092–1104, 1992, doi: 10.1002/aic.690380712.

[76] J. Qian, H. Liu, Y. Lin, W. Chen, and H. Gao, “A Mechanochemical Model of Cell Reorientation on Substrates under Cyclic Stretch,” *PLoS One*, vol. 8, no. 6, 2013, doi: 10.1371/journal.pone.0065864.

[77] A. Livne, E. Bouchbinder, and B. Geiger, “Cell reorientation under cyclic stretching,” *Nat. Commun.*, vol. 5, no. May, 2014, doi: 10.1038/ncomms4938.

[78] S. Jungbauer, H. Gao, J. P. Spatz, and R. Kemkemer, “Two characteristic regimes in frequency-dependent dynamic reorientation of fibroblasts on cyclically stretched substrates,” *Biophys. J.*, vol. 95, no. 7, pp. 3470–3478, 2008, doi: 10.1529/biophysj.107.128611.

[79] E. H. Barriga and R. Mayor, “Adjustable viscoelasticity allows for efficient collective cell migration,” *Semin. Cell Dev. Biol.*, vol. 93, pp. 55–68, 2019, doi: 10.1016/j.semcdb.2018.05.027.

[80] I. Pajic-Lijakovic and M. Milivojevic, “Viscoelasticity of multicellular systems caused by collective cell migration: dynamics at the biointerface,” *Eur. Biophys. J.*, vol. 49, no. 3–4, pp. 253–265, 2020, doi: 10.1007/s00249-020-01431-2.

[81] I. Casuso, F. Rico, and S. Scheuring, “Biological AFM: Where we come from - Where we are - Where we may go,” *J. Mol. Recognit.*, vol. 24, no. 3, pp. 406–413, 2011, doi: 10.1002/jmr.1081.

[82] M. Radmacher, “Measuring the elastic properties of biological samples with the AFM,” *IEEE Eng. Med. Biol. Mag.*, vol. 16, no. 2, pp. 47–57, 1997, doi: 10.1109/51.582176.

[83] M. Glaubitz *et al.*, “A novel contact model for AFM indentation experiments on soft spherical cell-like particles,” *Soft Matter*, vol. 10, no. 35, pp. 6732–6741, 2014, doi: 10.1039/c4sm00788c.

[84] S. V. Kontomaris, A. Stylianou, K. S. Nikita, and A. Malamou, “Determination of the linear elastic regime in AFM nanoindentation experiments on cells,” *Mater. Res. Express*, vol. 6, no. 11, 2019, doi: 10.1088/2053-1591/ab4f42.

[85] M. Thé *et al.*, “Anisotropy of cell adhesive microenvironment governs cell internal organization and orientation of polarity,” *Proc. Natl. Acad. Sci. U. S. A.*, vol. 103, no. 52, pp. 19771–19776, 2006, doi: 10.1073/pnas.0609267103.

[86] A. M. Collinsworth, S. Zhang, W. E. Kraus, and G. A. Truskey, “Apparent elastic modulus and hysteresis of skeletal muscle cells throughout differentiation,” *Am. J. Physiol. - Cell Physiol.*, vol. 283, no. 4 52-4, pp. 1219–1227, 2002, doi: 10.1152/ajpcell.00502.2001.

[87] K. E. Bremmell, A. Evans, and C. A. Prestidge, “Deformation and nano-rheology of red blood cells: An AFM investigation,” *Colloids Surfaces B Biointerfaces*, vol. 50, no. 1, pp. 43–48, 2006, doi: 10.1016/j.colsurfb.2006.03.002.

[88] F. M. Hecht, J. Rheinlaender, N. Schierbaum, W. H. Goldmann, B. Fabry, and T. E. Schäffer, “Imaging viscoelastic properties of live cells by AFM: Power-law rheology on the nanoscale,” *Soft Matter*, vol. 11, no. 23, pp. 4584–4591, 2015, doi: 10.1039/c4sm02718c.

[89] Z. Al-Rekabi and S. Contera, “Multifrequency AFM reveals lipid membrane mechanical properties and the effect of cholesterol in modulating viscoelasticity,” *Proc. Natl. Acad. Sci. U. S. A.*, vol. 115, no. 11, pp. 2658–2663, 2018, doi: 10.1073/pnas.1719065115.

[90] Y. M. Efremov, W. H. Wang, S. D. Hardy, R. L. Geahlen, and A. Raman, “Measuring nanoscale viscoelastic parameters of cells directly from AFM force-displacement curves,” *Sci. Rep.*, vol. 7, no. 1, pp. 1–14, 2017, doi: 10.1038/s41598-017-01784-3.

[91] B. R. Brückner, H. Nöding, and A. Janshoff, “Viscoelastic Properties of Confluent MDCK II Cells Obtained from Force Cycle Experiments,” *Biophys. J.*, vol. 112, no. 4, pp. 724–735, 2017, doi: 10.1016/j.bpj.2016.12.032.

[92] T. C. T. Ting, “The contact stresses between a rigid indenter and a viscoelastic half-space,” *J. Appl. Mech. Trans. ASME*, vol. 33, no. 4, pp. 845–854, 1964, doi: 10.1115/1.3625192.

[93] B. Shoelson, E. K. Dimitriadis, H. Cai, B. Kachar, and R. S. Chadwick, “Evidence and implications of inhomogeneity in tectorial membrane elasticity.,” *Biophys. J.*, vol. 87, no. 4, pp. 2768–2777, 2004, doi: 10.1529/biophysj.104.040774.

[94] D. C. Lin, E. K. Dimitriadis, and F. Horkay, “Robust strategies for automated AFM force curve analysis - I. Non-adhesive indentation of soft, inhomogeneous materials,” *J. Biomech. Eng.*, vol. 129, no. 3, pp. 430–440, 2007, doi: 10.1115/1.2720924.

[95] D. C. Lin, E. K. Dimitriadis, and F. Horkay, “Robust strategies for automated AFM force curve analysis - II: Adhesion-influenced indentation of soft, elastic materials,” *J. Biomech. Eng.*, vol. 129, no. 6, pp. 904–912, 2007, doi: 10.1115/1.2800826.

[96] D. Rudoy, S. G. Yuen, R. D. Howe, and P. J. Wolfe, “Bayesian change-point analysis for atomic force microscopy and soft material indentation,” *J. R. Stat. Soc. Ser. C Appl. Stat.*, vol. 59, no. 4, pp. 573–593, 2010, doi: 10.1111/j.1467-9876.2010.00715.x.

[97] R. Benítez, S. Moreno-flores, V. J. Bolós, and J. L. Toca-Herrera, “A new automatic contact point detection algorithm for AFM force curves,” *Microsc. Res. Tech.*, vol. 76, no. 8, pp. 870–876, 2013, doi: 10.1002/jemt.22241.

[98] D. Tranchida, S. Piccarolo, and M. Soliman, “Nanoscale mechanical characterization of polymers by AFM nanoindentations: Criticalr approach to the elastic characterization,” *Macromolecules*, vol. 39, no. 13, pp. 4547–4556, 2006, doi: 10.1021/ma052727j.

[99] V. Managuli and S. Roy, “Asymptotical Correction to Bottom Substrate Effect Arising in AFM Indentation of Thin Samples and Adherent Cells Using Conical Tips,” *Exp. Mech.*, vol. 58, no. 5, pp. 733–741, 2018, doi: 10.1007/s11340-018-0373-8.

[100] N. Gavara and R. S. Chadwick, “Determination of the elastic moduli of thin samples and adherent cells using conical atomic force microscope tips,” *Nat. Nanotechnol.*, vol. 7, no. 11, pp. 733–736, 2012, doi: 10.1038/nnano.2012.163.

[101] P. D. Garcia, C. R. Guerrero, and R. Garcia, “Nanorheology of living cells measured by AFM-based force-distance curves,” *Nanoscale*, vol. 12, no. 16, pp. 9133–9143, 2020, doi: 10.1039/c9nr10316c.

[102] S. L. Crick and F. C. P. Yin, “Assessing micromechanical properties of cells with atomic force microscopy: Importance of the contact point,” *Biomech. Model. Mechanobiol.*, vol. 6, no. 3, pp. 199–210, 2007, doi: 10.1007/s10237-006-0046-x.

[103] N. Gavara, “Combined strategies for optimal detection of the contact point in AFM force-indentation curves obtained on thin samples and adherent cells,” *Sci. Rep.*, vol. 6, no. January, pp. 1–13, 2016, doi: 10.1038/srep21267.

[104] N. Gavara and R. S. Chadwick, “Relationship between cell stiffness and stress fiber amount, assessed by simultaneous atomic force microscopy and live-cell fluorescence imaging,” *Biomech. Model. Mechanobiol.*, vol. 15, no. 3, pp. 511–523, 2016, doi: 10.1007/s10237-015-0706-9.

[105] A. Raman *et al.*, “Mapping nanomechanical properties of live cells using multi-harmonic atomic force microscopy,” *Nat. Nanotechnol.*, vol. 6, no. 12, pp. 809–814, 2011, doi: 10.1038/nnano.2011.186.

[106] H Hertz, “Hertz Model Reine,” *Angew. Math.*, 1881.

[107] I. N. Sneddon, “The relation between load and penetration in the axisymmetric boussinesq problem for a punch of arbitrary profile,” *Int. J. Eng. Sci.*, vol. 3, no. 1, pp. 47–57, 1965, doi: 10.1016/0020-7225(65)90019-4.

[108] F. Rico, P. Roca-Cusachs, N. Gavara, R. Farré, M. Rotger, and D. Navajas, “Probing mechanical properties of living cells by atomic force microscopy with blunted pyramidal cantilever tips,” *Phys. Rev. E - Stat. Nonlinear, Soft Matter Phys.*, vol. 72, no. 2, pp. 1–10, 2005, doi: 10.1103/PhysRevE.72.021914.

[109] M. Lekka *et al.*, “Cancer cell recognition - Mechanical phenotype,” *Micron*, vol. 43, no. 12, pp. 1259–1266, 2012, doi: 10.1016/j.micron.2012.01.019.

[110] C. Rotsch and M. Radmacher, “Drug-induced changes of cytoskeletal structure and mechanics in fibroblasts: An atomic force microscopy study,” *Biophys. J.*, vol. 78, no. 1, pp. 520–535, 2000, doi: 10.1016/S0006-3495(00)76614-8.

[111] Q. S. Li, G. Y. H. Lee, C. N. Ong, and C. T. Lim, “AFM indentation study of breast cancer cells,” *Biochem. Biophys. Res. Commun.*, vol. 374, no. 4, pp. 609–613, 2008, doi: 10.1016/j.bbrc.2008.07.078.

[112] M. Prabhune, G. Belge, A. Dotzauer, J. Bullerdiek, and M. Radmacher, “Comparison of mechanical properties of normal and malignant thyroid cells,” *Micron*, vol. 43, no. 12, pp. 1267–1272, 2012, doi: 10.1016/j.micron.2012.03.023.

[113] Y. M. Efremov, A. A. Dokrunova, D. V. Bagrov, K. S. Kudryashova, O. S. Sokolova, and K. V. Shaitan, “The effects of confluency on cell mechanical properties,” *J. Biomech.*, vol. 46, no. 6, pp. 1081–1087, 2013, doi: 10.1016/j.jbiomech.2013.01.022.

[114] E. H. Lee and J. R. M. Radok, “The Contact Problem for Visooelastia Bodies 1 Transactions of the ASME-asme/terms-of-use,” pp. 438–444, 1960, [Online]. Available: http://www.asme.org/about-asme/terms-of-use.

[115] S. Nawaz, P. Sánchez, K. Bodensiek, S. Li, M. Simons, and I. A. T. Schaap, “Cell Visco-Elasticity Measured with AFM and Optical Trapping at Sub-Micrometer Deformations,” *PLoS One*, vol. 7, no. 9, 2012, doi: 10.1371/journal.pone.0045297.

[116] L. M. Rebelo, J. S. De Sousa, J. Mendes Filho, and M. Radmacher, “Comparison of the viscoelastic properties of cells from different kidney cancer phenotypes measured with atomic force microscopy,” *Nanotechnology*, vol. 24, no. 5, 2013, doi: 10.1088/0957-4484/24/5/055102.

[117] A. B. Mathur, A. M. Collinsworth, W. M. Reichert, W. E. Kraus, and G. A. Truskey, “Endothelial, cardiac muscle and skeletal muscle exhibit different viscous and elastic properties as determined by atomic force microscopy,” *J. Biomech.*, vol. 34, no. 12, pp. 1545–1553, 2001, doi: 10.1016/S0021-9290(01)00149-X.

[118] M. A. Caporizzo *et al.*, “Strain-Rate Dependence of Elastic Modulus Reveals Silver Nanoparticle Induced Cytotoxicity,” *Nanobiomedicine*, vol. 2, pp. 1–15, 2015, doi: 10.5772/61328.

[119] P. D. Garcia and R. Garcia, “Determination of the viscoelastic properties of a single cell cultured on a rigid support by force microscopy,” *Nanoscale*, vol. 10, no. 42, pp. 19799–19809, 2018, doi: 10.1039/c8nr05899g.

[120] R. M. Hochmuth, “Micropipette aspiration of living cells,” *J. Biomech.*, vol. 33, no. 1, pp. 15–22, 2000, doi: 10.1016/S0021-9290(99)00175-X.

[121] N. H. Reynolds, W. Ronan, E. P. Dowling, P. Owens, R. M. McMeeking, and J. P. McGarry, “On the

role of the actin cytoskeleton and nucleus in the biomechanical response of spread cells," *Biomaterials*, vol. 35, no. 13, pp. 4015–4025, 2014, doi: 10.1016/j.biomaterials.2014.01.056.

[122] P. Fernández, P. A. Pullarkat, and A. Ott, "A master relation defines the nonlinear viscoelasticity of single fibroblasts," *Biophys. J.*, vol. 90, no. 10, pp. 3796–3805, 2006, doi: 10.1529/biophysj.105.072215.

[123] N. Desprat, A. Richert, J. Simeon, and A. Asnacios, "Creep function of a single living cell," *Biophys. J.*, vol. 88, no. 3, pp. 2224–2233, 2005, doi: 10.1529/biophysj.104.050278.

[124] M. Balland *et al.*, "Power laws in microrheology experiments on living cells: Comparative analysis and modeling," *Phys. Rev. E - Stat. Nonlinear, Soft Matter Phys.*, vol. 74, no. 2, pp. 1–17, 2006, doi: 10.1103/PhysRevE.74.021911.

[125] M.-T. Wei *et al.*, "A comparative study of living cell micromechanical properties by oscillatory optical tweezers," *Opt. Express*, vol. 16, no. 12, p. 8594, 2008, doi: 10.1364/oe.16.008594.

[126] B. D. Hoffman, G. Massiera, K. M. Van Citters, and J. C. Crocker, "The consensus mechanics of cultured mammalian cells," *Proc. Natl. Acad. Sci. U. S. A.*, vol. 103, no. 27, pp. 10259–10264, 2006, doi: 10.1073/pnas.0510348103.

[127] G. Massiera, K. M. Van Citters, P. L. Biancaniello, and J. C. Crocker, "Mechanics of single cells: Rheology, time dependence, and fluctuations," *Biophys. J.*, vol. 93, no. 10, pp. 3703–3713, 2007, doi: 10.1529/biophysj.107.111641.

[128] K. I. Schiffmann, "Nanoindentation creep and stress relaxation tests of polycarbonate: Analysis of viscoelastic properties by different rheological models," *Int. J. Mater. Res.*, vol. 97, no. 9, pp. 1199–1211, 2006, doi: 10.3139/146.101357.

[129] E. M. Darling, S. Zauscher, J. A. Block, and F. Guilak, "A thin-layer model for viscoelastic, stress-relaxation testing of cells using atomic force microscopy: Do cell properties reflect metastatic potential?," *Biophys. J.*, vol. 92, no. 5, pp. 1784–1791, 2007, doi: 10.1529/biophysj.106.083097.

[130] J. Alcaraz *et al.*, "Microrheology of human lung epithelial cells measured by atomic force microscopy," *Biophys. J.*, vol. 84, no. 3, pp. 2071–2079, 2003, doi: 10.1016/S0006-3495(03)75014-0.

[131] R. Takahashi and T. Okajima, "Mapping power-law rheology of living cells using multi-frequency force modulation atomic force microscopy," *Appl. Phys. Lett.*, vol. 107, no. 17, 2015, doi: 10.1063/1.4934874.

[132] S. G. Shroff, D. R. Saner, and R. Lal, "Dynamic micromechanical properties of cultured rat atrial myocytes measured by atomic force microscopy," *Am. J. Physiol. - Cell Physiol.*, vol. 269, no. 1 38-1, pp. 286–292, 1995, doi: 10.1152/ajpcell.1995.269.1.c286.

[133] A. X. Cartagena-Rivera, W. H. Wang, R. L. Geahlen, and A. Raman, "Fast, multi-frequency, and quantitative nanomechanical mapping of live cells using the atomic force microscope," *Sci. Rep.*, vol. 5, no. June, pp. 1–11, 2015, doi: 10.1038/srep11692.

[134] M. Dokukin and I. Sokolov, "High-resolution high-speed dynamic mechanical spectroscopy of cells and other soft materials with the help of atomic force microscopy," *Sci. Rep.*, vol. 5, no. July, pp. 1–14, 2015, doi: 10.1038/srep12630.

[135] S. Moreno-Flores, R. Benitez, M. d. M. Vivanco, and J. L. Toca-Herrera, "Stress relaxation microscopy: Imaging local stress in cells," *J. Biomech.*, vol. 43, no. 2, pp. 349–354, 2010, doi: 10.1016/j.jbiomech.2009.07.037.

[136] D. Stamenović *et al.*, "Rheological behavior of living cells is timescale-dependent," *Biophys. J.*, vol. 93, no. 8, pp. 39–41, 2007, doi: 10.1529/biophysj.107.116582.

[137] S. Tripathy and E. J. Berger, “Measuring viscoelasticity of soft samples using atomic force microscopy,” *J. Biomech. Eng.*, vol. 131, no. 9, pp. 1–6, 2009, doi: 10.1115/1.3194752.

[138] B. Wang, P. Lançon, C. Bienvenu, P. Vierling, C. Di Giorgio, and G. Bossis, “A general approach for the microrheology of cancer cells by atomic force microscopy,” *Micron*, vol. 44, no. 1, pp. 287–297, 2013, doi: 10.1016/j.micron.2012.07.006.

[139] B. Qiang, J. Greenleaf, M. Oyen, and X. Zhang, “Estimating material elasticity by spherical indentation load-relaxation tests on viscoelastic samples of finite thickness,” *IEEE Trans. Ultrason. Ferroelectr. Freq. Control*, vol. 58, no. 7, pp. 1418–1429, 2011, doi: 10.1109/TUFFC.2011.1961.

[140] P. P. Weafer *et al.*, “Stability enhancement of an atomic force microscope for long-term force measurement including cantilever modification for whole cell deformation,” *Rev. Sci. Instrum.*, vol. 83, no. 9, 2012, doi: 10.1063/1.4752023.

[141] O. Jonas and C. Duschl, “Force propagation and force generation in cells,” *Cytoskeleton*, vol. 67, no. 9, pp. 555–563, 2010, doi: 10.1002/cm.20466.

[142] J. Rother, H. Nöding, I. Mey, and A. Janshoff, “Atomic force microscopy-based microrheology reveals significant differences in the viscoelastic response between malign and benign cell lines,” *Open Biol.*, vol. 4, no. MAY, 2014, doi: 10.1098/rsob.140046.

[143] D. Schneider *et al.*, “Tension monitoring during epithelial-to-mesenchymal transition links the switch of phenotype to expression of moesin and cadherins in NMuMG cells,” *PLoS One*, vol. 8, no. 12, 2013, doi: 10.1371/journal.pone.0080068.

[144] Y. M. Efremov, A. A. Dokrunova, A. V. Efremenko, M. P. Kirpichnikov, K. V. Shaitan, and O. S. Sokolova, “Distinct impact of targeted actin cytoskeleton reorganization on mechanical properties of normal and malignant cells,” *Biochim. Biophys. Acta - Mol. Cell Res.*, vol. 1853, no. 11, pp. 3117–3125, 2015, doi: 10.1016/j.bbamcr.2015.05.008.

[145] T. Niu and G. Cao, “Finite size effect does not depend on the loading history in soft matter indentation,” *J. Phys. D. Appl. Phys.*, vol. 47, no. 38, 2014, doi: 10.1088/0022-3727/47/38/385303.

[146] P. Sollich, “Rheological constitutive equation for a model of soft glassy materials,” *Phys. Rev. E - Stat. Physics, Plasmas, Fluids, Relat. Interdiscip. Top.*, vol. 58, no. 1, pp. 738–759, 1998, doi: 10.1103/PhysRevE.58.738.

[147] P. Kollmannsberger and B. Fabry, “Linear and nonlinear rheology of living cells,” *Annu. Rev. Mater. Res.*, vol. 41, pp. 75–97, 2011, doi: 10.1146/annurev-matsci-062910-100351.

[148] J. D. Hemmer, J. Nagatomi, S. T. Wood, A. A. Vertegel, D. Dean, and M. LaBerge, “Role of cytoskeletal components in stress-relaxation behavior of adherent vascular smooth muscle cells,” *J. Biomech. Eng.*, vol. 131, no. 4, pp. 1–9, 2009, doi: 10.1115/1.3049860.

[149] R. L. Bagley, “Power law and fractional calculus model of viscoelasticity,” *AIAA J.*, vol. 27, no. 10, pp. 1412–1417, 1989, doi: 10.2514/3.10279.

[150] Wiliam N. Sharpe, *Springer Handbook of Experimental Solid Mechanics*. 2008.

[151] L. M. Rebêlo, J. S. De Sousa, J. M. Filho, J. Schäpe, H. Doschke, and M. Radmacher, “Microrheology of cells with magnetic force modulation atomic force microscopy,” *Soft Matter*, vol. 10, no. 13, pp. 2141–2149, 2014, doi: 10.1039/c3sm52045e.

[152] C. Mechanics and D. Stamenovic, “Two regimes, maybe three?,” vol. 5, no. August, pp. 597–598, 2006.

[153] L. Deng *et al.*, “Fast and slow dynamics of the cytoskeleton,” *Nat. Mater.*, vol. 5, no. 8, pp. 636–640, 2006, doi: 10.1038/nmat1685.

Chapter 3

Devices development

On-stage cell incubator for live cell imaging

In this section we will describe the step-by-step realization of a low-cost on-stage cell incubator Arduino-based. The first version of the cell incubator device was placed on the original stage of the optical microscope and was connected to the PC through a USB port and interfaced to a LabView control panel, this version allows to acquire a single petri dish area per session. The home-made setup includes also an automated autofocus algorithm exploitable for long-time live cell imaging sessions managed by a second Arduino, which work separately from the cell incubator device and was interfaced to a Python script (also a Matlab interface has been developed) for image contrast analysis.

After the first cell incubator design was published in Journal of Biological Education [1], we modified the initial enclosure chassis in order to host not a single dish but a multi-six petri-dish. Simultaneously, we designed an aluminum-based motorized stage that allows us to image several cell sample fields exposed to different treatments and to increase the cell migration statistical analysis in a single session. The motorized stage apparatus has been connected to the previously existing autofocus system, thus the final Arduino-setup can control the overall 3D cell incubator position (X-Y planar pane of the cell incubator and the Z vertical coordinate of the optical objective of the microscope). The stage-autofocus Arduino-setup has been interfaced to the PC using a USB port. A dedicated LabView control panel has been developed to select the cell sample regions of interest (X-Y coordinates) setting also the focus vertical position Z of each area. In Fig 1 is reported the LabView interface controlling the X-Y-Z displacements during regions assignment, the software can define from 4 up to 8 different areas.

The LabView program constituted the starting point of the subsequent automatic image acquisition, in fact is launched, exploited and finally closed before automatic image acquisition, representing a preliminary

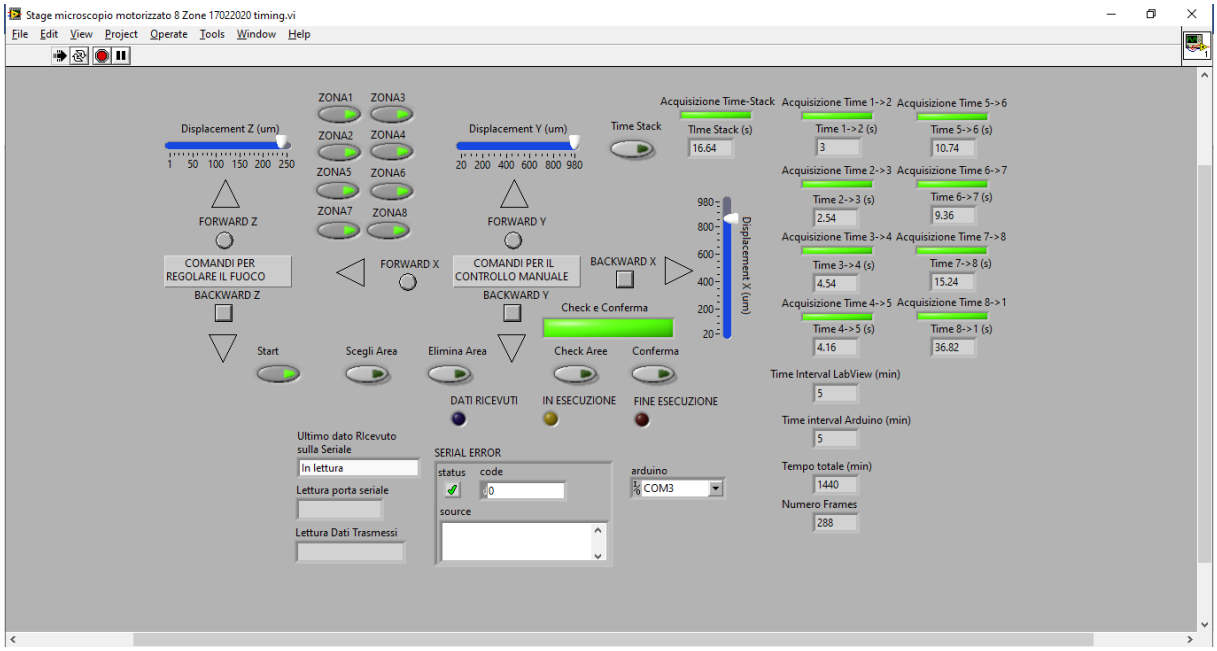

Figure 1: LabView controlling interface during cell sample regions assignment. The software automatically evaluates the time needed to cover the overall region set during acquisition phase.

procedure. Then, the automated cell image region acquisition loop is managed by a Python script, which has been designed to cyclically apply the autofocus algorithm on each pre-selected region. The LabView and Python programs has been realized to study an arbitrary number of different cell region. Our work treats from 4 up to 8 regions. The automated procedure for image acquisition has been written to maintain in focus each region independently along the entire time session, thus the focus is adjusted recursively during image

acquisition cycle. A third cell incubator design has been realized to host a PDMS-based stretcher substrate and it will be described in the next chapter.

• Introduction

One of the most diffuse and fundamental devices in cell-biology labs is certainly the cell incubator. Essentially, the task a cell incubator has to perform is to keep cells in the best conditions for their survival and proliferation as long as possible. The main ingredients to fulfill this aim are a constant temperature of 37 °C, stabilize the pH parameter, and relative humidity of about 90–95% to limit as much as possible water evaporation. Usually, 5% carbon dioxide (CO2) concentration is maintained to stabilize the pH of many of the cell culture media. Many other cell culture media namely "CO2 independent" have also been developed, which assure pH stability for several hours without requiring C02 pressure. Nevertheless, these culture media are less pH stable during time and are not suitable for long-time live cell imaging experiments. Instead they are more exploited for example in AFM sessions where complete chassis enclosure is not feasible. Thus, we will adopt the former cell culture media and a CO2 flux is driven into the cell incubator. At the same time, considering that cells are strongly active systems, in the past the possibility of observing in real-time with a microscope dynamic events occurring for example during cell duplication, cell migration or reactivity of cells exposed to exogenous molecules has been pursued [2]–[4]. For this task two different solutions have been considered: 1) the optical microscope has been almost completely included inside a system allowing to control all the required conditions; 2) smaller incubators could be positioned on top of the microscope stage have been developed. The first strategy is less feasible for several reasons like the optical microscope usury when exposed to high relative humidity level, or the higher volume chassis required to enclosure the optical apparatus. The second strategy is more portable and can be easily adapted to different microscopes preventing high risks of optical microscope usury. On-top stage incubators are commercially available but quite expensive for cell biology tutorial labs. In the recent years an activity called DIY (Do It Yourself) biology [5] allowed many small labs, which have not access to large fundings, to equip themselves with small devices to perform experiments in biology. The DIY biology movement allowed scientists, small organizations as well as young students, to approach biology and life science exploiting methods and devices similar to those used in traditional research institutions [5]–[7]. Cell incubators are among these devices. The DIY biology activity has benefitted from the development of open-source microcontrollers, like the popular Arduino microprocessor [8] homepage for Arduino creators covering hardware, software, applications and support; https://www.arduino.cc.pdf], which are very cheap and can also be used to train students with the programming and electronics procedures [9]. In addition, the Arduino board is an easily programmable platform based on C++ language that requires a basic secondary school electronic knowledge. Alternatively, the electronic basis can be possibly acquired during undergraduate formation. Recently, there have been works aimed at developing low cost cell incubators for live-cell imaging [4]. These attempts could allow many labs and also tutorial labs to equip themselves with a device for studying dynamical aspects of cells. Here we present the development of an on-stage cell incubator based on the Arduino microprocessor, which can be built for a total cost of about 260 euros. The incubator is easily mounted on the stage of any inverted microscope and allows to maintain cells in optimal conditions (temperature, CO2 concentration and humidity). The parameters are controlled by independent feedback systems that exploit the already developed routines for Arduino. We observed the evolution in time of different mammalian cells (see cell migration chapter for details) and we were also able to study in real time the effect of molecules delivered to the cells. This set-up allows to investigate long-term effects of drugs on cells while keeping them in good conditions taking advantage also of an autofocus system and automatic acquisition of images.

- **Cell incubator design**

The first version of the chassis of the cell incubator was made using plastic PMMA (polymethylmetacrylate) and Aluminum. The PMMA has been used for the base and the cover parts for several reasons. The base is in direct contact to the metallic microscope stage, thus a plastic material prevents high heat dispersion and lower temperature expansion contribution. The cover will host an ITO heating window driven by an appropriate PID feedback to adjust the underlying cell sample temperature, thus a surrounding thermo-electrical insulator surface is required as well.

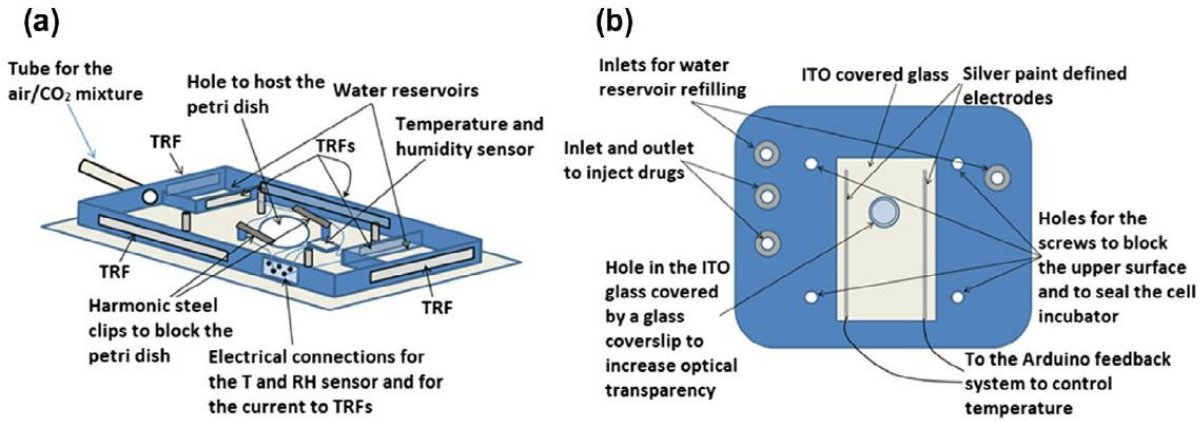

Figure 2: (a) scheme of the main components of the cell incubator; (b) scheme of the cell incubator cover showing the ITO covered

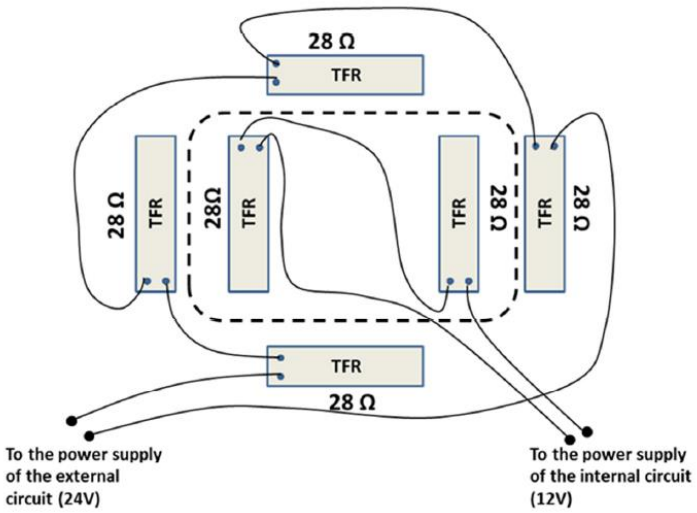

Figure 3: Electrical connection scheme of the TFRs used to heat the cell incubator and favor the increase of the relative humidity inside the cell incubator. The dashed line represents the boundary between the internal and the external TFRs.

The schematic representation of the case is reproduced in Fig 2.

To control the internal temperature, we used both Thick Film Resistors (TFRs) and an Indium Tin Oxide (ITO) covered glass slide, as mentioned above.

In Fig 3 are reported the detailed electrical connections of the TFRs, as showed in the figure the internal and the external TFRs series are power up by two independent power supplies, to better calibrate the cell incubator temperature during initial heating phase. In particular, external TFRs are not necessarily required

or needful but reduce noticeably the pre-heating phase time. When the cell incubator temperature reaches approximatively ≈34-35°C the external TFRs power supply can be turned off and the ITO PID feedback is

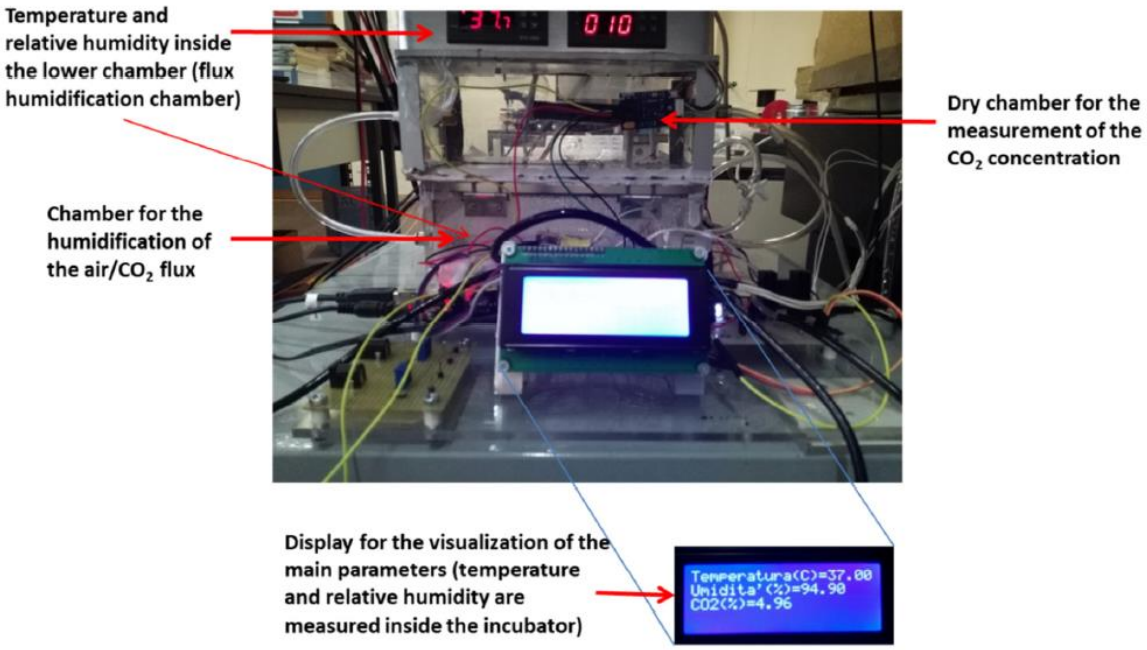

Figure 4: Picture of the set-up external to the on-stage cell incubator. It shows the chambers used to mix air and CO2 and to humidify the mixture before sending it to the incubator and the display used to visualize the parameters inside the incubator.

switched on. In fact, turning on the ITO window PID control when the chassis temperature is still far from the physiological condition will introduce a high rebound in temperature curve profile when the setpoint (37°C) is finally reached. The internal TFR are always powered up to assist the ITO window and prevent cell sample medium evaporation. In fact, the internal humidity is maintained by two water reservoirs that are heated by TFRs. The CO2 concentration is measured by a 10,000 ppm MH-Z16 NDIR CO2 sensor with I2C/UART 5V/3.3V Interface for Arduino from Sandbox Electronics. The internal humidity and temperature are measured by an Arduino sensor (DHT22 – AM2302, Aosong Electronics Co., Ltd) placed just aside from the petri-dish but still below the ITO window to reproduce accurately the cell sample condition. The whole system is controlled by the Arduino Uno microprocessor. The Arduino microprocessor is interfaced with the LabView software to allow the real-time monitoring and storing of the cell-incubator parameters. In particular, the cell incubator parameters are stored in a .txt file recording also the related time and date values in order to recover the actual cell sample conditions of each image frame once the session is concluded. The values of temperature, CO2 concentration and humidity are also visualized on an LCD Arduino display with four lines and are updated approximatively every 2 seconds. CO2 gas is taken from a pressure bottle typically used for controlling the CO2 presence inside aquariums (ASKOLL CO2 PRO GREEN SYSTEM). The CO2 source is connected to a reducer, which coarsely pre-regulates the gas flux. The humidified air/CO2 mixture is delivered inside the incubator using a 12V pump (AIRPO 12VDC). To control the amount of CO2 inside the cell incubator a solenoid valve (PARKER) is used and its open/close state is controlled by Arduino. A similar pump is used to mix the atmospheric air with CO2. In Fig 4 the external cell incubator set-up is reported: it includes the Arduino Uno board and circuit, the dry-chamber, the humidified pre-chamber and the LCD display.

The different parts of the chassis have been designed by a freeware program, which is able to produce a G-Code (Geometric Code) and the cuts have been obtained using a numerical control milling machine (Proxxon MF70). Anyway, any normal mechanical workshop could produce the chassis in about 5-6 hours working-time. The upper and lower surfaces of the case have been made of plastic PMMA, as mentioned above, whereas the lateral wall is made of aluminum to allow heat conduction. In the bottom surface a circular hole (30 mm diameter) has been milled in order to host petri dishes of different diameters. Additionally, a couple of harmonic steel clamps have been installed close to the circular hole in order to fix the petri position. Inside the chamber two water reservoirs have been constructed with a total volume of 40 ml. TFRs have been glued to the walls of both reservoirs in order to allow water heating. At the same time, along the external walls of the aluminum lateral barrier other 3 TFRs have been glued and 2 of them are located in a position corresponding to the internal water reservoirs. All the connections to the TFRs are reported in Fig 2. To obtain a good optical transparency for acquiring phase contrast images of the cells, part of the upper surface was made with an ITO coated glass. The ITO window must also prevent water condensation along the optical pathway, the glass has been then modified introducing two linear electrodes using silver paint (See Fig 5 right). In Fig 5 left the cell incubator chassis assembling is reported.

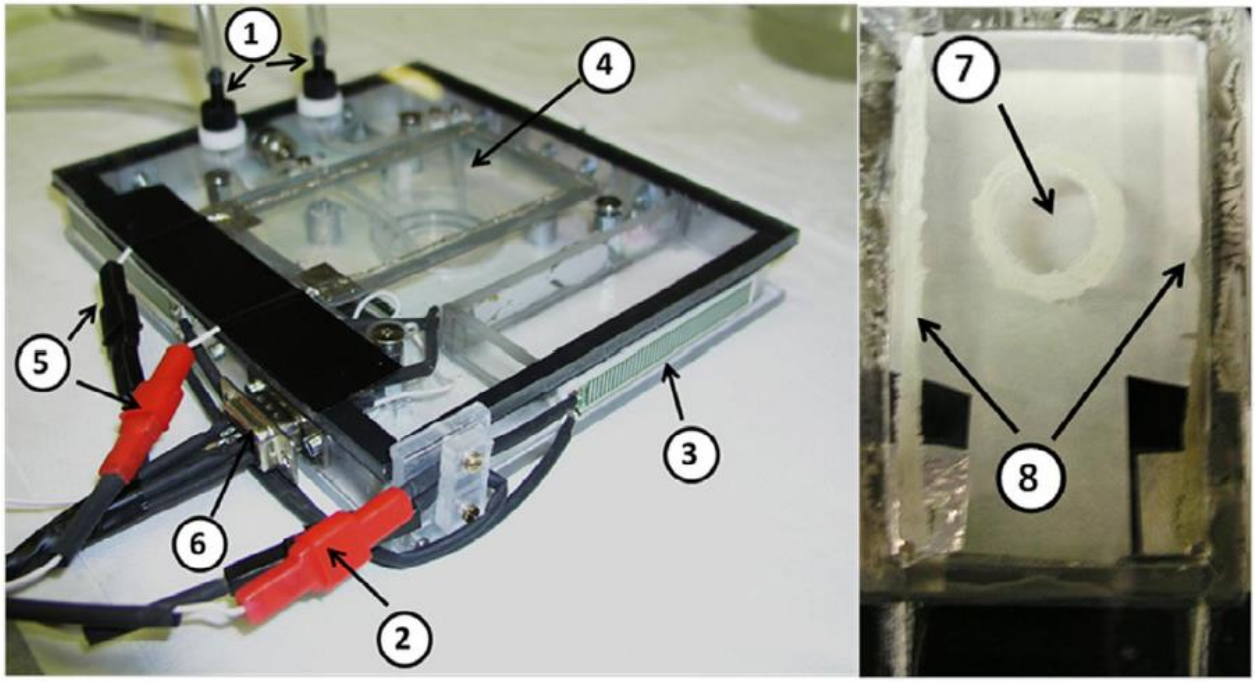

Figure 5: Picture of the assembling of the incubator chamber and of the ITO glass: (1) connections for the injection of drugs and perfusion of different media in the petri dish; (2) electrical connections for the TFRs external to the chamber; (3) TFR; (4) ITO glass before cutting the hole for the glass coverslip (see (7)); (5) electrical connections for the current to the ITO glass; (6) connections to the internal region of the chamber: T and RH sensor, internal TFRs circuit; (7) circular glass coverslip to increase the optical transparency; (8) silver paint electrodes on the ITO glass.

The electrodes are then connected to the Arduino feedback system to control the current going through the ITO glass. The aim of the ITO glass is that of providing heat to warm the cell incubator but at the same time to keep the upper surface at a higher temperature with respect to the internal chamber. Essentially, the current regulation through the ITO window slightly heats the underlying cell sample but does not constitute the main heating source that is managed instead by TFRs. The ITO glass functionality avoids water vapor condensation on the upper surface, which could hamper optical transparency. To further increase optical transparency, we cut the ITO glass in the region just above the petri dish producing a circular hole. The hole was then closed using a glass coverslip glued by a conductive glue to the ITO glass. In practice, the TFRs are powered by a constant power supply assuring a temperature just below 37 °C. The ITO glass is connected to a variable power supply controlled by an Arduino feedback system using a PWM signal (Pulse-Width-Modulation) to adjust the temperature exactly to 37 °C. Fig 4-5 and Fig 6 show pictures of the on-stage

incubator we constructed and of how the incubator is positioned on the stage of an inverted optical microscope.

In the upper surface of the chassis we made several holes for inlet and outlet tubes to inject reagents inside the culture medium and to perform exchange of the medium by using a syringe pump. We also inserted two inlets to perform a refilling of the water reservoirs for very long imaging sessions. To automate the image acquisition system, we implemented an autofocus process and the possibility of switching on and off the light of the microscope by Arduino. In fact, the light exposition results cytotoxic for the cell sample and must be reduces as much as possible, so it is only exploited during the image acquisition phase. The automatic autofocus is managed by another Arduino, which works independently from the cell incubator control system. The autofocus is based on a stepper motor connected to the focus knob and controlled by Python via Arduino and a motor shield. The same Arduino controls also the switching on an off of the microscope light by exploiting a relay and a 5V TTL signal. The details of the automation process and related algorithm are reported below. Before each imaging session the cell incubator was kept for at least 15 min under UV irradiation to sterilize the internal components of the device.

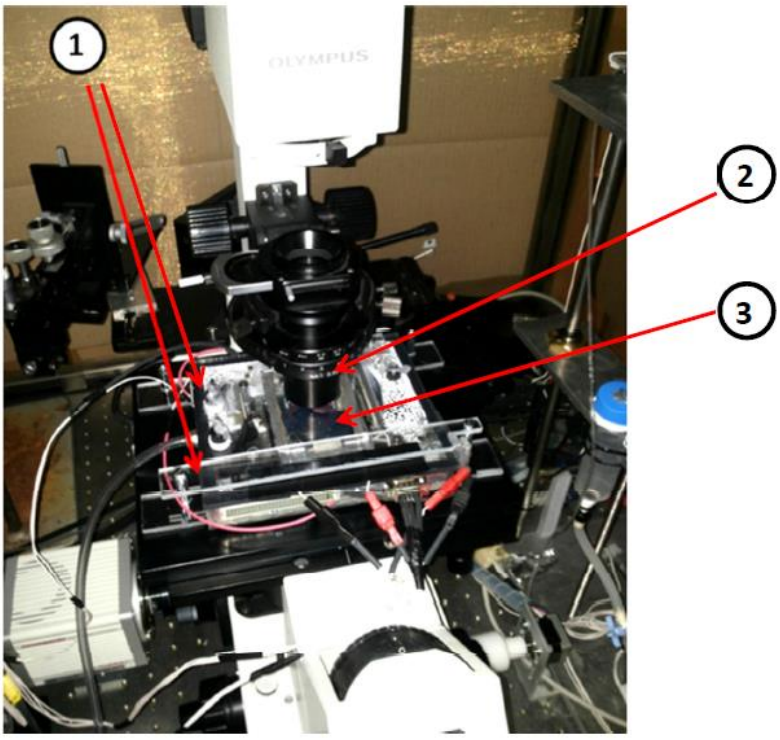

Figure 6: Cell-incubator mounted on the optical microscope stage. Two plexiglass bars (1) are used to rigidly couple the cell-incubator chassis (3) to the microscope stage. The microscope condenser (2) is positioned very near to the incubator. All the system is inside a box to protect cells from light exposure.

- # PID feedback and electronic development

In this section we will illustrate the PID (Proportional-Integral-Derivative) feedback system adopted for CO2 and temperature control, respectively. Then, we will show the PID controller parameters tuning for the CO2 and temperature management.

Briefly, the PID represents one of the fundamental (negative)-feedback control algorithms at infinite-loop. The PID controller manages a physical parameter measuring continuously the error signal $e(t)$, a time t dependent function defined as the difference between the required setpoint value and the current measurement [Eq 1]:

$$e(t) = r(t) - y(t)\ [1]$$

Where $y(t)$ is the physical parameter measurement and $r(t)$ is the required setpoint. The PID controller is connected to the sensor, which measures the physical parameter and to the actuator that influences the physical parameter value. The error signal $e(t)$ constitutes the input signal of the PID controller, then the output signal $u(t)$ [Eq 2] (a function depending of the error signal) is evaluated and exploited in order to the actuator action.

$$u(t) = K_p e(t) + K_i \int_0^t e(t')dt' + K_d \frac{d}{dt} e(t)\ [2]$$

The output signal $u(t)$ is composed of three different terms: The proportional term: $K_p e(t)$, the integral term: $K_i \int_0^t e(t')dt'$, and the derivative term: $\frac{d}{dt} e(t)$. These factors are in fact proportional to the error signal: $e(t)$, its time integral: $\int_0^t e(t')dt'$, and its time derivate: $\frac{d}{dt} e(t)$, respectively. [Eq 2] is a linear combination of these factors where: K_p, K_i, and K_d are the constant parameters (the PID controller parameters). The PID parameters must be finely tuned to obtain the fastest, precise, and accurate physical parameter response in order to reach the required setpoint. In Fig 7 the PID controller scheme, the input signal, $e(t)$ is reported , and the subsequent output signal $u(t)$ evaluated using [Eq 2] is highlighted. The plant/process block represents the actuator element, which is driven by the PID output signal.

The PID scheme shows the basic principle of the negative-feedback controller. In particular, current output

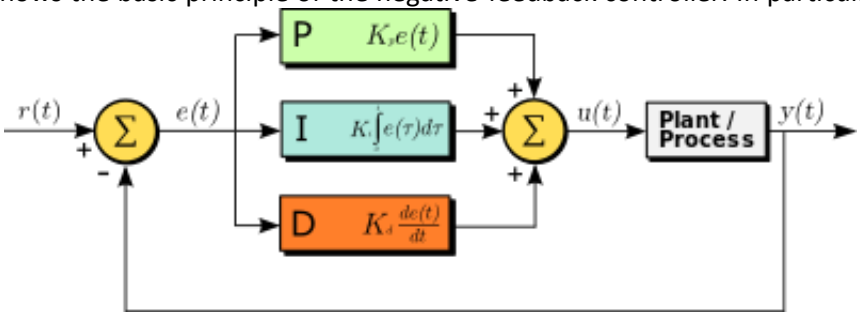

Figure 7: Representative PID controller scheme.

modification will alter actuator action and future physical parameter measurements, but new physical parameter measurements will introduce a new error (input) signal $e(t)$ and the output signal $u(t)$ will be subsequently re-computed and so on. Thus, changes in the output signal $u(t)$ evaluated from an initial error (input) signal $e(t)$ will provide a cascade effects that finally modify again the input signal. For this reason, this kind of controller is called negative-feedback controller since it is based on a loop mechanism depending on the subtraction between the setpoint and the current measurement [Eq 1]. Thus, in a PID controller the input $e(t)$ and the output $u(t)$ signals are reciprocally influenced and the controller is also called "closed-loop system". The crucial feature of a PID controller is its stability, whenever a new setpoint is assigned, the physical parameter reaches the setpoint with certain fluctuations. If the physical parameter measurement fluctuates systematically around the setpoint but fluctuation amplitudes increase during time then the system is unstable. If the physical parameter fluctuation amplitudes around the setpoint are stationary, then the system is partially stable. Finally, when the physical parameter stabilizes around the setpoint, and the fluctuation amplitudes reduce during time then the system is stable. During PID controller calibration the proportional, integral, and derivative parameters $[K_p; K_i; K_d]$ are finely tuned in order to prevent physical parameter over-oscillations, the ideal physical parameter response is the critical-damping profile.

Here we briefly summarize the role of the proportional, the integral, and derivative factor respectively.

The proportional contribution is based on the pure error signal: $e(t)$. Consequently, an active (not null) actuator response is provided only if the error (input) is not zero. Clearly a pure proportional controller (P) cannot reach the required setpoint since a net discrepancy between the setpoint and the measurement [Eq 1] is needed in order to apply a net contribution to the actuator state. This setpoint-measurement discrepancy becomes smaller during time reaching a stable and not zero value, even increasing the proportional coefficient K_p. Gradually increasing the proportional parameter, the asymptotic measurement approaches the setpoint and the speed response of the controller is also increased. Nevertheless, the initial fluctuation amplitudes and frequency of the physical parameter around the setpoint become higher and slowly reduce during time. Consequently, the controller is less stable for too high proportional parameter value. In Fig 8 the physical parameter response in a P controller for different proportional coefficient values is reported.

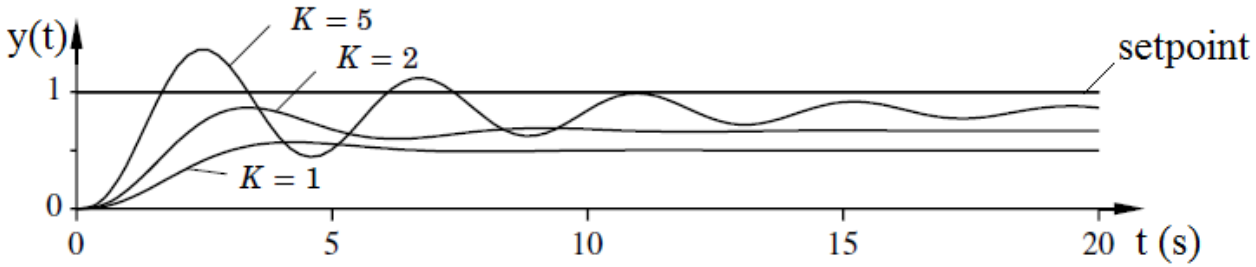

Figure 8: Physical parameter response y(t) obtained by pure P controller for several K_p proportional parameter values.

The integral factor essentially mediates the previous physical parameter measurements during time, starting from the controller initialization. Thus, the integral factor is proportional to the time-averaged of the physical parameter measurement. Now the output signal of the PI controller depends on the current measurement (like the pure P controller), but also on the previous measurements of the physical parameter. In Fig 9 is reported the physical parameter response produced by a PI controller.

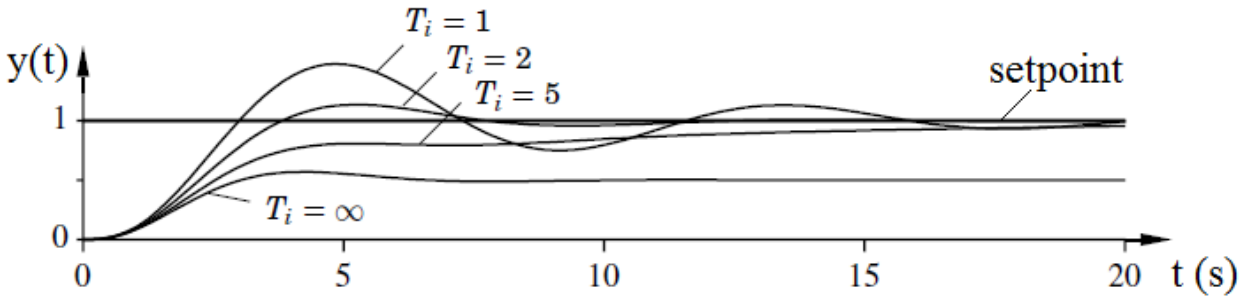

Figure 9: Physical parameter response y(t) obtained by a PI controller for several Ki integral parameter values at fixed K_p=1. The time constant T_i has been defined as follows: $T_i = {K_p}/{K_i}$

The response of the physical parameter in a PI controller becomes faster and more accurate than the pure P controller. In particular, the asymptotic setpoint-measurement discrepancy is removed. Even the controller stability is increased with respect to the P case. The PI controller introduced also an undesired effect called "Wind-up" (see Fig 10). When the current measurements remain systematically higher or lower than the setpoint for a certain amount of time the output signal can overcome the operating range of the actuator and the hypothetical response provided by the PI and the actual response applied on the actuator are different.

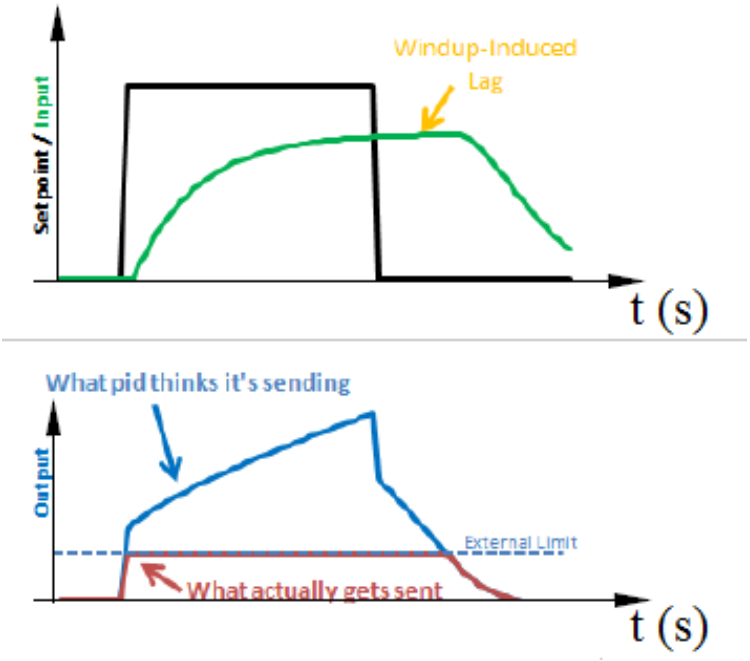

Figure 10: Wind-Up effect representation when the setpoint (black curve) vary as a step profile. A clear discrepancy between the actual output (red curve) which govern the actuator and the PID output (blue curve) signal is observed.

A possible solution of the Wind-Up effect is to remove temporary the integral contribution until the output signal return within the actuator operating range.

The last factor is the derivative term. This contribution measures the rate of change of the error signal and can provide a forecast of the future error values, for this reason the derivative term represents an "anticipatory role". As observed in Fig 9 in the PI controller the fluctuating transient in the response of the physical parameter is still present, using a PID the derivative term can dump these fluctuations delaying the setpoint achievement. In Fig 11 is reported the physical parameter response in PID controller for several derivative coefficient values keeping constant the K_p and K_i parameters, gradually increasing the derivative

term up to T_d=1.5. The transient fluctuations are dumped and a theoretical "critical-dumping" profile is achieved.

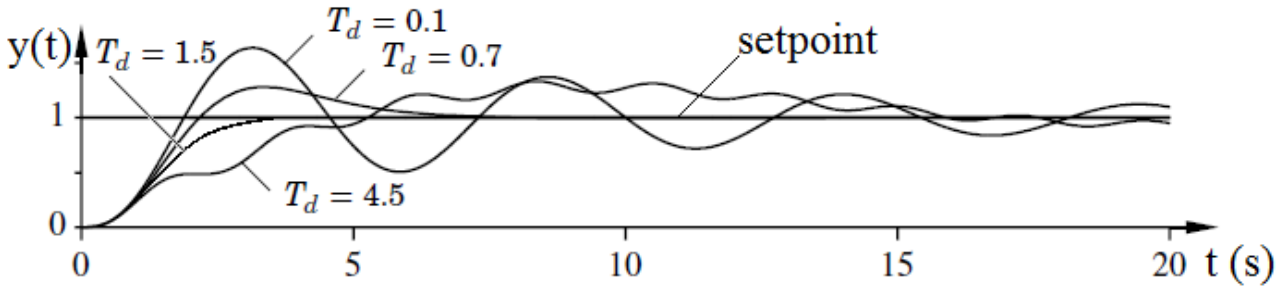

Figure 11: Physical parameter response y(t) obtained by a PID controller for several Kd derivative parameter values at fixed Kp and K_i values. The time constant Td has been defined as follows: $T_d = {K_d}/{K_p}$

The derivative factor has two possible undesired effects. Firstly, if the physical parameter measurement has a white noise contribution with amplitude A and frequency F, this periodic noise is magnified by a factor F when the temporal derivative is evaluated, and is finally transferred in the output signal with a net amplitude: $K_d AF$. This white noise amplification in the output signal and its subsequently transfer in the physical parameter measurement is highlighted in Fig 11 for T_d>1.5. Secondly, each time the setpoint is modified the temporal derivative of the error undergoes a fast change in the next output evaluation. This effect is called "Derivative Kick" and can produce large and undesired actions in the actuator, which could damage the actuator itself. This effect can be avoided evaluating only the derivative of the measurement ignoring the setpoint contribution. In Fig 12 an example the Derivative Kick effect is reported.

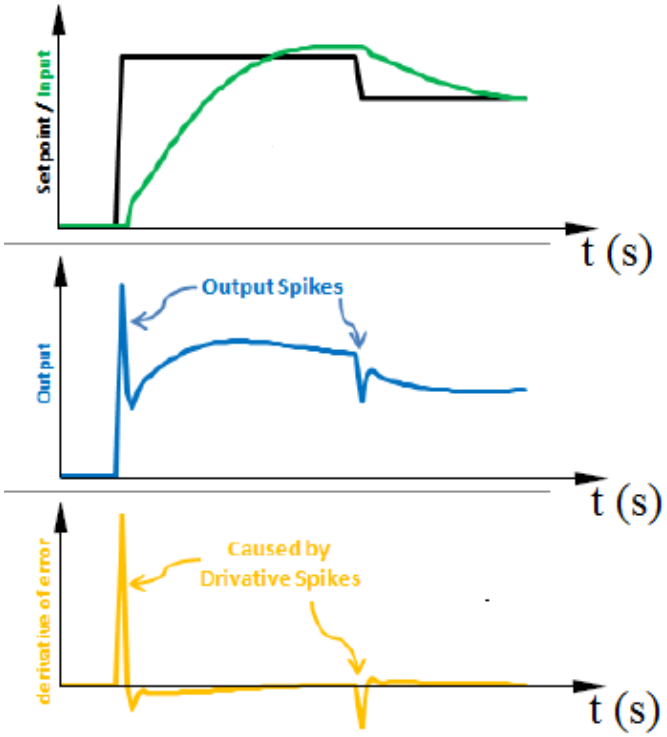

Figure 12: Derivative Kick effect representation when the setpoint (black curve) vary as a step profile. The derivative of error (yellow curve) and subsequently the output signal (blue curve) undergo fast variations assimilable to spikes profiles.

After this brief PID theory introduction we will calibrate the PID set parameter $[K_p; K_i; K_d]$ for the CO2 and temperature control, respectively.

The PID algorithm contained in the Arduino libraries already includes the Wind-Up and the Derivative Kick effects compensation. The PID function and its parameter set $[K_p; K_i; K_d]$ must be defined in the script initialization, since we have two physical parameters to control, two PID functions must be initialized. We first consider the CO2 concentration, we will must focus on the CO2 sensor and actuator mechanism of action, then we will calibrate the PID parameters $[K_p; K_i; K_d]$.

To measure the CO2 concentration, we used a NDIR (Non Dispersive InfraRed) sensor that measures the concentration of CO2 by recording the received IR light intensity through a defined pathway in the same environment. NDIR sensors detect the molar density of the gas from the number of CO2 molecules in the path of the beam, but the output is typically provided as volume percent. The amount of radiation that is absorbed by CO2 is proportional to the concentration of CO2 in the environment in terms of ppm. However, if the pressure, the temperature, or the amount of water humidity change, considering that the light-pathway is constant and that the molar density and percentage with respect to other gases could be affected in a different way, also the CO2 concentration detected by the sensor will change. In fact, an increase of the pressure will increase the density of CO2 molecules in the light-pathway whereas, in case of constant pressure, the increase of the water vapor pressure will remove part of the CO2 molecules in the pathway (dilution effect). Obviously, the number of water molecules in the pathway will not affect the signal recorded by the NDIR sensor for CO2. In our system we cannot use the CO2 sensor inside the cell incubator chamber because the high humidity produces a large condensation on the windows of the IR emitter and detector affecting the detected signal. To avoid this problem, we detect the CO2 concentration in a dry environment before sending the air/CO2 mixture inside the cell incubator. If we keep CO2 concentration in the dry environment to 5%, once inside the incubator CO2 will be 'diluted' by the presence of the water vapor molecules obtaining a lower concentration. Considering published conversion tables (see table 1) and the dewpoint inside the incubator (about 36 °C resulting from a temperature of 37 °C and 98% relative humidity), which can be calculated according to the August-Roche-Magnus approximation [10] [Eq 3 4a-b], and the dewpoint of the CO2 measurement chamber (about 9 °C resulting from a temperature of 25 °C and 40% RH) the correction factor is about 0.939. It results that for the CO2 setpoint in the dry environment we have to use a value of 5.3% which should correspond to 5% inside the cell incubator.

Td (°C)	-40	-30	-20	-10	0	10	20	30	40	50	60
-60	0.9999	0.9996	0.999	0.997	0.994	0.988	0.977	0.958	0.927	0.878	0.803
-50	0.9999	0.9997	0.999	0.997	0.994	0.988	0.977	0.958	0.927	0.878	0.803
-40	1.0000	0.9998	0.999	0.998	0.994	0.988	0.977	0.958	0.927	0.878	0.803
-30		1.0000	0.999	0.998	0.994	0.988	0.977	0.958	0.928	0.879	0.804
-20			1.000	0.998	0.995	0.989	0.978	0.959	0.928	0.879	0.804
-10				1.000	0.997	0.990	0.979	0.961	0.930	0.881	0.806
0					1.000	0.994	0.983	0.964	0.933	0.884	0.809
10						1.000	0.989	0.970	0.939	0.890	0.815
20							1.000	0.981	0.950	0.901	0.826
30								1.000	0.969	0.920	0.845
40									1.000	0.951	0.876
50										1.000	0.925

Table 1: CO_2 concentration correction factor.

$$T_{dew} = \frac{b\left[\ln\left(\frac{RH}{100}\right) + \frac{aT}{b+T}\right]}{a - \ln\left(\frac{RH}{100}\right) + \frac{aT}{b+T}} [3]$$

where $a = 17.625$ and $b = 243.04$, the temperatures T and T_{dew} are expressed in °C and RH the relative humidity in %. To obtain the environmental condition T and RH we can use the following set of equations [Eq 4a-b]:

$$\begin{cases} T = \dfrac{b\left[\frac{aT_{dew}}{b+T_{dew}} - \ln\left(\frac{RH}{100}\right)\right]}{a + \ln\left(\frac{RH}{100}\right) - \frac{aT_{dew}}{b+T_{dew}}} [4a] \\ RH = 100\dfrac{e^{\left(\frac{aT_{dew}}{b+T_{dew}}\right)}}{e^{\left(\frac{aT}{b+T}\right)}} [4b] \end{cases}$$

The CO2 is taken from a pressure bottle typically used to maintain the presence of CO2 inside aquariums. The bottle is connected to the measurement chamber by a tube passing through a solenoid valve (continuous regulation). The flux through the valve is controlled by a bias voltage provided by Arduino and controlled by a feedback scheme.

The air/CO2 mixture is then humidified passing through a chamber containing a large water reservoir and a rectangular piece of ITO glass glued to the wall of the reservoir and endowed with two electrodes produced by two lines of silver paint. The electrodes are connected to a power supply and the water is then heated and the humidity and temperature inside the chamber are measured (37 °C, 100% RH). The humidified mixture is then delivered to the incubator chamber by a vacuum pump and tubing provided with a valve manually controlled in order to obtain an equilibrium condition for all the parameters of interest. The circuit for the preparation of the air/CO2 mixture to inject inside the cell incubator is shown in Figure 13.

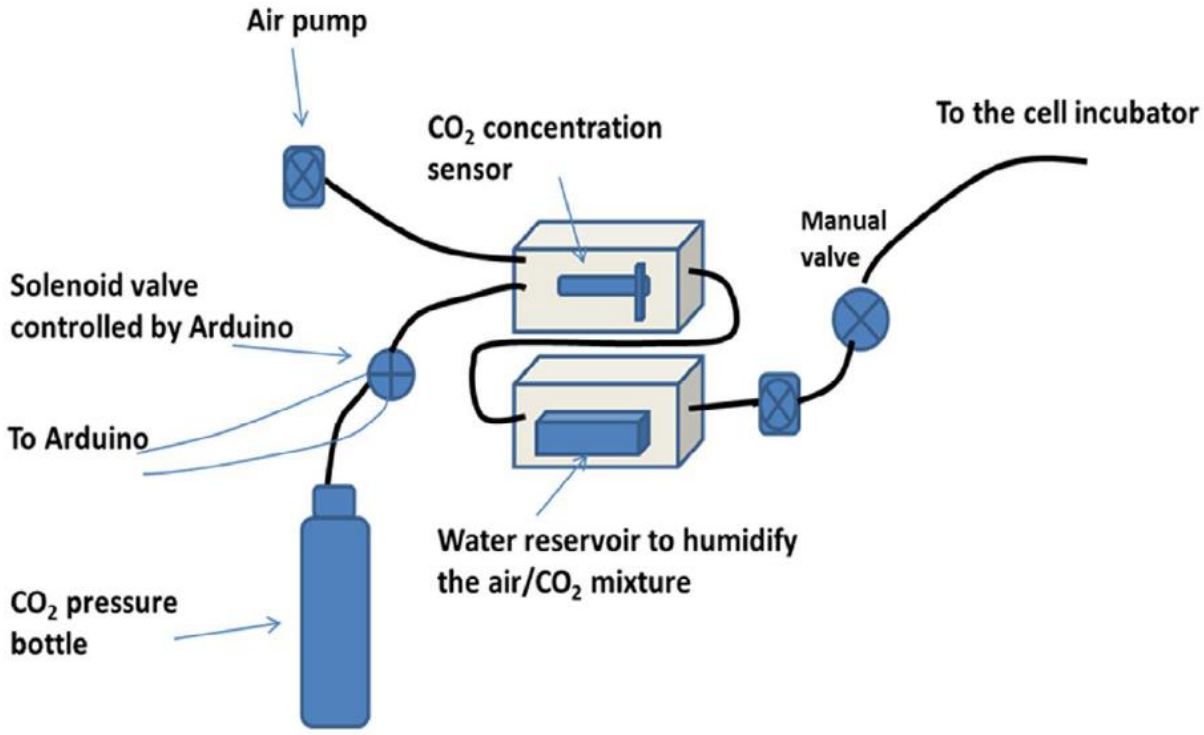

Figure 13: Scheme of the gas flux circuit used to inject the air/CO 2 mixture inside the cell incubator. The CO 2 concentration is measured outside the incubator in a dry environment at 25 °C. The setpoint is in this case set to 5.3% according to the dilution effect due to the water vapor.

The PID parameters calibration $[K_p; K_i; K_d]$ has been performed substituting the cell incubator chassis to an identical empty case and inserting inside a second CO2 sensor. This additional test verify that the CO2 amount measured in the pre-chamber is correctly transferred inside the incubator. We observed that the CO2 sensor measurement provides not negligible inertia and we decided to calibrate the PID controller focusing mainly on the derivative and proportional contributions.

Here we will focus on the PID parameters calibration for the temperature control. The temperature is acquired by a DHT22 sensor, which is placed below the ITO window, the current flux passing through the ITO is controlled by a transistor (IRF-740). The transistor is driven by a PWM Arduino output signal, which spans between [0;255] range. The PWM state is defined using the output signal evaluated by the PID controller using Eq 1-2 where y(t) is the current temperature measurement. Since the ITO glass is only able to heat but cannot cool down the underlying cell sample, when the current measurement overcomes the setpoint the current flux is interrupted using a relay. During the PID calibration procedure we focused on the derivative contribution required for a high level of inertia of the system, but also including a not null integral parameter.

The DHT22 sensor can also measure the relative humidity percentage. This physical parameter must be as high as possible to prevent cell medium evaporation (>90-95%) and is not directly managed by a PID controller.

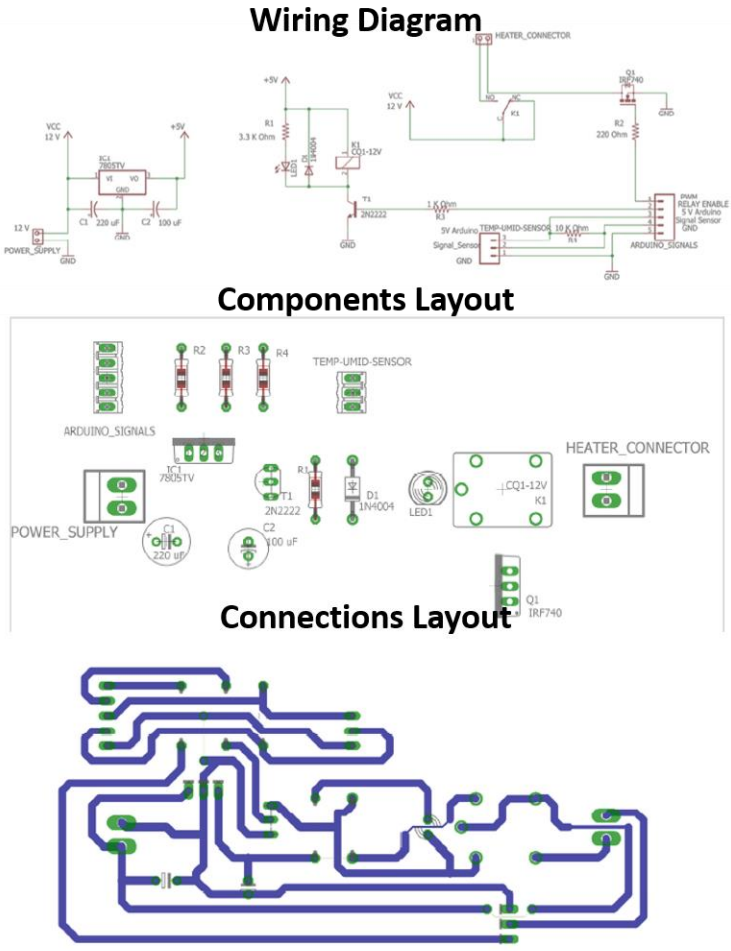

Figure 14: Detailed scheme of the DHT22-ArduinoUno circuit interface.

The whole system is controlled by the Arduino Uno microprocessor (the detailed circuit interface between DHT22 sensor and the Arduino Uno board is reported in Fig 14). Temperature, relative humidity and CO2

concentration are visualized on a LCD Display controlled by Arduino with a refresh time period of 2 seconds. To test the physiological cell incubator parameters (CO2 percentage, Temperature, and relative Humidity) and its stability during time, we plotted these parameters as a function of time (especially the Temperature). in Fig 15a is reported the temperature parameter profiles during 6-7 hours of live imaging session. During

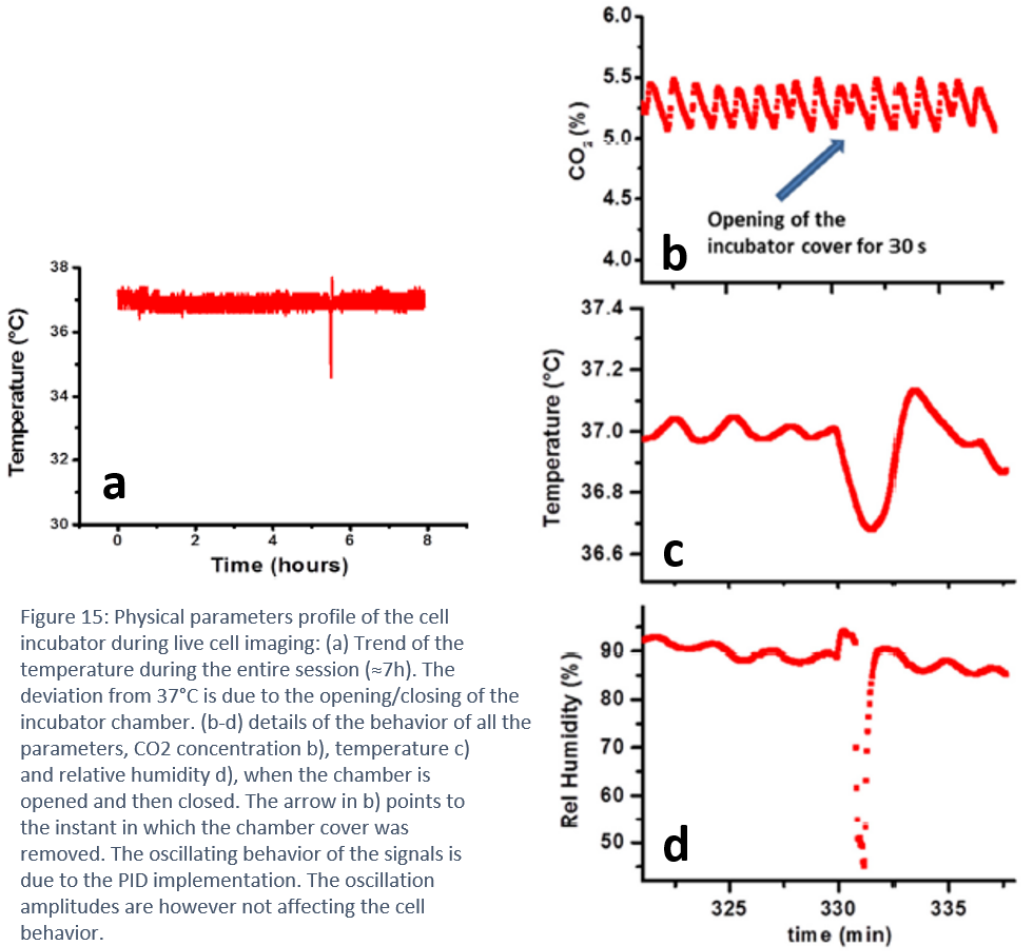

Figure 15: Physical parameters profile of the cell incubator during live cell imaging: (a) Trend of the temperature during the entire session (≈7h). The deviation from 37°C is due to the opening/closing of the incubator chamber. (b-d) details of the behavior of all the parameters, CO2 concentration b), temperature c) and relative humidity d), when the chamber is opened and then closed. The arrow in b) points to the instant in which the chamber cover was removed. The oscillating behavior of the signals is due to the PID implementation. The oscillation amplitudes are however not affecting the cell behavior.

the experiment, the cell incubator has been temporary opened to insert exogenous drug in the cell sample and immediately after has been closed again. In Fig 15b-d we can observe the time needed to recover the physiological state after cell incubator closure.

- **Autofocus algorithm**

To automate the image acquisition system we implemented an autofocus process and the possibility of switching on and off the light of the microscope by Arduino. The autofocus is based on a stepper motor connected to the focus knob and controlled by Python via Arduino Uno and a motor shield. When the motorized stage has been developed (see next section), we removed the Arduino Uno and the motor shield replacing them with an Arduino Mega 2560 and several stepper motor drivers. A vertical stack (Z-axis) of images is acquired with an adjustable step size. The contrast of each image is then calculated with a specific algorithm and the image with the highest contrast is selected and stored [11]. The contrast image function C is evaluated summing up the pixel intensity $p[i,j]$ difference (in absolute value) between adjacent pixels, the pixels intensity difference evaluated along the diagonal direction is weighted by a factor: $1/\sqrt{2}$ [Eq 5] (See also Fig 16). The focus knob is moved to the position corresponding to the highest contrast. This position will be the central position around which the focus of the next image will be looked for. The same Arduino

controls also the switching on an off of the microscope light by exploiting a relay and a 5V TTL signal. The details of the automation process are reported in Fig 17 flowcharts.

$$C = \sum_{i=1}^{N_{row}-1} \sum_{j=1}^{N_{column}-1} \|p[i,j] - p[i,j+1]\| + \|p[i,j] - p[i+1,j+1]\| \frac{1}{\sqrt{2}} + \|p[i,j] - p[i+1,j]\| \quad [5]$$

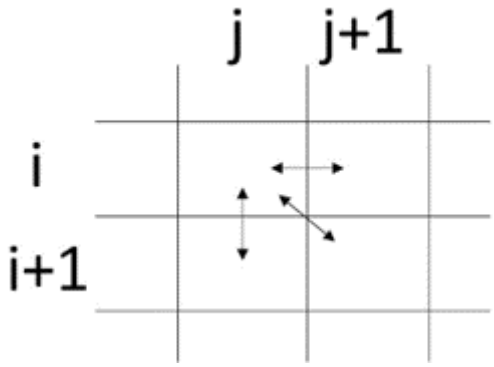

Figure 16: Image contrast evaluation scheme.

Python script scheme:

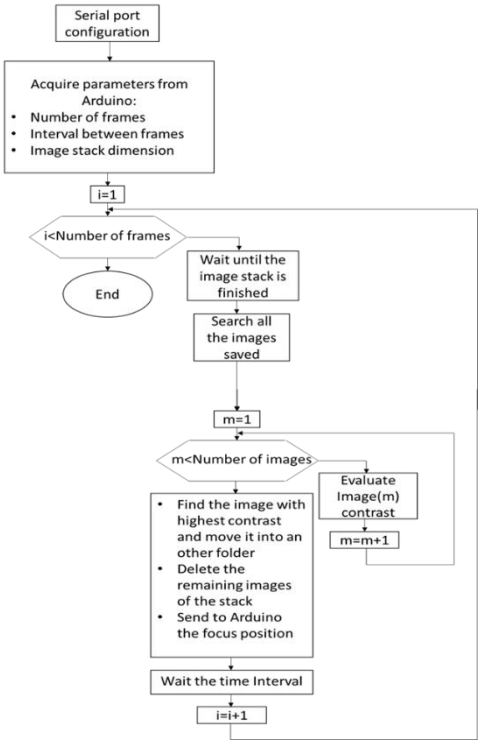

Arduino Uno algorithm scheme:

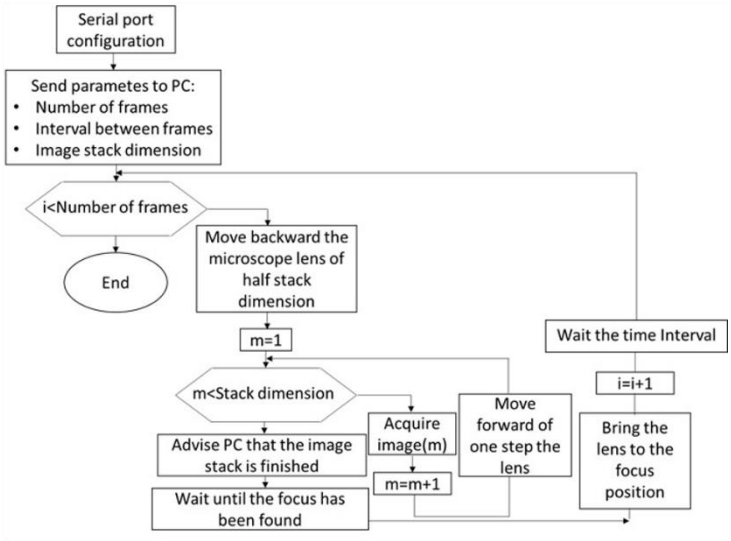

Figure 17: Autofocus algorithm flowcharts: Python script flowchart (left) and Arduino Uno flowchard (right).

In the following improvements (see next section and next chapter [12]) we applied also this automated autofocus algorithm (Eq 5) but we observed some deviations between the actual focal plane and the plane chosen by the algorithm. Essentially, when a PDMS-based substrate is used the substrate imperfections like micrometer-sized encapsulated bubbles falsify the autofocus research method. Thus, the autofocus algorithm based on Eq 5 try to follow the bubbles or other small artifacts present in the surface or inside the substrate. To overcome this issue, we defined as best on-focus plane that one which has the highest contrast variation, evaluated between adjacent planes. This correction is based on the fact that cells are typically larger than the artifacts pattern inside the PDMS substrate, consequently the contrast will vary more when

the objective lens is reaching the cells plane. Usually, the details coming from the inner part of the PDMS substrate are really small compared to the typical cell feature size, so, in the analysis of the contrast variation in the stack of images, the frames where the cells are in focus will have the major contrast variation contribution between consecutives slices. Instead, frames where the PDMS substrate inner details are in focus will present minor variation contributions, and will be discarded. We found that the method based on the maximum contrast can be easily used for images acquired in the Differential Interference Contrast mode or for phase contrast images in the case of an elevated density of cells on the surface. In the case of phase contrast images with mainly isolated cells, the method based on the contrast gradient provided more stable results.

• Cell lines tested

The cells used for the tests were from the U87MG cell line. This line represents a model for Glioblastoma Multiforme. Glial tumors are clinically classified in 4 groups according to their malignancy level. Glial tumors belonging to the IV group are called Glioblastoma Multiforme (GBM) and they are among the most aggressive brain tumors. We used this cell line because U87MG cells are endowed with a high motility and their movement is largely evident even for small incubation periods. U87MG cells (ATCC) were maintained in EMEM growth medium supplemented with 10% fetal bovine serum, 100 g/mL streptomycin, 100 U/mL penicillin and 1% non-essential amino acids (Euroclone Spa, Milan, Italy) under a humidified incubator at 37 °C and 5% CO2. Sub confluent cells were then detached using trypsin-EDTA solution (Sigma, Italy) in calcium-free phosphate buffered saline (PBS) and counted in hemocytometers. For the experiments the cells were seeded ($30\times10^4/cm^2$) in 9.6 cm^2 dishes, and culture medium was changed every 48 hr. The cells were treated using 1G compound in order to test its antimitotic and cytostatic effects (see dedicated chapter). The cells were also exposed to blebbistatin (Sigma-Aldrich, Italy), initially dissolved in dimethyl sulfoxide (DMSO), at 25 μM concentration. The final concentration of DMSO in the culture medium was ≤ 0.1%. Blebbistatin is a well-established inhibitor of myosin II activity. It is known that blebbistatin leaves myosin II in a configuration in which its head is not able to bind to actin in order to exert its contractile activity.

We tested the cell-incubator using the U87MG cell line. The cells were initially plated in a petri dish inside a conventional incubator and allowed to grow for one day. The petri dish was then transferred inside the on-stage incubator for live imaging. Before the transfer, the on-stage incubator was stabilized at 37 °C, 90–95% RH and 5% CO2. The stabilization step requires about 20-30 minutes. The developed apparatus allows to monitor in real-time and to store all the parameters of the incubator exploiting a custom-developed LabView software. Fig 15a shows the registration of temperature values during an imaging session of about 6-7 h. The temperature maintains a value of 37.0 ± 0.3 °C. The oscillation is due to the fact that the control system allows just to heat the system and not to cool it. Accordingly, once the temperature reaches a value lower than 36.8 °C (the setpoint value) the Arduino PID system provides the current to the ITO glass to increase the temperature and the value bounces above 37 °C by 0.3 °C. In this way temperature oscillations are centered around 37 °C. The same happens for the CO2 concentration value. We then evaluated the change in the parameters and the re-equilibration time when the incubator cover is opened and then closed again. This could be the case when the medium has to be changed or drugs have to be added without a perfusion process. Figure [Fig 15b-d] shows the trend of the different parameters when the cover remains open for 30 seconds. The value of the CO2 concentration is practically unaffected. The reason is that CO2 concentration is measured far from the cell chamber, in a dry environment and the concentration of CO2 in the flux that is delivered to the chamber is controlled. Temperature, during the brief opening of the chamber, decreases to about 36 °C and in about 2 minutes the system is again at equilibrium. The most affected parameter when the cover is opened is the relative humidity. However, even in this case, in about 2 minutes the system recovered the correct value for the relative humidity. We initially investigated the spreading phase of cells

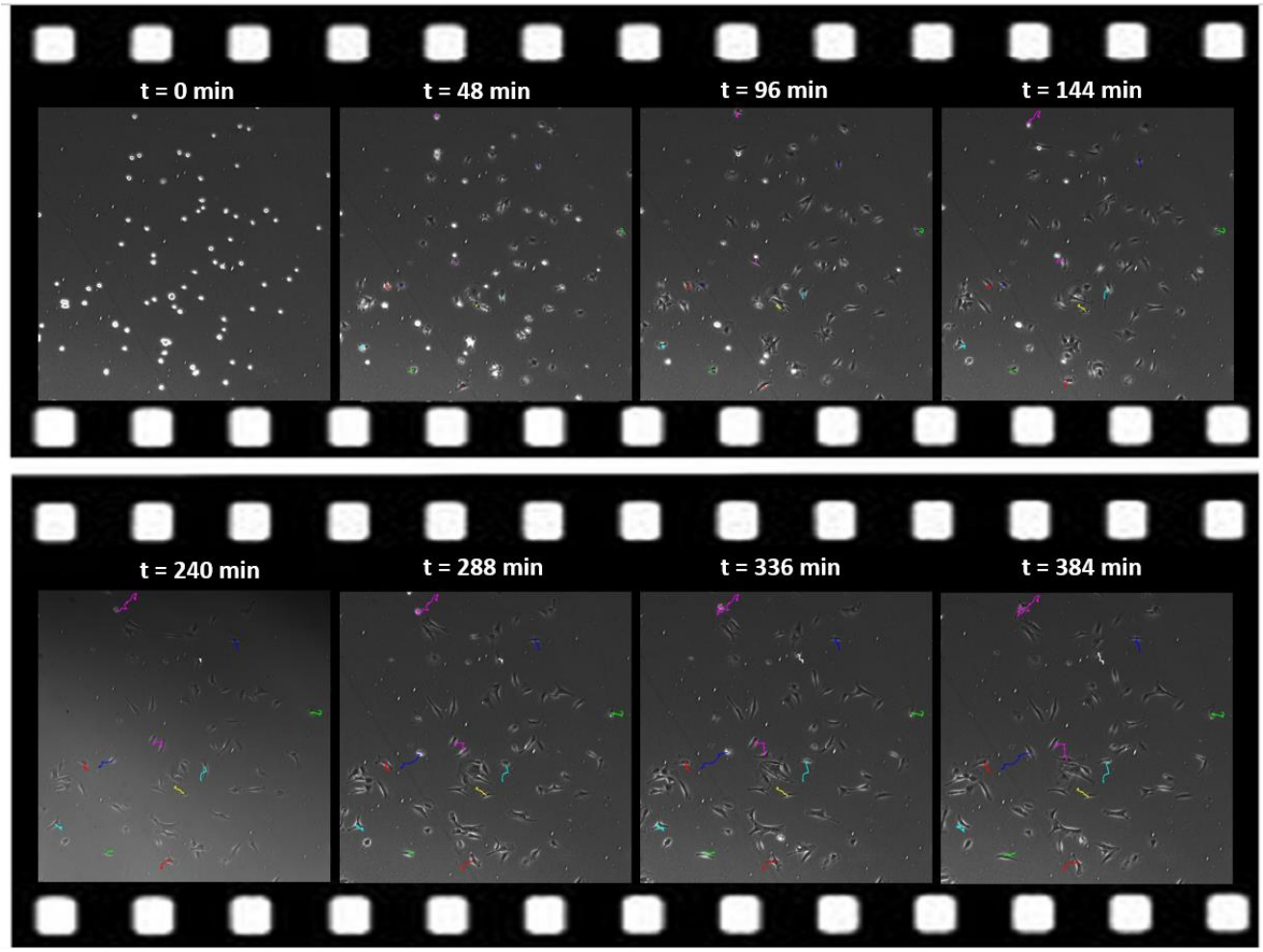

Figures 18 panel: U87MG cell seeding and spreading on plastic substrate over 6.5 hours. Several isolated cells have been manually tracked and the extrapolated paths are highlighted. The imaged area is ≈1330x1330 μm²

just seeded inside the petri dish already mounted inside the on-stage incubator. The images (Figs 18 panel) show that after approximatively two hours of incubation most of the cells spread on the substrate and after 4 hours well defined long processes can be observed.

Figs 18 panel highlights also several paths of manually tracked cells (12 cells) during an imaging period of about 6.5 hours. U87MG cells are moving on the substrate following the typical saltatory migration behavior. Figs 19 panel reports a sequence of images of a tracked cell in which the typical steps of the migration process are clearly evident [13]. Initially, there is a dilation of the leading process. Then, the centrosome and the Golgi

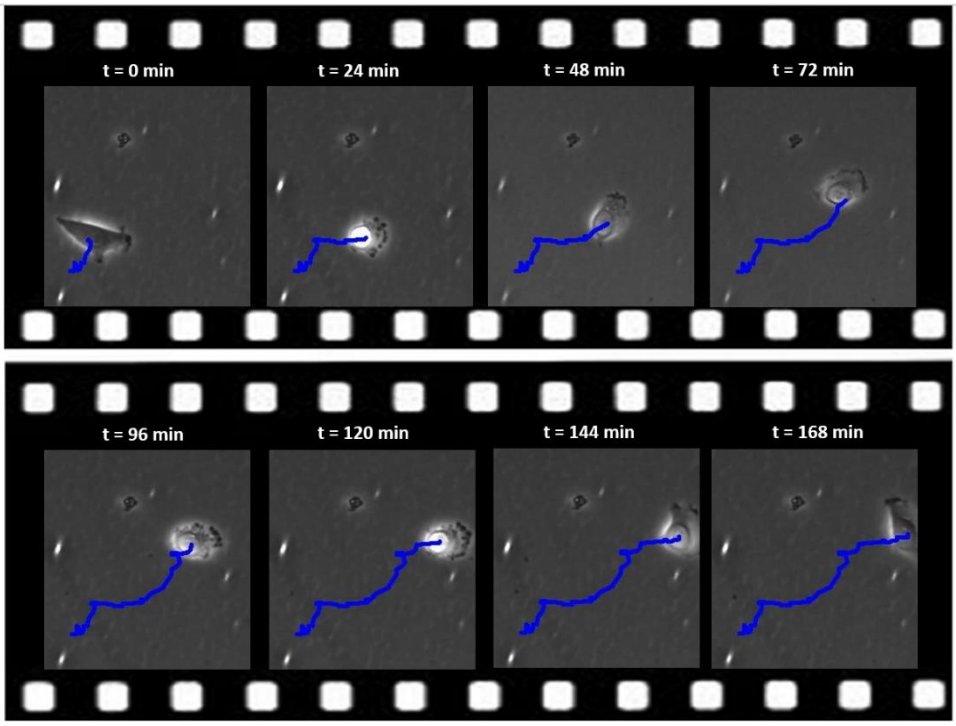

Figures 19 panel: Single cell migration path obtained from manual tracking analysis.

apparatus are transferred to the dilated leading process. Exploiting the contractile activity of the actin/myosin II system the nucleus is then forced to move to the dilated region. The rear part of the cell is then retracted and the cell completely moves to the forward direction.

We then investigated the effect of a drug on the cell behavior in real time. We have chosen to study the effect of blebbistatin on U87MG cells. The effect of blebbistatin on different cell lines has already been investigated [14], [15]. In the case of neurons, it has been found that blebbistatin induces an increase of the length of minor processes. In general, by acting on the myosin contractile motor, blebbistatin affects the stress fibers and the cells adopt a shrinking tendency. Figs 20 panel shows what we obtained in the case of U87MG cells. We exposed the cells to a 20 µM blebbistatin concentration for approximatively 8 hours. Blebbistatin is solubilized in DMSO and we verified that the cells are not affected by the DMSO amount that we insert in the culture medium together with blebbistatin (about 3.5 µL in a total of 2500 µL). Cells, after a few minutes of exposition to blebbistatin, start to retract their soma to a less spread conformation (see Figs 20 panel) and they adopt a largely dendritic conformation. The processes start to increase their length after a few minutes of incubation.

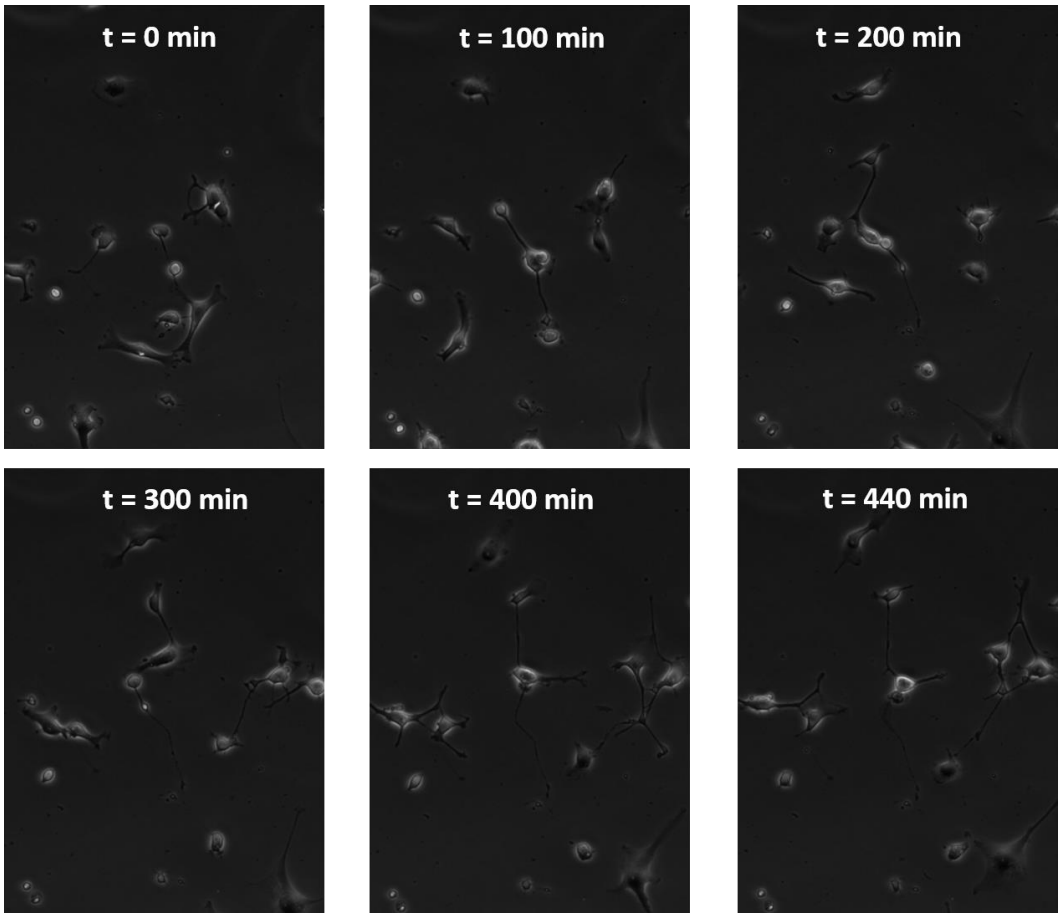

Figures 20 panel: U87MG cells exposed to blebbistatin 20 µM for approximatively 8 hours. The imaged area is approximatively 442x614 µm²

- **Further improvements**

The on-stage cell incubator development and its cell migration results described above refer to the first project, when the cell incubator is placed on the microscope stage. This configuration allows to acquire a single cell sample region per imaging session, limiting the statistical analysis and exogenous drug effect comparison. Here we will report additional modification we exploited to overcome these limitations. Firstly, we developed a custom-built motorized stage, which substitutes the original manual microscope stage, then we redesigned the cell incubator chassis in order to host a multi-six petri dish. Finally, we modified the autofocus algorithm in order to combine an epifluorescence imaging to the previous existing phase contrast technique.

- **Motorized stage**

Experiments where the analysis of cell morphology or migration trajectories have to be evaluated, require a large number of individual cells to be measured. In order to obtain large statistics from a single experiment, we implemented a motorized stage allowing to acquire 4 or 8 images during each time interval or stop in the cyclic stretching protocol. The motorized stage has been assembled using aluminum and PMMA plates, the different parts have been designed and cut using the same numerical control milling machine previously

mentioned. The motorized stage is able to move in the two in-plane directions (X,Y) independently. The X and Y displacements are provided by a couple of Nema 23 stepper motors (using the appropriate drivers DM542) driven by the same Arduino microcontroller used also for the autofocus system. This Arduino manage also additional features (the stretcher device described in the next section [12], and the epifluorescence imaging described below), since an higher number of input and output pins are required for these additional features the original Arduino Uno has been replaced by an Arduino Mega 2560. The stepper-motors does not include the encoder circuit used for counting the effective steps of the motors. Nevertheless, with the appropriate driver (DM542), the torque provided by the motors is in large excess compared to the torque required to move the stage. Moreover, in-plane movements are executed considering the backlash corrections by the software. Before starting the time-lapse imaging acquisition, the different areas of interest are selected and stored in the software (every step in each of the two perpendicular directions plus the vertical adjustments of the focus are counted and stored). They include the in-plane coordinates(X,Y) and the Z position for the best in-focus image. After all the required information for the process are stored, the experiment starts, in a fully automated way, for the total amount of established hours. The autofocus algorithm elaborates the best on-focus plane position for each selected region independently, the procedure is repeated at each image acquisition regions cycle. In Fig 21 the cell incubator mounted on motorized stage is reported (a) front and (b) side view, respectively.

- **Cell incubator chassis for multi-six petri dish**

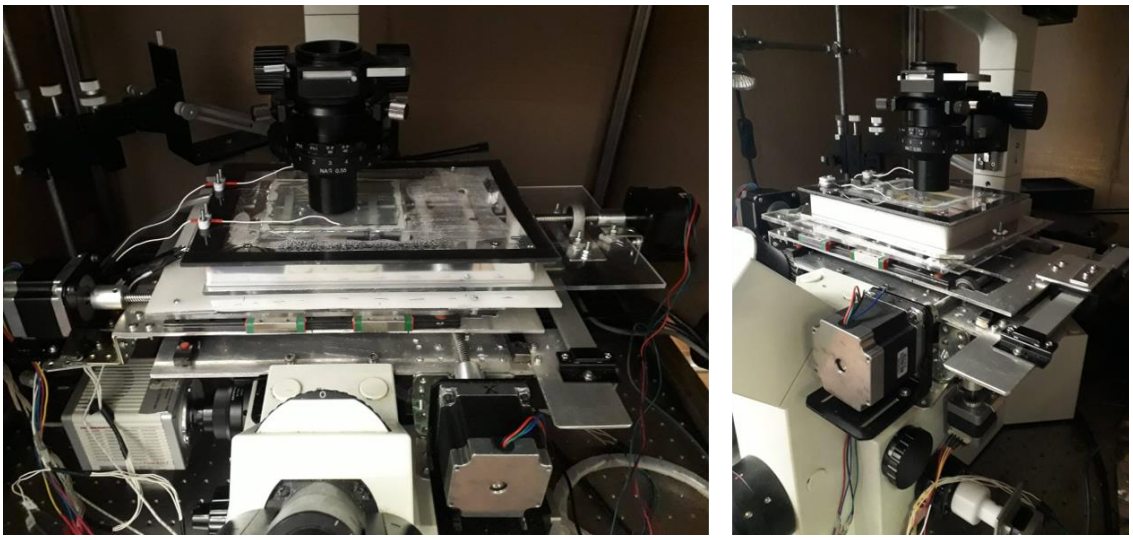

Figure 21: Cell incubator and the motorized stage combined set-up. (a) Front view of the stretcher device included in the cell incubator. (b) Side view of the cell incubator including inside the multi-six petri-dish.

In order to test several exogenous compounds simultaneously on a single live cell imaging session the original cell incubator chassis has been redesigned to host a multi-six petri dish plate. Since the cell incubator is placed on top of the motorized stage whose plate is made of PMMA we decided to use an aluminum plate for the bottom chassis surface. Thus, the heat is uniformly dispersed inside the cell incubator and the underlying PMMA plate of the motorized stage prevent heating flux toward the surrounding environment. In the bottom surface a rectangular hole has been made using the milling machine, which will host the multi-six plastic plate. Two water reservoirs have been placed symmetrically from the central rectangular hole and a couple of TFRs have been glued to the reservoirs walls. The cell incubator cover has been also modified, a rectangular hole in the PMMA surface has been cut in order to contain a larger ITO glass. The ITO glass has been redesigned with a rectangular shape equal to the multi-six plate and has been finally placed on top of the multi-six plate and glued on the cell incubator cover. In Fig 22c-d the new on-stage cell incubator design is reported. In Fig 22a-b the cell incubator device hosting a multi-six petri-dish and a couple of petri dishes is respectively showed. As reported in the figure the petri dishes placed on the top-left and the bottom-left

corners are used to acquire the physical parameters reference. In fact, the DHT22 sensor is put inside the former dish, while the latter dish can accommodate a thermocouple as additional temperature reference directly in liquid. The other 4 petri dishes are used for cell migration assay and can contain different combinations of exogenous compounds. For example, two different drugs can be studied simultaneously using the following scheme: the 4 dishes contain respectively the control, the 1st drug, the 2nd drug, and the 1st+2nd drugs.

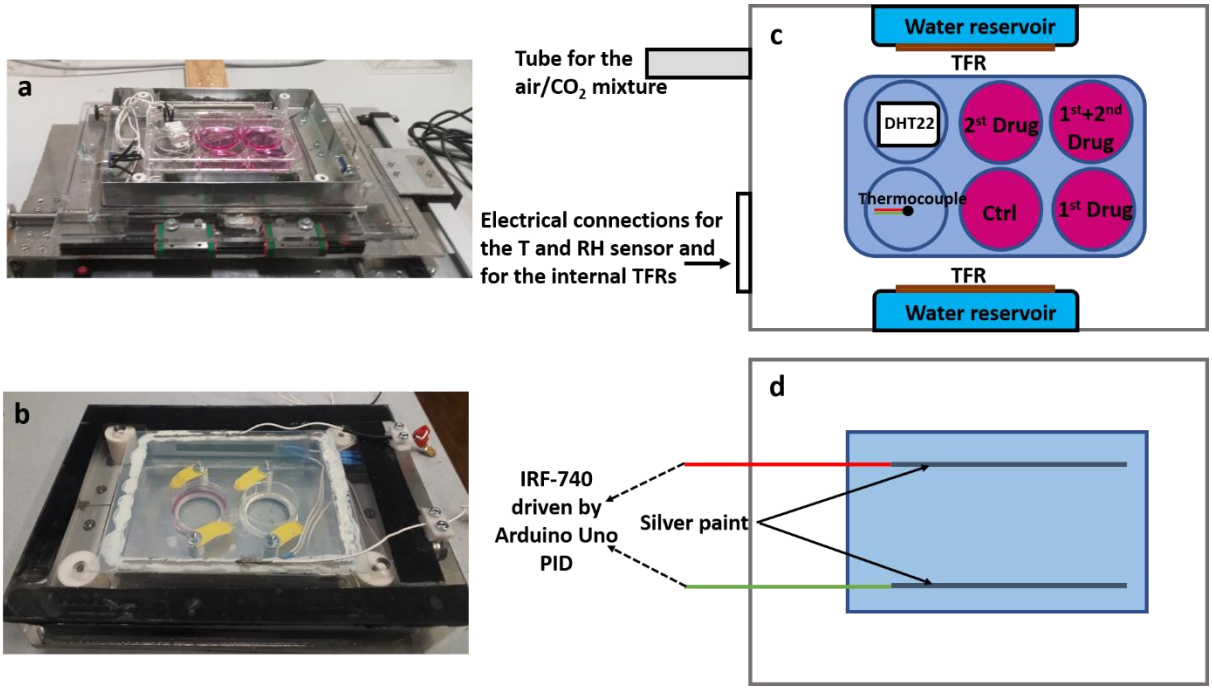

Figure 22: New cell incubator scheme and assembling. (a) cell incubator hosting a multi-six petri-dish. (b) cell incubator hosting a couple of petri dishes. (c-d) Top view of cell incubator scheme.

• Combined phase-contrast and epifluorescence microcopy

Since we are using an inverted optical microscope we could exploit also the epifluorescence microscopy technique. Thus, we modified the previous hardware and software setup that already includes the motorized stage and the autofocus system to accommodate also the epifluorescence imaging.

The epifluorescence acquisition is performed opening the shutter and taking several images and finally closing again the shutter. Normally, the shutter is manually managed and the integration time should be manually modified by the operator as well. The automated epifluorescence imaging acquisition has been performed introducing the following modifications. The shutter has been jointed to a gear that is in mechanical contact to a second gear driven by a stepper motor axis, the stepper motor is able to open and close the shutter and is connected (using the appropriate driver: TB6600) to the Arduino Mega 2560 setup. The issues regarding the different integration times between phase-contrast and epifluorescence microscopy has been resolved modifying the autofocus algorithm. Usually the integration time required for phase-contrast-based techniques is approximatively ≈30ms, while the time required for epifluorescence microscopy is at least ten times longer. During the image acquisition cycle, immediately after that the phase-contrast frame in a given region has been acquired, the shutter is opened and several fluorescence images are acquired using the same vertical plane of reference, whereupon the shutter is closed again. Then, the pixel

intensity arising from the images stack are summed and the resulting image is stored, the images stack is finally removed.

We tested the epifluorescence setup using a co-culture experiment where we superimposing a standard U87MG cell line, and a U87MG genetically modified to spontaneously emit fluorescence signal (luciferase reported). We followed the free migration of the co-culture sample for several hours and finally we overlapped the phase-contrast to the epifluorescence sequences obtained. In Fig 23 a single cell migration snap-shot where the phase-contrast and the epifluorescence images have been overlapped is rereported.

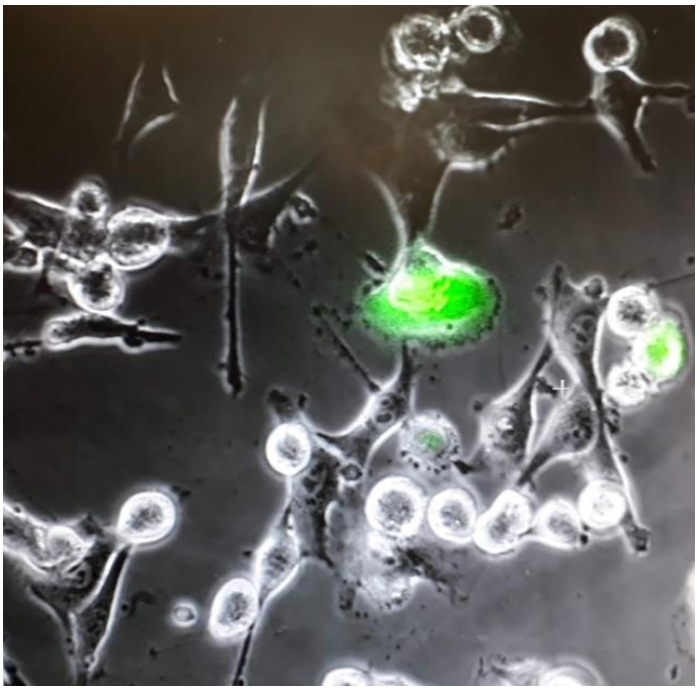

Figure 23: Snapshot obtained from live imaging assays from U87MG (scale gray signal) and U87MG luciferase (green signal) co-culture.

From phase-contrast and fluorescence image superposition we can clearly distinguish which cells belong to the standard U87MG cell line, and which belong to the luciferase-treated line. Furthermore, the cell migration assay confirms that the cell fluorescence signal is stable during time.

Periodic stretching device suitable for living cell assay

• Introduction

It has been largely demonstrated that living cells are affected by mechanical stimuli in a similar way to chemical ones [16]–[19]. Processes that can be modulated by mechanical cues include differentiation, migration and adhesion and living cells in their physiological environments are continuously exposed to stretching or compressing deformations. These situations include both the case of uniaxial stretching, such as for cells of the skeletal-muscle tissues or cells in the walls of vessels exposed to a periodic stretching given by the blood pressure oscillations, and of isotropic stretching, as in the case of hollow structures such as the heart or lungs. Stretching a cell could affect in different ways its behaviour. For example, stretch-activated ion channels such as piezo-channels [20] could be induced to activate, leading to a change of the flux across the membrane of Ca^{2+} ions, generating in this way a cascade of biochemical processes. At the same time, every deformation of the substrate on which cells are growing acts on the focal adhesion complexes, transmitting the mechanical signal to the cytoskeleton inside the cell [21], [22]. Given the mainly dynamic nature of the cell cytoskeleton, a stretching acting on the sticking points of the cells to the substrate, could interfere with the polymerization and depolymerisation processes of its elementary units. To shed light on the role of mechanical stimulation on the cell activity, devices that are able to apply well defined deformations to the substrate have been developed [17], [23]. If cells sufficiently adhere to the underlying substrate, without sliding, a strain of the substrate can be transmitted to their internal structures. Typically, these devices exploit polymer-based compounds where cells can adhere, proliferate and migrate. Among synthetic polymers, polydimethylsiloxane (PDMS) is largely used as substrate for living cells due to its good biocompatibility and the possibility to tune its rigidity by varying the amount of the crosslinking agent. It should be emphasized that cell adhesion is ultimately regulated by the presence of cell-adhesive molecules, which, depending on the cell type and on the applications, can be natural (e.g. components of the extracellular matrix ECM such as fibronectin or laminin) [24] or obtained with synthetic approaches [25]. These molecules are generally deposited on the substrate surface in contact with cells and are able to locally modify the chemical-physical properties promoting cell adhesion. The substrates can then be stretched periodically by the use of a transducer system. These devices, even if they cannot recapitulate the very complex scenario occurring *in vivo*, can provide very useful information on the biological effects of mechanical deformations of the cells, better approaching specific physiological situations. Indeed, the physiological environment of several cells includes periodic mechanical stimuli, but cells that physiologically reside in regions without mechanical signals also share the same type of reactions when exposed to periodic stretching. This behaviour appears so as a common aspect of the molecular machinery constituting the parts of the cells in mechanical contact with the external environment. It has been demonstrated that cyclic stretching can lead to alterations of the gene expression profile of cells. This phenomenon typically concerns the proteins of the cytoskeleton or associated with it and the proteins of the extracellular matrix [26]–[28]. One of the effects of periodic stretching on cells that has been deeply investigated is their reorientation relative to the stretching direction in order to maintain a tensional homeostasis [29]–[35]. There is large evidence that cells with a bipolar shape such as fibroblasts tend to reorganize their orientation almost perpendicularly to the direction of periodic stretching as a consequence of the development of an oriented structure of stress fibers. Studying the details of this effect can largely help in understanding the mechanobiology of the cell/substrate interaction.

The development of mechanical stretching devices represents a sort of interdisciplinary enterprise in which mechanical and medical engineers, together with physicist, biologists and chemists are involved. Several home-developed devices have been described in the literature [36]–[45]. Commercial devices are also available (for example FlexCell, (http://www.flexcellint.com/) [46] or STREX (www.strexcell.com) but, in many cases, they have limitations in providing *ad-hoc* stimuli researchers might be interested to test (for

example specific periodic signals different from the usual simple sinusoidal, triangular or square patterns) [47]. Moreover, they are typically costly to purchase and many laboratories, especially the ones dedicated to educational training, might find it difficult to buy one of them. Moreover, it would also be very interesting to study the kinetics of orientation at high time resolution to understand how a cell responds to a mechanical stimulus transmitted by the environment and what are the main determinants of the phenomenon. For example, the characterization of the relaxation time of the cell orientation process as a function of the applied frequency could be compared with the output of different models that have been developed to describe the overall phenomenon [48]–[50]. In this case, it would be useful to have a stretcher device integrated with a cell incubator. This result could be pursued both by constructing cell stretcher devices with optical access compatible with an optical microscope [51] and then exploiting an enclosure to maintain all the microscope in the best conditions for cell survival (presence of a CO_2 environment, 37°C and high relative humidity) or by integrating the stretcher device inside an on-stage cell incubator. Only a few devices of the latter type are commercially available and they are typically expensive.

The stretching device development will provide some examples of investigation to get in touch with cutting-edge experiments in the field of mechanobiology. Mechanobiology has in fact developed into a well-established research field that should now be part of undergraduate curricula for biologists, biotechnologists and biomedical engineers. The team of instructors for the project should include both researchers working in laboratories focused on cell biology experiments, where an optical microscope with basic phase imaging systems is typically present, and researchers working in labs more familiar with engineering approaches, where skills such as CAD (Computer Aided Design) knowledge, programming, CNC (Computer Numerical Control) milling techniques and basic electronics are typically present and where there is also the possibility of exploiting a mechanical workshop. The best context for this activity would therefore be a Faculty of Biomedical Engineering. The project presented also includes some ideas on the construction of a motorized stage for optical microscopy (a device available on the market but usually quite expensive and not included in basic optical microscopes), but, if a large statistical analysis relating to the dynamic behaviour of the cell population is not required, this part can be skipped. Several basic concepts of continuum mechanics are required for stretcher pre-calibration, and also to compare the cell reorientation results with the proposed theoretical frameworks. Finally, several knowledge regarding programming skills and PC-microcontroller interface are strictly needed, like Python, LabView or Matlab. The uniaxial stretching device that we present can be exploited with cell populations growing on a PDMS support while observing how the cells are affected by the mechanical cue with time-lapse optical microscopy imaging. In fact, the stretching device is built inside an on-stage cell incubator [1]. The PDMS substrate can be chemically functionalized or coated to allow other cell-substrate interaction studies. All the different modules are controlled by the Arduino microprocessor and the movements are driven by stepper motors. For the apparatus controlling the cell culturing conditions such as the feedback mechanisms for controlling the temperature and CO_2 concentration, we refer to our previous work [1] (also mentioned in previous section). As a proof-of-concept, we will investigate the effect of the periodic stretching stimulus on cell reorientation and migration processes. We present also a brief overview of the different working principles of the stretching devices that have been presented in the literature and a short introduction to mechanobiology as far as mechanical stretching cues are involved.

In the literature there are works that have been carried out exploiting different types of cell stretching devices [52]. The large majority of the devices are custom-made, although some systems are also commercially available. The stretcher can be uniaxial, bi-axial or radial (isotropic). In the first case, due to the volume conservation of the stretched material, in addition to the elongation of the substrate in the direction of the actively induced stretching, there will also be a contraction in the perpendicular directions. The ratio between the deformation in mutually perpendicular directions is, in ideal conditions, provided by the Poisson ratio of the exploited material but in real experiments it is partly controlled by the geometry of the PDMS chamber and its connection to the stretcher device (in particular the clamping or boundary conditions). As a result, in the case of the typical substrates used for cell culturing, the ratio of the deformations in the two

perpendicular directions of the cell plane is different from the Poisson ratio of the exploited material. This is due to the presence of structures like the borders of the culture chamber that confer directional asymmetries to the system. Bi-axial stretchers are able to apply deformations to the PDMS substrate in two perpendicular directions. In this case, in both directions it is possible to have a positive elongation at the same time. In the case of isotropic stretchers, the elongation is applied at the same time in all planar directions and they are typically exploited to reproduce deformation stimuli experienced by cells residing in hollow organs like the heart or lungs. The deformation can be obtained exploiting different actuation systems [41], [42], [53]–[55]. One possibility is represented by pneumatic stretching devices. In this case, both negative and positive pressures could be used to decrease or increase the volume of a deformable chamber that is able to transmit the deformation to a substrate on which the cells are adhering [56], [57]. This system, which microfabrication and lithography skills are required, offers the possibility of obtaining deformations in a very clean way. The pneumatic actuation allows to obtain uniaxial, bi-axial and radial strains of the substrate. Another actuation system is based on electromagnetic signals and this includes both the use of stepper motors and voice coils actuators [39], [58], [59]. This method is very simple to implement and offers the possibility of interfacing the devices with easily programmable low-cost microprocessors. Their compatibility with incubators may be more difficult than pneumatic systems due to possible contamination related to the motor lubricants and motor heating. Another possible actuation system is based on the use of DEAs (Dielectric Elastomer Actuators) which allow the application of very fast strain deformations (sub-ms resolution) and at the same time are compatible with optical inspection [60], [61]. In this case, an elastomer is sandwiched between two stretchable electrodes and the application of a high voltage potential difference induces the approaching of the two electrodes and the stretching of the elastomer. Another advantage of DEA-based stretchers is that they can be easily miniaturized to make them compatible with other instruments such as incubators and optical microscopes. For this actuation system, it is necessary to pay attention to the fact that strong electric fields could affect cell behaviour in addition to the effect on the cells produced by the mechanical substrate deformation [60].

Here, we revising the general mechanobiology concepts seen in the introduction chapter, focusing on cycling stretching framework.

In the context of mechanosensing, any deformation in the geometry of the substrate where the cells are growing can be transmitted inside the cell causing a sequence of biochemical reactions to begin if there is a mechanical connection between the cell and the substrate [62]. Focal adhesions (FAs) are complexes working as mechanonsensors used by the cells to probe their mechanical environment and integrins are transmembrane proteins inside FAs used by cells to establish this connection [22], [63]. They provide a bridge between the internal cytoskeleton and the extracellular matrix. The stretching action is able to affect the activation of relevant molecules inside the FA complexes such as the FA kinase (FAK) [64]. Forces applied from outside to the cytoskeleton are able to affect the dynamical structure of this molecular construct. As far as mechanochemistry is concerned, it is important to consider that the mechanical transmission chain in composed by proteins interacting with each other with mainly two different types of bonds [65]. The first type is the “slip bond” and its lifetime decreases if a force trying to break it is applied to the partners [66]. The second type is called “catch bond” [67] and is characterized by the fact that there is an initial increase of the bond lifetime when a force is applied to it. After a maximum lifetime has been reached, upon a further increase of the force, the lifetime starts decreasing. Many of the proteins associated with the cell cytoskeleton, and in general the proteins whose physiological role is to withstand forces, establish catch bonds. It means that, if a force is applied to them, the stability of the bonds increases. Accordingly, the stability of actin subunits in the actin filaments and their interaction with actin-bounding molecules, can be affected by the application of a force. This modulation can in turn be regulated by other molecules, such as the Rho A protein, which has been found to be directly involved in the orientation of the stress fibers in the presence of a cyclic stretch [33]. In fact, the presence of interacting molecules could transform a catch bond in a slip bond, altering the polymerization dynamics of actin [68], [69]. It is relevant for cyclic stretching experiments that some molecular interactions have memory of what happened previously. It means that the

history of force application to a bond determines the evolution of the same bond. So, if the same force value is applied to the bond of two molecular partners, the lifetime of the bond will depend on how that force value was achieved. In this context, the stretching-ramp frequency can be relevant to determine the type of bond of a specific interaction and a shift from a catch to a slip bond can be observed by changing the force-ramp rate [70]. Also the cyclic application of forces can induce a modification of the lifetime of a bond. In some cases, reaching a peak force before releasing the applied force produces a stabilization of a bond and, in other cases, the bond stabilization can be reached as a consequence of a cyclic stretching of the bond. Accordingly, it is clear that the history of the force applied to a molecular bond affects its stability. The important aspect is to be able to measure *in-vivo* the waveform of the mechanical stimuli applied to cells from the outside and, vice-versa, from the cell to the external environment. If the stretching waveform of a self-oscillating cell on the extracellular matrix is registered, the measured waveform could be transmitted to cells *in vitro* to better reproduce the *in-vivo* situation [71]. Of relevance in this context, it has been found that the rate of force application by a stretchable substrate is more relevant than the overall frequency of the signal [72]. For example, in the case of the cardiac stimulation or in the connected vascular system, different rates of force increase are present during the cycle and the different rates might be biochemically relevant. The cell could work as a filter capturing the presence of specific frequencies and force application rates to activate specific biochemical processes.
What we just described represents the complicated ensemble of possible molecular interactions controlled by the application of a force. The stability of a bond could be affected by the amplitude, the frequency and the waveform of the applied force. The cell has then to integrate all these signals to obtain a specific behaviour [62]. This last step is what concerns the mechanobiology. In addition to the effect on the lifetime of molecular bonds, mechanical force can also induce partial denaturation of molecular partners making cryptic sequences accessible to effector proteins. An example is constituted by the focal adhesion complex where the talin protein, partially unfolded by the force transmitted via integrin attachment to the extracellular matrix, interacts with the protein vinculin [73]. This allowed interaction leads to the stabilization of focal adhesion complexes and their reinforcement. Of relevance, it has also been found that talin undergoes dynamic stretch and relaxation cycles at the level of single molecule in cells [74]. Also the plasma membrane deformations induced by cell stretching can have a mechanobiological effect [75]. Considering the concept of forces mediated by lipids [76], the activity of ion channels, and in general membrane proteins, can be modulated by the lateral tension of the lipid bilayer. This is valid for truly mechanosensitive channels (channels whose open-closed state can be completely controlled by a change of the lateral tension, such as piezo-channels or MSLC channels), but also for many other membrane proteins whose functionality is somehow affected by a modification of the lateral tension in the membrane.

In addition to the biochemical transmission based on the interaction between molecular partners, the mechanical transmission chain has also to be considered [77]. In this case, a mechanical stimulus first sensed by integrins and the FA complexes could be transmitted directly to the interior of the nucleus exploiting mechanical lines of transmission like actin filaments, structurally connected via the LINC (Linkers of the Nucleoskeleton and Cytoskeleton) complexes to the nucleus [78], [79]. The main advantage of this transmission line is its rapidity compared to a chemically travelling signal exploiting diffusion or even an active transport system.

- # Stretcher design

After a brief introduction of the existing cell stretcher devices and description of their relevance recalling mechanosensing related evidences we will illustrate the design and fabrication of our stretcher device, incapsulated in the on-stage home-made cell incubator previously developed.

The stretching device is installed inside an on-stage cell incubator based on a work we recently published [1]. The case is made by a PMMA base and an aluminium wall. The overall scheme of the stretching chamber is shown in Figure 1. The heating system is composed by thick film resistors mounted on the external wall of

two water reservoirs positioned inside the chamber, as shown in Figure 1a, and by an ITO (indium-tin-oxide) window positioned on the top cover of the chamber. The window is endowed with two silver-painted lines that assure electrical connection with an external circuit [1]. The heated ITO window provides optical accessibility for time-lapse imaging while avoiding water condensation. The temperature inside the chamber is measured by a DH22 sensor and is controlled by an Arduino driven circuit exploiting the PID routines already available for this microprocessor. The sensor is positioned inside the chamber very close to the region where the cells are seeded. The position of the cell culture PDMS support is symmetric with respect to the heating apparatus and we can assume the absence of temperature gradients in the incubator chamber in the region close to the cells. The same sensor measures also the relative humidity inside the chamber. The two water reservoir assure the high humidity level inside the incubator with negligible liquid evaporation from the cell medium. For very long imaging sessions (> 24h), the water reservoirs can be refilled from the outside of the chamber by a tubing system. The CO_2 atmosphere is assured by the same system exploited in our previous work [1]. The mechanical stretching is obtained by a stepper motor controlled by Arduino. The stepper motor produces the rotation of a stainless steel screw with a pitch of 2 mm producing the linear translation of a PVC bar that transmits, via two wires, a symmetrical uniaxial stretching to the cell chamber. All the moving PVC bars of the stretcher device move along two 4 mm diameter aluminium bars using Ball Bearing Linear Bushing typically used for CNC systems. To ensure a completely closed chamber, the region under the PDMS cell substrate was also closed using a glass window. During normal operation of the incubator, this glass window could be subjected to humidity condensation and a consequent deterioration of the image quality. To eventually avoid this problem, a liquid water film can be sandwiched between the bottom of the PDMS chamber and the glass window. This system avoids the formation of a condensation film on the internal face of the window and it is stable without significant evaporation for more than 10 hours.

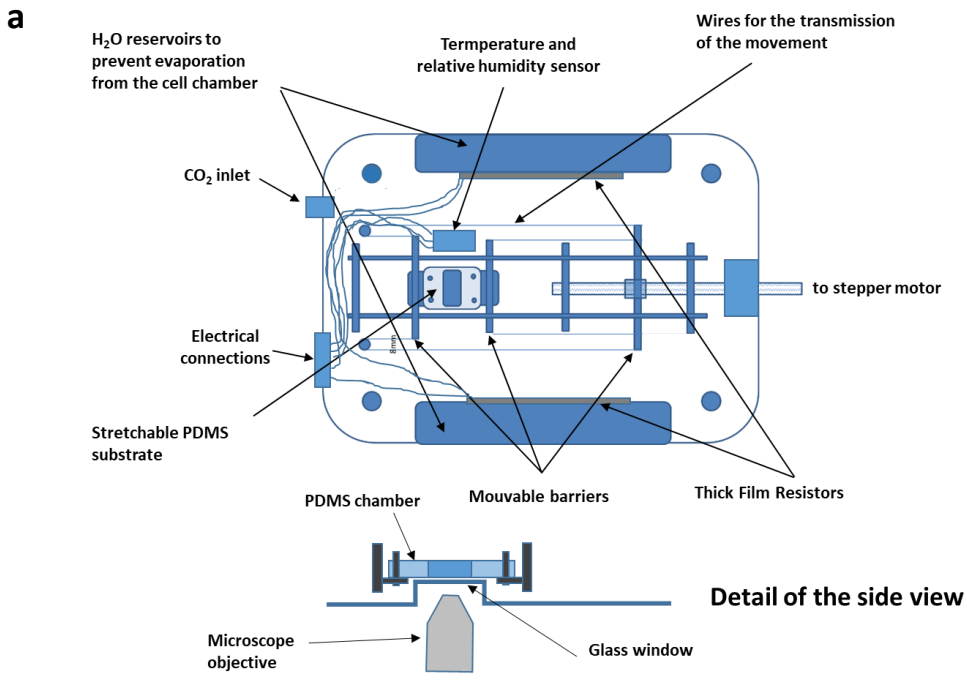

b

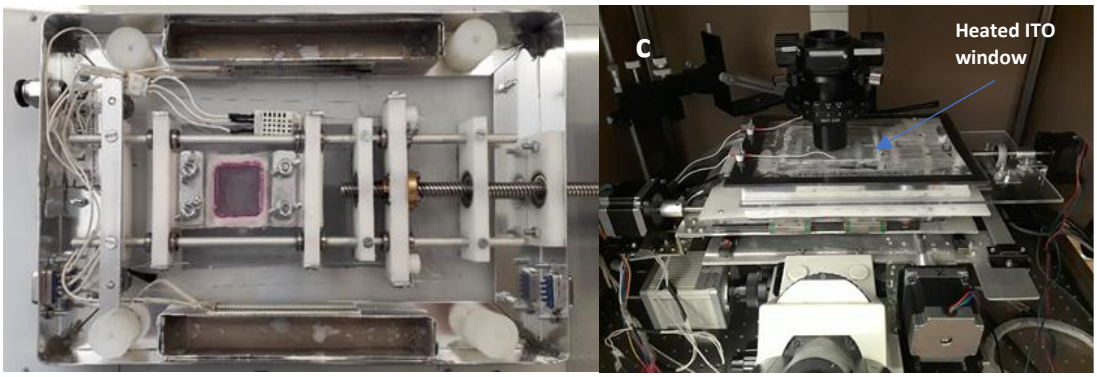

Figure1: a) scheme of the cell stretcher apparatus. The different parts are highlighted together with the elements used to obtain the controlled environment for the temperature, humidity and CO_2 concentration. B) top view pictureof the stretcher. C) image of the stretcher mounted on the motorized stage of the inverted optical microscope.

- **Design and fabrication of PDMS substrates for cell culture**

As reported in figure 1a the stretchable PDMS substrate is placed between a couple of barriers, which constituted the geometrical boundary condition of the cycling stretching. Here we will illustrate the fabrication protocol adopted for the PDMS substrates.

The PDMS substrate for cell culture is made exploiting the 184 Sylgard from Dow-Syl. We used a cross-linker/polymer weight ratio from 1:10 to 1:20. This particular composition assured a good mechanical stability of the cell culture chamber with a Young modulus in the order of 150 kPa. The chamber is prepared in a polytetrafluoroethylene (PTFE) mould as shown in Figure S2. The PTFE mould, in the region corresponding to the area where cells are seeded, is covered by a piece of glass that avoids the appearance on the surface of the PDMS substrate of topographic irregularities coming from mechanical machining of the mould. This strategy allows obtaining the best transparency of the substrate for optimal imaging conditions. The PDMS region where the cells are seeded and imaged has a typical thickness < 1 mm and its value can be decreased to about 200 µm. The use of high numerical aperture objectives is however prevented (unless they have a working distance longer than 3 mm) as the PDMS substrate is inside the incubator and is also separated from the objective by a glass window as shown in Figure 1a. To avoid as much as possible the formation of air bubbles in the PDMS substrate, once the mixture is poured in the mould, all the system is inserted in a vacuum apparatus for about 30’ and then put in the oven to accelerate the polymerization process. Before seeding the cells, the PDMS surface is treated in a Plasma cleaner with Nitrogen atmosphere and is exposed to a solution containing proteins of the extracellular matrix as detailed in the text. Considering that the exposition of PDMS surfaces to a plasma cleaning procedure could produce a texturing of the surface [80], which will deteriorate the image quality, the power was kept at a maximum of 25 W and the exposition time to 2 minutes.

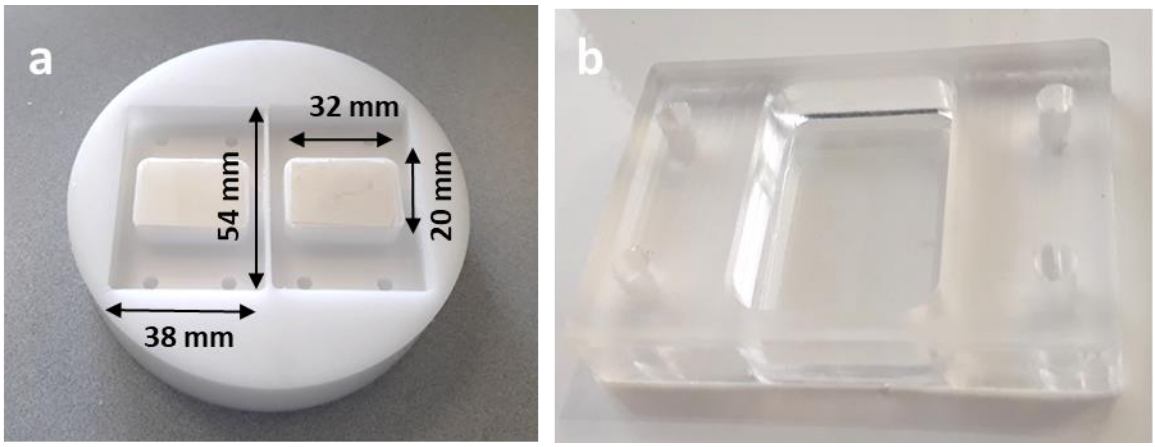

Figure 2: a) Teflon stamp for the fabrication of the PDMS; b) example of a PDMS substrate

- **Generating the arbitrary strain waveform**

There are several pieces of evidence showing how the specific shape of the waveform may have an influence on the effect produced by cyclic stretching on cells. Accordingly, the ability to deliver different waveforms to cells is crucial. In this section we will show how our set-up can generates arbitrary periodic waveforms. In fact, we developed a software able to provide a periodic deformation resulting from the composition of sinusoidal signals of different frequencies. In this way, a periodic signal of interest can be analysed by a Fourier decomposition process and then reconstructed with the desired fidelity including the required number of harmonic components.

Suppose to have a periodic deformation signal obtained from *in vivo* experimental assay. Firstly, using OriginLab software or Python routines we spectrally decomposed (using Fourier basis) the periodic signal we want to transfer to cell substrate. Using the appropriate harmonics set the original signal is reconstructed, and finally the reconstructed signal is adapted for stepper motor mechanical transmission.

In fact, the stretching deformation is applied to the PDMS substrate through a stepper motor, which is connected to the screw. We expected to observe the major deformation along the axis direction, driven by the rotations of the stepper motor. Every single step of the motor (corresponding to 10 µm for a 200 steps/revolution motor) will correspond to a specific quantized displacement of the two clamped PDMS substrate edges (considering the specific configuration of the device, the stretching amount per each step if the motor is equal to twice the step size, see Fig 1a for details). The displacement amplitude related to a single step of the motor depends on the technical specification of the screw, in particular, its screw-pitch, and of the stepper motor (steps per revolution). This parameter specifies the amount of displacement that can be provided by a single step, and is equal to [Eq 1]:

$$Single\_Step\_Displacement = \frac{Screw\_Pitch}{N_{Step\_per\_Revolution}} [1]$$

[Eq 1] condition holds at least at the movable barriers, while inside the cell sample just a fraction of the original displacement is transmitted.

The amplitude of the periodic signal we want to apply to the substrate can be converted from the metric scale to the corresponding number of single steps of the motor obtaining the y = *f* (t) rescaled function, the conversion can be performed after imposing the maximum strain level we want to transfer to the cell sample. The mechanical actuators, the stepper motor, is driven by the Arduino microcontroller managing the delays

between consecutive steps, even at the microsecond scale if necessary. Thus, the time interval between two consecutive steps must be subsequently evaluated, the overall time intervals sum will corresponds to the period T of the function. Since the displacements provided by the stepper-motor are discretized, the periodic function will be discretized as well. In order to reconstruct the entire periodic function profile, the appropriate time intervals between two consecutive steps must be evaluated while keeping the single step amplitude constant. Starting from an arbitrary periodic function y = *f* (t) with *f* (t) = *f* (t+T), where T is the periodicity, it is possible to invert the function in order to resume t [Eq 2]:

$$t = f^{-1}(y)\ [2]$$

Since the periodic function has been discretized, we can define the different stepper motor processes: $y_0 = f(t_0)$, $y_1 = f(t_1)$, $y_2 = f(t_2)$ and so on, where the subscript enumerates the number of the sub-processes out of *N* the total motor processes in which the period has been divided. Similarly, y_i represents the actual stepper motor position related to the time frame: t_i. The boundary condition to ensure the periodicity is the following [Eq 3]:

$$y_0 = f(t_0) = f(0) = y_N = f(t_N) = f(T)[3]$$

Inverting the periodic function, we can estimate the different time intervals $t_{i,i+1}$ [Eq 4]:

$$t_{i,i+1} = t_{i+1} - t_i = f^{-1}(y_{i+1}) - f^{-1}(y_i)\ [4]$$

Where the subscript "i" runs from *0* to *N-1*. This approach can be used for an arbitrary complex periodic function, from a single sinusoidal profile, up to a superposition of many harmonic functions. In Fig 3 are reported 3 examples of strain waveform discretization starting from theoretical behaviour (Sinusoidal Fig 3a, Triangular Fig 3b, and superposition of several harmonics Fig 3c).

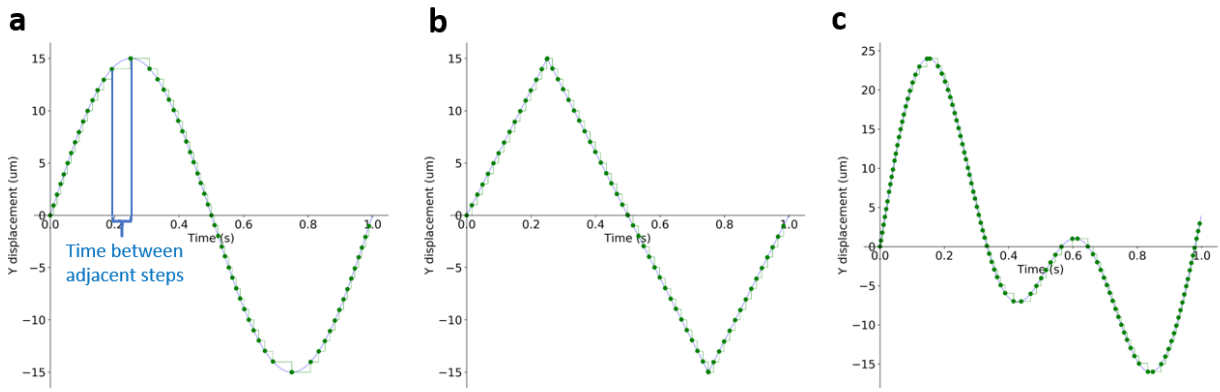

Figure 3: Periodic waveform examples panel: (a) Sinusoidal shape, (b) Triangular shape, and (c) superposition of several harmonics.

- **Validation of the stretcher signal to the PDMS substrate**

The signal transmitted to the substrate has been analysed by acquiring images during the stretching cycle at a high frame rate (1 image every 20 ms). Since the typical waveform period range is ≈[0.5÷1.5]s we have enough frames for signal test evaluation. The sequence of images has been then analysed exploiting the ImageJ plug-in that allows the alignment of images exploiting a feature present in all images as a reference. A large defect in the substrate has been selected in order to be able to use the same reference for all the images, notwithstanding the focussing problems connected to variations of the z position of the substrate during the stretching process. Once the sequence of images has been aligned, a second feature in the images is selected and the plug-in for the alignment is applied again. The list of the x-y coordinates of the displacements gives variations of the distance between the two selected features during the stretching cycle

in the two perpendicular directions. Fig 4 shows two examples for a sinusoidal and a triangular signal. The results related to the validation of the transmission of the stretching signals to cells are reported in the next section. We verified that cells effectively are stretched following the signal imposed by the substrate.

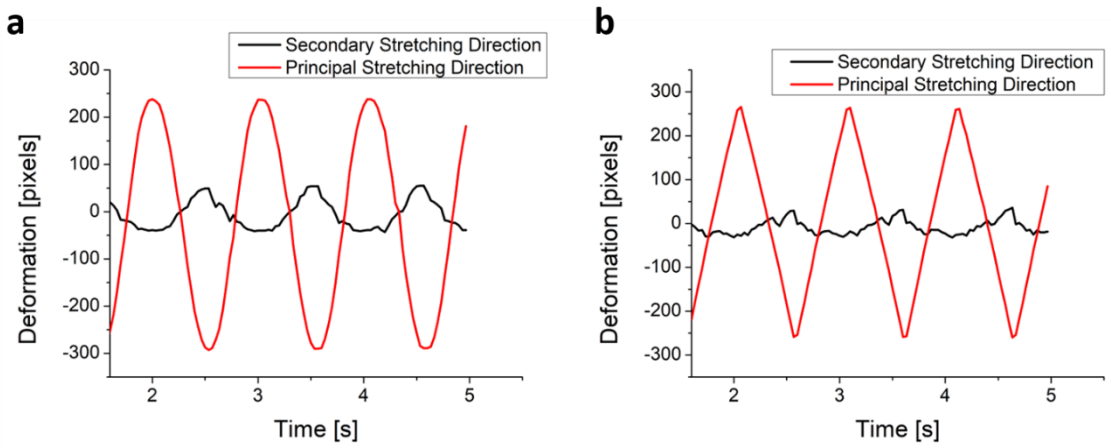

Figure 4: analysis of the distance variation between two features in the PDMS substrate for a sinusoidal (a) and a triangular (b) signal. The red line refers to principal stretching direction, black line refers to secondary stretching direction.

- **Validation of the stretcher signal from PDMS substrate to cells**

After validation of the periodic signal transmission to the PDMS substrate another important aspect of a stretcher device is the validation of the transmission of the deformation signal to cells. In fact, the substrate could slip under the cell body due to an insufficient adhesion configuration that could prevent the complete transmission of the signal to the cells. Moreover, it could be interesting to understand the maximum strain that could be applied to the substrate without the cells detaching from it. Typically, above a strain of about 20% cells could easily detach from the substrate. To verify these aspects, we acquired a series of images for different values of static strain and we marked the perimeter of a cell (see Fig 5,6). The lines following the cell perimeter in the conditions of zero stretch, maximum stretch and again zero stretch, are reported and compared to each other. From the analysis it appears that cells are able to follow the substrate deformations we applied (10%).

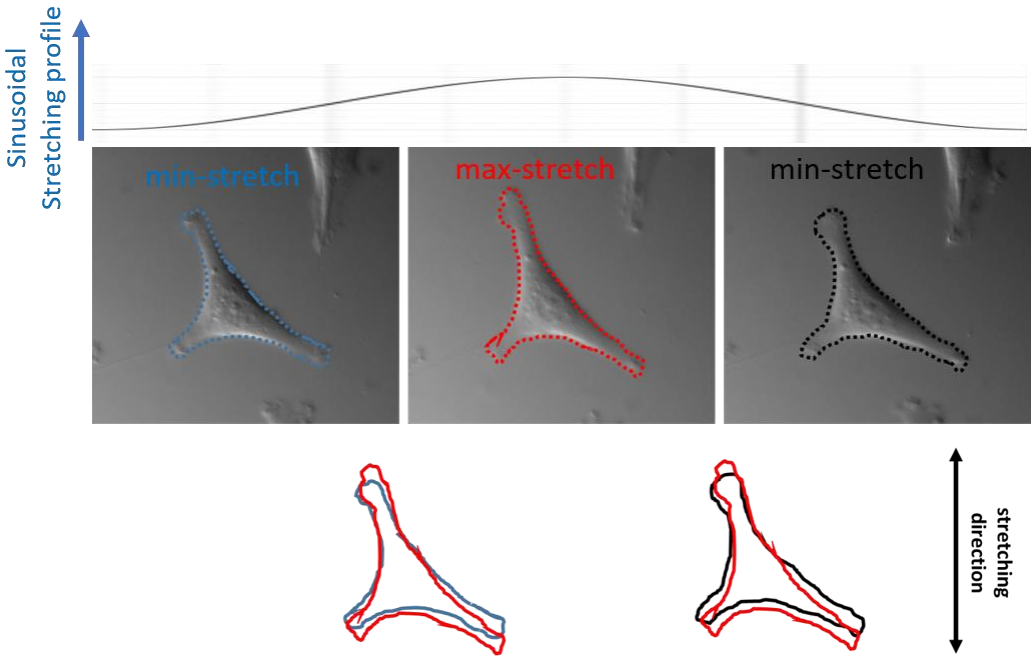

Figure 5: example of a stretching cycle for a U87MG cell. At the top a cycle of the sinusoidal signal applied to the PDMS substrate is reported and the corresponding images at the minimum, maximum and again minimum stretching conditions are reported in the middle. In the bottom section, the contour lines of the cells in the different conditions have been overlaid to highlight the transmission of the substrate extension to the cell body. (marker = 10 µm)

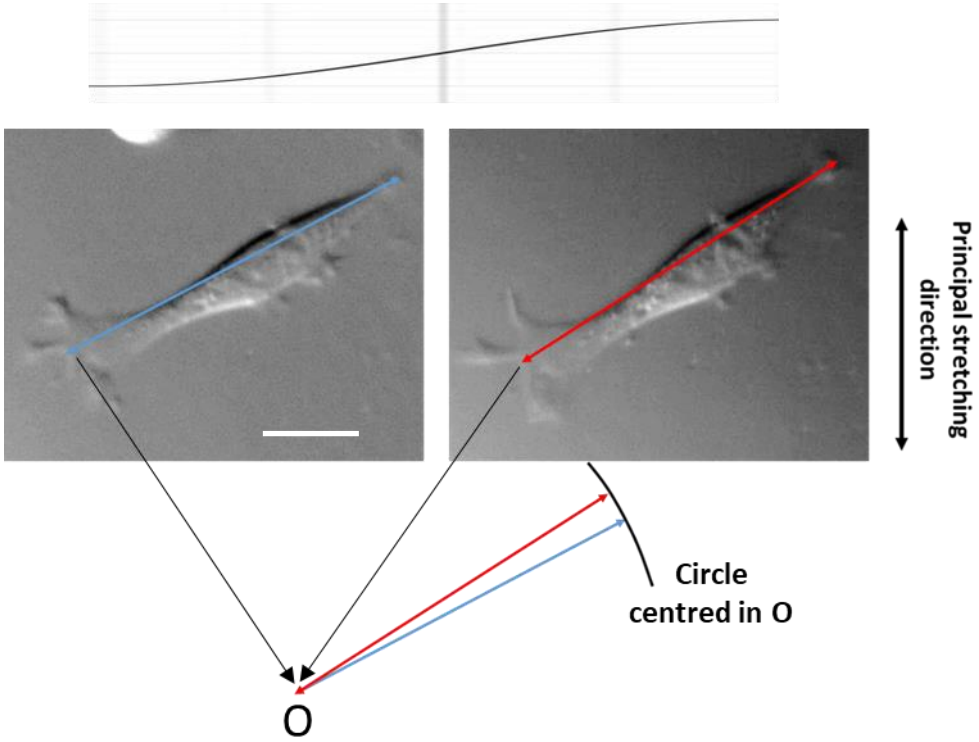

Figure 6: orientation of a Balb-3T3 cell during a cycle of the stretching process. The figure shows the variation of the orientation of the cell while keeping an almost constant length during one stretching cycle schematized at the top of the image. The two arrows (red and blue) represent the cell length and in the bottom they are reported (by a parallel translation) as rays of the same circle (centred in O) to highlight their almost equal length. This situation is useful to stress the fact that the angle of the cell orientation with respect to the stretching direction depends on the specific position during the cycle. (marker = 10 µm)

- # Theoretical basis for the strain calibration procedure

Here we introduce all the theory required to better understand the calibration method for the substrate strains. Suppose that in the not-stretched condition we have a feature of our support in the position **X** and that, after a certain amount of stretch and at time t, the position of the same feature, in the same reference system is **x** = x(**X**,t) (we are using a reference system that is fixed in space, another possibility would be that of considering a reference system that is fixed with the stretched support). We can define, according to Fig 7, the vector **u** (u,v,w) joining the initial position of a feature identified by **X** (X,Y,Z) with its final position identified by the vector **x** (x,y,z). Accordingly:

$$\boldsymbol{x} = \boldsymbol{X} + \boldsymbol{u} \; [5]$$

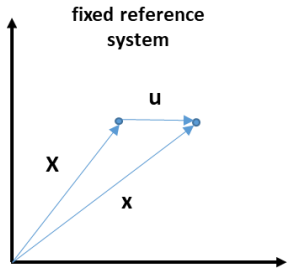

Figure 7: deformation in a fixed reference system (2D case)

It is possible to define a deformation matrix according to the following expression [Eq 6]:

$$\boldsymbol{F} = \frac{\partial \boldsymbol{x}}{\partial \boldsymbol{X}} = I + \frac{\partial \boldsymbol{u}}{\partial \boldsymbol{X}} \; [6]$$

where *I* is the identity matrix and whose terms will be given accordingly by [Eq 7]:

$$\boldsymbol{F} = \begin{pmatrix} 1 + \frac{\partial u}{\partial X} & \frac{\partial u}{\partial Y} & \frac{\partial u}{\partial Z} \\ \frac{\partial v}{\partial X} & 1 + \frac{\partial v}{\partial Y} & \frac{\partial v}{\partial Z} \\ \frac{\partial w}{\partial X} & \frac{\partial w}{\partial Y} & 1 + \frac{\partial w}{\partial Z} \end{pmatrix} \; [7]$$

If we consider an initial segment of length d**X** in the support, the matrix **F** will be able to provide the transformation of this segment d**x** after the deformation simply by [Eq 8]:

$$d\boldsymbol{x} = \boldsymbol{F} d\boldsymbol{X} \; [8]$$

Another parameter defining the action of a stretcher is the “stretch value”, defined as [Eq 9]:

$$\lambda = \left| \frac{d\boldsymbol{x}}{d\boldsymbol{X}} \right| \; [9]$$

It is different from strain, the last being defined, for a segment of length L increased by ΔL, as [Eq 10]:

$$\varepsilon = \frac{\Delta L}{L} \; [10]$$

whereas the stretch is defined as [Eq 11]:

$$\lambda = \frac{\mathrm{L} + \Delta L}{L} \; [11]$$

and it has to be considered just in the direction of the segment neglecting its possible rotation. In fact, as we already considered, the strain is a parameter that can have also a shear component. It is also evident that, considering the definitions [Eq 10] and [Eq 11], $\varepsilon = \lambda - 1$. In the case of the stretching evaluation in a plane, segments along two different directions joining specific features are selected and the change of the length of the resulting segments are measured. If the two directions are selected along the principal axis, equivalent to consider a diagonal matrix **F**, the segments will maintain their direction in the space. In this case, the matrix **F**, in 2 dimensions, will be represented by [Eq 12]:

$$\boldsymbol{F} = \begin{pmatrix} \lambda_1 & 0 \\ 0 & \lambda_2 \end{pmatrix} [12]$$

F matrix diagonalization can be numerically evaluated starting from a triad of distinct points observed in the images before and after deformation, the two images correspond to the initial condition and the condition of maximum stretch of the substrate. The triangle located at the centre of the images is constructed by exploiting three different features in the PDMS substrate. These three features are identified in the images labelling the vertices of the corresponding triangle, ABC and A'B'C' respectively, and three segments joining the selected couples are reported. The coordinates of the points (in pixels) are given by the fixed reference system is provided by the camera frame, below we will show a numerical example using B=B' as frame of reference (see Fig 8). Using the segments set: $d\mathbf{X}_1$=BA, $d\mathbf{X}_2$=BC, $d\mathbf{x}_1$=B'A', and $d\mathbf{x}_2$=B'C' we can define two equations [Eq 13a-b], which allow us to extrapolate the non-diagonalized form of **F**:

$$\begin{cases} d\boldsymbol{x_1} = \begin{pmatrix} F_{11} & F_{12} \\ F_{21} & F_{22} \end{pmatrix} d\boldsymbol{X_1} \, [13a] \\ d\boldsymbol{x_2} = \begin{pmatrix} F_{11} & F_{12} \\ F_{21} & F_{22} \end{pmatrix} d\boldsymbol{X_2} \, [13b] \end{cases}$$

From the above derived equations, it is possible to obtain the ***F*** matrix and eventually diagonalize it. However, the matrix **F** includes possible rotations together with the distortions. Considering the matrix ***F***, it can be expressed as the product of a rotation matrix ***R*** and a distortion matrix ***U***, where the translation is performed before the rotation [Eq 14]:

$$\boldsymbol{F} = \boldsymbol{RU} \, [14]$$

Obviously, if the deformation is just a distortion without rotation, the matrix ***F*** will be equal to ***U***. If the distortion is performed after the rotation, the corresponding matrix will be ***V*** and we will have:

$$\boldsymbol{F} = \boldsymbol{VR} \, [15]$$

Considering the properties of the matrices, we have:

$$\boldsymbol{V} = \boldsymbol{FR^T} \, [16]$$

and, exploiting [Eq 14], we can write [Eq 17]:

$$\boldsymbol{V} = \boldsymbol{RUR^T} \, [17]$$

Two matrices [Eq 18a-b] can be defined so that they are related just to deformation, neglecting rotation. They can be obtained considering the following expressions:

$$\boldsymbol{F^T F} = (\boldsymbol{RU})^{\boldsymbol{T}}(\boldsymbol{RU}) = \boldsymbol{U^T R^T RU} = \boldsymbol{U^T U} = \boldsymbol{U^2} = \boldsymbol{C} \, [18\, a]$$

$$\boldsymbol{FF^T} = (\boldsymbol{VR})(\boldsymbol{VR})^{\boldsymbol{T}} = \boldsymbol{VRR^T V^T} = \boldsymbol{V^T V} = \boldsymbol{V^2} = \boldsymbol{D} \, [18\, b]$$

where we have considered that the product of a rotation matrix and its transpose is the identity matrix. The two matrices **C** and **D** are the right and left Cauchy-Green deformation tensors, respectively. The advantage

of the Cauchy-Green tensor is that it depends just on the distortion or stretch and not on the rotation. Moreover, exploiting the matrix **C**, we can write [Eq 19]:

$$d\boldsymbol{x}^2 = (d\boldsymbol{X})\boldsymbol{C}(d\boldsymbol{X}) \text{ [19]}$$

It is then possible to introduce the Green strain tensor E [Eq 20] as:

$$\boldsymbol{E} = \frac{1}{2}(\boldsymbol{F}^T\boldsymbol{F} - \boldsymbol{I}) \text{ [20]}$$

The term 1/2 is due to the fact that ***E*** is a tensor and the mixed elements of the matrix, corresponding to the shear elements will explicitly contain this term. The Green strain tensor can be considered as the sum of a small strain tensor and a quadratic term that is to be taken into account for large deformations. Once the ***F*** matrix has been calculated, it is possible to derive the Green strain tensor ***E*** according to [Eq 20]. The advantage of using ***E*** instead of simply ***F***, is particularly evident when considering large deformations.

After a brief introduction of the theoretical deformation tools needed for stretch calibration here we detail the specific calibration procedure obtained in our set-up.

To be sure that the stretching of the PDMS substrate responds to the desired stimulus and to calibrate the quantitative substrate stretching we performed a series of experiments with and without cells. We started considering a PDMS substrate without any applied stretch, looking for different features or imperfections of the substrate, such as bubbles encapsulated in the inner part. All these details identify points of reference needed to quantify the amount of deformation reached after gradually increasing the stretching on the substrate. Each time the stretching is increased, a new image is acquired, in order to follow the evolution of the different points identified in the initial frame. In this way we can test if the deformation applied behaves following a homogeneous/linear regime response. The only mechanical boundary condition [81] that we impose to our PDMS substrate is a mechanical clamping. For the procedure, we concentrated on the central region of the PDMS substrate. Considering that our set-up provides a symmetric stretching, the central position is found by looking for almost static-point during the stretching procedure. Calibration analysis is performed studying the evolution of triads of adjacent points for different regions of the substrate. In this way we can confirm whether the deformations are homogeneous throughout the area, and which are the principal axis along which the deformations act. The amount of strains evaluated along the principal axis are also needed to quantify which is the minimum strain direction in the PDMS substrate (see below). In the following, the complete procedure, is reported for a substrate region.

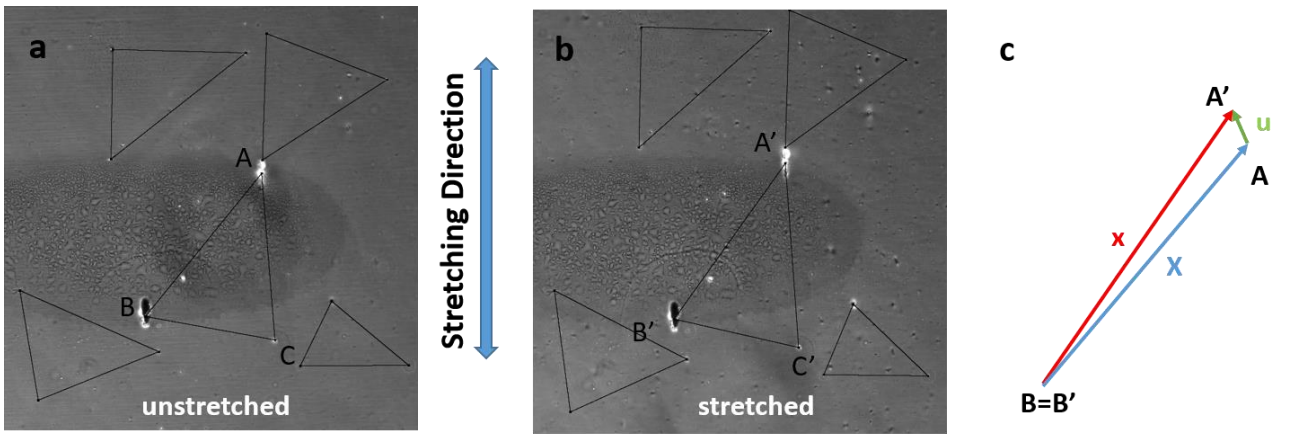

*Figure 8: a) PDMS substrate without any applied stretch, b) PDMS substrate exposed to stretching along the vertical direction via stepper motor rotation. c) Example (enlarged for clarity) of the vector analysis of **X** = **AB** (blue) and **x** = **A'B'** (red), and the associated **u** = **AA'** (green) representing the translational displacement.*

In Fig 8, images of the PDMS substrate in unstretched (a) and stretched (b) conditions are reported. In the images we identified five triangles placed at the centre and the four corners of the area. The vertexes of the triangles are identified by features of the substrate. Figure 8c shows an example of the vector analysis. Assuming a common origin in B = B' of the two vectors **BA** and **B'A'**, the deformation vector **AA'** is obtained. For each triangle we can evaluate the associated gradient-deformation matrix ***F*** inverting [Eq 13a-b]. This matrix contains the transformations involved during the stretching process, in particular, rigid rotation, strain and shear deformation. We can separate rotational contribution from strain and shear by evaluating the right Cauchy-Green deformation tensor, directly ($\boldsymbol{F}^T\boldsymbol{F}=\boldsymbol{C}$) or by polar decomposition of ***F*** [Eq 14] and evaluating the product $\boldsymbol{U}^T\boldsymbol{U}=\boldsymbol{C}$. By choosing the polar decomposition we have the possibility to verify if rotational contributions are negligible during deformation. Experimental results obtained from deformation analysis of the five triangles confirm that rigid rotations are negligible. In fact, we obtain $\theta_{Rotation}$= (3.02±2.87)°. This evidence confirm that we are deforming the PDMS substrate along two perpendicular directions without introducing any significant rotation. Finally, using the ***C*** tensor we can measure the actual strain deformation via the Green-Lagrange strain matrix ***E*** [Eq 20], which can be also used for large deformation conditions, since ***F*** is only a first order strain approximation, useful only for small deformation conditions. We can obtain strain amount along the principal directions using ***E***, and compare this result to its first order approximation, provided by ***F*** matrix. In fact, we expect from the theory $\boldsymbol{E} \sim \boldsymbol{F}$-I.

From experimental data analysis, performed for a well-defined rotation of the stepper motor, we have observed that the strain amount obtained using the Green-Lagrange strain (already diagonalized) is:

$$\boldsymbol{E}(\%) = \begin{pmatrix} \varepsilon_{xx} & 0 \\ 0 & \varepsilon_{yy} \end{pmatrix} = \begin{pmatrix} -3.63 \pm 0.36 & 0 \\ 0 & 10.43 \pm 0.78 \end{pmatrix}$$

Instead, strains obtained using the gradient-deformation matrix ***F*** (already diagonalized and subtracting the identity matrix) is:

$$\boldsymbol{F} - \boldsymbol{I}(\%) = \begin{pmatrix} F_{xx} - 1 & 0 \\ 0 & F_{yy} - 1 \end{pmatrix} = \begin{pmatrix} -3.67 \pm 0.35 & 0 \\ 0 & 9.90 \pm 0.68 \end{pmatrix}$$

The experimental results confirm that ***F*** is just a first approximation of the measured strain, which is well described by the matrix ***E***. Comparing ε_{xx} with F_{xx}-1 and ε_{yy} with F_{yy}-1, we can observe that the relative error associated to the *y* axis $\frac{\varepsilon_{yy}-(F_{yy}-1)}{\varepsilon_{yy}} \approx 5.1\%$, the maximum strain direction, is much higher than its counterpart along *x* axis $\frac{\varepsilon_{xx}-(F_{xx}-1)}{\varepsilon_{xx}} \approx 1.1\%$, the minimum strain direction. This observation is in total agreement with the fact that ***F*** is only valid for small deformation. Furthermore, exploiting diagonalization of ***E*** we can measure the principal axis strain directions, which are placed at $\theta_{Max\text{-}Strain}$≈91.48±3.7° and $\theta_{Min\text{-}Strain}$≈1.48±3.7° for the maximum and minimum strain axis, respectively (using the camera frame as reference). Note that the motor axis producing the stretch is placed at +90°, completely in agreement with the measured value of $\theta_{Max\text{-}Strain}$. Also note that the uncertainty associated to $\theta_{Max\text{-}Strain}$ is perfectly comparable to $\theta_{Rotation}$, the rotation measured by polar decomposition, confirming again that rigid rotation is negligible.

• Minimum strain and stress directions evaluation

There is large consensus about the fact that cells belonging to several lines are able to align themselves in a direction almost perpendicular to the direction of the main deformation stimulus in the case of cyclic stretching. The kinetics and the amount of the average reorientation of a cell population has been found to depend on the amplitude of the stretching stimulus [33], [82], on the frequency [32], [83], [84] and also on the rate of deformation (the wave shape) for the same value of the overall frequency using non-harmonic stretching protocols [72], [85], [86]. Even if this behaviour has a physiological relevance for some types of cells, like for example smooth muscle or endothelial cells of blood vessels exposed to period stretching, many

cell lines share the same behaviour, even if they don't undergo a stretching cycle *in-vivo*, pointing to a general mechanism connected to common molecular constructs. Several analytical models have been developed to explain and quantify this phenomenon [83], [87]–[91]. Their validity is evaluated on the basis of the relevant aspects of the phenomenon that they are able to reproduce, such as the dependence upon the frequency and the rate of deformation, the difference between a static stretch and a cyclic stretch, the direction of stress fiber orientation with respect to the substrate strain and the kinetics of cell reorientation. Some of these models are based on methods of statistical mechanics and they rely on the minimization of the potential energy accumulated by the cell cytoskeleton during the stretching process. Accordingly, the orientation of the cells will correspond to the situation where the stress fibers of the cells are minimally deformed by the substrate.

These theoretical methods based on statistical mechanics proposed a crucial dilemma regarding the potential energy minimization of the cell cytoskeleton. "Are cells more sensible to stress or strain mechanical stimuli under substrate deformation?". Here we will recall briefly the theoretical framework required to evaluate the minimum strain and stress directions in a 2D planar system.

Let us concentrate on the determination of the direction corresponding to the minimum deformation of the cells as a function of substrate strain. We consider a transformation from the x-y plane where x is the main stretching direction and y the orthogonal direction (we will assume that the stretching is without shear) to a polar coordinate system defined by the direction of a segment we are considering, as shown in Fig 9. The polar coordinates can be interpreted as a new Cartesian system with x' along the direction of the segment we identified and y' along the perpendicular direction. The displacements in the two coordinate systems are connected by the following equations [92]:

$$\begin{cases} u_x = u_r cos\vartheta - u_\vartheta sin\vartheta \ [21a] \\ u_y = u_r sin\vartheta + u_\vartheta cos\vartheta \ [21b] \end{cases}$$

where the transformation matrix is given by R, the rotation matrix:

$$R = \begin{pmatrix} cos\vartheta & sin\vartheta \\ -sin\vartheta & cos\vartheta \end{pmatrix} \ [22]$$

We can find the elements of the strain matrix considering the following conversions [Eq 23a-c]:

$$\begin{cases} \varepsilon_{rr} = \varepsilon_{x'x'} \ [23a] \\ \varepsilon_{\vartheta\vartheta} = \varepsilon_{y'y'} \ [23b] \\ \varepsilon_{r\vartheta} = \varepsilon_{x'y'} \ [23c] \end{cases}$$

and we can apply the transformation rule for the strain tensor [Eq 24]:

$$\boldsymbol{\varepsilon'} = \boldsymbol{R\varepsilon R^T} \ [24]$$

where R is the rotation matrix [Eq 22] and:

$$\boldsymbol{\varepsilon'} = \begin{pmatrix} \varepsilon_{x'x'} & \varepsilon_{x'y'} \\ \varepsilon_{x'y'} & \varepsilon_{y'y'} \end{pmatrix} = \begin{pmatrix} \varepsilon_{rr} & \varepsilon_{r\vartheta} \\ \varepsilon_{r\vartheta} & \varepsilon_{\vartheta\vartheta} \end{pmatrix} \ [25]$$

Accordingly, we obtain:

$$\begin{pmatrix} \varepsilon_{rr} & \varepsilon_{r\vartheta} \\ \varepsilon_{r\vartheta} & \varepsilon_{\vartheta\vartheta} \end{pmatrix} = \begin{pmatrix} cos\vartheta & sin\vartheta \\ -sin\vartheta & cos\vartheta \end{pmatrix} \begin{pmatrix} \varepsilon_{xx} & \varepsilon_{xy} \\ \varepsilon_{xy} & \varepsilon_{yy} \end{pmatrix} \begin{pmatrix} cos\vartheta & -sin\vartheta \\ sin\vartheta & cos\vartheta \end{pmatrix} \ [26]$$

$$\varepsilon_{rr} = \varepsilon_{xx} cos^2\vartheta + \varepsilon_{yy} sin^2\vartheta + 2\varepsilon_{xy} sin\vartheta cos\vartheta \ [27]$$

$$\varepsilon_{\vartheta\vartheta} = \varepsilon_{xx} sin^2\vartheta + \varepsilon_{yy} cos^2\vartheta - 2\varepsilon_{xy} sin\vartheta cos\vartheta \ [28]$$

$$\varepsilon_{r\vartheta} = (\varepsilon_{yy} - \varepsilon_{xx}) sin\vartheta cos\vartheta + \varepsilon_{yy}(cos^2\vartheta - sin^2\vartheta) \ [29]$$

If we consider the definition of the cross-strain element [Eq 30]:

$$\varepsilon_{xy} = \frac{1}{2}\left(\frac{\partial u_x}{\partial y} + \frac{\partial u_y}{\partial x}\right) \text{ [30]}$$

and we remind that we assumed that there is no shear in the transformation ($\varepsilon_{xy} = 0$), the ε_{rr} term is given by:

$$\varepsilon_{rr} = \varepsilon_{xx} cos^2\vartheta + \varepsilon_{yy} sin^2\vartheta \text{ [31]}$$

From this expression it is easy to consider the condition of zero strain in the *r* direction. In fact, if we consider the matrix describing the plane deformation of the PDMS substrate, the relative deformation of an initially segment of length l_o can also be written as:

$$\frac{\Delta l}{l_0} = \varepsilon_{xx} + (\varepsilon_{yy} - \varepsilon_{xx}) sin^2\vartheta = \varepsilon_{xx}[1 - (k+1) sin^2\vartheta] \text{ [32]}$$

where ε_{xx} and ε_{yy} represent the relative deformation of the substrate in the *x* and *y* directions, respectively, ϑ is the angle defining the direction with respect to the direction of main stretching and *k* is the ratio – $\varepsilon_{yy}/\varepsilon_{xx}$. The condition of zero strain requires, for a specific value of $\vartheta = \alpha$:

$$1 - (k+1) sin^2\alpha = 0 \text{ [33]}$$

$$\alpha_{Min-Strain} = arcsin\sqrt{\frac{1}{k+1}} = arctg\sqrt{\frac{1}{k}} = arctg\sqrt{-\frac{\varepsilon_{xx}}{\varepsilon_{yy}}} \text{ [34]}$$

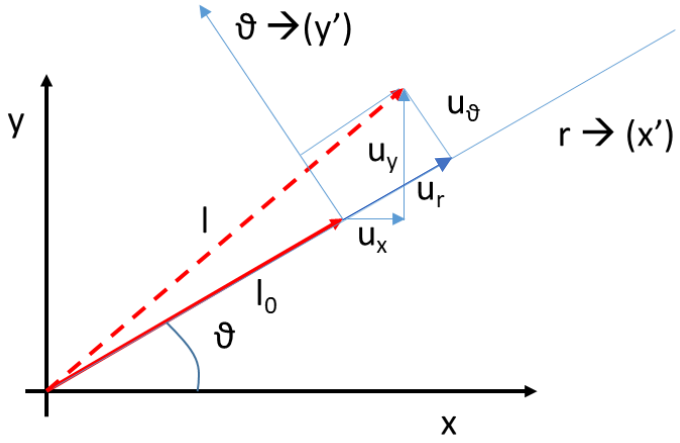

Figure 9: scheme of the transition from Cartesian to polar coordinates and the relation among the corresponding deformations of a segment.

Following the question proposed above, we can also evaluate the zero-stress direction condition. The zero-stress direction is achieved rewriting [Eq 31] for the stress components, and requiring σ_{rr}=0 obtaining [Eq 35]:

$$\sigma_{rr} = \sigma_{xx} cos^2\vartheta + \sigma_{yy} sin^2\vartheta = 0 \text{ [35]}$$

In the case where the orientation is controlled by the stress [48], we have to consider the relations connecting strain and stress of the substrate (plane stress in 2D) [Eq 36a-c]:

$$\begin{cases} \sigma_{xx} = \dfrac{E}{1-\nu^2}\left(\varepsilon_{xx} + \nu\varepsilon_{yy}\right) [36a] \\ \sigma_{yy} = \dfrac{E}{1-\nu^2}\left(\varepsilon_{yy} + \nu\varepsilon_{xx}\right) [36b] \\ \sigma_{xy} = \dfrac{E}{1+\nu}\varepsilon_{xy} [36c] \end{cases}$$

Where we have introduced the Young modulus E and the Poisson ratio υ of the material we are using (PDMS). If we consider the ratio σ_{yy}/σ_{xx} we have [Eq 37]:

$$\frac{\sigma_{yy}}{\sigma_{xx}} = \frac{\varepsilon_{yy} + \nu\varepsilon_{xx}}{\varepsilon_{xx} + \nu\varepsilon_{yy}} = \frac{\nu - k}{1 - \nu k} \; [37]$$

Where we used the same symbol $k = -\varepsilon_{yy}/\varepsilon_{xx}$ adopted above, and the orientation angle will be [Eq 38]:

$$\alpha = arctg\sqrt{-\frac{\sigma_{xx}}{\sigma_{yy}}} = arctg\sqrt{\frac{1-\nu k}{\nu - k}} \; [38]$$

Anyway, as has been reported in Livne et al. [50], the value obtained by this second possibility is not consistent with the experimental data assuming a value of 0.5 for the Poisson ratio and the experimentally determined value for *k*. Livne et al. proposed an interesting explanation for this deviation.

Bibliography

[1] G. Ragazzini, A. Mescola, L. Corsi, and A. Alessandrini, “Fabrication of a low-cost on-stage cell incubator with full automation,” *J. Biol. Educ.*, vol. 53, no. 2, pp. 165–173, 2019, doi: 10.1080/00219266.2018.1451772.

[2] M. Baker, “Taking a long, hard look,” *Nature*, vol. 466, no. 7310, pp. 1137–1140, 2010, doi: 10.1038/4661137a.

[3] D. J. Stephens and V. J. Allan, “Light microscopy techniques for live cell imaging,” *Science (80-.).*, vol. 300, no. 5616, pp. 82–86, 2003, doi: 10.1126/science.1082160.

[4] M. P. Walzik *et al.*, “A portable low-cost long-term live-cell imaging platform for biomedical research and education,” *Biosens. Bioelectron.*, vol. 64, pp. 639–649, 2015, doi: 10.1016/j.bios.2014.09.061.

[5] T. Landrain, M. Meyer, A. M. Perez, and R. Sussan, “Do-it-yourself biology: Challenges and promises for an open science and technology movement,” *Syst. Synth. Biol.*, vol. 7, no. 3, pp. 115–126, 2013, doi: 10.1007/s11693-013-9116-4.

[6] A. Delgado, “DIYbio: Making things and making futures,” *Futures*, vol. 48, pp. 65–73, 2013, doi: 10.1016/j.futures.2013.02.004.

[7] H. Wolinsky, “Kitchen biology,” *EMBO Rep.*, vol. 10, no. 7, pp. 683–685, 2009, doi: 10.1038/embor.2009.145.

[8] G. A. Mabbott, “Teaching electronics and laboratory automation using microcontroller boards,” *J. Chem. Educ.*, vol. 91, no. 9, pp. 1458–1463, 2014, doi: 10.1021/ed4006216.

[9] J. H. Arrizabalaga, A. D. Simmons, and M. U. Nollert, “Fabrication of an Economical Arduino-Based Uniaxial Tensile Tester,” *J. Chem. Educ.*, vol. 94, no. 4, pp. 530–533, 2017, doi: 10.1021/acs.jchemed.6b00639.

[10] Alduchov O. A. ; Eskirdge R. E., “Improved Magnus Approximation of Saturation Vapor Pressure,” *Appl. Metereology*, vol. 35, pp. 601–609, 1996.

[11] T. Ehang, M. A. Othman, N. H. Mahmood, and M. A. A. Razak, “Autofocus microscope system using contrast measurement approach,” *J. Teknol.*, vol. 74, no. 6, pp. 35–39, 2015, doi: 10.11113/jt.v74.4665.

[12] G. Ragazzini, J. Guerzoni, A. Mescola, D. Di Rosa, L. Corsi, and A. Alessandrini, “A Fully Integrated Arduino-Based System for the Application of Stretching Stimuli to Living Cells and Their Time-Lapse Observation: A Do-It-Yourself Biology Approach,” *Ann. Biomed. Eng.*, 2021, doi: 10.1007/s10439-021-02758-3.

[13] M. O. Valiente, Manuel, “Neuronal Migration Mechanisms in Development and Disease,” *Curr. Opin. Neurobiol.*, vol. 20, no. (1), pp. 68–78, 2010.

[14] K. M. Kollins, J. Hy, P. C. Bridgman, Y. Q. Hyang, and G. Gallo, “Myosin-II negatiwely regulates minor process extension and the temporal development of neuronal polarity,” *Dev. Neurobiol.*, vol. 69, no. 5, pp. 279–298, 2009, doi: 10.1002/dneu.20704.

[15] Z. Liu *et al.*, “Blebbistatin inhibits contraction and accelerates migration in mouse hepatic stellate cells,” *Br. J. Pharmacol.*, vol. 159, no. 2, pp. 304–315, 2010, doi: 10.1111/j.1476-5381.2009.00477.x.

[16] T. Iskratsch, H. Wolfenson, and M. P. Sheetz, “Appreciating force and shape-the rise of mechanotransduction in cell biology,” *Nat. Rev. Mol. Cell Biol.*, vol. 15, no. 12, pp. 825–833, 2014, doi: 10.1038/nrm3903.

[17] A. W. Holle *et al.*, “Cell-Extracellular Matrix Mechanobiology: Forceful Tools and Emerging Needs for Basic and Translational Research,” *Nano Lett.*, vol. 18, no. 1, pp. 1–8, 2018, doi: 10.1021/acs.nanolett.7b04982.

[18] V. Marx, “May mechanobiology work forcefully for you,” *Nat. Methods*, vol. 16, no. November, pp. 1083–1086, 2019, doi: 10.1038/s41592-019-0621-6.

[19] K. A. Jansen, D. M. Donato, H. E. Balcioglu, T. Schmidt, E. H. J. Danen, and G. H. Koenderink, “A guide to mechanobiology : Where biology and physics meet ☆,” *BBA - Mol. Cell Res.*, vol. 1853, no. 11, pp. 3043–3052, 2015, doi: 10.1016/j.bbamcr.2015.05.007.

[20] B. Coste *et al.*, “Piezo1 and Piezo2 Are Essential Components of Distinct Mechanically Activated Cation Channels,” *Science*, vol. 330, no. October, pp. 7–12, 2010.

[21] M. A. Schwartz, “Integrins and Extracellular Matrix in Mechanotransduction,” *Cold Spring Harb Perspect Biol*, pp. 1–13, 2010, doi: 10.2147/CHC.S21829.

[22] J. Z. Kechagia, J. Ivaska, and P. Roca-Cusachs, “Integrins as biomechanical sensors of the microenvironment,” *Nat. Rev. Mol. Cell Biol.*, vol. 20, no. 8, pp. 457–473, 2019, doi: 10.1038/s41580-019-0134-2.

[23] D. Y. M. Leung, S. Glagov, and M. B. Mathews, “A new in vitro system for studying cell response to mechanical stimulation,” *Exp. Cell Res.*, vol. 109, no. 2, pp. 285–298, 1977, doi: 10.1016/0014-4827(77)90008-8.

[24] V. P. Terranova, M. O. N. I. Q. U. E. Aumailley, L. H. Sultan, G. R. Martin, and H. Y. N. D. A. K. Kleinman, “Regulation of Cell Attachment and Cell Number by Fibronectin and Laminin,” vol. 479, pp. 473–479, 1986.

[25] A. Mescola *et al.*, “Speci fi c Neuron Placement on Gold and Silicon Nitride-Patterned Substrates through a Two-Step Functionalization Method,” 2016, doi: 10.1021/acs.langmuir.6b01352.

[26] M. Reichenbach, K. Reimann, and H. Reuter, “Gene expression in response to cyclic mechanical stretch in primary human dermal fibroblasts,” *Genomics Data*, vol. 2, pp. 335–339, 2014, doi: 10.1016/j.gdata.2014.09.010.

[27] T. Korff, K. Aufgebauer, and M. Hecker, “Cyclic stretch controls the expression of CD40 in endothelial cells by changing their transforming growth factor-β1 response,” *Circulation*, vol. 116, no. 20, pp. 2288–2297, 2007, doi: 10.1161/CIRCULATIONAHA.107.730309.

[28] S. Lehoux and A. Tedgui, “Cellular mechanics and gene expression in blood vessels,” *J. Biomech.*, vol. 36, no. 5, pp. 631–643, 2003, doi: 10.1016/S0021-9290(02)00441-4.

[29] K. Hayakawa, N. Sato, and T. Obinata, “Dynamic reorientation of cultured cells and stress fibers under mechanical stress from periodic stretching,” *Exp. Cell Res.*, vol. 268, no. 1, pp. 104–114, 2001, doi: 10.1006/excr.2001.5270.

[30] K. Kurpinski, J. Chu, C. Hashi, and S. Li, “Anisotropic mechanosensing by mesenchymal stem cells,” *Proc. Natl. Acad. Sci. U. S. A.*, vol. 103, no. 44, pp. 16095–16100, 2006, doi: 10.1073/pnas.0604182103.

[31] V. P. Shirinsky *et al.*, “Mechano-chemical control of human endothelium orientation and size,” *J. Cell Biol.*, vol. 109, no. 1, pp. 331–339, 1989, doi: 10.1083/jcb.109.1.331.

[32] B. Liu *et al.*, “Role of cyclic strain frequency in regulating the alignment of vascular smooth muscle cells in vitro,” *Biophys. J.*, vol. 94, no. 4, pp. 1497–1507, 2008, doi: 10.1529/biophysj.106.098574.

[33] U. S. Kaunas R, Nguyen P, R. Kaunas, P. Nguyen, S. Usami, and S. Chien, “Cooperative effects of Rho and mechanical stretch on stress fiber organization,” *Proc Natl Acad Sci U S A. 2005 Nov*

1;102(44)15895-900., vol. 102, no. 44, p. 900, 2005, doi: 10.1073/pnas.0506041102.

[34] R. A. Brown, R. Prajapati, D. A. McGrouther, I. V. Yannas, and M. Eastwood, "Tensional homeostasis in dermal fibroblasts: Mechanical responses to mechanical loading in three-dimensional substrates," *J. Cell. Physiol.*, vol. 175, no. 3, pp. 323–332, 1998, doi: 10.1002/(SICI)1097-4652(199806)175:3<323::AID-JCP10>3.0.CO;2-6.

[35] K. D. Webster, W. P. Ng, and D. A. Fletcher, "Tensional homeostasis in single fibroblasts," *Biophys. J.*, vol. 107, no. 1, pp. 146–155, 2014, doi: 10.1016/j.bpj.2014.04.051.

[36] M. J. Yost *et al.*, "Design and construction of a uniaxial cell stretcher," vol. 29208, pp. 3124–3130, 2021.

[37] O. R. Rana *et al.*, "A simple device to apply equibiaxial strain to cells cultured on flexible membranes," pp. 532–540, 2021, doi: 10.1152/ajpheart.00649.2007.

[38] G. Rápalo, J. D. Herwig, R. Hewitt, K. R. Wilhelm, C. M. Waters, and E. Roan, "Live Cell Imaging during Mechanical Stretch 1 . Construction of Membrane with Well Walls for Retention of Cell Culture Media (see 2 . Correlation of Motor Rotations with Clamp Displacement or Radial Growth for Calibration," no. August, pp. 1–12, 2015, doi: 10.3791/52737.

[39] L. P. H. Huang, P. S. M. Mathieu, and B. R. P. H. Helmke, "A Stretching Device for High-Resolution Live-Cell Imaging," vol. 38, no. 5, pp. 1728–1740, 2010, doi: 10.1007/s10439-010-9968-7.

[40] S. Schürmann, S. Wagner, S. Herlitze, C. Fischer, S. Gumbrecht, and A. Wirth-hücking, "Biosensors and Bioelectronics The IsoStretcher : An isotropic cell stretch device to study mechanical biosensor pathways in living cells," *Biosens. Bioelectron.*, vol. 81, pp. 363–372, 2016, doi: 10.1016/j.bios.2016.03.015.

[41] Y. H. N. Nguyen, "A polymeric cell stretching device for real-time imaging," 2013, doi: 10.1007/s10544-013-9796-2.

[42] C. P. Ursekar, S. Teo, H. Hirata, I. Harada, and K. Chiam, "Design and Construction of an Equibiaxial Cell Stretching System That Is Improved for Biochemical Analysis," vol. 9, no. 3, 2014, doi: 10.1371/journal.pone.0090665.

[43] S. Seriani, G. Del Favero, J. Mahaffey, D. Marko, P. Gallina, and C. S. Long, "The cell-stretcher : A novel device for the mechanical stimulation of cell populations The cell-stretcher : A novel device for the mechanical stimulation of cell populations," vol. 084301, 2016, doi: 10.1063/1.4959884.

[44] C. T. Davis, N. R. Sullivan, T. D. Smith, S. Anis, and Z. R. Robinson, "A Low-Cost Mechanical Stretching Device for Uniaxial Strain of Cells : A Platform for Pedagogy in Mechanobiology," vol. 140, no. August, pp. 1–9, 2018, doi: 10.1115/1.4039949.

[45] E. Boulter, F. S. Tissot, J. Dilly, S. Pisano, and C. C. Féral, "Cyclic uniaxial mechanical stretching of cells using a LEGO ® parts-based mechanical stretcher system," no. December, 2019.

[46] A. J. Banes, "Out of Academics : Education , Entrepreneurship and Enterprise," vol. 41, no. 9, pp. 1926–1938, 2013, doi: 10.1007/s10439-013-0839-x.

[47] J. J. L. Lau, R. M. W. Wang, and L. D. B. III, "Development of an Arbitrary Waveform Membrane Stretcher for Dynamic Cell Culture," 2014, doi: 10.1007/s10439-014-0976-x.

[48] R. De and S. A. Safran, "Dynamical theory of active cellular response to external stress," no. April, 2008, doi: 10.1103/PhysRevE.78.031923.

[49] R. De, A. Zemel, and S. A. Safran, "Dynamics of cell orientation," vol. 3, no. September, pp. 655–659, 2007, doi: 10.1038/nphys680.

[50] A. Livne, E. Bouchbinder, and B. Geiger, “Cell reorientation under cyclic stretching,” *Nat. Commun.*, vol. 5, no. May, 2014, doi: 10.1038/ncomms4938.

[51] D. Wang, Y. Xie, B. Yuan, and J. Xu, “A stretching device for imaging real-time molecular dynamics of live cells adhering to elastic membranes on inverted microscopes during the entire process of the stretch,” pp. 288–293, 2010, doi: 10.1039/b920644b.

[52] H. Kamble, M. J. Barton, M. Jun, S. Park, and N. T. Nguyen, “Cell stretching devices as research tools: Engineering and biological considerations,” *Lab Chip*, vol. 16, no. 17, pp. 3193–3203, 2016, doi: 10.1039/c6lc00607h.

[53] K. B. Roth, K. B. Neeves, J. Squier, and D. W. M. Marr, “Imaging of a linear diode bar for an optical cell stretcher,” vol. 6, no. 3, pp. 422–426, 2015, doi: 10.1364/BOE.6.000807.

[54] R. Fior, S. Maggiolino, M. Lazzarino, and O. Sbaizero, “A new transparent Bio-MEMS for uni-axial single cell stretching,” pp. 1581–1587, 2011, doi: 10.1007/s00542-011-1325-8.

[55] S. Dhein *et al.*, “Mechanical control of cell biology . Effects of cyclic mechanical stretch on cardiomyocyte cellular organization,” *Prog. Biophys. Mol. Biol.*, vol. 115, no. 2–3, pp. 93–102, 2014, doi: 10.1016/j.pbiomolbio.2014.06.006.

[56] W. Tan, D. Scott, and D. Belchenko, “Development and evaluation of microdevices for studying anisotropic biaxial cyclic stretch on cells,” pp. 869–882, 2008, doi: 10.1007/s10544-008-9201-8.

[57] J. Garvin, J. I. E. Qi, M. Maloney, A. J. Banes, D. Ph, and G. E. T. Al, “Novel System for Engineering Bioartificial Tendons and Application of Mechanical Load *†,” vol. 9, no. 5, pp. 967–979, 2003.

[58] B. Engineering and C. Street, “Design of a New Stretching Apparatus and the Effects of Cyclic Strain and Substratum on Mouse Lung Epithelial-12 Cells,” vol. 35, no. 7, pp. 1156–1164, 2007, doi: 10.1007/s10439-007-9262-5.

[59] W. W. Ahmed *et al.*, “Biomaterials Myoblast morphology and organization on biochemically micro-patterned hydrogel coatings under cyclic mechanical strain,” vol. 31, pp. 250–258, 2010, doi: 10.1016/j.biomaterials.2009.09.047.

[60] A. Poulin *et al.*, “An ultra-fast mechanically active cell culture substrate,” no. April, pp. 1–10, 2018, doi: 10.1038/s41598-018-27915-y.

[61] Z. Li, C. Gao, S. Fan, J. Zou, G. Gu, and M. Dong, “Cell Nanomechanics Based on Dielectric Elastomer Actuator Device,” *Nano-Micro Lett.*, vol. 11, no. 1, pp. 1–19, 2019, doi: 10.1007/s40820-019-0331-8.

[62] B. D. Hoffman, C. Grashoff, and M. A. Schwartz, “Dynamic molecular processes mediate cellular mechanotransduction,” *Nature*, vol. 475, no. 7356, pp. 316–323, 2011, doi: 10.1038/nature10316.

[63] B. Geiger, J. P. Spatz, and A. D. Bershadsky, “Environmental sensing through focal adhesions,” *Nat. Rev. Mol. Cell Biol.*, vol. 10, no. 1, pp. 21–33, 2009, doi: 10.1038/nrm2593.

[64] J. I. Andersen, C. P. Pennisi, T. Fink, and V. Zachar, “Focal Adhesion Kinase Activation Is Necessary for Stretch-Induced Alignment and Enhanced Differentiation of Myogenic Precursor Cells,” *Tissue Eng. - Part A*, vol. 24, no. 7–8, pp. 631–640, 2018, doi: 10.1089/ten.tea.2017.0137.

[65] Y. Wang, J. Yan, and B. T. Goult, “Force-Dependent Binding Constants,” *Biochemistry*, vol. 58, no. 47, pp. 4696–4709, 2019, doi: 10.1021/acs.biochem.9b00453.

[66] E. Evans, “Probing the Relation Between Force Lifetime and Chemistry,” *Annu. Rev. Biophys. Biomol. Struct.*, vol. 30, pp. 105–128, 2001.

[67] B. T. Marshall, M. Long, J. W. Piper, T. Yago, R. P. McEver, and C. Zhu, “Direct observation of catch bonds involving cell-adhesion molecules,” *Nature*, vol. 423, no. 6936, pp. 190–193, 2003, doi:

10.1038/nature01605.

[68] C. Lee, J. Lou, K. Wen, M. Mckane, S. G. Eskin, and S. Ono, “Actin depolymerization under force is governed by lysine 113 : glutamic acid 195-mediated,” pp. 1–6, 2013, doi: 10.1073/pnas.1218407110/-/DCSupplemental.www.pnas.org/cgi/doi/10.1073/pnas.1218407110.

[69] C. Lee *et al.*, “Regulation of actin catch-slip bonds with a RhoA-formin module,” *Nat. Publ. Gr.*, no. September, pp. 1–10, 2016, doi: 10.1038/srep35058.

[70] K. K. Sarangapani *et al.*, “Regulation of Catch Bonds by Rate of Force Application *,” *J. Biol. Chem.*, vol. 286, no. 37, pp. 32749–32761, 2011, doi: 10.1074/jbc.M111.240044.

[71] I. Nitsan, S. Drori, Y. E. Lewis, S. Cohen, and S. Tzlil, “Mechanical communication in cardiac cell synchronized beating,” vol. 12, no. January, 2016, doi: 10.1038/NPHYS3619.

[72] A. Tondon, H. Hsu, and R. Kaunas, “Dependence of cyclic stretch-induced stress fiber reorientation on stretch waveform,” *J. Biomech.*, vol. 45, no. 5, pp. 728–735, 2012, doi: 10.1016/j.jbiomech.2011.11.012.

[73] A. Rio, R. Perez-jimenez, R. Liu, P. Roca-cusachs, J. M. Fernandez, and M. P. Sheetz, “Stretching Single Talin Rod,” vol. 323, no. January, pp. 638–641, 2009.

[74] F. Margadant *et al.*, “Mechanotransduction In Vivo by Repeated Talin Stretch- Relaxation Events Depends upon Vinculin,” vol. 9, no. 12, 2011, doi: 10.1371/journal.pbio.1001223.

[75] A. L. Le Roux, X. Quiroga, N. Walani, M. Arroyo, and P. Roca-Cusachs, “The plasma membrane as a mechanochemical transducer,” *Philos. Trans. R. Soc. B Biol. Sci.*, vol. 374, no. 1779, 2019, doi: 10.1098/rstb.2018.0221.

[76] A. Anishkin, S. H. Loukin, J. Teng, and C. Kung, “Feeling the hidden mechanical forces in lipid bilayer is an original sense,” vol. 111, no. 22, 2014, doi: 10.1073/pnas.1313364111.

[77] N. Wang, J. D. Tytell, and D. E. Ingber, “Mechanotransduction at a distance: mechanically coupling the extracellular matrix with the nucleus,” vol. 10, no. JANuARy, pp. 75–82, 2009.

[78] S. Na *et al.*, “Rapid signal transduction in living cells is a unique feature of mechanotransduction,” vol. 105, no. 18, 2008.

[79] I. D. E. MANIOTIS A. J.,CHEN C. S., “Demonstration of mechanical connections between integrins , cytoskeletal filaments , and nucleoplasm that stabilize,” *Cell Biol.*, vol. 94, pp. 849–854, 1997.

[80] H. Hillborg, J. F. Ankner, U. W. Gedde, G. D. Smith, H. K. Yasuda, and K. Wikstro, “Crosslinked polydimethylsiloxane exposed to oxygen plasma studied by neutron reflectometry and other surface specific techniques,” vol. 41, pp. 6851–6863, 2000.

[81] K. Chen, A. Vigliotti, M. Bacca, R. M. Mcmeeking, and V. S. Deshpande, “Role of boundary conditions in determining cell alignment in response to stretch,” pp. 1–6, 2017, doi: 10.1073/pnas.1715059115/-/DCSupplemental.www.pnas.org/cgi/doi/10.1073/pnas.1715059115.

[82] J. J. Wille, C. M. Ambrosi, and F. C. Yin, “Comparison of the Effects of Cyclic Stretching and Compression on Endothelial Cell,” vol. 126, no. October, pp. 11–13, 2004, doi: 10.1115/1.1798053.

[83] H. Hsu, C. Lee, and R. Kaunas, “A Dynamic Stochastic Model of Frequency-Dependent Stress Fiber Alignment Induced by Cyclic Stretch,” vol. 4, no. 3, 2009, doi: 10.1371/journal.pone.0004853.

[84] S. Jungbauer, H. Gao, J. P. Spatz, and R. Kemkemer, “Two characteristic regimes in frequency-dependent dynamic reorientation of fibroblasts on cyclically stretched substrates,” *Biophys. J.*, vol. 95, no. 7, pp. 3470–3478, 2008, doi: 10.1529/biophysj.107.128611.

[85] H. Hsu, C. Lee, A. Locke, S. Q. Vanderzyl, and R. Kaunas, “Stretch-Induced Stress Fiber Remodeling

and the Activations of JNK and ERK Depend on Mechanical Strain Rate , but Not FAK," vol. 5, no. 8, 2010, doi: 10.1371/journal.pone.0012470.

[86] C. Lee, C. Haase, S. Deguchi, and R. Kaunas, "Cyclic stretch-induced stress fiber dynamics – Dependence on strain rate, Rho-kinase and MLCK," *Biochem. Biophys. Res. Commun.*, vol. 401, no. 3, pp. 344–349, 2010, doi: 10.1016/j.bbrc.2010.09.046.

[87] Wang James H.-C., "Substrate Deformation Determines Actin Cytoskeleton Reorganization : A Mathematical Modeling and Experimental Study," *Theor. Biol.*, vol. 202, pp. 33–41, 2000.

[88] R. K. Ã and H. Hsu, "A kinematic model of stretch-induced stress fiber turnover and reorientation," vol. 257, pp. 320–330, 2009, doi: 10.1016/j.jtbi.2008.11.024.

[89] C. O. C. W. J. Oomens, S. Loerakker, J. Foolen, C. V. C. Bouten, and F. P. T. Baaijens, "Computational model predicts cell orientation in response to a range of mechanical stimuli," 2013, doi: 10.1007/s10237-013-0501-4.

[90] R. M. Mcmeeking and A. G. Evans, "Analysis and Interpretation of Stress Fiber Organization in Cells Subject to Cyclic Stretch," vol. 130, no. June, 2008, doi: 10.1115/1.2907745.

[91] G. Xu, B. Li, X. Feng, and H. Gao, "Article A Tensegrity Model of Cell Reorientation on Cyclically Stretched Substrates," pp. 1478–1486, 2016, doi: 10.1016/j.bpj.2016.08.036.

[92] YC Fung, *A First Course in Continuum Mechanics for Physical and Biological Engineers and Scientists*. 1994.

Chapter 4

Results

Effects of a benzodiazepine-derived molecule (1G) on U87MG cell-line

• Introduction

Glioblastoma multiforme (GBM) is one of the most common malignant primary brain tumors and, despite a strong effort dedicated to finding an effective therapy, it is still characterized by a very poor prognosis [1]. Among others, one feature that makes GBM difficult to be defeated is its ability to migrate and to infiltrate into the surrounding brain parenchyma and all of these properties are strongly related to a continuous dynamic reorganization of the actin cytoskeleton [2], [3]. At the same time, the cellular dynamic changes that occur during tumor progression induce significant changes in the architecture and mechanical properties of both the tumor and surrounding host tissue. It is known that cellular biomechanics are involved in a number of biological functions in eukaryotic cells, such as migration, differentiation, morphogenesis, and proliferation [4], [5]. The cytoskeleton and the associated proteins are responsible for both transducing external mechanical stimuli into biochemical processes and for the application of stresses on the external matrix. This sort of mechanical homeostasis is strictly dependent on the activity of cytoskeleton-associated motor proteins and to the cell/matrix adhesion molecules and it is altered in the case of developing and migrating tumors [6]–[8]. Thus, the motor-clutch hypothesis becomes crucial in this framework. In particular, cell adhesion is related to integrin clustering, leading to the formation of focal adhesions and actin stress fibers that, in turn, alter the rheological properties of the cells [9]. Although the available standard therapy for GBM has evolved into multimodality approaches, comprising temozolomide and the antiangiogenic monoclonal recombinant antibody bevacizumab, corticosteroids and immunotherapy, unfortunately, the improvements of patients survival have been only modest [10], [11]. This has led to an important effort to identify new molecular targets of GBM tumor specially focusing on motility and proliferation properties of the associated cells [12]–[15]. Specific microtubule associated proteins, especially the ones related to the dynamic behavior of microtubules, could represent a good target to simultaneously act on invasion and proliferation activity of GBM cells. However, especially in the brain, the role of microtubules is crucial, and their unspecific depolimerization should be avoided as much as possible. From this point of view, compounds that produce only a slowdown in microtubule dynamics avoiding its depolimerization could more selectively fight cancer cells in which the dynamic activity is strongly enhanced. Affecting microtubule dynamics could also result in an alteration of the actin cytoskeleton [16]. It has been found that the depolymerization of microtubules induces for example an increase of the formation of actin stress fibers by the activation of RhoA [17], [18] and, in general, by affecting the Rho family GTPases and the nucleotide exchange factors involved in the dynamic activity of microtubules. As a consequence, molecules targeting microtubules associated proteins can have an effect on cell mechanical properties, largely ascribable to the structure of the actin cytoskeleton, and on cell migration properties. In recent years, several studies reported that some types of cancer cells have a stiffness inversely proportional to their metastatic potential, due to increased ability of more deformable cells to migrate in the narrow pores of the extracellular matrix. In general, cancer cell rheological properties are different with respect to the case of healthy cells [19]–[21]. Softer cancer cells are typically embedded in more rigid tissues thanks to the production of a stiffer extracellular matrix. Cells and matrix reciprocally interact on the basis of mechanical stimuli in a sort of mechanoreciprocity process [22]. Even if the tissue scale mechanics is the definite mechanical descriptor of the cancer behavior, analysis of rheological properties of single cells could be used as a marker of cell metastatic potential. At the same time, alteration of cell or tissue mechanical properties could be exploited as a target to which drugs can be directed [23], [24].

Some of us recently demonstrated the ability of a new 2-benzodiazepine-3-one derivative (in the following named 1G) to arrest the cell cycle progression of human leukemia Jurkat T cells and HeLa cells by altering mitotic spindle formation during mitosis [25]. Since the new molecule is supposed to be able to cross the blood brain barrier, it could represent an interesting candidate for fighting brain tumors. In this section we will illustrate how 1G interferes with the replicating, migrating and mechanical properties of the GBM cell line U87MG. We show that 1G, starting from a concentration of 5 μM, is able to slow down duplication times of GBM cells and, at concentrations higher than 20 μM, to almost completely block their duplication in the G2/M phase by disorganizing the mitotic spindle. At the same time, starting from a concentration of 5 μM, 1G induces strong and almost instantaneous shape changes leading to a polarity loss of the cells and strongly decreases the 2D migration capabilities of the cells regardless of the stiffness of their substrate. We found, exploiting Atomic Force Microscopy, that cell polarity loss is also coupled with an increased cell stiffness.

- # Cell migration assay

GBM cells are endowed with a very high infiltration ability exploiting physical structures in the brain environment such as blood vessels and axons. The molecular basis for their migration of glioma cells has been largely investigated and it has been found that their proliferative and migration capabilities are mutually exclusive, meaning that conditions that favor their migration at the same time slow down their proliferation [26]–[28]. This correlation between proliferation and migration poses a critical limit in clinical treatments. Accordingly, a strategy to block GBM proliferation could have the increase of their migration ability as a side effect. Moreover, the GBM cell migration process has been found to be sensitive to the mechanical properties of the substrate on which cells reside. This situation could depend on the specific GBM cell lines that are considered, and the behavior of primary cell from patients could be different [29].

At the same time, it has been shown that the effect of drugs on the same type of cells depends on the mechanical environment of the cells [30], [31]. Moreover, also drugs affecting molecular motors or cell substrate adhesion could have different effect on cell migration properties, in terms of relative speed variation, depending on the stiffness of the substrate [32]. Our initial findings were focused on cell migration capabilities when the U87MG cells are exposed to different concentrations of 1G compound (5-10-20 μM). Accordingly, we measured the effect of 1G on the 2D cell migration properties of U87MG cells on PDMS substrates with different Young modulus and on plastic. The range of substrate stiffness (Young modulus) we considered spans the interval from 0.2 kPa to 300 kPa for PDMS supports (0.2-8-32-300 kPa in order to span over 3 orders of magnitudes focusing on the relevant substrate rigidity range well resuming the brain extracellular-matrix) and we also considered the plastic substrate for which we can assume a Young modulus of a few GPa. The different PDMS substrate rigidities have been studied acquiring a multi-six dish set by “Advanced Biomatrix CytoSoft® Discovery Kit”. The set was composed by seven multi-six with different rigidity (nominal value): 0.2-0.5-2.0-8.0-16.0-32.0 and 64.0 kPa, respectively. We did not check the accuracy of the nominal value rigidities provided by the seller. Regarding the repeatability of the overall experimental findings reported below for the different rigidities, we repeated the live imaging assays twice.

- # Wind Rose Plots

Firstly, we provide a qualitative comparison of the averaged area explored during live cell imaging assays using the Wind rose plot, Fig 1. At fixed row we showed how the substrate rigidity can modulate cell motility capability, especially under control conditions (below we will provide a brief account recalling the motor

clutch theory), the last column report the results obtained on plastic-dish. At fixed column we demonstrated the gradual cell migration inhibition while the 1G concentration is increased.

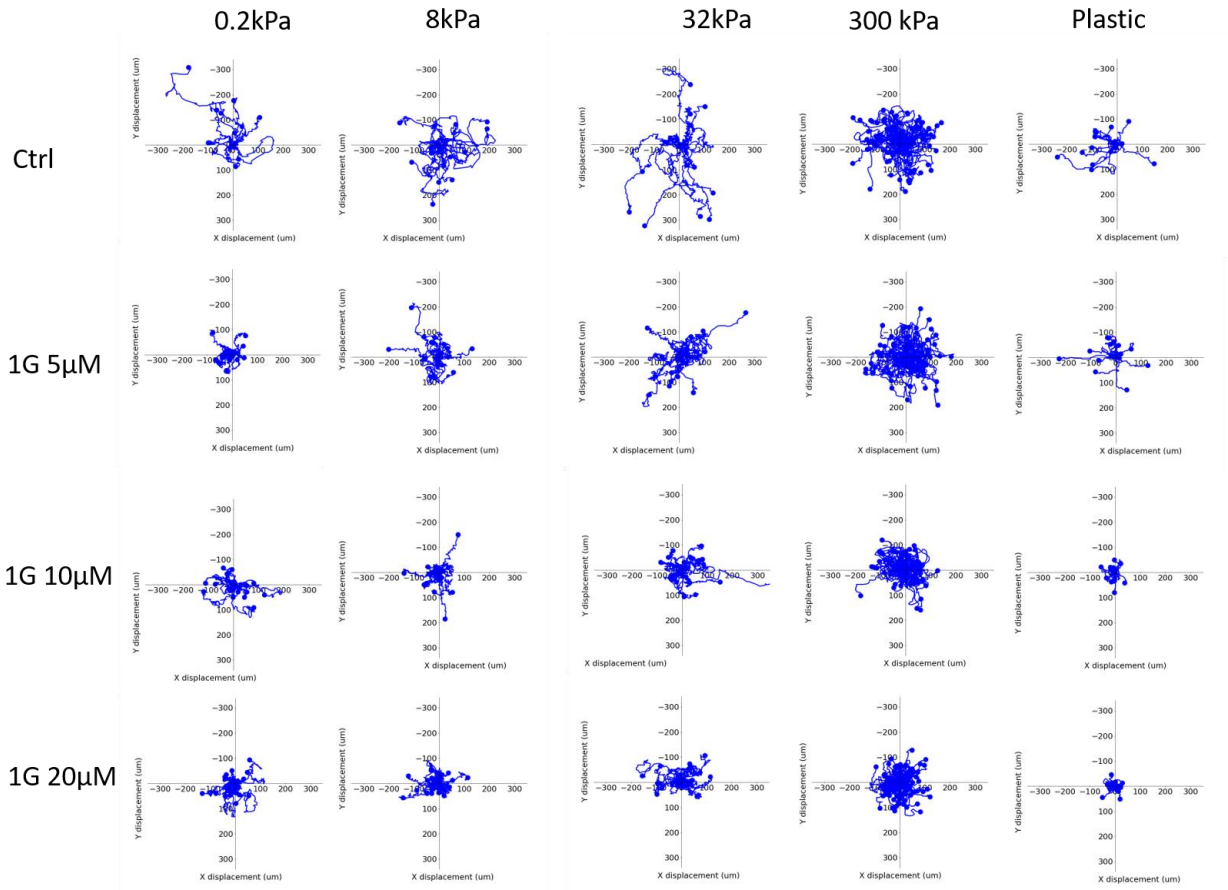

Figure 1: Wind-Rose plots panel: At fixed column is investigated the 1G effect gradually increasing its concentration for a given substrate rigidity condition. At fixed row is explored a specific 1G concentration condition varying the substrate rigidity.

- **MSD and PRW model**

After Wind Rose plot illustration (Fig 1), which qualitatively confirms the efficiency of the 1G compound for all the substrate rigidity under study, we moved toward a more quantitative analysis. Firstly, we measured the experimental MSD after approximatively 8 hours of live imaging session. The experiments were performed using a multi-six plate with a nominal fixed rigidity and moving repeatedly the motorized stage to follow 4 dishes that represent respectively: control, 1G 5µM, 1G 10µM and 1G 20µM. In Fig 2 the MSD panel is reported. In the first row (Fig 2a-e) the MSD results for a fixed substrate rigidity are plotted [0.2kPa;8.0kPa;32kPa;300kPa;Plastic], in the second row (Fig 2f-i) the MSD for a specific 1G concentration are plotted [Control;1G 5µM;1G 10µM;1G 20µM]. Focusing on the finding obtained in control conditions, we showed how the substrate rigidity can modulate cell motility capability. In the first row the 1G compound concentration is gradually increased (5µM red line; 10µM green line; 20µM blue line) and its effect on the cell sample motility is investigated. The tracked cells used for the averaged MSD evaluation have been chosen using the protocol described in the methods chapter, thus only ≈75% of the entire observing time is exploited in the graphs.

For the control case, where no drug was injected, we can see that the cell migration ability shows mechano-sensitivity; the MSD for all the time intervals is higher for substrates of intermediate stiffness with a maximum, considering the different substrates we tested, for 32 kPa. We have to recall that U87MG cells are

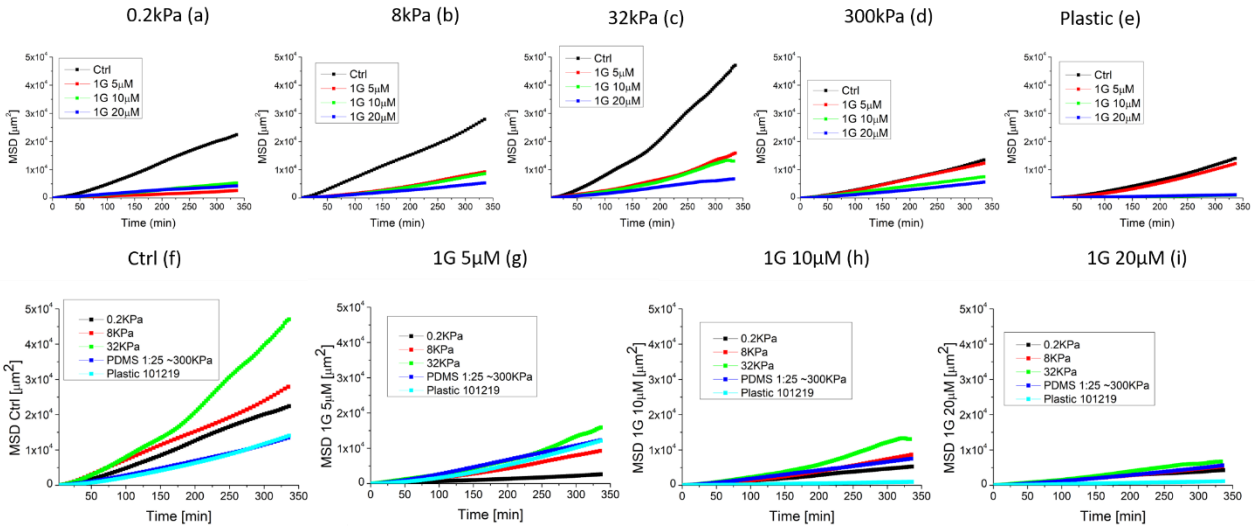

Figure 2: MSD-vs-Time profiles panel: (a-e)Experimental MSD evaluated for the different substrate rigidities, the 1G concentrations effect are compared in each subplot. (f-i) Experimental MSD for a fixed 1G concentration condition, the substrate rigidities role if compared in each subplot.

mainly representative of the mesenchymal subclass among all the GBM types and the presence of mechano-sensitivity for migration ability could depend of the specific subclass [33]. Dealing with the MSD parameter, the overall behavior we observed is biphasic, as found for other cell types. This behavior can be attributed to a balance between cell adhesion on the support and the dynamics of actin polymerization and traction force [34]. On a soft substrate, cell adhesion area is lower and the focal adhesion complexes of the leading edge and the cells are not strongly attached to the substrate to induce an efficient forward movement of the cell. On the other hand, on a too much stiff substrate, the strong development of adhesion complexes makes the necessary release for the migration of the rear portion of the cell more difficult. We must emphasize how the blue and the light-blue lines in control condition (Fig 2 f, which represent the 300kPa and the plastic substrate, respectively) are almost superimposable. Thus, 300kPa and few GPa values provide an almost equal MSD behavior and confirm how U87MG cell are insensitive above certain substrate rigidity limit. An intermediate stiffness could produce the optimal compromise between the two opposite situations to enhance cell migration. A quantitative model of this mechanism with predictive ability can be based on the motor-clutch mechanism [32], [35]–[37], which specifically applies to the force transmission process. A combination of different modules with different orientations can produce a balance of traction forces resulting in an effective cell migration. In each module, myosin contractility is partially transmitted to the adhesion complexes that assure the connection between the cytoskeleton elements and the cell substrate establishing a cytoplasmatic retrograde flow of actin. The binding and unbinding rate constants, together with the force rate increase on the substrate, finely tune an optimal intermediate substrate rigidity value for which the rate of force increase is not too fast to impede the formation of a relevant number of integrin/substrate attachment points before disengagement and not too slow to induce detachment of the adhesion complexes before a relevant force value is transmitted to the substrate. Considering that the traction force has an effect on the actin retrograde flow, a connection can be established between the motor-clutch hypothesis and the migration speed, especially in the case where different pseudopods are included in the prediction analysis. In this context, a biphasic behavior of glioma cells as the substrate rigidity is varied has been experimentally obtained [32]. The motor clutch mechanism deals with the role of the cytoskeletal actin polymers. However, as already mentioned, it has been demonstrated in several cases that a drug that is able to affect microtubules can have a secondary effect also on actin stress fibers. Including the effect of the 1G compound in Fig 2a-e and g-i we observe a gradual reduction of the MSD increasing the compound concentration, which is not uniform for the different substrate rigidities analyzed. In fact, at higher substrate rigidities (300kPa and Plastic) the 1G 5µM curve and the control condition are almost superimposable. At lower rigidities (0.2kPa;8.0kPa;32.0kPa) even at 1G 5µM concentration we have a drastic MSD slow down if

compared to the related control reference. Although, the MSD magnitude at 5µM and 10µM conditions for 32kPa (where the motility is maximized) are comparable to MSD in control condition for 300kPa and Plastic substrate. Concluding, the substrate stiffnesses can modulate the motility in control condition, as explained above, but also in presence of the 1G compound.

• Experimental mean speed modulus

Another motility index is the experimental mean speed modulus evaluated between adjacent frames. In Fig 3 our findings comparing the substrate stiffness role for a fixed 1G compound concentration are reported.

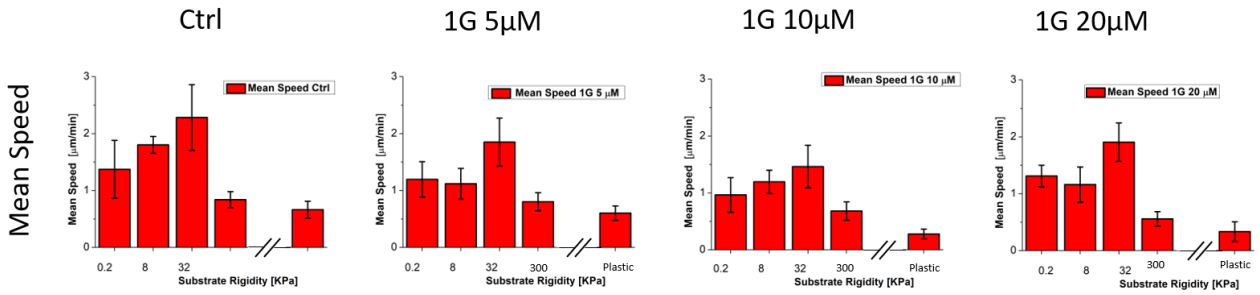

Figure 3: Experimental mean speed panel: The subplots reports the results for fixed 1G concentration condition comparing the substrate rigidities role.

Observing Fig 3, the mechano-sensitive biphasic migration behavior, already observed in the MSD analysis (Fig 2), is confirmed for the mean speed even for all 1G concentrations we considered. Furthermore, the experimental mean speed remains almost unchanged (or little reduced at most) gradually increasing 1G concentration for all the substrate rigidities explored, even at the highest level (20µM). The drastic MSD reduction seen in Fig 2 is not ascribable to the instantaneous experimental mean speed. The cell motility capability inhibition under 1G exposition must be related to directional index. Firstly, we tried to apply the PRW mathematical model on the experimental MSD in order to extrapolate the [S;P] fitting parameters and to compare them when the 1G concentration is gradually increased. Then, we measured and compared the angular correlation function.

• S (Speed fit) and P (Persistence Time) parameters

The PRW model is applied singularly on the cells tracked set, then the $[S_i;P_i]$ where S_i and P_i refer to the i-th cell are statistically analyzed following the protocol described in the Methods Chapter. Thus, the most probable <S> and <P> for a given substrate rigidity and 1G concentration are extrapolated. We must emphasize that <S> and <P> are evaluated starting from the statistical distribution arising from the single MSD cell fitting procedure, not from the overall MSD plotted in Fig 2. Furthermore, not all the tracked cells follow the PRW model, but most of them do. In Fig 4a-d the extrapolated <S> fitting parameters are reported.

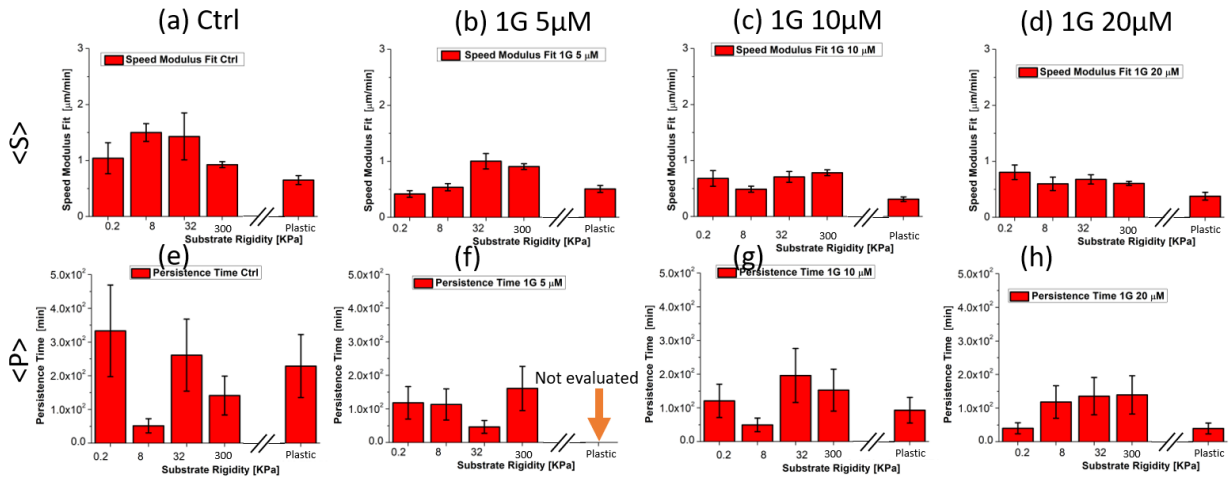

Figure 4: <S> and <P> fitting parameters panel:(a-d) <S> and (e-h) <P> parameter comparison, each subplot refers to specific 1G concentration condition.

In Fig 4e-h the related <P> parameters are shown. The findings are organized splitting up the data for each 1G concentration we considered (similarly to the experimental mean speed Fig 3), and each graph compares the substrate rigidities for a given 1G concentration.

The most probable speed fitting parameters <S>, unlike the corresponding experimental average speed (Fig 3) gradually decreases significantly with respect to the control reference when the 1G concentration is increased. Even the extrapolated persistence time <P> follows a similar trend for the overall substrate rigidities set (except for the 8.0kPa case). Summing up, the <S> and <P> results comparison in Fig 4 shows how cells gradually lose their capability to maintain their starting direction during time when they ate exposed to 1G molecule, especially at higher concentrations (10µM and 20µM). Simultaneously, the fitting speed parameter <S> reduction can provide some guess regarding the deep cytoskeleton reorganization under 1G exposition, while experimental mean speed does not show. This discrepancy between <S> and the experimental mean speed, together with the fact that cells exposed to 1G explore a reduced area with respect to the control case, can be interpreted as a continuous attempt but without success to produce stable pseudopodia.

Now we can evaluate and compare the angular autocorrelation function to estimate a complete motility overview including also a directional parameter.

• Direction-Autocorrelation

In Fig 5 the Direction-Autocorrelation (DA) function results are reported: in the first row (Fig 5a-d) the findings obtained at fixed 1G concentration are summarized, and in the second row (Fig 5e-i) the results extrapolated at fixed substrate stiffness are reported.

The DA graph obtained under control condition (Fig 5a) shows that the 300kPa and plastic rigidity substrate provide similar finding and their curves decay slowly during time if compared to DA at low substrate rigidities regime. This behavior could once again be attributed to the larger adhesion area of cells on harder substrates and to the cytoskeleton dynamics. Higher substrate rigidity produces a more structured cytoskeleton with stress fibers resulting from the enlargement of adhesion complexes and enhanced myosin activation.

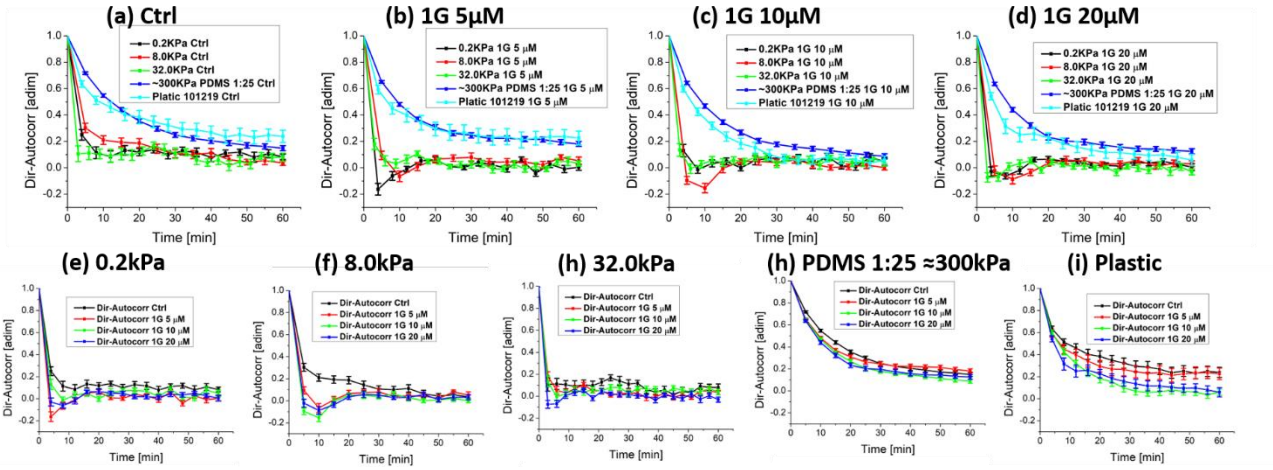

Figure 5: Direction-Autocorrelation panel: (a-d) AD profiles rearranged for a specific 1G concentration, each subplot reports the substrate rigidity comparison. (e-i) AD profiles rearranged for a specific substrate rigidity, each subplot reports the 1G concentration comparison.

Accordingly, when the cell is organized for migration along a specific direction, it takes longer time to nucleate a new pseudopod and to change the migration direction. Instead, softer substrates allow a more rapid and similar change of migration direction for U87MG cells and the DA function decays faster. Thus, the direction-autocorrelation provides an estimation of the change of the migration direction rate unbiased from the instantaneous cell speed. In fact, the DA profiles for softer substrates under control condition, 0.2kPa, 8.0kPa and 32.0kPa are almost superimposable. Including the effect of the 1G compound for the different substrate rigidities (Fig 5e-i) we observe a minimal DA decrement but well distinguishable when the 1G concentration is increased to 300kPa and to the plastic cases (Fig 5h-i). The 300kPa and the plastic curves are superimposable and strictly positive at the different 1G concentrations. Similarly, the DA profiles for low substrate stiffnesses are fairly superimposable for a fixed 1G concentration condition (Fig 5b-d 0.2kPa-8.0kPa-32.0kPA, black, red and green dotted line respectively). Gradually increasing the 1G amount for a given low substrate rigidity (Fig 5e-g) we observe a noticeable DA decrement, especially at first time points, where DA assumes even negative magnitude. Since the DA decays faster for low substrate rigidities, the relevant DA comparison between different 1G concentration for 0.2kPa-8.0kPa-32kPa cases must be performed in the first time-frame points, while for longer times the 1G concentrations and control conditions are indistinguishable. Differently, at high substrate rigidities regime (300kPa and plastic) the DA profiles are well separated even for longer times (>30min).

• Cell Polarization Loss

An additional parameter that quantified the cytoskeletal reorganization under 1G exposition, like the lamellipodia or pseudopodia protrusion stability is the shape-factor introduced in the Methods Chapter. In

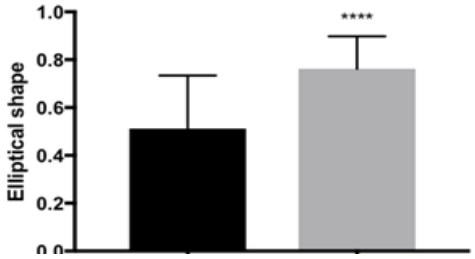

Figure 6: Aspect-Ratio comparison between control (black column bar) and 1G 20µM (gray column bar) after 8h from initial seeding.

fact, one of the immediate effects once 1G is injected is the retraction of the processes and the prevalent round shape adopted by the cells, as shown by the shape-factor parameter reported in Fig 6 after elliptical fitting (Figure already showed as example in the aspect-ratio introduction).

The loss of polarity and the processes retraction of U87MG cells upon exposure to 1G have been initially observed during live cell imaging analysis for migration assays, but not quantitively measured. These preliminary findings suggested us to investigate by time-lapse imaging what happens when cells are directly seeded in the presence or in the absence of 1G. In fact, symmetry breaking occurs in cells after they started to adhere to the substrate. Whereas U87MG cells in the absence of 1G, after about two hours required for the adhesion process, start elongating processes, in the case of cells seeded in the presence of 1G, the elongation of processes was completely prevented. It appears such as 1G is able to block a stable symmetry breaking in cells leading to the formation of protrusions and directed cell migration. The initial step in the formation of cell protrusions is mainly the result of actin polimerization but the stability of the formed protrusions against the myosin contractile action could be attributed to the mechanical role of microtubules. If microtubule dynamics and organization is affected by 1G, the establishment of cell polarization is more difficult and the directed migration is strongly reduced. Cells are however active in producing many attempts to extend pseudopods.

- **Cell viscoelasticity characterization**

The large cell cytoskeletal reorganization after 1G exposition suggested us to investigate how the mechanical properties of the cells are affected by 1G compound. Mechanical properties have been often related to the migratory ability of cells, but a general rules set framework has not yet been defined. Although it has been found that in many cases a reduced stiffness of cancer cells ensures a higher metastatic degree, each cell type must be specifically analyzed in this regard. Moreover, the migration ability should be considered in a specific environment. In fact, the relevant mechanical features are the cell viscoelasticity combined to the substrate extracellular matrix stiffness. For example, 3D migration in a dense polymer network could require the deformation of the nucleus, whereas this property is not relevant if migration is considered in an obstacle-free 2D environment. Here we studied using AFM the mechanical properties of U87MG cells before and after their exposure to 1G. The comparisons have been performed under the same conditions and different experiments have been performed. We investigated by force spectroscopy control cells and cells exposed for 5h and 24h to 20 µM 1G concentration, respectively, inside a cell incubator. Considering long time live cell imaging, we observed that, in the case of a 24h treatment, there are two different populations in the petri dish: rounded cells corresponding to cells in mitosis and blocked in this phase, and flattened cells corresponding to both cells in interphase and still waiting to enter the first attempt of mitosis after 1G has been added and cells that exited from mitosis after a prolonged attempt to divide.

We adopted the AFM experimental protocol acquisition mention in the methods chapter (chapter 2), acquiring ≈ 10 Force-Indentation curves per cell.

In AFM characterization we concentrated on flat cells given that, for untreated cells, the rounded cell population is scarcely represented and a statistical meaningful analysis for a comparison is difficult. Secondly, the rounded and unpolarized cells have usually higher height profiles, which pose serious limits for AFM analysis since the piezo scan-limit is approximatively ≈14µm. The viscoelasticity analysis has been performed acquiring several Force-Indentation curves in the central region of the cell, studying approximatively ≈20 cells for each condition (1G 20µM after 3h and 24h since 1G initial addition and corresponding controls reference). The Force-Indentation curves have been acquired for several scan-displacement speeds $V_{Scan\text{-}Displacement}$ in order to validate the robustness of the findings. The viscoelastic results, analyzed exploiting the Ting model, reported below refer to two distinct $V_{Scan\text{-}Displacement}$ [2µm/s;5µm/s]. Then, the raw data are pre-processed for

Contact-Point evaluation and hydrodynamic force subtraction following the protocol explained in the Method Chapter. Finally, the Ting model solution has been exploited. In Fig 7a-b the mean [E_0;α] parameters extrapolated from the analysis after 3h of 1G exposition and corresponding control condition are reported and compared. In Fig 7c-d are reported the mean [E_0;α] parameters after 24h from initial 1G addition and related control condition reference. In Fig 8 are showed the histograms for the viscoelasticity parameters [E_0;α] obtained from cell sample after 24h 1G 20μM exposure. After 3h of 1G treatment both the cell stiffness E_0 and viscosity index α are almost unchanged if compared to the initial control state. Instead, after 24h of 1G 20μM treatment the cell stiffness E_0 is significantly higher with respect to control reference, and the viscosity parameter is more spread toward higher values (see the histograms in Fig 8). Concluding, these comparisons between control and 1G exposition after 3h and 24h focalized on flattened cells reveals a drastic viscoelasticity modification only for longer time 1G treatment. Subsequently, we can observe that the depolarization of the cell shape that acts immediately after 1G treatment is not related to immediate

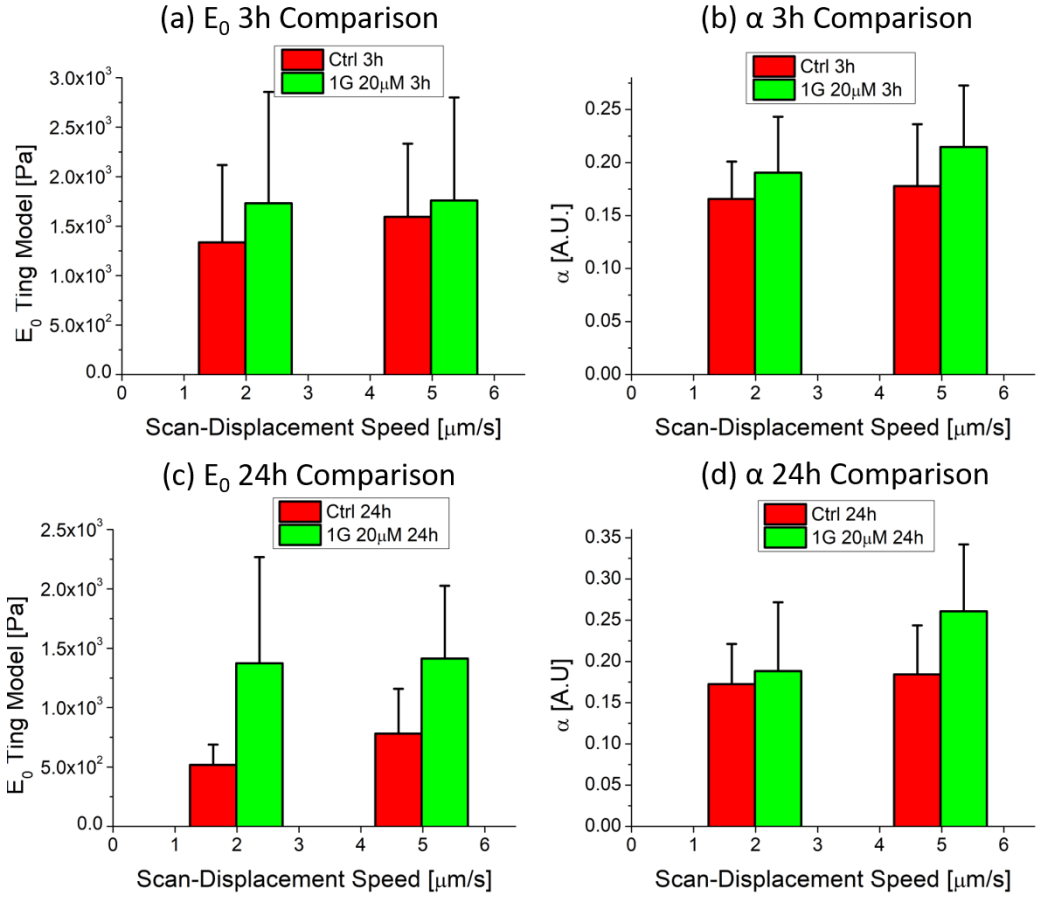

Figure 7: E_0 and α viscoelastic parameters obtained applying the power-law-rheology (PLR) relaxation function for two different $V_{Scan\text{-}Displacement}$: (a-b) E_0 and α comparison after 3h from 1G 20μM insertion. (c-d) E_0 and α comparison after 24h from 1G 20μM insertion.

viscoelasticity changes in the cytoskeleton. However, after long time 1G exposition also the viscoelastic modifications are involved. Finally, comparing our findings with respect to the Scan-Displacement speed we can observe a small shift of the viscoelastic parameters when we moved to higher speeds. This is probably due to hydrodynamic drag force, although it has been removed in the previous pre-treating steps.

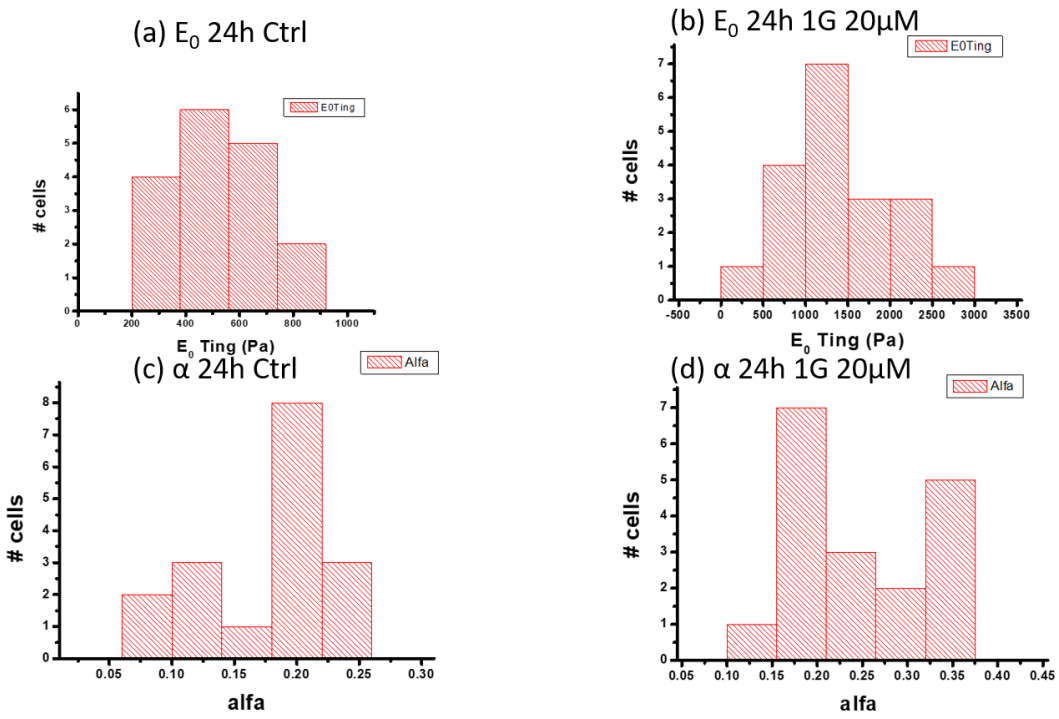

Figure 8: E_0 and α histograms after 24h from 1G 20µM insertion: (a,c) control condition, (b,d) 1G 20µM exposition

- **Effect of 1G on tubulin in mitosis and mitotic time**

During the mitotic stage, some attempts to start the cytokinesis step can be observed as deduced from the shape changes of the cells rounded cells start to adopt an oblong configuration and then they go back to the rounded shape when we performed long-time live imaging assays [38].

In Fig 9 is reported the "cell-state-progression" during the long-time cell imaging assays under 1G 20µM exposition. In particular, 26 different cells have been analyzed from their entrance in mitosis. In many cases, the attempts are stopped and the cell goes back to the rounded shape. It happens that, after a prolonged period of time rounded cells start adopting a flat configuration escaping the mitotic stop. These cells are probably going back to the interphase stage of their cycle in a multinucleated configuration. There are mechanical actions to be performed to proceed with cell shape changes during cytokinesis. Work has to be done against the cortical tension to deform the cell from a spherical shape that minimizes the total cell area. An increased cell cortical tension could be a limiting factor for the cytokinesis process. Moreover, the disorganization of the mitotic spindle could produce the absence of the right coupling of microtubules and actin filaments to proceed in the cytokinesis stage. For example, the right coupling between the two cytoskeletal elements is required for the correct positioning of the furrow stiffening ring.

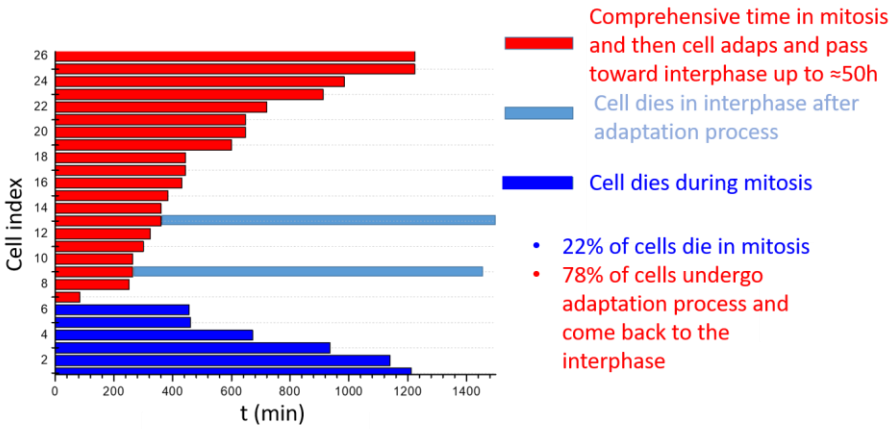

Figure 9: cell-state-progression graph obtained from long-time live imaging assay under 1G exposition

- **Immunofluorescence assays**

A recent study from some of us showed that, in HeLa cells, 1G affects the dynamics of microtubules, slowing down their growth [39]. Microtubule dynamics is controlled by several Microtubule Associated Proteins (MAPs) which, by their binding-unbinding kinetics control the dynamic stability of the polymers. To directly check the effect of 1G on cytoskeleton organization, we decided to analyze, by immunofluorescence, U87MG cells exposed to 1G for different time intervals. Firstly, we analyzed on actin filaments, then we moved toward microtubule and FAK structures. Fig 10 shows typical fluorescence microscopy images of U87MG cells where actin filaments have been stained. It is evident that, after just a few hours of exposition, 1G induced the formation of stress fibers in the cells, similarly to what happens in the case of nocodazole [40]. The action mechanism of nocodazole is based on microtubule depolimerization, a situation highly toxic for cells in the brain, where a lot of signals travel along microtubules. It has been shown that microtubule depolimerization is often coupled to an increase of the stress in cells and the formation of actin stress fibers [17], [40], [41]. This effect could be the result of the elimination of the resisting role played by microtubules against the acto-myosin contraction. Alternatively, microtubule depolimerization could induce enhance myosin light chain (MLC) phosphorylation inducing the formation of the stress fibers. At the same time, by affecting other MAPs, or by modifying the association/dissociation rate of proteins that couple actin filaments to microtubules they could affect the organization of actin. Fig 11a-b show a couple of cells that were exposed to 1G 20µM (Fig 11b) and under control condition (Fig 11a), respectively, both stained for tubulin. Whereas in the elongated structure of control cells microtubules are aligned forming bundles, in cells exposed to 1G, microtubules appear as a disordered network composed by not depolymerized filaments, similarly to what has been observed in HeLa cells [39].

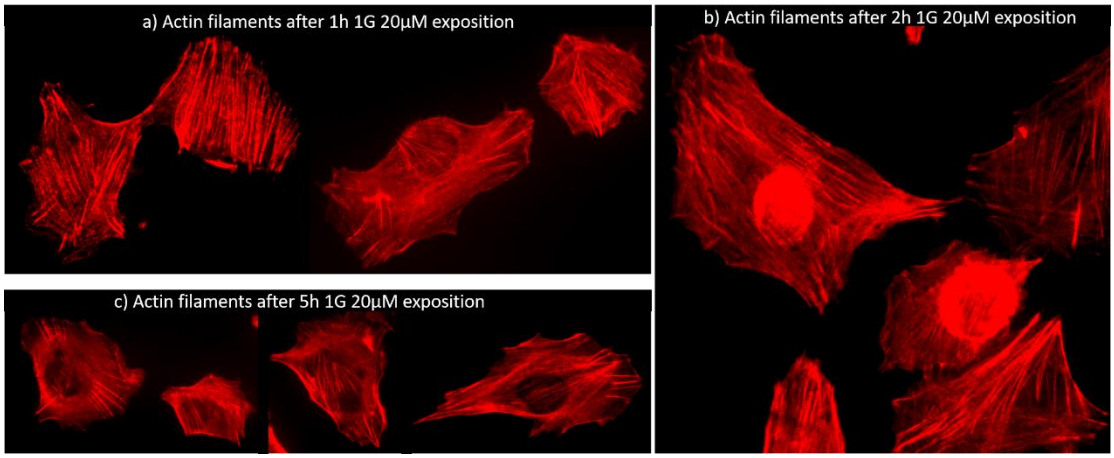

Figure 10:Actin filaments panel: Several U87MG stained cells exposed to 1G 20µM compound at different times (a) 1h,(b) 2h and (c) 5h

We also considered the distribution of FAK molecules (Fig 12a-b), confirming their coupling with the formation stress fibers and cofilin, noting that 1G favors the translocation of this molecule from the cytoplasm to the nucleus.

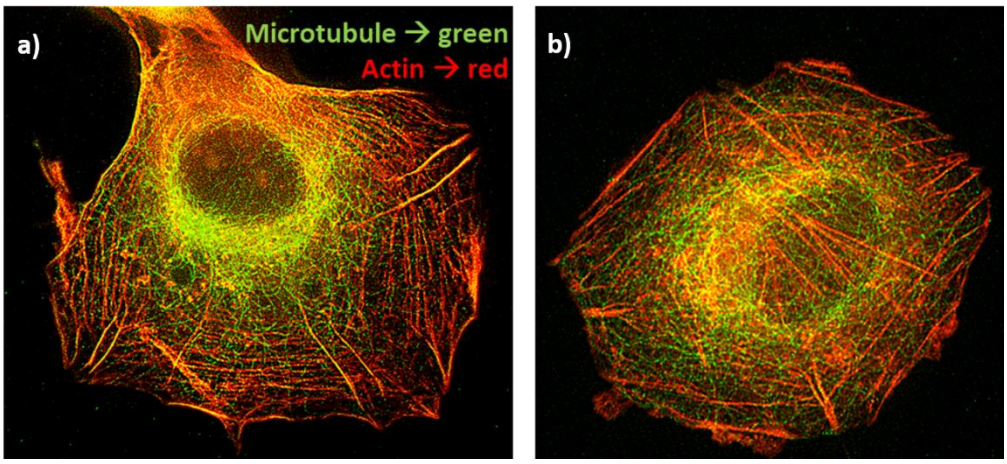

Figure 11: Microtubule (tubulin) and actin filaments staining of U87MG cell during control condition (a) and exposed to 1G 20µM (b)

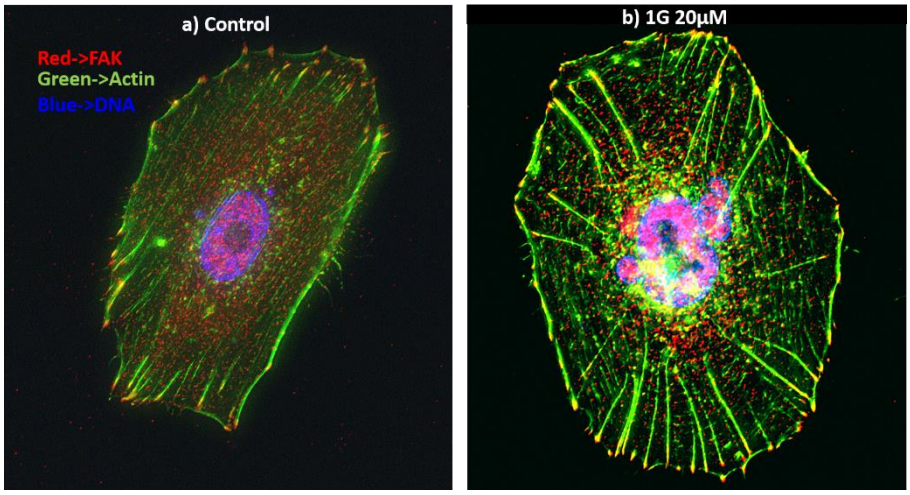

Figure 12: FAK, actin filaments and DNA staining of U87MG cell during control condition (a) and exposed to 1G 20µM (b)

Regarding the effects of 1G on the cell cytoskeleton and the associated proteins, we can conclude that after

just a few hours (effects are visible even after 1 hour of exposition to 20 uM 1G), an increase in the formation of stress fibers is observed, whereas microtubules appear as disordered but they are not depolimerized.

One of the immediate effects of 1G on U87MG cells is the retraction of the processes and the loss of polarity all leading to the adoption of a circular shape, as evidenced in Fig 6. The fact that the effect is almost instantaneous (occurring on the time-scale of a few minutes) suggested us to investigate for processes occurring at or near the plasma membrane. Among the proteins that can regulate cell shape and the structure of the cortical layer there are the proteins ezrin, radixin and moesin (ERM proteins) that mediate the interactions between membrane proteins and F-actin of the cortical layer. Accordingly, we investigated the distribution of pERM proteins during control condition (Fig 13a) at long time (24 hours) 1G 20µM exposure (Fig 13b) of U87MG cells. Fig 13a-b shows that, whereas in control cells pERMs are mainly localized in microvilli of the flattened cells, when cells are exposed to 1G and retract the processes, pERMs aggregate at the periphery of the cells forming hollow structures.

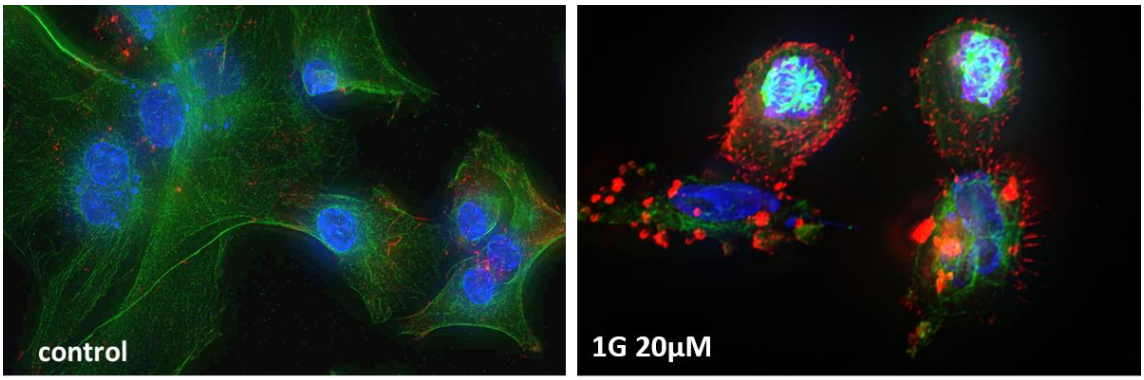

Figure 13: FAK (red), actin filaments (green) and DNA (blue) staining of U87MG cell during control condition (left) and exposed to 1G 20µM (right)

Bibliography

[1] Y. C. P. Q.T, D, J. Dowling, Y. W. P. D, C. K. B. A, and J. B. P. D, "CBTRUS Statistical Report: Primary Brain and Central Nervous System Tumors Diagnosed in the United States in 2007–2011 Quinn," *Neuro. Oncol.*, 2014, doi: 10.1093/neuonc/nou223.

[2] T. D. Pollard, G. G. Borisy, and N. Haven, "Cellular Motility Driven by Assembly and Disassembly of Actin Filaments," vol. 112, pp. 453–465, 2003.

[3] A. Nürnberg, T. Kitzing, and R. Grosse, "Nucleating actin for invasion," *Nat. Publ. Gr.*, vol. 11, no. March, pp. 177–187, 2011, doi: 10.1038/nrc3003.

[4] A. Hall, "Rho GTPases and the Actin Cytoskeleton," vol. 279, no. January, 1998.

[5] P. P. Provenzano and P. J. Keely, "Mechanical signaling through the cytoskeleton regulates cell proliferation by coordinated focal adhesion and Rho GTPase signaling," 2011, doi: 10.1242/jcs.067009.

[6] C. S. Chen, "Mechanotransduction – a field pulling together ?," 2008, doi: 10.1242/jcs.023507.

[7] V. Vogel and M. Sheetz, "Local force and geometry sensing regulate cell functions," *Nat. Rev. Mol. Cell Biol.*, vol. 7, no. 4, pp. 265–275, 2006, doi: 10.1038/nrm1890.

[8] M. J. Paszek *et al.*, "Tensional homeostasis and the malignant phenotype," vol. 8, no. September, pp. 241–254, 2005, doi: 10.1016/j.ccr.2005.08.010.

[9] M. Nagano, D. Hoshino, N. Koshikawa, T. Akizawa, and M. Seiki, "Turnover of Focal Adhesions and Cancer Cell Migration," vol. 2012, 2012, doi: 10.1155/2012/310616.

[10] A. M. P. Omuro, S. Faivre, and E. Raymond, "Review Lessons learned in the development of targeted therapy for malignant gliomas," vol. 6, no. July, pp. 1909–1920, 2007, doi: 10.1158/1535-7163.MCT-07-0047.

[11] A. Woehrer, L. Bauchet, and J. S. Barnholtz-sloan, "Glioblastoma survival : has it improved ? Evidence from population-based studies," vol. 27, no. 6, pp. 666–674, 2014, doi: 10.1097/WCO.0000000000000144.

[12] M. L. Sciences, "Review Molecular targets of glioma invasion," vol. 64, pp. 458–478, 2007, doi: 10.1007/s00018-007-6342-5.

[13] C. Beadle, M. C. Assanah, P. Monzo, R. Vallee, S. S. Rosenfeld, and P. Canoll, "The Role of Myosin II in Glioma Invasion of the Brain," vol. 19, no. August, pp. 3357–3368, 2008, doi: 10.1091/mbc.E08.

[14] T. J. Manning, J. C. Parker, and H. Sontheimer, "Role of Lysophosphatidic Acid and Rho in Glioma Cell Motility," vol. 199, no. November 1999, pp. 185–199, 2000.

[15] B. Salhia *et al.*, "Inhibition of Rho-Kinase Affects Astrocytoma Morphology , Motility , and Invasion through Activation of Rac1," no. 19, pp. 8792–8801, 2005, doi: 10.1158/0008-5472.CAN-05-0160.

[16] D. Meiri *et al.*, "Article Mechanistic Insight into the Microtubule and Actin Cytoskeleton Coupling through Dynein-Dependent RhoGEF Inhibition," *Mol. Cell*, vol. 45, no. 5, pp. 642–655, 2012, doi: 10.1016/j.molcel.2012.01.027.

[17] B. A. Danowski, "Fibroblast contractility and actin organization are stimulated by microtubule inhibitors," no. 3280, 1988.

[18] Y. Chang, P. Nalbant, Z. Chang, and G. M. Bokoch, "GEF-H1 Couples Nocodazole-induced Microtubule Disassembly to Cell Contractility via RhoA," vol. 19, no. May, pp. 2147–2153, 2008, doi: 10.1091/mbc.E07.

[19] S. E. Cross, Y. Jin, J. Rao, and J. K. Gimzewski, “Nanomechanical analysis of cells from cancer patients,” vol. 2, no. December, pp. 1–4, 2007, doi: 10.1038/nnano.2007.388.

[20] S. Suresh *et al.*, “Connections between single-cell biomechanics and human disease states: Gastrointestinal cancer and malaria,” *Acta Biomater.*, vol. 1, no. 1, pp. 15–30, 2005, doi: 10.1016/j.actbio.2004.09.001.

[21] T. P. Sciences *et al.*, “A physical sciences network characterization of non-tumorigenic and metastatic cells,” 2013, doi: 10.1038/srep01449.

[22] S. Van Helvert, C. Storm, and P. Friedl, “Mechanoreciprocity in cell migration,” *Nat. Cell Biol.*, vol. 20, no. January, 2018, doi: 10.1038/s41556-017-0012-0.

[23] A. Surcel *et al.*, “Pharmacological activation of myosin II paralogs to correct cell mechanics defects,” vol. 112, no. 5, 2015, doi: 10.1073/pnas.1412592112.

[24] P. E., A. Surcel, and D. N. Robinson, “The Mechanobiome: A Goldmine for Cancer Therapeutics,” *Cell Physiol.*, 2020.

[25] S. Parenti *et al.*, “A novel 2 , 3-benzodiazepine-4-one derivative AMPA antagonist inhibits G 2 / M transition and induces apoptosis in human leukemia Jurkat T cell line ☆,” *Life Sci.*, vol. 152, pp. 117–125, 2016, doi: 10.1016/j.lfs.2016.03.051.

[26] A. Giese, M. A. Loo, N. Tra, D. Haskett, S. W. Coons, and M. E. Berens, “DICHOTOMY OF ASTROCYTOMA MIGRATION AND PROLIFERATION,” vol. 282, pp. 275–282, 1996.

[27] M. Medicine, I. M. Oncology, H. L. Moffitt, and H. Computing, “‘ Go or Grow ’: the key to the emergence of invasion in tumour progression ?,” pp. 49–65, 2012, doi: 10.1093/imammb/dqq011.

[28] H. D. Dhruv *et al.*, “Reciprocal Activation of Transcription Factors Underlies the Dichotomy between Proliferation and Invasion of Glioma Cells,” vol. 8, no. 8, 2013, doi: 10.1371/journal.pone.0072134.

[29] T. J. Grundy *et al.*, “Differential response of patient- derived primary glioblastoma cells to environmental stiffness,” *Nat. Publ. Gr.*, no. March, pp. 4–13, 2016, doi: 10.1038/srep23353.

[30] C. Zhang *et al.*, “Exploration of the E ff ects of Substrate Sti ff ness on Biological Responses of Neural Cells and Their Mechanisms,” 2020, doi: 10.1021/acsomega.0c04279.

[31] J. Feng, Y. Tang, Y. Xu, Q. Sun, F. Liao, and D. Han, “Substrate stiffness influences the outcome of antitumor drug screening in vitro,” vol. 55, pp. 121–131, 2013, doi: 10.3233/CH-131696.

[32] B. L. Bangasser *et al.*, “Shifting the optimal stiffness for cell migration,” *Nat. Commun.*, vol. 8, no. May, pp. 1–10, 2017, doi: 10.1038/ncomms15313.

[33] T. A. Ulrich, E. M. D. J. Pardo, and S. Kumar, “The Mechanical Rigidity of the Extracellular Matrix Regulates the Structure , Motility , and Proliferation of Glioma Cells,” no. 10, pp. 4167–4175, 2009, doi: 10.1158/0008-5472.CAN-08-4859.

[34] P. A. Dimilla, K. Barbee, and D. A. Lauffenburger, “Mathematical model for the effects of adhesion and mechanics on cell migration speed,” *Biophys. J.*, vol. 60, no. 1, pp. 15–37, 1991, doi: 10.1016/S0006-3495(91)82027-6.

[35] A. Elosegui-artola, X. Trepat, and P. Roca-Cusachs, “Control of Mechanotransduction by Molecular Clutch Dynamics,” *Trends Cell Biol.*, vol. 28, no. 5, pp. 356–367, 2018, doi: 10.1016/j.tcb.2018.01.008.

[36] B. L. Bangasser, S. S. Rosenfeld, and D. J. Odde, “Determinants of maximal force transmission in a motor-clutch model of cell traction in a compliant microenvironment,” *Biophys. J.*, vol. 105, no. 3, pp. 581–592, 2013, doi: 10.1016/j.bpj.2013.06.027.

[37] B. L. Bangasser and D. J. Odde, “Master equation-based analysis of a motor-clutch model for cell traction force,” *Cell. Mol. Bioeng.*, vol. 6, no. 4, pp. 449–459, 2013, doi: 10.1007/s12195-013-0296-5.

[38] D. N. Robinson and J. A. Spudich, “Mechanics and regulation of cytokinesis,” doi: 10.1016/j.ceb.2004.02.002.

[39] V. Pirani *et al.*, “RESEARCH ARTICLE A novel benzodiazepine derivative that suppresses microtubule dynamics and impairs mitotic progression,” 2020, doi: 10.1242/jcs.239244.

[40] B. P. L. I. U. M. Chrzanowska-wodnicka and K. Burridge, “Microtubule Depolymerization Induces Stress Fibers , Focal Adhesions , and DNA Synthesis via the GTP- Binding Protein Rho,” vol. 5, no. 919, pp. 249–255, 1998.

[41] P. W. Grabham, B. Reznik, and D. J. Goldberg, “Microtubule and Rac 1-dependent F-actin in growth cones,” vol. 1, pp. 3739–3748, 2003, doi: 10.1242/jcs.00686.

- **Bending constant findings**

In chapter 2 we recalled the Flickering spectroscopy theory, which allows us to estimate the bending constant and the domain line tension parameters from GUVs. Here we will report our results regarding bending constant characterization of mono-component GUVs.

In the work reported below we studied the Magainin-H2 (Mag H2) antimicrobial peptide (AMPs), a mutant form of the well-known Magainin 2 wild-type (wt Mag 2). AMPs constitute a novel and encouraging therapeutic alternative with respect to traditional antibiotics to fight bacterial infections. AMPs are endowed with a strong advantage if compared to classical antibiotics. In fact, they strongly interact directly at the plasma membrane level targeting mainly the lipid bilayer physical-chemical properties among that also mechanical properties, and bacteria can hardly successfully evolve a drug resistance from AMPs. Thus, AMPs can provide a rapid and a wide-spectrum action against bacterial infections. A correct, wide and comprehensive understanding of the mechanisms underlying the AMPs and bacterial membrane interactions is required. In the paper we will focus on Mag H2 action on GUVs exploiting several techniques (for example Micropipette aspiration MAT and Flickering spectroscopy) proving a general mechanical characterization of the lipid bilayer, and of the dynamics of the permeabilization process in order to investigate the underlying possible molecular pathways like pore formation. Mag H2 owns a higher hydrophobicity level with respect to Mag 2, and this additional feature deeply influence its target due the electrostatic interactions. Nevertheless, the intrinsic spontaneous monolayer curvature is also relevant thus we focused also on GUVs composed by PG groups verifying how these specific groups play a protective role.

Journal of Colloid and Interface Science 553 (2019) 247–258

Contents lists available at ScienceDirect

Journal of Colloid and Interface Science

journal homepage: www.elsevier.com/locate/jcis

Regular Article

Magainin-H2 effects on the permeabilization and mechanical properties of giant unilamellar vesicles

Andrea Mescola [a,1], Nathaly Marín-Medina [b,1], Gregorio Ragazzini [a,c], Maurizio Accolla [c], Andrea Alessandrini [a,c,*]

[a] CNR-Nanoscience Institute-S3, Via Campi 213/A, 41125 Modena, Italy
[b] Department of Physics, University of Los Andes, Carrera 1 N° 18A – 12, Bogotá, Colombia
[c] Department of Physics, Informatics and Mathematics, University of Modena and Reggio Emilia, Via Campi 213/A, 41125 Modena, Italy

GRAPHICAL ABSTRACT

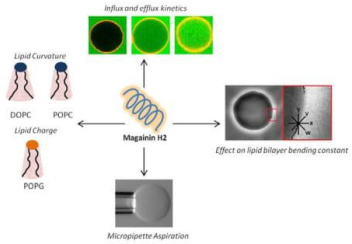

ARTICLE INFO

Article history:
Received 22 March 2019
Revised 28 May 2019
Accepted 9 June 2019
Available online 10 June 2019

Keywords:
Antimicrobial peptides
Magainin H2
Micropipette aspiration
Giant unilamellar vesicles
Flickering spectroscopy
Optical microscopy

ABSTRACT

Among the potential novel therapeutics to treat bacterial infections, antimicrobial peptides (AMPs) are a very promising substitute due to their broad-spectrum activity and rapid bactericidal action. AMPs strongly interact with the bacterial membrane, and the need to have a correct understanding of the interaction between AMPs and lipid bilayers at a molecular level prompted a wealth of experimental and theoretical studies exploiting a variety of AMPs. Here, we studied the effects of magainin H2 (Mag H2), an analog of the well-known magainin 2 (*wt* Mag 2) AMP endowed with a higher degree of hydrophobicity, on giant unilamellar vesicles (GUVs) concentrating on its permeabilization activity and the effect on the lipid bilayer mechanical properties. We demonstrated that the increased hydrophobicity of Mag H2 affects its selectivity conferring a strong permeabilization activity also on zwitterionic lipid bilayers. Moreover, when lipid mixtures including PG lipids are considered, PG has a protective effect, at variance from *wt* Mag 2, suggesting that for Mag H2 the monolayer curvature could prevail over the peptide-membrane electrostatic interaction. We then mechanically characterized GUVs by measuring the effect of Mag H2 on the bending constant of lipid bilayers by flickering spectroscopy and, by using micropipette aspiration technique, we followed the steps leading to vesicle permeabilization. We found that Mag H2,

Abbreviations: AMP, antimicrobial peptide; CF, carboxyfluorescein; CL, cardiolipin; DHPE, 1,2-dihexadecanoyl-*sn*-*glycero*-3-phosphoethanolamine; DOPC, 1,2-dioleoyl-*sn*-*glycero*-3-phosphocholine; EC_{50}, Effective concentration 50%; GUV, giant unilamellar vesicle; *wt* Mag 2, magainin 2; Mag H2, magainin H2; MAT, micropipette aspiration technique; MIC, minimum inhibitory concentration; P/L, peptide-to-lipid ratio; POPC, 1-palmitoyl-2-oleoyl-*sn*-*glycero*-3-phosphocholine; POPG, 1-palmitoyl-2-oleoyl-*sn*-*glycero*-3-phospho-(1′-*rac*-glycerol).

* Corresponding author at: Department of Physics, Informatics and Mathematics, University of Modena and Reggio Emilia, 41125 Modena, Italy.
E-mail addresses: andrea.mescola@nano.cnr.it (A. Mescola), nmarinm@uniandes.edu.co (N. Marín-Medina), gregorio.ragazzini@unimore.it (G. Ragazzini), andrea.alessandrini@unimore.it (A. Alessandrini).

[1] These two authors contributed equally to the work

https://doi.org/10.1016/j.jcis.2019.06.028

notwithstanding its enhanced hydrophobicity, has a pore formation mechanism compatible with the toroidal pore model similar to that of *wt* Mag 2.

1. Introduction

The continuous misuse of antibiotics in the medical and agricultural sectors together with a substantial lack in the discovery of new active molecules has led to a worldwide incidence of multidrug resistant bacteria. Various international organizations such as the World Health Organization (WHO) and United Nations, as well as the USA government and several European countries, have identified the uncontrolled spread of these resistant microorganisms as one of the most dangerous threats of this century, carrying serious consequences at different social levels, not only in public health but even within macroeconomic sectors [1-5].

Among the alternative solutions to fight bacterial infections, the use of antimicrobial peptides (AMPs) has been considered a very promising strategy given their broad spectrum of activity and rapid bactericidal action [6,7]. AMPs are evolutionarily conserved host-defense molecules found in most complex living organisms, and they selectively target the bacterial membrane through a variety of non-specific interactions. The exploitation of non-specific interactions hinders bacteria from developing definite resistance mechanisms to peptide binding and action [8,9]. Research on AMPs activity during the last three decades have suggested that their interaction with the cytoplasmic membrane could be the first step of the bactericidal mechanism and that inhibition of enzymatic activity, induction of protein degradation, inhibition of protein, nucleic acid or cell wall synthesis, and interference in the transport and energy metabolism could subsequently be involved [8,10,11]. Regarding the first step of their mechanism of action, several scenarios involving or not the formation of pores have been proposed. Among them there are the formation of barrel-stave pores or toroidal pores, a carpet mechanism, sinking raft, lipid clustering and interfacial activity models [11-14]. AMPs have also been found to be active against fungi, viruses, and even cancer cells [15]. Studies aimed at developing AMP-based pharmaceuticals used either engineered synthetic peptides or modified native peptides to improve their antimicrobial properties and stability, and reduce toxicity to host cells. For this to be achieved, a full understanding of the molecular aspects of the AMP-membrane interaction is required. Even if significant advances have been recently done to shed light on the various mechanisms of action of AMPs, some molecular details still remain unknown.

Research about the effects of AMP activity on both biological membranes and lipid bilayer model systems have been performed by means of various experimental techniques [16]. These studies have revealed that the bound-peptide concentration plays a crucial role. The model systems are strongly sensitive to small changes in the peptide-to-lipid (P/L) ratio, requiring low P/L values to observe the peptides' effects, whereas much higher peptide concentrations are needed to obtain significant effects on bacteria [14]. Liposomes are among the mostly exploited model systems to study the interaction of AMPs with lipid bilayers. Liposomes can be classified according to their size and, different sizes allow different techniques to be exploited for their investigation. Whereas Large Unilamellar Vesicles (LUVs, diameter up to about 120 nm) can be used for the analysis of fluorescence signals due to vesicle permeabilization processes at well-established P/L ratios [17], Giant Unilamelar Vesicles (GUVs, diameter from 1 μm up to about 100 μm) can be studied also by optical microscopy techniques including fluorescence techniques [18]. Moreover, GUVs could also be used to investigate the effect of AMPs on the lipid bilayer area changes or on their mechanical properties by using the Micropipette Aspiration Technique (MAT) [19-25] or flickering spectroscopy [26]. At the same time, exploiting GUVs it is possible to establish the effects of mechanical properties modulation on peptide activity [27].

Notwithstanding the variety of biophysical experimental analysis, at present the details about the molecular mechanisms of the AMP/membrane interaction at nanometer scale resolution can be grasped mainly by molecular dynamics (MD) simulations [28-30]. Due to the restrictions in the time covered by simulations and number of included molecules, MD investigations typically target AMPs which are strongly active on lipids which have been well characterized in terms of simulation. This is the case of Magainin H2 (Mag H2), an analog of magainin 2 (*wt* Mag 2) which is one of the best characterized short cationic AMPs. *wt* Mag 2, a 23 amino acids long peptide secreted on the skin of the African clawed frog *Xenopus laevis*, permeabilizes bacterial membranes via toroidal pores without exhibiting significant toxicity against mammalian cells [31-34]. The Mag H2 analog differs on five amino acids that confer it a higher hydrophobicity compared to *wt* Mag 2, consequently enhancing the permeabilizing activity on zwitterionic membranes due to a higher binding affinity, while leaving nearly unchanged its antimicrobial activity [35]. Particularly, Mag H2 shows an ED_{50} for hemolysis of 16 μM, whereas *wt* Mag 2, has practically no activity on red blood cells, and, concerning the bactericidal activity against *Escherichia coli*, Mag H2 has just a four-fold lower MIC with respect to *wt* Mag 2 (2 μM *vs* 8 μM) [35]. This loss of membrane selectivity (zwitterionic host cell *vs* anionic bacterial membranes) might be undesirable from a medical point of view. In fact, due to its activity on zwitterionic lipids, Mag H2 cannot be considered a peptide with therapeutic applications. Nevertheless, in order to infer the molecular details of the peptide/membrane interaction it is important to investigate what happens when the properties of the peptides are changed in order to establish a correlation between the peptide chemical and physical properties and its mechanism of action. On the other hand, zwitterionic lipids such as phosphatidylcholines (PC) are well characterized in MD simulations, and AMPs strongly active on PC membranes like Mag H2 are preferred in this type of studies. In fact, most of the few studies about Mag H2 activity in the literature are of simulation character [30,35-38] whereas the performed experimental studies involved just the analysis of the permeabilization of LUVs [35].

Aimed at filling the gap between simulation and experimental studies about the interaction of Mag H2 with model membranes and at understanding if the different hydrophobicity could induce also a different mechanism of action apart from selectivity with respect to *wt* Mag 2, here we studied the action of Mag H2 on GUVs by using phase contrast optical microscopy, fluorescence microscopy, flickering spectroscopy and MAT. The results have been compared with the results on *wt* Mag 2 taken from the literature. Our results reveal that Mag H2 strongly interacts with lipid bilayers inducing a rapid permeabilization. The permeabilization process is anticipated by a large increase of lipid bilayer area and a strong decrease of the bilayer bending constant. The mechanism of action seems however similar to that of *wt* Mag 2, implying the probable formation of toroidal pores that decrease their diam-

eter as the permeabilization process proceeds. Mag H2 has a strong permeabilization activity on bilayers composed of zwitterionic lipids and is less effective on GUVs including PG or cardiolipin (CL) lipids suggesting that the monolayer curvature could prevail over the peptide-membrane electrostatic interaction partly inhibiting the formation of pores and the permeabilization process.

2. Material and methods

2.1. Lipids, fluorescent markers and peptides

DOPC (1,2-dioleoyl-*sn-glycero*-3-phosphocholine), POPC (1-palmitoyl-2-oleoyl-*sn-glycero*-3-phosphocholine), POPG (1-palmitoyl-2-oleoyl-*sn-glycero*-3-phospho-(1′-*rac*-glycerol), Cardiolipin (CL) (Heart, Bovine), and cholesterol (chol) were bought from Avanti Polar Lipids (Alabaster, USA). 1,2-dihexadecanoyl-*sn-glycero*-3-phosphoethanolamine-Texas Red (DHPE-Texas Red) was bought from Life Technologies (Thermofisher. Carlsbad, CA, USA). Carboxyfluorescein (CF) was bought from Sigma-Aldrich Corporation (Saint Louis, MO, USA). Specific lipid mixtures were prepared by mixing chloroform lipid solutions in the desired amount (the proportions used in this work are to be intended as molar). The peptide Mag H2 (Ile – Ile – Lys – Lys – Phe – Leu – His – Ser – Ile – Trp – Lys – Phe – Gly – Lys – Ala – Phe – Val – Gly – Glu – Ile – Met – Asn – Ile) was purchased in powder from United BioSystems Inc, with a 95.6% purity, and used without further purification (see Par S1 and Fig. S1 for the aminoacid sequence and hydropathy of Mag H2 compared to the natural Magainin 2). It was dissolved in Millipore water at a high peptide concentration (4 mg/mL) and stored at −20 °C until required for use.

2.2. Preparation of GUVs

GUVs were prepared according to the usual electroformation method [39] with minor modifications. Briefly, lipid mixtures were suspended in chloroform, and small drops (2–3 μL from a 2 mg/ml lipid solution) were deposited on two opposing platinum (Pt) wires positioned inside a Teflon chamber. The chloroform was initially removed via a Nitrogen flux and then the chamber was positioned inside a vacuum system (10^{-2} mBar) for 0.5–1 h. Thereafter, the Pt wires were connected to an electric function generator providing a sinusoidal voltage potential difference. The Teflon chamber was then filled with a 100 mM sucrose solution, and sealed. The electroformation protocol was as follows: (i) 10 Hz, 4.0 V_{p-p} for 105 min; (ii) 5 Hz, 2 V_{p-p} for 45 min; (iii) a 5 Hz square-wave for 5 min in order to promote the final detachment of the vesicles from the wires. All the procedure was performed at a temperature of 40 °C. GUVs were then extracted from the Teflon chamber and resuspended in a 105 mM glucose solution. The presence of the osmotic difference across the bilayer (the external glucose concentration is 5 mM higher than the sucrose concentration) makes the vesicles a little bit flaccid increasing their bending fluctuations, and approaching the behavior of biological membrane which are typically not tensed. When GUVs were prepared for fluorescence microscopy investigation, a 0.5–1% molar amount of DHPE-Texas Red was included in the lipid mixtures in order to mark the bilayer. When studying Mag H2-induced membrane permeabilization via fluorescence microscopy, CF was added to the imaging or formation medium. In the first case, we measured the influx of CF, and we injected the GUVs in a chamber already containing 10 μM CF in 105 mM glucose + the desired Mag H2 concentration. In the second case, we formed the vesicles in the presence of 100 mM sucrose + 10 μM CF. The vesicles were then washed by at least 5 cycles of centrifugation and exchange of the supernatant with 105 mM glucose before injecting them in a chamber already containing the desired concentration of Mag H2. The chambers we used to study the permeabilization of the GUVs were made with glass slides and Teflon and the bottom glass surface was pretreated with BSA (10 mg/mL) to avoid adhesion between glass and lipid bilayers. The BSA solution was then removed and the chamber abundantly rinsed with the working solution. We did not observe any effect ascribable to residual BSA in the chamber.

2.3. Micropipette aspiration

Micropipettes were made by pulling glass capillaries (World Precision Instruments, Sarasota, FL, USA) of 1.2 mm initial-internal diameter, reaching a final cylindrical shape and an internal diameter of ∼10 μm. To pull the micropipettes, we initially used a HEKA temperature controlled pipette puller PIP5 followed by the use of a home-developed pipette puller to obtain the final cylindrical shape. A home-made microforge was used to cut the micropipette perpendicularly to its axis; the capillaries were then tip-polished to smooth their break-point in order to ensure good membrane/micropipette contact. The micropipettes were pretreated with BSA (10 mg/mL) to avoid adhesion between glass and lipid bilayers by neutralizing the charge on the bare glass surface, and then the pipettes were abundantly rinsed with the working solution. The micropipettes were then filled with a 105 mM glucose solution, assuring the absence of internal air bubbles. Finally, the micropipette is connected to the aspiration system, and immersed in a home-made Teflon/glass chamber where the vesicles were deposited.

To apply lateral tensions to the vesicles, the micropipette was connected to a pneumatic pressure transducer (Lorenz MPCU-3) to exert pressure differences between the internal side of the pipette and the external solution at the same height, with a sensitivity of 0.1 cm H_2O. The pressure difference was applied by controlling the air pressure on top of a cylindrical tube containing the same external solution and initially kept at the height providing a negligible pressure difference. The negligible initial pressure was evidenced by the absence of movement of small particles in front of the pipette aperture. Controlling the height difference of the solution levels in two tubes, we are able to aspirate the vesicle into the micropipette, and the progressive membrane deformation (projection) into the micropipette can be measured as a function of time at constant pressure difference. To study the kinetics of the interaction of the molecules with a lipid bilayer, a fast perfusion system would be required (the measurement time should start with an already established constant concentration of the peptides). To circumvent this problem, we assembled a cell with two chambers [23,25,40], and we transferred the vesicles to be studied from one chamber without the peptide to another chamber with the already homogeneous peptide concentration. In particular, the chambers are prepared using Teflon in order to have a hydrophobic surface and to avoid the contact between the liquids of the two compartments (see Fig. S2). To better insulate the two compartments we also used two small pieces of a Teflon foil (25 μm thick) in contact with the glass in the channel. One compartment is filled with the vesicle solution in glucose. Using a micromanipulator, a pipette with an external diameter of about 0.5/1 mm and filled with the glucose solution is inserted through the hole from the compartment opposite to the vesicle in order to reach the vesicle solution. The other compartment is then filled with the solution already containing the Mag H2 concentration we want to investigate. A vesicle from the first compartment is aspirated by the micropipette and the vesicle with the micropipette are then inserted inside the bigger pipette (see Fig. S2). The chamber is then moved by using the microscope stage in order to take the aspirated vesicle to the chamber containing the peptide solution. The bigger pipette is then removed and the interaction kinetics starts. Time

t = 0 in our analysis corresponds to the removal of the bigger pipette and the exposure of the vesicle to the Mag H2 solution. All the formulas used to analyze the experiments performed by MAT are reported in the Supplementary Material section (see Par S2).

2.4. Flickering spectroscopy

GUVs have been observed using 40X phase contrast objective (NA 0.60), mounted on an Olympus IX 70 microscopy. An additional lens incorporated in the microscope was used to increase the total magnification, up to 60X. A CCD high-resolution video camera (QIcam FAST Cooled Mono 12-bits) was used to store GUVs movies of 1500 phase images with a frame rate of 25 images/s, and an integration time of 15 ms. The samples have been prepared using an O-ring chamber sealed with two cover glasses. During sample preparation, GUVs were suspended in 112 mM glucose solution in order to make fluctuations easily visible by optical microscopy at our resolution level. The images of fluctuating vesicles represent the evolution in time of the GUVs contour at the equatorial plane. Using a home-made software developed in Python, the vesicle contour for each image of the sequence is detected with a sub-pixel resolution [41]. The 2D contour coordinates are used to obtain the radial fluctuations: $r(\frac{\pi}{2},\varphi,t)=r(\varphi,t)$ in polar coordinates at the equatorial plane at a given time t, corresponding to the analyzed image.

Starting from radial fluctuations, the angular autocorrelation function is evaluated by:

$$\xi(\gamma,t)=\frac{1}{2\pi R^2}\int_0^{2\pi}[r(\varphi+\gamma,t)-r(t)]\cdot[r(\varphi,t)-r(t)]d\varphi \qquad (1)$$

where $r(t)=\frac{1}{2\pi}\int_0^{2\pi}r(\varphi,t)d\varphi$ is the averaged radius of the vesicle, and $R=\sum_{i=0}^{Nf}\frac{r(t_i)}{N_f}$ is the mean radius obtained from the entire sequence containing N_f frames. The autocorrelation functions are then decomposed using a Legendre Polynomials basis, $\xi(\gamma,t)=\langle B_0\rangle P_0(\cos\gamma)+\sum_{n=2}^{N_{max}}\langle B_n\rangle\cdot P_n(\cos\gamma)$, obtaining the corresponding B_n coefficients for each frame. Finally, the mean value$\langle B_n\rangle=\sum_{i=0}^{Nf}\frac{B_n(t_i)}{Nf}$ is evaluated. Using a Levenberg-Marquardt procedure, the experimental $\langle B_n\rangle$ values are fitted following the theoretical expression:

$$B_n\left(\kappa,\bar{\sigma}\right)=\frac{2n+1}{4\pi}\cdot\frac{k_bT}{\kappa(n+2)(n-1)\left[\bar{\sigma}+n(n+1)\right]} \qquad (2)$$

wherek_b is the Boltzmann constant,κ and $\bar{\sigma}$ are the bending constant and the reduced surface tension, respectively, and $n>1$. For the fitting procedure, coefficients between the 3° and 14° mode number were used. Since the coefficients are defined as greater than 0, following Eq. (2), all negative contributions have been neglected.

2.5. Fluorescence microscopy

Epifluorescent images were acquired using an Olympus IX 70 microscope equipped with a 20X or 40X objective (NA 0.4 and 0.75, respectively). All procedures were performed at minimal light exposition (using neutral filters) to avoid fluorophores' photobleaching. A CCD high-resolution video camera (QIcam FAST Cooled Mono 12-bits) or a CMOS camera (Hamamatsu ORCA-flash 4.0LT - C11440) connected to a computer were used for image and video capture. Analysis of images and videos was made using ImageJ [42]. For confocal imaging, we used a Leica SP2 microscope with AOBS (Acoustic Optical Beam Splitter), and 40X and 63X-oil immersion objectives. The excitation wavelengths for CF and Texas-Red were 488 nm and 594 nm, respectively; the emission wavelengths were 517 nm and 615 nm, respectively as well. Analysis of the evolution of the fluorescence intensity inside GUVs was performed with ImageJ+Time Series V3 plugins. Briefly, the images corresponding to the time sequence of each vesicle, were selected, properly aligned, and joined in a single sequence. Images corresponding to the fluorescence reference value (outside the vesicle) were inserted in the sequence, as well.

3. Results and discussion

3.1. Strategies for the study of the permeabilization of GUVs by peptides

Typically, three different strategies can be exploited to verify the permeabilization activity of AMPs on GUVs: (i) the GUVs being inside a chamber, the AMPs are delivered by using a micropipette positioned near to a single vesicle (single GUV method); (ii) the vesicles are injected in a glucose solution already containing a homogeneous peptide concentration (GUV dispersion method); (iii) the vesicles are injected in a chamber and, after they have been settled down, the peptides are injected into the medium. Among them, just strategy (ii) allows the measurement of the peptide-vesicle interaction at a well-defined AMP concentration. Obviously, the adsorption of the peptides on the vesicles implies a decrease of the peptide concentration in solution but, in most cases, it can be considered anyway as an equilibrium situation given the usually high amount of peptides in solution in experiments involving GUVs. This strategy presents the impossibility of having data at a very short time after exposing the vesicle to the peptides because enough time has to elapse (about 40–50 s) before the vesicles settle at the bottom of the imaging chamber in order to have a time lapse visualization of their state. In strategy (iii) the exact peptide concentration near to the GUVs is not known, or it changes during the measurements. When GUVs are exposed to a peptide flux (strategy (i)), vesicles not adhering to the surface are easily moved. Vesicles not moving are probably physically adhered to the substrate, and this condition could alter the tension in the bilayer. If the possibility of blocking the vesicles on the support by a specific chemistry such as biotin/avidin is exploited [43], it is possible to flux a solution with a well-defined peptide concentration and this method, repeated on several vesicles, could provide valuable results even if the uncertainty on the concentration and effects related to mass diffusion in solution should be considered. Different methods of vesicles exposure to peptides could give different results. In the experiments performed in this study, we mainly worked with strategy (ii), i.e. the vesicle dispersion method. With this method we never measured the permeabilization kinetics. What we were able to measure is the percentage of intact and permeabilized vesicles after a quite long interval from the vesicle injection (about 30 min) or the kinetics of influx or efflux between the vesicle lumen and the external solution from the moment when these events start. In these cases, we considered time t = 0 as the time at which the permeabilization starts without reporting the real time after the initial exposure of the vesicles to the Mag H2 solution. The overall time at which the influx or efflux start is stochastic. More results obtained with the other strategies are reported in the Supplementary Material Section.

3.2. Role of lipid composition on the Mag H2 effect

In order to identify which types of lipids could promote or disfavor the permeabilization effect of Mag H2, GUVs with different lipid compositions have been studied. We initially measured the percentage of permeabilized vesicles for different lipids and for different peptide concentrations after 30 min incubation time with

Mag H2 [44,45]. For this analysis we exploited phase microscopy imaging. The permeabilization efficiency is detected by the contrast change due to an equilibration process between sucrose inside the GUV and glucose outside the GUVs once pores have been formed. To be sure that the leakage process by itself could not affect the time analysis, we followed the leakage process of several vesicles by time lapse phase contrast imaging with a time resolution of just a few seconds. Fig. 1 reports a representative example for a DOPC/chol (88%/12%) vesicle.

Once it starts, the leakage process reaches an equilibrium situation in about 30 s. In some cases, the leakage process was not complete but it stopped producing a partially permeabilized situation. This scenario was more evident at low peptide concentrations for all the lipid compositions we studied. Anyway, in the case of partial permeabilization, after a fast first step (see below) a second very slow leakage process follows. The fact that the leakage process is much faster than the observation time of 30 min assures us that it is the rate of pore formation what is relevant, and not the time required for the equilibration of the internal and external solutions of the GUVs. Table 1 reports the percentage of still intact vesicle at the end of the 30 min incubation time for different lipid composition of the GUVs.

As a first analysis, we compared the permeabilization activity of Mag H2 on DOPC and POPC vesicles in order to understand the role of chain unsaturation on the activity of Mag H2. Due to its higher hydrophobicity, Mag H2 is much more effective on PC lipids than Mag 2 and very low concentrations of Mag H2 are enough to induce permeabilization of the vesicles (1–2 μM) whereas concentrations starting from 15 μM are required for Mag 2 [46]. The fraction of not-permeabilized vesicles shown in Table 1 reveals that DOPC bilayers are more resistant to Mag H2 permeabilization than POPC bilayers. This is quite interesting because DOPC, having two unsaturated chains, is expected to be more disordered than POPC at the same temperature (the analysis have been performed at a controlled temperature of 27 °C) and more prone to be destabilized by the peptide. A possible explanation for this behavior is related to the spontaneous curvature of the monolayers. In fact, given the increased volume of the acyl chain region of DOPC monolayers, it is expected that they will have a higher tendency to adopt negative curvature with respect to POPC monolayers. Experimental data on the spontaneous curvature for DOPC and POPC report a higher negative curvature for DOPC (-0.091 nm^{-1}) with respect to POPC (-0.022 nm^{-1}) [47]. Given that simulations of the activity of Mag H2 show the formation of toroidal pores [30], lipids with a higher negative curvature will protect the bilayer from the formation of Mag H2 pores [48]. The same protective behavior was observed in vesicles containing CL (see Par S5), a lipid with the tendency to form monolayers with high negative curvature, and to easily adopt the inverted hexagonal phase structure (H_{II}).

Table 1
Permeabilization effect of Mag H2 at different concentrations for GUVs with different lipid compositions, estimated as the fraction of not-permeabilized vesicles after ≈30 min. All the measurements have been performed at a constant controlled temperature of 27 °C, and more than 100 vesicles have been considered for each experiment. Each experiment was repeated 3 times giving consistent results. The reported error is the standard deviation of the repetition of the experiments (n = 3). ND = Not Determined.

Compositions	*Percent of intact GUVs after 30* min	
	1 μM Mag H2	2 μM Mag H2
DOPC	ND	26 ± 9
POPC	47 ± 7	0.3 ± 0.1
POPC/POPG 3:1	73 ± 10	30 ± 8
DOPC/chol 88:12	ND	32 ± 10
DOPC/chol 76:24	ND	79 ± 8
DOPC/chol 60:40	ND	84 ± 12

We then compared the permeabilization activity of Mag H2 on vesicles including negatively charged lipids -such as POPG- in order to understand their role on the activity of Mag H2. We found that a POPC/POPG (3:1) lipid bilayer is more protective than a pure POPC bilayer (Table 1). It is important to point out that the measurements in this case were performed in water plus 105 mM glucose without any buffering agent, obtaining a solution with pH between 5 and 5.5 that assures a negative charge to the PG headgroup (the pK_a of phosphatidylglycerol is ∼3). In the case of Mag 2, it has been found in previous works that the presence of PG favors the permeabilization of the vesicles [46]. The presence of negatively charged lipids typically increases the effect of cationic AMPs due to the electrostatically increased adsorption of peptides on the lipid bilayer. This is exactly what happens in the case of Mag 2, while in the case of Mag H2 the presence of PG acts as a protection against permeabilization. It is also to be stressed that in water solution (even if residual Na^+ ions are present in the solution according to how lipids are provided by Avanti Polar Lipids) the electrostatic effect is even more intense with respect to buffer solutions in which the charges are shielded, and the tendency to adopt inverted phases is reduced. In other cases, it has been recently found that the electrostatic force is relevant in the AMP/lipids interaction but it is not the only relevant parameter and, in specific cases, the geometry of the bilayer, the number of defects and the lipid-to-lipid average distance could overwhelm the electrostatic interaction [49]. The protective effect of PG groups is present for both 1 and 2 μM Mag H2 concentrations that we analyzed (Table 1). A similar result has been obtained in the case of LUVs [35] and it has been interpreted as a result of the intrinsic more negative curvature of PG with respect to PC [50]. Even in this case it is important to highlight that our experiments could be different with respect to experiments performed in buffer solution; in

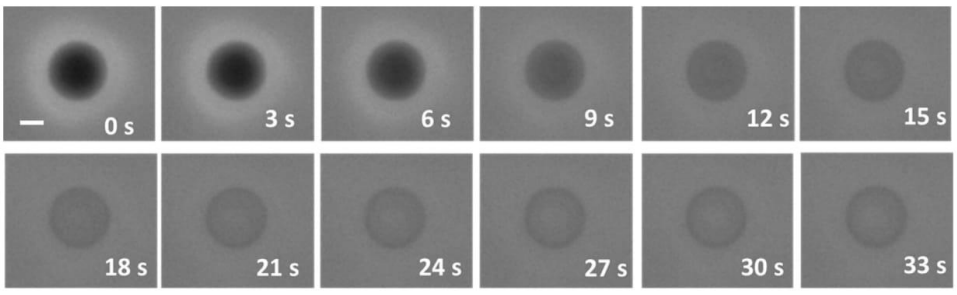

Fig. 1. Sequence of phase contrast optical microscopy images of a DOPC/chol (12% cholesterol molar content) GUV exposed to a 2 μM Mag H2 concentration. Once it starts, in about 30 s all the permeabilization process is complete. The contrast loss is related to equilibration of the internal (sucrose) and external (glucose) solutions of the GUV. The time reported on each image starts from the starting of the vesicle leakage (bar = 10 μm).

particular, the higher negative curvature value for PG is reported for buffer solutions; therefore, in our case, the presence of the positively charged peptides could play a role similar to poly-electrolytes in solution. Our results suggest that, for Mag H2-induced permeabilization, the intrinsic monolayer curvature could be more relevant than the electrostatic interaction between the peptide and the bilayer. Another case in which a protective effect of POPG lipids has been obtained is related to a modification of the maculin peptide by the insertion of a proline amino acid [51].

We also evaluated the role of cholesterol on the permeabilization activity of Mag H2. Cholesterol has typically a protective effect against AMPs, and this aspect is one of the mechanisms conferring specificity to the activity of AMPs towards bacteria with respect to host-cell membranes [52]. We demonstrated that cholesterol has a protective effect also in the case of Mag H2. Whereas in the case of DOPC/chol (with cholesterol molar content equal to 12%) the fraction of permeabilized vesicles is comparable to the case of pure DOPC, at a cholesterol molar fraction of 24%, the protective effect is greatly enhanced, and it seems to reach a saturation effect for larger concentrations considering that 40% cholesterol concentration provides similar results (Table 1). A similar non-linear behavior as a function of cholesterol concentration has already been obtained for MSI-78 [53], a 22 amino acids long AMP commercially known as pexiganan. The non-linear behavior has been interpreted as the result of a phase change of the DOPC/chol binary mixture for cholesterol concentrations higher than ~20%. In fact, for cholesterol concentrations above 20%, regions of L_o phase should form, and the activity of the peptides on these domains should be strongly inhibited. We speculated that the protective effect of cholesterol is mainly related to its effect on the phase state of the bilayer and on their mechanical properties; in fact, the presence of cholesterol in lipid bilayers confers a much higher value to the their stretching and bending constants [54]. On the other hand, in many cases, the formation of black dots or spots on the surface of vesicles was observed by phase contrast microscopy after the exposure to the peptide, in particular in the case of vesicles containing CL (see Fig. S7 and Fig. S12a). By including 1% DHPE-Texas Red in the bilayer of the vesicles, we were able to confirm that the black dots are due to lipid accumulation (see Fig. S12b); for example, in case of high Mag H2 concentrations, we observed formation of large spots on the surface of the vesicles before they collapse (see Fig. S6). Furthermore, the presence of these spots does not imply the permeabilization of the involved vesicle. We do not know which could be the organization of the lipids within these regions, and we just refer to these structures as accumulation of lipids, as suggested also by other studies [55,56].

3.3. Quantitative analysis of the influx kinetics

For a quantitative analysis of the kinetics of the influx process we exploited a fluorescent dye and confocal microscopy using strategy (ii). Fig. 2 shows GUVs composed of POPC +1% DHPE-Texas Red dispersed in a solution containing 105 mM glucose + 10 μM CF. Even in this case the exact P/L ratio is difficult to establish due to the impossibility of knowing the lipid concentration in the sample. Fig. 2a shows the vesicles in the absence of Mag H2. At the beginning of the experiment, the internal region of the GUVs showed the complete absence of CF. On the time scale of several minutes no permeabilization event was observed in the absence of the peptides. Vesicles exposed to Mag H2 showed different behaviors depending on the peptide concentration. In all the reported experiments, time t = 0 corresponds to the starting of the influx of efflux process, independently from the overall time of exposure of the GUVs to the peptide. Fig. 2b shows the effect of a 1 μM Mag H2 concentration on POPC GUVs. In this case most of the vesicles become partially permeabilized: after an initial rapid influx of CF molecules, the flux slows down, and it proceeds at a very low rate probably due to a size reduction of the pore diameter (see also Fig. S3 for a photobleaching experiment, and Fig. S4 for an example of influx kinetics after the initial fast step). The decrease of the pore size after the initial influx (or efflux) of a dye has been already reported both for Mag 2 [57] and for Mag H2 [35]. Fig. 2c shows a completely permeabilized vesicle which was exposed to a 2 μM peptide concentration. The same behavior was observed for both CF influx and efflux. The behavior of the influx process for some of the analyzed GUVs is shown in Fig. 3. To analyze quantitatively the data, we used a simple exponential decay function similar to the one reported in [58]:

$$I(t) = (1 - A) + Ae^{-kt} \quad (3)$$

where $I(t)$ represents the difference of the fluorescence intensity between the external region and the region inside the vesicle, normalizing to 1 the difference at time t = 0 when no permeabilization has occurred, (1-A) is the permeabilization fraction (where A is the percentage of fluorescence increase inside the vesicle. A = 1 would correspond to a total permeabilization of the vesicle), and k is the

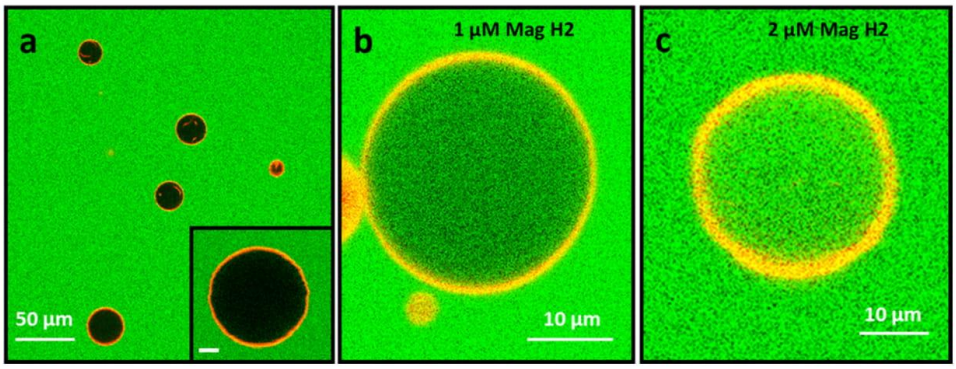

Fig. 2. Confocal fluorescence microscopy images of POPC+1% DHPE-Texas Red GUVs dispersed in a solution containing 105 mM glucose + 10 μM CF. (a) GUVs not exposed to Mag H2; scale bar in the inset = 5 μm; (b) example of a POPC vesicle partially permeabilized after exposing the GUVs to a 1 μM Mag H2 concentration; (c) example of a vesicle completely permeabilized after being exposed to a 2 μM Mag H2 concentration. (For interpretation of the references to colour in this figure legend, the reader is referred to the web version of this article.)

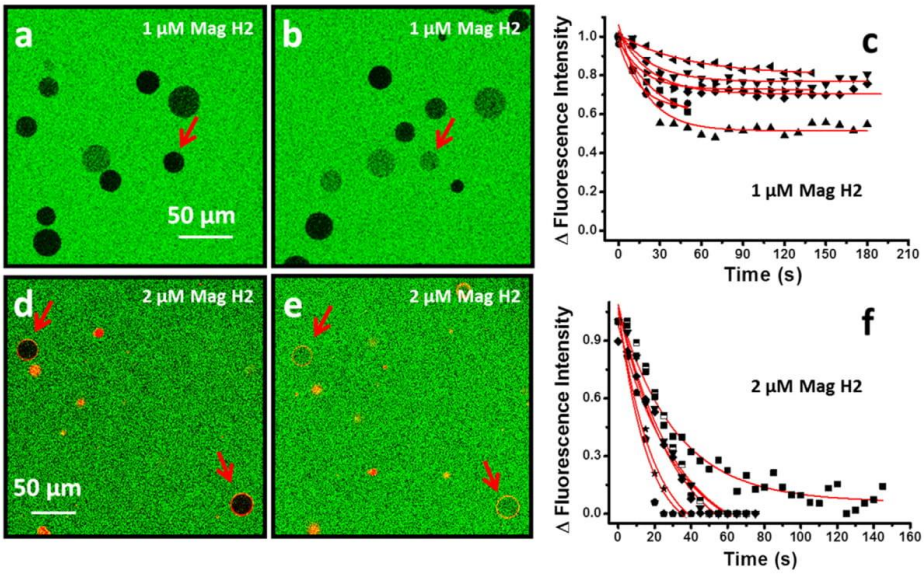

Fig. 3. Analysis of the influx kinetics of a POPC GUV by confocal microscopy. (a) and (b) POPC GUVs dispersed in a solution containing 105 mM glucose + 10 μM CF, exposed to a 1 μM Mag H2 concentration. A GUV initially not-permeabilized (indicated by a red arrow in panel (a), appears partially permeabilized 200 s later (indicated by a red arrow in panel b – the vesicles slowly moved in the chamber and we had to follow their positions); (c) normalized fluorescence signal difference between the regions outside and inside the vesicles. The black dots correspond to representative traces of the kinetics of the fluorescence marker influx whereas the red continuous lines represent the best fit by Eq. (1). The influx process occurs by an initial fast step corresponding to the opening of the pores, followed by a very slow influx process which is not noticeable on this time scale; (d) and (e) POPC GUVs dispersed in a solution containing 105 mM glucose + 10 μM CF, exposed to a 2 μM Mag H2 concentration. Two GUVs initially not-permeabilized (indicated by the red arrows in panel (d)) appear completely permeabilized in panel (e); (f) normalized fluorescence signal difference between the regions outside and inside the vesicles. The black dots correspond to representative traces of the kinetics of the fluorescence marker influx whereas the red continuous lines represent the best fit by a simple exponential decay function. All the curves have been aligned in such a way that t = 0 s corresponds to the beginning of the influx process for all the vesicles. (For interpretation of the references to colour in this figure legend, the reader is referred to the web version of this article.)

inverse of the time constant (in s^{-1}). Before fitting the data with the exponential function, we aligned the fluorescence intensity trends so that $t = 0$ s corresponds to the stochastic beginning of the CF influx process. The rate constant k is about (0.048 ± 0.016) s^{-1} (mean ± s.d. for n = 9) in the case of partial permeabilization (Fig. 3a–c), and (0.041 ± 0.012) s^{-1} (mean ± s.d. for n = 9) for total permeabilization (Fig. 3d–f). The permeabilization of the vesicles loaded with CF (efflux kinetics) occurs on similar time-scales (see Fig. S5). We also performed an analysis of the initial volume flux J_V across the bilayer in the cases of both transient and complete permeabilization exploiting the method presented in [44,45] (see Par S4). The results are reported in Fig. 4 showing that by doubling the Mag H2 concentration from 1 μM to 2 μM we have an initial dye influx changing from (0.04 ± 0.02) μm/s to (0.29 ± 0.08) μm/s (mean ± s.d, n = 9) . This result can be interpreted as an increased number of pores initially formed at higher Mag H2 concentration

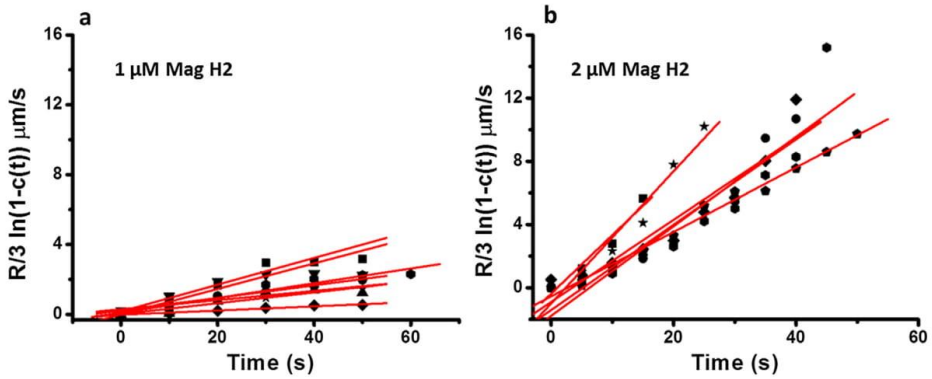

Fig. 4. (a) Log-linear plots of time-dependent initial dye influx (−R/3ln(1 − c)) versus time for partial permeabilization of POPC GUVs exposed to 1 μM Mag H2 concentration. The average flux value is (0.04 ± 0.02) μm/s (average ± sd); (b) The same plots as in (a) in the case of POPC GUVs exposed to 2 μM Mag H2 concentration in the case of total permeabilization. The average flux value is (0.29 ± 0.08) μm/s (average ± sd).

leading to a complete influx of the dye during the period in which the pores remain completely open. In the case of partial permeabilization, the number of pores could be not enough to obtain a complete equilibration of CF concentration during their open time.

If Mag H2 concentration is further increased to greater than 5 μM, we observed a very fast complete influx kinetics with the GUVs rapidly losing their stability resulting in the formation of spots where lipids accumulate as evidenced by the localized increase of the lipid fluorescence signal (see Fig. S6). The partial permeabilization phenomenon can be interpreted on the basis of the fact that once the pores are formed, they can close or reduce their size even if we do not know the mechanistic details of this phenomenon. In this case, the level of permeabilization depends on the rate constant of the fluorophore flux: if the flux rate is high (large pores or high number of pores for example), it is possible to obtain a complete permeabilization before pore closure or size reduction, whereas if the flux is slow (narrow pores for example), the vesicles will show just a transient permeabilization followed by a second phase characterized by a very low permeabilization rate (~0.0019 s^{-1}, see Fig S4). This behavior could also be interpreted in the context of the translocation of the peptides from one leaflet to the other. From our results, in the case of Mag H2 the behavior is mainly related to its concentration and to the initial value of the influx of the fluorescent dye.

3.4. Investigation by micropipette aspiration of GUVs exposed to Mag H2

The MAT technique is typically exploited to study the mechanical properties of lipid bilayers in the form of GUVs or to investigate the bilayer area expansion or volume variation providing information about the interaction kinetics of the lipid bilayer with exogenous molecules [20-25]. Usually, to study the interaction of the lipid bilayer with exogenous molecules, a single GUV is grabbed by a micropipette which is covered by a bigger pipette, and moved to a different compartment already prepared with a solution of homogeneous concentration of the molecule of interest. The removal of the bigger pipette marks the beginning of the interaction kinetics [25,59]. The expansion or retraction of the vesicle area is detected by the movement of the vesicle projection inside the micropipette (increase or decrease, respectively) which works as an amplifier of the effect of the peptides on the bilayer area (see the Supplementary Information Par S2 for details of the analysis). The data we will show are mainly representative of the qualitative behavior of the lipid bilayer exposed to the peptides given that a rigorous quantitative analysis in terms of peptide concentration could strongly depend on the initial conditions, such as vesicle size and applied lateral tension.

MAT experiments on DOPC GUVs at different Mag H2 concentrations were performed. Fig. 5a–c shows the results of the exposure of a DOPC GUV to a 5.37×10^{-13} M Mag H2 concentration [40], corresponding to P/L ≈ 1/30 (to obtain this estimate we considered that there is only one GUV in the chamber, the vesicle is composed by approximately 5.8×10^{9} lipids according to its size and the area-*per*-lipid and we evaluated the total number of peptides in the chamber on the basis of the peptide concentration and the volume of the chamber ~0.6 mL). From all the performed experiments (n = 7) at this peptide concentration, in ~70% of the cases the projection increased like in the case shown in Fig. 5a-c, whereas in the remaining 30% the vesicle projection remained

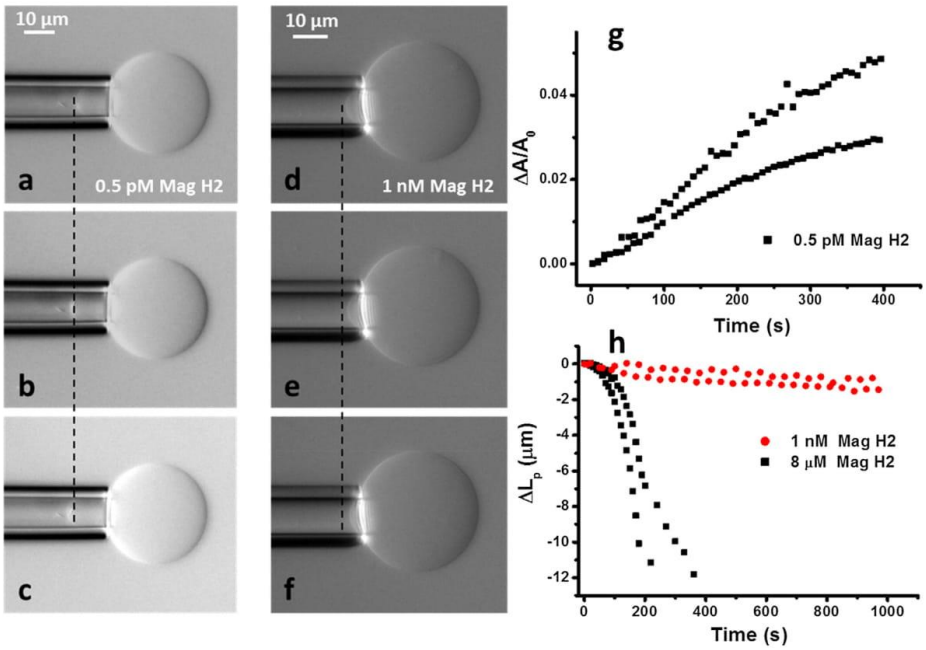

Fig. 5. (a)–(c) Evolution of the vesicle protrusion inside the micropipette for a DOPC vesicle (t = 0 s, 150 s, 350 s, respectively) exposed to a 5×10^{-13} M Mag H2 concentration. The vertical dashed line highlights the position of the vesicle projection inside the micropipette with respect to the first snapshot; (d)–(f) sequence of images acquired on a DOPC vesicle exposed to a Mag H2 concentration of 10^{-9} M. The lipid bilayer protrusion retracts as a consequence of the interaction with the peptides; (g) evolution of the relative area variation as a function of time for two representative cases for 5.13×10^{-13} M Mag H2; (h) representative plots of the protrusion retraction for two Mag H2 concentrations, 10^{-9} M (black squares) and 8 μM (red circles). In the case of the 8 μM concentration, the vesicle disrupted after 200 s. (For interpretation of the references to colour in this figure legend, the reader is referred to the web version of this article.)

stationary. Fig. 5g shows the relative area increase associated with the overall projection increase as a function of time for two representative experiments. When the Mag H2 concentration is increased to 10^{-9} M, we observed the opposite effect, i.e. the vesicle projection retracted such as in the sequence shown in Fig. 5d–f (n = 5). The retraction rate depended on the Mag H2 concentration, increasing with peptide concentration, as shown in Fig. 5h. In the case of the vesicle projection retraction we did not analyze its behavior in terms of relative area variation because it cannot be excluded that the lipid bilayer is adopting structures in which lipids accumulate in some points, having an effect on the quantitative analysis. In fact, in some cases we observed the formation of dots on the lipid bilayer during the projection retraction. Qualitatively, the decrease of the vesicle projection can be interpreted as due to a volume increase of the vesicle. In this case, the volume increase could be related to the formation of pores in the membrane inducing the influx of glucose molecules in the vesicle lumen.

Considering the extreme sensitivity of the bilayer to the peptide concentration, and looking for the transition from the expansion to the retraction behavior on the same vesicle, we decided to change the method of vesicle exposure to the peptides. To this aim, we grabbed one POPC vesicle using the MAT system, and then injected in the chamber a peptide amount equivalent to a final concentration of 2 and 4 μM without any stirring procedure. By this way, the concentration of the peptide near the vesicle increases as the diffusion of the molecules proceeds. Before injecting Mag H2, we measured the background effect on the position of the vesicle projection inside the micropipette due to the evaporation of water in the imaging chamber. Fig. 6 shows the trend of the relative area variation as a function of time for different POPC vesicles. For 2 μM Mag H2, we generally observed a slow increase of the area up to a relative variation of 4% followed by a projection retraction and the final collapse of the vesicle. For 4 μM Mag H2, the typical behavior consists of an initial rapid area increase, a decrease of the growth rate which is then followed, after a relative area variation of about 8%, by a rapid retraction of the vesicle projection; the sequence ends with the collapse of the vesicle (see Movie S1 for the complete sequence of one experiment). The average area increase for the two concentrations, 2 and 4 μM, are 3.3 ± 1.0% and 6.3 ± 1.6% (n = 9 in both cases), respectively. The behavior of the vesicle projection can be explained as follows: an initial area increase takes place due to the adsorption of the peptide and the decrease of the lipid bilayer thickness (it is not excluded that a contribution comes also from the decrease of the bending constant – see below – of the lipid bilayer affecting the GUV projection position). It is to be stressed that the second region of slow increase of the area should be considered taking into account also the reported area variation just due to solvent evaporation (thin dashed line in Fig. 6). If this effect is taken into account, we can say that after the initial increase, the lipid bilayer area stays constant until the permeabilization and the increase of the volume starts. This behavior is similar to the one observed for Mag 2 in ref [19]. The increase of the volume always leads to the destruction of the vesicle, probably due to the strong effect of the peptide on the mechanical properties of the bilayer and the lateral tension applied by the micropipette.

3.5. Vesicle area variation before permeabilization

We then tried to deepen the understanding of the lipid bilayer changes while it interacts with Mag H2 before the permeabilization process starts. To do this, we decided to continuously follow the shape changes of the vesicles during the exposure to the peptides by measuring the equatorial shape of the vesicles using phase contrast imaging. We then reconstructed the approximate perimeter of the equatorial image of the vesicle using the same profiling technique exploited for flickering spectroscopy (see below) and, at the same time, we measured the changes of the phase contrast inside the vesicles as a marker of the permeabilization process. In this case we can report the ratio between the average contrast inside the vesicle and the average contrast value measured outside the vesicle as a function of time. The initial contrast difference between the two regions is due to the fact that the solution inside the vesicle contains sucrose whereas outside it is mainly glucose. Upon permeabilization, the solutions inside and outside the vesicle equilibrate and the ratio approaches 1. Fig. 7 shows an example for this kind of analysis on a POPC vesicle exposed to 2 μM Mag H2. If a GUV had a spherical shape it could be possible to measure the area from the measurement of the circle obtained at the equatorial region. In the case of a fluctuating vesicle, the measurement of the perimeter at the equatorial region can be exploited only to have an idea of fluctuations but not as a parameter from which to obtain the exact vesicle area. Accordingly, the trend of the perimeter reported in Fig. 7 shows the behavior of the fluctuations as the interaction of the vesicle with Mag H2 proceeds. The images reported in Fig. 7 show the vesicle frames at the different time points reported in the plot (the complete sequence of images is reported in Movie S2). As already pointed out, the first effect of peptides adsorbing onto the lipid bilayer is an increase of the visible lipid bilayer fluctuations. Both, the excess area and the

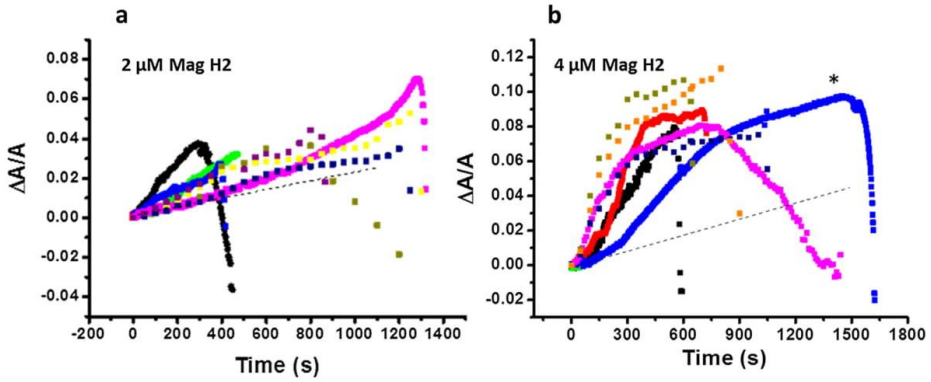

Fig. 6. Evolution of the relative area change as a function of time of POPC GUVs exposed to (a) 2 μM and (b) 4 μM Mag H2 concentrations. The dotted light grey line represents the extrapolation of the drift of the relative area variation due to water evaporation measured for 500 s in (a) and 200 s in (b) on the same vesicle at the beginning of each experiment. (see movie S1 for the experiment indicated by the asterisk).

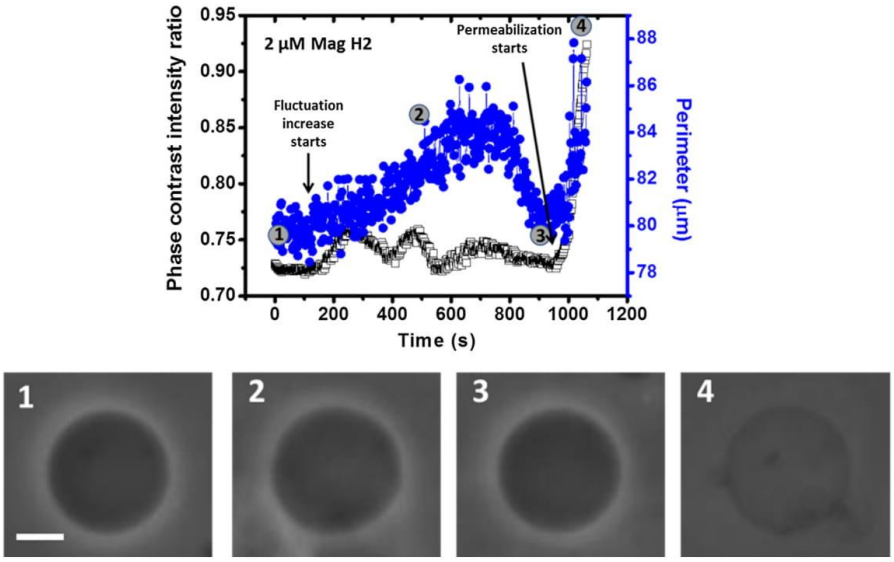

Fig. 7. Variation of the phase contrast and the perimeter value measured at the equatorial plane of a POPC GUV as it interacts with a 2 μM Mag H2 concentration. Hollow squares represent the phase contrast intensity ratio obtained by considering the average intensity of a region external to the vesicle and the average contrast value inside the vesicle. The blue circles represent the approximate value of the perimeter of the vesicle at the equatorial plane as an observable used to report lipid bilayer fluctuations. The phase contrast images of the vesicle reported below have been obtained at the instants numbered in the plot (bar = 10 μm). (For interpretation of the references to colour in this figure legend, the reader is referred to the web version of this article.)

possible thickness decrease could induce this effect as well as a bending constant decrease. The increase of fluctuations however proceeds without any change in the phase contrast between the internal and external regions of the vesicle (the instabilities in the plot of Fig. 7 are due to the overlapping of floating structures in the chamber as it is evident from Movie S2). At point 3 in the plot, fluctuations of the bilayer rapidly decrease without producing any change in the internal contrast of the vesicle. We tentatively associate this phase to the translocation of the peptides from the external to the internal leaflet of the bilayer. Immediately after this rapid phase, the permeabilization starts and the area of the vesicle increases. In the Supplementary Material section we report the analysis of the area variation measured by phase contrast for POPC vesicles exposed to different Mag H2 concentrations (Fig S11) as well as a sequence of images obtained by confocal microscopy showing a similar process (Fig S8). The sequence of the events could be summarized in the following steps: (i) the peptides adsorb onto the external vesicle leaflet increasing its area and generating a strong asymmetry between the two leaflets, introducing softening of the bilayer and strong visible fluctuations; (ii) the internal leaflet of the bilayer expands due to the interleaflet coupling, probably inducing the formation of highly disordered structures which allow (iii) the translocation of the peptides to the internal leaflet restoring a symmetry between the two leaflets and recovering the spherical shape of the vesicle; (iv) after restoring the spherical shape with a symmetric situation for the two leaflets, pores are formed and the equilibration of the internal and external solutions starts with an increase of the vesicle volume. The behavior that we observed for vesicles exposed to Mag H2 is in part consistent with a model developed for Mag 2 in the literature [57] and is also consistent with experimental results in which fluorescently labeled Mag 2 accumulation on the surface of a GUV has been tracked together with the efflux from the vesicle of a fluorescent species [19]. In particular Karal et al. [19] show the presence of a small lag time between the moment in which the peptide starts to translocate to the inner leaflet of the vesicle and the starting of the fluorescent dye efflux from the vesicle. The average lag time that has been found in [19] is about 24 s, whereas, using a different observable (fluctuations with respect to the intensity of the labeled peptide) we observed a lag time of about 100 s. Accordingly, the main source for the fluctuations that we observe could be related to the leaflet asymmetry in the peptide concentration whereas pore formation is highly favored when the peptide is distributed in the two bilayer leaflets. On the basis of our data we cannot obtain any evidence about the mechanistic process that eventually leads to the decrease of the pore diameter.

3.6. Effect of Mag H2 on the lipid bilayer bending constant

In MAT experiments, the vesicle projection inside the pipette is a sort of amplification of the lipid bilayer area changes. However, in the MAT set-up, changes in the bending constant of the lipid bilayer could produce a variation of the apparent vesicle area. Accordingly, we decided to study the changes of the bending constant of lipid bilayers due to the adsorption of the peptides by flickering spectroscopy. The effect of AMPs on lipid bilayer fluctuations has already been studied by flickering microscopy [60,61] establishing for example in the case of Mag 2 a strong effect, in particular a decrease, on the bending constant of POPC membranes [26]. Table 2 shows the effects of low Mag H2 concentrations

Table 2
Bending constant values for POPC and DOPC vesicles measured by flickering spectroscopy before and after the exposure to low Mag H2 concentrations (before producing the permeabilization effect).

	Control	Mag H2[C]
POPC	**(26 ± 6) k_BT** (n = 3)	**(11 ± 2) k_BT 0.25 μM** (n = 7)
DOPC	**(21 ± 2) k_BT** (n = 7)	**(7 ± 2) k_BT 0.3 μM** (n = 17)

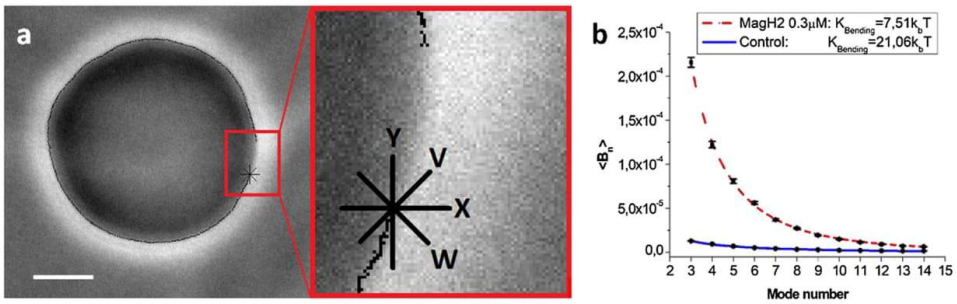

Fig. 8. (a) Image of a DOPC GUV exposed to 0.30 μM Mag H2. Part of the GUV contour is zoomed in order to show the different directions used for gradient of pixels evaluation. Scale bar = 10 μm; (b) fit of experimental $<B_n>$ coefficients obtained from a fluctuating POPC GUV observed at room temperature (22C°) in control condition (continuous blue line), and exposed to Mag H2 0.3 μM (dashed red line). (For interpretation of the references to colour in this figure legend, the reader is referred to the web version of this article.)

(0.25–0.3 μM) on the bending constant of DOPC and POPC bilayers. The low concentration of Mag H2 assures that the permeabilization processes is not obtained. This is necessary because the permeabilization typically produces an increase of the vesicle volume producing a tensed bilayer for which the fluctuations are difficult to be measured. Fig. 8 shows an example of the procedure used to identify the vesicle contour (see Par S6 for the details and Movie S7 for the complete contour reconstruction) and the comparison between a pure POPC vesicle and a POPC vesicle exposed to a 0.3 μM Mag H2 solution. The results show that Mag H2 decreases the bending constant of the bilayer, with a similar effect for both DOPC and POPC. This effect could be related to a decrease of the bilayer thickness as has been detected for Mag H2 [62,63].

4. Conclusion

In this work, we studied, by exploiting GUVs, the permeabilization activity of Mag H2, a peptide obtained by changing 5 residues to the natural antimicrobial peptide Mag 2. Mag H2 is endowed with increased hydrophobicity with respect to Mag 2 and, to the best of our knowledge, no previous studies used GUVs and the related optical microscopy approaches to study the activity of this peptide. The aim of the study was to shed light on the mechanism of action of Mag H2 compared to the well-studied mechanism of Mag 2 with particular emphasis on figuring out of the role played by the enhanced hydrophobicity on the poration mechanism. In fact, together with the different selectivity which is associated to the increased hydrophobicity it is possible that the different physical and chemical properties of the peptides could give rise to different mechanism for the permeabilization activity. We found that Mag H2 has a strong activity also on zwitterionic bilayers and the presence of negatively charged lipids such as PG has a protective effect on the permeabilization activity at variance with the natural Mag 2. We associated this behavior to an increased role of the monolayer curvature in the pore formation mechanism, probably due to deeper penetration of Mag H2 in the hydrophobic region of the bilayer. Accordingly, the increased hydrophobicity of peptides could make the intrinsic monolayer curvature aspects more relevant than the electrostatic effects. In the future, detailed experiments as a function of temperature could shed new light on this aspect. In fact, the intrinsic monolayer curvature can be modulated by temperature and the tendency to form toroidal pores could be consequently affected. Concerning the mechanism of pore formation, our results can be interpreted as consistent with the formation of a toroidal structure and the sequence of steps leading to the permeabilization that we observed are consistent with what has been obtained in other previous studies for Mag 2 [19]. In particular, it seems that pore formation occurs only after the peptide has translocated to the internal leaflet of the GUV, The results we obtained are in agreement with the MD simulation studies in which the formation of disordered toroidal pores has been obtained in the specific case of Mag H2 in PC lipid bilayers [30]. It could be interesting to extend the simulation studies to the case of PG lipids to investigate in more details the role of lipid curvature with respect to electrostatic effects.

Appendix A. Supplementary material

Supplementary data to this article can be found online at https://doi.org/10.1016/j.jcis.2019.06.028.

References

[1] K. Mølbak, Spread of resistant bacteria and resistance genes from animals to humans - the public health consequences, J. Vet. Med. Ser. B Infect. Dis. Vet. Public Heal. 51 (2004) 364–369, https://doi.org/10.1111/j.1439-0450.2004.00788.x.
[2] D.I. Andersson, D. Hughes, J.Z. Kubicek-Sutherland, Mechanisms and consequences of bacterial resistance to antimicrobial peptides, Drug Resist. Updat. 26 (2016) 43–57, https://doi.org/10.1016/j.drup.2016.04.002.
[3] J.O'. Neill, Antimicrobial resistance: tackling a crisis for the health and wealth of nations the review on antimicrobial resistance chaired, HM Gov. Wellcome Trust. (2014) 1–20, https://doi.org/10.1038/510015a.
[4] E.Y. Furuya, F.D. Lowy, Antimicrobial-resistant bacteria in the community setting, Nat. Rev. Microbiol. 4 (2006) 36–45, https://doi.org/10.1038/nrmicro1325.
[5] World Health Organization, ed., Antimicrobial resistance: global report on surveillance, World Health Organization, Geneva, Switzerland, 2014.
[6] A. Giuliani, G. Pirri, S.F. Nicoletto, Antimicrobial peptides: an overview of a promising class of therapeutics, Cent. Eur. J. Biol. 2 (2007) 1–33.
[7] W. Aoki, M. Ueda, Characterization of antimicrobial peptides toward the development of novel antibiotics, Pharmaceuticals 6 (2013) 1055–1081.
[8] M. Zasloff, Antimicrobial peptides of multicellular organisms, Nature 415 (2002) 389–395, https://doi.org/10.1038/415389a.
[9] T. Koprivnjak, A. Peschel, Bacterial resistance mechanisms against host defense peptides, Cell. Mol. Life Sci. 68 (2011) 2243–2254, https://doi.org/10.1007/s00018-011-0716-4.
[10] K.A. Brogden, Antimicrobial peptides: pore formers or metabolic inhibitors in bacteria?, Nat Rev. Microbiol. 3 (2005) 238–250, https://doi.org/10.1038/nrmicro1098.
[11] L.T. Nguyen, E.F. Haney, H.J. Vogel, The expanding scope of antimicrobial peptide structures and their modes of action, Trends Biotechnol. 29 (2011) 464–472, https://doi.org/10.1016/j.tibtech.2011.05.001.
[12] A. Pokorny, T.H. Birkbeck, P.F.F. Almeida, Mechanism and kinetics of δ-lysin interaction with phospholipid vesicles, Biochemistry 41 (2002) 11044–11056, https://doi.org/10.1021/bi020244r.
[13] R.F. Epand, W.L. Maloy, A. Ramamoorthy, R.M. Epand, Probing the "charge cluster mechanism" in amphipathic helical cationic antimicrobial peptides, Biochemistry 49 (2010) 4076–4084.
[14] W.C. Wimley, Describing the mechanism of antimicrobial peptide action with the interfacial activity model, ACS Chem. Biol 5 (2010) 905–917, https://doi.org/10.1021/cb1001558.

[15] D.W. Hoskin, A. Ramamoorthy, Studies on anticancer activities of antimicrobial peptides, Biochim. Biophys. Acta (BBA)-Biomembranes 1778 (2008) 357–375.
[16] H.W. Huang, N.E. Charron, Understanding membrane-active antimicrobial peptides, Q. Rev. Biophys. 50 (2017) 1–13, https://doi.org/10.1017/S0033583517000087.
[17] P.F. Almeida, A. Pokorny, Mechanisms of antimicrobial, cytolytic, and cell-penetrating peptides: from kinetics to thermodynamics, Biochemistry 48 (2009) 8083–8093, https://doi.org/10.1021/bi900914g.
[18] M.Z. Islam, J.M. Alam, Y. Tamba, M.A.S. Karal, M. Yamazaki, The single GUV method for revealing the functions of antimicrobial, pore-forming toxin, and cell-penetrating peptides or proteins, Phys. Chem. Chem. Phys. 16 (2014) 15752–15767, https://doi.org/10.1039/c4cp00717d.
[19] M.A.S. Karal, J.M. Alam, T. Takahashi, V. Levadny, M. Yamazaki, Stretch-activated pore of the antimicrobial peptide, magainin 2, Langmuir 31 (2015) 3391–3401, https://doi.org/10.1021/la503318z.
[20] E. Evans, D. Needham, Physical properties of surfactant bilayer membranes: thermal transitions, Elasticity, Rigidity, Cohesion, Colloid. Interact. 2 (1987) 4219–4228.
[21] E. Evans, W. Rawicz, Entropy-driven tension and bending elasticity in condensed-fluid membranes, Phys. Rev. Lett. 64 (1990) 2094–2097, https://doi.org/10.1103/PhysRevLett. 64.2094.
[22] K. Olbrich, W. Rawicz, D. Needham, E. Evans, Water permeability and mechanical strength of polyunsaturated lipid bilayers, Biophys. J. 79 (2000) 321–327, https://doi.org/10.1016/S0006-3495(00)76294-1.
[23] Y. Sun, C.C. Lee, W.C. Hung, F.Y. Chen, M.T. Lee, H.W. Huang, The bound states of amphipathic drugs in lipid bilayers: Study of curcumin, Biophys. J. 95 (2008) 2318–2324, https://doi.org/10.1529/biophysj.108.133736.
[24] R. Kwok, E. Evans, Thermoelasticity of large lecithin bilayer vesicles, Biophys. J. 35 (1981) 637–652, https://doi.org/10.1016/S0006-3495(81)84817-5.
[25] Y. Sun, W.C. Hung, F.Y. Chen, C.C. Lee, H.W. Huang, Interaction of tea catechin (-)-epigallocatechin gallate with lipid bilayers, Biophys. J. 96 (2009) 1026–1035, https://doi.org/10.1016/j.bpj.2008.11.007.
[26] H. Bouvrais, P. Méléard, T. Pott, K.J. Jensen, J. Brask, J.H. Ipsen, Softening of POPC membranes by magainin, Biophys. Chem. 137 (2008) 7–12, https://doi.org/10.1016/j.bpc.2008.06.004.
[27] M.Z. Islam, S. Sharmin, V. Levadnyy, S.U. Alam Shibly, M. Yamazaki, Effects of mechanical properties of lipid bilayers on the entry of cell-penetrating peptides into single vesicles, Langmuir 33 (2017) 2433–2443, https://doi.org/10.1021/acs.langmuir.6b03111.
[28] S. Arasteh, M. Bagheri, Molecular dynamics simulation and analysis of the antimicrobial peptide-lipid bilayer interactions, In Antimicrob. Pept. (2017) 103–118, https://doi.org/10.1007/978-1-4939-6737-7_8.
[29] P. La Rocca, P.C. Biggin, D.P. Tieleman, M.S.P. Sansom, Simulation-studies-of-the-interaction-of-antimicrobial-peptides-and-lipid-bilayers_1999_Biochimica-et-Biophysica-Acta-BBA-Biomembranes.pdf, 1462 (1999) 185–200.
[30] H. Leontiadou, A.E. Mark, S.J. Marrink, Antimicrobial peptides in action, J. Am. Chem. Soc. 128 (2006) 12156–12161, https://doi.org/10.1021/ja062927q.
[31] M. Zasloff, Magainins, a class of antimicrobial peptides from *Xenopus* skin: isolation, characterization of two active forms, and partial cDNA sequence of a precursor, Proc. Natl. Acad. Sci. 84 (1987) 5449–5453.
[32] K. Matsuzaki, K.I. Sugishita, M. Harada, N. Fujii, K. Miyajima, Interactions of an antimicrobial peptide, magainin 2, with outer and inner membranes of Gram-negative bacteria, Biochim. Biophys. Acta - Biomembr. 1327 (1997) 119–130, https://doi.org/10.1016/S0005-2736(97)00051-5.
[33] S.J. Ludtke, K. He, W.T. Heller, T.A. Harroun, L. Yang, H.W. Huang, Membrane pores induced by magainin, Biochemistry 35 (1996) 13723–13728, https://doi.org/10.1021/bi9620621.
[34] L. Yang, T.M. Weiss, R.I. Lehrer, H.W. Huang, Crystallization of antimicrobial pores in membranes: magainin and protegrin, Biophys. J. 79 (2000) 2002–2009, https://doi.org/10.1016/S0006-3495(00)76448-4.
[35] T. Tachi, R.F. Epand, R.M. Epand, K. Matsuzaki, Position-dependent hydrophobicity of the antimicrobial magainin peptide affects the mode of peptide-lipid interactions and selective toxicity, Biochemistry 41 (2002) 10723–10731, https://doi.org/10.1021/bi0256983.
[36] A.J. Rzepiela, D. Sengupta, N. Goga, S.J. Marrink, Membrane poration by antimicrobial peptides combining atomistic and coarse-grained descriptions, Faraday Discuss. 144 (2010) 431–443, https://doi.org/10.1039/B901615E.
[37] A. Goliaei, K.P. Santo, M.L. Berkowitz, Local pressure changes in lipid bilayers due to adsorption of melittin and magainin-h2 antimicrobial peptides: results from computer simulations, J. Phys. Chem. B 118 (2014) 12673–12679, https://doi.org/10.1021/jp507919p.
[38] A. Pino-Angeles, J.M. Leveritt, T. Lazaridis, Pore structure and synergy in antimicrobial peptides of the magainin family, PLoS Comput. Biol. 12 (2016) 1–17, https://doi.org/10.1371/journal.pcbi.1004570.
[39] D.S. Dimitrov, M.I. Angelova, Lipid swelling and liposome formation mediated by electric fields, J. Electroanal. Chem. Interfacial Electrochem. 253 (1988) 323–336, https://doi.org/10.1016/0022-0728(88)87069-4.
[40] M.-T. Lee, W.-C. Hung, F.-Y. Chen, H.W. Huang, Mechanism and kinetics of pore formation in membranes by water-soluble amphipathic peptides, Proc. Natl. Acad. Sci. 105 (2008) 5087–5092, https://doi.org/10.1073/pnas.0710625105.
[41] J. Pécréaux, H.G. Döbereiner, J. Prost, J.F. Joanny, P. Bassereau, Refined contour analysis of giant unilamellar vesicles, Eur. Phys. J. E. 13 (2004) 277–290, https://doi.org/10.1140/epje/i2004-10001-9.
[42] W.S. Rasband, ImageJ, U. S. National Institutes of Health, Bethesda, Maryland, USA, 1997-2018, (2018) 2018. 1997-2018. <https://imagej.nih.gov/ij/>, <https://imagej.nih.gov/ij/>.
[43] M.J. Sarmento, M. Prieto, F. Fernandes, Reorganization of lipid domain distribution in giant unilamellar vesicles upon immobilization with different membrane tethers, Biochim. Biophys. Acta - Biomembr. 2012 (1818) 2605–2615, https://doi.org/10.1016/j.bbamem.2012.05.028.
[44] P. Schön, A.J. García-Sáez, P. Malovrh, K. Bacia, G. Anderluh, P. Schwille, Equinatoxin II permeabilizing activity depends on the presence of sphingomyelin and lipid phase coexistence, Biophys. J. 95 (2008) 691–698, https://doi.org/10.1529/biophysj.108.129981.
[45] N.B. Leite, A. Aufderhorst-Roberts, M.S. Palma, S.D. Connell, J.R. Neto, P.A. Beales, PE and PS lipids synergistically enhance membrane poration by a peptide with anticancer properties, Biophys. J. 109 (2015) 936–947, https://doi.org/10.1016/j.bpj.2015.07.033.
[46] Y. Tamba, M. Yamazaki, Magainin 2-induced pore formation in the lipid membranes depends on its concentration in the membrane interface, J. Phys. Chem. B. 113 (2009) 4846–4852, https://doi.org/10.1021/jp8109622.
[47] B. Kollmitzer, P. Heftberger, M. Rappolt, G. Pabst, Monolayer spontaneous curvature of raft-forming membrane lipids, Soft Matter. 9 (2013) 10877, https://doi.org/10.1039/c3sm51829a.
[48] K. Matsuzaki, K.I. Sugishita, N. Ishibe, M. Ueha, S. Nakata, K. Miyajima, et al., Relationship of membrane curvature to the formation of pores by magainin 2, Biochemistry 37 (1998) 11856–11863, https://doi.org/10.1021/bi980539y.
[49] D. Bhattacharyya, M. Kim, K.H. Mroue, M. Park, A. Tiwari, M. Saleem, et al., Role of non-electrostatic forces in antimicrobial potency of a dengue-virus derived fusion peptide VG16KRKP: Mechanistic insight into the interfacial peptide-lipid interactions, Biochim. Biophys. Acta - Biomembr. 2019 (1861) 798–809, https://doi.org/10.1016/j.bbamem.2019.01.011.
[50] S.H. Alley, O. Ces, M. Barahona, R.H. Templer, X-ray diffraction measurement of the monolayer spontaneous curvature of dioleoylphosphatidylglycerol, Chem. Phys. Lipids. 154 (2008) 64–67, https://doi.org/10.1016/j.chemphyslip.2008.03.007.
[51] E.E. Ambroggio, F. Separovic, J.H. Bowie, G.D. Fidelio, L.A. Bagatolli, Direct visualization of membrane leakage induced by the antibiotic peptides: maculatin, citropin, and aurein, Biophys. J. 89 (2005) 1874–1881, https://doi.org/10.1529/biophysj.105.066589.
[52] E. Glukhov, M. Stark, L.L. Burrows, C.M. Deber, Basis for selectivity of cationic antimicrobial peptides for bacterial versus mammalian membranes, J. Biol. Chem. 280 (2005) 33960–33967, https://doi.org/10.1074/jbc.M507042200.
[53] A.J. McHenry, M.F.M. Sciacca, J.R. Brender, A. Ramamoorthy, Does cholesterol suppress the antimicrobial peptide induced disruption of lipid raft containing membranes?, Biochim Biophys. Acta - Biomembr. 2012 (1818) 3019–3024, https://doi.org/10.1016/j.bbamem.2012.07.021.
[54] L.R. Arriaga, I. López-Montero, F. Monroy, G. Orts-Gil, B. Farago, T. Hellweg, Stiffening effect of cholesterol on disordered lipid phases: a combined neutron spin echo + dynamic light scattering analysis of the bending elasticity of large unilamellar vesicles, Biophys. J. 96 (2009) 3629–3637, https://doi.org/10.1016/j.bpj.2009.01.045.
[55] K.A. Riske, Optical Microscopy of Giant Vesicles as a Tool to Reveal the Mechanism of Action of Antimicrobial Peptides and the Specific Case of Gomesin, 1st ed., Elsevier Inc., 2015. 10.1016/bs.adplan.2014.12.001.
[56] E.F. Haney, S. Nathoo, H.J. Vogel, E.J. Prenner, Induction of non-lamellar lipid phases by antimicrobial peptides: a potential link to mode of action, Chem. Phys. Lipids. 163 (2010) 82–93, https://doi.org/10.1016/j.chemphyslip.2009.09.002.
[57] Y. Tamba, H. Ariyama, V. Levadny, M. Yamazaki, Kinetic pathway of antimicrobial peptide magainin 2-induced pore formation in lipid membranes, J. Phys. Chem. B 114 (2010) 12018–12026, https://doi.org/10.1021/jp104527y.
[58] Y. Tamba, M. Yamazaki, Single giant unilamellar vesicle method reveals effect of antimicrobial peptide magainin 2 on membrane permeability, Biochemistry 44 (2005) 15823–15833, https://doi.org/10.1021/bi051684w.
[59] M. Sacchi, D. Balleza, G. Vena, G. Puia, P. Facci, A. Alessandrini, Effect of neurosteroids on a model lipid bilayer including cholesterol: an atomic force microscopy study, Biochim. Biophys. Acta - Biomembr. 2015 (1848) 1258–1267, https://doi.org/10.1016/j.bbamem.2015.01.002.
[60] T. Pott, C. Gerbeaud, N. Barbier, P. Méléard, Melittin modifies bending elasticity in an unexpected way, Chem. Phys. Lipids. 185 (2015) 99–108, https://doi.org/10.1016/j.chemphyslip.2014.05.004.
[61] V. Vitkova, P. Méléard, T. Pott, I. Bivas, Alamethicin influence on the membrane bending elasticity, Eur. Biophys. J. 35 (2006) 281–286, https://doi.org/10.1007/s00249-005-0019-5.
[62] N. Marín-Medina, A. Mescola, A. Alessandrini, Effects of the peptide magainin H2 on supported lipid bilayers studied by different biophysical techniques, Biochim. Biophys. Acta - Biomembr. 2018 (1860) 2635–2643, https://doi.org/10.1016/j.bbamem.2018.10.003.
[63] S. Ludtke, K. He, H. Huang, Membrane thinning caused by magainin 2, Biochemistry 34 (1995) 16764–16769, https://doi.org/10.1021/bi00051a026.

Supplementary Material for:

Magainin-H2 effects on the permeabilization and the mechanical properties of Giant Unilamellar Vesicles

Andrea Mescola[a], Nathaly Marín-Medina[b], Gregorio Ragazzini[a,c], Maurizio Accolla[c], Andrea Alessandrini[a,c]

[a]CNR-Nanoscience Institute-S3, Via Campi 213/A, 41125, Modena, Italy , andrea.mescola@nano.cnr.it

[b]Department of Physics, University of Los Andes, Carrera 1 N° 18A – 12, 111711,Bogotá, Colombia, nmarin@uniandes.edu.co

[c]Department of Physics, Informatics and Mathematics, University of Modena and Reggio Emilia, Via Campi 213/A, 41125, Modena, Italy, andrea.alessandrini@unimore.it

Index

1) Magainin H2 vs Magainin 2 sequences

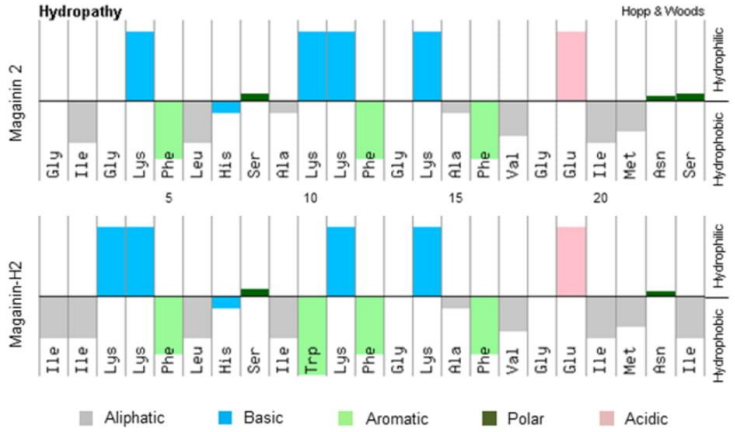

Figure S1: Aminoacid sequence and hydropathy of Mag H2 compared to the natural Magainin 2

2) Micropipette aspiration set-up and formulas for analysis of results

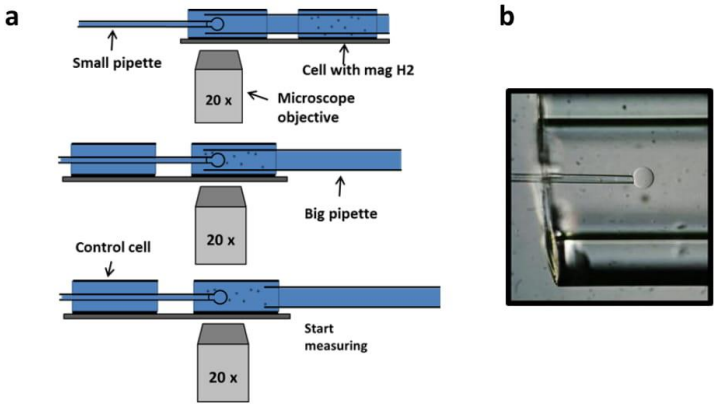

Figure S2: a) Schematics of the set-up used to perform transfer experiments in order to measure the interaction kinetics between a single GUV and mag-H2 peptides; b) picture of the aspirated GUV inside the bigger pipette to be transferred from one compartment to the other one.

In Micropipette Aspiration Experiments, the vesicle area variation ΔA can be measured from the optical images. It is given by[1]:

$$\Delta A = 8\pi R_v \Delta R_v + 2\pi R_p \Delta L_p \quad [S1]$$

where R_v is the GUV radius, R_p is the internal micropipette radius and L_p is the length of the vesicle projection inside the micropipette. At the same time we can also measure the volume variation ΔV:

$$\Delta V = 4\pi R_v^2 \Delta R_v + \pi R_p^2 \Delta L_p \quad [S2]$$

Performing experiments with GUVs and antimicrobial peptides we can have two possible cases: at low P/L ratios the peptides induce an area expansion without the formation of pores; at high P/L ratios the peptides induce the formation of pores. In the first case we can have GUVs with constant volume and increasing area, whereas in the second case the area could be considered constant and the vesicle volume can change due to water or electrolyte fluxes. In the first case, i.e. at constant volume, the expression for the area change can be simplified to:

$$\Delta A = 2\pi R_p \left(1 - R_p/R_v\right) \Delta L_p \quad [S3]$$

The above formula has been used to calculate the area variation when the GUVs were exposed to the antimicrobial peptides. According to Eq. S3, a positive value of ΔL_p (an increase of the projection inside the micropipette) corresponds to an increase of the vesicle area. For values of the peptide concentration which are expected to form pores, the projection of the GUV inside the micropipette decreases. In the case of an isosmotic situation (between the inside and outside of the vesicle), the formation of pores should not induce a volume variation. However, it has been considered that the permeability of the pores for the different species in solution could be different. For example, narrow pores could allow glucose to pass through while blocking the flux of sucrose. In this case, the volume of the GUV will increase because glucose from the external solution will move inside the vesicle, carrying also water molecules. At constant area (it has been found that once pores are formed the lipid bilayer area remains constant) the expression for the volume variation could be simplified to:

$$\Delta V = -\pi R_p \left(R_v - R_p\right) \Delta L_p \quad [S4]$$

A negative variation of the vesicle projection can be interpreted as a volume increase of the vesicle. We observed that for peptide concentrations in the order of 10^{-6} μM (for a single vesicle) the vesicle projection retracted. For higher peptide concentrations the retraction was very evident leading to the complete destruction of the vesicle.

3) Experiments by epifluorescence and confocal microscopy

Here we present supplementary experiments by epifluorescence and confocal microscopy on the permeabilization activity of Mag H2 on GUVs. Figure S3 shows what happens when a GUV has been permeabilized and the internal region of the GUV is photobleached. GUVs were prepared without CF inside and they were injected in a chamber containing 105 mM

glucose, 10 µM CF and 2 µM Mag H2. Once the GUVs have been permeabilized, the region was photobleached. Then, we waited for 10 minutes to see if a re-equilibration with external CF molecules occurs. We found that no re-equilibration occurred. This result evidences that the pores formed by Mag H2 close or decrease their size after the initial opening.

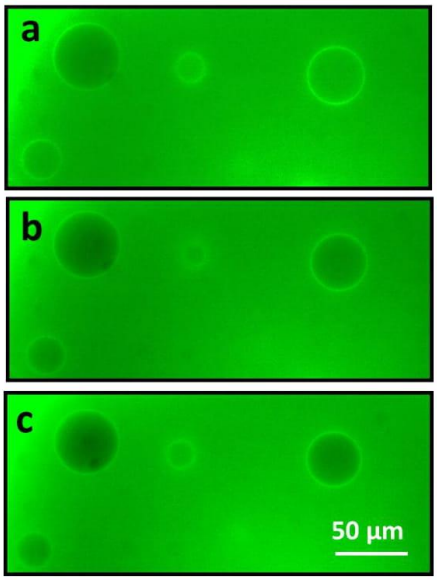

Figure S3: Example of photobleaching inside permeabilized vesicles of POPC + 1% DHPE-Texas Red dispersed in a solution containing 105 mM glucose + 10 µM CF + 2 µM Mag H2. The Texas Red is excited at the same wavelength used for CF. a) First image acquired by fluorescence microscopy to show the presence of permeabilized vesicles; b) fluorescence image of the same area after exposition to high intensity fluorescence light in order to produce CF photobleaching; c) fluorescence image of the same sample area as in a) and b) acquired 10 minutes after the photobleaching step. No recovery of the fluorescence intensity is observed.

In the following figures (Figures S4, S5 and S6) we represent the kinetics of GUVs influx and efflux exposed to different Mag H2 concentrations. As a general comment, we found that for both POPC and DOPC vesicles, the permeabilization is mainly partial at low Mag H2 concentrations whereas a total permeabilization takes place at high concentrations. Moreover, at low peptide concentrations the permeabilization typically occurs with a partial fast initial process that is followed by a very slow process. This behavior is probably related to the closure or size decrease of the pores after the initial formation. We present data both for GUVs internally loaded with CF (CF flux is from inside to outside the vesicle - efflux) and GUVs that initially have no CF inside (CF flux is from outside to inside the vesicle - influx).

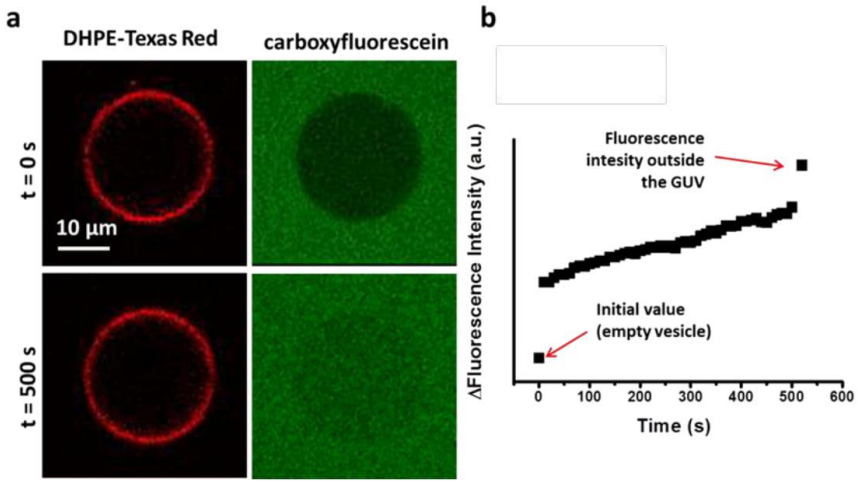

Figure S4: a) Confocal microscopy images showing the slow permeabilization step of a DOPC GUV exposed to a 1 µM Mag H2 concentration. The images have been acquired after an initial fast partial permeabilization step (see for example Fig. 3 in the main manuscript). (t = 0 s corresponds to an instant after the fast permeabilization step). 1% DHPE-Texas Red was added to the lipids and the vesicles were injected in a 105 mM glucose + 50 µM CF + 1 µM Mag H2 solution; b) plot of the fluorescence intensity variation during the slow permeabilization process. After an initial fast permeabilization step, the influx of CF slows down and it proceeds for several minutes at a low rate probably due to a closure or a reduction of the pore size. The initial value of the fluorescence intensity inside the vesicle (no fluorescence) and the value of the fluorescence signal outside the vesicle are reported as well in b) but they are not to be considered according to the reported time scale.

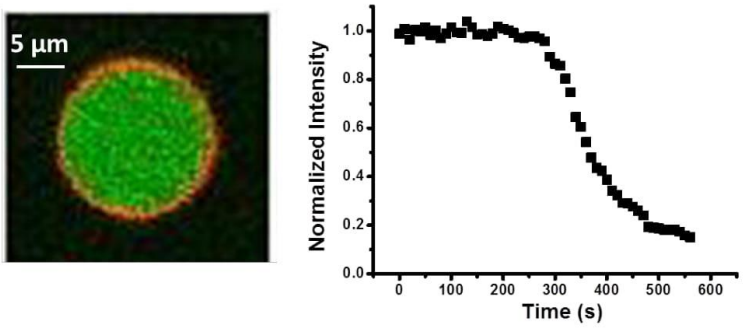

Figure S5: Efflux kinetics of a DOPC + 1% DHPE-Texas Red GUV loaded with 10 µM CF exposed to a 2 µM Mag H2 concentration. The confocal fluorescence image on the left shows the vesicle at the beginning of the experiment. The diagram on the right reports the fluorescence intensity inside the vesicle as a function of time. See the corresponding Movie S3 and S4 for the case of a GUV with CF initially present outside the vesicle.

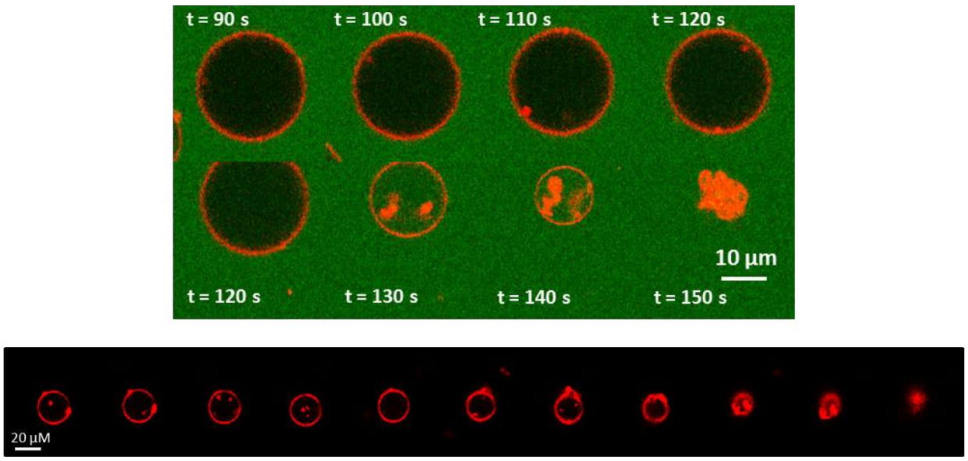

Figure S6: Upper panel: Sequence of images obtained by confocal microscopy showing a DOPC lipid bilayer (in red – 1% DHPE-Texas Red) and the influx of CF (in green) when the vesicle has been exposed to an 8 µM concentration of Mag H2. The time in each image reports the acquisition instant of the pictures starting from the GUVs injection. It is evident that the lipid bilayer collapses by a burst event and the vesicle diameter decreases due to the formation of spots where lipids accumulate. Lower panel: another example of a DOPC GUV (+ 1% DHPE-Texas Red) which has been exposed to a 5 µM concentration of Mag H2. The snapshots have been acquired every 10 seconds. In the case of concentrations higher than 5 µM all the permeabilized vesicles underwent burst events.

4) Measurement of the fluorescent dye influx in GUVs

The calculation of the fluorescent dye vesicle influx is based on the work by Schön et al [2]. In brief, the variation of the fluorophore concentration *c(t)* inside the vesicle is given by:

$$c(t+dt) = c(t) + \frac{dN}{V} \quad [S4]$$

where *dN* is the change in the number of fluorophore molecules inside the vesicle and *V* is the volume of the vesicle. If we normalize the fluorophore concentration outside the vesicle to 1, the overall flux of molecules in the time interval *dt* can be assumed to be proportional to the concentration difference (1 – *c(t)*). Accordingly:

$$dN = \big(1 - c(t)\big) J_V A_V dt \quad [S5]$$

where J_V is the net volume flux across the vesicle of area A_V. By this equation J_V is assumed to be independent of time if the flux mechanism remains the same. We can then write the following differential equation:

$$\frac{c(t+dt)-c(t)}{dt} = \frac{\big(1-c(t)\big) J_V A_V}{V} = \frac{3}{R}\big(1 - c(t)\big) J_V \quad [S6]$$

Considering that *c(0) = 0*, we can integrate the equation S6 to obtain:

$$\frac{c(t+dt)-c(t)}{dt} = \frac{\big(1-c(t)\big)J_V A_V}{V} = \frac{3}{R}\big(1-c(t)\big)J_V \quad [S7]$$

The solution of eq. S7 is given by:

$$c(t) = 1 - e^{-\frac{3J_V}{R}t} \quad [S8]$$

$$\big(1-c(t)\big) = e^{-\frac{3J_V}{R}t}$$

$$ln\big(1-c(t)\big) = -\frac{3J_V}{R}t$$

Accordingly:

$$-\frac{R}{3}ln\big(1-c(t)\big) = J_V t \quad [S9]$$

5) Vesicles containing cardiolipin

We assembled GUVs composed of DOPC:CL (3:1). Cardiolipin is a lipid endowed with a large tendency to adopt a negative curvature and to form the inverted hexagonal phase. GUVs containing CL were more resistant to the Mag H2 permeabilization . Exposing GUVs to a 4 µM Mag H2 concentration did not induce any permeabilization event. At the same time, we observed the formation of black dots on the surface of vesicles in phase contrast images (Figure S7) which might be attributed to accumulation of lipids in an unknown structure.

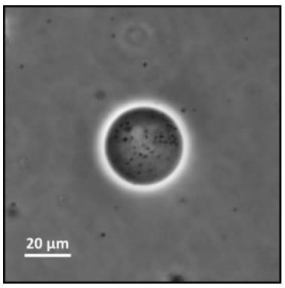

Figure S7: Phase contrast image of a DOPC:CL (3:1) GUV showing the formation of dark spots on the vesicle surface apparently due to the accumulation of lipids. The presence of these spots is particularly evident with CL, even if it is not to be completely excluded the fact that the dark spots could be due to smaller vesicles in solution adhering to the observed GUVs as we did not use filtered vesicles.

6) Fluctuations induced by Mag H2 in GUVs

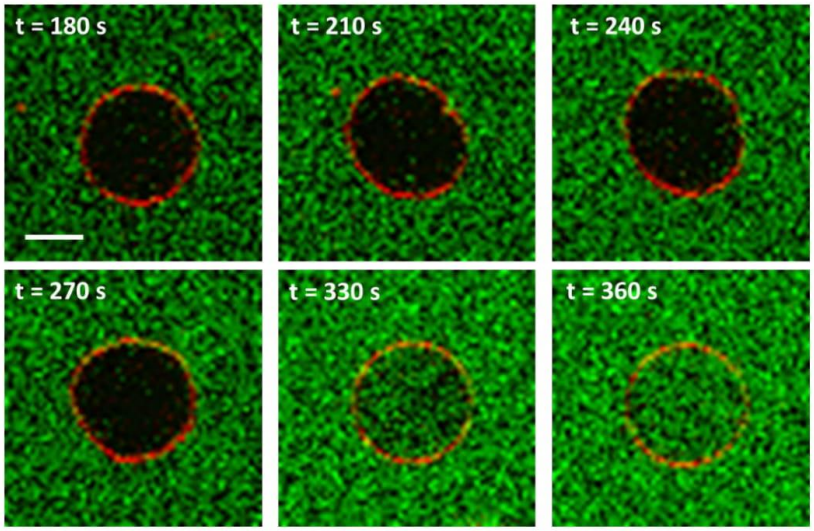

Figure S8: Sequence of confocal fluorescence images showing the permeabilization of a POPC vesicle exposed to a 2 µM Mag H2 concentration (see also the corresponding Movie S5). The external solution contains 105 mM glucose + 10 µM carboxyfluorescein + 2 µM Mag H2. The vesicle has been prepared with 0.5 % DHPE Texas Red. The time reported in each image corresponds to the time since the exposure of the vesicles to the peptide solution. The images show that, the period just before the vesicle permeabilization is characterized by an increased area fluctuation of the lipid bilayer with the tendency to adopt an oval shape. (Bar = 10 µm).

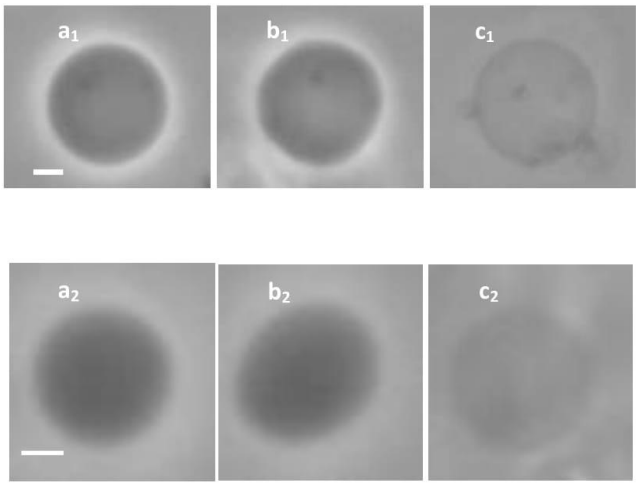

Figure S9: Sequences of phase contrast images of two POPC vesicles undergoing the permeabilization process when exposed to 2 µM Mag H2. a_1-a_2) the vesicle before the permeabilization; b_1-b_2) the vesicle undergoing large fluctuations; c_1-c_2) the vesicle after the permeabilization with a spherical shape. Bar = 10 µm (see also the corresponding Movie S6)

Flickering Spectroscopy measurement

We investigated the changes in the bending constant of POPC and DOPC GUVs exposed to Mag H2 using the classical Flickering Spectroscopy method based on Legendre polynomials decomposition of the autocorrelation function [3].

The algorithm used for contour evaluation of the images is based on iterative procedure which analyses the pixel-intensity slopes for four different directions (X,Y,V,W; see Fig S10a and Movie S7). Since the V and W directions correspond to the diagonals of the pixels, their contributions are weighed by a factor $\frac{1}{\sqrt{2}}$. Starting from a given initial point (X_o;Y_o) belonging to the contour, the first eight close neighbours pixels are analysed. For each pixel the intensity slopes along X,Y,V and W directions are evaluated, and summed (in modulus). The pixel having the greater sum is considered as the next-contour-point, neglecting pixels which already belong to the contour. The procedure can be considered concluded when the last point of the contour (X_{Final};Y_{Final}) collapses to the initial one (X_o;Y_o). This first procedure provides a contour-evaluation with pixel resolution $(x_i; y_i)$. In order to achieve a sub-pixel resolution $(\tilde{x}_i; \tilde{y}_i)$, we introduce a post-processing analysis on contour points obtained previously [4]. This second step consists of a weighted average as shown in Eqs. S10 a-b:

$$\tilde{x}_i = \frac{S_i^y * x_i + S_i^x * \overline{x_i} + S_i^v * \overline{v_{x_i}} + S_i^w * \overline{w_{x_i}}}{S_i^y + S_i^x + S_i^v + S_i^w} \quad \text{[S10a]}$$

$$\tilde{y}_i = \frac{S_i^x * y_i + S_i^y * \overline{y_i} + S_i^v * \overline{v_{y_i}} + S_i^w * \overline{w_{y_i}}}{S_i^y + S_i^x + S_i^v + S_i^w} \quad \text{[S10b]}$$

where the slopes (S_i^x , S_i^y ...) represent the weights. The barred values ($\overline{x_1}$, $\overline{y_1}$…) are obtained by searching the interception between the fitted line (red), and the mean pixel intensity (see Fig S10b). The fitted red line represents the linearization of the pixel intensity close to the maximum slope in that direction.

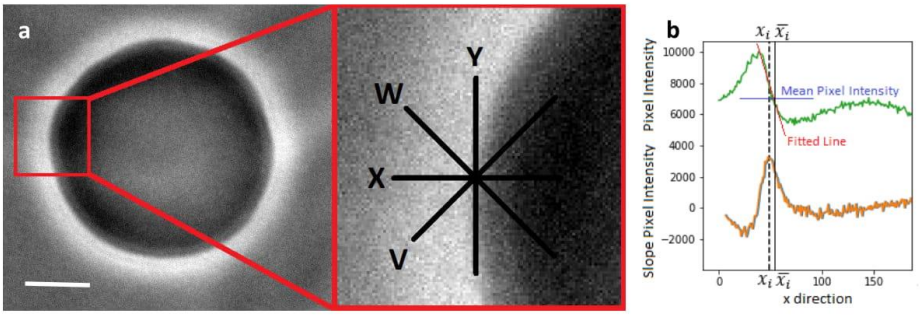

Figure S10: a) Image of a DOPC GUV exposed to Mag H2 0.30µM. Part of the GUV contour is zoomed in order to show the different directions used for gradient of pixels evaluation. Bar = 10 µm; b) Plot of pixel intensity (green) and its slope (orange) along x direction close to x_i point.

Starting from the contour coordinates it is possible to numerically evaluate the autocorrelation function, and then decompose it using Legendre polynomials. Before proceeding with the non-linear fitting procedure, we consider a time integration correction factor [5]. Since the images of the GUVs are taken every t_s=40 μs, modes having a relaxation time smaller then t_s cannot be observed. For this reason, all contributions coming from these not-observable modes must be mediated, and the experimental values $B_n(t)$ must be multiplied by a correction coefficient. In order to obtain $B_n(t)$', the corrected value of the experimental $B_n(t)$, a couple of non-linear equations (S11 a-b) must be numerically solved:

$$\tau_n{}^m = \frac{4\pi\eta R^3}{k_b T}\left(2 - \frac{1}{n(n+1)}\right) B_n \quad \text{[S11 a]}$$

$$B'_n = 2\left(\frac{\tau_n{}^m}{\tau_s}\right)^2 \left[\frac{\tau_s}{\tau_n{}^m} + e^{-\frac{\tau_s}{\tau_n{}^m}} - 1\right] B_n \quad \text{[S11 b]}$$

A correlation time $\tau_n{}^m$ is introduced for each B_n mode. The parameter η represents the viscosity of the medium surrounding the liposome. R is the GUV radius, k_B is the Boltzmann constant and T is the temperature (in Kelvin). The new set of coefficients $B_n(t)$' is then used for the fitting procedure of eq. S12:

$$B_n(\kappa, \bar{\sigma}) = \frac{2n+1}{4\pi} \frac{K_b T}{\kappa(n+2)(n-1)[\bar{\sigma}+n(n+1)]} \quad \text{[S12]}$$

7) Measurement of the area variation of GUVs by phase contrast microscopy

The area variation of GUVs can be estimated considering spherical shapes due to the fact that we have just an image representing a 2D projection of a 3D object. Accordingly, we measured the area of the initial and final spherical GUVs once they have been permeabilized by Mag H2. We concentrated on the average relative area variation in the case of 1 μM and 1.5 μM Mag H2 concentrations for POPC vesicles. To measure the area of the vesicles we used the following strategy: 1) we acquired phase contrast images at the equatorial plane of the vesicles; 2) the borders of the vesicles in the equatorial plane were reconstructed using a protocol developed in the context of flickering spectroscopy of GUVs to determine the bending constant (Fig. S11); 3) the obtained profile is then fitted to a circular shape and the resulting radius is extracted. Using this strategy we obtained the following features for the area increase of POPC vesicles: (4.7 ± 2.1)% (n = 8) for 1 μM Mag H2 and (14.5 ± 3.0)% (n = 8) for 1.5 μM Mag H2.

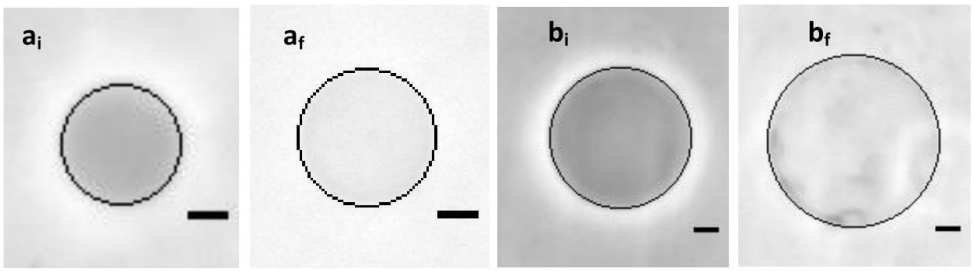

Figure S11: Two examples showing how the area variation of the vesicles has been measured are reported above. The continuous lines represent the best fitted circle to the POPC GUV profile before (a_i, b_i) and after (a_f, b_f) exposing the vesicles to a 1 μM Mag H2 concentration. The scale bars are 5 μm in all images.

8) Formation of spots on the surface of GUVs exposed to Mag H2

In several cases, when the vesicles were exposed to Mag H2, we observed the formation of black spots on the GUVs' surface in phase contrast images (Figure S12a). Using the DHPE-Texas Red fluorescent marker, we established that the black spots correspond to accumulation of lipids (Figure S12b). As already mentioned, it is not to be completely excluded the fact that the dark spots could be due to smaller vesicles in solution adhering to the observed GUVs as we did not use filtered vesicles. However, the fact that the amount of these spots correlates with the lipid composition of the vesicles supports our conclusion that they are due to lipid accumulation from the same vesicle.

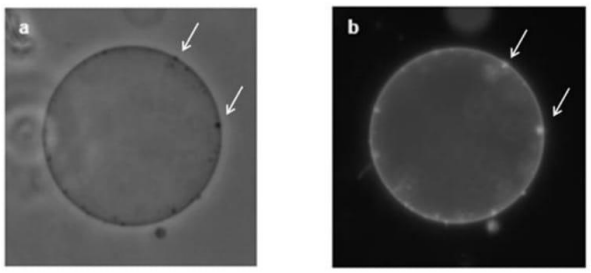

Figure S12: a) Phase contrast image of a DOPC + 1% DHPE-Texas Red GUV exposed to a 2.5 μM Mag H2 concentration; b) the corresponding fluorescence microscopy image. The arrows point to the black dots in the phase contrast image and the corresponding bright dots in the fluorescence image.

9) Description of the Movies

Movie S1: Movie representing the deformations of a POPC GUV aspirated by a micropipette and exposed to a 4 µM Mag H2 concentration. The movie covers a period of about 1600 s.

Movie S2: Example of a POPC vesicle imaged by phase contrast microscopy undergoing the permeabilization process when exposed to 2 µM Mag H2

Movie S3: Permeabilization kinetics of a DOPC + 1% DHPE Texas Red GUV loaded with 10 µM CF exposed to a 2 µM Mag H2 concentration.

Movie S4: Permeabilization kinetics of a DOPC + 1% DHPE Texas Red GUV in a 10 µM CF solution and exposed to a 1.5 µM Mag H2 concentration.

Movie S5: Confocal fluorescence microscopy movie showing the permeabilization of a POPC vesicle exposed to a 2 µM Mag H2 concentration. The external solution contains 105 mM glucose + 10 µM carboxyfluorescein + 2 µM Mag H2. The vesicle has been prepared with 0.5 % DHPE Texas Red.

Movie S6: Example of a POPC vesicle imaged by phase contrast microscopy undergoing the permeabilization process when exposed to 2 µM Mag H2.

Movie S7: Example of a vesicle contour tracking for the flickering spectroscopy technique.

References

[1] R. Kwok, E. Evans, Thermoelasticity of large lecithin bilayer vesicles, Biophys. J. 35 (1981) 637–652. doi:10.1016/S0006-3495(81)84817-5.

[2] P. Schön, A.J. García-Sáez, P. Malovrh, K. Bacia, G. Anderluh, P. Schwille, Equinatoxin II permeabilizing activity depends on the presence of sphingomyelin and lipid phase coexistence, Biophys. J. 95 (2008) 691–698. doi:10.1529/biophysj.108.129981.

[3] H. Bouvrais, P. Méléard, T. Pott, K.J. Jensen, J. Brask, J.H. Ipsen, Softening of POPC membranes by magainin, Biophys. Chem. 137 (2008) 7–12. doi:10.1016/j.bpc.2008.06.004.

[4] J. Pécréaux, H.G. Döbereiner, J. Prost, J.F. Joanny, P. Bassereau, Refined contour analysis of giant unilamellar vesicles, Eur. Phys. J. E. 13 (2004) 277–290. doi:10.1140/epje/i2004-10001-9.

[5] J.F. Faucon, M.D. Mitov, P. Méléard, I. Bivas, P. Bothorel, Bending elasticity and thermal fluctuations of lipid membranes. Theoretical and experimental requirements, J. Phys. 50 (1989) 2389–2414. doi:10.1051/jphys:0198900500170238900.

- **Line tension findings**

After showing the bending constant findings obtained by successfully applying the flickering spectroscopy analysis in the AMPs framework now we will focus on line tension evaluation of GUV fluctuating domains obtained from ternary lipid mixtures.

In the following paper we investigated the phase behavior of ternary mixtures composed by a low melting temperature phospholipid, a high melting temperature phospholipid, and cholesterol. Ternary lipid mixtures resemble the main thermodynamical features of real cell membrane of mammalian cells and constitute a valid physical model for the complex cell barrier. We used diphytanoyl-phosphatidylcholine (DiphyPC) for the low melting component, while we used several sphingomyelin types (SM) or 1,2-dipalmitoyl-snglycero-3-phosphocholine (DPPC) for the high melting component. Adopting fluorescence microscopy investigation combined to micropipette aspiration set-up (MAT) we analyzed the complex phase behavior of ternary mixtures, especially mixtures containing SM. When GUVs obtained from ternary mixture containing cholesterol are imaged with fluorescence microscopy, up to three coexisting phases can be observed under certain thermodynamical conditions. These phases refer to the: Solid-ordered (S_o), Liquid-Ordered (L_o), and Liquid-Disordered (L_d) respectively. Nevertheless, in standard condition like mixture containing DPPC only two phases coexistence, typically the L_o-L_d coexistence is clearly observable.

When we exploited mixtures containing SM we observe the presence of three coexisting phases upon specific conditions: 1) the presence in the SM specie of asymmetric and long acyl chains 2) low temperature regimes. Additionally, adopting MAT we also observed that these phases are easily modulated applying a lateral tension. Thus, we decided to measure the line tension exploiting the flickering protocol for fluctuating domains of mixtures containing SM and DPPC according to the theory presented in Chapter xxx and finally to compare their findings. Our results show how fluctuating domains of mixtures containing SM with long acyl chains have a lower line tension with respect to domains obtained from mixture containing DPPC.

Biophysical *Journal*
Article

Biophysical Society

Complex Phase Behavior of GUVs Containing Different Sphingomyelins

Daniel Balleza,[1] Andrea Mescola,[1] Nathaly Marín–Medina,[2] Gregorio Ragazzini,[1,3] Marco Pieruccini,[1] Paolo Facci,[4] and Andrea Alessandrini[1,3,*]

[1]Istituto Nanoscienze CNR, S3, Modena, Italy; [2]Departamento de Física, Universidad de Los Andes, Bogotá, Colombia; [3]Dipartimento di Scienze Fisiche, Matematiche e Informatiche, Università di Modena e Reggio Emilia, Modena, Italy; and [4]CNR – Istituto di Biofisica, Genova, Italy

ABSTRACT Understanding the lateral organization of biological membranes plays a key role on the road to fully appreciate the physiological functions of this fundamental barrier between the inside and outside regions of a cell. Ternary lipid bilayers composed of a high and a low melting temperature lipid and cholesterol represent a model system that mimics some of the important thermodynamical features of much more complex lipid mixtures such as those found in mammal membranes. The phase diagram of these ternary mixtures can be studied exploiting fluorescence microscopy in giant unilamellar vesicles, and it is typically expected to give rise, for specific combinations of composition and temperature, to regions of two-phase coexistence and a region with three-phase coexistence, namely, the liquid-ordered, liquid-disordered, and solid phases. Whereas the observation of two-phase coexistence is routinely possible using fluorescence microscopy, the three-phase region is more elusive to study. In this article, we show that particular lipid mixtures containing diphytanoyl-phosphatidylcholine and cholesterol plus different types of sphingomyelin (SM) are prone to produce bilayer regions with more than two levels of fluorescence intensity. We found that these intensity levels occur at low temperature and are linked to the copresence of long and asymmetric chains in SMs and diphytanoyl-phosphatidylcholine in the lipid mixtures. We discuss the possible interpretations for this observation in terms of bilayer phase organization in the presence of sphingolipids. Additionally, we also show that in some cases, liposomes in the three-phase coexistence state exhibit extreme sensitivity to lateral tension. We hypothesize that the appearance of the different phases is related to the asymmetric structure of SMs and to interdigitation effects.

INTRODUCTION

Understanding the lateral organization of biological membranes could be extremely relevant to grasp some aspects of their functional role. Many of the mechanical and chemical stimuli that affect cell behavior must somehow interact with the cell membrane, and the physical-chemical properties of this barrier could contribute to signal transduction (1). Biophysicists usually exploit different kinds of model systems of the biological membrane to shed light on the fundamental physical aspects ruling its behavior (2–4). Lipids are one of the main constituents and structure-determining elements of biological membranes, and the most common model systems are composed of two, three, or even four different types of lipids (5–9). Moreover, these model systems can be assembled in the form of monolayers, liposomes, supported lipid bilayers (SLBs), or black lipid membranes (2,4). As thermodynamic structures, lipid bilayers might present different phases characterized by order/disorder of the hydrophobic chains and by solid or liquid lateral dynamics of lipid molecules. The relevance of model systems has recently been highlighted by the evidence that ternary lipid mixtures composed by a high-melting-temperature (high T_m) lipid, a low-melting-temperature (low T_m) lipid, and cholesterol, assembled in giant unilamellar vesicles (GUVs), show a thermodynamic behavior very similar to that of giant plasma membrane vesicles (10). Typically, the phase diagram for ternary mixtures is characterized by the occurrence of a large region in which two immiscible liquid phases coexist, named liquid-disordered (L_d) and liquid-ordered (L_o) phases (11–14). Immiscibility

Submitted September 5, 2018, and accepted for publication December 20, 2018.

*Correspondence: andrea.alessandrini@unimore.it

Daniel Balleza and Andrea Mescola contributed equally to this work.

Daniel Balleza's present address is Department of Chemistry ICET, Universidad Autonoma de Guadalajara, Lomas del Valle, Zapopan, Jalisco, Mexico.

Marco Pieruccini's present address is CNR Institute for Microelectronics and Microsystems, Bologna, Italy.

Editor: Simon Scheuring.

https://doi.org/10.1016/j.bpj.2018.12.018

is ascribed to the different distribution of cholesterol, which shows a higher affinity for the high T_m lipids, especially if they are represented by sphingolipids (15). The biological relevance in this case is related to the presence of the L_o phase, which has been connected to the "lipid-raft hypothesis" in biological membranes (16). The formation of lateral heterogeneities in a lipid bilayer could be in fact a lipid-based mechanism for the compartmentalization of membrane proteins, and it could be connected to fundamental biochemical processes (17,18). Apart from the liquid-liquid coexistence region, the phase diagram for ternary lipid mixtures foresees the presence of a triangular three-phase coexistence area (19). This triangular region includes, along with the L_d and L_o phases, the solid-ordered (S_o) phase as well.

Ternary lipid mixtures, including sphingolipids, have been deeply studied. Both natural (frequently found in mixtures) and synthetic sphingolipids have been considered in biophysical studies. This class of lipids has a strong biological relevance because of their abundance in the external leaflet of eukaryotic cells and, in the case of mammals, because of their peculiar interaction with cholesterol (20–23). Notwithstanding their relevance and profusion of previous studies devoted to understand the thermotropic behavior of sphingolipids, several aspects are still far from being well understood, and their behavior in mixtures with other lipids is to be considered as particularly complex. Part of this complexity arises from the possible presence of acyl chain asymmetry (24–27).

Together with the sphingosine chain, many different saturated and unsaturated alkyl chains of different length, ranging from 12 to 26 carbon atoms, might be found in sphingolipids composing biological membranes (28). The two main species of natural sphingolipids contain a chain with 16 or 24 carbon atoms (C16 and C24). With their very long acyl chains, C24 sphingolipids have been observed to interact with cholesterol distinctly from C16 sphingolipids (29–31). As an example, it has been recently shown that substituting C24 with C16 sphingolipids (particularly ceramides) results in metabolic defects in mice, an effect probably related to their different interface with cholesterol (32). This outcome clearly points to the critical biological relevance of sphingolipids. In addition, the thermotropic behavior of these lipids is strongly affected by their headgroup, as well. For example, the main transition for the C24:1 ceramide occurs at 44°C, whereas the C24:1 sphingomyelin (SM), sharing the same acyl chain structure, has a transition temperature of 24°C (33). Strictly connected to the chain asymmetry of these lipids is the possibility for the acyl chains to exhibit interdigitation states (29,34–37) in which part of the acyl chain of lipids in one leaflet explores the region of the opposing one. This phenomenon is expected to be relevant for ordered phases, but its relevance also in disordered phases cannot be excluded (38). Finally, considering the strong asymmetry in the composition of the biological membranes (39), the possibility of interdigitation provides a mechanism for interleaflet coupling and confers a potentially remarkable physiological role to these kinds of lipids (40). Interdigitation could in principle also alleviate the relevant hydrophobic thickness difference between ordered and disordered phases acting as a sort of interfacial attenuation of the line tension energy cost.

Here, we studied the phase behavior of ternary lipid mixtures composed of DiPhyPC (low T_m), cholesterol, and different types of SMs (high T_m). We analyzed both natural and synthetic SMs at different molar ratios, temperatures, and lateral tensions of the bilayer. As model systems, we considered GUVs, lipid monolayers at the water-air interface, and SLBs. We used fluorescence microscopy, micropipette aspiration, atomic force microscopy (AFM), and the Langmuir trough technique coupled to fluorescence microscopy so as to highlight the presence of phase separation in both mono- and bilayers. We found that more than two fluorescence intensity levels on the surface of GUVs can appear when specific lipids are present and for particular physical parameters. This situation is interesting both because of the supposed presence of a region of three-phase coexistence in the phase diagram of ternary lipid mixtures and its elusive character when GUVs are observed by fluorescence microscopy, and because it could be evidence of a more complex phase behavior in the presence of specific SMs in the membrane with respect to other high-T_m lipids. The micropipette aspiration technique (MAT) allowed us to study the effect of the lateral tension on the phase state and on the shape of domains on GUVs, taking account of an additional control parameter to temperature and composition (41–44). Likewise, we compared the effect of the lateral pressure on lipid bilayers with the effect of the surface pressure on lipid monolayers of the same composition. Interesting analogous behaviors were found pointing to a relevant role of line tension in shaping lipid bilayer domains.

MATERIALS AND METHODS

GUV preparation and imaging

1,2-dioleoyl-*sn*-glycero-3-phosphocholine (DOPC), 1,2-dipalmitoyl-*sn*-glycero-3-phosphocholine (DPPC), brain SM (bSM) (porcine), egg-SM, diphytanoyl-phosphatidylcholine (DiPhyPC), dihydrocholesterol (dichol), cholesterol (Chol), (24:1)SM (N-nervonoyl-D-erythro-sphingosylphosphorylcholine), (24:0)SM (N-lignoceroyl-D-erythro-sphingosylphosphorylcholine), (18:0)SM (N-stearoyl-D-erythro-sphingosylphosphorylcholine) were purchased from Avanti Polar Lipids (Alabaster, AL) and used without further purification. Texas Red-DHPE (Texas Red 1,2-Dihexadecanoyl-*sn*-Glycero-3-Phosphoethanolamine) was purchased from Thermo Fischer Scientific (Waltham, MA). Specific lipid mixtures were prepared by mixing chloroform lipid solutions in the desired amount (the lipid fractions reported in this work are molar proportions). Bovine serum albumin (BSA) was acquired from Sigma Aldrich (St. Louis, MO).

GUVs were prepared by the electroformation method with minor modifications (45). Briefly, lipid mixtures were dissolved in chloroform, and small drops (2–3 μL; 2 mg/mL lipid concentration) of this mixture were deposited on two opposing Pt wires (distance between the wires equal to

~3 mm) inside a Teflon chamber. Chloroform was initially removed by exposing the Pt wires to a continuous N_2 flux and then by using a vacuum pump (10^{-2} mbar) for at least 30 min. The two Pt wires were then connected to an electric wave generator set to produce a sinusoidal potential difference. The Teflon chamber was then filled with a 100-mM sucrose solution and sealed using glass coverslips and vacuum grease (Dow Corning, Midland, MI). The applied electroformation protocol was as follows: 1) 10 Hz, 2.0–3.0 $V_{p\text{-}p}$ peak to peak voltage for 1 h and 30 min; 2) 5 Hz, 2–2.5 $V_{p\text{-}p}$ for 30 min; and 3) 2 Hz, 1.5 $V_{p\text{-}p}$ for 15–20 min. The vesicle formation process was performed at 50°C. As a final step, we applied a square wave at 5 Hz to promote vesicle detachment from the wires. After formation, GUVs were extracted from the Teflon chamber and suspended in a 105-mM glucose solution (in some cases, we resuspended the samples in a 200-mM glucose solution to make the vesicles more flaccid). Vesicles were then allowed to cool slowly to room temperature. In place of cholesterol, we also tested dichol. It has been suggested that dichol, especially in the case of Langmuir monolayers, is more resistant than cholesterol to oxidation (46,47). However, changing cholesterol for dichol resulted in no appreciable differences in the results of the experiments both with GUVs and monolayers.

Fluorescence microscopy was performed with an Olympus IX 70 microscope (Olympus, Tokyo, Japan). Texas Red-DHPE was included in the lipid mixtures at a molar concentration of 0.5–1% or lower. Imaging was performed at controlled temperature. A home-developed imaging chamber consisting of two cover glass slides separated by a Teflon spacer was used. A small hole was made in the spacer to insert the thermocouple probe inside the water solution. The bottom slide was pretreated with 10 mg/mL BSA to remove surface charges and to avoid strong adhesion between the bilayers and the glass, which could affect the phase behavior of the vesicles. About 200 μL of a 105-mM glucose solution was inserted into the chamber, and 50 μL of vesicle suspension was added. The chamber was sealed by vacuum grease and put in direct contact with a Peltier cell. From the opposite side, the Peltier cell was in contact with a circulating water chamber whose temperature was controlled by a circulating temperature control unit (Lauda-Brinkmann, Delran, NJ). The Peltier cell was connected to a custom-developed control unit exploiting the proportional integral derivative system of an Arduino microprocessor. The system allowed for temperature jumps as fast as 15°C/min as well as controlled cooling or heating ramps (see Fig. S1 for details).

AFM

AFM imaging was performed with a BioScope I microscope equipped with a Nanoscope IIIA controller (Veeco Metrology, Plainview, NY). We used a custom temperature-controlled stage based on a circulating water bath on which we could mount the BioScope head. The sample's temperature was continuously monitored by a digital thermometer Fluke 16 (Fluke, Brugherio MB, Italy) equipped with a small K-thermocouple probe (Thermocoax, Heidelberg, Germany) in direct contact with the imaging buffer. Temperature stability was within ± 0.3°C of the specified temperature value. Triangular silicon nitride cantilevers (DNP-S; Bruker, Billerica, MA) with nominal spring constant of 0.32 N/m were used for tapping-mode imaging. All the images presented in this work have been obtained in tapping-mode AFM.

SLBs were prepared by the vesicle fusion technique. Briefly, small unilamellar vesicles were prepared by initially mixing the lipids in chloroform at the desired molar proportions. The chloroform was then removed by initially using a N_2 flux and then by keeping the lipids in vacuum for at least 1 h. The lipids were then resuspended in a 450 mM KCl, 100 mM phosphate-buffered saline, 10 mM $CaCl_2$ (pH 7) solution (the high ionic strength of the buffer favors the formation of SLBs). The lipid suspension was then sonicated at ~40°C, and 70 μL were deposited onto a freshly cleaved mica sheet (SPI Supplies/Structure Probe, West Chester, PA) fixed on a polytetrafluoroethylene (Teflon) disk attached to a metal disk, incubated for 15 min at a temperature above 40°C and then the sample was extensively rinsed with the imaging buffer (150 mM KCl, 50 mM phosphate-buffered saline (pH 7)). Finally, the sample was slowly cooled to the desired imaging temperature.

Micropipette aspiration setup

Microaspiration was performed by means of pulled glass capillaries (World Precision Instruments, Sarasota, FL) with a cylindrical shape to a final internal diameter in the order of ~10 μm. Pipettes were tip polished to ensure good membrane-pipette contact and pretreated with BSA (10 mg/mL) to avoid adhesion phenomena between the glass and vesicles. For each experiment, a micropipette was connected to a pneumatic pressure controller (MPCU-3; Lorenz, Dayton, OH) to apply pressure differences between the internal side of the pipette and the external solution at the same height with a sensitivity of 1 mm H_2O. The pressure difference was applied by controlling the air pressure on top of a cylindrical tube containing the same external solution and initially kept at a height to assure an initial negligible pressure difference. The vesicles were manipulated inside a homemade chamber. We assembled a specific chamber in which the solution temperature could be controlled by two Peltier cells in contact with a metallic base and, from the opposite side, with a water circuit whose temperature was controlled by a temperature control unit. See Fig. S2 for the details of the setup.

In response to pressure, the vesicle is aspirated into the pipette and the lateral applied tension can be measured by the Laplace law according to the following:

$$\Delta P = \frac{2\tau}{R_p}\left(1 - \frac{R_p}{R_v}\right), \tag{1}$$

where τ is the lateral tension in the bilayer (in N/m), R_p is the internal diameter of the micropipette, ΔP is the pressure difference, and R_v is the external vesicle radius.

Langmuir monolayers

For the lipid monolayer experiments, we used a Langmuir trough (Nima Technology, Coventry, UK). Before usage, the Langmuir trough was cleaned with ethanol and chloroform and then repeatedly rinsed with distilled water until it did not show any significant increase ($\Pi <$ 0.2 mN/m) in the surface pressure upon barrier closure. The trough's temperature was controlled by circulating water from a water heat bath. At open barriers (surface area = 80 cm^2), we injected 4–5 μL of the lipids dissolved at a concentration of 1 mg/mL in chloroform. The chloroform was allowed to evaporate for 5 min; subsequently, barriers were closed at a speed of 5–10 cm^2/min. The lipids contained a 0.5–1% molar proportion of Texas Red-DHPE to visualize the formation of domains by epifluorescence microscopy.

RESULTS

Effect of the temperature and composition on the phase behavior of GUVs

The first ternary lipid mixture that we considered was DiPhyPC/bSM/Chol 1:1:1. DiPhyPC (a branched-chained lipid) was chosen as the low T_m lipid of the mixture mainly because we mostly used fluorescence microscopy to inspect the phase state of lipid bilayers, and DiPhyPC provides an elevated resistance against oxidation induced by radiation damage. DiPhyPC is a synthetic lipid that adopts the L_o state

for a very large temperature range (no phase transition has been found from −120 to 120°C) (48), although an order-disorder phase transition has been described as a function of the degree of hydration (49). DiPhyPC can be considered an archetypical model for methylated lipids. This kind of lipid is present in archaebacteria conferring high stability to the membrane even in extreme temperature conditions. Methyl-branched lipids have also been found in bacteria and eukaryotic cells (some SMs have been found to include chain branching) even if their physiological role has not been completely established (50,51). The lateral methyl groups on each of the isoprenoid chains of DiPhyPC confers to this lipid the tendency to form expanded states in the bilayer with a large area-per-lipid value in comparison with normal linear acyl chains. In addition, methylated phosphatidylcholines have been shown to be more fluid than the corresponding unbranched counterparts at a given temperature (46). It has also been found that a phosphatidylcholine with two phytanoyl chains packs very poorly with cholesterol, and this behavior can have a role in the formation of L_o and L_d domains (47). Additionally, the methyl groups in DiPhyPC have been shown to favor a negative monolayer curvature (52,53).

bSM is a natural extract containing many different species, the dominant ones being (18:0)SM (50%) (https://avantilipids.com) and (24:1)SM (∼20%). Phase diagrams of similar ternary mixtures have been previously investigated using different techniques (27,54–57), and a phase coexistence region with two types of liquid domains has been observed. The coexistence of three phases, including also an S_o phase, has remained more elusive. The occurrence of the different phases depends on temperature, but it should be kept in mind that the lateral organization of the lipid bilayer can also be influenced by properties related to line tension and membrane curvature, which are both affected by the lateral tension applied to the vesicle.

When GUVs of the ternary lipid mixture DiPhyPC/bSM/Chol 1:1:1 plus 0.5–1% molar proportion of Texas Red-DHPE are prepared by the electroformation method and imaged by fluorescence microscopy at 16°C, the population has mainly a bimodal distribution. As shown in Fig. 1, apart from a large population of vesicles presenting the usual two fluorescence intensity levels that we assign to L_o and L_d phases, a small group of vesicles exhibits three fluorescence levels (which from now on we will call 3-ph vesicles). Considering the intensity levels, it seems that the new appearing level has an intermediate fluorescence between the ones attributed to L_o and L_d phases. We also found that the probability of finding 3-ph vesicles increases upon decreasing temperature and after the vesicles have been stored for a long period (a few hours) at 4°C. Remarkably, at 12°C the percentage of vesicles with three fluorescence intensity levels is ∼7% ($n = 300$ vesicles). We then tried to follow the formation of regions with three different intensity levels by decreasing the temperature. To this aim, we

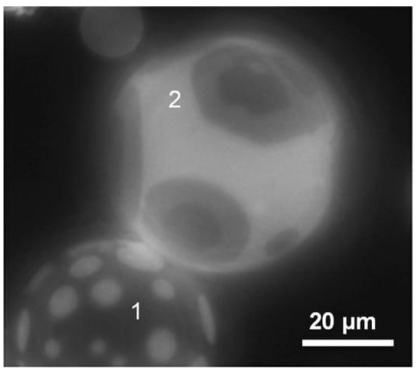

FIGURE 1 Fluorescence microscopy image of representative GUVs composed by an equimolar mixture of DiPhyPC/bSM/dichol + 1% Texas Red-DHPE at 16°C. A GUV presenting two different phases (GUV 1) and a GUV with three fluorescence intensity levels (GUV 2) are observed.

initially increased temperature to 50°C to make the liposomes completely homogeneous. According to the phase diagram for the ternary lipid system at issue or with very similar composition, at 50°C, most of the vesicles are in the homogeneous L_d phase. To keep the vesicle constantly in the field of view of the camera during the cooling step, we aspirated and kept at low constant tension one uniform vesicle with a micropipette. Fig. 2 shows a sequence of snapshots of a representative 3-ph vesicle during this cooling ramp (see the corresponding Video S1). We observed that the lipid demixing starts at a temperature of 34°C producing what are typically interpreted as L_o domains (*dark regions*) surrounded by the L_d phase (*brighter matrix*). By further decreasing temperature, the newly formed domains tend to enlarge and coalesce. Starting from a temperature around 16°C, a third fluorescence intensity level appears in the lipid bilayer (Fig. 2 *e*). The new intensity level is intermediate between the previously observed ones, and it seems to completely surround the darkest regions. If the temperature is further decreased, we observe an increase of the area occupied by the region with the intermediate level of fluorescence intensity (see Fig. S3 for an analysis of the fluorescence intensity levels for 3-ph vesicles). Furthermore, the above described evolution can be observed when the vesicles are not grabbed by a micropipette as well (see Fig. S4), demonstrating that the behavior cannot be ascribed to the lateral tension applied by the micropipette setup. Overall, the intermediate region seems to grow mainly at the expense of the brighter one (see Fig. S5 for the quantitative analysis), and it completely wets the darkest regions. Carrer et al. (58) reported a case in which three intensity levels were observed on GUVs by fluorescence microscopy. However, in the latter case, the vesicles had four components, and the geometry of the domains strongly depended on the amount of brain ceramides in the vesicles. By

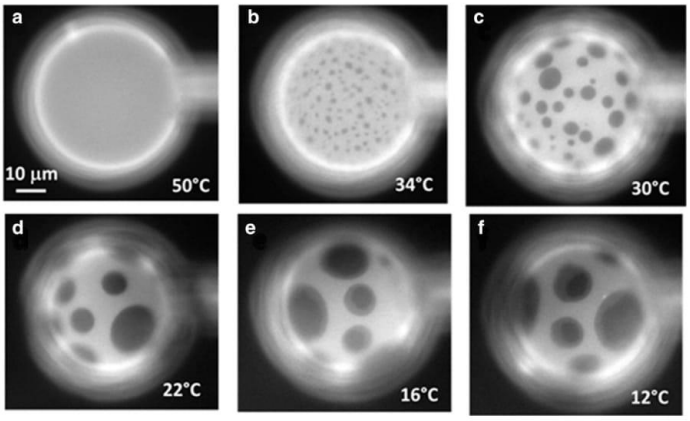

FIGURE 2 (*a–f*) Sequence of fluorescence microscopy images of a 3-ph GUV composed of an equimolar proportion of DiPhyPC/bSM/Chol (plus 1% Texas Red DHPE) for decreasing temperature values. To have an easier tracking of the vesicle during the temperature quench, the vesicle has been grabbed using a small negative pressure applied with a glass micropipette (on the *right* in the image). The same behavior has been observed for the other five vesicles.

performing fluorescence correlation spectroscopy, they were able to exclude the possibility of leaflet decoupling as an explanation for the different intensity levels. The authors attributed the intermediate level to an intermediate phase between the L_o and the L_d one.

We also studied the effect of a change in Chol concentration while keeping the same proportion of DiPhyPC and bSM. Our results indicate that for a Chol concentration of 25%, we never observed the third fluorescent intensity level appearance, whereas, for concentrations from 29 up to 40%, the three fluorescence intensities were always observed in a similar percentage of vesicles (see Fig. S6).

Effect of the lateral tension

If a 3-ph GUV grabbed by a micropipette is exposed to an increasing lateral tension by increasing the negative pressure, the intermediate fluorescent region is always removed. Under such conditions, this region is transformed to round domains showing the lowest or the highest fluorescence intensity levels. An example of this behavior is reported in Fig. 3 (see Fig. S7; Video S2 for other examples). On the other hand, if temperature is increased, the removal of the intermediate level occurs mainly by the appearance of bright domains, which progressively increase their area until only two fluorescence intensity levels are left (see Fig. S8).

AFM of SLBs

We also performed an AFM analysis on the same lipid mixture (DiPhyPC/bSM/Chol 1:1:1) prepared as an SLB. In AFM analysis of lipid bilayers, the presence of different phases is inferred by the appearance of regions with different heights (i.e., bilayer thickness). Fig. 4 shows a representative image of effects on an SLB at decreasing temperature. Starting from 25°C, we observed the presence of two height levels on the lipid bilayer, which we attribute to L_d and L_o phases. At 16°C, the regions surrounding the thicker domains adopt an intermediate height as evidenced in Fig. 4 *c*, which shows line sections obtained across the lines in Fig. 4, *a* and *b*. As in the case of GUVs, these data further confirm the formation of new domains upon decreasing the temperature. The fact that some domains decrease their thickness upon decreasing temperature is a strong indicator of interdigitation effects. In general, even if we have found several cases in which the behavior was like the one described in Fig. 4, this was not observed in all the SLBs having the same lipid composition. This fact is also consistent to what we observed for GUVs. Even if AFM could be very useful for the investigation of lipid bilayer phases given that nanodomains are easily detected, it is possible to have leaflet decoupling in SLBs (59). However, it is very difficult to know if the different occurring domains are due to phases that span the whole bilayer or if they involve just one of them. We performed force spectroscopy analysis of the SLBs as well, yet the curves showed no evidence of leaflet decoupling (see Fig. S9). Under different conditions, three phases have been found on SLBs of ternary mixtures by AFM (60). In that case, it has been observed that S_o regions had a lower thickness than L_o areas because of the amount of Chol that is not enough to create a L_o phase but is able to induce an order decrease of the S_o region. This phase has been called the "disordered gel phase," and its formation is favored at low Chol concentration (10–15%) and by cooling the bilayer at a low rate (~1°C/min). In our case, the concentration of Chol is quite high (30–40%), and it should therefore disfavor the appearance of this type of domain.

Synthetic SMs

In principle, a bilayer composed by a lipid mixture containing a high-T_m lipid, a low T_m-lipid, and Chol should be

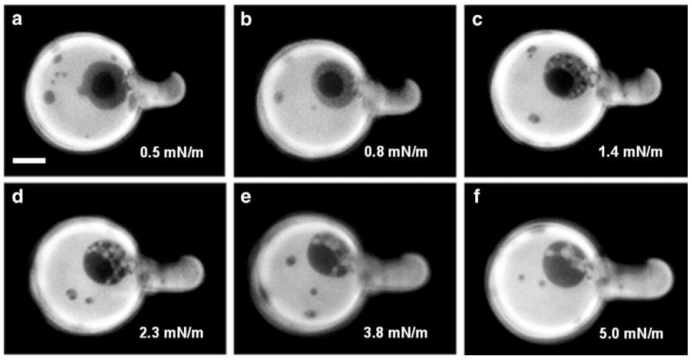

FIGURE 3 (*a–f*) Sequence of images of a typical 3-ph GUV upon increasing the lateral tension at 15°C (from 0.5 to 5 mN/m). The aspirating micropipette is to the right of the vesicle, and the increasing lateral pressure is evidenced by the growth of the vesicle projection inside the micropipette. Scale bar, 10 μm. (See Video S2.) A similar behavior has been observed for at least seven vesicles under similar circumstances.

considered equivalent to a system with five components. This is due to the fact that the membrane is composed by two separate leaflets and two types of lipids (high and low T_m), which cannot easily translocate from one leaflet to the other, whereas Chol is more free to diffuse transversally. In the case of GUVs prepared by electroformation, it is assumed there is no asymmetry in the lipid composition, and domains in the two leaflets are kept in register by an interleaflet coupling mechanism. Accordingly, the effective number of components should be reduced to three. However, bSM is already a mixture by itself with two main species, (18:0)SM and (24:1)SM, which represent 50 and 20% of the total composition, respectively. Hence, the appearance of three fluorescence intensity levels could also be explained by the number of components being higher than three. In particular, we hypothesized that at 16°C, the (24:1)SM component could segregate from the other bSM species giving rise to a new phase. Moreover, C24:1 chains interact differently with Chol with respect to chains with a lower number of C atoms. To understand the possible role of all species in the mixture, we firstly considered a more pure natural SM, egg-SM, which is a mixture too, yet the dominant phase, 16:0 SM, represents ∼86% of the total composition. In this case, we were not able to observe the coexistence of the three fluorescence intensities (see Fig. S10). We then used synthetic SMs, starting from (18:0)SM. The mixture of DiPhyPC/(18:0)SM/Chol was not able to produce 3-ph GUVs (see Fig. S11). In addition, with (18:0)SM, the typical features of the S_o phase were observed at low temperature (see Fig. S11 *b*), including dendritic domains with not rounded borders. We then moved to the second major component of the bSM mixture, specifically (24:1)SM. In this case, the percentage of 3-ph vesicles increased (up to ∼15% at 12°C) ($n = 250$ vesicles). Interestingly, the presence of the intermediate fluorescence level is not strictly confined to the boundary with the darkest domains and, in many cases, it is the most abundant phase.

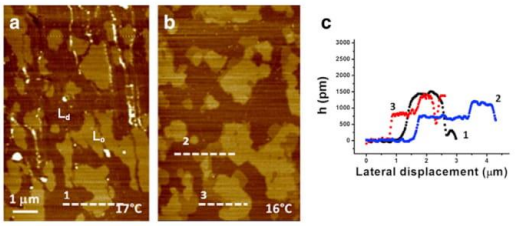

FIGURE 4 AFM images showing the phase state of a DiPhyPC/bSM/Chol 1:1:1 SLB at two different temperatures: (*a*) 17°C; (*b*) 16°C; (*c*) line sections corresponding to the dashed lines reported in (*a–b*). To see this figure in color, go online.

Different possibilities exist for the appearance of the three levels. Fig. 5 *a* shows the case in which bright domains surrounded by the intermediate level appear (type I case), whereas Fig. 5, *b* and *c* shows the case in which the darkest and intermediate fluorescence intensity regions are surrounded by the brightest region (type II case). Fig. 5 *d* shows the case in which isolated circular domains appear for each fluorescence intensity level (type III case).

It is important to note that when regions of the darkest fluorescence intensity are inside a larger domain of intermediate fluorescence level, the dark domains apparently cannot cross the border between the highest level of fluorescence and the intermediate one, a phenomenon that supports the fact that the different domains come from a single bilayer. In principle, there could be not-in-register domains present in the bilayer, which could provide an explanation for the appearance of the three fluorescence levels. Nonetheless, the analysis of domain behavior upon coalescence (see Fig. S12) confirms the fact that the three different fluorescence intensity levels must be attributed to configurations spanning the whole bilayer. Then we analyzed the behavior of the 3-ph GUVs upon variation of the temperature. Fig. 6 shows the behavior when the temperature is increased until the GUV reaches homogeneous fluorescence intensity.

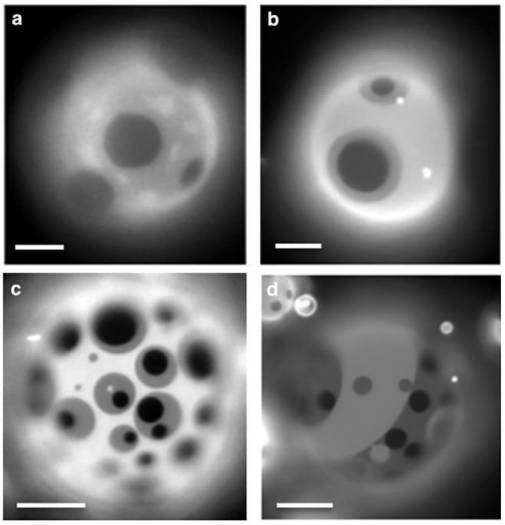

FIGURE 5 Examples of domains appearing in the case of the ternary mixture DiPhyPC/(24:1)SM/Chol 1:1:1 plus 0.5–1% Texas Red DHPE. (*a*) Appearance of the brighter and not rounded domains in the intermediate fluorescent intensity region (type I); (*b* and *c*) darkest domains completely wetted by the intermediate fluorescence intensity region (type II); (*d*) appearance of rounded domains of all the three fluorescent intensity levels (type III). Scale bar, 10 μm.

Increasing the temperature results immediately in a decrease of the line tension between the brightest and the intermediate fluorescence intensity regions as deduced from the irregular boundaries. Moreover, the two brighter phases become very similar to each other with a fading interface region, whereas the darkest regions are removed. At a temperature of ~34°C, the GUV becomes homogeneous (i.e., without any apparent lipid segregation). Fig. S13 reports also the behavior corresponding to the subsequent cooling of the same GUV down to 12°C, showing that the formation of the different regions is completely reversible. Another example of phase behavior of DiPhyPC/(24:1)SM/Chol GUVs upon temperature increase is included in Fig. S14, as well.

Considering the peculiar behavior of the DiPhyPC/(24:1) SM/Chol mixture, we analyzed different molar proportions of the three lipids. By increasing the amount of DiPhyPC with respect to (24:1)SM, keeping constant the cholesterol concentration to 33.3%, we found that for the mixture DiPhyPC/(24:1)SM/Chol 53.3/13.3/33.3, just a few vesicles clearly showed the 3-ph condition, whereas at a temperature <20°C, most of the vesicles showed only two fluorescence levels with multilobe-shaped domains (see Fig. S15). It is to be remarked that the fluorescence intensity differences could be so small as to be undetectable. For the mixture DiPhyPC/(24:1)SM/Chol 13.3/53.3/33.3, we were not able to find 3-ph GUVs, and they typically showed just two regions (bright domains on a dark background). According to these results, a similar amount of DiPhyPC and (24:1) SM is required for the appearance of the three domains. We also exchanged (24:1)SM for (24:0)SM. In this case, three fluorescence intensity levels with a behavior similar to that observed for (24:1)SM were detected (see Fig. S16), yet the 3-ph state was typically detected up to 35°C. It is to be stressed that (24:0)SM has a higher transition temperature with respect to (24:1)SM (61), but, at the same time, (24:1)SM and (24:0)SM have different properties, with (24:0)SM more similar to (18:0)SM than (24:1)SM.

AFM of SLBs with synthetic SM

We next obtained AFM images of SLBs prepared from small unilamellar vesicles that were of the DiPhyPC/(24:1)SM/Chol 1:1:1 ternary mixture. Previous AFM studies showed that in presence of ethanol, supported bilayers can adopt, for specific lipid compositions, an interdigitated phase (62). Nevertheless, interdigitation has also been observed by AFM for pure DHPC bilayers in the absence of ethanol (33,63). The appearance of the new phase in AFM experiments is deduced from the lower thickness of the interdigitated domains (62,64). Interestingly, when the interdigitated domains are studied by polarized total-internal-reflection fluorescence microscopy in SLBs, a contrast inversion is obtained by changing the light polarization. This behavior is related to the orientation of the Texas Red DHPE fluorescence probe. By changing the light polarization from s- to p-, the interdigitated and the L_d regions invert their relative fluorescence intensity. For the s-polarization (parallel to the substrate), which is the case closely resembling the conditions found in epifluorescence microscopy (65), the interdigitated phase is brighter than the L_d phase. This aspect stresses again the fact that the association of the fluorescence intensity with the order parameter should be evaluated with care.

AFM can provide directly the analysis of the bilayer thickness, offering another way to reveal the order of different domains in the lipid bilayer. Fig. 7 shows the results we obtained at low temperature for the specific mixture we used. At higher temperatures, the lipid bilayer appears uniform, whereas at 20°C, the formation of thicker domains occurs. By further decreasing temperature, starting from ~12°C, another type of domain appears. These new domains are characterized by a circular or semicircular region of lower thickness, and the region inside this border has a height that is just a fraction of a nanometer thicker than the surrounding bilayer (see Fig. S17). This height difference is very small (~0.2–0.3 nm), which could be undetectable in many cases. This very small height difference points to very tiny differences in the lipid chain order of the different domains. The absolute height of the bilayers is ~4–4.5 nm. This value is not consistent with a bilayer

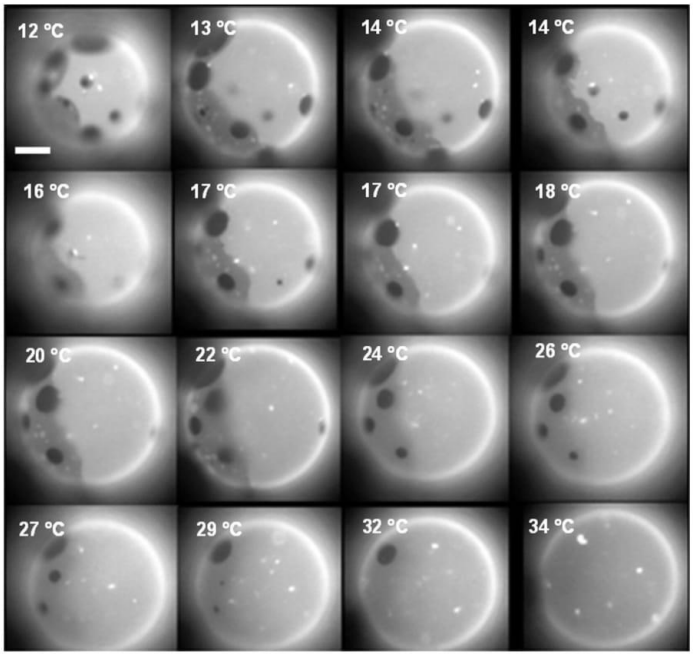

FIGURE 6 Sequence of fluorescence microscopy images of a DiPhyPC/(24:1)SM/Chol + 0.5% Texas Red DHPE as the temperature is increased from 12 to 34°C. The border between the brightest and the intermediate fluorescence intensity regions gradually disappears without apparently changing the relative area, whereas the darkest regions shrink until they disappear. Scale bar, 10 μm.

composed of 24.1 SM in the straight conformation in both leaflets unless we consider interdigitation effects. Hence, in general terms, at low temperatures, three phases are observed in SLB (see Fig. S18 for other examples).

Effect of lateral tension on vesicles containing (24:1)SM

Another interesting aspect of this mixture is the appearance of modulated phases at low temperature (8–9°C) involving the brightest and the intermediate fluorescence intensity regions (see Fig. S19). The appearance of this particular phase is highly favored by releasing the lipid bilayer lateral tension via an increase of the external osmotic pressure, which is obtained by an increment of the sugar concentration outside the vesicle. In other cases, the formation of modulated phases is observed while increasing the temperature (see Fig. S20) just after the decrease of the line tension between the intermediate and brightest fluorescence intensity regions where the trend of the line tension is deduced from the increasing irregularity of the borders separating the two regions. The modulated phases start with linear structures and then tend to small rounded regions. Considering the dependence of the modulated phase on the tension in the lipid bilayer, we concentrated on the effect of the lateral tension on the appearance and the shapes of the domains for the DiPhyPC/(24:1)SM/Chol mixture. Fig. 8 shows the effects on a type I vesicle grabbed by the micropipette at increasing lateral tension (see Video S3). The vesicle initially showed the presence of bright domains in

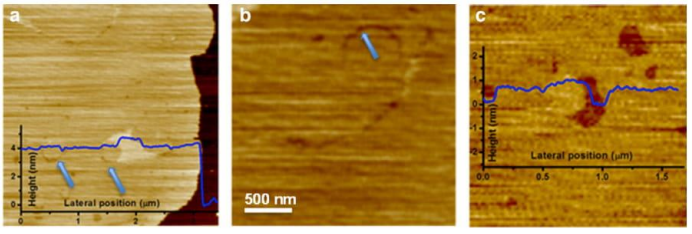

FIGURE 7 (*a–c*) AFM images of DiPhyPC/(24:1)SM/Chol 1:1:1 SLBs obtained at 12°C. In (*a*) and (*c*), the line sections on specific regions of the sample are reported evidencing the presence of more than two height levels. In (*a*) and (*b*), the presence of annular regions with lower height with respect to the surrounding bilayer is highlighted by arrows. To see this figure in color, go online.

a background, which can be associated with the intermediate intensity level. These domains typically show a large fluctuation of their borders with an estimated line tension of (0.066 ± 0.035) pN (see Supporting Materials and Methods for the details of the calculation). At higher resolution, some of these domains show the presence of modulations with stripes of different fluorescence intensity inside the domains with the highest fluorescence intensity (Fig. 8 *a*), whereas, in other cases, no structures were observed (see Fig. S21; Videos S4 and S5 for other examples). Fig. S22 reports the detailed shape changes of a domain when the lateral tension of the GUV is increased by MAT. The quantitative analysis of the area of the different domains shows that the increase of the lateral tension corresponds to an increase of the region characterized by the brightest fluorescence intensity as well as a decrease of the area with the darkest fluorescence intensity. This behavior points to the connection between the brightest region and an area with greater disorder than the latter one.

Fig. 8 shows that upon an increase of the pressure difference between the inside and the outside of the micropipette, a strong reorganization of the domains occurs. The stripes inside the bright domains increase their width until they fuse in dark subdomains near the boundary of the bright domain. At the same time, the bright regions assume a higher fluorescence intensity and a quarter moon-like shape. Notably, the shape changes are fully reversible (see Videos S3, S4, and S5) and occur over a lateral tension range going from $\sim 10^{-2}$ to 1 mN/m where the vesicle bending fluctuations are dominant. From these results, we speculate that the shape changes are mainly related to the removal of fluctuations and not to a molecular area increase in the lipid bilayer (stretching component). According to this evidence, it seems the modulated phases are ascribable to different spontaneous fluctuations of the curvatures from different domains in the bilayer. In the case of type II vesicles in which the background region is the brightest one, the lateral tension increase produces a negligible effect on the shape of the domains (see Fig. S23).

Langmuir monolayers of DiPhyPC/(24:1)SM/Chol

The shapes adopted by the domains in the case of the DiPhyPC/(24:1)SM/Chol 1:1:1 mixture upon changes in the GUV lateral tension are reminiscent of what happens in the case of lipid monolayers when three different phases (i.e., gas, liquid expanded, and liquid condensed) are present at the air-water interface and the lateral pressure is varied. Theoretical approaches that are able to explain what happens to domains in the three-phase coexistence region have been developed (66–68). Accordingly, we investigated the possible equivalence of GUVs under the effect of an increasing lateral tension and monolayers in a Langmuir trough for which we controlled the lateral pressure. Fig. 9 reports examples of the similarities we observed. We found changes in the domain shapes when the bilayer lateral tension was increased (greater molecule-to-molecule distance), which corresponds to a lateral pressure decrease in the Langmuir trough (increase of area-per-molecule). Theories developed for the analysis of lipid monolayers ascribe most of the observed behavior to effects related to the competition between line tension among the different

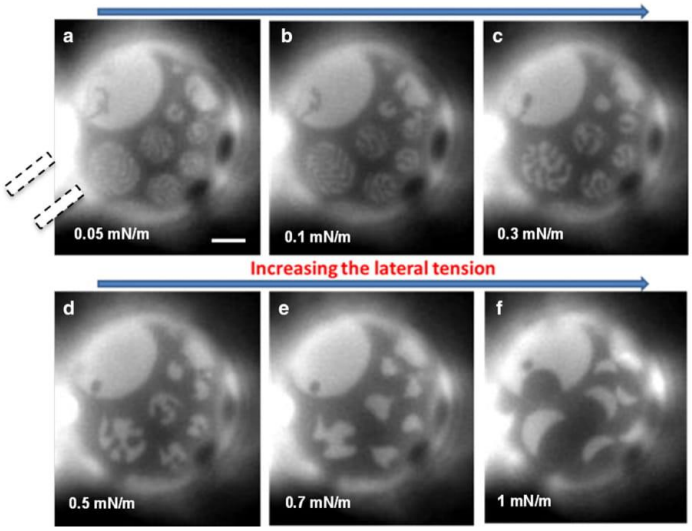

FIGURE 8 (*a–f*) Fluorescence microscopy images of a DiPhyPC/(24:1)SM/Chol + 1% DHPE Texas Red undergoing a lateral tension increase. The micropipette is on the left of the image (*dashed lines* in the first frame). See also Video S3. Scale bar, 10 μm. To see this figure in color, go online.

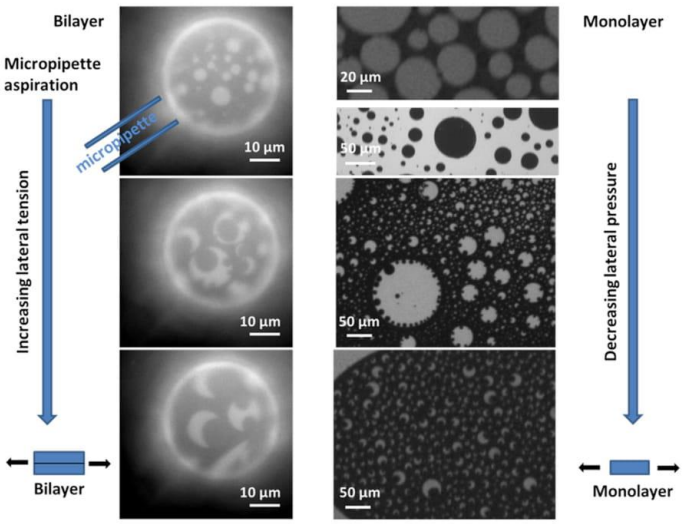

FIGURE 9 Analogies between the appearance of domains in a DiPhyPC/(24:1)SM/Chol 1:1:1 + 1% Texas Red DHPE GUV as a function of the applied lateral tension (*left column*) in a MAT setup and domains of the same lipid composition in a Langmuir monolayer upon decreasing the lateral pressure (*right column*). The lateral tension in the GUV on the left column ranges from 0.3 to 0.8 mN/m moving from the upper to the lower case, whereas the lateral tension in the monolayer is 12 mN/m in the first two images and less than 0.5 mN/m in the remaining two cases. To see this figure in color, go online.

domains, dipole repulsion, and wetting phenomena (66). The wetting phenomena in Langmuir monolayers presenting three different phases have been largely investigated (68). Upon changes in the values of both the dipole density difference among the different domains and the line tension, wetting and dewetting transitions associated with large shape changes of the domains occur (see for example Figs. 2 and 3 in (68)). Similar changes take place when the above parameters are held constant and the areas of different domains are modified (68).

DISCUSSION

Unraveling the phase behavior of sphingolipids represents a difficult task because of the many different types of molecular structure they have, the different types of bonds they form with other lipids in the bilayer, and the presence of very asymmetric acyl chains (69). Sphingolipids have been associated to the raft hypothesis for lipid bilayers because, in model systems, they typically form complexes with Chol in the L_o domain, suggesting a clue relevance of sphingolipids in plasma membranes. Here, we found that a mixture including a natural SM extract, like bSM or synthetic analogs ((24:1)SM and (24:0)SM), together with cholesterol and DiPhyPC, can give rise to a phase behavior in which three fluorescence intensity levels might appear. Domains with an intermediate fluorescence intensity appear when the temperature is decreased, completely surrounding darkest domains in the case of bSM. Considering that the new domains with an intermediate fluorescence intensity level are formed at the interface between the brightest and darkest domains, we exclude the possibility that we are observing the formation of the typical S_o phase. In fact, the S_o phase would be expected to form in the central part of an already dark region. Moreover, AFM images of SLBs of ternary mixtures containing bSM showed the formation of new domains with intermediate thickness at low temperature (~16°C). At first, we tentatively attributed the formation of the new domains to the fact that bSM is already a mixture (the two main components are (18:0) and (24:1) SMs). It is not unusual to observe three different types of domains when more than three types of molecule are present in a lipid mixture. This is observed when, for example, ceramides are added to ternary lipid mixtures (58). Nonetheless, the experiments we performed with synthetic SMs clearly showed that the appearance of the intermediate phase is not strictly related to the presence of more than three components. When a purely ternary mixture including the synthetic (24:1) or (24:0)SM lipids and DiPhyPC is considered, three fluorescence intensity levels are still obtained. Our experiments clearly showed that these specific SMs, in combination with DiPhyPC, are responsible for this three-phases phenomenon. However, whereas in the case of bSM, the intermediate phase always wet the darkest regions, in the case of (24:1) or (24:0)SM, we found that the intermediate phase can also be present in the form of isolated domains, pointing to a possible different explanation for the formation of the different domains.

We used the MAT to study the behavior of different phases when the lateral tension in the bilayer is increased. It has been recently reported that the osmotic differences between the inside and outside regions of GUVs strongly affect the shape and size of L_o and L_d domains (70). It is to be stressed that temperature decrease induces on its

own an increase of the lateral tension of the GUV because of the fact that the area decrease of the lipid bilayer prevails over volume decrease (71,72). Accordingly, effects related to the lateral tension increase could be evident also when temperature is decreased. In particular, any undulated or ripple phases present in the vesicle will be removed simply by increasing the lateral tension resulting in a planar structure. Actually, the role of lateral tension on the phase behavior of lipid bilayers has been already considered both in theoretical (41,73) and experimental investigations (42–44,74). In principle, considering the 2D version of the Clausius-Clapeyron law, an increase of lateral tension should favor more expanded phases. For example, it has been found that the demixing temperature from a completely L_d phase to the coexistence of L_o and L_d phases decreases upon an increase of the lateral tension (43). Moreover, theoretical analysis showed that a lateral tension increase produces a line tension rise when domains of different hydrophobic thickness are present (73). The variation of the line tension in the case of a domain thicker than the surrounding lipids (like in the case of a lipid raft) has been predicted to be appreciable. This effect is related to the curvature and elastic moduli of the domains and to the tilt and splay deformations at the borders of the domains. In this context it is also possible that the molecular details of the lipids could be equally important to determine the extent to which line tension is affected by the lateral pressure. In light of all these considerations, the intermediate phase in the case of bSM cannot be ascribed to an increase of the lateral tension in the bilayer during the cooling step because the transformation of a bright region into an intermediate fluorescence intensity region should correspond to an increase of the lateral order. Furthermore, we noticed that the intermediate region is removed by an increase of the lateral tension applied by the micropipette.

The line tension increase could induce the coalescence of nanodomains, which are not optically detectable. These dark L_o nanodomains on the bright L_d background would result in an intermediate fluorescence intensity level. Thus, when temperature is decreased, the height difference between the L_o and L_d domains could increase up to the point at which a wetting layer made by L_o nanodomains is energetically favored (see Fig. S9). The coalescence of nanodomains into microdomains allows the possibility to observe them by fluorescence microscopy. A similar explanation has been hypothesized previously by Li and Cheng (75) even in the absence of Chol (DLPC/DPPC GUVs prepared at high (1M) sucrose concentration or DLPC/DPPC plus DOPG GUVs were used). This mechanism could in principle explain the effect observed for bSM upon lateral pressure increase.

If we consider the coexistence of three different phases as suggested by AFM, we have to understand their nature. It has been shown that (24:1)SM has a very broad and complex differential scanning calorimetry thermogram, and it is not prone to form well-ordered domains (76). Different temperatures have been associated to (24:1)SM bilayer reorganizations; from high to low temperature, two reorganizations occur at 25 and 16°C even if the exact nature of these transitions has not been clarified. Even in the case of (24:0)SM, a complex thermotropic behavior with multiple transitions has been observed, being strongly dependent on the hydration degree of the molecules and the thermal history of the sample. Notably, these behaviors have been attributed also to transitions between a tilted, partially interdigitated to an almost untilted, interdigitated gel phase at low temperatures (39.4°C), with major changes in lipid thickness (77). In general, it has been observed that for SMs with different chain length, the appearance of complex thermograms starts for chains with more than 18–20 carbon atoms. This fact coincides with the appearance of chain asymmetry in the acyl chains (33).

According to these considerations, a possible explanation for the formation of the third type of domains is given by the formation of interdigitated phases upon a temperature decrease due to the presence of the strongly asymmetric (24:1)SM species (bSM contains ~34 mol % of asymmetric molecules, including C22, and of this 34 mol %, 59% is unsaturated). The detection of the phase diagram just by fluorescence microscopy presents the problem of associating the intensity of the fluorescent emission, strictly related to the partition coefficients of the marker, to the different lipid phases (i.e., lipid order) that can be present. This is particularly critical in our case in which (24:1)SM is prone to adopt interdigitated phases at low temperature, and the partitioning of fluorescence markers in this phase is unclear. Moreover, different lipid organizations giving rise to interdigitated conditions (i.e., mixed, partial, and complete interdigitation) are possible (78), and different lipid packing is expected in different situations. Concomitantly, the fully and mixed interdigitated phases imply an increase of the lateral area and a strong decrease of the bilayer thickness. Considering AFM images, the height difference among the different domains is small (~0.5 nm), and it allows us to exclude the possibility of a complete interdigitation state. In the case of (24:1)SM, the height differences are even smaller, and if the different domains are due to interdigitation effects, the overlap of the acyl chains of the two leaflets is also very small. At the same time, the absolute thickness of the bilayers measured by AFM (~4–4.5 nm) is consistent with at least a partial interdigitation phenomenon of the chains (61). Pinto et al. (79) studied the phase behavior of (24:1) nervonoylceramide in the binary mixture with 1-palmitoyl-2-oleoyl-*sn*-glycero-3-phosphocholine. They found a complex behavior of the mixture at low temperature, which was attributed to an initial change from a mixed interdigitated gel phase to a partially interdigitated one and then to a fluid phase at increasing temperature. They also found regions of phase coexistence with lines in the phase diagram in which three phases could coexist. Similar results have been found for SM (80). Because the main phase transition

of (24:1)SM occurs at ~16–20°C and the intermediate phase appears at a very similar temperature, it is feasible to relate the appearance of the intermediate phase to a change in the organization of the (24:1)SM molecules. In this case, the first dark domains that are formed by decreasing temperature are due to the L_o phase in which mainly (18:0)SM is involved, whereas (24:1)SM remains in the L_d phase. At a temperature of ~16°C, (24:1)SM adopts a more ordered state, and the possible interdigitation of (24:1)SM, probably favored by the large area-per-molecule of DiPhyPC, explains the lower thickness of the newly formed L_o phase with respect to the (18:0)SM related L_o region as observed by AFM (see Fig. 4). This interdigitated phase could have a reduced area-per-molecule occupation, and this would explain, at least in part, the fact that the intermediate phase collapses by increasing the lateral tension.

Previous studies using the ternary mixture DOPC/(24:1)SM/Chol reported that (24:1)SM inhibits the formation of laterally heterogeneities like the formation of L_o domains, yet the behavior at low temperature has not been considered (81). In the same study, it was established that exchanging (24:1)SM for (24:0)SM leads to the formation of separated domains. In this context, DiPhyPC could have a role in the interdigitation effects. Indeed, the ether derivative of DiPhyPC has been shown to form interdigitated phases, as well (63). In light of this fact, it is probable that DiPhyPC could favor the formation of interdigitated phases via SM with long chains even if it does not interdigitate when considered as a single component.

The images we obtained for the case of the DiPhyPC/(24:1 or 24:0)SM/Chol mixtures are quite similar to those reported in a work by Collins and Keller (82) in which they used a ternary mixture of DiPhyPC/DPPC/Chol in a lipid bilayer with asymmetric leaflet composition. They found three different fluorescence intensity levels, and their appearance was related to the asymmetry of the bilayer. However, they found that the three levels should be associated to bilayer spanning phases and the three intensity levels could also be found in just one leaflet. Because in our case we should have a symmetric bilayer, the reason for the appearance of the different fluorescence levels should be different. In one recent molecular dynamics investigation, it has been found that the presence of C24 SM in just one leaflet forces cholesterol to the opposite one (83). At the same time, cholesterol in the opposite leaflet is able to push C24 SM slightly out from the bilayer, and its interaction with cholesterol in the same leaflet is reduced. The asymmetric structure of the bilayer could produce bilayer spanning phases with different values of fluorescence intensity because of a nonsymmetric partitioning of the fluorophore. Accordingly, in our case, the asymmetry in leaflet composition could be a process that is induced by the presence of C24 SM. We also observed, especially in the case of a largely reduced tension of the lipid bilayer obtained by an osmotic unbalance, that modulated phases involving the two brighter regions appeared.

One interesting aspect of the domain shape in the case of the DiPhyPC/(24:1)SM/Chol mixture is its extreme dependence on the lateral tension of the bilayer. The behavior we observed in GUVs is similar to what is observed at the interface of three phases in Langmuir monolayers. The shape of the domains formed in the case of phase coexistence is finely tuned by the mutual line tension between the phases and by the area of each phase according to the Young equation. Both parameters can in turn be affected by the applied lateral tension. In the case of monolayers, a parameter ruling the wettability of different phase domain is related to both the dipole moment difference and the line tension between each pair of phases (68). For example, it is possible to induce wettability transitions in two-dimensional systems by reducing the area-per-molecule. Considering the behavior of lipid bilayers, we can hypothesize that aspects related to line tension and wetting phenomena are relevant for the shape of domains when three phases characterized by different lipid density are present simultaneously and they have very similar thicknesses. In this case, we have to consider that the main contribution of the dipole moment in ester-linked lipid membranes has to be associated with the carbonyl group of each leaflet (50). Their dipole moments are quite far from each other and, as a consequence, the possibility to be mutually neutralized becomes unlikely. Accordingly, dipole interactions should play a role in the shape of the domains in bilayers as it has been established for monolayers.

Considering all the possibilities, we hypothesize that in the presence of highly asymmetric and very long chain SMs and DiPhyPC, one L_d phase and two different L_o phases exist, with the latter associated to two different interdigitation states of SM. Generally, interdigitated phases are associated with gel or ordered phases, but it is not to be excluded that interdigitation can also have effects on liquid phases. The L_d phase and one of the two L_o phases have a very similar thickness as highlighted by our AFM results. In some cases, it is possible to have the copresence of three phases in which the shape of the domains is strongly dependent on the lateral tension in the bilayer as a result of variations in the mutual area fraction and line tension. In the case of monolayers, it has been proposed that for long acyl chains, as is the case of 24:1 ceramide, a transition from a "mushroom" to a "brush" configuration might occur by increasing the lateral pressure, like in the case of grafted polymers (24). It is not clear yet how these findings could be translated to the bilayer case, but it is to be considered that temperature and lateral tension might affect the configuration of the long acyl chains inside the bilayer.

CONCLUSIONS

We have found that the appearance of more than two fluorescence intensity levels occurs at low temperature for ternary lipid mixtures, including the highly asymmetric

lipid (24:1) SM, a methyl-branched ester lipid, DiPhyPC, and Chol. If (24:1)SM is substituted for (24:0)SM, the three fluorescent levels are present even at higher temperature (up to 35°C). We attributed the presence of the three intensity levels to the asymmetric and very long chains of SMs and the formation of different interdigitated structures, which can favor phases with different lipid densities. This is relevant because very long chain sphingolipids (>20 C) are largely present in specialized tissues, and some functional properties of the membranes are affected if these specific lipids are lacking. Notably, we have found that when the 3-ph state is present on a GUV, the shape of domains involving the phase with the brightest fluorescence level can be strongly dependent on the lateral tension applied to the vesicle. Based on the strong similarities between the behavior of domains in the GUVs when the lateral tension is increased and domains in lipid monolayers when the surface pressure is released, we assigned a strong relevance to line tension and wetting phenomena in the organization of lipid domains in bilayers. This experimental evidence, although obtained on a model system, could have biological relevance considering the typical very low lateral tension of plasma membranes in living cells. Moreover, the complex alteration of the membrane state induced by the presence of (24:0) or (24:1)SM could be one of the reasons for their biological effect (83). Thus, the possible interdigitation of very long and asymmetric SM lipid species could contribute to the coupling of the inner and outer leaflets in biological membranes.

SUPPORTING MATERIAL

Supporting Materials and Methods, thirty figures, and five videos are available at http://www.biophysj.org/biophysj/supplemental/S0006-3495(18)34532-6.

AUTHOR CONTRIBUTIONS

D.B., A.M., and A.A. designed research's strategy. D.B., A.M., N.M-M., G.R., and A.A. performed experiments. All authors analyzed the data and contributed to the manuscript writing.

REFERENCES

1. Anishkin, A., S. H. Loukin, …, C. Kung. 2014. Feeling the hidden mechanical forces in lipid bilayer is an original sense. *Proc. Natl. Acad. Sci. USA.* 111:7898–7905.
2. Mouritsen, O. G. 2011. Model answers to lipid membrane questions. *Cold Spring Harb. Perspect. Biol.* 3:a004622.
3. Mouritsen, O. G., and L. A. Bagatolli. 2015. Lipid domains in model membranes: a brief historical perspective. *Essays Biochem.* 57:1–19.
4. Simons, K., and W. L. Vaz. 2004. Model systems, lipid rafts, and cell membranes. *Annu. Rev. Biophys. Biomol. Struct.* 33:269–295.
5. Goh, S. L., J. J. Amazon, and G. W. Feigenson. 2013. Toward a better raft model: modulated phases in the four-component bilayer, DSPC/DOPC/POPC/CHOL. *Biophys. J.* 104:853–862.
6. Feigenson, G. W. 2009. Phase diagrams and lipid domains in multicomponent lipid bilayer mixtures. *Biochim. Biophys. Acta.* 1788:47–52.
7. McConnell, H. M., and M. Vrljic. 2003. Liquid-liquid immiscibility in membranes. *Annu. Rev. Biophys. Biomol. Struct.* 32:469–492.
8. Radhakrishnan, A., T. G. Anderson, and H. M. McConnell. 2000. Condensed complexes, rafts, and the chemical activity of cholesterol in membranes. *Proc. Natl. Acad. Sci. USA.* 97:12422–12427.
9. Veatch, S. L., and S. L. Keller. 2005. Seeing spots: complex phase behavior in simple membranes. *Biochim. Biophys. Acta.* 1746:172–185.
10. Veatch, S. L., P. Cicuta, …, B. Baird. 2008. Critical fluctuations in plasma membrane vesicles. *ACS Chem. Biol.* 3:287–293.
11. Ipsen, J. H., O. G. Mouritsen, and M. J. Zuckermann. 1989. Theory of thermal anomalies in the specific heat of lipid bilayers containing cholesterol. *Biophys. J.* 56:661–667.
12. Ipsen, J. H., G. Karlström, …, M. J. Zuckermann. 1987. Phase equilibria in the phosphatidylcholine-cholesterol system. *Biochim. Biophys. Acta.* 905:162–172.
13. Veatch, S. L., and S. L. Keller. 2003. Separation of liquid phases in giant vesicles of ternary mixtures of phospholipids and cholesterol. *Biophys. J.* 85:3074–3083.
14. Veatch, S. L., and S. L. Keller. 2002. Organization in lipid membranes containing cholesterol. *Phys. Rev. Lett.* 89:268101.
15. Veatch, S. L., and S. L. Keller. 2005. Miscibility phase diagrams of giant vesicles containing sphingomyelin. *Phys. Rev. Lett.* 94:148101.
16. Lingwood, D., and K. Simons. 2010. Lipid rafts as a membrane-organizing principle. *Science.* 327:46–50.
17. Rayermann, S. P., G. E. Rayermann, …, S. L. Keller. 2017. Hallmarks of reversible separation of living, unperturbed cell membranes into two liquid phases. *Biophys. J.* 113:2425–2432.
18. Phillips, R., T. Ursell, …, P. Sens. 2009. Emerging roles for lipids in shaping membrane-protein function. *Nature.* 459:379–385.
19. Clarke, J. A., J. M. Seddon, and R. V. Law. 2009. Cholesterol containing model membranes studied by multinuclear solid state NMR spectroscopy. *Soft Matter.* 5:369–378.
20. Carreira, A. C., A. E. Ventura, …, L. C. Silva. 2015. Tackling the biophysical properties of sphingolipids to decipher their biological roles. *Biol. Chem.* 396:597–609.
21. Westerlund, B., and J. P. Slotte. 2009. How the molecular features of glycosphingolipids affect domain formation in fluid membranes. *Biochim. Biophys. Acta.* 1788:194–201.
22. Ramstedt, B., and J. P. Slotte. 2002. Membrane properties of sphingomyelins. *FEBS Lett.* 531:33–37.
23. Maggio, B., M. L. Fanani, …, N. Wilke. 2006. Biophysics of sphingolipids II. Glycosphingolipids: an assortment of multiple structural information transducers at the membrane surface. *Biochim. Biophys. Acta.* 1758:1922–1944.
24. Holopainen, J. M., H. L. Brockman, …, P. K. Kinnunen. 2001. Interfacial interactions of ceramide with dimyristoylphosphatidylcholine: impact of the N-acyl chain. *Biophys. J.* 80:765–775.
25. Zhai, X., X. M. Li, …, R. E. Brown. 2006. Lactosylceramide: lateral interactions with cholesterol. *Biophys. J.* 91:2490–2500.
26. Goñi, F. M., A. Alonso, …, J. L. Thewalt. 2008. Phase diagrams of lipid mixtures relevant to the study of membrane rafts. *Biochim. Biophys. Acta.* 1781:665–684.
27. de Almeida, R. F., A. Fedorov, and M. Prieto. 2003. Sphingomyelin/phosphatidylcholine/cholesterol phase diagram: boundaries and composition of lipid rafts. *Biophys. J.* 85:2406–2416.
28. Fahy, E., S. Subramaniam, …, E. A. Dennis. 2005. A comprehensive classification system for lipids. *J. Lipid Res.* 46:839–861.
29. Jaikishan, S., and J. P. Slotte. 2011. Effect of hydrophobic mismatch and interdigitation on sterol/sphingomyelin interaction in ternary bilayer membranes. *Biochim. Biophys. Acta.* 1808:1940–1945.

30. Quinn, P. J., and C. Wolf. 2009. Thermotropic and structural evaluation of the interaction of natural sphingomyelins with cholesterol. *Biochim. Biophys. Acta.* 1788:1877–1889.

31. Quinn, P. J. 2013. Structure of sphingomyelin bilayers and complexes with cholesterol forming membrane rafts. *Langmuir.* 29:9447–9456.

32. Sas, K. M., V. Nair, …, S. Pennathur. 2015. Targeted lipidomic and transcriptomic analysis identifies dysregulated renal ceramide metabolism in a mouse model of diabetic kidney disease. *J. Proteomics Bioinform (Suppl. 14)*:002.

33. Jiménez-Rojo, N., A. B. García-Arribas, …, F. M. Goñi. 2014. Lipid bilayers containing sphingomyelins and ceramides of varying N-acyl lengths: a glimpse into sphingolipid complexity. *Biochim. Biophys. Acta.* 1838:456–464.

34. Lewis, R. N., R. N. McElhaney, …, S. M. Gruner. 1994. Enigmatic thermotropic phase behavior of highly asymmetric mixed-chain phosphatidylcholines that form mixed-interdigitated gel phases. *Biophys. J.* 66:207–216.

35. Mehlhorn, E. I., E. Florio, …, C. W. M. Grant. 1988. Evidence that trans-bilayer interdigitation of glycosphingolipid long chain fatty acids may be a general phenomenon. *Biochim. Biophys. Acta.* 939:151–159.

36. Róg, T., A. Orłowski, …, I. Vattulainen. 2016. Interdigitation of long-chain sphingomyelin induces coupling of membrane leaflets in a cholesterol dependent manner. *Biochim. Biophys. Acta.* 1858:281–288.

37. Boggs, J. M., and K. M. Koshy. 1994. Do the long fatty acid chains of sphingolipids interdigitate across the center of a bilayer of shorter chain symmetric phospholipids? *Biochim. Biophys. Acta.* 1189:233–241.

38. Schram, V., and T. E. Thompson. 1995. Interdigitation does not affect translational diffusion of lipids in liquid crystalline bilayers. *Biophys. J.* 69:2517–2520.

39. Devaux, P. F. 1991. Static and dynamic lipid asymmetry in cell membranes. *Biochemistry.* 30:1163–1173.

40. Fujimoto, T., and I. Parmryd. 2017. Interleaflet coupling, pinning, and leaflet asymmetry-major players in plasma membrane nanodomain formation. *Front. Cell Dev. Biol.* 4:155.

41. Uline, M. J., M. Schick, and I. Szleifer. 2012. Phase behavior of lipid bilayers under tension. *Biophys. J.* 102:517–522.

42. Chen, D., and M. M. Santore. 2014. Large effect of membrane tension on the fluid-solid phase transitions of two-component phosphatidylcholine vesicles. *Proc. Natl. Acad. Sci. USA.* 111:179–184.

43. Portet, T., S. E. Gordon, and S. L. Keller. 2012. Increasing membrane tension decreases miscibility temperatures; an experimental demonstration via micropipette aspiration. *Biophys. J.* 103:L35–L37.

44. Hamada, T., Y. Kishimoto, …, M. Takagi. 2011. Lateral phase separation in tense membranes. *Soft Matter.* 7:9061–9068.

45. Dimitrov, D. S., and M. I. Angelova. 1988. Lipid swelling and liposome formation mediated by electric fields. *J. Electroanal. Chem. Interfacial Electrochem.* 253:323–336.

46. Silvius, J. R., and R. N. McElhaney. 1980. Effects of phospholipid acyl chain structure on thermotropic phase properties. 3. Phosphatidylcholines with (−), and (±)-anteiso acyl chains. *Chem. Phys. Lipids.* 26:67–77.

47. Bakht, O., P. Pathak, and E. London. 2007. Effect of the structure of lipids favoring disordered domain formation on the stability of cholesterol-containing ordered domains (lipid rafts): identification of multiple raft-stabilization mechanisms. *Biophys. J.* 93:4307–4318.

48. Lindsey, H., N. O. Petersen, and S. I. Chan. 1979. Physicochemical characterization of 1,2-diphytanoyl-sn-glycero-3-phosphocholine in model membrane systems. *Biochim. Biophys. Acta.* 555:147–167.

49. Hung, W. C., F. Y. Chen, and H. W. Huang. 2000. Order-disorder transition in bilayers of diphytanolyl phosphatidylcholine. *Biochim. Biophys. Acta.* 1467:198–206.

50. Ohashi, Y., T. Tanaka, …, Y. Nagai. 2000. Squid nerve sphingomyelin containing an unusual sphingoid base. *J. Lipid Res.* 41:1118–1124.

51. Carter, H. E., and C. B. Hirschberg. 1968. Phytosphingosines and branched sphingosines in kidney. *Biochemistry.* 7:2296–2300.

52. Shinoda, K., W. Shinoda, …, M. Mikami. 2004. Comparative molecular dynamics study of ether- and ester-linked phospholipid bilayers. *J. Chem. Phys.* 121:9648–9654.

53. Yasmann, A., and S. Sukharev. 2015. Properties of diphytanoyl phospholipids at the air-water interface. *Langmuir.* 31:350–357.

54. Veatch, S. L., and S. L. Keller. 2003. A closer look at the canonical 'Raft Mixture' in model membrane studies. *Biophys. J.* 84:725–726.

55. Konyakhina, T. M., and G. W. Feigenson. 2016. Phase diagram of a polyunsaturated lipid mixture: brain sphingomyelin/1-stearoyl-2-docosahexaenoyl-sn-glycero-3-phosphocholine/cholesterol. *Biochim. Biophys. Acta.* 1858:153–161.

56. Petruzielo, R. S., F. A. Heberle, …, G. W. Feigenson. 2013. Phase behavior and domain size in sphingomyelin-containing lipid bilayers. *Biochim. Biophys. Acta.* 1828:1302–1313.

57. Veatch, S. L., K. Gawrisch, and S. L. Keller. 2006. Closed-loop miscibility gap and quantitative tie-lines in ternary membranes containing diphytanoyl PC. *Biophys. J.* 90:4428–4436.

58. Carrer, D. C., E. Kummer, …, P. Schwille. 2009. Asymmetry determines the effects of natural ceramides on model membranes. *Soft Matter.* 5:3279–3286.

59. Seeger, H. M., G. Marino, …, P. Facci. 2009. Effect of physical parameters on the main phase transition of supported lipid bilayers. *Biophys. J.* 97:1067–1076.

60. Aufderhorst-Roberts, A., U. Chandra, and S. D. Connell. 2017. Three-phase coexistence in lipid membranes. *Biophys. J.* 112:313–324.

61. Niemelä, P. S., M. T. Hyvönen, and I. Vattulainen. 2006. Influence of chain length and unsaturation on sphingomyelin bilayers. *Biophys. J.* 90:851–863.

62. Vanegas, J. M., R. Faller, and M. L. Longo. 2010. Influence of ethanol on lipid/sterol membranes: phase diagram construction from AFM imaging. *Langmuir.* 26:10415–10418.

63. Balleza, D., A. B. Garcia-Arribas, …, F. M. Goñi. 2014. Ether- versus ester-linked phospholipid bilayers containing either linear or branched apolar chains. *Biophys. J.* 107:1364–1374.

64. Ngo, A. T., Z. J. Jakubek, …, L. J. Johnston. 2014. Membrane order parameters for interdigitated lipid bilayers measured via polarized total-internal-reflection fluorescence microscopy. *Biochim. Biophys. Acta.* 1838:2861–2869.

65. Oreopoulos, J., and C. M. Yip. 2008. Combined scanning probe and total internal reflection fluorescence microscopy. *Methods.* 46:2–10.

66. Perković, S., and H. M. McConnell. 1997. Cloverleaf monolayer domains. *J. Phys. Chem. B.* 101:381–388.

67. Heinig, P., S. Wurlitzer, …, T. M. Fischer. 2002. Stability criteria for two-dimensional wetting in monolayers. *J. Phys. Chem. B.* 106:11951–11960.

68. Khattari, Z., P. Heinig, …, T. M. Fischer. 2002. Wetting in asymmetric quasi-2D systems. *Langmuir.* 18:2273–2279.

69. García-Arribas, A. B., E. J. González-Ramírez, …, F. M. Goñi. 2017. Complex effects of 24:1 sphingolipids in membranes containing dioleoylphosphatidylcholine and cholesterol. *Langmuir.* 33:5545–5554.

70. Cornell, C. E., A. D. Skinkle, …, S. L. Keller. 2018. Tuning length scales of small domains in cell-derived membranes and synthetic model membranes. *Biophys. J.* 115:690–701.

71. Käs, J., and E. Sackmann. 1991. Shape transitions and shape stability of giant phospholipid vesicles in pure water induced by area-to-volume changes. *Biophys. J.* 60:825–844.

72. Needham, D., and E. Evans. 1988. Structure and mechanical properties of giant lipid (DMPC) vesicle bilayers from 20 degrees C below to 10 degrees C above the liquid crystal-crystalline phase transition at 24 degrees C. *Biochemistry.* 27:8261–8269.

73. Akimov, S. a., P. I. Kuzmin, …, F. S. Cohen. 2007. Lateral tension increases the line tension between two domains in a lipid bilayer membrane. *Phys. Rev. E Stat. Nonlin. Soft Matter Phys.* 75:011919.

74. Chen, D., and M. M. Santore. 2014. Three dimensional (temperature-tension-composition) phase map of mixed DOPC-DPPC vesicles: two solid phases and a fluid phase coexist on three intersecting planes. *Biochim. Biophys. Acta.* 1838:2788–2797.

75. Li, L., and J. X. Cheng. 2006. Coexisting stripe- and patch-shaped domains in giant unilamellar vesicles. *Biochemistry.* 45:11819–11826.

76. Björkqvist, Y. J., J. Brewer, …, B. Westerlund. 2009. Thermotropic behavior and lateral distribution of very long chain sphingolipids. *Biochim. Biophys. Acta.* 1788:1310–1320.

77. Maulik, P. R., and G. G. Shipley. 1996. Interactions of N-stearoyl sphingomyelin with cholesterol and dipalmitoylphosphatidylcholine in bilayer membranes. *Biophys. J.* 70:2256–2265.

78. Slater, J. L., and C. H. Huang. 1988. Interdigitated bilayer membranes. *Prog. Lipid Res.* 27:325–359.

79. Pinto, S. N., L. C. Silva, …, M. Prieto. 2008. Membrane domain formation, interdigitation, and morphological alterations induced by the very long chain asymmetric C24:1 ceramide. *Biophys. J.* 95:2867–2879.

80. Levin, I. W., T. E. Thompson, …, C. Huang. 1985. Two types of hydrocarbon chain interdigitation in sphingomyelin bilayers. *Biochemistry.* 24:6282–6286.

81. Maté, S., J. V. Busto, …, F. M. Goñi. 2014. N-nervonoylsphingomyelin (C24:1) prevents lateral heterogeneity in cholesterol-containing membranes. *Biophys. J.* 106:2606–2616.

82. Collins, M. D., and S. L. Keller. 2008. Tuning lipid mixtures to induce or suppress domain formation across leaflets of unsupported asymmetric bilayers. *Proc. Natl. Acad. Sci. USA.* 105:124–128.

83. Courtney, K. C., W. Pezeshkian, …, X. Zha. 2018. C24 sphingolipids govern the transbilayer asymmetry of cholesterol and lateral organization of model and live-cell plasma membranes. *Cell Rep.* 24:1037–1049.

Biophysical Journal, Volume *116*

Supplemental Information

Complex Phase Behavior of GUVs Containing Different Sphingomyelins

Daniel Balleza, Andrea Mescola, Nathaly Marín–Medina, Gregorio Ragazzini, Marco Pieruccini, Paolo Facci, and Andrea Alessandrini

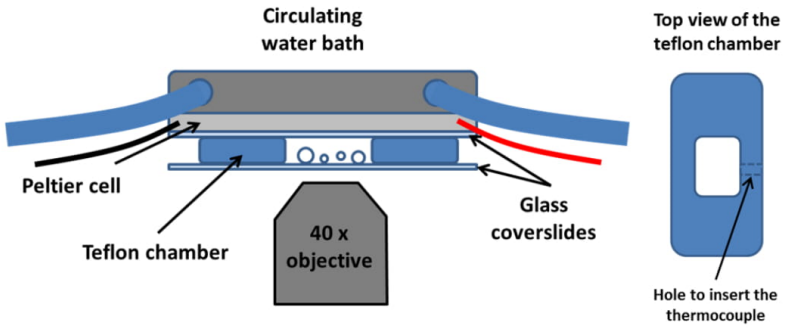

Fig. S1:Scheme of the set-up used to analyze the GUVs at different temperatures with the epifluorescence microscope. The Peltier cell is connected to a home-developed temperature controller device implementing a PID control by the Arduino Uno board. The circulating water bath is exploited as fast heat sink.

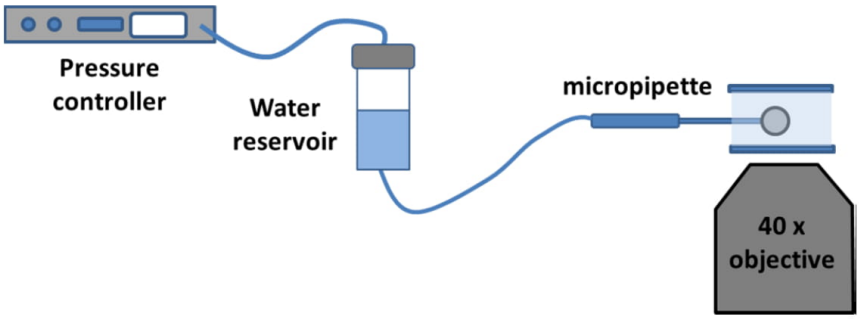

Fig. S2: Scheme of the Micropipettte aspiration set-up exploited to change the lateral tension of the GUVs. The pressure controller is used to control the pressure on top of the water reservoir. The water reservoir is connected to the micropipette.

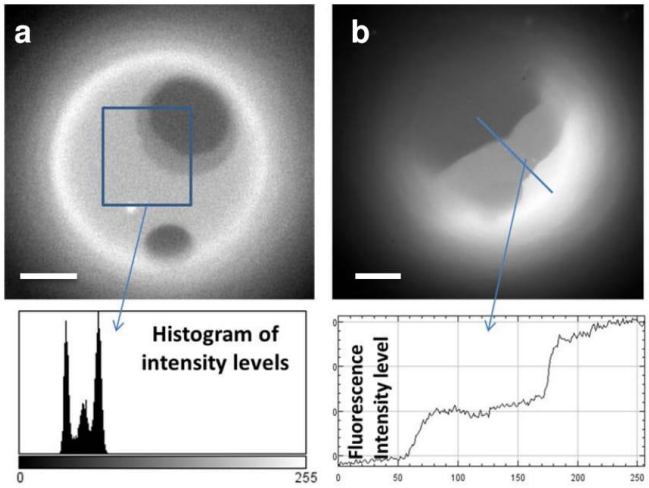

Fig. S3: Fluorescence intensity analysis (histogram of intensity levels in a) and line section in b)) for DiPhyPC/bSM/Cho 1/1/1 GUVs showing three intensity levels. (Bar = 10 µm)

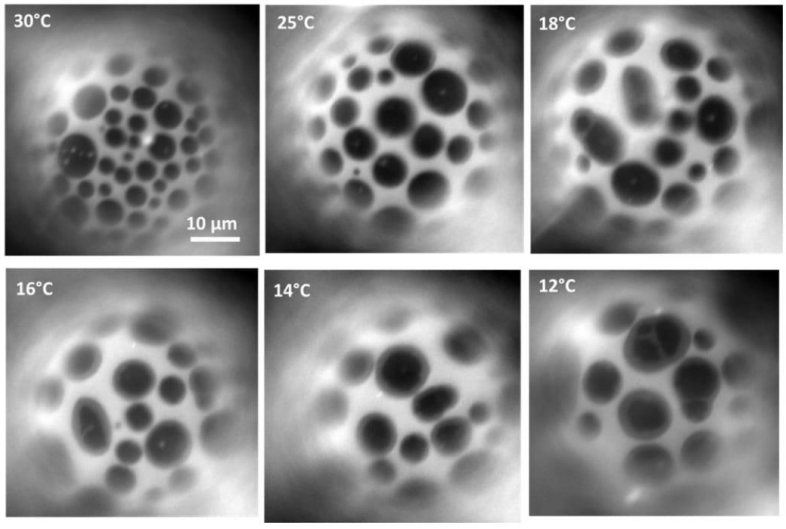

Fig S4: Example of the formation of the intermediate fluorescence intensity level for a DiPhyPC/bSM/Chol 1/1/1 vesicle not grabbed by a micropipette upon a decreasing temperature run.

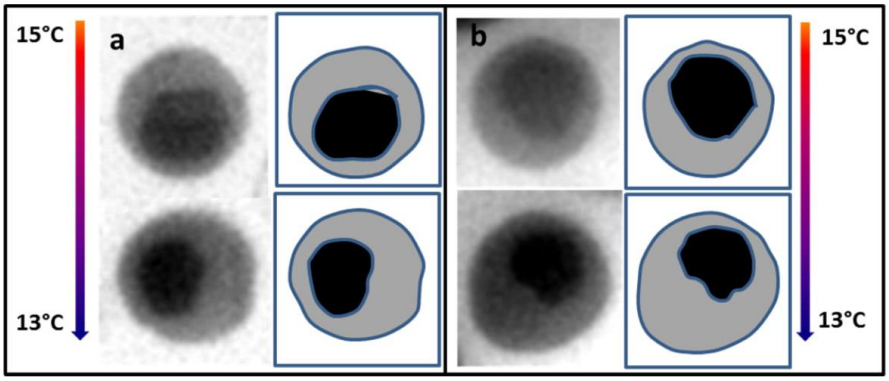

	15°C		13°C	
	Grey region	Black region	Grey region	Black region
a	79	48	103	39
b	82	51	109	42

Fig. S5: Analysis of the area variation as a function of temperature for the darkest and the intermediate region in the case of two domains (a and b) from the sequence reported in Fig. 2 of the manuscript and Movie S1. Both the fluorescence images and schemes of how the domains have been calculated are reported. The Table reports the area of the different domains for two different temperatures (15°C and 13°C). The grey region is the region defined by the external border of the intermediate fluorescence level whereas the black region is the area of the region with the lowest fluorescence intensity level. The unit for area quantification is μm^2.

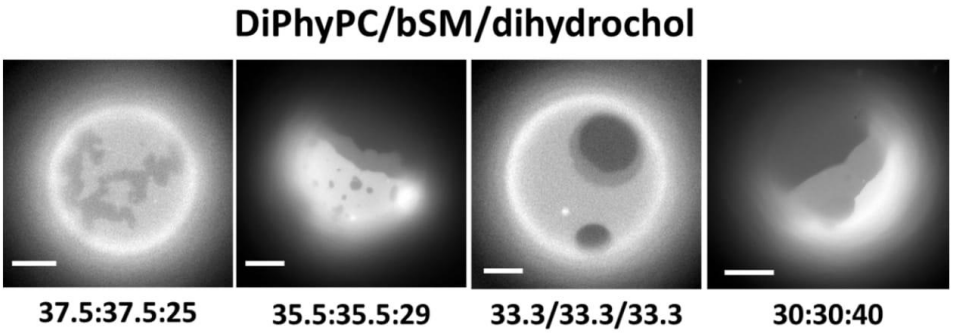

Fig. S6: We considered different molar proportions of the DiPhyPC/bSM/dihydrochol mixture. In particular, keeping an equal molar proportion between DiPhyPC and bSM (1:1) we changed the amount of cholesterol. We found that a low amount of cholesterol (~25%) easily produced the S_o phase coexisting with the L_d phase and the three different fluorescent intensities were never observed. For higher cholesterol concentrations (up to 40%) the coexistence of the three intensities was always observed with no evidence of a dependence of the percentage of GUVs in this state on the cholesterol amount. (Bar = 10 μm)

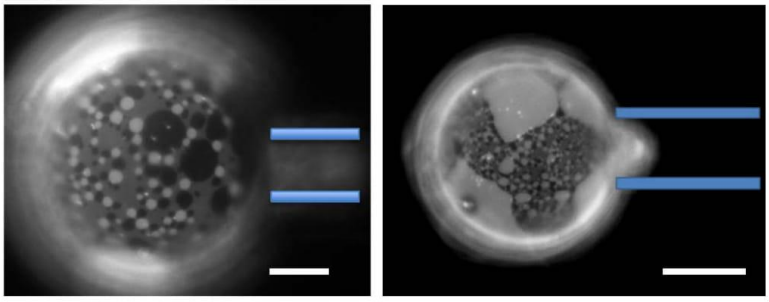

Fig. S7: Examples of other GUVs for which the application of the lateral tension by the MAT set-up induces the appearance in the intermediate fluorescence intensity level region of bright and dark round domains. The blue bars represent the position of the micropipette. (Bar = 10 μm)

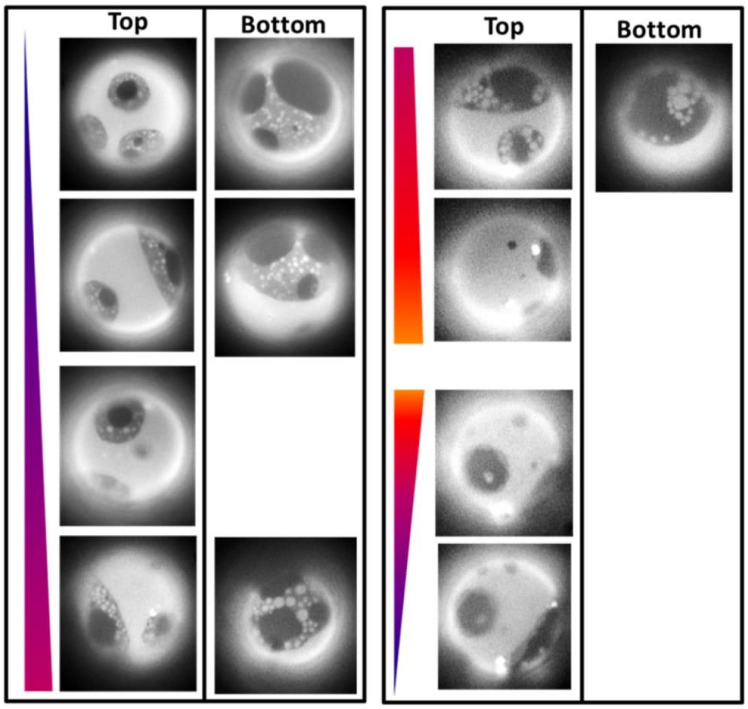

Fig. S8: Sequence of fluorescence microscopy images of a DiPhyPC/bSM/chol 1/1/ 1 GUV (+ 1% Texas Red-DHPE) upon a temperature cycle. The colored triangles and the arrows show the temperature variation trend. Couples of images have been reported when both the top and bottom surfaces of the GUVs have been captured

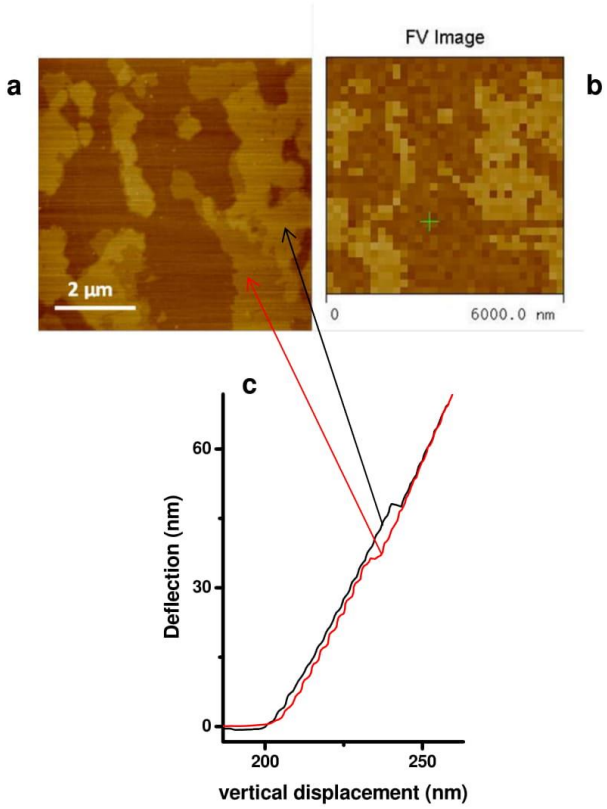

Fig. S9: a) Topography image of a DiPhyPC/bSM/Chol 1/1/1 SLB at 16°C; b) Force Volume image corresponding to the force spectroscopy analysis of the same region in a). The threshold value for the deflection has been chosen to show the punch-through force difference among the different domains; c) two examples of force curves coming from the regions pointed by the arrows.

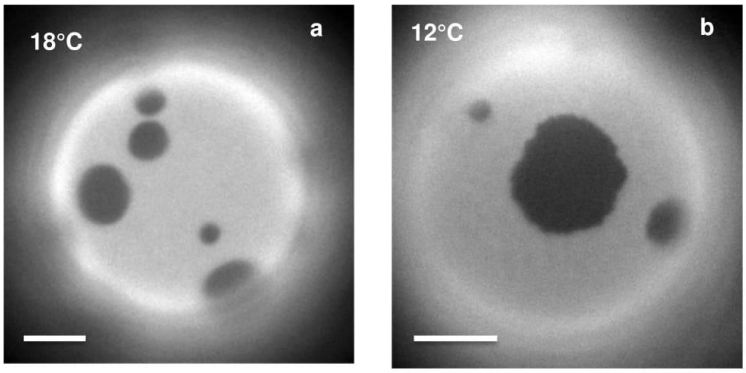

Fig. S10: Examples of fluorescence microscopy images of DiPhyPC/eggSM/chol 1/1/1 (+ 1% Texas Red-DHPE) GUVs. In no cases the presence of more than 2 fluorescence intensity levels has been observed. Bar = 10 µm.

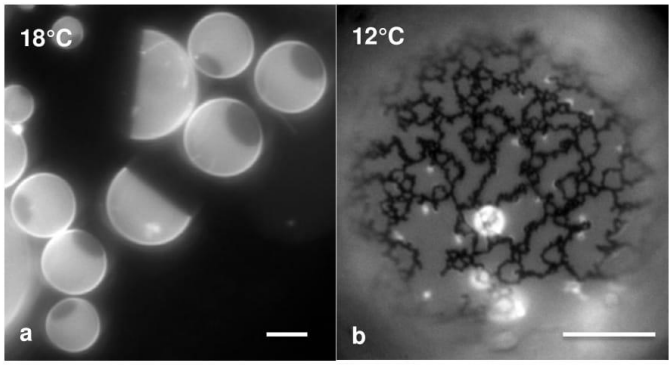

Fig. S11: Examples of fluorescence microscopy images of DiPhyPC/(18:0)SM/Chol 40/40/20 (+ 1% Texas Red-DHPE) GUVs. The presence of more than 2 fluorescence intensity levels has never been observed. Bar = 10 µm.

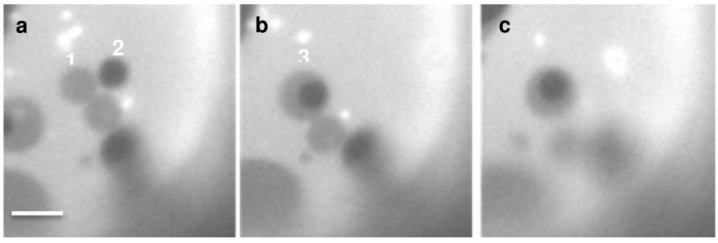

Fig. S12: The sequence shows what happens when a region with the darkest fluorescence intensity merges with an intermediate region. The darkest region is completely included in the intermediate region and the overall area of the domains at the end of the coalescence event is approximately equal to the sum of the two initially separated regions. This behavior is not in accordance with the confinement of the two different domains to the two opposite leaflets Quantitative analysis of the area of different domains upon coalescence: The area (in pixel^2) of domain 1 in a) is 168, for domain 2 we have 102. Upon merging of the two domains, the overall area of the formed domain (3) is 298. The fact that the area of the new domain is almost equal to the sum of the two initial domains points to the fact that the two domains span the overall bilayer thickness and they are not confined to a single leaflet. (Bar = 10 μm)

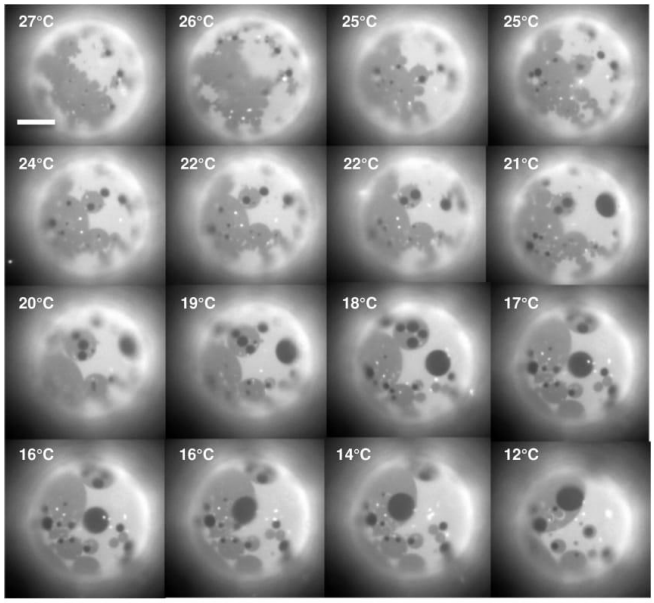

Fig. S13: Sequence of fluorescence microscopy images of a DiPhyPC/(24:1) SM/Chol + 0.5% DHPE Texas Red GUV as the temperature is decreased from 27°C to 12°C. The border between the brightest and the intermediate fluorescence intensity regions gradually gets more defined and regular and the darkest domains, once included inside a larger intermediate domain, get trapped in that position. The sequence corresponds to the vesicle shown in Fig. 7 of the manuscript. (Bar = 10 μm)

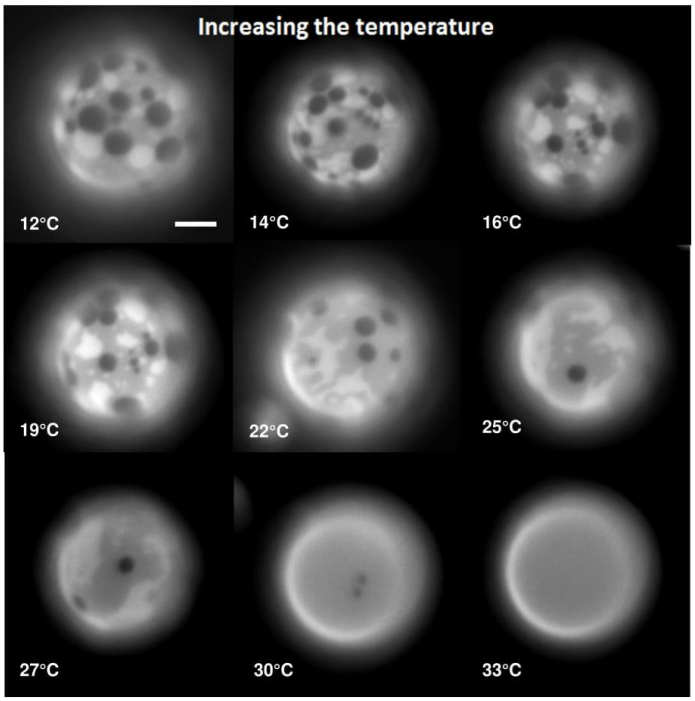

Fig. S14: Phase behavior of a DiPhyPC/(24:1)SM/Chol 1/1/1 (+ 0.5% Texas Red-DHPE) upon temperature increase. Bar = 10 μm.

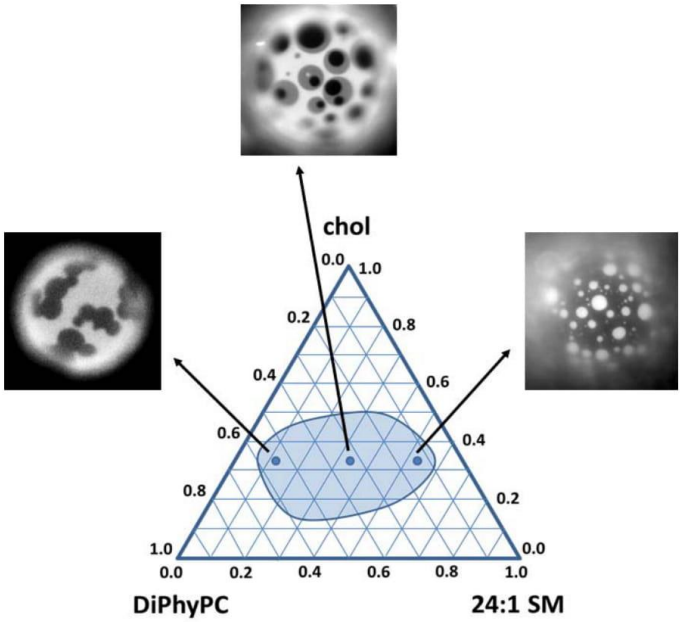

Fig. S15: Appearance of the different fluorescence intensity levels as a function of composition for the ternary mixture DiPhyPC/24:1 SM/chol + 1% Texas Red. The highest fraction of vesicles presenting three fluorescence intensity levels is obtained for a lipid composition with an approximately equal concentration of DiPhyPC and (24:1)SM.

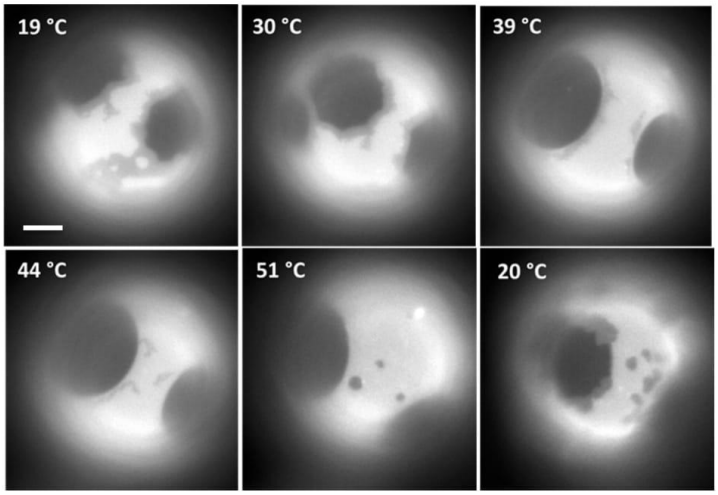

Fig. S16: Sequence of fluorescence microscopy images of a GUV composed by DiPhyPC/(24:0)SM/Chol 1/1/1 plus 1 % DHPE Texas Red. The vesicle has been exposed to a temperature cycle: from 19°C to 51°C and back. The presence of an intermediate fluorescence intensity level wetting the darkest domains is removed at 51°C and reappears at around 25°C. Bar = 10 μm.

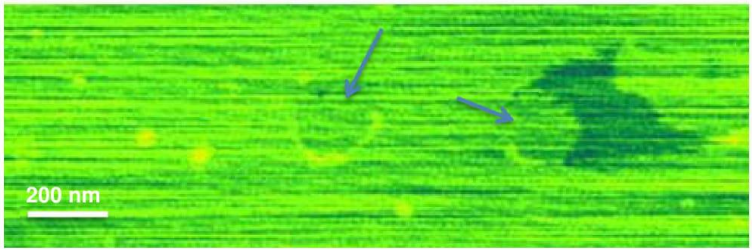

Fig. S17: Higher magnification of Fig. 8a with false colors to highlight the fact that the regions inside the arcs (arrows) have a different height (higher) with respect to the surrounding bilayer. In the false colors representation darkest regions are thicker.

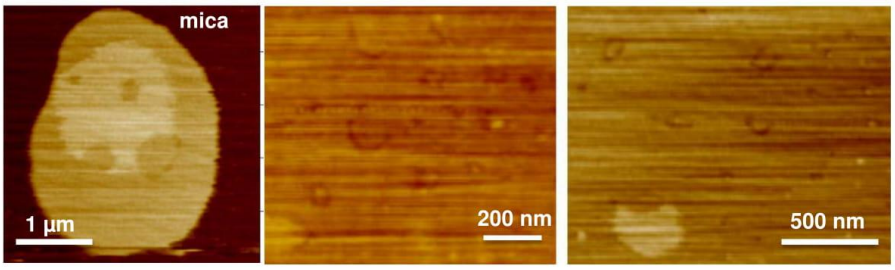

Fig. S18: AFM images of DiPhyPC/(24:1)SM/Chol 1/1/1 SLBs showing the presence of more than two height levels corresponding to the presence of more than two different domain thicknesses. The images have been acquired at a temperature of 12°C

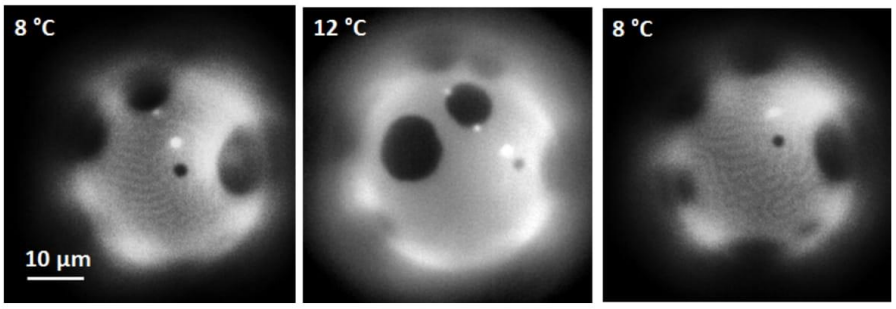

Fig. S19: Appearance of a modulated phase as a function of temperature for a DiPhyPC/(24:1)SM/Chol 1/1/1 +1% Texas Red DHPE GUV. The appearance and disappearance of the modulation is reversible.

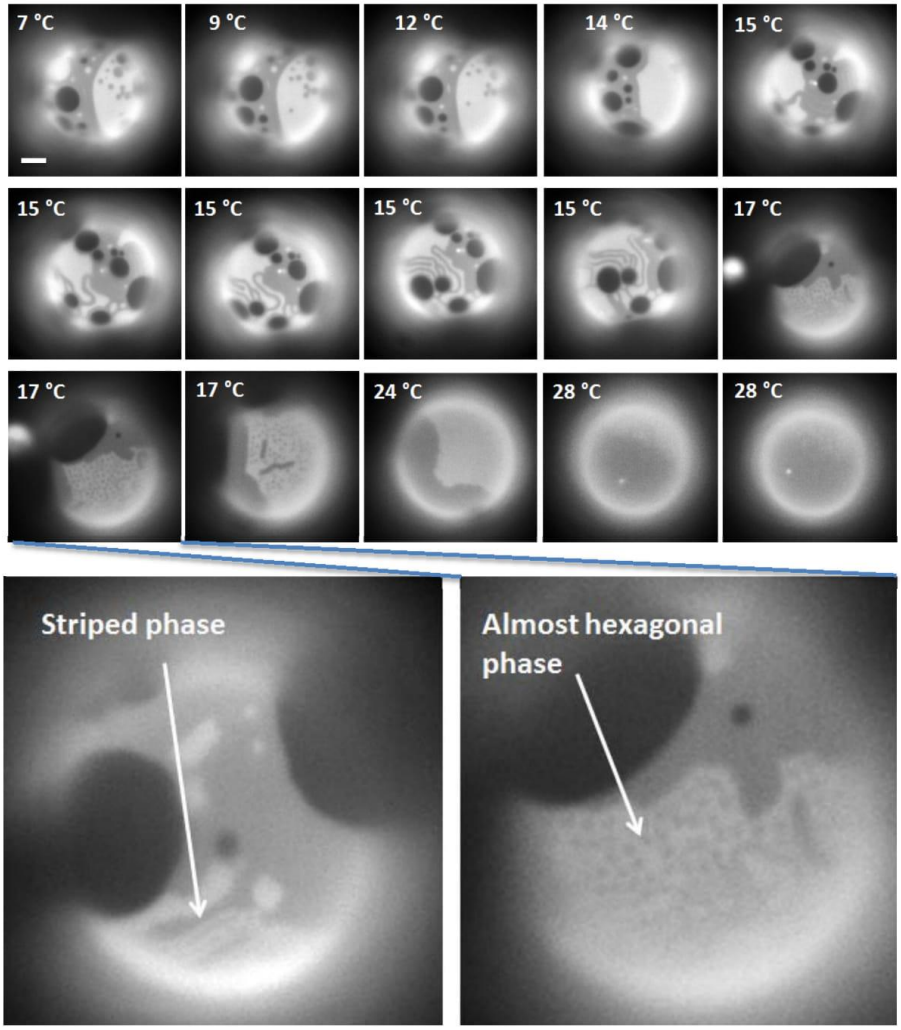

Fig. S20: Example of the appearance of striped domains upon temperature increase for a DiPhyPC/(24:1)SM/chol 1/1/1 + 1% Texas Red DHPE GUV. The striped domains appear after the decrease of the line tension between the domains with the highest fluorescence intensity and the domains with the intermediate intensity. Scale bar for the upper images = 10 µm.

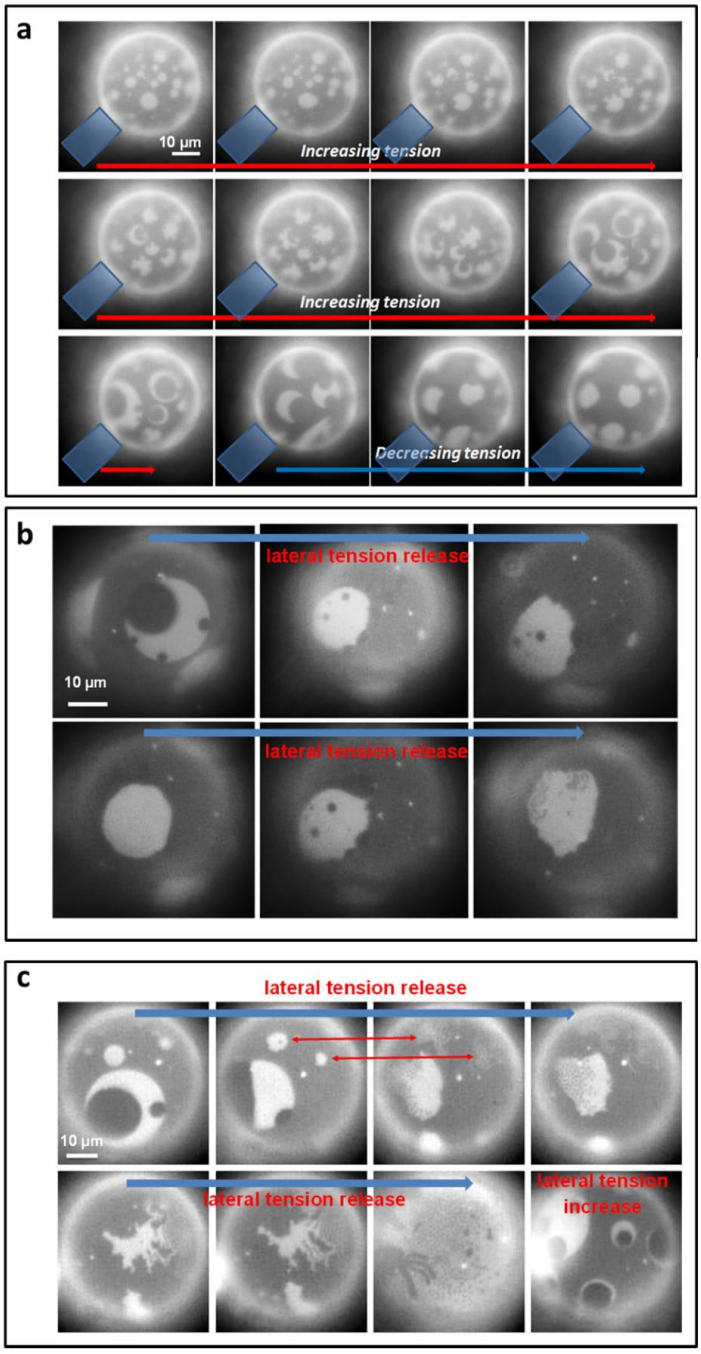

Fig. S21: a,b,c) Examples of shape changes of domains for DiPhyPC/(24:1)SM/Chol 1/1/1 (+ 1% Texas Red DHPE) GUVs upon an increase or release of the lateral tension obtained by a Micropipette Aspiration set-up at 15°C. The blue object in a) represents the position of the micropipette.

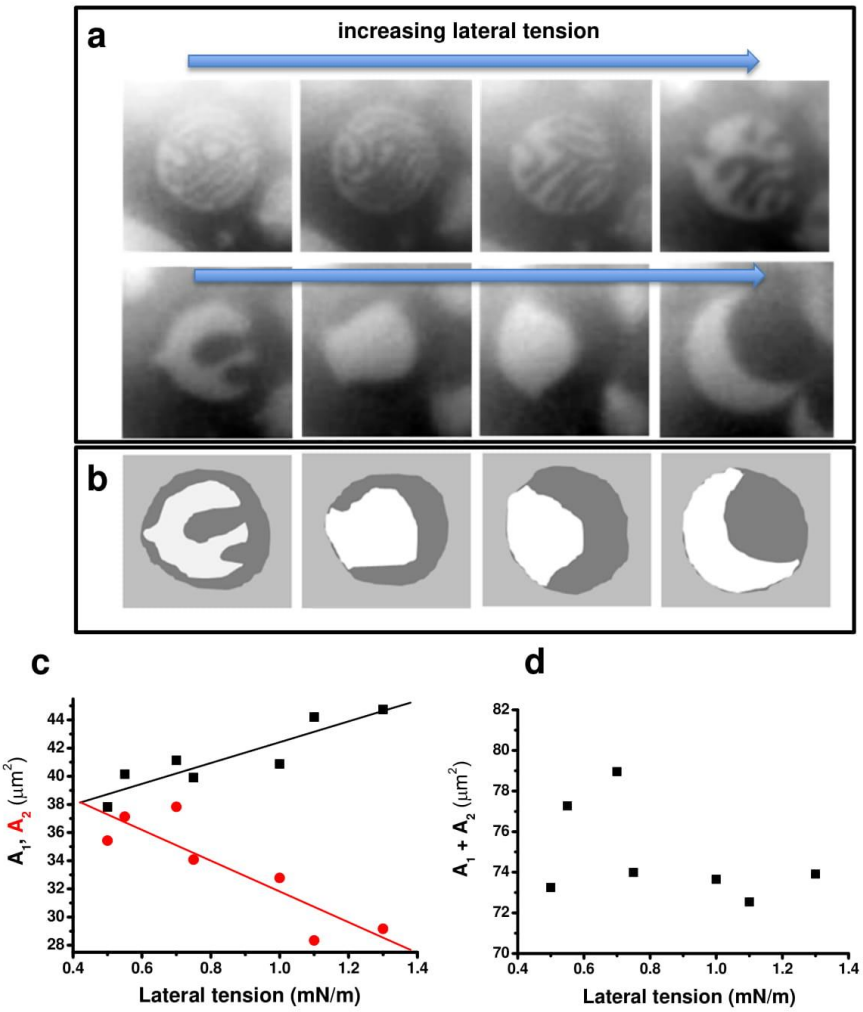

Fig. S22: a) Sequence of fluorescence microscopy images showing the detailed analysis of a domain in Fig. 10. b) Schematic representation of the domains corresponding to the second row in a); c) Quantitative analysis of the white (black squares) and dark grey (red dots) regions as a function of the applied lateral tension; d) Sum of the dark grey and white regions as a function of the applied lateral tension.

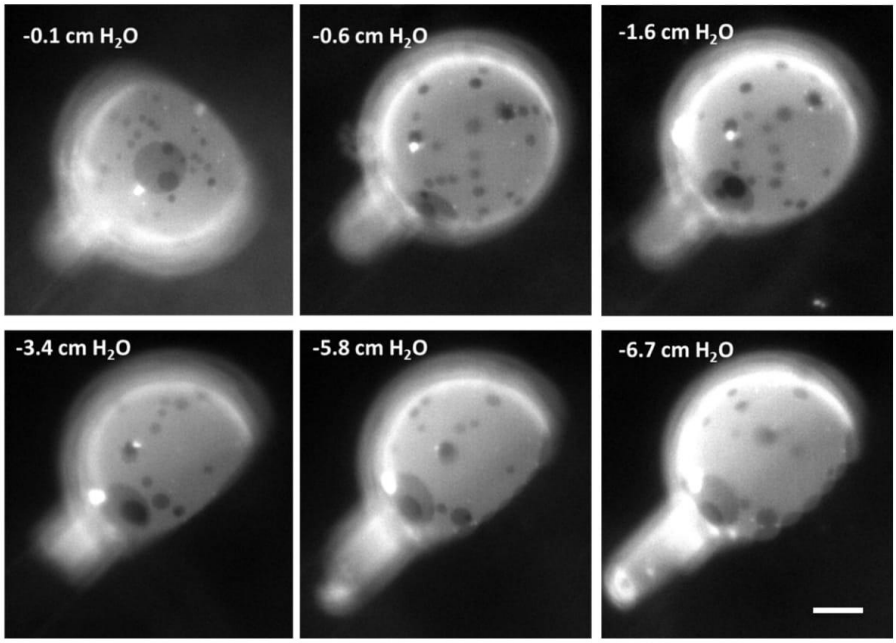

Fig. S23: Effect of the lateral tension on the shape of domains for a DiPhyPC/(24:1)SM/Chol 1/1/1 (+1% Texas Red DHPE) in the case of Type II domains of Fig. 5. Upon a lateral tension increase little effect is observed on the shape of the domains. Bar = 10 μm.

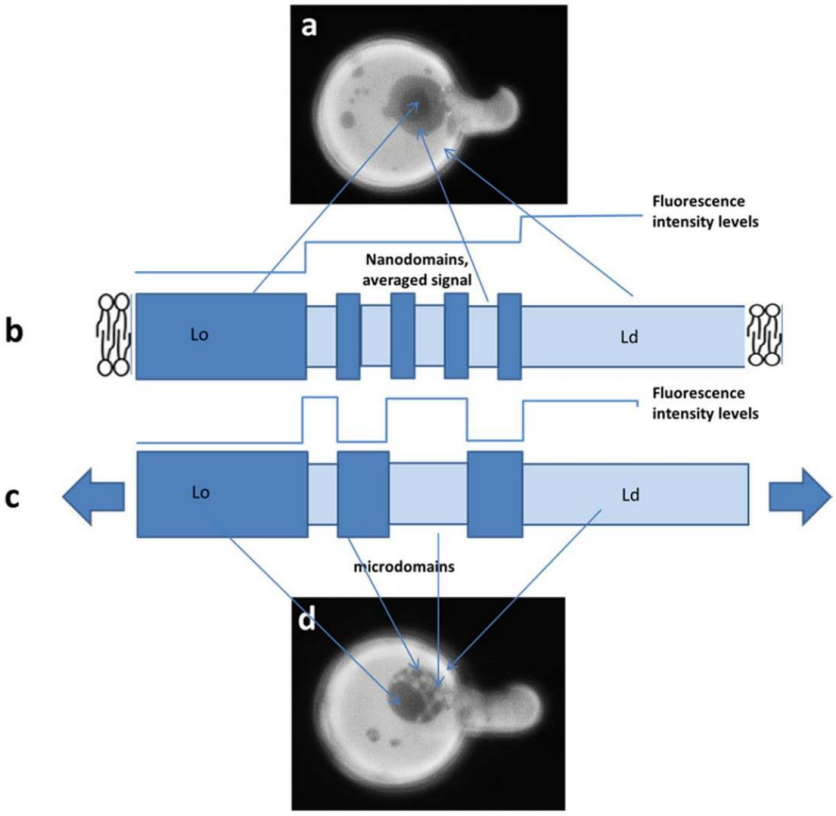

Fig. S24: Scheme of a possible interpretation for the appearance of the intermediate fluorescence intensity level upon temperature decrease and of its removal in favor of black (the darkest fluorescence level) and white (the highest fluorescence level) regions upon an increase of the lateral tension.

Line tension measurement

Theory

The line tension can be estimated from the (Fast) Fourier analysis of the L_o and L_d domains' contour fluctuations. The method is illustrated in detail in refs. [1], [2] but we provide here a brief account.

Given a selected domain, its image is recorded in time with a sufficient number of frames; for each frame, the radius as a function of the angle, $r(\vartheta)$, is extracted and the associated n-mode amplitudes $|u_n|$ are derived either by direct analysis or from the autocorrelation function $c(\delta) = \langle r(\vartheta)r(\vartheta+\delta)\rangle_\vartheta = (R_0^2/2)\Sigma_n\ |u_n|^2\ \cos(n\delta)$, being R_0 the radius of a circle with the same area of the analyzed domain. The averages of the square amplitudes yield the line tension σ through [1]

$$\sigma = \frac{k_B T}{\pi R_0 (n^2-1)\langle |u_n|^2\rangle},$$

where $k_B T$ is the thermal energy.

A 40x objective lens has been used, and the pixel size approximately corresponds to 114 nm. The exposure times range from 20 to 30 ms and the cycle times from 30 to 50 ms (if we increase the cycle time up to 250 ms the obtained results are very similar). Being the number of images for each sequence in the order of 600, the overall acquisition time takes 18-30 s. The domains are selected following the criteria indicated in [1,2], namely:

- Their area must not exceed 1/5 of the total area of a GUV
- Their shape must be almost circular
- Their radius must be not less than 3 μm
- They must be planar and located at about the center of the GUV imaged surface
- Their area must remain constant during the whole acquisition time

Selection of GUVs with appropriate domains is performed using as low as possible light intensity to prevent photo-oxidation. The images are collected by fluorescence microscopy; then, discrete approximations of the domain contours are obtained by superposing a square mesh mask to the images, which are converted to binary afterwards (the ImageJ software was used).

The length Δx_{lim} = 114 nm corresponding to the pixel size, poses a limit on the maximum mode number n_{max} which makes sense to be analyzed: the wavelengths of the Fourier components (e.g. in the autocorrelation function) are 2^n submultiples of the fundamental wavelength $\lambda_1 \equiv 2\pi R_0$, so that it is readily found that $n_{max} = \log_2(\lambda_1/\Delta x_{lim})$. Contours of domains with approximately 3 μm radius can be analyzed up to the 6th mode.

The problem of photo-oxidation has been considered already in ref. [2] and it is addressed here because we used a fluorophore concentration significantly higher (~5 times) than in that work. To check the relevance of induced photo-oxidation on the domains, we partitioned the image sequence in four sub-sets made of the same number of frames. For each sub-set the line tension was estimated in order to reveal whether any systematic drift of σ in time was detectable; our results did

not show any such tendency. Eventually, we analyzed the dependence of the line tension as a function of domain radius and, within errors, no influence on the domain size was observed.

Results

We compared the value of the line tension in the case of domains for a well-known lipid mixture (DiPhyPC/DPPC/Chol) with the case of domains of Type I (see manuscript) for the DiPhyPC/(24:1) SM/Chol mixture which showed the maximum sensitivity to the applied lateral tension. Fig. S24 shows typical examples of the domains we analyzed.

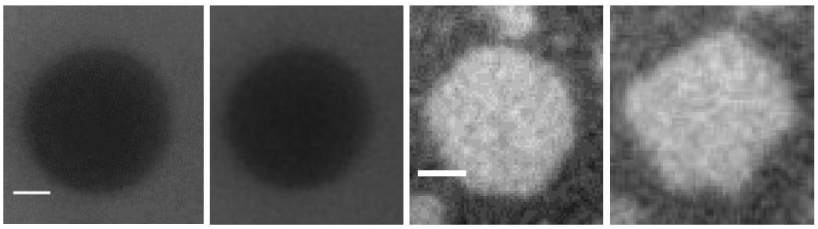

Fig. S25: a) and b) represent a L_o domain obtained from the DiPhyPC/DPPC/Chol mixture (1/1/1 molar ratio), as it appears in the initial and final frame of the analysis respectively . c) and d) represent a L_d domain obtained from the DiPhyPC/(24:1) SM/Chol mixture (1/1/1 molar ratio), as it appears in the initial and final frame respectively. Bar = 2 μm

Line tension components (Variance and mean amplitude):

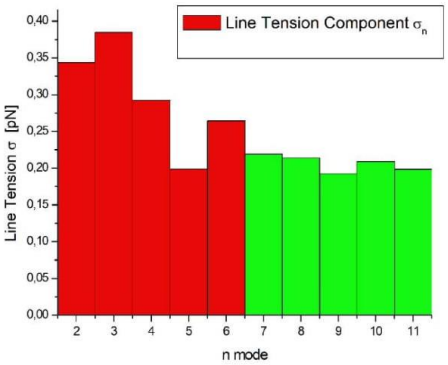

Fig. S26: Example of line tension estimate from different Fourier mode amplitudes as a function of mode number n. Only the first terms (up to the 6^{th} mode) are relevant (red bars).

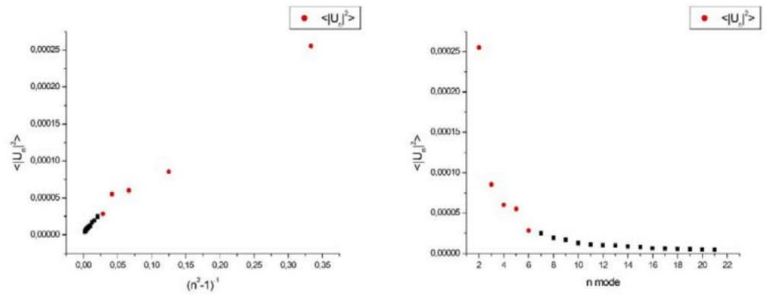

Fig. S27: Mean square amplitudes $\langle |u_n|^2 \rangle$ of the autocorrelation function as functions of $(n^2 - 1)^{-1}$ (left) and mode number n (right). Amplitudes from the 2nd to the 6th mode are plotted as red dots.

Line tension subsets

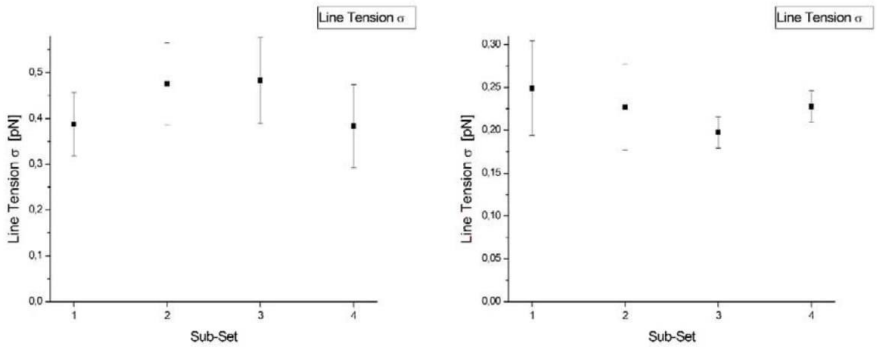

Fig. S28: Examples of estimated line tension for progressive sub-set number. The results do not show a significant dependence on the sub-sets; thus, the photo-oxidation process should be minimal.

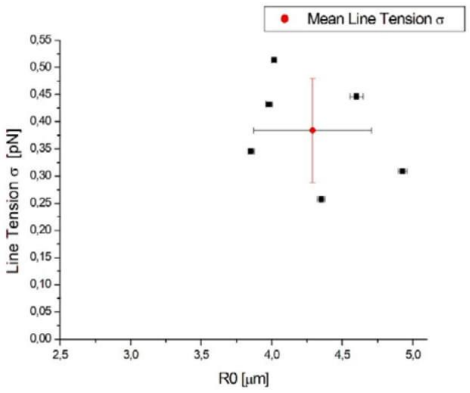

Line tension as a function of domain radius

Fig. S29: Line tension as a function of domain radius for six L_o domains of a DiphyPC/DPPC/Chol 1/1/1 mixture. Only the domains with radius larger than 3 μm have been considered, as they allow to access a larger number of modes (up to the 6th one at least).

Line tension comparison

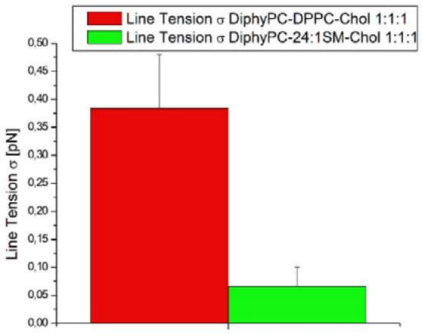

Fig. S30: Comparison of line tension estimates from L_o domains of DiPhyPC/DPPC/Chol 1/1/1 mixture (red) and L_d domains of DiPhyPC/(24:1) SM/Chol 1/1/1 mixture (green): The line tension for the domains in the first type of mixture (0.384 ± 0.096 pN) is larger than in the case of the second mixture (0.066 ± 0.035 pN).

References

[1] Esposito C, Tian A, Melamed S, Johnson C, Tee SY, Baumgart T., Flicker spectroscopy of thermal lipid bilayer domain boundary fluctuations. Biophys J. 2007 Nov 1;93(9):3169-81

[2] Usery RD, Enoki TA, Wickramasinghe SP, Weiner MD, Tsai WC, Kim MB, Wang S, Torng TL, Ackerman DG, Heberle FA, Katsaras J, Feigenson GW.,Line Tension Controls Liquid-Disordered + Liquid-Ordered Domain Size Transition in Lipid Bilayers. Biophys J. 2017 Apr 11;112(7):1431-1443.

Movies' legends

Movie S1: Fluorescence microscopy movie of a DiPhyPC/bSM/Chol 1/1/1 (plus 1% Texas Red DHPE) vesicle undergoing a decreasing temperature ramp. The vesicle is grabbed by a micropipette (on the right of the vesicle, not visible in the fluorescence microscopy image). The temperature decreases from 50°C to 12°C. (see Figure 2 in the manuscript for other details).

Movie S2: Fluorescence microscopy movie of a DiPhyPC/bSM/Chol 1/1/1 (plus 1% Texas Red DHPE) vesicle showing the presence of three fluorescence intensity levels and undergoing an increase of the lateral tension at a constant temperature of 15°C. (See Figure 3 in the manuscript for other details).

Movie S3: Fluorescence microscopy movie of a DiPhyPC/(24:1)SM/Chol 1/1/1 (plus 1% Texas Red DHPE) vesicle at 15°C undergoing repetitive cycles of lateral tension increase and decrease. The lateral tension is increased by a micropipette aspiration set-up (the micropipette, not visible in the image, is positioned on the left of the vesicle at 45° with respect to the horizontal direction). (see Figure 10 in the manuscript for other details).

Movie S4: Another example of the same type of vesicle as in Movie S2. The vesicle undergoes a sequence of lateral tension increase and decrease. See Figure S20a for other details.

Movie S5: Another example of the same type of vesicle as in Movie S2. The vesicle undergoes a rapid lateral tension decrease. See Figure S20b for other details.

- **Jump-Through-Force on SLB exposed to Daptomycin**

In the previous sections we illustrated two possible mechanical characterizations of GUVs based on the flickering spectroscopy. Here we will mechanically characterize another cell plasma membrane physical model, the Supported-Lipid-Bilayer (SLB) model, adopting the Jump-Through-Force parameter.

In the following paper the antimicrobial role of Daptomycin has been investigated exploiting SLBs. We analyzed several SLB two-component compositions resembling mainly the classical bacterial membrane features. Daptomycin is an antimicrobial cyclic lipopeptide, which requires calcium ions to correctly targets bacterial membrane. Daptomycin is especially efficient against gram positive bacteria, which hardly can contrast Daptomycin action and provide subsequent resistance. Furthermore, this drug has a high affinity for phospholipids containing phosphatidylglycerol (PG) headgroups and owns an intrinsic fluorescence emission which make it reliable and suitable for fluorescence analysis. Even if Daptomycin has been released on the market since 2003 several mechanism of action details that could provide some guidelines for further drugs development are still controversial.

In this work we exploited AFM and fluorescence microscopy techniques to shed light on the still debated questions related to the role of the presence of phase separation in the lipid bilayer for the Daptomycin mechanism of action. Thus, we focused on SLB incorporating two different lipid species both containing the PG headgroup and reproducing the S_o-L_d phases coexistence. We developed the data-analysis protocol to detect the events and evaluate the Jump-Through-Force (JTF) writing the software able to read the Force-Volume map data and then search the possible JTF for each event. Finally, the obtained results are illustrated in JTF maps. The AFM topography analysis has been combined to quantitative JTF mechanical characterization.

Our finding confirm that Daptomycin preferentially interacts with PG headgroup, regardless of whether the PG lipids are in the L_d or S_o phase. From S_o and L_d topography profiles analysis the solid and the liquid phase reach progressively a similar height under Daptomycin exposure. Considering also the JTF analysis, Daptomycin appears to produce a stiffening effect of the domains where PG lipids are mainly in the fluid phase, whereas it causes fluidification of the domains where PG lipids are in the solid phase.

THE JOURNAL OF PHYSICAL CHEMISTRY B

pubs.acs.org/JPCB Article

Daptomycin Strongly Affects the Phase Behavior of Model Lipid Bilayers

Andrea Mescola,* Gregorio Ragazzini, and Andrea Alessandrini

Cite This: *J. Phys. Chem. B* 2020, 124, 8562−8571 Read Online

ACCESS | Metrics & More | Article Recommendations | Supporting Information

ABSTRACT: Daptomycin (DAP) is a calcium-dependent cyclic lipopeptide with great affinity for negatively charged phospholipids bearing the phosphatidylglycerol (PG) headgroup and has been used since 2003 as a last resort antibiotic in the treatment of severe infections caused by Gram-positive bacteria. The first step of its mechanism of action involves the interaction with the bacterial membrane, which not only represents a physical barrier but also accommodates transmembrane proteins, such as receptors, transporters, and enzymes, whose activity is crucial for the survival of bacteria. This results in a less efficient development of resistance strategies by pathogens compared to common antibiotics that activate or inhibit biochemical pathways connected to specific target proteins. Although already on the market, the molecular mechanism of action of DAP is still a controversial subject of investigation and it is most likely the result of a combination of distinct effects. Understanding how DAP targets the membrane of pathogens could be of great help in finding its analogues that could better avoid the development of resistance. Here, exploiting fluorescence microscopy and atomic force microscopy (AFM), we demonstrated that DAP affects the thermodynamic behavior of lipid mixtures containing PG moieties. Regardless of whether the PG lipids are in the liquid or solid phase, DAP preferably interacts with this headgroup and is able to penetrate more deeply into the lipid bilayer in the regions where this headgroup is present. In particular, considering the results of an AFM/spectroscopy investigation, DAP appears to produce a stiffening effect of the domains where PG lipids are mainly in the fluid phase, whereas it causes fluidification of the domains where PG lipids are in the solid phase.

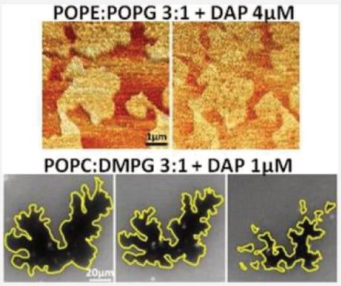

INTRODUCTION

The development of strategies to fight antimicrobial resistance is today a very active research field.[1−3] The effort aims to find new molecules capable of attacking bacteria and preventing the occurrence of their resistance mechanism as much as possible. To this end, much research has been devoted to the study of molecules that affect physical aspects of bacterial structures such as the barrier provided by their plasma membrane. In fact, the membrane plays a fundamental role in the vital processes of microbes, and any drug that influences its physical structure can be harmful to them and their effects can hardly be bypassed by redundant mechanisms or mutations. This is the case for many antimicrobial peptides (AMPs), whose effects on the lipid bilayer *in vitro* and *in vivo* have been extensively explored.[4−8] In fact, the first step on the way to the inactivation of pathogens by AMPs is the interaction with their cytoplasmic membranes and, typically, their permeabilization to relatively large molecules.[9−13] Apart from the formation of pores, other mechanisms of action have been suggested for AMPs and a combination of different processes is more plausible.[14] For example, it has been proposed that the AMPs activity could be related to their effect on the lipid domain organization within the bacterial membrane, including phase separation, variations in their fluidity and/or the formation of domains. These effects could be mainly a consequence of the selective grouping of anionic lipids and the lipid demixing induced by the AMPs.[15−20] The effect of AMPs on the formation of domains in bacterial membranes could for example alter both the partitioning of relevant membrane proteins and the membrane permeability by promoting ion leakage.[10,21] In some cases, the effect of AMPs could also be seen in the absence of permeabilization phenomena, at least as regards the formation of large pores. For example, the appearance, after interaction with AMPs, of two distinct peaks or the shift of the peaks in differential scanning calorimetry (DSC) experiments performed on lipid mixtures containing phosphatidylethanolamine (PE), phosphatidylglycerol (PG), and cardiolipin (CL), which are lipid headgroups typically present in bacterial membranes, could be explained by a stronger segregation of the different lipids.[18,19] The mechanistic explanation of this behavior could be related to the preferential electrostatic interactions between cationic peptides and anionic lipids such as PG. A related class

Received: July 20, 2020
Revised: September 4, 2020
Published: September 4, 2020

https://dx.doi.org/10.1021/acs.jpcb.0c06640
J. Phys. Chem. B 2020, 124, 8562−8571

of molecules of significant interest for their antimicrobial effect is represented by lipopeptides (LPs).[22,23] These are molecules in which a small number of amino acids organized in a linear or circular chain are connected to a lipid chain. For example, daptomycin (DAP), a cyclic LP active on Gram-positive bacteria, is the representative of the latest class of antibiotics that was introduced to the market in 2003.[24−27] Although negatively charged, DAP, in the presence of Ca^{2+}, has several aspects in common with AMPs as regards the interaction with lipid bilayers. For example, there are several pieces of evidence showing that its mechanism of action does not implicate any direct DAP−protein interactions and is related to the interaction with the bacterial membrane.[28−31] Indeed, the development of resistance is typically related to changes in the composition of the lipid membrane. In particular, in many cases, DAP-resistant bacteria present a significant decrease in the amount of lipids with PG headgroups and increased conversion of PG to Lys-PG.[32−34] The DAP mechanism of action requires the simultaneous presence of PG lipids and Ca^{2+} ions and involves the formation of a dimeric complex at a specific stoichiometric ratio,[35] both in bacteria and in lipid membrane model systems.[24,30,35−38] Interestingly, DAP has been recently demonstrated to specifically interact also with undecaprenyl-coupled cell wall precursors (lipid II) in the presence of PG lipids by forming a tripartite complex.[39] Considering the pivotal role of lipid II precursor in the enzymatic arrangement involved in peptidoglycan biosynthesis as well as in cell division, these findings offer an explanation about the cell wall synthesis inhibition observed in the presence of DAP; the mentioned interaction with lipid II precursor can induce the recruitment of fundamental protein complexes affecting physiological cellular processes. In several studies, it has been discovered that DAP, in the presence of Ca^{2+} ions, induces an increase in K^+ ions leakage which affects the difference in electrical potential across the membrane and the biosynthesis of basic molecules for the assembly of the cell wall,[28,40] even if it seems that DAP does not directly inhibit peptidoglycan synthesis.[41] Another possible scenario is linked to the DAP effect on the membrane curvature: in this case, the different geometries of some membrane regions could lead to a non-physiological distribution of specific membrane proteins, affecting their activity,[42] even if this mechanism of action has been questioned in other works.[43]

Interestingly, several *in vivo* studies have shown that the membrane depolarization in bacteria is just partially present when DAP is used at a typical minimum inhibitory concentration (MIC), but it can occur completely at much higher concentrations and, at the same time, this phenomenon has a slow kinetics.[44−46] This behavior is not consistent with the formation of ion channels by DAP. It has been recently shown that lethal DAP concentrations for different bacteria are able to affect the organization of bacterial membranes by altering the formation of fluid domains and, as an indirect effect, to inhibit cell wall synthesis.[42,43] Moreover, it has also been found that DAP is able to target fluid domains in the membrane and to produce a rigidification of the lipid bilayer, as revealed by an increase in the Laurdan general polarization signal.[43] From these studies, it appears that the presence of DAP in bacteria involves lipid segregation and alteration of lipid domains organization, particularly, domains where functionally relevant transmembrane proteins are located. All these effects are present when working at the MIC. Another recent investigation established that similar rules are valid also for model lipid bilayers assembled in the form of liposomes.[47] It has been discovered that the K^+ ions leakage is a transient phenomenon that appears just immediately after DAP is added to the solution, and the binding of DAP with the lipid bilayers depends on their thermodynamic phase state. Accordingly, further investigations on DAP effects on the thermodynamics and the organization of model lipid bilayers could be relevant to shed light on its mechanism of action on bacterial membranes, helping thus the development of new substitutes able to counter the bacterial resistance.

Here we studied, using fluorescence microscopy (FM) and atomic force microscopy (AFM)/spectroscopy, how DAP can affect the structure of supported lipid bilayers (SLBs) assembled with different lipid mixtures relevant in the context of bacterial membranes. Using the FM technique on SLBs, we can take the advantage of the presence of a kynurenine (Kyn 13) residue in DAP and its intrinsic fluorescent properties. In fact, even if the quantum yield is very low for this peptide (it increases when it is buried inside the lipid bilayer[37]), the stable configuration of a SLB allows the use of prolonged integration times for signal acquisition. The Kyn residue has already been exploited to obtain images of model lipid bilayers in the form of liposomes.[38] In the lipid bilayers studied by FM, we also included a fluorescent lipid probe which is known to preferentially partition into more fluid domains and whose fluorescence does not overlap with the intrinsic one of DAP. In this way, we are able to simultaneously detect the localization of more fluid domains and of DAP.[30] The use of AFM allows to distinguish the changes in the thermodynamic state of the bilayer by exploiting the presence of lipid domains characterized by different thicknesses (see Figure S1). Unlike FM, using AFM, it is possible to detect the formation of even nanometric domains if these are characterized by a different hydrophobic thickness and, using the related force spectroscopy capabilities,[48−51] it is possible to study the mechanical stability of the different lipid domains to understand if they are differently affected by the LP.

■ MATERIALS AND METHODS

Materials and Reagents. DAP was bought from Sigma-Aldrich Corporation (Saint Louis, MO, USA) and dissolved in dimethyl sulfoxide (DMSO) at its solubility limit (5 mg/mL). Final concentrations were then obtained by diluting the mother solution with distilled water. The amount of DMSO inside the imaging chambers at the final concentration does not affect the structure of SLBs. 1-palmitoyl-2-oleoyl-*sn*-glycero-3-phosphoethanolamine (POPE), 1-palmitoyl-2-oleoyl-*sn*-glycero-3-phosphocholine (POPC), 1-palmitoyl-2-oleoyl-*sn*-glycero-3-phospho-(1′-*rac*-glycerol) (POPG), and 1,2-dimyristoyl-*sn*-glycero-3-phospho-(1′-*rac*-glycerol) (DMPG) were all purchased from Avanti Polar Lipids, Inc. (Alabaster, USA). 1,2-dihexadecanoyl-*sn*-glycero-3-phosphoethanolamine-Texas Red (DHPE-Texas Red) was purchased from Life Technologies (Thermo Fisher, Carlsbad, CA, USA). Each lipid was dissolved in the proper amount of chloroform (Sigma-Aldrich Corporation) and then mixed with the other lipids of interest to create the desired lipid proportion. The lipid ratios in the reported mixtures must be considered as molar ratios. DHPE-Texas Red was included in the lipid mixtures at a molar concentration ranging from 0.5 to 1%.

SLBs Preparation Exploiting Small Unilamellar Vesicles. SLBs were prepared, exploiting the vesicle fusion technique on mica substrates starting form small unilamellar

https://dx.doi.org/10.1021/acs.jpcb.0c06640
J. Phys. Chem. B 2020, 124, 8562−8571

vesicles (SUVs).[52] Briefly, after transferring with glass syringes the right amount of lipids in chloroform in a small glass vial, the chloroform was evaporated under a gentle flow of nitrogen and under vacuum to obtain a complete removal of the solvent. Thin lipid films formed on the walls of the vial were then rehydrated with the proper amount of buffer solution (150 mM KCl, 8 mM HEPES, 3 mM $CaCl_2$, pH 7) and vortexed till their complete resuspension in the form of large multilamellar vesicles (LMVs) of various sizes. SUVs were then obtained by reducing the size of LMVs exploiting energy input in the form of sound energy (sonication) for 30 min at ∼ 40 °C. For FM, SLBs were assembled in a home-made chamber equipped with a temperature control system (see the Fluorescence Microscopy section) mounted on the microscope stage. It consisted of a polytetrafluoroethylene (PTFE-Teflon) drilled disk (with a diameter of 20 mm), equipped with an O-ring to keep the liquid solution confined inside; to avoid further liquid leakage, the outer edges were sealed with high vacuum grease (Dow Corning, USA). The bottom of the chamber was a freshly cleaved mica substrate (Supplies/Structure Probe, West Chester, PA) with a thickness that guarantees the best compromise between optical transparency and mechanical stability. SLBs for FM measurements have been prepared by adding 100 μL of the SUV suspension (0.25 mg/mL) to 1.5 mL of imaging buffer solution, whereas, for the AFM analysis, samples were prepared by depositing 70 μL of the SUV suspension onto the cleaved mica substrate. In both cases, lipids were incubated for 15 min at ∼40 °C and then vigorously rinsed with buffer solution before being analyzed.

As for the DAP concentration, we must emphasize that the method of preparation for SLBs does not allow to know the accurate surface percentage covered by the membrane and, at the same time, the exact packing density of the lipids in the bilayer is not known. Consequently, it is difficult to convert the concentration of DAP in the chamber into a specific lipid−LP ratio. Concerning the peptide-to-lipid ratio, we can consider a lower limit assuming a complete coverage of the chamber surface used for the experiments by the SLBs and a value of the lateral surface area-per-lipid taken from the literature. In the specific case of FM analysis, for the circular area of our chamber (diameter = 2 cm) and a volume of the solution of 1.5 mL, a DAP concentration of 1 μM corresponds to a peptide-to-lipid ratio of about 2:1. In the experiments we performed, we focused on what happens when the DAP is introduced into the imaging chamber and when its concentration is gradually increased. To characterize the experiments, we refer to the DAP concentration considering the volume of the imaging chamber. In all cases, we performed experiments with a DAP concentration lower than its critical aggregation concentration in the presence of Ca^{2+}, which is reported to be around 120 μM.[53]

Fluorescence Microscopy. Epifluorescent images were acquired using an Olympus IX 70 microscope equipped with a 20× or 40× objective (NA 0.4 and 0.75, respectively). All procedures were performed at minimal light exposure (using neutral filters) to avoid fluorophores' photobleaching. A CMOS camera (Hamamatsu ORCA-flash 4.0LT—C11440) connected to a computer was used to acquire images and videos. Excitation wavelengths at around 380 and 594 nm for Kyn 13 and Texas-Red, respectively, have been used. Emission wavelengths at around 450 nm for Kyn 13 and 615 nm for Texas Red were used. The home-made sample chamber was equipped with a temperature control system based on the use of a pair of Peltier cells. One surface of both Peltier cells was indirectly in contact with the sample (they were in direct contact with a thin metallic plate on which the mica was positioned). The opposite side of both Peltier cells was in contact with chambers where water with controlled temperature (Lauda-Brinkmann, Delran, NJ) was flowing. Peltier cells were connected to a custom-developed control unit using the proportional integral derivative feedback system provided by an Arduino microcontroller. The microcontroller is connected to a PC by USB port and interfaced to a custom-developed LabView program. The LabView control panel is used to manage the setpoint temperature and save the temperatures acquired by the thermocouple inserted in the home-made chamber. In this way, the system allowed fast cooling and heating ramps that were performed every time before the DAP insertion in order to have well-mixed and uniform lipid bilayers and avoid artifacts because of the thermal history of the sample. The public domain software ImageJ was used to analyze all images presented in the manuscript.

Atomic Force Microscopy/Spectroscopy. AFM analysis was performed with a BioScope I microscope equipped with a Nanoscope IIIA controller (Veeco Metrology, Plainview, NY, USA). A custom temperature-controlled stage based on a circulating water bath has been exploited to control sample temperature. The BioScope head was mounted on the home-developed stage. The sample's temperature was continuously monitored by a digital thermometer Fluke 16 (Fluke, Brugherio MB, Italy) equipped with a small K-thermocouple probe (Thermocoax, Heidelberg, Germany) in direct contact with the buffer solution. AFM was used in both imaging (tapping-mode) and force spectroscopy configurations using triangular silicon nitride cantilevers (Bruker DNP-S) with nominal spring constants of 0.32 N/m. Processing of AFM images was carried out using the free software Gwyddion (version 2.41). Force−distance ($F-D$) curves on SLBs and force−volume maps were analyzed using a home-developed software (Python). The algorithm we developed automatically finds, if present, the jump-through event in each curve at every specific point of the force−volume map. All jump-through events and their corresponding coordinates are recorded in order to reconstruct the jump-through force map.

■ RESULTS AND DISCUSSION

To design a suitable model system able to best mimic bacterial membrane properties, the complexity of membrane's architecture as well as the variance of lipid composition represent two fundamental aspects to be carefully considered. Bacterial membranes contain a huge assortment of lipids, including the common phospholipids PE, PG, and CL; for most bacteria, the predominant zwitterionic phospholipid is PE. Generally, Gram-negative bacteria show a higher content of PE than Gram-positive bacteria. Some Gram-positive bacteria have a very low content of zwitterionic phospholipids, even if some exceptions of Gram-positive bacteria with a high content of PE have been reported.[54] PG and CL represent the predominant anionic lipids in bacterial membranes. The total amount of anionic lipids present in all bacteria, be they Gram-negative or Gram-positive organism, is at least 15%. It is the presence of these anionic lipids that confer selectivity of the AMPs, generally cationic, against bacteria and not against mammalian cells. Considering Gram-positive membranes, although their lipid composition can vary from one species to another, they typically contain high amounts of anionic lipids such as PG and

https://dx.doi.org/10.1021/acs.jpcb.0c06640
J. Phys. Chem. B 2020, 124, 8562−8571

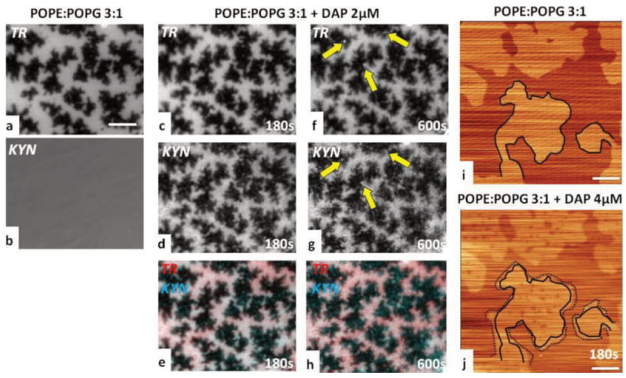

Figure 1. FM and AFM images of POPE/POPG 3:1 SLBs exposed to DAP at 20 °C. (a) SLB in phase separation comprising solid ordered domains (dark regions) in a liquid disordered background (bright region) rich in a fluorescence lipid probe (DHPE-Texas-Red). (b) Same region with signal absence from the KYN channel before interacting with DAP. (c–h) Fluorescence images of the same region in (a) exposed to 2 μM DAP and acquired after 180 s (c–e) and 600 s (f–h), respectively, exploiting TR and KYN channels and the overlapped image. Scale bar corresponds to 20 μm. (i) AFM topographic image of a POPE/POPG 3:1 SLB before and (j) 180 s after exposure to 4 μM DAP; full and dotted lines correspond to the domain boundaries before and after the interaction with 4 μM DAP, respectively. Scale bar is 1 μm.

they usually contain phospholipids species characterized by a high content of branched-fatty acids, which were shown to influence the activity of AMPs.[55]

With this understanding, we decided to exploit two different lipid model systems. As a first model system, we investigated the POPE/POPG 3:1 (molar proportion) lipid mixture. The POPE/POPG mixture is a well-studied system with regard to its phase behavior,[56] and the presence of the PG headgroup allows one to investigate the specific interaction with DAP. The POPE/POPG mixture has a phase transition temperature which depends on the molar proportion of the two components, going from about 23 °C in the case of pure POPE to a temperature lower than 0 °C for pure POPG. When the bilayer is in phase separation, the liquid disordered regions are rich in POPG, whereas solid ordered regions are rich in POPE, with a non-ideal mixing in the solid phase.[56] The phase diagram of the POPE/POPG 3:1 lipid mixture allows rough quantification of the distribution of PG lipid between the two phases at 20 °C, around 15% for the solid regions and 38% for liquid regions, respectively.[56] When this model system is assembled in the form of SLBs, a small shift to higher temperatures (2–3 °C) of the main phase transition could be found due to the interaction of the bilayer, in particular the proximal leaflet, with the substrate which, in all cases in this work was mica.[57,58] Figure 1a shows a FM image of a POPE/POPG 3:1 SLB at a temperature of 20 °C using the fluorescence signal coming from the lipid probe (DHPE-Texas-Red, in the following TR). The image shows the presence of solid ordered domains (darker regions) embedded in a liquid disordered background (brighter regions), as expected from the phase diagram of the lipid mixture at issue. If the signal is taken from the channel at about 445 nm (maximum emission wavelength of the Kyn residue, in the following KYN), no contrast is observed (Figure 1b). Figure 1c–e represents FM images acquired on the same area of panel (1a) 180 s after the injection of 2 μM DAP for the TR and KYN channels, together with the corresponding merged images. As expected, considering the KYN signal (Figure 1d), DAP mainly interacts with the PG-rich region, corresponding to the disordered liquid phase, and the regions producing the two fluorescence signals mainly coincide. However, it is possible to see an apparent expansion of the solid ordered domains rich in PE at the expense of the disordered region, quantified at around 45%. This behavior could be ascribed to the surplus of lateral pressure resulting from the insertion of DAP into the liquid disordered phase of the bilayer and from the consequently induced lateral expansion. In fact, in the case of SLBs, a prevented or limited expansion of the bilayer lateral area because of the interaction with the substrate could produce an increase in the lateral pressure in the bilayer and an enlargement of the solid regions.[59,60] FM images taken 600 s after DAP injection (1f–h) reveal the formation of bright spots especially along the boundaries of solid domains. The spots formed are brighter in both fluorescence channels, TR as well as KYN, as indicated by the yellow arrows. This evidence suggests an aggregation of lipids together with DAP consistent with a sort of lipid extraction mechanism, as suggested in previous investigations.[30] Furthermore, the occurrence of these spots along the boundaries of solid domains probably points to a phenomenon favored by the presence of defects in the bilayer. The increased fluorescence cannot be simply explained by the increased penetration of the KYN residue into the hydrophobic environment of the bilayer because we have also observed an increase in the TR fluorescence for these spots. We also observed the prevalence of the KYN signal in some spots embedded in the solid regions (Figure 1g). It is important to emphasize that all these phenomena are not observed if the experiments are performed in the absence of Ca^{2+}. In order to see the consequences on the phase organization at higher spatial resolution, the DAP effect on SLBs has also been studied by AFM. Panels (1i) and (1j) show topographic images of POPE/POPG 3:1 SLBs at a temperature of 20 °C before and after DAP insertion to reach a final concentration of 4 μM; an expansion of the external boundaries of solid phase domains, in association with a partial lipid fluidification within the domains, is clearly observable. The observed fluidification could reasonably be ascribed to the clustering of the PG

https://dx.doi.org/10.1021/acs.jpcb.0c06640
J. Phys. Chem. B 2020, 124, 8562–8571

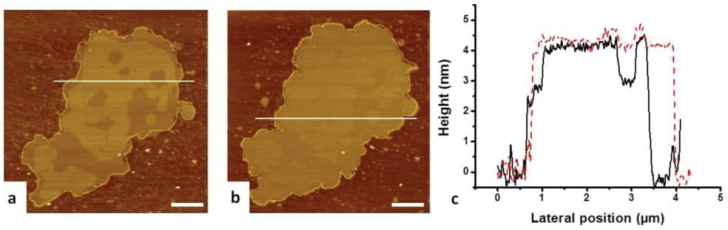

Figure 2. AFM images and relative height profiles of POPE/POPG 3:1 SLB, prepared as a bilayer patch, exposed to DAP at 20 °C. (a) Topographic image of the bilayer patch. (b) Same patch as in (a) after its exposure to 8 μM DAP concentration. (c) Averaged profiles of the two images relative to the regions highlighted by a white line in both images [continuous black line for (a) and dashed red line for (b)]. Scale bar is 1 μm.

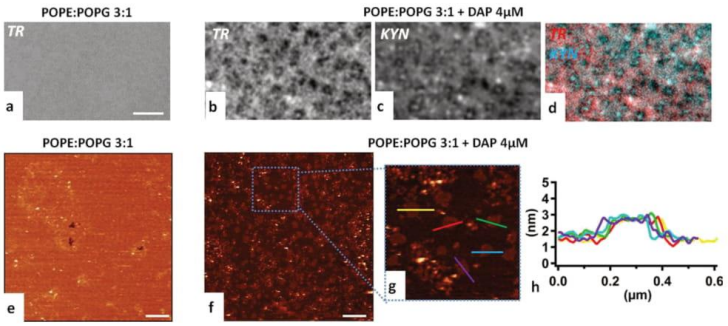

Figure 3. FM and AFM images of POPE/POPG 3:1 SLBs at 25 °C exposed to 4 μM DAP; (a) completely homogeneous SLB. (b,c) Fluorescence images of the same region in (a) after exposure to a 4 μM DAP concentration, as seen from TR and KYN channels, respectively, and (d) overlapped image. Scale bar corresponds to 10 μm; (e) topographic image of a SLB and the (f) same region after exposure to a 4 μM DAP concentration. (g) Magnification of the 2 × 2 μm^2 region corresponding to the blue dotted rectangle in (f). Scale bars correspond to 1 μm; (h) height profiles reconstruction of five randomly selected solid domains. The height of the newly formed solid domains is ≈1.0 nm.

fraction within solid domains by means of DAP.[22,61,62] This behavior is consistent with the appearance of the KYN signal from the solid region, as shown in Figure 1g. At the same time, the enlargement of the external boundaries of the solid domains could be the result of the fluidification of the PG moieties inside solid domains.

AFM does not provide direct analytical information to evaluate the order of lipid domains with the aim of analyzing whether DAP is affecting it. However, an indirect method frequently exploited to have an indication of changes in the lipid order is to measure the changes in the domain's thickness. If we consider the images in Figure 1i,j, we obtain that the difference in height between the liquid and solid domains decreases from (0.46 ± 0.04) to (0.24 ± 0.05) nm after the interaction with DAP, highlighting the fact that they become more similar to each other. However, to get an idea of the absolute variation in the height of the domain, we need to also image the solid substrate, exploiting bilayer patches instead of uniformly covered substrates. Furthermore, although the increase in the lateral area in SLBs could be limited by the interaction of the bilayer with the substrate (see Figure S2 for an example of the consequence of the presence of the substrate), this situation could be partially reduced if the experiments were performed on bilayer patches instead of on complete bilayers.[60,63] Accordingly, we performed AFM analysis on POPE/POPG 3:1 patches and Figure 2 reports a typical example. In this case, after exposing the lipid bilayer patch to a DAP concentration equal to 8 μM, we observe an increase in the global area of the patch of about 20% and an increase also in the area occupied by the solid domains. This result points to the fact that the increase in the solid domains could also be due to the other factors besides the fluidification within the domains, as shown in Figure 1i. We can speculate that, apart from the formation of clusters of POPG lipids followed by their fluidification within solid domains and part of the POPE lipids from the liquid domains that join solid domains, we have a general rigidification of the bilayer and an enlargement because of the incorporation of DAP. In the case of a patch, we can measure the thickness of both domains, liquid and solid, relative to the substrate, together with the difference between the two domains. In the case of the patch of Figure 2, we found that both types of domains become thicker when DAP is inserted (Figure 2c). This situation could be explained by an increase in the order of lipids in both phases, with a greater increase in the case of liquid domains rich in PG where DAP is mainly concentrated. Indeed, the height difference between the two domains decreases, as shown in Figure 1h,i. If the DAP concentration is increased, a saturation effect is obtained for the height variation and, in the specific case of Figure 2, for concentrations from 10 μM up to 20 μM, no variations in the thickness of the lipid domains are observed. Unlike AMPs, even a high LP concentration (20 μM) is not able to destroy the double-layer structure of the membrane. These observations suggest that DAP can produce

https://dx.doi.org/10.1021/acs.jpcb.0c06640
J. Phys. Chem. B 2020, 124, 8562−8571

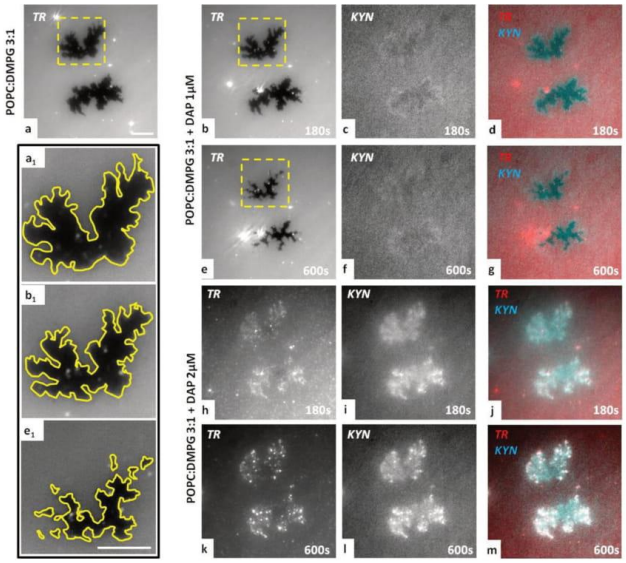

Figure 4. FM images of POPC/DMPG 3:1 SLBs at 20 °C exposed to a concentration of 1 and 2 μM DAP. (a) SLB in phase separation showing two solid ordered domains (dark regions) in a liquid disordered background (bright region) rich in the fluorescence lipid probe (DHPE-Texas-Red). (b–g) Fluorescence images of the same region in (a) exposed to a concentration of 1 μM DAP acquired after 180 s (b–d) and 600 s (e–g) obtained from TR, KYN, and overlapped channels, respectively. (h–m) Fluorescence images of the same region in (a) exposed to a concentration of 2 μM DAP, acquired after 180 s (h–j) and 600 s (k–m), from TR, KYN, and overlapped channels, respectively. (a_1,b_1,e_1) Highlighted boundaries of the solid ordered domain inside the dashed square in (a) before (a_1) and after interaction with 1 μM DAP after 180 s (b_1) and 600 s (e_1). Scale bars correspond to 40 μm.

an increase in the lateral area of the lipid bilayer and an increase in the lipid order. This effect recalls of the rigidification effect observed in the case of bacteria.[43] At the same time, a strong reorganization of the domain distribution is observed when the DAP concentration is increased (see Figure S3 for another example of domain reorganization induced by DAP). It is to be stressed that, in the case of many AMPs, their interaction with the lipid bilayer causes a decrease in the order as well as thickness of the bilayer. The results obtained with DAP are similar to those obtained in analogous investigations with surfactin, another LP.[64] In ref 64, it was found that the surfactin insertion into DOPC and DPPC lipid bilayers induced an increase in the lipid order, as revealed by Laurdan. The behavior resembles what happens when cholesterol is inserted in a lipid bilayer. At the same time, surfactin started to interact with the lipid bilayer from the boundaries of the domain.

We then considered the influence of DAP on a specific aspect of the thermodynamic behavior of the POPE/POPG 3:1 lipid mixture; in particular, keeping the temperature slightly above the melting one ($T \approx 25$ °C), DAP was inserted in the imaging chamber. Under these conditions, at the beginning of the experiment, the system is totally fluid, as confirmed by the absence of darker regions (Figure 3a) using FM and the observation of a substantially homogeneous flat bilayer using AFM (Figure 3e). The DAP injection at a concentration of 4 μM induces a strong rearrangement of the SLB inducing the formation of solid domains. In fact, Figure 3b–d reveals the different fluorescent signals coming from TR, KYN, and merged channels. In particular, solid domains in the TR signal are observed. It is shown as the phase transition region of the bilayer shifted to a higher temperature and, keeping the bilayer at a constant temperature, it entered the phase transition region. A similar behavior has been obtained for a POPE/TOCL SLB exposed to PR-9 peptides, investigated by AFM and polarized total internal reflection FM.[65] Furthermore, it is possible to note the presence of spherical aggregates at the center of solid domains which show a higher fluorescence intensity in both channels. These observations allow us to hypothesize that DAP, by recruiting and forming co-clusters of DAP–POPG lipids, promotes the solidification of POPE-rich domains above the melting temperature of the pure lipid mixture. An analogous result is obtained studying the behavior of the bilayer by AFM, as shown in Figure 3e–g. Indeed, it is possible to clearly notice the formation of solid domains having dimensions of the order of tens of nanometers in diameter consequent to DAP insertion (Figure 3f,g). Height profiles of solid domains are shown in panel (3h) and height differences are in the range of 1 nm, in agreement with the solid phase separation. These findings are biologically relevant if we consider that bacterial membranes in physiological conditions are in the fluid phase but very near to the main phase transition, and this condition is assured even in the case of a variation of the growth temperature by adjusting the lipid composition.[66] Accordingly, even a small amount of DAP could induce a lipid phase transition greatly affecting the membrane structure.

As a second model system, the POPC/DMPG 3:1 lipid mixture was considered. The choice of this lipid mixture has been dictated by its phase transition behavior which allows to

https://dx.doi.org/10.1021/acs.jpcb.0c06640
J. Phys. Chem. B 2020, 124, 8562–8571

obtain solid domains rich in PG at around 15 °C unlike the previous case; in fact, at this temperature, because of the different melting behavior of the two lipids, the system is in phase separation, with POPC-rich liquid disordered regions and DMPG-rich solid ordered regions. Now, PG headgroups are in the solid phase. Figure 4a shows an experiment that has been performed at constant temperature on a system in phase separation by adding DAP initially at the concentration of 1 μM, followed by another injection of the LP to reach the concentration of 2 μM. Considering that, apart from concentration, the kinetics of DAP/lipid bilayer is also a relevant aspect, we reported the images as a function of the time since injection: in particular, after 180 and 600 s. The second DAP injection has been made after 600 s, when the lipid system appeared as stable and no further significant changes were recorded. We initially observed a slightly higher presence of DAP on liquid phosphatidylcholine (PC) domains than on PG domains. This could be due to the KYN residue being able to better approach the hydrophobic region on less dense bilayers. A basal binding of DAP to neutral membranes exposing PC groups in SLBs was also observed in other investigations.[39] However, this initial situation was followed by a strong interaction between DAP and solid PG lipids, together with a gradual fluidization of solid domains edges, as deduced from the TR signal (see also Figure S4). Figure 4a_1−e_1 shows an extensive size reduction of the solid domains, equal to 59%, after the interaction with DAP at the concentration of 1 μM. Over time, it is possible to observe an increase of the fluorescent signal because of DAP along the edges of solid domains.

This behavior could be explained by a DAP-induced fluidification of the solid lipid domains which is initially stronger at the edges because of the higher lipid disorder in these regions. The fluidization induces a higher penetration of the TR lipid probe. In turn, the increase in the fluorescent signal from DAP could be related to a greater penetration of the LP into the hydrophobic region of the lipid bilayer. When the DAP concentration is increased to 2 μM (Figure 4h−m), the previously solid domains seem to enrich in DAP, as deduced from the increase of the KYN fluorescent signal and, if the overall fluorescence signal coming from the DAP is considered, the domains restored their initial area. However, if we consider the signal from TR, the lipid domains become visible again, but they appear as brighter with respect to the background. This behavior is ascribable to the appearance of bright spots in both fluorescence signals, reasonably due to the interaction between DAP and PG-fused moieties and the extraction mechanisms previously mentioned. Therefore, DAP interacts with PG moieties regardless of their physical state by promoting fluidization in PG-rich domains starting from their boundaries when this type of lipid is in the solid phase and a rigidification when this type of lipid is in the liquid phase. From these results, it emerges that PG is probably the moiety that allows DAP to penetrate deeply into the lipid bilayer, in contrast with PC moieties, for example, and this ability does not depend on the thermodynamic state of the lipids. In the case of different proportions of the same mixture (POPC/DMPG 1:1), we obtained a similar behavior. In another experiment, we exploited AFM to shed light on the effect of DAP on the edges of solid domains in the POPC/DMPG 1:1 mixture. We observed a sharp increase in the length of the edges and the formation of finger-like structures, as shown in Figure 5. The observed behavior suggests a decrease in the line tension because of the hydrophobic mismatch between the different domains, as already obtained for other LPs.[64] This result agrees with the observation of a strong increase of the fluorescent intensity due to DAP along the boundaries of the domains.

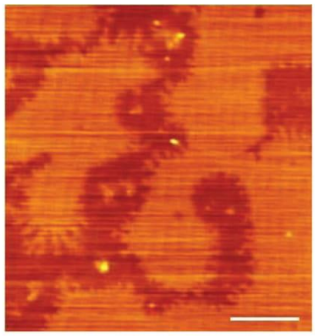

Figure 5. AFM image of POPC/DMPG 1:1 SLBs at 15 °C exposed to a concentration of 8 μM DAP. Finger-like structures at the boundaries of the domains when they are exposed to DAP reveal a preferential interaction of DAP with the domain boundaries. Scale bar is 1 μm.

To obtain further information on the fluidization or solidification of lipid domains by DAP, we also investigated the mechanical stability of SLBs using force spectroscopy measurements. The typical jump-through force obtained in force−distance curves on SLBs by AFM is considered to be a marker of the fluctuations in the lipid bilayer, and it could provide hints on the mechanical and order properties of the bilayer.[50] In the case of the AMPs interaction with lipid bilayers, the force spectroscopy technique has already been used, revealing the action of peptides on the order of the lipids in the membrane.[60,67] We concentrated on the POPC/DMPG 1:1 mixture, and the data in Figure 6 show the results. Upon the addition of DAP, we observe an initial increase in the jump-through force for both types of domains (Figure 6b,b_1,d). This behavior points to an initial rigidification of the bilayer, equivalent to an increase of the lipid order. A parallel could be established with an initial increase of bilayer bending constant that has been observed when AMPs interact with model lipid bilayers that mimic bacterial composition.[68] Upon increasing DAP concentrations, we observed a decrease of the jump-through force for both domains (Figure 6c,c_1,d), corresponding to a fluidification of the domains. By measuring the domain height from the topographic images of the patch, we observed that for the fluid domains, at a DAP concentration of 4 μM, it was (4.7 ± 0.5) nm compared to (6.5 ± 0.6) nm in the control bilayer, whereas for the solid domains, it was (5.7 ± 0.6) nm with respect to (7.0 ± 0.4) nm in the control. The decrease in the height of the domain is in accordance with a decrease in the jump-through force. Moreover, the interaction of DAP with the solid domains produces regions of decreased bilayer thickness and an enlargement of the area delimited by the external boundary of the domain (see Figure 6e,f). This behavior could be interpreted as a demixing of the different lipids in the domains, producing clusters of more solid PG lipids and a fluidification of the remaining PC lipids.

https://dx.doi.org/10.1021/acs.jpcb.0c06640
J. Phys. Chem. B 2020, 124, 8562−8571

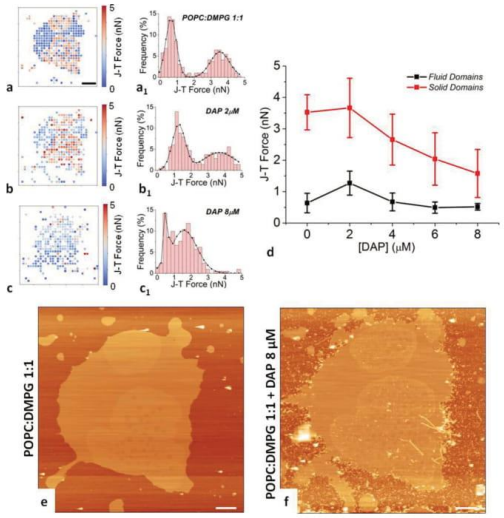

Figure 6. Force spectroscopy analysis and AFM images of a POPC/DMPG 1:1 SLB exposed to increasing DAP concentrations (2, 4, 6, and 8 μM). (a,a_1) Jump-through force maps and the corresponding histogram distribution (red pattern) with the corresponding Gaussian fitting (black) of jump-through events for pure SLB and after the exposure to 2 μM (b,b_1) and 8 μM (c,c_1) DAP concentrations; maps resolution (32 × 32 pixels); scale bar corresponds to 2 μm. The evaluation of the peak value, and its error, has been performed applying a double Gaussian fit to the experimental data. (d) Comparison of solid and fluid domains jump-through force upon increasing concentrations of DAP. (e) Topographic image of SLB before and after (f) exposure to a 8 μM concentration of DAP. Scale bars correspond to 1 μm.

CONCLUSIONS

The present study showed that DAP interacts with phase-separated lipid bilayers, producing a strong modification of their phase state. We found that DAP preferentially interacts with domains rich in PG lipids, regardless of whether their phase state is fluid or solid. It appears that PG allows DAP to access more deeply into the lipid bilayer producing a change in its phase state. However, whereas in the case of PG lipid in the fluid phase, DAP induces a stiffening in the bilayer with an increase in solid domains, probably due to lipid demixing, when PG lipids represent the solid fraction of the bilayer, DAP produces a fluidification. The observed behavior is similar to what cholesterol produces on lipid bilayers. Analogously, a similar behavior has been suggested for another LP, surfactin.[64] The preferential interaction of DAP with PG headgroups could be related to the ability of the LP to affect the configuration of the hydrogen bond networks of lipid headgroups. The main effect of DAP on lipid bilayers would be to modify their phase state by affecting, in bacteria, the distribution of proteins relevant for essential processes. The observed transient ionic flux observed in model bilayers could be due to the strong reorganization of the bilayer structure induced by the LP and may not be strictly related to the length of the domain boundaries. Even in the absence of domains, the lipid flip-flop due to the initial binding of DAP on the external leaflet of the bilayer could in part explain the observed transient transmembrane ion current.

ASSOCIATED CONTENT

Supporting Information

The Supporting Information is available free of charge at https://pubs.acs.org/doi/10.1021/acs.jpcb.0c06640.

AFM topographic image and FM image of a POPE/POPG 3:1 + 1% DHPE-Texas-Red SLB on mica; POPE/POPG 3:1 SLB imaged at 20°C; and FM image of a POPC/DMPG 3:1 + 1% DHPE-Texas Red (PDF)

AUTHOR INFORMATION

Corresponding Author

Andrea Mescola − *CNR-Nanoscience Institute-S3, 41125 Modena, Italy;* orcid.org/0000-0002-1667-7564; Phone: +39 059 2055191; Email: andrea.mescola@nano.cnr.it

Authors

Gregorio Ragazzini − *CNR-Nanoscience Institute-S3, 41125 Modena, Italy; Department of Physics, Informatics and Mathematics, University of Modena and Reggio Emilia, 41125 Modena, Italy*

Andrea Alessandrini − *CNR-Nanoscience Institute-S3, 41125 Modena, Italy; Department of Physics, Informatics and Mathematics, University of Modena and Reggio Emilia, 41125 Modena, Italy*

Complete contact information is available at: https://pubs.acs.org/10.1021/acs.jpcb.0c06640

Notes

The authors declare no competing financial interest.

REFERENCES

(1) Neill, J. O. *Antimicrobial Resistance: Tackling a Crisis for the Health and Wealth of Nations The Review on Antimicrobial Resistance Chaired*; HM Gov. Wellcome Trust, 2014; pp 1−20.

(2) Thabit, A. K.; Crandon, J. L.; Nicolau, D. P. Antimicrobial resistance: impact on clinical and economic outcomes and the need for new antimicrobials. *Expert Opin. Pharmacother.* **2015**, *16*, 159−177.

(3) Molbak, K. Spread of resistant bacteria and resistance genes from animals to humans—The public health consequences. *J. Vet. Med., Ser. B* **2004**, *51*, 364−369.

(4) Hollmann, A.; Martinez, M.; Maturana, P.; Semorile, L. C. Antimicrobial Peptides : Interaction With Model and Biological Membranes and Synergism With Chemical Antibiotics. *Front. Chem.* **2018**, *6*, 204.

(5) Zhang, L.-J.; Gallo, R. L. Antimicrobial peptides. *Curr. Biol.* **2016**, *26*, R14−R19.

(6) Steiner, H.; Hultmark, D.; Engström, Å.; Bennich, H.; Boman, H. G. Sequence and specificity of two antibacterial proteins involved in insect immunity. *Nature* **1981**, *292*, 246−248.

(7) Jenssen, H.; Hamill, P.; Hancock, R. E. W. Peptide Antimicrobial Agents. *Clin. Microbiol. Rev.* **2006**, *19*, 491−511.

(8) Wimley, W. C. Describing the Mechanism of Antimicrobial Peptide Action with the Interfacial Activity Model. *ACS Chem. Biol.* **2010**, *5*, 905−917.

(9) Matsuzaki, K.; Sugishita, K. I.; Harada, M.; Fujii, N.; Miyajima, K. Interactions of an antimicrobial peptide, magainin 2, with outer and inner membranes of Gram-negative bacteria. *Biochim. Biophys. Acta, Biomembr.* **1997**, *1327*, 119−130.

(10) Fuertes, G.; Giménez, D.; Esteban-Martín, S.; Sánchez-Muñoz, O. L.; Salgado, J. A lipocentric view of peptide-induced pores. *Eur. Biophys. J.* **2011**, *40*, 399−415.
(11) Huang, H. W.; Charron, N. E. Understanding membrane-active antimicrobial peptides. *Q. Rev. Biophys.* **2017**, *50*, No. e10.
(12) Almeida, P. F. Membrane-active peptides: Binding, translocation, and flux in lipid vesicles. *Biochim. Biophys. Acta, Biomembr.* **2014**, *1838*, 2216−2227.
(13) Mescola, A.; Marín-Medina, N.; Ragazzini, G.; Accolla, M.; Alessandrini, A. Magainin-H2 effects on the permeabilization and mechanical properties of giant unilamellar vesicles. *J. Colloid Interface Sci.* **2019**, *553*, 247−258.
(14) Brogden, K. A. Antimicrobial peptides: pore formers or metabolic inhibitors in bacteria? *Nat. Rev. Microbiol.* **2005**, *3*, 238−250.
(15) Epand, R. M.; Epand, R. F. Lipid domains in bacterial membranes and the action of antimicrobial agents. *Biochim. Biophys. Acta, Biomembr.* **2009**, *1788*, 289−294.
(16) Omardien, S.; Drijfhout, J. W.; Vaz, F. M.; Wenzel, M.; Hamoen, L. W.; Zaat, S. A. J.; Brul, S. Bactericidal activity of amphipathic cationic antimicrobial peptides involves altering the membrane fluidity when interacting with the phospholipid bilayer. *Biochim. Biophys. Acta, Biomembr.* **2018**, *1860*, 2404−2415.
(17) Scheinpflug, K.; Wenzel, M.; Krylova, O.; Bandow, J. E.; Dathe, M.; Strahl, H. Antimicrobial peptide cWFW kills by combining lipid phase separation with autolysis. *Sci. Rep.* **2017**, *7*, 44332.
(18) Arouri, A.; Dathe, M.; Blume, A. Peptide induced demixing in PG/PE lipid mixtures: A mechanism for the specificity of antimicrobial peptides towards bacterial membranes? *Biochim. Biophys. Acta, Biomembr.* **2009**, *1788*, 650−659.
(19) Wadhwani, P.; Epand, R. F.; Heidenreich, N.; Bürck, J.; Ulrich, A. S.; Epand, R. M. Membrane-Active Peptides and the Clustering of Anionic Lipids. *Biophys. J.* **2012**, *103*, 265−274.
(20) Joanne, P.; Galanth, C.; Goasdoué, N.; Nicolas, P.; Sagan, S.; Lavielle, S.; Chassaing, G.; El Amri, C.; Alves, I. D. Lipid reorganization induced by membrane-active peptides probed using differential scanning calorimetry. *Biochim. Biophys. Acta, Biomembr.* **2009**, *1788*, 1772−1781.
(21) Oliva, R.; Del Vecchio, P.; Grimaldi, A.; Notomista, E.; Cafaro, V.; Pane, K.; Schuabb, V.; Winter, R.; Petraccone, L. Membrane disintegration by the antimicrobial peptide (P)GKY20: lipid segregation and domain formation. *Phys. Chem. Chem. Phys.* **2019**, *21*, 3989−3998.
(22) Balleza, D.; Alessandrini, A.; Beltrán García, M. J. Role of Lipid Composition, Physicochemical Interactions, and Membrane Mechanics in the Molecular Actions of Microbial Cyclic Lipopeptides. *J. Membr. Biol.* **2019**, *252*, 131−157.
(23) Balleza, D.; Mescola, A.; Alessandrini, A. Model lipid systems and their use to evaluate the phase state of biomembranes, their mechanical properties and the effect of non-conventional antibiotics: the case of daptomycin. *Eur. Biophys. J.* **2020**, *49*, 401−408.
(24) Taylor, S. D.; Palmer, M. The action mechanism of daptomycin. *Bioorg. Med. Chem.* **2016**, *24*, 6253−6268.
(25) Steenbergen, J. N.; Alder, J.; Thorne, G. M.; Tally, F. P. Daptomycin: a lipopeptide antibiotic for the treatment of serious Gram-positive infections. *J. Antimicrob. Chemother.* **2005**, *55*, 283−288.
(26) Kern, W. V. Daptomycin: first in a new class of antibiotics for complicated skin and soft-tissue infections. *Int. J. Clin. Pract.* **2006**, *60*, 370−378.
(27) Eliopoulos, G. M.; Willey, S.; Reiszner, E.; Spitzer, P. G.; Caputo, G.; Moellering, R. C. In vitro and in vivo activity of LY 146032, a new cyclic lipopeptide antibiotic. *Antimicrob. Agents Chemother.* **1986**, *30*, 532−535.
(28) Silverman, J. A.; Perlmutter, N. G.; Shapiro, H. M. Correlation of Daptomycin Bactericidal Activity and Membrane Depolarization in Staphylococcus aureus. *Antimicrob. Agents Chemother.* **2003**, *47*, 2538−2544.
(29) Tran, T. T.; Munita, J. M.; Arias, C. A. Mechanisms of drug resistance: daptomycin resistance. *Ann. N.Y. Acad. Sci.* **2015**, *1354*, 32−53.
(30) Chen, Y. F.; Sun, T. L.; Sun, Y.; Huang, H. W. Interaction of daptomycin with lipid bilayers: A lipid extracting effect. *Biochemistry* **2014**, *53*, 5384−5392.
(31) Huang, H. W. DAPTOMYCIN, its membrane-active mechanism vs. that of other antimicrobial peptides. *Biochim. Biophys. Acta, Biomembr.* **2020**, *1862*, 183395.
(32) Hachmann, A.-B.; Angert, E. R.; Helmann, J. D. Genetic Analysis of Factors Affecting Susceptibility of Bacillus subtilis to Daptomycin. *Antimicrob. Agents Chemother.* **2009**, *53*, 1598−1609.
(33) Hachmann, A.-B.; Sevim, E.; Gaballa, A.; Popham, D. L.; Antelmann, H.; Helmann, J. D. Reduction in Membrane Phosphatidylglycerol Content Leads to Daptomycin Resistance in Bacillus subtilis. *Antimicrob. Agents Chemother.* **2011**, *55*, 4326−4337.
(34) Miller, W. R.; Bayer, A. S.; Arias, C. A. Mechanism of Action and Resistance to Daptomycin in Staphylococcus aureus and Enterococci. *Cold Spring Harbor Perspect. Med.* **2016**, *6*, a026997.
(35) Lee, M. T.; Hung, W. C.; Hsieh, M. H.; Chen, H.; Chang, Y. Y.; Huang, H. W. Molecular State of the Membrane-Active Antibiotic Daptomycin. *Biophys. J.* **2017**, *113*, 82−90.
(36) Lakey, J. H.; Maget-Dana, R.; Ptak, M. The lipopeptide antibiotic A21978C has a specific interaction with DMPC only in the presence of calcium ions. *Biochim. Biophys. Acta, Biomembr.* **1989**, *985*, 60−66.
(37) Lakey, J. H.; Ptak, M. Fluorescence indicates a calcium-dependent interaction between the lipopeptide antibiotic LY 146032 and phospholipid membranes. *Biochemistry* **1988**, *27*, 4639−4645.
(38) Kreutzberger, M. A.; Pokorny, A.; Almeida, P. F. Daptomycin-Phosphatidylglycerol Domains in Lipid Membranes. *Langmuir* **2017**, *33*, 13669−13679.
(39) Grein, F.; Müller, A.; Scherer, K. M.; Liu, X.; Ludwig, K. C.; Klöckner, A.; Strach, M.; Sahl, H.-G.; Kubitscheck, U.; Schneider, T. Ca^{2+}-Daptomycin targets cell wall biosynthesis by forming a tripartite complex with undecaprenyl-coupled intermediates and membrane lipids. *Nat. Commun.* **2020**, *11*, 1455.
(40) Allen, N. E.; Hobbs, J. N.; Alborn, W. E. Inhibition of peptidoglycan biosynthesis in gram-positive bacteria by LY146032. *Antimicrob. Agents Chemother.* **1987**, *31*, 1093−1099.
(41) Tantibhedhyangkul, W.; Wongsawat, E.; Matamnan, S.; Inthasin, N.; Sueasuay, J.; Suputtamongkol, Y. Anti-mycoplasma activity of daptomycin and its use for mycoplasma elimination in cell cultures of rickettsiae. *Antibiotics* **2019**, *8*, 123.
(42) Pogliano, J.; Pogliano, N.; Silverman, J. A. Daptomycin-Mediated Reorganization of Membrane Architecture Causes Mislocalization of Essential Cell Division Proteins. *J. Bacteriol.* **2012**, *194*, 4494−4504.
(43) Müller, A.; Wenzel, M.; Strahl, H.; Grein, F.; Saaki, T. N. V.; Kohl, B.; Siersma, T.; Bandow, J. E.; Sahl, H.-G.; Schneider, T.; et al. Daptomycin inhibits cell envelope synthesis by interfering with fluid membrane microdomains. *Proc. Natl. Acad. Sci. U.S.A.* **2016**, *113*, E7077−E7086.
(44) Cotroneo, N.; Harris, R.; Perlmutter, N.; Beveridge, T.; Silverman, J. A. Daptomycin exerts bactericidal activity without lysis of Staphylococcus aureus. *Antimicrob. Agents Chemother.* **2008**, *52*, 2223−2225.
(45) Hobbs, J. K.; Miller, K.; O'Neill, A. J.; Chopra, I. Consequences of daptomycin-mediated membrane damage in Staphylococcus aureus. *J. Antimicrob. Chemother.* **2008**, *62*, 1003−1008.
(46) Mensa, B.; Howell, G. L.; Scott, R.; DeGrado, W. F. Comparative mechanistic studies of brilacidin, daptomycin, and the antimicrobial peptide LL16. *Antimicrob. Agents Chemother.* **2014**, *58*, 5136−5145.
(47) Lee, M.-T.; Yang, P.-Y.; Charron, N. E.; Hsieh, M. H.; Chang, Y. Y.; Huang, H. W. Comparison of the Effects of Daptomycin on Bacterial and Model Membranes. *Biochemistry* **2018**, *57*, 5629−5639.

https://dx.doi.org/10.1021/acs.jpcb.0c06640
J. Phys. Chem. B 2020, 124, 8562−8571

(48) Alessandrini, A.; Seeger, H. M.; Caramaschi, T.; Facci, P. Dynamic Force Spectroscopy on Supported Lipid Bilayers: Effect of Temperature and Sample Preparation. *Biophys. J.* **2012**, *103*, 38−47.
(49) Alessandrini, A.; Facci, P. Phase transitions in supported lipid bilayers studied by AFM. *Soft Matter* **2014**, *10*, 7145−7164.
(50) Alessandrini, A.; Seeger, H. M.; Di Cerbo, A.; Caramaschi, T.; Facci, P. What do we really measure in AFM punch-through experiments on supported lipid bilayers? *Soft Matter* **2011**, *7*, 7054.
(51) Garcia-Manyes, S.; Sanz, F. Nanomechanics of lipid bilayers by force spectroscopy with AFM: A perspective. *Biochim. Biophys. Acta, Biomembr.* **2010**, *1798*, 741−749.
(52) Tamm, L. K.; McConnell, H. M. Supported phospholipid bilayers. *Biophys. J.* **1985**, *47*, 105−113.
(53) Qiu, J.; Kirsch, L. E. Evaluation of Lipopeptide (Daptomycin) Aggregation Using Fluorescence, Light Scattering, and Nuclear Magnetic Resonance Spectroscopy. *J. Pharm. Sci.* **2014**, *103*, 853−861.
(54) Epand, R. F.; Savage, P. B.; Epand, R. M. Bacterial lipid composition and the antimicrobial efficacy of cationic steroid compounds (Ceragenins). *Biochim. Biophys. Acta, Biomembr.* **2007**, *1768*, 2500−2509.
(55) Mitchell, N. J.; Seaton, P.; Pokorny, A. Branched phospholipids render lipid vesicles more susceptible to membrane-active peptides. *Biochim. Biophys. Acta, Biomembr.* **2016**, *1858*, 988−994.
(56) Pozo Navas, B.; Lohner, K.; Deutsch, G.; Sevcsik, E.; Riske, K. A.; Dimova, R.; Garidel, P.; Pabst, G. Composition dependence of vesicle morphology and mixing properties in a bacterial model membrane system. *Biochim. Biophys. Acta, Biomembr.* **2005**, *1716*, 40−48.
(57) Seeger, H. M.; Marino, G.; Alessandrini, A.; Facci, P. Effect of Physical Parameters on the Main Phase Transition of Supported Lipid Bilayers. *Biophys. J.* **2009**, *97*, 1067−1076.
(58) Seeger, H. M.; Di Cerbo, A.; Alessandrini, A.; Facci, P. Supported Lipid Bilayers on Mica and Silicon Oxide: Comparison of the Main Phase Transition Behavior. *J. Phys. Chem. B* **2010**, *114*, 8926−8933.
(59) Domanov, Y. A.; Kinnunen, P. K. J. Antimicrobial Peptides Temporins B and L Induce Formation of Tubular Lipid Protrusions from Supported Phospholipid Bilayers. *Biophys. J.* **2006**, *91*, 4427−4439.
(60) Marín-Medina, N.; Mescola, A.; Alessandrini, A. Effects of the peptide Magainin H2 on Supported Lipid Bilayers studied by different biophysical techniques. *Biochim. Biophys. Acta, Biomembr.* **2018**, *1860*, 2635−2643.
(61) Lohner, K. A sponge against fungal infections. *Nat. Chem. Biol.* **2014**, *10*, 411−412.
(62) Anderson, T. M.; Clay, M. C.; Cioffi, A. G.; Diaz, K. A.; Hisao, G. S.; Tuttle, M. D.; Nieuwkoop, A. J.; Comellas, G.; Maryum, N.; Wang, S.; et al. Amphotericin forms an extramembranous and fungicidal sterol sponge. *Nat. Chem. Biol.* **2014**, *10*, 400−406.
(63) Henderson, J. M.; Waring, A. J.; Separovic, F.; Lee, K. Y. C. Antimicrobial Peptides Share a Common Interaction Driven by Membrane Line Tension Reduction. *Biophys. J.* **2016**, *111*, 2176−2189.
(64) Deleu, M.; Lorent, J.; Lins, L.; Brasseur, R.; Braun, N.; El Kirat, K.; Nylander, T.; Dufrêne, Y. F.; Mingeot-Leclercq, M. P. Effects of surfactin on membrane models displaying lipid phase separation. *Biochim. Biophys. Acta, Biomembr.* **2013**, *1828*, 801−815.
(65) Oreopoulos, J.; Epand, R. F.; Epand, R. M.; Yip, C. M. Peptide-induced domain formation in supported lipid bilayers: Direct evidence by combined atomic force and polarized total internal reflection fluorescence microscopy. *Biophys. J.* **2010**, *98*, 815−823.
(66) Koga, Y. Thermal Adaptation of the Archaeal and Bacterial Lipid Membranes. *Archaea* **2012**, *2012*, 789652.
(67) García-Sáez, A. J.; Chiantia, S.; Salgado, J.; Schwille, P. Pore Formation by a Bax-Derived Peptide: Effect on the Line Tension of the Membrane Probed by AFM. *Biophys. J.* **2007**, *93*, 103−112.
(68) Kumagai, A.; Dupuy, F. G.; Arsov, Z.; Elhady, Y.; Moody, D.; Ernst, R. K.; Deslouches, B.; Montelaro, R. C.; Peter Di, Y.; Tristram-Nagle, S. Elastic behavior of model membranes with antimicrobial peptides depends on lipid specificity and d-enantiomers. *Soft Matter* **2019**, *15*, 1860−1868.

https://dx.doi.org/10.1021/acs.jpcb.0c06640
J. Phys. Chem. B 2020, 124, 8562−8571

SUPPORTING INFORMATION

Supporting Figures

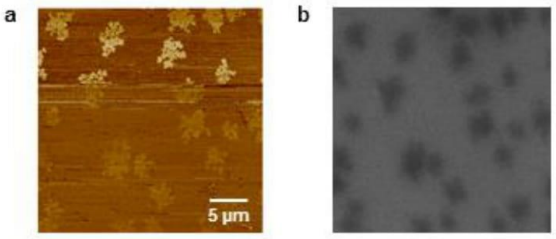

Figure S1: a) AFM topographic image of a POPE/POPG 3:1 + 1% DHPE-Texas-Red SLB on mica at 20°C; b) Fluorescence Microscopy image of the same area in a). The thicker regions in a) correspond to dark regions in b) in which the fluorescence lipid marker is preferentially excluded. These higher regions correspond to solid ordered areas of the lipid bilayer

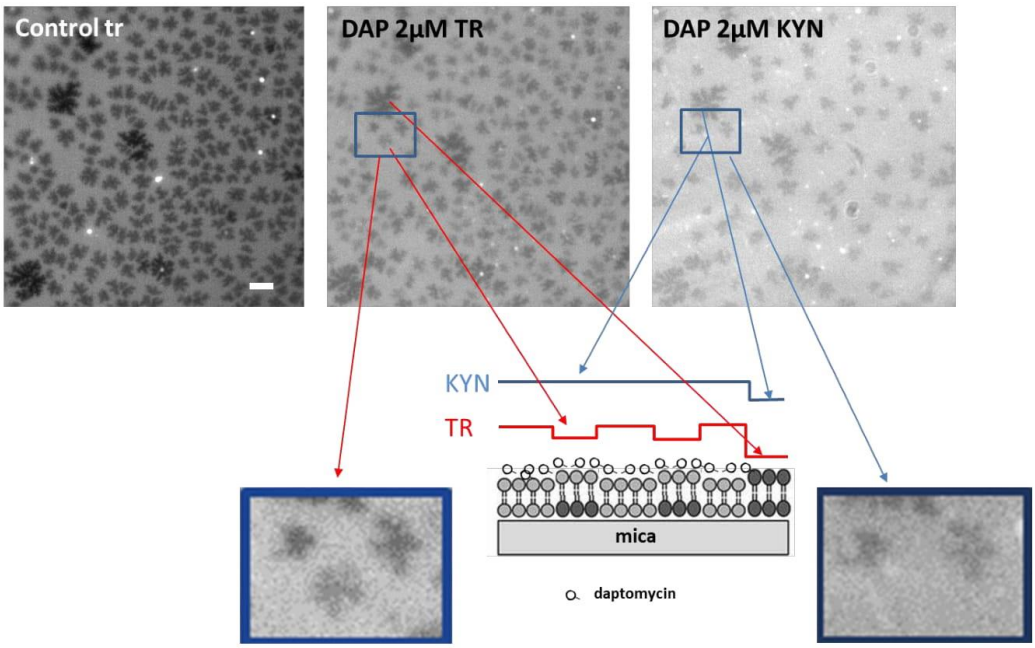

Figure S2: a) Fluorescence Microscopy image (TR signal) of a POPE/POPG 3:1 + 1% DHPE-Texas Red on mica: the different fluorescence intensity of the solid domains could be ascribed to the uncoupling of the two

leaflets and the presence of solid domain only in the lower leaflet, as reported in several reports in the literature. The situation is described in the scheme in the bottom part of the image, where darker lipids represent solid lipids. b) TR signal after the SLB in a) has been exposed to a 2 μM DAP concentration. We still see the different intensity of the domains due to the fact that the TR probe is present in both leaflets. Accordingly, the signal intensity can be explained by the schematic red line on the bilayer scheme (TR). c) KYN signal from the same region of a) and b). The darkest regions in b) are dark also in c) whereas the regions with an intermediate dark signal in b) are not dark in c). This behavior can be explained considering that, where the solid regions are limited to the lower leaflet of the bilayer, the upper layer is affected by the presence of DAP and its penetration in the bilayer. The signal from the KYN residue is schematized in the blue line above the bilayer scheme.

The two insets show magnification of a specific region of the bilayer obtained from the TR and KYN signals after the bilayer has been exposed to DAP. Note that not all the dark regions observed in the magnification of b) are visible as dark domains in c). The bar corresponds to 10 μm.

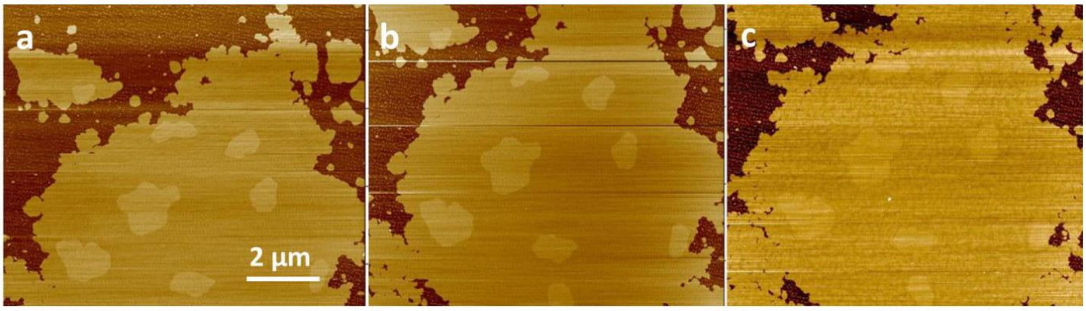

Figure S3: a) POPE/POPG 3:1 SLB imaged at 20°C; b) the same area of a) is imaged immediately after DAP has been added to the imaging chamber in order to have 3 μM DAP concentration: we observe an immediate increase of the lipid bilayer area; c) the same area of a) with 3 μM DAP concentration 10 minutes after the lipopeptide has been added. The bilayer shows a strong reorganization of its phase state, with higher domains appearing in the previously completely fluid regions.

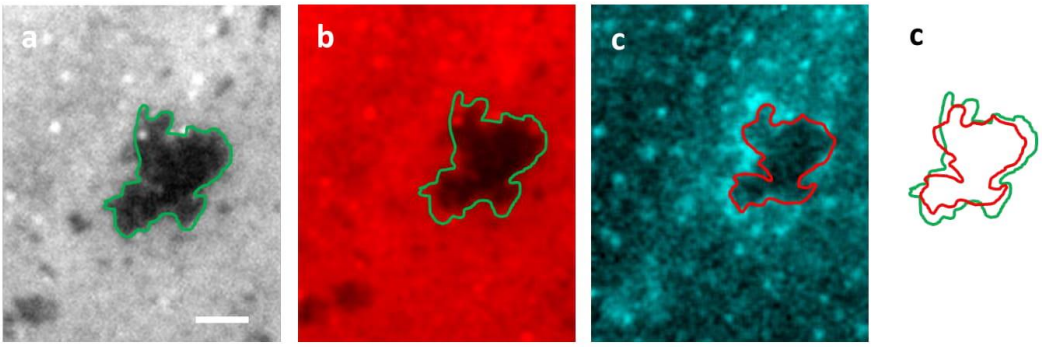

Figure S4: a) Fluorescence microscopy image of a POPC/DMPG 3:1 + 1% DHPE-Texas Red. The image has been obtained exploiting the fluorescence signal from Texas-Red. The boundaries of a solid domains have been highlighted by the green line; b) the same bilayer as in a) has been exposed to a 2 μM DAP

concentration and imaged exploiting the Texas-Red signal. The green line represents the boundaries of the same solid domain in a). It is evident that the borders of the solid domain have been fluidified by the lipopeptide; c) the same region of b) has been imaged exploiting the fluorescence signal from KYN. It is evident that the borders of the solid domain have the strongest signal; d) the borders of the solid initial solid domain have been overlapped with the borders of the solid area observed in b). It appears that the brighter region observed in c) corresponds to the fluidified borders of the initial solid domains.

Chapter 5
Conclusions

Final remarks

Following the previous findings mentioned in the introduction chapter, mechanobiology constitutes an interdisciplinary research field, which has gradually increased its relevance in the last decade toward the new horizons of advanced medicine-based research. Cell samples and their microenvironment scaffolds clearly require a combined investigation where AFM and optical microscopies found their places. Nevertheless, an adequate comprehension of the vast variety of mechanical processes and subsequent cell capabilities relationship, both under physiological and pathological conditions is still elusive. The development of new devices able to reproduce particular microenvironmental conditions is also highly required.

These main topics have been tackled in this PhD thesis. Here we will summarize the main contributions and aims achieved regarding the implementation of novel and useful analysis and devices, both for cell membrane and the underlying cytoskeleton scaffolds. The following results have been obtained:

1. Two analysis protocols for mechanical characterization of biological models describing the plasma membrane have been successfully implemented. Firstly, the bending constant analysis of GUVs obtained from mono-component phospholipid species (DOPC and POPC) has been evaluated and the resulting findings are in good agreement with previous works (using both the “classical” and the “statistical” approach). Then, the protocol has been exploited to investigate exogenous molecule effects on GUVs (an antimicrobial peptide and a lipopeptide). Secondly, the line tension of fluctuating domains in GUVs composed by ternary mixtures has been successfully extrapolated. After protocol validation, the method has been exploited to investigate the sphingomyelins role in the phase behavior of ternary mixtures containing cholesterol. These methods belong to the Flickering-based analysis family.
2. An adequate analysis protocol to investigate and quantify single cell migration, reorientation and polarization has been successfully implemented and validated exploiting the vast data acquired from time-lapse cell imaging assays. A “Persistence Random Walk” mathematical model has been also successfully implemented and tested.
3. Since a deep lack in the appropriate devices development for *in-vitro* assay as mentioned above still exist, and sometimes are economically not accessible for small research groups, we successfully developed several tools and devices useful to investigate live cell behavior both from a “first-step” undergraduate level and a “higher” level for state of the art investigations in the mechanobiology fields. In particular, starting from an initial education-based project dedicated to build a low-cost on-stage cell incubator we moved toward a stretcher suitable for live cell imaging assay, an useful investigating tool that can reproduce not so obvious cell microenvironmental conditions.
4. In order to assist the previous live cell imaging assays results, we successfully implemented and test the robustness of a method to investigate cell viscoelasticity based on Ting model applied to Force-Indentation raw curves. This protocol analysis combined to time lapse assays is highly helpful to provide possible guess and interpretations of exogenous molecules mechanism of actions on cells. Furthermore, the usual Hertzian models clearly do not resemble the entire viscoelastic overview of living cell sample.

PhD activities

I implemented an on-stage cell incubator with an automated autofocus system exploiting an Arduino Uno microcontroller communicating to a Python script for time-lapse live imaging assay. The Arduino Uno controls the microscope objective lens vertical position through a stepper motor, the Python script analyzes the images acquired and exploits an autofocus algorithm developed by me to evaluate the best on-focus frame.

The on-Stage cell incubator can be placed on the optical microscope stage for live cell imaging assay. I developed the hardware and software set-up of this project using and Arduino Uno microcontroller and creating a dedicated LabView control panel interface. The Arduino board controls the cell incubator temperature T, relative humidity RH, and CO_2 concentration maintaining the best conditions for cell cultures (T=37°C, RH>90-95%, pH=7). The pH value is stabilized through a CO_2 flux, the temperature T and CO_2 concentration are controlled exploiting the PID feedback controller libraries already included in the Arduino Uno microprocessor. The LabView interface plots and stores the physical parameters during live cell imaging session. The cell incubator works together with the autofocus system and the corresponding Arduino boards are completely independent from each other. The set-up project allows to follow a cell sample region in a completely automated way up to 12-24 hours. The cell incubator has been validated using U87MG cell line during control condition and exposing the cells to blebbistatin 20μM [1]. The On-Stage cell incubator combined to the automated autofocus acquisition have been refined adding several features.

In order to increase the statistical analysis of live cell imaging a custom-built motorized stage has been realized. I focused on the hardware and software implementation of this project. The stage controls the cell incubator position (X-Y) using a couple of stepper motors and has been integrated with the autofocus system. The resulting set-up can follow up to 8 different cell sample areas and their focus position independently of each other. The cell incubator has been redesigned to host a multi-six petri dish, I dealt with the required hardware and software modifications.

A stretcher device able to reproduce a periodic waveform with arbitrary shape on a PDMS-based cell substrate has been developed. This device can be hosted in a modified version of the previously mentioned cell incubator. I focused on the hardware and software implementation required to filter and reconstruct an experimental periodic signal (obtained for example from AFM measurements on cells), which must be reproduced on a PDMS-based cell substrate. I managed the hardware and software implementation required to combine the stretcher and previous existing cell incubator and the motorized stage devices. The resulting set-up is able to follows live cell imaging sessions in a completely automated way studying up to 8 different regions exploiting also the autofocus procedure. Essentially, the periodic stimulation is provided continuously (>75% of the entire time session) and, periodically, the stretcher is interrupted and the automated image region acquisition is performed. The periodic substrate deformation has been achieved using an Arduino-based actuation system exploiting stepper motors. I wrote the software (Arduino and LabView) needed to reproduce an arbitrary periodic signal exploiting the spectral Fourier decomposition. I dealt with the strain substrate calibration based on continuum mechanics theory. I developed the data-analysis protocols for cell migration and reorientation exploiting the Python language. I also developed the experimental procedure to produce and functionalize the PDMS substrate for cell seeding and live imaging application.

The time-lapse live cell imaging assay is performed using phase-contrast or differential-interference-contrast (DIC) techniques. The automated autofocus protocol has been modified in order to combine these techniques with the epi-fluorescence microscopy. I managed the hardware and software implementation required to integrate the epifluorescence microscopy technique.

The On-stage cell incubator has been exploited to study several cell lines. Firstly, I investigated the U87MG line, which is a biological model for the GMB tumor, during control condition. Then U87MG cells where exposed to exogenous myosin II inhibitor drugs like blebbistatin or Y-27632, and to a potential antimitotic and cytostatic compound called 1G. The 1G was tested for different rigidities of the PDMS-based cell substrate [2]. The On-Stage cell incubator combined with the automated motorized stage has been exploited to investigate the cell response activity of the THP-1 cell line previously differentiated into M0 macrophages (M0-THP-1) following exposure to exogenous mineral fibres. Three different mineral fibres: chrysotile,

crocidolite and fibrous erionite classified as carcinogens by the International Agency for Research on Cancer have been analyzed and their cytotoxic effects have been compared [3].

The stretcher device has been validated using two different cell lines, U87MG and the BALB-3T3 [4].

I implemented the data-analysis protocol to evaluate the cell migration and reorientation capabilities during time-lapse cell imaging assays. I focused on single cell migration using a manual tracking tool and I exploited several migration and orientation indexes. Among the different models for cell migration, I implemented and specifically adopted the Persistence-Random-Walk (PRW) mathematical model to describe the mean-square-displacement (MSD) of single cells. The cell migration analysis on substrates of different rigidities showed that. For U87MG cells there is an optimal value for the MSD value. The existence of this optimal value can be explained on the basis of the molecular clutch model for force transmission to the substrate.

After the implementation of the on-Stage cell incubator set-ups for live cell imaging assays I developed a viscoelastic nanomechanical analysis protocol suitable for AFM experiments on living cells. The data-analysis protocol is based on the Ting model, which is able to extrapolate the viscoelasticity parameters starting from simple Force-Indentation raw curves. In particular, the implemented algorithm is able to identify which is the best viscoelastic constitutive equation describing the cell viscoelastic properties. The Ting-based analysis has been validated using U87MG and hADSC cell lines. The live cell imaging experiments and results were analyzed according to cell nanomechanical characterizations exploiting the AFM technique. In the case of 1G investigation on U87MG cells the obtained findings revealed the cytostatic and antimitotic effect of 1G compound on the different substrate rigidities, whereas the viscoelasticity characterization showed a strong variation of the elastic parameter when U87MG are exposed to 1G 20μM for 24 h. Instead, for lower time exposure, the viscoelastic parameters are almost unchanged [2]. The Ting-based viscoelastic analysis has been also exploited to investigate the nanomechanical response of Human Adipose-derived Stem Cells under exposure to the Cytochalasin B drug [5].

In the context of AFM-based mechanical characterizations, I developed also the data-analysis protocol to detect and evaluate the Jump-Through-Force (JTF) events in SLB (supported by mica) obtained from binary lipid mixtures. In particular, I wrote the software to read the Force-Volume map data and then search the possible JTF events. Finally, the obtained results can be presented in JTF maps. All the programs have been written using Python language. The aim of this analysis was to investigate the S_o-L_d phases coexistence thermodynamical changes under exogenous drug exposure like Daptomycin. Our findings show how POPC:DMPG 1-1 SLB mixture exposed to gradually higher Daptomycin concentrations progressively alter the JTF parameter for the S_0 and L_d phase, respectively [6].

In the context of physical simplified models of the plasma-membrane I focused also on GUVs analysis. I acquired the skills to produce GUVs from ternary lipid mixture using the electro-formation procedure. I developed and exploited a protocol for the Flickering spectroscopy analysis in order to measure the bending constant of GUVs under control condition and exposed to exogenous molecule (antimicrobial peptides and lipopeptides). Firstly, I developed a custom algorithm able to evaluate the liposome contour from frames of fluctuating GUVs at sub-pixel resolution level. This algorithm has been written in Python language and is based on the pixel intensity slope profile along different directions. Secondly, I implemented the data-analysis procedure to extrapolate the angular autocorrelation function from contour coordinates and then decompose this function to evaluate the bending constant. In particular, I developed and compared two different methods: 1) the “classical” approach, which exploits the Legendre Polynomial decomposition; 2) the “statistical” approach, which is based on spectral Fourier decomposition. The bending constant has been evaluated using a non-linear fitting procedure based on Levenberg-Marquardt algorithm. The “classical” and “statistical” models provide similar findings in agreement with previous literature results. The data-analysis has been written using Python language. I also compared different experimental protocols for fluctuation vesicles selection and movie acquisition. I compared the bending constant parameter obtained from DOPC

and POPC vesicles under control conditions and exposed to Magainin and Magainin-H2 [7]. The results showed how Magainin-H2 reduces dramatically the bending constant, even more than natural Magainin with respect to control conditions. The contour evaluation algorithm has been also exploited to study the (dynamic) time evolution of the permeabilization effect.

I also focused on line-tension evaluation of L_o or L_d fluctuating domains of GUVs electro-formed from ternary mixtures composed by high melting temperature, low melting temperature phospholipids and cholesterol, respectively. Line-tension analysis, similarly to bending constant, is a Flickering-spectroscopy-based technique. The frames of the GUVs domains have been obtained exploiting fluorescence microscopy technique and the contour evaluation is straightforward derived from phase contrast microscopy. The domain contour has been evaluated applying a square mesh mask to the fluctuating domain images. I numerically evaluated the angular autocorrelation from contour fluctuations and I spectrally decomposed this function to extrapolate the square power modes. The line-tension is finally extrapolated. In [8] we compared the line tension obtained from DiphyPC-DPPC-Cholesterol and DiphyPC-24:1 Sphingomyelin-Cholesterol mixture, in the former case the measured line tension is significantly higher than in the latter case.

• Published papers

[1] G. Ragazzini, A. Mescola, L. Corsi, and A. Alessandrini, "Fabrication of a low-cost on-stage cell incubator with full automation," *J. Biol. Educ.*, vol. 53, no. 2, pp. 165–173, 2019, doi: 10.1080/00219266.2018.1451772.

[4] G. Ragazzini, J. Guerzoni, A. Mescola, D. Di Rosa, L. Corsi, and A. Alessandrini, "A Fully Integrated Arduino-Based System for the Application of Stretching Stimuli to Living Cells and Their Time-Lapse Observation: A Do-It-Yourself Biology Approach," *Ann. Biomed. Eng.*, 2021, doi: 10.1007/s10439-021-02758-3.

[6] A. Mescola, G. Ragazzini, and A. Alessandrini, "Daptomycin Strongly Affects the Phase Behavior of Model Lipid Bilayers," *J. Phys. Chem. B*, vol. 124, no. 39, pp. 8562–8571, 2020, doi: 10.1021/acs.jpcb.0c06640.

[7] A. Mescola, N. Marín-Medina, G. Ragazzini, M. Accolla, and A. Alessandrini, "Magainin-H2 effects on the permeabilization and mechanical properties of giant unilamellar vesicles," *J. Colloid Interface Sci.*, vol. 553, pp. 247–258, 2019, doi: 10.1016/j.jcis.2019.06.028.

[8] D. Balleza *et al.*, "Complex Phase Behavior of GUVs Containing Different Sphingomyelins," *Biophys. J.*, vol. 116, no. 3, pp. 503–517, 2019, doi: 10.1016/j.bpj.2018.12.018.

• Articles in preparation

[2] G. Ragazzini, A. Mescola, L. Corsi, and A. Alessandrini, "Study of antitumoral effects and mechanism of action of a new compound with antimitotic and antimigration properties."

• Articles under review

[3] D. Di Giuseppe *et al.*, "Acute cytotoxicity of mineral fibres observed by time-lapse video microscopy," *Toxicology*.

[5] E. Bianconi *et al.*, “Cytochalasin B Modulates Nanomechanical Patterning and Fate in Human Adipose-derived Stem Cells,” *Pharmaceuticals*.